POLISH ANATOMICAL SOCIETY

FOLIA
MORPHOLOGICA

Vol. 82   2023   No. 3

The journal is published at: https://journals.viamedica.pl/folia_morphologica in one volume per year consisting of four numbers.

Subscription rates: Paper subscription, 4 issues incl. package and postage institutional — 210 euro. The above prices are inclusive of regular postage costs. Payment should be made to: VM Media Group sp. z o.o., Grupa Via Medica, BNP Paribas Bank Polska SA account number: 15 1600 1303 0004 1007 1035 9021; SWIFT: PPABPLPK. Single issues, subsriptions orders and requests for sample copies should be send to e-mail: prenumerata@viamedica.pl. Electronic orders option available at: https://journals.viamedica.pl/folia_morphologica. The publisher must be notified of a cancellation of access to electronic version not later then two months before the end of a calendar year. After that date electronic access will be automatically prolonged for another year.

Advertising. For details on media opportunities within this electronic version of journal please contact the advertising sales department, ul. Świętokrzyska 73, 80–180 Gdańsk, Poland, tel: (+48 58) 320 94 94, e-mail: viamedica@viamedica.pl
The editors accept no responsibility for advertisement contents.

Folia Morphologica is the official journal of the Polish Anatomical Society. For information about the Society, please contact: Prof. Janusz Moryś, Departent of Normal Anatomy, Pomeranian Medical University, Al. Powstańców Wielkopolskich 72, 70–111 Szczecin, Poland, tel. (+48 91) 466 15 43, e-mail: jmorys@pum.edu.pl

Editorial policies and author guidelines are published on journal website: https://journals.viamedica.pl/folia_morphologica

Legal note: https://journals.viamedica.pl/folia_morphologica/about/legalNote

Folia Morphologica is indexed by: BIOSIS Previews, CAS, CINAHL, CrossRef, Dental Abstracts, EBSCO, Elsevier BIOBASE, EMBIOLOGY, FMJ, Google Scholar, Index Copernicus (159.83), Index Medicus/MEDLINE, Index Scholar, Polish Ministry of Education and Science (140), NCBI/National Center for Biotechnology Information, Polish Medical Bibliography, Scopus, SJR, Thomson Reuters, Thomson Scientific Products — Biological Abstracts, Ulrich's Periodicals Directory, Veterinary Bulletin, WorldCat and Zoological Record. Position in Index Copernicus ranking systems is available at: www.indexcopernicus.com. Current Impact Factor of Folia Morphologica (2022) is 1.2.

22-6110.003.001

FOLIA MORPHOLOGICA

EDITORIAL ADVISORY BOARD

VM VIA MEDICA

R E V I E W A R T I C L E

Thiel embalming method used for anatomy dissection as an educational tool in teaching human anatomy, in research, and in training in comparison of different methods for long term preservation

M. Rakuša, L. Kocbek Šaherl

University of Maribor, Faculty of Medicine, Institute of Anatomy, Histology, and Embryology, Maribor, Slovenia

The use of human cadavers is beneficial in teaching gross human anatomy, training, and development in medicine. Fresh-frozen cadavers initially exhibit natural colour, tenderness, and flexibility. They also present innumerable difficulties, including the requirement of freezers for storage and a few weeks' work time because of fast decay. The risk of infection is also significant. A possible choice for fresh-frozen cadavers is embalmed cadavers. The requested characteristic needed for successful embalming is acceptable long-term structural preservation of organs and tissues with minimal deformity and prevention of outward aspects. Scientists are trying to develop an ideal embalming solution to preserve the human body. Such a solution renders the flexibility of internal organs, preventing dryness, and reducing fungal or bacterial growth. Cadavers should be in a condition comparable to that of an unembalmed cadaver, and the chemicals used in the solution should not be harmful to persons during manipulation. The promising results have been obtained by the use of different embalming techniques by many faculties of medicine as a tool to enhance the teaching of anatomy to students. (Folia Morphol 2023; 82, 3: 449–456)

Key words: anatomy, embalming method, cadaver dissection, education

INTRODUCTION

Human cadaveric dissection has been used as the base teaching tool in anatomy for centuries [1, 44]. Fresh-frozen cadaver is the closest to learning anatomical structures under realistic conditions although it can be properly well-used in a very limited time [1, 44]. There are several insecurities when working with a fresh-frozen cadaver for the reason that the fresh corpse disintegrates immediately, the risk of infection is high as the bacteria multiply rapidly and further use due to freezing and thawing is no longer

endorsed [31, 32]. Embalming with formalin is safe against infections with microorganisms, suitable for long-term storage, and is an inexpensive method. On the other hand, the tissue becomes more compacted over time and less comparable to the natural structures in the body. In addition, continuous inhalation of formalin in high concentrations may be harmful to health and carcinogenicity has been reported [11]. Soft-fix and flexible cadavers are formed by Thiel's method. The colour of the tissues remains natural, the cadaver is manageable and very suitable for use. In

contrast, the preparation of the deceased is relatively expensive and demanding, even though the time for dissection is defined [5–9]. A saturated salt solution (continued as SSS) can also be used for embalming the dead human body. As a method, it has many advantages, including technical implementation, not having a lot of risk of infection and it is cost-effective. It seems to be adequately useful for surgical training and has characteristics for clinical training [35, 36, 63].

We made several observations as outlined in the publication describing fresh-frozen cadavers, formalin-embalmed cadavers, Thiel-embalmed cadavers, and in a SSS embalmed cadavers [35, 36]. We are convinced about the positive effects of structures due to the anatomical dissection of the Thiel-embalmed cadaver, also because we use the method by ourselves. Not only does it enhance the students' learning of anatomy, thus improves the students' long-term ability to identify anatomical structures [47].

HISTORY OF HUMAN BODY PRESERVATION

The intent to preserve the body in response to questions of a religious nature has existed since ancient times [11, 26, 27]. Different techniques were used in the early beginnings of embalming, like exenteration or the corpse being immersed for a while in an alcohol solution, plus herbs imprinted in the corpse served for preservation as well as cadavers were wrapped in waxed or tar sheets [25–27]. Ancient civilizations invented the embalming process, while for Europe it had been unprecedented for a very long time [1, 26, 27, 44, 58]. Embalming became influenced by scientific developments in medicine. Bodies were needed for dissection purposes and preservation required more refined embalming techniques [50]. The German chemist August Wilhelm von Hofman 1869 discovered and determined formaldehyde to be an excellent preservative [19, 28]. In improving the embalming method a combination of salts, chloral hydrate, and formaldehyde [42, 43] along with solutions based on alcohol, glycerine, and phenol [69] were experimented with by scientists. By modifying the original embalming procedures researchers presupposed a simple method for longer persistence of cadavers and thus its use for learning intentions [10, 12, 23, 48, 68]. A visionary scientific leader Walter Thiel [24, 29] presented 1992 an embalming method that maintains the natural look, colour, flexibility, and characteristics of a living body [26, 27, 66, 67].

THIEL'S EMBALMING METHOD

The introduction of soft fixed cadavers using the Thiel embalming method has dramatically improved the flexibility and colour retention of cadavers used for teaching anatomy [29, 40]. Intravascular Thiel's embalming technique keeps the cadaver soft to physical contact and permanent movable, all anatomical structures retain in natural colour and due to learning, comparability with the properties of living people is of paramount importance. Those typical characteristics of cadavers [40] have been suitable in fields such as thyroid surgery, echography, regional anaesthesia [20, 48] and ultrasound-guided anaesthesia [7], laparoscopy, tendon repair, flap raising, and microsurgery [68], including maxillofacial surgery. Although the insertion of dental implants is a predictable and successful method of replacement, the insertion of dental implants into the jawbone with all possible complications could first be made on embalmed corpse models [38]. Thiel-embalmed cadavers have been applicable for intubation and ventilation, suturing, biopsies. The chest radiographs of Thiel-embalmed cadavers were also described. Workshops for several medical disciplines have been arranged. Despite the many positive properties of Thiel's method, the technical process of preparing the solution is exacting and expensive. Some of the chemicals are poisonous, inflammable, explosive, extremely unhealthy, and environmentally unfriendly. The imperfection of Thiel-embalmed cadavers has been muscular disorganization and a limited time for dissection as well as noticeable histological alterations [36]. Also for learning to insert a central venous canal, Thiel-embalmed cadavers are less or even inappropriately. Other embalming methods were tested with better results. Nonetheless, Thiel's embalming method shows significant properties. There are advantages to joint and muscle flexibility and because of that, we can bend the limbs. The colour of the corpse is very similar to the physiological appearance. Due to the work and handling of the preparations, a completely reduced exposure to microorganisms has been improved so that it is safe to work against infections. Further, good flexibility and plasticity preservation in organs and tissues are remarkable characteristics as well [57, 66–68]. At autopsy, tissue and organ samples are taken for

histological examination. The embalmed cadaveric tissue is already fixed and opinions on compliance for all histological studies have been divided [54].

Many authors have repeated the original procedure since Thiel's method was introduced. And in current studies modifications, a fixative according to Thiel's formulation of solutions has been used for better fixation of cells of the central nervous system. By inserting a needle into the subarachnoid space the fixative can penetrate the tissue promptly and thus ensure the persistence of the brain and spinal cord for further research or for learning the anatomy of the central nervous system [21, 22]. Eljamel received good imaging with clear differentiation of white and grey matters in studies of Thiel-embalmed cadavers with magnetic resonance imaging. They could be relevant for practical training and microsurgical workshops for scientific investigation inside the brain or other parts of the body [18]. Thiel's method could be used for the progress in otoneurosurgery for which mechanisms of normal and pathological events are involved here [2]. Additionally, morphometric studies of anatomical muscle variations [59], insertions, perforating vessels, repairs and reinforcement of tendons, and prophylaxis were done by Thiel-embalmed cadavers. Thiel-embalmed cadavers have accelerated possibilities for extending experimental laparoscopic surgery, the establishment of new endoscopic surgical methods [33, 55], principally in urinary tract surgery [37] as well as proceeding in angiology [33, 55], thyroidectomies, cricothyroidotomies [9], liver surgery simulations, arthroplasty, artery sutures, peripheral nerve repair, flap surgeries [34], neurosurgery, and anastomosis techniques [56, 57]. In principle, they would be constructively practical in improving the efficiency of surgical techniques together with the development of various surgical techniques.

All these numerous characteristics [57] of Thiel-embalmed cadavers are very appropriate and relevant for undergraduate and graduate education, training, and specialised surgical abilities. Their complex handling is preferred from formalin-embalmed cadavers, and even fresh cadavers [7–9].

FORMALIN EMBALMING METHOD

The earliest research on using formalin solution (FAS) as an embalming agent has occurred in 1899 [53]. Not much has changed in the basic technique of formalin maintaining. FAS stands as the most frequently used embalming solution. It is an excellent tissue fixative without destroying its delicate structure [4, 53]. Assures protection against pathogenic microorganisms and prevents infection [4, 7, 11, 30]. On the contrary, tissues, and organs impregnated with formalin become even more rigorous, with the lost appearance of natural colour and with the loss of all other characteristics of living organs [53]. The smell of formalin is very strong and later high exposure, it can be irritating for the nose, eyes, skin, and airways, along with chronic toxic effects [11, 39, 51, 53].

Imaging techniques such as ultrasound and radiography in formalin-embalmed human cadavers were poorly detectable [61] and are not preferable for a detailed examination of the skeleton, body cavities, and all present pathologies in the body cavities, as well as the accumulation of gas in the intestine [4, 5, 13, 15, 16, 40].

Despite all these effects, FAS is still the most frequently in use in the Faculty of Medicine all over the world because is a good detection solution [53]. The influence of re-evaluation of formalin concentration, appropriate ventilation, and assessment of working practices in the dissecting rooms at the Anatomy Departments provided FAS as commonly used as a preservative [53].

SATURATED SALT SOLUTION EMBALMING METHOD

Cadavers were also excellently preserved by using the SSS embalming method and might become an alternate method for embalming. The salt solution was described as readily available, uncomplicated, and inexpensive. Cadavers embalmed by the SSS method had a minimal structural deformity, their colours remained natural, and the blood remained liquefied. The X-ray and ultrasound images were also used in cadavers embalmed by the SSS method where very intense fluid was observed in pericardial, pleuroperitoneal, and peritoneal spaces. Central venous catheterisation could be inserted in the SSS-embalmed cadavers too. The indicated cadavers were presentable for laparoscopic and microvascular surgery, pulmonary ventilation, auto suture-stapling material, and echo-guided peripheral nerve block. Lungs and intestines could be incised with an electrosurgical knife and closed using an auto suture-stapling device. Softness and mobility of tissues and joints are important aspects found in embalmed cadavers. But most excellent properties have been described and tested with Thiel-embalmed cadavers, compared to

embalmed cadavers in salt solutions. Those cadavers have been considered as being too consolidated to perform surgical practice [35, 36, 63].

FRESH CADAVERS

Fresh-frozen cadavers have been repeatedly described as suitable in many studies for their most natural appearance and consistency. Even though the fresh cadavers were considered as being not applicative for usual procedures [50, 52, 60, 62, 64]. They present innumerable difficulties, including the specification for adequate cooling space and time-delayed work because of fast decay. The risk of infection is also significant [3, 15–17, 30].

THE USE OF HUMAN BODIES IN EDUCATIONAL SETTINGS AND FUTURE DIRECTION

According to the literature, the appropriate preservation of the cadaver is essential [1, 44].

The embalmment method was developed as a response to teaching anatomy, as a valuable educational tool [1, 44] to ensure a well-preserved cadaver, and to prevent destruction, decomposition, and contamination [4]. The dilemma in a well-developed new method for embalming cadavers is only funding involved in establishing [1, 44].

In terms of visual and tactile assessment, regarding its usefulness in teaching undergraduate students, postgraduate students, and surgical specialists, many medical educational institutions have included in the curriculum plastic anatomy models, three-dimensional (3D) atlases, and virtual human models [1, 44]. According to students, it is important to note that only a traditional method like cadaveric dissection includes the concepts of gross anatomy, structural details, and anatomical variations. The limited availability of corpses, location for storage, preparation, or dissection of the cadaverous parts, and the ascending development of modern technologies, like anatomical models and 3D visual implements, are taking the place of human cadavers in the teaching of human anatomy [1, 44].

Feedback from students undertaken through questionnaires or evaluation forms presented with studies by authors Alamneh [1] and Kalthur et al. [44] illustrated the impact of the usefulness and importance of dissection in today's teaching of anatomy. Two-thirds of students realised the relevance of anatomy and agreed that adequate knowledge and understanding of anatomy can only be acquired when medical students are exposed to the tissues and structures within the body. Those students felt confident with the cadaveric dissection. In addition, one-third of students perceived the role of the tissue dissection module as unprogressive and inapplicable. A few had a negative attitude towards death, and emotional trauma [1, 44]. A similar response has been observed from our students.

Students are technologically sufficiently educated and skilled in obtaining all information, including in the field of anatomy. But all of the above is not enough for the acquired knowledge of human anatomy or for objectively learning and developing surgical skills. Anatomy is one of the most prominent and necessary subjects of medical and nursing education. Dissection has been an important part of medical education as the complete preservation of the body contributes to learning not only the theoretical concepts of structure, framing, and the relationship between body parts, but visualization of the basic components of the body might help detect tissue characteristics or any other important clinical benefits [1, 44]. Withal, training on cadavers is important in appropriate training to evaluate skills in surgical experience and in diagnostic as well as therapeutic endoscopic skills [1, 44]. Practice and work on the appearance of the cadavers according to the tissue quality, colour and consistency have been recognized as excellent compared to real-life patients. The four preservation methods reviewed so far with different advantages and disadvantages are certainly no less useful in comparison. Each technique in microsurgery, endoscopy, laparoscopic and arthroscopic surgery, and interventional radiology is consistent with special skills programmes, and diagnostic and therapeutic interventions. According to the literature Thiel-embalmed cadavers are more eligible than formalin-embalmed cadavers or fresh-frozen cadavers [40]. Thiel embalmed cadavers allow the muscular and connective tissue to retain most of its premortem texture and tone [45, 46]. Most cadavers are used for laparoscopic procedures and more realistic representations of the movement and function of the musculoskeletal system [1, 44]. Thiel-embalmed cadavers are applied in workshops on ultrasound-guided regional anaesthesia [45, 46], thoracic surgery, abdominal surgery, urology, arthroscopy, and other fields of surgery, together with magnetic resonance imaging-guided procedures involving vascular devices and focused ultrasound [7]. They have been

used to evaluate new ultrasound-guided regional anaesthesia techniques and equipment, laparoscopic equipment, laryngoscopes, retractors, and hip and shoulder prosthesis. Thiel-embalmed cadavers are becoming useful in making imaging diagnoses and performing guided therapeutic procedures [7, 18]. Farther, dental surgeons have been testing inferior alveolar nerve blocks and extractions [38, 57].

The visualisation and manipulation of cadavers remain the gold standard to teach anatomy and are suitable for extension activities in the medical faculty, especially in surgical and clinical training [1, 44]. Focusing on the values of learning the human anatomy through the active voluntary body donation programme in the medical curriculum, awareness of the ethical and humanistic values of cadaveric dissection must be carried out respectfully. Because the use of the cadavers is an assessment of knowledge and practice, ethical consideration with profound respect for the deceased person among graduate and undergraduate students, ultimately for all medical professionals is expected undoubtedly [1, 41, 44, 65].

We will continue further work at our institute with the Thiel embalming method as we are very satisfied with the method. Only for one-day or short-term workshops, where the corpses would be used once, we are considering another method. For more assessment of appropriateness, the parallel use of cadavers, each in another solution of embalming, and for the same learning purposes allow our further evaluation of the advantages and disadvantages of all methods described above. According to the results in the articles, the use of SSS for embalming has similar positive properties as Thiel's method does and the use of these cadavers may be perfectly suitable in anatomy education [35, 36], for postgraduate students in training to evaluate their skills, and also for surgeons who are constantly being trained in their work in general surgeries on soft tissues, laparoscopic surgical procedures and a surgical subspecialty of the vascular system, minimally-invasive catheter procedures, and plastic and reconstructive surgery. The use of cadavers is effective and helps surgeons to gain technical competence before performing any procedures on patients. The fresh-frozen and formalin methods are also suitable but perhaps only for short-term learning interventions such as emergency procedures or with reduced exposure to practical anatomy in education.

For teaching anatomy, where students work and learn on cadavers by themselves, cadavers must en-

sure competent tissue properties, durability, and long-standing perseverance. Additionally, methods must ensure that the tissues of the cadavers maintain a similar appearance to their premortem condition, and provide good conditions for the cadavers for a longer period. All cadavers will differ from living patients but these differences allow re-use across a range of procedures.

CONCLUSIONS

We focused on the analysis of the potential effects of four embalming methods in terms to choose a method that can be very useful for learning anatomy and for a variety of learning events for academic and teaching employees and workshops for medical students. Regarding the procedure, Thiel's method is favoured and pleasantly evaluated among teachers, students, surgeons, and instructors. It has brought benefits to the study, decreases the level of toxicity, and offers long-term preservation that combines flexible tissues and a good cosmetic appearance similar to *in vivo* conditions. Compared with other methods, general surgeries were performed mostly with SSS embalmed cadavers [26], formalin has shown superior bactericidal and bacteriostatic properties, and without destroying tissue's delicate structure [13]. Thiel's method is increasingly widely known [67], it is overpriced, and complex components are required, while SSS is simpler and low-priced but its use in anatomy education has been limited [4, 5].

Teaching practices in anatomy education are based on either demonstrating dissected specimens or human cadaveric dissection individually [1, 14, 44]. The most frequently used was formaldehyde and since 1992 use of the Thiel embalming method has been implemented for the long-term preservation of cadavers, with a minimum and non-toxic amount of formaldehyde [14]. It seemed therefore to preserve body with low health risk and suitable for the palpable experience. It cannot be harmful to the students and its use is ethical. Soft consistency allows students to perform dissection practices in conditions very similar to those they would present *in vivo*.

Dissection should be reinforced and enriched in undergraduate medical school, considering that learning basic anatomy by using human cadavers is still the most important learning tool for educational anatomy as well as for understanding and respecting ethical principles. Only in this way can students study the topographic and regional anatomy, the continu-

ous veins and nerves, the lymphatic system, and all variations that are not so rare. Commonly, students study anatomy from atlases, books, and lecture notes although the experience of the general aspects of the dimensional relationships in the body even modern and contemporary technology cannot replace. As a part of good practices in the context of human dissection, medical students can observe these details of anatomical structures of the body and the reciprocal relationships between body parts [1, 44].

The current study has some limitations. It is based on our opinion and hence does not provide objective data on tissue properties used with the other technique. Our experience is currently based on Thiel-embalmed cadavers. And formaldehyde is also used to store organs. The experience of teachers, researchers as well as students, is good so far.

Each embalming method has advantages and disadvantages for different fields of study and education, all of which are influenced by working conditions, finances, suitable space, and also by the interest of employees and students. Due to the many advantages, and good responses from students, teachers, surgeons, and technicians, we will continue to use Thiel's method and also improve it for academic and didactic purposes. And at the same time known advantages of other methods, especially when it comes to storing and using the cadavers for a short-term preservation period or use in surgical training programmes.

Through further research to assess the knowledge, it is substantial to evaluate concepts of studying anatomy through whole-body dissection accessible to students, expose students and all medical professionals to ideas on the point of the regular use of human cadavers for learning and training purposes still rely on cadavers, and how valuable it is to identify disease sites that they might otherwise not have come into contact with [1, 41, 44].

Dissection has been an important part of medical education and still contributes positively to teaching purposes at many medical faculty. It requires fundamental educational, moral, and ethical values and should be strictly within the directives of medical institutions.

Acknowledgements

Conflict of interest: None declared

REFERENCES

1. Alamneh Y. Knowledge and attitude towards ethical cadaver dissection among medical and health sciences students, 1997–2020: A systematic review and meta-analysis. Transl Res Anat. 2021; 25: 100149, doi: 10.1016/j.tria.2021.100149.

2. Alberty J, Filler TJ, Schmäl F, et al. [Thiel method fixed cadaver ears. A new procedure for graduate and continuing education in middle ear surgery]. HNO. 2002; 50(8): 739–742, doi: 10.1007/s00106-001-0601-9, indexed in Pubmed: 12243029.

3. Anderson SD. Practical light embalming technique for use in the surgical fresh tissue dissection laboratory. Clin Anat. 2006; 19(1): 8–11, doi: 10.1002/ca.20216, indexed in Pubmed: 16287109.

4. Balta JY, Cronin M, Cryan JF, et al. Human preservation techniques in anatomy: A 21st century medical education perspective. Clin Anat. 2015; 28(6): 725–734, doi: 10.1002/ca.22585, indexed in Pubmed: 26118424.

5. Balta JY, Lamb C, Soames RW. A pilot study comparing the use of Thiel- and formalin-embalmed cadavers in the teaching of human anatomy. Anat Sci Educ. 2015; 8(1): 86–91, doi: 10.1002/ase.1470, indexed in Pubmed: 24996059.

6. Benkhadra M, Bouchot A, Gérard J, et al. Flexibility of Thiel's embalmed cadavers: the explanation is probably in the muscles. Surg Radiol Anat. 2011; 33(4): 365–368, doi: 10.1007/s00276-010-0703-8, indexed in Pubmed: 20632174.

7. Benkhadra M, Faust A, Ladoire S, et al. Comparison of fresh and Thiel's embalmed cadavers according to the suitability for ultrasound-guided regional anesthesia of the cervical region. Surg Radiol Anat. 2009; 31(7): 531–535, doi: 10.1007/s00276-009-0477-z, indexed in Pubmed: 19225711.

8. Benkhadra M, Gérard J, Genelot D, et al. Is Thiel's embalming method widely known? A world survey about its use. Surg Radiol Anat. 2011; 33(4): 359–363, doi: 10.1007/s00276-010-0705-6, indexed in Pubmed: 20665059.

9. Benkhadra M, Lenfant F, Nemetz W, et al. A comparison of two emergency cricothyroidotomy kits in human cadavers. Anesth Analg. 2008; 106(1): 182–185, doi: 10.1213/01.ane.0000296457.55791.34, indexed in Pubmed: 18165576.

10. Bradbury SA, Hoshino K. An improved embalming procedure for long-lasting preservation of the cadaver for anatomical study. Acta Anat (Basel). 1978; 101(2): 97–103, doi: 10.1159/000144954, indexed in Pubmed: 565573.

11. Brenner E. Human body preservation: old and new techniques. J Anat. 2014; 224(3): 316–344, doi: 10.1111/joa.12160, indexed in Pubmed: 24438435.

12. Coleman R, Kogan I. An improved low-formaldehyde embalming fluid to preserve cadavers for anatomy teaching. J Anat. 1998; 192(Pt 3): 443–446, doi: 10.1046/j.1469-7580.1998.19230443.x, indexed in Pubmed: 9688512.

13. Coskey A, Gest TR. Effectiveness of various methods of formaldehyde neutralization using monoethanolamine. Clin Anat. 2015; 28(4): 449–454, doi: 10.1002/ca.22534, indexed in Pubmed: 25832967.

14. Denis Rodriguez E. Thiel soft-fix method for long term preservation. Rev Mex Med Forense. 2017; 3(2): 91–98.

15. Eisma R, Lamb C, Soames RW. From formalin to Thiel embalming: What changes? One anatomy department's experiences. Clin Anat. 2013; 26(5): 564–571, doi: 10.1002/ca.22222, indexed in Pubmed: 23408386.

16. Eisma R, Mahendran S, Majumdar S, et al. A comparison of Thiel and formalin embalmed cadavers for thyroid surgery training. Surgeon. 2011; 9(3): 142–146, doi: 10.1016/j.surge.2010.09.001, indexed in Pubmed: 21550519.

17. Eisma R, Wilkinson T. From "silent teachers" to models. PLoS Biol. 2014; 12(10): e1001971, doi: 10.1371/journal.pbio.1001971, indexed in Pubmed: 25333490.

18. Eljamel S, Volovick A, Saliev T, et al. Evaluation of Thiel cadaveric model for MRI-guided stereotactic procedures in neurosurgery. Surg Neurol Int. 2014; 5(Suppl 8): S404–S409, doi: 10.4103/2152-7806.140199, indexed in Pubmed: 25289170.

19. Ezugworie J, Anibeze C, Ozoemena F. Trends in the development of embalming methods. Int J Altern Med. 2009; 7(2), doi: 10.5580/29b.

20. Feigl G, Anderhuber F, Schwarz G, et al. [Training methods for regional anaesthesia. Evaluation and comparison]. Anaesthesist. 2007; 56(5): 437–443, doi: 10.1007/s00101-007-1149-1, indexed in Pubmed: 17285320.

21. Feigl G, Fuchs A, Gries M, et al. A supraomohyoidal plexus block designed to avoid complications. Surg Radiol Anat. 2006; 28(4): 403–408, doi: 10.1007/s00276-006-0113-0, indexed in Pubmed: 16680393.

22. Feigl GC, Fasel JH, Anderhuber F, et al. Superior vestibular neurectomy: a novel transmeatal approach for a denervation of the superior and lateral semicircular canals. Otol Neurotol. 2009; 30(5): 586–591, doi: 10.1097/MAO.0b013e3181ab9164, indexed in Pubmed: 19574943.

23. Frewein J, Steinmann W, Müller U. [Experiences with reduced formalin fixation of specimens and formalin-free preservation of anatomic samples]. Anat Histol Embryol. 1987; 16(3): 250–253, indexed in Pubmed: 3326428.

24. Fürstner A, List B, Ritter T, et al. Walter Thiel (1949-2019). Angew Chem Int Ed Engl. 2020; 59(4): 1382–1383, doi: 10.1002/anie.201915463, indexed in Pubmed: 31917510.

25. Fylaktou A, Haidopoulou K, Goutaki M, et al. Measles and mumps immunity in Northern Greece, 2004-2007. Euro Surveill. 2008; 13(16): 18841, indexed in Pubmed: 18768118.

26. Ghosh SK. Human cadaveric dissection: a historical account from ancient Greece to the modern era. Anat Cell Biol. 2015; 48(3): 153–169, doi: 10.5115/acb.2015.48.3.153, indexed in Pubmed: 26417475.

27. Ghosh SK. Paying respect to human cadavers: We owe this to the first teacher in anatomy. Ann Anat. 2017; 211: 129–134, doi: 10.1016/j.aanat.2017.02.004, indexed in Pubmed: 28279760.

28. Grönroos H. Zusammenstellung der üblichen Conservierungsmethoden für Prä-pariersaalzwecke. Anat Anz. 1898; 15: 61–84.

29. Hachabizwa C, Banda M, Hainza J, et al. Cadaveric embalming using a modified Thiel method as an alternative to the formalin method. Anat J Afr. 2020; 9(2): 1797–1806, doi: 10.4314/aja.v9i2.199945.

30. Hammer N, Löffler S, Bechmann I, et al. Comparison of modified Thiel embalming and ethanol-glycerin fixation in an anatomy environment: Potentials and limitations of two complementary techniques. Anat Sci Educ. 2015; 8(1): 74––85, doi: 10.1002/ase.1450, indexed in Pubmed: 24706536.

31. Hammer N, Löffler S, Feja C, et al. Ethanol-glycerin fixation with thymol conservation: a potential alternative to formaldehyde and phenol embalming. Anat Sci Educ. 2012; 5(4): 225–233, doi: 10.1002/ase.1270, indexed in Pubmed: 22434588.

32. Hammer N, Schröder C, Schleifenbaum S. On the suitability of Thiel-fixed samples for biomechanical purposes: Critical considerations on the articles of Liao et al. "Elastic Properties of Thiel-Embalmed Human Ankle Tendon and Ligament" and Verstraete et al. "Impact of Drying and Thiel Embalming on Mechanical Properties of Achilles Tendons". Clin Anat. 2016; 29(4): 424–425, doi: 10.1002/ca.22679, indexed in Pubmed: 26679099.

33. Hassan S, Eisma R, Harry LE. Surgical training of anastomotic technique using Thiel cadavers. J Plast Reconstr Aesthet Surg. 2014; 67(10): e250–e251, doi: 10.1016/j.bjps.2014.06.016, indexed in Pubmed: 25034316.

34. Hassan S, Eisma R, Soames R, et al. Raising of microvascular flaps using the Thiel cadaveric model. J Plast Reconstr Aesthet Surg. 2014; 67(4): e107–e108, doi: 10.1016/j.bjps.2013.12.003, indexed in Pubmed: 24365567.

35. Hayashi S, Homma H, Naito M, et al. Saturated salt solution method: a useful cadaver embalming for surgical skills training. Medicine (Baltimore). 2014; 93(27): e196, doi: 10.1097/MD.0000000000000196, indexed in Pubmed: 25501070.

36. Hayashi S, Naito M, Kawata S, et al. History and future of human cadaver preservation for surgical training: from formalin to saturated salt solution method. Anat Sci Int. 2016; 91(1): 1–7, doi: 10.1007/s12565-015-0299-5, indexed in Pubmed: 26670696.

37. Healy SE, Rai BP, Biyani CS, et al. Thiel embalming method for cadaver preservation: a review of new training model for urologic skills training. Urology. 2015; 85(3): 499–504, doi: 10.1016/j.urology.2014.11.009, indexed in Pubmed: 25582818.

38. Hölzle F, Franz EP, Lehmbrock J, et al. Thiel embalming technique: a valuable method for teaching oral surgery and implantology. Clin Implant Dent Relat Res. 2012; 14(1): 121–126, doi: 10.1111/j.1708-8208.2009.00230.x, indexed in Pubmed: 19673955.

39. Hubbell DS, Dwornik JJ, Alway SE, et al. Teaching gross anatomy using living tissue. Clin Anat. 2002; 15(2): 157–159, doi: 10.1002/ca.1113, indexed in Pubmed: 11877797.

40. Hunter A, Eisma R, Lamb C. Thiel embalming fluid: a new way to revive formalin-fixed cadaveric specimens. Clin Anat. 2014; 27(6): 853–855, doi: 10.1002/ca.22392, indexed in Pubmed: 24639210.

41. Iwanaga J, Singh V, Ohtsuka A, et al. Acknowledging the use of human cadaveric tissues in research papers: Recommendations from anatomical journal editors. Clin Anat. 2021; 34(1): 2–4, doi: 10.1002/ca.23671, indexed in Pubmed: 32808702.

42. Jores L. Die Conservirung anatomischer Praparate in Blutfarbe mittelst Formalin. Zbl Path Jena. 1896; 7: 134.

43. Jores L. Ueber eine verbesserte Methode der Konservierung anatomischer. Objekte Münchn Med Wschr. 1913; 60: 976.

44. Kalthur S, Pandey A, Prabhath S. Benefits and pitfalls of learning anatomy using the dissection module in an indian medical school: A millennial Learner's perspective. Transl Res Anat. 2022; 26: 100159, doi: 10.1016/j.tria.2021.100159.

45. Karakitsios I, Bobeica M, Saliev T, et al. Thermometry during MR-guided focused ultrasound in a preclinical model based on Thiel embalmed tissue. Minim Invasive Ther Allied Technol. 2014; 23(2): 120–126, doi: 10.3109/13645706.2013.839950, indexed in Pubmed: 24079349.

46. Karakitsios I, Dogadkin O, Le N, et al. Measurement of proton resonance frequency shift coefficient during MR-guided focused ultrasound on Thiel embalmed tissue. Magn Reson Med. 2015; 74(1): 260–265, doi: 10.1002/mrm.25378, indexed in Pubmed: 25056821.

47. Kocbek Šaherl L, Rakuša M. Thiel's embalming method: review of the literature and our institute's experience. Acta Medico-Biotechnica. 2021; 10(2): 34–42, doi: 10.18690/actabiomed.152.

48. Lirk P, Colvin JM, Biebl M, et al. [Evaluation of a cadaver workshop for education in regional anesthesia]. Anaesthesist. 2005; 54(4): 327–332, doi: 10.1007/s00101-005-0811-8, indexed in Pubmed: 15711813.

49. Logan BM. The long-term preservation of whole human cadavers destined for anatomical study. Ann Royal Coll Surg Engl. 1983; 65: 333.

50. Macchi V, Munari PF, Brizzi E, et al. Workshop in clinical anatomy for residents in gynecology and obstetrics. Clin Anat. 2003; 16(5): 440–447, doi: 10.1002/ca.10176, indexed in Pubmed: 12903067.

51. Mayer RG. Embalming: History, Theory, and Practise. New York 2012.

52. Mitchell EL, Sevdalis N, Arora S, et al. A fresh cadaver laboratory to conceptualize troublesome anatomic relationships in vascular surgery. J Vasc Surg. 2012; 55(4): 1187–1194, doi: 10.1016/j.jvs.2011.09.098, indexed in Pubmed: 22209607.

53. Musiał A, Gryglewski RW, Kielczewski S, et al. Formalin use in anatomical and histological science in the 19th and 20th centuries. Folia Med Cracov. 2016; 56(3): 31–40, indexed in Pubmed: 28275269.

54. Nicholson HD, Samalia L, Gould M, et al. A comparison of different embalming fluids on the quality of histological preservation in human cadavers. Eur J Morphol. 2005; 42(4-5): 178–184, doi: 10.1080/09243860500473306, indexed in Pubmed: 16982474.

55. Odobescu A, Moubayed SP, Harris PG, et al. A new microsurgical research model using Thiel-embalmed arteries and comparison of two suture techniques. J Plast Reconstr Aesthet Surg. 2014; 67(3): 389–395, doi: 10.1016/j.bjps.2013.12.026, indexed in Pubmed: 24507964.

56. Okada R, Tsunoda A, Momiyama N, et al. [Thiel's method of embalming and its usefulness in surgical assessments]. Nihon Jibiinkoka Gakkai Kaiho. 2012; 115(8): 791–794, doi: 10.3950/jibiinkoka.115.791, indexed in Pubmed: 23016272.

57. Ottone N, Vargas C, Fuentes R, et al. Walter Thiel's embalming method: review of solutions and applications in different fields of biomedical research. Int J Morphol. 2016; 34(4): 1442–1454, doi: 10.4067/s0717-95022016000400044.

58. Papageorgopoulou C, Xirotiris NI, Iten PX, et al. Indications of embalming in Roman Greece by physical, chemical and histological analysis. J Arch Sci. 2009; 36(1): 35–42, doi: 10.1016/j.jas.2008.07.003.

59. Pichler W, Tesch NP, Grechenig W, et al. Anatomic variations of the musculotendinous junction of the soleus muscle and its clinical implications. Clin Anat. 2007; 20(4): 444–447, doi: 10.1002/ca.20421, indexed in Pubmed: 17022026.

60. Reed AB, Crafton C, Giglia JS, et al. Back to basics: use of fresh cadavers in vascular surgery training. Surgery. 2009; 146(4): 757–762, doi: 10.1016/j.surg.2009.06.048, indexed in Pubmed: 19789036.

61. Schramek GG, Stoevesandt D, Reising A, et al. Imaging in anatomy: a comparison of imaging techniques in embalmed human cadavers. BMC Med Educ. 2013; 13: 143, doi: 10.1186/1472-6920-13-143, indexed in Pubmed: 24156510.

62. Sharma M, Horgan A. Comparison of fresh-frozen cadaver and high-fidelity virtual reality simulator as methods of laparoscopic training. World J Surg. 2012; 36(8): 1732–1737, doi: 10.1007/s00268-012-1564-6, indexed in Pubmed: 22484566.

63. Shirai T, Hayashi S, Itoh M. Experience of raising flaps using cadavers embalmed by saturated salt solution method. Plast Reconstr Surg Glob Open. 2015; 3(10): e543, doi: 10.1097/GOX.0000000000000523, indexed in Pubmed: 26579349.

64. Shiwani MH. Fresh frozen cadaver: a model for laparoscopic surgery training. J Coll of Physicians Surg Pak. 2010; 20(7): 425–426, indexed in Pubmed: 20642938.

65. Souza A, Kotian SR, Pandey AK, et al. Cadaver as a first teacher: a module to learn the ethics and values of cadaveric dissection. J Taibah Univ Med Sci. 2020; 15(2): 94–101, doi: 10.1016/j.jtumed.2020.03.002, indexed in Pubmed: 32368204.

66. Thiel W. Die Konservierung ganzer Leichen in natürlichen Farben. Ann Anat. 1992; 174(3): 185–195, doi: 10.1016/s0940-9602(11)80346-8.

67. Thiel W. Ergänzung für die Konservierung ganzer Leichen nach W. Thiel. Ann Anat. 2002; 184(3): 267–269, doi: 10.1016/s0940-9602(02)80121-2.

68. Wolff KD, Kesting M, Mücke T, et al. Thiel embalming technique: a valuable method for microvascular exercise and teaching of flap raising. Microsurgery. 2008; 28(4): 273–278, doi: 10.1002/micr.20484, indexed in Pubmed: 18383351.

69. Woodburne RT, Lawrence CA. An improved embalming fluid formula. Anat Rec. 1952; 114(3): 507–514, doi: 10.1002/ar.1091140309, indexed in Pubmed: 12996887.

VM VIA MEDICA

REVIEW ARTICLE

Systematic literature study of trachea and bronchus morphology in children and adults

Z.K. Coşkun, K. Atalar, B. Akar

Department of Anatomy, Faculty of Medicine, Gazi University, Ankara, Turkey

Understanding the dimensions of the lower airway is critical for performing respiratory surgery, selecting and designing appropriate airway equipment, and removing aspirated foreign bodies via bronchoscopy, anaesthesia, and radiography. The purpose of this study was to analyse the trachea and bronchus morphologically in children and adults, as well as to standardise the data for these structures' measurements. Various databases were reviewed for studies on lower airway dimensions. The criteria for inclusion and exclusion were established. Finally, it was agreed to look into 28 studies that took place between 1984 and 2021. The length of the trachea, its anterior-posterior (AP) and transverse dimensions, the lengths and transverse diameters of the right and left major bronchus, and the subcarinal angle were also investigated in the study. In studies where measurements were performed with different methods and procedures. It was revealed that age and gender were effective in the difference in lower respiratory tract dimensions. The mean values of all parameters were greater in adults than in children, the AP diameter of the trachea in adults was greater than the transverse diameter. In children, it was observed that the transverse diameter was larger than the AP diameter on average, the left main bronchus was longer than the right main bronchus, and the transverse diameter was smaller than the right main bronchus in most of the studies. The articles reviewed for this study revealed that measurements were done using a variety of different procedures and approaches, and the resulting data were inconsistent and could not be standardized. The data collected will be beneficial both conceptually and clinically; we believe that additional comparison research involving children and adults in bigger groups are necessary. (Folia Morphol 2023; 82, 3: 457–466)

Key words: trachea, bronchus, morphology, adult, child

INTRODUCTION

The trachea is a tubular organ 10–13 cm long with muscles and membranes [1, 39]. It begins at the lower edge of the C6 vertebra and divides into two bronchi: bronchus principalis dexter and bronchus principalis sinister at the T4–T5 vertebra level. After giving rise to the superior lobar bronchus, the right main bronchus descends as the intermediate bronchus. The middle and inferior lobar bronchi separate the intermediate bronchus into two lobar bronchi. Two lobar bronchi, bronchus lobaris superior and inferior, split the left main bronchus [29]. The term "normality" in anatomy refers to a variety of morphologies, including the

most prevalent ones, and "variations" are used to describe uncommon anatomical variation [40, 43]. In the medical literature, anatomical differences are referred to as anomalies [43]. Variations can influence disease susceptibility, symptomatology, clinical examination, and patient care in operational surgery and can affect any area of the human body [40]. Contrary to its overall anatomical structure, the tracheobronchial tree may also have distinctive characteristics and numerous variations [3]. The accessory cardiac bronchus and tracheal bronchus are frequently major anomalies or variations in the tracheobronchial tree [41]. The accessory cardiac bronchus is an excess bronchus that extends from the inner wall of the right main bronchus or intermediate bronchus to the pericardium [13], whereas the tracheal bronchus is an abnormal or accessory bronchus that primarily arises from the right lateral wall of the trachea [26]. Tracheobronchial abnormalities occur between 0.1% and 2% of cases [41]. Clinical practice should take anatomical variances into account [43]. Surgeons must have a thorough understanding of anatomical variations in order to appropriately identify anatomical structures during surgery [40]. In anaesthesia and respiration, knowing these airway dimensions are critical in conditions such as endotracheal tube, double lumen tube, rigid and flexible bronchoscopes, bronchial blockers, or stent size selection [11]. Furthermore, understanding the standard reference values for airway dimensions in radiology allows for the differentiation of normal and pathological airway findings in various age groups, as well as the design and manufacture of appropriate airway equipment [10]. In surgical approaches to the thoracic cavity, in the application of various airway techniques in anaesthesiology, and in the removal of aspirated foreign bodies by bronchoscopy, accurate knowledge of the anatomy and morphology of the tracheobronchial tree is essential [17]. Airways can be measured using computed tomography (CT) scans, cadaver measurements, chest X-ray and three-dimensional (3D) reconstruction, ultrasound, and bronchoscopy [38].

The purpose of this study was to compare the dimensions of the trachea and bronchus in children and adults using existing data and to standardise the measurement values. Our study of the literature revealed no systematic study comparing the morphological measurements of the trachea and bronchus in children and adults.

MATERIALS AND METHODS

Our study's methodology was developed in accordance with a paper from the Annals of Anatomy journal titled "Methods of Evidence-Based Anatomy: a guide to conducting systematic reviews and meta-analysis of anatomical studies" [16]. After conducting a literature analysis, it was decided that the focus of our study would be a review of the morphological structure of the trachea and bronchi in both children and adults. Our study's objective was to standardise the data and compare the diameters of the trachea and bronchi in children and adults. The inclusion criteria were carefully chosen. Children under the age of 18 and adults over the age of 18, from any ethnic origin, without airway pathology were included study. We used articles that examined CT scans, cadavers, chest radiographs, and 3D reconstructions as the basis for our work. Our study is a retrospective study that clearly defined the anatomical definitions of the trachea and bronchus. In order to avoid any interviewer bias in our study, care was taken to include articles that presented anatomical data in tabular form. Case reports, letters to the editor, conference summaries, unpublished articles, studies on fetuses, published articles with incomplete or uncertain results, age criteria, and the number of people in the article were excluded from our study. Researchers have identified a broad search strategy to reduce location bias. For literature searches on lower respiratory tracts such the trachea and bronchus, researchers used Google academic, PubMed, and Scopus databases. Searches in these databases returned 45 articles using keywords like "adult," "child," "human," "trachea," "bronchus," "diameter," "dimensions," "bronchial angles," "airway morphology," and their permutations. During the database search, neither historical date nor language restrictions were identified. In addition, the search has been expanded to include additional articles in the study from the journals' websites and by utilizing references from previously selected papers. In deciding the study, the title and abstract of the search-result articles were examined first, followed by the full text of the articles, if relevant to the subject of the study. To reduce the possibility of language and multi-publication bias in the article selection process, we also included data from incomprehensible languages and avoided using duplicate publications of the same study data. Twenty-eight articles that were published between 1984 and 2021 were selected for our study after the articles had been examined by the

Table 1. General descriptive data on lower airway studies in children

Studies	Age	Number of people	Parameter	Method
Griscom and Wohl (1986)	0–18 years	119 people (64 M, 55 F)	Trachea length, AP and transverse diameters, cross-sectional area, volume	CT
Herek et al. (2017)	0–18 years	118 children (67 M, 51 F)	SCA, RBA, LBA, IBA	CT
Breatnach et al. (1984)	10–18 years	48 children (26 M, 22 F)	AP and transverse diameters of trachea	Chest X-ray
Kuo et al. (2018)	0–18 years	240 people (155 M, 85 F)	Trachea length, transverse diameter, right and left main bronchus diameters	CT
Ulusoy et al. (2016)	0–18 years	41 people (26 M, 15 F)	AP and transverse diameters of trachea, trachea cross-sectional area, RBA, LBA, IBA	Multidetector CT
Jit and Jit (2000)	0–18 years	60 children (30 M, 30 F)	Trachea length, AP and transverse diameters, right and left main bronchus lengths and transverse diameters, subcarinal angle	Cadaver study
Chalwadi et al. (2021)	0–18 years	110 children (54 M, 56 F)	AP, transverse diameters and cross-sectional areas of trachea, right and left main bronchus	CT
Tan and Tan-Kendrick (2002)	2 days–16 years	250 children (133 M, 117 F)	Right and left main bronchus transverse diameters	CT
Luscan et al. (2020)	1 day–14 years	192 children (127 M, 65 F)	Trachea length, AP and transverse diameters, right and left main bronchus lengths, AP and transverse diameters	CT
Aslan et al. (2015)	0–16 years	520 people (246 M, 274 F)	Trachea diameters of right and left main bronchus	Chest X-ray
Szelloe et al. (2017)	0–16 years	195 people (118 M, 77 F)	Trachea, right and left main bronchus, AP diameter, transverse diameter, cross-sectional area	CT
Tahir et al. (2009)	< 16 years	156 people (84 M, 72 F)	Trachea, right and left main bronchus transverse diameters, RBA, LBA, SCA	Chest X-ray
Kubota et al. (1986)	0–13 years	259 babies and children	RBA, LBA, SCA	Chest X-ray

M — male; F — female; AP — anterior-posterior diameter; RBA — right bronchial angle; LBA — left bronchial angle; IBA — interbronchial angle; SCA — subcarinal angle; CT — computed tomography image

researchers. Tables 1 and 2 show general descriptive information gathered from papers, including the articles' authors and the year they were published, the number of participants and age groups, the anatomical structures that were measured, and the methodologies that were used. The length of the trachea, the anterior-posterior (AP) and transverse diameters of the trachea, the subcarinal angle, the lengths of the right and left major bronchus, and their transverse diameters, in both adults (> 18 years) and children (under 18 years) are defined independently in the publications included in our analysis.

Analytical statistics

The data was analysed using the SPSS 24.0 software within the scope of this study. For each parameter, the data in the studies were grouped and represented according to child and adult age groups. Minimum and maximum values, range, mean, standard deviation, median, quartiles, and confidence intervals were generated for each parameter as descriptive statistics (Tables 3, 4). Due to the varying age group distributions in the studies and the fact that the parameter measuring method was not consistent, further statistical analysis of the data was limited.

RESULTS

In the scanned studies, total of 2308 children were examined in 13 and 7148 adults in 18 were examined. Eighteen studies were examined used CT scan, 9 relied on cadaver examination, 6 used chest X-ray, and 3 used 3D reconstruction method. Tables 3 and 4 provide descriptive data for trachea and bronchus measurements in children and adults. In Tables 5 and 6, studies that include measurements of trachea and bronchus sizes are presented in detail in children and adults.

As a result of the studies analysed, the mean values in children and adults, respectively, were as follows: trachea length 7.52 (6.19–9.36) and 10.08 (8.13–13.25) cm; the AP diameter of the trachea 1.19 (0.78–1.58) cm and 1.75 (1.11–2.14) cm; the transverse diameter of the trachea 1.28 (0.95–1.74) cm and 1.66 (1.23–2.57) cm. It was observed that the pa-

Table 2. General descriptive data on lower airway studies in adults

Studies	Age	Number of people	Parameter	Method
Breatnach et al. (1984)	20–79 years	760 people (404 M, 356 F)	Trachea length, AP and transverse diameters, cross-sectional area, volume	CT
Tuncer (2019)	Average: 52 years	150 people (81 M, 69 F)	Trachea length, AP and transverse diameters, right and left main bronchus lengths, lobar bronchus lengths	CT
Ulusoy et al. (2016)	19–74 years	212 people (116 M, 96 F)	AP and transverse diameters of trachea, cross-sectional area of trachea, RBA, LBA, IBA	Multidetector CT
Jit and Jit (2000)	18–75 years	370 people (220 M, 150 F)	Trachea length, AP and transverse diameters, right and left main bronchus lengths and diameters, RBA, LBA, SCA	Cadaver study
Zahedi-Nejad et al. (2011)	20–85 years	200 people (132 M, 68 F)	AP and transverse diameters of trachea, cross-sectional area of trachea, diameters of right and left main bronchus	CT
Mi et al. (2015)	18–89 years	2107 people (1143 M, 964 F)	Trachea length, AP and transverse diameters, right and left main bronchus lengths and diameters, RBA, LBA, right upper lobe bronchus length and angle	CT 3D
Tamang et al. (2017)	Adult individuals	40 people (20 M, 20 F)	Length and transverse diameter of trachea, SCA	Cadaver study
Sakuraba et al. (2010)	Average: 58 years	146 people (55 M, 91 F)	Trachea transverse diameter	Chest X-ray CT
Chen et al. (2020)	18–89 years	2093 people (1136 M, 957 F)	Length and diameter of right main bronchus, right upper lobe length, diameter and angle of the bronchus, RBA	CT
Premakumar et al. (2018)	70–96 years	10 people (8 M, 2 F)	Trachea, AP and transverse diameters	Cadaver study
Lee et al. (2014)	21–78 years	160 people (80 M, 80 F)	Right-left main bronchus length, AP and transverse diameters	3D CT
Kim and Song (2017)	47–91 years	48 cadavers (33 M, 15 F)	Right and left main bronchus, lenght, AP and transverse diameters, SCA	Cadaver study
Bhandari et al. (2018)	over 18 years	182 cadavers (132 M, 50 F)	Trachea, AP and transverse diameters	Cadaver study
Kamel et al. (2009)	CT image: 22–88 years Cadaver study: 68–101 years	CT: 60 people (40 M, 20 F) Cadaver: 10 people (7 M, 3 F)	Trachea length, AP and transverse diameters, tracheal volume, SCA	CT Cadaver study
Otoch et al. (2013)	18–83-years-old male patients	134 people	Trachea, length of right main bronchus	Cadaver study
Datta et al. (2019)	20–65 years	60 cadavers (30 M, 30 F)	Trachea, AP and transverse diameters	Cadaver study
Hampton et al. (2000)	Adult individuals	206 people (130 M, 76 F)	Trachea diameter, right and left main bronchus diameters	Chest X-ray
Kim et al. (2014)	19–80 years	200 people (100 M, 100 F)	Right and left main bronchus lengths, AP and transverse diameters	CT 3D

M — male; F — female; AP — anterior-posterior diameter; RBA — right bronchial angle; LBA — left bronchial angle; IBA — interbronchial angle; SCA — subcarinal angle; CT — computed tomography image; 3D — three-dimensional reconstruction

rameters increased with age. The transverse diameter of the trachea was greater than the AP diameter in children, and the AP diameter was greater than the transverse diameter in adults.

When the mean values in children and adults were compared, the length of the right main bronchus was 2.05 (1.76–2.47) and 2.93 (1.23–11.35) cm, the length of the left main bronchus was 4.09 (3.48–5.17) cm and 5.25 (3.68–10.15) cm, the transverse diameter of the right main bronchus was 0.97 (0.73–1.34) cm and 1.40 (1.08–1.91) cm, and the transverse diameter of the left main bronchus was 0.85 (0.68–1.10) cm and 1.26 (0.94–1.69) cm. The mean subcarinal angle was 71.53° (56.1°–83°) and 72.14° (52.48°–82.12°) in children and adults, respectively. It has been observed that the left main bronchus is longer than the right main bronchus in children and adults, and the transverse diameters of the right main bronchus are wider than the left main bronchus. On average, all parameter values were found to be higher in adults than in children.

When the parameters were compared according to gender, all values, except the subcarinal angle, were

Table 3. Descriptive statistics of measurements of trachea and bronchus in children

	LMB TR diameter	LMB length	RMB TR diameter	RMB length	SCA	Trachea AP diameter	Trachea TR diameter	Trachea length
Age	0–18	0–18	0–18	0–18	0–18	0–18	0–18	0–18
Min	0.68	3.48	0.73	1.76	56.10	0.78	0.95	6.19
Max	1.10	5.17	1.34	2.47	83.00	1.58	1.74	9.36
Range	0.42	1.69	0.61	0.71	26.90	0.80	0.79	3.17
Mean	0.85	4.09	0.97	2.05	71.53	1.19	1.28	7.52
SD	0.14	0.94	0.20	0.37	10.25	0.29	0.27	1.36
95.0% lower CI for mean	0.73	1.77	0.81	1.13	60.77	0.92	1.07	5.36
95.0% upper CI for mean	0.96	6.42	1.14	2.97	82.28	1.46	1.49	9.68
Median	0.83	3.63	0.98	1.93	73.12	1.10	1.14	7.27
95.0% lower CI for median	0.70	3.48	0.75	1.76	63.25	0.94	1.13	6.19
95.0% upper CI for median	0.96	5.17	1.10	2.47	80.56	1.58	1.60	9.36
Percentile 05	0.68	3.48	0.73	1.76	56.10	0.78	0.95	6.19
Percentile 25	0.75	3.48	0.83	1.76	63.25	0.94	1.13	6.56
Percentile 75	0.92	5.17	1.06	2.47	80.56	1.50	1.50	8.48
Percentile 95	1.10	5.17	1.34	2.47	83.00	1.58	1.74	9.36

Values are presented as centimetre and degree; LMB — left main bronchus; RMB — right main bronchus; SCA — subcarinal angle; AP — anterior-posterior; TR — transvers; CI — confidence interval; SD — standard deviation; Min — minimum; Max — maximum

Table 4. Descriptive statistics of measurements of trachea and bronchus in adults

	LMB TR diameter	LMB length	RMB TR diameter	RMB length	SCA	Trachea AP diameter	Trachea TR diameter	Trachea length
Age	18–89	18–89	18–89	18–89	18–89	18–89	18–89	18–89
Min	0.94	3.68	1.08	1.23	52.48	1.11	1.23	8.13
Max	1.69	10.15	1.91	11.35	82.12	2.14	2.57	13.25
Range	0.75	6.47	0.83	10.12	29.64	1.03	1.34	5.12
Mean	1.26	5.25	1.40	2.93	72.14	1.75	1.66	10.08
SD	0.28	2.19	0.27	3.24	10.48	0.25	0.33	1.39
95.0% lower CI for mean	1.02	3.22	1.20	0.44	61.14	1.59	1.47	9.09
95.0% upper CI for mean	1.49	7.28	1.61	5.42	83.14	1.91	1.84	11.08
Median	1.17	4.59	1.32	1.68	74.44	1.80	1.65	10.20
95.0% lower CI for median	1.07	4.29	1.25	1.36	71.37	1.72	1.58	9.20
95.0% upper CI for median	1.66	10.15	1.76	3.30	78.00	1.85	1.75	10.38
Percentile 05	0.94	3.68	1.08	1.23	52.48	1.11	1.23	8.13
Percentile 25	1.08	4.29	1.25	1.36	71.37	1.72	1.51	9.20
Percentile 75	1.46	4.83	1.46	2.55	78.00	1.85	1.75	10.38
Percentile 95	1.69	10.15	1.91	11.35	82.12	2.14	2.57	13.25

Values are presented as centimetre and degree; LMB — left main bronchus; RMB — right main bronchus; SCA — subcarinal angle; AP — anterior-posterior; TR — transvers; CI — confidence interval; SD — standard deviation; Min — minimum; Max — maximum

found to be higher in males than females on average. In 4 of the 6 studies in which the subcarinal angle was measured, the values were higher in women than in men, while it was observed that it was higher in men than in women in 2 studies.

DISCUSSION

Twenty-eight studies were analysed in the review of the literature, and lower airway dimensions in children and adults were compared. In both children and adults, measurement values vary. Among the possible

Table 5. Studies examining the sizes of trachea and bronchus in children

Studies	Parameters	
	RMB TR diameter	**LMB TR diameter**
Kuo [23]	M: 1.12; F: 1.06	M: 0.87; F: 0.78
Jit [18]	Average: 0.9	Average: 0.82
Chalwadi [6]	Average: 1.02	Average: 0.96
Tan [35]	Average: 0.75	Average: 0.7
Luscan [25]	Average: 1.01	Average: 0.88
Aslan [2]	Average: 0.94	Average: 0.8
Tahir [33]	M: 0.77; F: 0.68	M: 0.7; F: 0.67
	RMB length	**LMB length**
Jit [18]	Average: 1.93	Average: 3.48
Luscan [25]	Average: 1.76	Average: 3.63
	Trachea AP diameter	**Trachea TR diameter**
Griscom [14]	M: 1.1; F: 1.08	M: 1.14; F: 1.14
Breatnach [5]	M: 1.54; F: 1.45	M: 1.55; F: 1.44
Ulusoy [37]	M: 1.22; F: 0.94	M: 1.37; F: 0.99
Jit [18]	Average: 1.32	Average: 1.13
Chalwadi [6]	Average: 1.1	Average: 1.16
Luscan [25]	Average: 0.78	Average: 1.02
Szelloe [32]	Average: 0.94	–
Kuo [23]	–	M: 1.32; F: 1.2
Aslan [2]	–	Average: 1.14
Tahir [33]	–	M: 1.02; F: 0.91
	Trachea length	**Subcarinal angle**
Griscom [14]	M: 9.45; F: 9.28	–
Kuo [23]	M: 7.06; F: 6.09	–
Jit [18]	Average: 6.09	Average: 56.10°
Luscan [25]	Average: 7.6	–
Herek [17]	–	Average: 80.56°
Ulusoy [37]	–	M: 72.55; F: 69.6°
Aslan [2]	–	Average: 63.25°
Kubota [22]	–	Average: 83°

Values are presented as centimetre and degree; LMB — left main bronchus; RMB — right main bronchus; AP — anterior-posterior; TR — transverse; M — male; F — female

explanations for this are the participants' ages, the various assessment methods and procedures performed, gender disparities, and research conducted on various ethnic communities. Due to these discrepancies, standardizing measurement values is difficult.

Length of trachea

The mean value of the length of the trachea was found to be greater in adults than in children (Tables 3, 4). In studies on children and adults, it was found

Table 6. Studies examining the sizes of trachea and bronchus in adult

Studies	Parameters	
	RMB TR diameter	**LMB TR diameter**
Ulusoy [37]	Average: 1.34	Average: 1.1
Jit [18]	M: 1.36; F: 1.1	M: 1.16; F: 0.94
Mi [27]	M: 1.41; F: 1.21	M: 1.16; F: 1.0
Lee [24] (2D)	M: 1.98; F: 1.84	M: 1.82; F: 1.56
Lee [24] (3D)	M: 1.56; F: 1.21	M: 1.35; F: 1.01
Kim [21]	M: 1.89; F: 1.65	M: 1.7; F: 1.44
Kim [20]	M: 1.51; F: 1.18	M: 1.3; F: 0.99
Hampton [15]	M: 1.5; F: 1.38	M: 1.3; F: 1.18
Zahedi-Nejad [42]	M:1.16; F: 0.93	M: 1.02; F: 0.8
Chen [7]	M: 1.41; F: 1.21	–
	RMB length	**LMB length**
Tuncer [36]	M: 12.56; F: 10,15	M: 11.38; F: 8.71
Ulusoy [37]	Average: 2.47	Average: 5.17
Jit [18]	M: 2.68; F: 2.37	M: 4.81; F: 4.37
Mi [27]	M: 1.41; F: 1.29	M: 5.0; F: 4.62
Lee [24] (2D)	M: 1.38; F: 1.37	M: 4.36; F: 4.19
Lee [24] (3D)	M: 1.34; F: 1.18	M: 4.82; F: 4.36
Kim [21]	M: 1.68; F: 1.69	M: 3.72; F: 3.6
Kim [20]	M: 1.29; F: 1.17	M: 4.78; F: 4.35
Chen [7]	M: 2.37; F: 2.15	–
Otoch [28]	Average: 3.3	–
	Trachea AP diameter	**Trachea TR diameter**
Breatnach [5]	M: 2.01; F: 1.63	M: 1.92; F: 1.62
Tuncer [36]	M: 1.98; F: 1.55	M: 1.85; F: 1.49
Ulusoy [37]	M: 1.76; F: 1.35	M: 1.94; F: 1.51
Jit [18]	M: 2.0; F: 1.62	M: 1.65; F: 1.3
Zahedi-Nejad [42]	M: 1.96; F: 1.47	M: 1.8; F: 1.43
Mi [27]	M: 1.9; F: 1.49	M: 1.71; F: 1.49
Premakumar [30]	Average: 1.72	Average: 1,73
Bhandari [4]	M: 1.89; F: 1.58	M: 1.32; F: 1.05
Kamel [19] (CT)	M: 2.26; F: 1.92	M: 2.71; F: 2.29
Kamel [19] (Cadaver)	M: 2.17; F: 1.55	M: 2.13; F: 1.78
Datta [9]	M: 1.55; F: 1.37	M: 1.29; F: 1.2
Sakuraba [31] (CT)	–	M: 1.74; F: 1.48
Sakuraba [31] (Chest X-ray)	–	M: 1.77; F: 1.58
Otoch [28]	Average: 1.85	–
Tamang [34]	–	M: 1.85; F: 1.34
Hampton [15]	–	Average: 1.79
	Trachea length	**Subcarinal angle**
Jit [18]	M: 8.93; F: 8.19	M: 51.2°; F: 54.3°
Tamang [34]	M: 11.13; F: 9.58	M: 72.15°; F: 70.6°
Kamel [19] (CT)	M: 10.5; F: 9.83	M: 76°; F: 81°

→

Table 6. cont. Studies examining the sizes of trachea and bronchus in adult

Studies	Parameters	
Kamel [19] (Cadaver)	M: 10.26; F: 9.6	–
Mi [27]	M: 10.7; F: 10.1	M: 75.2°; F: 80.1°
Tuncer [36]	M: 14.24; F: 12.26	–
Premakumar [30]	Average: 10.38	–
Bhandari [4]	M: 8.28; F: 7.75	–
Otoch [28]	Average: 9.2	–
Datta [9]	M: 10.42; F: 9.81	–
Ulusoy [37]	–	M: 71.5°; F: 76.4°
Kim [20]	–	M: 83.4°; F: 79°

Values are presented as centimetre and degree; LMB — left main bronchus; RMB — right main bronchus; AP — anterior-posterior; TR — transverse; CT — computed tomography; 2D — two-dimensional image; 3D — three-dimensional image; M — male; F — female

that the length of the trachea increases with age (Tables 5, 6). Studies in children have shown that the length of the trachea increases with age and is close to each other in males and females. When the studies conducted by Griscom and Wohl (1986) [14] and Kuo et al. (2018) [23] were examined, it was seen that there was no difference between men and women until puberty, and the main difference began to occur after puberty and the length of the trachea was higher in men than in women. However, in a study by Chunder et al. (2010) [8], it was found that the trachea is shorter in women than in men, who were aged 0–15 years old. Chunder et al. (2010) [8] stated that this may be due to the puberty of children.

In all studies on adults, the length of the trachea increased with age, and it was found to be greater in males than females. However, in the study conducted by Chunder et al. (2010) [8] in the age groups of 41–55 and over 55 years old, it was stated that the length of the trachea decreased in both men and women depending on age. Chunder et al. (2010) [8] stated that this may be due to excessive contraction of the trachea by fibrous tissue due to aging.

Trachea lengths differ according to the method used in the studies. For example, in studies conducted by examining CT images of children [14, 23, 25] and adults [19, 36], it was found that trachea lengths were higher than that reported in studies performed on child [18] and adult [4, 18, 19, 28] cadavers.

AP and transverse diameters of trachea

It was noticed in comparative studies of children and adults that the diameters increased with age

[5, 8, 18, 32, 37]. In every study that compared men and women, the diameters of men were found to be greater than those of women.

In studies comparing the AP and transverse diameters of the trachea in children and adults, it was discovered that there were differences (Tables 5, 6). The mean value of the transverse diameter of the trachea was found to be greater than the AP diameter in children's studies [6, 14, 25, 37]. While the average value of the diameters was equal in the study by Breatnach et al. (1984) [5], the mean value of the AP diameter of the trachea was found to be larger than the transverse diameter in the study by Jit and Jit (2000) [18]. In a study conducted by Chunder et al. (2010) [8] in the 0–15 age group, it was discovered that men had a larger AP diameter and women had a larger transverse diameter. Jit and Jit (2000) [18] stated that these differences may be racial, due to the variability of the subjects' height and neck length.

Studies in adults were reviewed and studies were found in which the mean value of the AP diameter of the trachea was larger [4, 5, 9, 18, 36, 42] and smaller [19, 30, 37] than the mean value of the transverse diameter.

The trachea's AP and transverse diameters differ depending on how they are measured. The values of the transverse and AP diameters of the trachea measured on CT images were larger than the values measured on cadavers, according to Kamel et al. (2009) [19]. The transverse diameter of the trachea measured on the chest X-ray was found to be higher than the value of the transverse diameter measured on the CT images in studies conducted by Sakuraba et al. (2010) [31].

Lengths of right and left main bronchus

In studies comparing the lengths of the right and left main bronchus in children and adults, the average values of main bronchus lengths in adults were found to be higher than in children (Tables 3, 4). In studies conducted on adults, the lengths of the main bronchus were found to be greater in males than in females [7, 18, 20, 24, 27, 36]. In studies examining the lengths of the right and left main bronchus in children [18, 25] and adults [18, 20, 21, 24, 27, 37] comparatively, the length of the left main bronchus is compared to the length of the right main bronchus and found to be larger.

The lengths of the main bronchus differ according to the measurement methods. In a study by Lee et al. (2014) [24], in which measurements were made on two-dimensional (2D) and 3D images in adults, it was

found that the length of the right main bronchus was larger in 2D images than in 3D images. The length of the left main bronchus was found to be smaller in 2D images than in 3D images.

Transverse diameters of right and left main bronchus

The mean values of the transverse diameters of the main bronchus in adults were larger than in children, according to studies comparing the transverse diameters of the right and left main bronchus in children and adults (Tables 3, 4). The diameters of the right and left main bronchus were found to be larger in men than in women in all of the studies (Tables 5, 6). All studies measuring the transverse diameters of the right and left main bronchus in children [2, 6, 18, 23, 25, 33, 35] and adults [15, 18, 20, 21, 24, 27, 37, 42] found that the right main bronchus was larger than the left main bronchus.

The transverse diameters of the main bronchus vary depending on the method of measurement. Lee et al. (2014) [24] determined that the transverse diameters of the right and left main bronchus were smaller in 3D images than in 2D images in adults.

Subcarinal angle

Considering the studies examining the subcarinal angle in children [2, 17, 18, 22, 37] and adults [18, 19, 20, 27, 34, 37], it is seen that the mean value of the subcarinal angle is higher in adults than in children (Tables 3, 4). In a comparative study by Ulusoy et al. (2016) [37] in children and adult, it was reported that the mean value of the subcarinal angle was higher in adults. In the studies conducted by Jit and Jit (2000) [18] and Chunder et al. (2010) [8], the mean value of the subcarinal angle was found to be higher in children. It was stated by Farrukhabad and Chunder (2015) [12] that with increasing age, the ossification of the chest wall and ribs is about to be completed, relatively hardening and causing the subcarinal angle to narrow by directing the lower growth of the lungs.

The subcarinal angle varies by gender. It was found to be higher in men than women in some studies [8, 20, 34], but higher in women in others [18, 19, 27, 37].

Understanding the subcarinal angle is critical in some clinical scenarios. Enlargement of mediastinal structures or pulmonary diseases can dramatically modify the subcarinal angle. Due to the fact that the

Figure 1. Three-dimensional model of tracheobronchial tree; a — trachea length; b — trachea anterior-posterior diameter; c — trachea transvers diameter; d — right main bronchus length; e — left main bronchus length; f — right main bronchus transvers diameter; g — left main bronchus transvers diameter; h — subcarinal angle.

right main bronchus is almost parallel to the trachea, the right subcarinal angle, which is a component of the subcarinal angle, is smaller than the left subcarinal angle. For this reason, the probability of foreign bodies entering the right lung is higher [12].

CONCLUSIONS

The literature reviews on the trachea and bronchus in children and adults were compared according to age and gender in this study. The mean values of all parameters in the studies increased with age, and gender differences were found to have an impact on the differences in measured parameter values. The AP diameter of the trachea was discovered to be lower than the transverse diameter in children, whereas the AP diameter of the trachea was found to be higher than the transverse diameter in adults. According to studies, the right main bronchus transverse diameter is greater than the left main bronchus transverse diameter in children and adults. Despite the fact that the mean value in subcarinal angle studies is higher in adults than in children, there are research that contradict these findings [8, 18]. The data collected from the parameters varies since the measurements were done with varied methods and techniques in the investigations, and it is assumed that standardisation is difficult. We believe that the data gained will be valuable in terms of theory and clinic, and that it will be useful to perform additional research in a larger population, including children and adults, in a comparative manner, in conjunction with creating methodologies and procedures.

Acknowledgements

REFERENCES

1. Arıncı K. Arıncı Anatomi. 4. Baskı, Güneş Kitabevi, Ankara 2005.

2. Aslan A, Aslan M, Soysal A, et al. Pediatrik yaş grubunda akciğer grafisi bulguları. Kocatepe Tıp Dergisi. 2015; 15(1): 32–40.

3. Beder S, Küpeli E, Karnak D, et al. Tracheobronchial variations in Turkish population. Clin Anat. 2008; 21(6): 531–538, doi: 10.1002/ca.20667, indexed in Pubmed: 18698650.

4. Bhandari R, Ranjit N, Shrestha R, et al. Morphometric study of trachea in adult cadavers. J Institute Med. 2018; 40(1): 59–63.

5. Breatnach E, Abbott GC, Fraser RG. Dimensions of the normal human trachea. Am J Roentgenol. 1984; 142(5): 903–906, doi: 10.2214/ajr.142.5.903, indexed in Pubmed: 6609569.

6. Chalwadi UK, Swamy N, Agarwal A, et al. Determining normal values for lower trachea and bronchi size in children by computed tomography (CT). Pediatr Pulmonol. 2021; 56(9): 2940–2948, doi: 10.1002/ppul.25536, indexed in Pubmed: 34133085.

7. Chen Y, Guo Y, Mi W, et al. Anatomy of the right upper lobe revisited and clinical considerations in Chinese population. PLoS One. 2020; 15(11): e0242178, doi: 10.1371/journal.pone.0242178, indexed in Pubmed: 33237948.

8. Chunder R, Nandi S, Guha R, et al. A morphometric study of human trachea and principal bronchi in different age groups in both sexes and its clinical implications. Nepal Med Coll J. 2010; 12(4): 207–214, indexed in Pubmed: 21744760.

9. Datta D, Kundu D, Pal P, et al. A morphometric study of adult human trachea in West Bengal population. Int J Med Res Rev. 2019; 7(1): 36–42, doi: 10.17511/ijmrr.2019.i01.07.

10. Dave MH, Kemper M, Schmidt AR, et al. Pediatric airway dimensions: a summary and presentation of existing data. Paediatr Anaesth. 2019; 29(8): 782–789, doi: 10.1111/pan.13665, indexed in Pubmed: 31087466.

11. Dave MH, Schmid K, Weiss M. Airway dimensions from fetal life to adolescence: A literature overview. Pediatr Pulmonol. 2018; 53(8): 1140–1146, doi: 10.1002/ppul.24046, indexed in Pubmed: 29806162.

12. Farrukhabad UP, Chunder RA. morphometric study of human subcarinal angle in different age groups in both sexes and its clinical implications. Indian J Basic Applied Med Res. 2015; 4(2): 424–430.

13. Ghaye B, Szapiro D, Fanchamps JM, et al. Congenital bronchial abnormalities revisited. Radiographics. 2001; 21(1): 105–119, doi: 10.1148/radiographics.21.1.g01ja06105, indexed in Pubmed: 11158647.

14. Griscom NT, Wohl ME. Dimensions of the growing trachea related to age and gender. Am J Roentgenol. 1986; 146(2): 233–237, doi: 10.2214/ajr.146.2.233, indexed in Pubmed: 3484568.

15. Hampton T, Armstrong S, Russell WJ. Estimating the diameter of the left main bronchus. Anaesth Intensive Care. 2000; 28(5): 540–542, doi: 10.1177/0310057X0002800510, indexed in Pubmed: 11094671.

16. Henry BM, Tomaszewski KA, Walocha JA. Methods of Evidence-Based Anatomy: a guide to conducting systematic reviews and meta-analysis of anatomical studies. Ann Anat. 2016; 205: 16–21, doi: 10.1016/j.aanat.2015.12.002, indexed in Pubmed: 26844627.

17. Herek D, Herek O, Ufuk F. Tracheobronchial angle measurements in children: an anthropometric retrospective study with multislice computed tomography. Clin Exp Otorhinolaryngol. 2017; 10(2): 188–192, doi: 10.21053/ceo.2016.00185, indexed in Pubmed: 27334508.

18. Jit H, Jit I. Dimensions and shape of the trachea in the neonates, children and adults in northwest India. Indian J Med Res. 2000; 112: 27–33, indexed in Pubmed: 11006658.

19. Kamel KS, Lau G, Stringer MD. In vivo and in vitro morphometry of the human trachea. Clin Anat. 2009; 22(5): 571–579, doi: 10.1002/ca.20815, indexed in Pubmed: 19544298.

20. Kim D, Son JS, Ko S, et al. Measurements of the length and diameter of main bronchi on three-dimensional images in Asian adult patients in comparison with the height of patients. J Cardiothorac Vasc Anesth. 2014; 28(4): 890–895, doi: 10.1053/j.jvca.2013.05.029, indexed in Pubmed: 24103712.

21. Kim I, Song C. The morphometric study of main bronchus in Korean cadaver. Korean J Physical Anthropol. 2017; 30(1): 7, doi: 10.11637/kjpa.2017.30.1.7.

22. Kubota Y, Toyoda Y, Nagata N, et al. Tracheo-bronchial angles in infants and children. Anesthesiology. 1986; 64(3): 374–376, doi: 10.1097/00000542-198603000-00015, indexed in Pubmed: 3954135.

23. Kuo W, Ciet P, Andrinopoulou ER, et al. Reference values for central airway dimensions on CT images of children and adolescents. AJR Am J Roentgenol. 2018; 210(2): 423–430, doi: 10.2214/AJR.17.18597, indexed in Pubmed: 29261353.

24. Lee JW, Son JS, Choi JW, et al. The comparison of the lengths and diameters of main bronchi measured from two-dimensional and three-dimensional images in the same patients. Korean J Anesthesiol. 2014; 66(3): 189–194, doi: 10.4097/kjae.2014.66.3.189, indexed in Pubmed: 24729839.

25. Luscan R, Leboulanger N, Fayoux P, et al. Developmental changes of upper airway dimensions in children. Paediatr Anaesth. 2020; 30(4): 435–445, doi: 10.1111/pan.13832, indexed in Pubmed: 31995659.

26. McLaughlin FJ, Strieder DJ, Harris GB, et al. Tracheal bronchus: association with respiratory morbidity in childhood. J Pediatr. 1985; 106(5): 751–755, doi: 10.1016/s0022-3476(85)80348-6, indexed in Pubmed: 3998915.

27. Mi W, Zhang C, Wang H, et al. Measurement and analysis of the tracheobronchial tree in Chinese population using computed tomography. PLoS One. 2015; 10(4): e0123177, doi: 10.1371/journal.pone.0123177, indexed in Pubmed: 25894917.

28. Otoch JP, Minamoto H, Perini M, et al. Is there a correlation between right bronchus length and diameter with age? J Thorac Dis. 2013; 5(3): 306–309, doi: 10.3978/j.issn.2072-1439.2013.03.12, indexed in Pubmed: 23825764.
29. Ozan H. Ozan Anatomi. 3. Baskı, Tıp Kitabevi, Ankara 2014.
30. Premakumar Y, Griffin MF, Szarko M. Morphometric characterisation of human tracheas: focus on cartilaginous ring variation. BMC Res Notes. 2018; 11(1): 32, doi: 10.1186/s13104-018-3123-1, indexed in Pubmed: 29338790.
31. Sakuraba S, Serita R, Kuribayashi J, et al. Comparison of tracheal diameter measured by chest x-ray and by computed tomography. Anesthesiol Res Pract. 2010; 2010, doi: 10.1155/2010/269171, indexed in Pubmed: 20827310.
32. Szelloe P, Weiss M, Schraner T, et al. Lower airway dimensions in pediatric patients: a computed tomography study. Paediatr Anaesth. 2017; 27(10): 1043–1049, doi: 10.1111/pan.13210, indexed in Pubmed: 28846178.
33. Tahir N, Ramsden WH, Stringer MD. Tracheobronchial anatomy and the distribution of inhaled foreign bodies in children. Eur J Pediatr. 2009; 168(3): 289–295, doi: 10.1007/s00431-008-0751-9, indexed in Pubmed: 18500537.
34. Tamang BK, Lakhi K, Sinha P, et al. Study of tracheal dimension in adult cadavers from Eastern India. Indian J Clin Anat Physiol. 2017; 4(2): 144–147, doi: 10.18231/2394-2126.2017.0036.
35. Tan GM, Tan-Kendrick APA. Bronchial diameters in children: use of the Fogarty catheter for lung isolation in children. Anaesth Intensive Care. 2002; 30(5): 615–618, doi: 10.1177/0310057X0203000512, indexed in Pubmed: 12413262.
36. Tuncer I. İnsan Trakeobronşial Ağacının Her İki Cınsıyetin Farklı Yaş Gruplarında Ct ile Morfometrik Çalışması. DÜSTAD Dünya Sağlık ve Tabiat Bilimleri Dergisi. 2018; 1(1): 19–35.
37. Ulusoy M, Uysal II, Kivrak AS, et al. Age and gender related changes in bronchial tree: a morphometric study with multidedector CT. Eur Rev Med Pharmacol Sci. 2016; 20(16): 3351–3357.
38. Wani TM, Simion C, Rehman S, et al. Mainstem bronchial diameters and dimensions in infants and children: a systematic review of the literature. J Cardiothorac Vasc Anesth. 2021; 35(10): 3078–3084, doi: 10.1053/j.jvca.2020.07.002, indexed in Pubmed: 32732101.
39. Waschke J, Böckers TM, Paulsen F. Sobotta Anatomi Konu Kitabı. In: Mustafa Fevzi Sargon (ed.). İmge Kitabevi, Ankara 2016.
40. Willan P, Humpherson J. Concepts of variation and normality in morphology: Important issues at risk of neglect in modern undergraduate medical courses. Clin Anat. 1999; 12(3): 186–190, doi: 10.1002/(sici)1098-2353(1999)12:3<186::aid-ca7>3.0.co;2-6.
41. Wong LM, Cheruiyot I, de Oliveira MH, et al. Congenital anomalies of the tracheobronchial tree: a meta-analysis and clinical considerations. Ann Thorac Surg. 2021; 112(1): 315–325, doi: 10.1016/j.athoracsur.2020.08.060, indexed in Pubmed: 33159867.
42. Zahedi-Nejad N, Bakhshayesh-Karam M, Kahkoei S, et al. Normal dimensions of trachea and two main bronchi in the Iranian population. Pol J Radiol. 2011; 76(4): 28–31, indexed in Pubmed: 22802851.
43. Żytkowski A, Tubbs R, Iwanaga J, et al. Anatomical normality and variability: Historical perspective and methodological considerations. Transl Res Anat. 2021; 23: 100105, doi: 10.1016/j.tria.2020.100105.

VM
VIA MEDICA

R E V I E W   A R T I C L E

Clinical significance of morphological variations of the inferior phrenic arteries

W. Marcinkowska[1], M. Malicki[1], P. Karauda[1], R.S. Tubbs[2-7], N. Zielińska[1], Ł. Olewnik[1]

[1]Department of Anatomical Dissection and Donation, Medical University of Lodz, Poland
[2]Department of Neurosurgery, Tulane University School of Medicine, New Orleans, LA, United States
[3]Department of Neurology, Tulane University School of Medicine, New Orleans, LA, United States
[4]Department of Surgery, Tulane University School of Medicine, New Orleans, LA, United States
[5]Department of Structural and Cellular Biology, Tulane University School of Medicine, New Orleans, LA, United States
[6]Department of Neurosurgery and Ochsner Neuroscience Institute, Ochsner Health System, New Orleans, LA, United States
[7]Department of Anatomical Sciences, St. George's University, Grenada, West Indies
[8]Department of Normal and Clinical Anatomy, Medical University of Lodz, Poland

The rapid development of sciences such as genetics and molecular biology offers hope that better therapeutic methods can be developed and diagnosis and treatment made more effective. However, we must not forget that the basis for understanding the complex mechanisms of diseases and associated symptoms is knowledge of the relevant location and correlation among organs. In the present study, we focus on the clinical significance of the inferior phrenic artery. The diaphragm is a muscular structure that separates the abdominal and chest cavities. Thanks to this position, the inferior phrenic artery is much more significant than formerly assumed. A rich network of collaterals makes this vessel important in the development of neoplasms and metastases. Knowledge of anatomical variants of the inferior phrenic artery is also crucial for radiological procedures such as embolisation. The main aim of this study is to review the involvement of the inferior phrenic artery in physiological and pathophysiological processes. This work has value for all practicing doctors, especially radiologists and surgeons. (Folia Morphol 2023; 82, 3: 467–477)

Key words: inferior phrenic artery, diaphragm vascularisation, morphological variations, accessory inferior artery, hepatocellular carcinoma, pseudoaneurysm, embolisation

INTRODUCTION

The diaphragm is a dome-shaped muscular structure that separates the thoracic and abdominal cavities [5]. It is vascularised from several sources. Its cranial side is supplied by the pericardiacophrenic, musculophrenic, and superior phrenic arteries [32, 33]. However, the main donors of arterial blood to the diaphragm are the inferior phrenic arteries (IPAs) [5]. In the most common anatomical pattern, these ves-

sels branch off the abdominal aorta. Each then crosses the crus of the diaphragm. The IPAs are located on the abdominal surface at an angle. Each vessel then divides into ascending and descending branches. The bifurcation is near the dorsal part of the central tendon of the diaphragm [21]. The ascending branch creates anastomoses with other arteries that supply the organ, namely the musculophrenic and pericardiacophrenic arteries and the same vessels on

the opposite side [21]. The ascending branch of the left inferior phrenic artery (LIPA) crosses behind the oesophagus. It is then located on the left side of the aortic hiatus. The ascending branch of the right inferior phrenic artery (RIPA) runs behind the inferior vena cava. Thereafter, it is located on the right side of the vena cava foramen [21]. The descending branches of the IPAs anastomose with branches of the 8th to 12th intercostal arteries and the musculophrenic artery [5].

The provision of fresh arterial blood rich in oxygen is a precondition for keeping every organ alive [36]. The RIPA and LIPA are the most important sources of arterial blood for the diaphragm. This is highly physiologically significant because the diaphragm is crucial for respiration. It enables the thoracic cavity to expand during inspiration so that fresh air reaches the chest. Moreover, it prevents the withdrawal of gastric contents from the stomach into the oesophagus by occluding the gastroesophageal junction [5]. Branches of both the RIPA and LIPA also supply other organs such as the stomach, spleen, and oesophagus [37].

Anatomical variations of the RIPA and LIPA are well-known. Arteries often branch off abdominal arteries such as the gastric and renal arteries. The most common variant for both IPAs is an origin from the coeliac trunk. Interestingly, they can originate independently or via a common trunk [2, 3, 6, 7, 21].

Apart from providing blood to the diaphragm, the IPAs are also implicated in pathological conditions including pseudoaneurysm. The rupture of an IPA is life-threatening and requires early diagnosis and treatment [32]. Moreover, IPAs are particularly involved in the formation of extrahepatic collateral pathways that especially supply hepatocellular carcinomas [7]. They are also important in disorders caused by thoracic trauma, such as haemothorax [1].

The aim of this study is to assemble current knowledge about the physiological and clinical importance of IPAs and their anatomical variants. An important part of this review is the description of clinical syndromes related to these vessels. This knowledge is necessary for clinical practice, especially for radiologists and surgeons performing procedures pertaining to IPAs such as embolisation.

ANATOMICAL VARIANTS

Various types of IPA origin have been thoroughly described in recent studies. Aslaner et al. [2] proposed an interesting division of these arteries, distinguishing two main groups:

— arteries originating independently without a trunk (Table 1, Figs. 1–5);
— arteries originating via a common trunk (Tables 2, 3, Fig. 6).

The tables present the frequency of each type according to previous investigations. The papers by various researchers differ in the number of cases analysed, the type of arterial detection method, and the classification system [2, 3, 6, 7, 17, 21, 38].

Aslaner et al. [2] examined 1190 patients by abdominal computed tomography (CT) angiography (CTA). The images assessed included those obtained from patients with histories of mesenteric ischaemia, peripheral arterial disease, renal artery stenosis, and aortic aneurysm and donors for renal transplantation. Patients with histories of hepatocellular carcinoma, liver disease, or severe atherosclerosis and those who had undergone transarterial chemoembolisation or endovascular or surgical treatment of the aorta were excluded from this investigation. Each image was assessed for IPA origin by radiologists, followed by statistical analysis [2]. Their classification was very accurate. This is the only study that described four possible origins of the RIPA and LIPA via a common trunk (Table 1, Fig. 6). Greig et al. [6] examined 425 cases by dissection. American whites and blacks of both sexes were included in their study, which described all the patterns of arterial derivation found. Interestingly, Greig et al. [6] described a LIPA branching from the accessory left hepatic artery (Fig. 4) and a RIPA originating from the accessory right hepatic artery and spermatic artery (Fig. 2). These variants have not been described elsewhere.

Kimura et al. [17] analysed the type of origin of RIPA only. They examined 178 patients with hepatocellular carcinoma who required transcatheter arterial chemoembolisation via the RIPA. They used angiography to detect the origin pattern and relationship of the vessel to the coeliac, superior mesenteric, and right renal arteries. They described a RIPA arising from the dorsal pancreatic artery (Fig. 2). This type has not been reported in other investigations.

Gürses et al. [7] examined 26 cadavers (24 males and 2 females) by classical anatomical dissection. They resected the diaphragm, abdominal aorta, both kidneys, and the suprarenal glands in order to visualise the course of the IPAs. Their dissection also revealed branches of the RIPA and LIPA (Figs. 1, 3).

Szewczyk et al. [37] dissected the upper abdominal regions of 48 Caucasian cadavers (29 males and 19 females). All the specimens were free of trauma,

Table 1. Types of right inferior phrenic artery and left inferior phrenic artery origin by a common trunk

Types of origin	Greig et al., 1951	Loukas et al., 2005	Kimura et al., 2007	Basile et al., 2008	Gürses et al., 2015	Aslaner et al., 2017	Szewczyk et al., 2020
Abdominal aorta	18.1%	31%	21%	21%	11.53%	16.4%	6.24%
Coeliac trunk	12.1%	11%	9%	16%	7.69%	12.6%	–
Right renal artery	–	–	–	–	-	0.4%	–
Left gastric artery	0.7%	–	–	-	–	0.1%	–

Table 2. Types of separate origin of right inferior phrenic artery (without common trunk)

Types of origin	Greig et al., 1951	Loukas et al., 2005	Kimura et al., 2007	Basile et al., 2008	Gürses et al., 2015	Aslaner et al., 2017
Abdominal aorta	28%	30.67%	36%	28%	50%	25.2%
Coeliac trunk	29.2%	36%	20.79%	25%	3.85%	30.7%
Right renal artery	–	17%	11%	5.5%	7.69%	10.4%
Left gastric artery	1.9%	3%	2%	4%	3.85%	4.1%
Common hepatic artery	–	–	–	–	–	0.1%
Accessory right hepatic artery	0.2%	–	–	–	–	–
Spermatic artery	0.2%	–	–	–	–	–
Dorsal pancreatic artery	–	–	1%	–	–	–
Proper hepatic artery	–	2%	–	0.5%	–	–

Table 3. Types of separate origin of left inferior phrenic artery (without common trunk)

Types of origin	Greig et al., 1951	Loukas et al., 2005	Basile et al., 2008	Gürses et al., 2015	Aslaner et al., 2017
Abdominal aorta	25.9%	37.67%	26.5%	34.61%	25.2%
Coeliac trunk	40%	43%	28%	23.07%	40.3%
Left gastric artery	1.9%	2%	–	–	2.4%
Left renal artery	–	5%	1%	–	2%
Left hepatic artery	–	–	–	–	0.5%
Right renal artery	–	–	–	–	0.1%
Accessory left hepatic artery	0.2%	–	–	–	–
Proper hepatic artery	–	1%	–	–	–
Splenic artery	–	–	1%	–	–

pathology, or prior surgery in the upper abdominal organs. The authors examined the origins of the LIPA and RIPA and their diameters.

Loukas et al. [21] examined 300 adult human cadavers (120 females and 180 males) by dissection. They excised the inferior vena cava, liver, superior and inferior mesenteric arteries, stomach, pancreas, and coeliac and superior mesenteric nerve plexuses. This allowed a clear field of visualisation to be obtained. The spleen, both kidneys, and the suprarenal glands were not removed. In this study, the termination of the IPAs was also examined. The diameter of each IPA was measured. Interestingly, the authors described a case of a LIPA branching from the proper hepatic artery (Fig. 5). This has not been seen in other studies [21].

Basile et al. [3] examined 200 patients with hepatocellular carcinoma by 16-section CT during the arterial phase. They found a very rare case of a LIPA arising from the splenic artery (Fig. 5). This type of LIPA origin has not been presented in other investigations.

LIPA and RIPA branching by a common trunk have significantly less varied types. All authors presented in Table 1 agree that the most common type of such or-
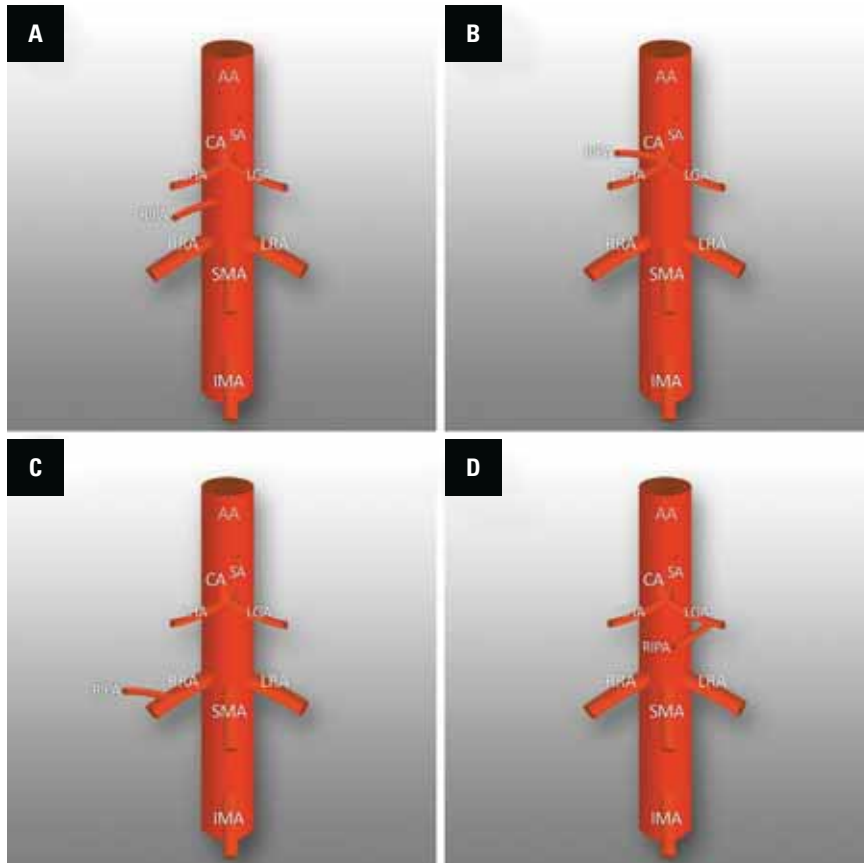
Figure 1. A. Right inferior phrenic artery (RIPA) (without common trunk) from abdominal aorta; **B.** RIPA (without common trunk) from coeliac trunk; **C.** RIPA (without common trunk) from right renal artery; **D.** RIPA (without common trunk) from the left gastric artery; AA — abdominal aorta; CA — coeliac artery; SA — splenic artery; CHA — common hepatic artery; LGA — left gastric artery; RRA — right renal artery; LRA — left renal artery; SMA — superior mesenteric artery; IMA — inferior mesenteric artery.

Figure 2. A. Right inferior phrenic artery (RIPA) (without common trunk) from common hepatic artery; **B.** RIPA (without common trunk) from accessory right hepatic artery; **C.** RIPA (without common trunk) from spermatic artery; **D.** RIPA (without common trunk) from the dorsal pancreatic artery; AA — abdominal aorta; CA — coeliac artery; SA — splenic artery; CHA — common hepatic artery; LGA — left gastric artery; RRA — right renal artery; LRA — left renal artery; SMA — superior mesenteric artery; IMA — inferior mesenteric artery; LHA — left hepatic artery; RHA — right hepatic artery; PSP — posterior superior pancreaticoduodenal artery; PSA — superior pancreaticoduodenal artery; PHA — proper hepatic artery; AGD — gastroduodenal artery; aRHA — accessory right hepatic artery; SpA — spermatic artery; DPA — dorsal pancreatic artery.
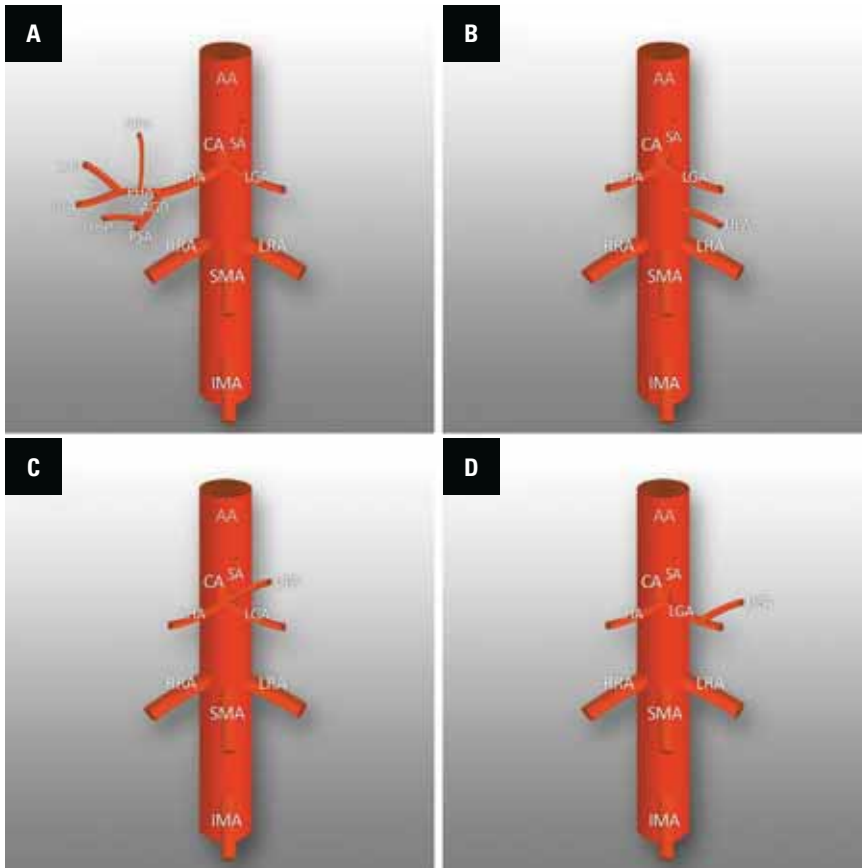
Figure 3. A. Right inferior phrenic artery (RIPA) (without common trunk) from proper hepatic artery; B. Left inferior phrenic artery (LIPA) (without common trunk) from abdominal aorta; **C.** LIPA (without common trunk) from coeliac trunk; **D.** LIPA (without common trunk) from the left gastric artery; AA — abdominal aorta; CA — coeliac artery; SA — splenic artery; CHA — common hepatic artery; LGA — left gastric artery; RRA — right renal artery; LRA — left renal artery; SMA — superior mesenteric artery; IMA — inferior mesenteric artery; LHA — left hepatic artery; RHA — right hepatic artery; PSP — posterior superior pancreaticoduodenal artery; PSA — superior pancreaticoduodenal artery; PHA — proper hepatic artery; AGD — gastroduodenal artery.
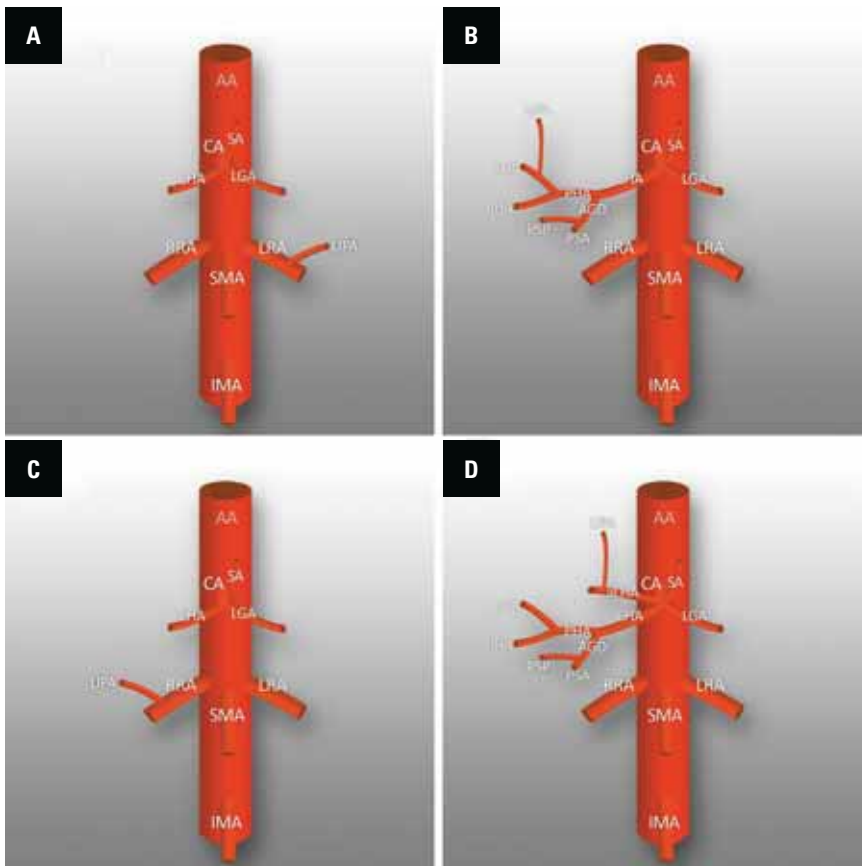
Figure 4. A. Left inferior phrenic artery (LIPA) (without common trunk) from left renal artery; **B.** LIPA (without common trunk) from left hepatic artery; **C.** LIPA (without common trunk) from right renal artery; **D.** LIPA (without common trunk) from accessory left hepatic artery; AA — abdominal aorta; CA — coeliac artery; SA — splenic artery; CHA — common hepatic artery; LGA — left gastric artery; RRA — right renal artery; LRA — left renal artery; SMA — superior mesenteric artery; IMA — inferior mesenteric artery; LHA — left hepatic artery; RHA — right hepatic artery; PSP — posterior superior pancreaticoduodenal artery; PSA — superior pancreaticoduodenal artery; PHA — proper hepatic artery; AGD — gastroduodenal artery; aLHA — accessory left hepatic artery.
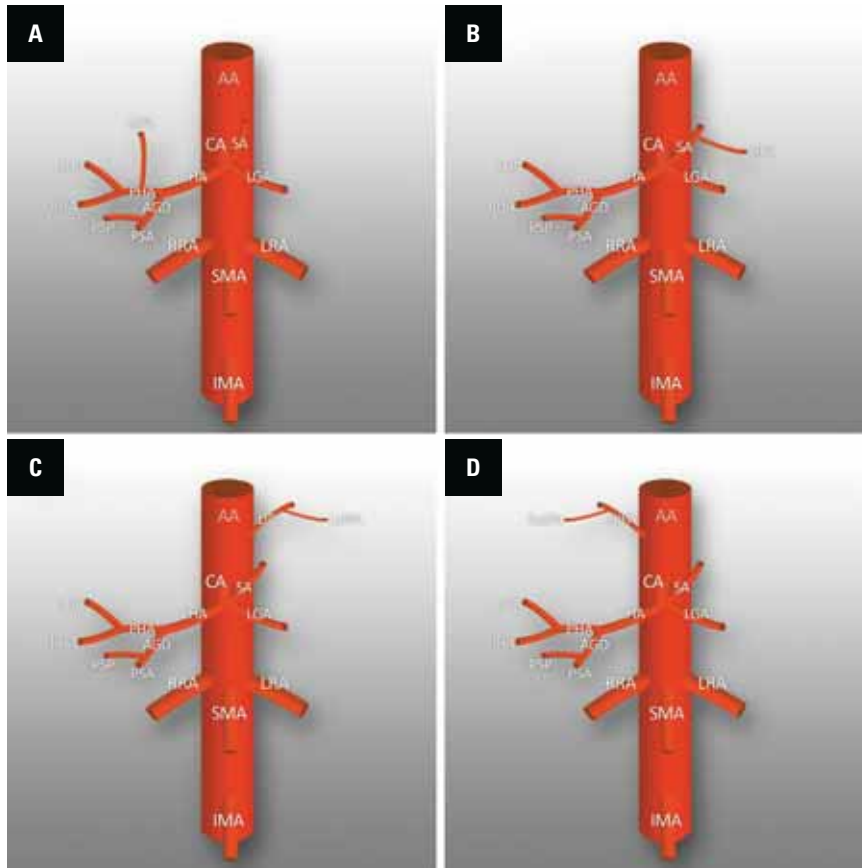
Figure 5. A. Left inferior phrenic artery (LIPA) (without common trunk) from proper hepatic artery; **B.** LIPA (without common trunk) from splenic artery; **C, D.** Accessory inferior phrenic artery from the inferior phrenic artery; AA — abdominal aorta; CA — coeliac artery; SA — splenic artery; CHA — common hepatic artery; LGA — left gastric artery; RRA — right renal artery; LRA — left renal artery; SMA — 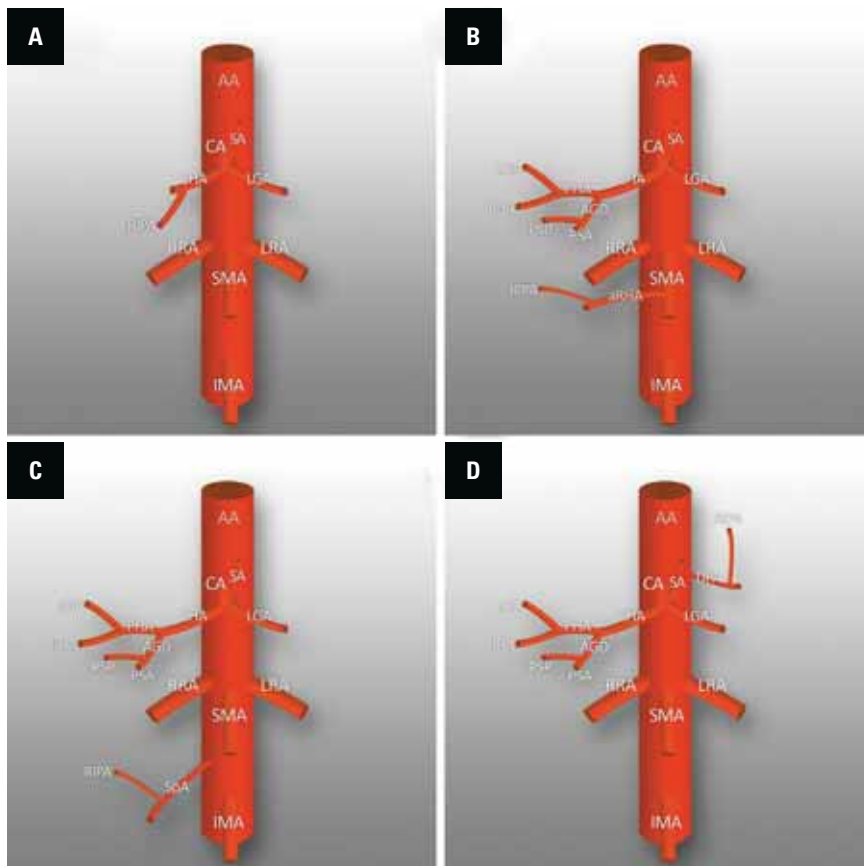superior mesenteric artery; IMA — inferior mesenteric artery; LHA — left hepatic artery; RHA — right hepatic artery; PSP — posterior superior pancreaticoduodenal artery; PSA — superior pancreaticoduodenal artery; PHA — proper hepatic artery; AGD — gastroduodenal artery; LaIPA — left accessory inferior phrenic artery; RaIPA — right accessory inferior phrenic artery.
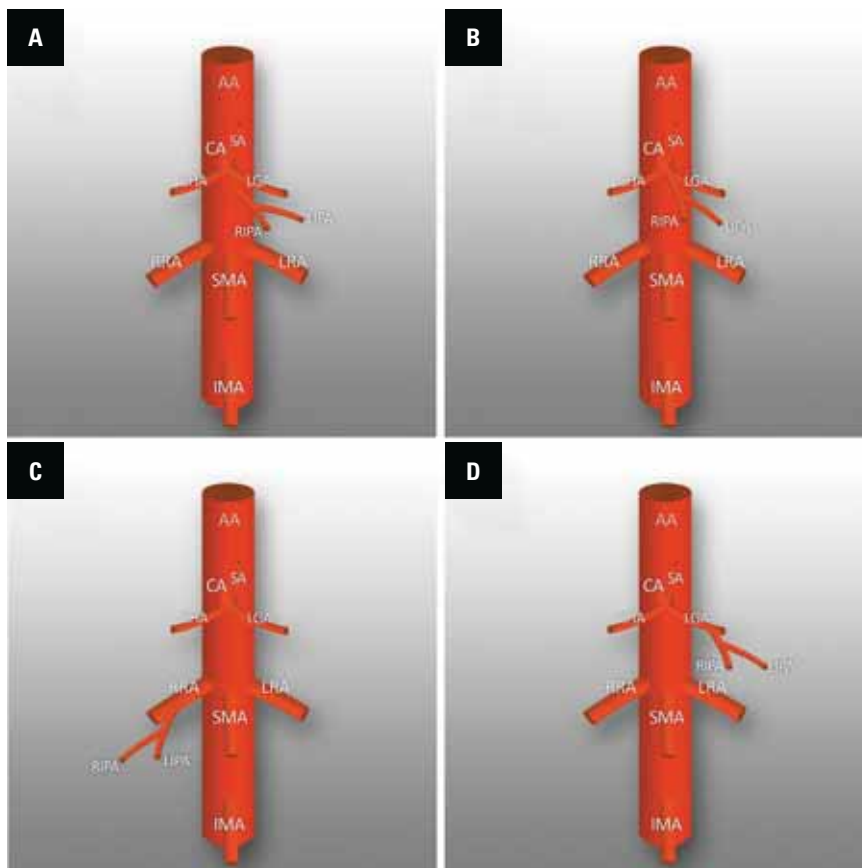
Figure 6. A. Right inferior phrenic artery (RIPA) and left inferior phrenic artery (LIPA) origin by a common trunk from the abdominal aorta; **B.** RIPA and LIPA origin by a common trunk from coeliac artery; **C.** RIPA and LIPA origin by a common trunk from right renal artery; **D.** RIPA and LIPA origin by a common trunk from the left gastric artery; AA — abdominal aorta; CA — coeliac artery; SA — splenic artery; CHA — common hepatic artery; LGA — left gastric artery; RRA — right renal artery; LRA — left renal artery; SMA — superior mesenteric artery; IMA — inferior mesenteric artery.

igin is from the abdominal aorta. Therefore, this trait is definitely well established in the human population.

According to Kimura et al. [17], Basile et al. [3], and Gürses et al. [7], RIPA branching from the abdominal aorta is the most common type of origin of this artery. These studies are in line with the classical anatomical pattern. However, according to Greig et al. [6], Loukas et al. [21], and Aslaner et al. [2], the RIPA arises much more frequently from the coeliac trunk. In our opinion, more investigations are necessary to determine whether the current anatomical pattern should be changed.

Interestingly, the most common type of LIPA origin according to Greig et al. [6], Loukas et al. [21], Basile et al. [3], and Aslaner et al. [2] is a branch from the coeliac trunk. This is not in line with the accepted anatomical pattern, which assumes that both the LIPA and RIPA arise most frequently from the abdominal aorta. The study by Gürses et al. [7] is the only one that confirmed the classical pattern accepted by medical universities, raising the question of whether it should be changed.

The foregoing tables present the frequency of occurrence of IPAs arising from various arterial vessels. However, we propose our own classification of IPA origins based on the available literature (Table 4). The most important feature of our classification is the presentation of complex correlations in a simple, easy-to-remember way. This system focuses on the location of origin only. We do not include the frequency, side of the body, or kind of branching (by a common trunk or direct). Therefore, it is more readable and potentially valuable in the clinical setting, where knowledge of the origins of various arteries is crucial for surgical or radiological procedures.

RELATIONSHIP BETWEEN ORIGIN OF IPA AND AORTA

The above tables present the frequency of IPAs arising from the aorta. However, the exact location in relation to the aorta is not shown; these arteries can branch off from it at different levels or sides. Several researchers have described this type of IPA origin more precisely [3, 17, 35]. Basile et al. [3] found cases of the RIPA and LIPA originating via a common trunk from the aorta at the left side of the coeliac trunk (12%) or from the middle ventral aortic wall above the origin of the coeliac trunk (9%). Kimura et al. [17] distinguished three classes of RIPA branches from the aorta: supracoeliac (32%), between the

Table 4. New classification system based on the available literature proposed by Marcinkowska et al.

Type	Description
I	Hepatic arteries*
	A — common hepatic artery
	B — proper hepatic artery
	C — left hepatic artery
	D — accessory left hepatic artery
	E — accessory right hepatic artery
II	Coeliac trunk and its branches**
	A — coeliac trunk
	B — left gastric artery
	C — splenic artery
III	Renal arteries
	A — right renal artery
	B — left renal artery
IV	Abdominal aorta
V	Dorsal pancreatic artery
VI	Spermatic artery

*This type contains blood vessels that are the main arterial supply to the liver
**This type includes the coeliac trunk and its branches without the common hepatic arteries, which are included in type I

coeliac trunk and superior mesenteric artery (17%), and between the superior mesenteric and right renal arteries (8%). So et al. [35] also examined RIPA origin sites and offered more precise descriptions. They distinguished five origin types: supracoeliac (20.5%), juxtacoeliac (11.7%), between the coeliac trunk and superior mesenteric artery (12.3%), juxta-superior mesenteric artery (7.9%), and suprarenal (5.5%).

BRANCHES OF THE INFERIOR PHRENIC ARTERY

Inferior phrenic arteries give off several branches and arteries that supply other structures [2, 6, 21, 22, 37]:
— superior adrenal artery — this vessel is one of three arteries that supply the suprarenal gland, which is known for its rich vascularity. The other two are the inferior adrenal and middle adrenal arteries, branching from the renal artery and aorta respectively;
— branches to the spleen;
— branches to the liver;
— branches to the stomach;
— branches to the oesophagus;
— branches to the inferior vena cava;
— branches to the retroperitoneum;
— branches to the kidney and renal capsule.

It has also been reported that IPA scan gives off aberrant vessels:

— accessory left gastric artery — Heymann et al. [11] presented five cases of such abnormalities as revealed by angiography. In these patients, a conventional left gastric artery arose from the coeliac trunk, but each patient had an additional vessel supplying the gastric fundus. The frequency of an accessory gastric artery is unknown. However, its appearance can be significant in surgical procedures involving the gastric fundus; for example, in bariatric embolisation and angiography for upper gastrointestinal bleeding;

— dorsal pancreatic artery — this vessel supplies blood to the dorsal part of the pancreatic body. It is divided into two branches. The right branch creates anastomoses with branches from the gastroduodenal artery. The left branch (called the transverse pancreatic artery) anastomoses with the great pancreatic artery. A dorsal pancreatic artery arising from the splenic artery is the most common anatomical pattern. However, Hagiwara et al. [9] presented a case in which this artery branched from the IPA; it was noted during transarterial chemoembolisation and subsequently confirmed by computed tomography;

— accessory inferior phrenic arteries.

Several studies have characterised the ascending and posterior branches of the LIPA, which can arise from various sources as independent arteries [7, 8]. Gürses et al. [7] presented an interesting case in which the ascending branch of the LIPA originated from the coeliac trunk and the posterior branch from the aorta. According to their statistical analysis, this variant occurs in 3.85% of cases. The same vascular variant was previously reported by Kim et al. [16].

A rare case of accessory phrenic arteries was described by Zeng et al. [38]. In a 69-year-old male, interventional radiography revealed a LIPA supplying the lesser curvature of the stomach and a right accessory phrenic artery conveying blood to the duodenum. Such variants of the gastrointestinal vascular system are significant in the planning of upper abdominal surgery.

DIAGNOSTICS

Effective surgical intervention for vascular disease depends on accurate diagnosis and identification of the location and type of lesion [26].Owing to the variable anatomy of the IPA, preoperative diagnosis is very helpful in planning surgical procedures and thus optimizing treatment outcomes [3].

A method that is currently widely used in the diagnosis of vascular pathology is magnetic resonance angiography [24]. It is gaining popularity because it is a safer and non-invasive alternative to digital X-ray angiography [14]. In addition, this technique avoids ionizing radiation and employs a contrast agent that is not nephrotoxic and is much less frequently associated with allergic reactions [12]. Magnetic resonance angiography (MRA) can be used with a variety of techniques. In particular, we distinguish between techniques that require contrast and those that do not [24]. One technique that does not use contrast is balanced steady-state free precession, which is a method of visualisation aneurysms. Imaging with this procedure allows differentiation of blood in the vessel lumen and thrombus. However, contrast-enhanced MRA (CE-MRA) is a more precise and reproducible technique that can be performed in seconds with relatively few artifacts, especially in comparison to non-contrast techniques [24]. Dynamic magnetic resonance (MR) imaging using three-dimensional (3D) gradient-echo with fat-suppression has become important in abdominal MR studies. Thin-segmented, multiphase, 3D contrast-enhanced dynamic MR sequences with fat suppression are potentially useful for imaging small abdominal vessels such as the IPAs [13]. These are clinically relevant because, for example, they can be a source of bleeding resulting from trauma or can be the vessels supplying hepatocellular carcinoma. Fat suppression is essential for evaluating small IPAs because high signals from fat and chemical shift artifacts impair the visualisation of these vessels. Fat suppression by increasing the contrast between enhanced vessels and low-signal fat can improve the visualisation of IPAs [13].

Computed tomography angiography is another important tool in vascular imaging. Furthermore, it is also employed to detect complications after treatment, such as thrombosis or internal leakage after aneurysm repair [18]. CTA is a quick diagnostic imaging procedure that produces images of blood vessels after injecting a contrast agent and using X-rays. Two-dimensional (2D) and 3D visualisation methods are routinely used in CTA to obtain images comparable to those obtained via catheter angiography. There are also several post-processing methods that include multiplanar reconstruction, maximum intensity projection (MIP), curved planar

reconstruction, and volume rendering. Multiplanar reconstruction produces images in arbitrary planes, resulting in quantitative analysis of both the lumen and the vessel wall. However, it can only generate 2D images [20]. Curved planar reconstruction is also a 2D image, displaying a cross-section of the vessel along its entire length, which is clearly visualized [31]. Volume rendering images preserve the original anatomical spatial relationships and have a 3D appearance, so vascular interrelationships can be visualised. In contrast, MIP is valuable as an additional display, especially for imaging smaller vessels [29]. Noninvasive vascular imaging by CTA has become an increasingly relevant diagnostic technique. Multidetector computed tomography angiography (MDCTA) is a quick and precise method for vascular anatomical assessment and diagnosis of vascular abnormalities [15]. This technique allows the anatomy of the IPA to be assessed in a relatively short time, which can be valuable in planning embolisation treatment sessions [3]. Specific advantages of MDCTA vascular imaging include more accurate visualisation of details, including stenoses and the presence and location of vascular anomalies. In addition, MIP rendering is valuable as an additional display, especially when smaller vessels are imaged [29]. MDCTA can reveal the real sizes of lesions such as aneurysms, thrombi, or arterial ruptures. Advances in MDCTA technology have contributed significantly to diagnosis and treatment planning in vascular disease [15]. Owing to the variable anatomy of the IPA, preoperative diagnostic MDCTA is very helpful in planning surgical procedures. This technique is also significant in imaging the different variants of the IPA, which helps in selective catheterisation of the vessel and eliminates the need for repeated contrast injections and angiograms in different projections [3].

CLINICAL RELEVANCE

It has been reported in the literature that IPAs are involved in several disorders and pathologic conditions. We reviewed the role of these arteries in diseases and clinical management below.

Inferior phrenic arteries are the main vessels supplying the diaphragm. In addition, they constitute extrahepatic collateral arterial pathways that supply hepatic malignancies. The RIPA and LIPA constitute more than half of the collaterals involved in forming the arterial pathways supplying hepatic malignancies,

the RIPA being the more common [7]. It has been estimated that RIPA is involved in 70–83% of extrahepatic arteries supplying hepatocellular carcinoma. Because it runs in direct contact with the bare area of the liver, the RIPA can form anastomoses with intrahepatic arteries. This facilitates the blood supply from the extrahepatic arteries to hepatic lesions when the natural tumour supply is impaired [23]. Apart from being an important extrahepatic artery for tumours of the liver, especially those located in the uncovered part of this organ, IPA also provides the essential blood supply to lung metastases [39].

Branches of the LIPA supply blood to the stomach and oesophagus and can also be involved in arterial bleeding at the oesophagus-gastric junction and Mallory-Weiss tears [7, 27, 34].

The LIPA can also be involved in atherosclerotic ischaemic heart disease, anastomosing with trans-diaphragmatic collaterals, and the left anterior descending coronary artery. This anastomosis arises from a connection between the LIPA and pericardiophrenic musculophrenic arteries [2].

The development of IPA pseudoaneurysm also has been described in the literature [19, 25, 32]. Such disorders are a consequence of partial or complete rupture of the vessel wall, leading to haemorrhage [28]. It is worth emphasizing that IPAs can be responsible for haemoperitoneum or haemothorax as a result of their pseudoaneurysm rupture [10, 19].

The IPA can also have a role in diaphragm injury. A very rare case of diaphragmatic rupture during cardiopulmonary resuscitation has been reported. Digital subtraction angiography revealed active bleeding from a branch of the RIPA. Thus, it is important to recognize the possibility that organs such as the diaphragm can be injured during energetic cardiopulmonary resuscitation [30].

The IPAs can also have a major role in diaphragmatic hernia repair, especially when rare anatomical defects or abnormal-looking vessels are involved. Calin et al. [4] described a rare case of diaphragmatic hernia in which an abnormally-sized LIPA presented a challenge to surgery. Knowledge of IPA variants is also necessary for treating surgical and traumatic vessel injuries and haemoptysis, especially when caused by pulmonary pathologies. However, when the arteries of vital organs are stenosed, the IPAs are key to preventing the development of ischaemia in those organs [2].

CONLUSIONS

The IPA has the ability to form rich collaterals with other arteries located in the thoracic and abdominal cavities. Thanks to this, it has an important role in pathological processes, the most common of which is supplying hepatic malignancies. Moreover, the IPA can become a pathway of lung metastasis. IPA injuries almost always result in life-threatening bleeding. On the other hand, this arterial vessel has great potential for protecting vital organs when their main arteries are stenosed. The present study demonstrates that knowledge of the anatomy of human blood vessels is helpful for better understanding of physiological and pathophysiological processes.

Ethical approval and consent to participate

Acknowledgements

Conflict of interest: None declared

REFERENCES

1. Ahn HJ, Lee JW, Kim KD, et al. Phrenic arterial injury presenting as delayed hemothorax complicating simple rib fracture. J Korean Med Sci. 2016; 31(4): 641–643, doi: 10.3346/jkms.2016.31.4.641, indexed in Pubmed: 27051252.

2. Aslaner R, Pekcevik Y, Sahin H, et al. Variations in the origin of inferior phrenic arteries and their relationship to celiac axis variations on CT angiography. Korean J Radiol. 2017; 18(2): 336–344, doi: 10.3348/kjr.2017.18.2.336, indexed in Pubmed: 28246513.

3. Basile A, Tsetis D, Montineri A, et al. MDCT anatomic assessment of right inferior phrenic artery origin related to potential supply to hepatocellular carcinoma and its embolization. Cardiovasc Intervent Radiol. 2008; 31(2): 349–358, doi: 10.1007/s00270-007-9236-x, indexed in Pubmed: 18071790.

4. Calin ML, Arevalo G, Harris K, et al. Large sized left inferior phrenic artery and parahiatal type of diaphragmatic hernia generating confusion during robotic surgical repair. J Laparoendosc Adv Surg Tech A. 2017; 27(3): 283–287, doi: 10.1089/lap.2016.0392, indexed in Pubmed: 27585397.

5. Downey R. Anatomy of the normal diaphragm. Thorac Surg Clin. 2011; 21(2): 273–279, ix, doi: 10.1016/j.thorsurg.2011.01.001, indexed in Pubmed: 21477776.

6. Greig HW, Anson BJ, Coleman SS. The inferior phrenic artery; types of origin in 850 body-halves and diaphragmatic relationship. Q Bull Northwest Univ Med Sch. 1951; 25(4): 345–350, indexed in Pubmed: 14892223.

7. Gürses İA, Gayretli Ö, Kale A, et al. Inferior phrenic arteries and their branches, their anatomy and possible clinical importance: an experimental cadaver study. Balkan Med J. 2015; 32(2): 189–195, doi: 10.5152/balkanmedj.2015.150052, indexed in Pubmed: 26167344.

8. Gwon DIl, Ko GY, Yoon HK, et al. Inferior phrenic artery: anatomy, variations, pathologic conditions, and interventional management. Radiographics. 2007; 27(3): 687–705, doi: 10.1148/rg.273065036, indexed in Pubmed: 17495287.

9. Hagiwara A, Akai H, Kosaka T, et al. A dorsal pancreatic artery originating from the right inferior phrenic artery. J Vasc Interv Radiol. 2016; 27(1): 143–145, doi: 10.1016/j.jvir.2015.06.010, indexed in Pubmed: 26723925.

10. Handa A, Dhooria S, Sehgal IS, et al. Primary cavitary sarcoidosis: A case report, systematic review, and proposal of new diagnostic criteria. Lung India. 2018; 35(1): 41–46, doi: 10.4103/lungindia.lungindia_225_17, indexed in Pubmed: 29319033.

11. Heymann G, Shin DS, Johnson GE. Accessory left gastric artery arising from inferior phrenic artery: angiographic findings in 5 patients. J Vasc Interv Radiol. 2019; 30(10): 1687–1689, doi: 10.1016/j.jvir.2019.07.004, indexed in Pubmed: 31547929.

12. Insko EK, Carpenter JP. Magnetic resonance angiography. Semin Vasc Surg. 2004; 17(2): 83–101, doi: 10.1053/j.semvascsurg.2004.03.010, indexed in Pubmed: 15185174.

13. Ito K, Kim MJ, Mitchell DG, et al. Inferior phrenic arteries: depiction with thin-section three-dimensional contrast-enhanced dynamic MR imaging with fat suppression. J Magn Reson Imaging. 2001; 13(2): 201–206, doi: 10.1002/1522-2586(200102)13:2<201::aid-jmri1030>3.0.co;2-l, indexed in Pubmed: 11169825.

14. Ivancevic MK, Geerts L, Weadock WJ, et al. Technical principles of MR angiography methods. Magn Reson Imaging Clin N Am. 2009; 17(1): 1–11, doi: 10.1016/j.mric.2009.01.012, indexed in Pubmed: 19364596.

15. Kang PS, Spain JW. Multidetector CT angiography of the abdomen. Radiol Clin North Am. 2005; 43(6): 963–976, vii, doi: 10.1016/j.rcl.2005.07.007, indexed in Pubmed: 16253657.

16. Kim HC, Chung JW, An S, et al. Left inferior phrenic artery feeding hepatocellular carcinoma: angiographic anatomy using C-arm CT. Am J Roentgenol. 2009; 193(4): W288––W294, doi: 10.2214/AJR.09.2417, indexed in Pubmed: 19770297.

17. Kimura S, Okazaki M, Higashihara H, et al. Analysis of the origin of the right inferior phrenic artery in 178 patients with hepatocellular carcinoma treated by chemoembolization via the right inferior phrenic artery. Acta Radiol. 2007; 48(7): 728–733, doi: 10.1080/02841850701376334, indexed in Pubmed: 17729002.

18. Kumamaru KK, Hoppel BE, Mather RT, et al. CT angiography: current technology and clinical use. Radiol Clin North Am. 2010; 48(2): 213–235, vii, doi: 10.1016/j.rcl.2010.02.006, indexed in Pubmed: 20609871.

19. Lee JW, Kim S, Kim CW, et al. Massive hemoperitoneum due to ruptured inferior phrenic artery pseudoaneurysm after blunt trauma. Emerg Radiol. 2006; 13(3): 147–149, doi: 10.1007/s10140-006-0524-6, indexed in Pubmed: 17039340.

20. Lell MM, Anders K, Uder M, et al. New techniques in CT angiography. Radiographics. 2006; 26 (Suppl 1): S45––S62, doi: 10.1148/rg.26si065508, indexed in Pubmed: 17050518.

21. Loukas M, Hullett J, Wagner T. Clinical anatomy of the inferior phrenic artery. Clin Anat. 2005; 18(5): 357–365, doi: 10.1002/ca.20112, indexed in Pubmed: 15971218.

22. Mitty HA. Embryology, anatomy, and anomalies of the adrenal gland. Semin Roentgenol. 1988; 23(4): 271–279, doi: 10.1016/s0037-198x(88)80037-3, indexed in Pubmed: 3055310.

23. Moustafa AS, Abdel Aal AK, Ertel N, et al. Chemoembolization of hepatocellular carcinoma with extrahepatic collateral blood supply: anatomic and technical considerations. Radiographics. 2017; 37(3): 963–977, doi: 10.1148/rg.2017160122, indexed in Pubmed: 28362557.

24. Muhs BE, Verhagen HJM, Huddle MG, et al. Theory, technique, and practice of magnetic resonance angiography. Vascular. 2007; 15(6): 376–383, doi: 10.2310/6670.2007.00052, indexed in Pubmed: 18053424.

25. Nagar N, Dubale N, Jagadeesh R, et al. Unusual locations of pseudo aneurysms as a sequel of chronic pancreatitis. J Interv Gastroenterol. 2011; 1(1): 28–32, doi: 10.4161/jig.1.1.14597, indexed in Pubmed: 21686110.

26. Nonent M, Thouveny F, Simons P, et al. Iodixanol in multidetector-row computed tomography angiography (MDCTA): diagnostic accuracy for abdominal aorta and abdominal aortic major-branch diseases using four-, eight- and 16-detector-row CT scanners. Acta Radiol. 2007; 48(1): 48–58, doi: 10.1080/02841850601067629, indexed in Pubmed: 17325925.

27. Northrop CH, Studley MA, Smith GR. Hemorrhage from the gastroesophageal junction. A cryptic angiographic diagnosis. Radiology. 1975; 117(3 Pt 1): 531–532, doi: 10.1148/117.3.531, indexed in Pubmed: 1081239.

28. Núñez DB, Torres-León M, Múnera F. Vascular injuries of the neck and thoracic inlet: helical CT-angiographic correlation. Radiographics. 2004; 24(4): 1087–1100, doi: 10.1148/rg.244035035, indexed in Pubmed: 15256630.

29. Ozbulbul NI, Yurdakul M, Tola M, et al. Can multidetector row CT visualize the right and left inferior phrenic artery in a population without disease of the liver? Surg Radiol Anat. 2009; 31(9): 681–685, doi: 10.1007/s00276-009-0504-0, indexed in Pubmed: 19367353.

30. Rossi UG, Ierardi AM, Cariati M. Diaphragmatic rupture with inferior phrenic artery bleeding caused by cardiopulmonary resuscitation. Clin Exp Emerg Med. 2020; 7(3): 238–240, doi: 10.15441/ceem.19.044, indexed in Pubmed: 32482019.

31. Saba L, Mallarini G. Multidetector row CT angiography in the evaluation of the hepatic artery and its anatomical variants. Clin Radiol. 2008; 63(3): 312–321, doi: 10.1016/j.crad.2007.05.023, indexed in Pubmed: 18275872.

32. Salem JF, Haydar A, Hallal A. Inferior phrenic artery pseudoaneurysm complicating drug-induced acute pancreatitis. BMJ Case Rep. 2014; 2014, doi: 10.1136/bcr-2013-201049, indexed in Pubmed: 24385392.

33. Schumpelick V, Steinau G, Schlüper I, et al. Surgical embryology and anatomy of the diaphragm with surgical applications. Surg Clin North Am. 2000; 80(1): 213–239, xi, doi: 10.1016/s0039-6109(05)70403-5, indexed in Pubmed: 10685150.

34. Smith DC, Kitching GB. Angiographic demonstration of esophagogastric bleeding from the inferior phrenic artery. Radiology. 1977; 125(3): 613–614, doi: 10.1148/125.3.613, indexed in Pubmed: 303782.

35. So YH, Chung JW, Yin Y, et al. The right inferior phrenic artery: origin and proximal anatomy on digital subtraction angiography and thin-section helical computed tomography. J Vasc Interv Radiol. 2009; 20(9): 1164–1171, doi: 10.1016/j.jvir.2009.05.036, indexed in Pubmed: 19631560.

36. Sperryn PN. Blood. Br J Sports Med. 1989; 23(2): 129–131, doi: 10.1136/bjsm.23.2.129, indexed in Pubmed: 2605442.

37. Szewczyk B, Karauda P, Olewnik Ł, et al. Types of inferior phrenic arteries: a new point of view based on a cadaveric study. Folia Morphol. 2021; 80(3): 567–574, doi: 10.5603/FM.a2020.0079, indexed in Pubmed: 32710792.

38. Zeng R, Yao Z, Chen Y, et al. Variant arterial supply to the lesser curvature of the stomach and duodenum from double inferior phrenic arteries. Surg Radiol Anat. 2015; 37(7): 867–869, doi: 10.1007/s00276-014-1392-5, indexed in Pubmed: 25380829.

39. Zhu LZ, Yang RJ, Zhu Xu. Role of inferior phrenic artery in the interventional treatment of lung metastases tumor: a report of 11 cases. J Cancer Res Ther. 2018; 14(1): 61–67, doi: 10.4103/jcrt.JCRT_742_17, indexed in Pubmed: 29516961.

VIA MEDICA

REVIEW ARTICLE

The divided zygoma: a meta-analysis of its prevalence with a review of the literature

D. Plutecki[1], M. Bonczar[2], P. Ostrowski[2], R. Canon[2], M. Dziedzic[2], I. Zamojska[2], J. Walocha[2], M. Koziej[2]

[1]Collegium Medicum, Jan Kochanowski University, Kielce, Poland
[2]Department of Anatomy, Jagiellonian University Medical College, Krakow, Poland

Background: Divided zygoma (DZ) is an important structure in the midfacial region. The anatomy of DZ is poorly researched, but knowledge about this entity could be useful during posttraumatic facial reconstructions. The aim of this study was to estimate the prevalence and anatomy of DZ in different regions around the world. Therefore, the authors performed a meta-analysis, including all studies that report extractable data on the DZ.

Materials and methods: The main online medical databases such as PubMed, EBSCO, ScienceDirect, Web of Science, SciELO, BIOSIS, Current Content Connect, Korean Journal Database and Russian Citation Index, were utilised to gather all studies on anatomical characteristics, prevalence, symmetry, and a number of divisions of zygomatic bone.

Results: A total of 20 studies were included in this meta-analysis. Data were grouped and analysed in five categories: (1) prevalence of DZ bone, (2) prevalence of DZ skulls, (3) gender prevalence of DZ with sides, (4) divisions of zygomatic bone, (5) symmetry of DZ.

Conclusions: In conclusion, the authors of the present study believe that this study can be considered an up-to-date meta-analysis regarding the prevalence, divisions, and symmetricity of the DZ. The data provided by the present study may be useful information for physicians in recognizing the DZ of the fracture and may be important information during zygomatic bone osteotomy. Detailed anatomical knowledge of the midfacial region can prevent surgical complications when operating in this area. (Folia Morphol 2023; 82, 3: 478–486)

Key words: os japonicum, divided zygoma, zygomatic bone, bipartite zygomatic bone, tripartite zygomatic bone, facial surgery, facial reconstruction

Address for correspondence: Dr. M. Koziej, Department of Anatomy, Jagiellonian University Medical College, ul. Mikołaja Kopernika 12, 33–332 Kraków, Poland, e-mail: mateusz.koziej@gmail.com

INTRODUCTION

Divided zygoma (DZ), also called os japonicum (OJ) because of its relatively high frequencies among modern human populations in Japan [19], is a division of zygomatic bone into two or more partitions. The division of the malar bone is accepted as an epigenetic variation [35]. Hilgendorf [17] observed two zygomatic bones out of 11 Japanese skulls showing bipartition, and that was the reason for the name OJ. Although some authors pointed out that the frequency of DZ in the Japanese population is too low to consider this character as a Japanese trait [30], many authors still use this synonym. Typically, the zygoma is a single midfacial bone and plays a significant role in the support and integration of the craniofacial skeleton, and the masticatory apparatus by its attachment to the masseter muscle [47]. It also contributes to the formation of the lateral wall and floor of the orbit, parts of the temporal and infratemporal fossa [44]. The zygomatic bone has three surfaces: malar, temporal and orbital. The malar surface has a small aperture for the passage of zygomatico-facial vessels and nerves [25].

There are great differences in opinion regarding the ossification of the zygomatic bone. Generally, it is thought that the human zygoma has only one ossification centre, which appears in the fetus at 8 weeks [5, 11, 28, 31, 45]. However, Buchanan's Manual of Anatomy [22] emphasizes that three ossification centres of the anterior, posterior, and inferior parts of the zygoma fuse to form the mature bone. Consequently, the DZ will occur if these three ossification centres fail to fuse, resulting in zygomaticum bipartitum or more divisions [22].

The sutures of the craniofacial skeleton are described as fibrous joints, serving as important loci of craniofacial growth through their interactions with surrounding tissues and structures, especially the zygomatico-facial vessels and nerves [34, 38]. Biomechanically, sutures are relatively weak sites in the otherwise rigid skull [41–43]. Zygomatic fractures are one of the most common facial bone fractures due to the prominent location of the zygoma that makes it prone to injuries [4]. This type of injury is common in contact sports or car accidents, which cause extensive and multiple fractures [25]. Supernumerary sutures could be misinterpreted as fracture lines in the radiograph plain, even if these lines do not have a typical appearance of a zygomatic fracture [32, 49]. It is crucial to differentiate fracture lines from sutures on the malar bone during craniofacial, maxillofacial, or zygomatic bone osteotomy reconstruction procedures [29].

The "norm" in anatomy is not as precise a concept as one would wish, and can be considered an approximation [50]. Understanding the variability of the zygomatic bone can be of great clinical significance when performing facial plastic and reconstructive surgeries, such as posttraumatic facial reconstructions. Detailed and precise anatomical knowledge is essential for surgeons in order to minimise potential complications associated with the craniofacial area. Therefore, the objective of the present study was to provide physicians, especially surgeons, with useful data on the prevalence of DZ and its anatomical features. To achieve this, a systematic search of the literature and a meta-analysis were performed.

MATERIALS AND METHODS

Search strategy

Online medical databases such as PubMed, ScienceDirect, EBSCO, Web of Science, SciELO, BIOSIS, Current Content Connect, Korean Journal Database, and Russian Citation Index, were used to gather all studies on anatomical characteristics, prevalence, symmetry, and a number of divisions of zygoma. The study collection ended in May 2022. In agreement with the Boolean technique, the following search terms were employed: (os japonicum) OR (divided zygoma) OR (bipartite zygomatic bone) OR (tripartite zygomatic bone). Search terms were individually adapted to each database to minimise potential bias. Neither the date, language, type of article, nor text availability conditions were applied. An additional search was conducted through the references of the identified studies at the end of the search stage to ensure the accuracy of the process. During the study, the Preferred Reporting Items for Systematic Reviews and Meta-Analyses (PRISMA) guidelines were followed. Furthermore, the Critical Appraisal Tool for Anatomical Meta-analysis (CATAM) was used to provide the highest quality findings [6].

Eligibility assessment

The database search and the manual search identified a total of 347 studies that were initially evaluated by two independent reviewers. In addition, nine studies were added through reference searching. After removing duplicates and irrelevant records, a total of

479

22 articles were qualified for full text evaluation. To minimise potential bias and maintain accurate statistical methodology, articles such as case reports, case series, conference reports, reviews, letters to editors, and studies that provided incomplete or irrelevant data were excluded. The inclusion criteria consisted of original studies with extractable numerical data on the subject of this study. Finally, a total of 20 studies were included in this meta-analysis. Additionally, the AQUA Tool, which was specifically designed for anatomical meta-analyses, was used to minimise the potential bias of included studies [16].

Data extraction

Data from qualified studies were extracted by two independent reviewers. Qualitative data, such as year of publication, country and continent of origin, data collection methodology, and information on diseases in the studied groups, were collected. Quantitative data, such as sample size, numerical data on anatomical characteristics, prevalence, symmetry, and divisions of zygomatic bone, were also collected. Any discrepancies between studies identified by the two reviewers, were resolved by contacting the authors of the original studies whenever possible or by consensus with a third reviewer.

Statistical analysis

To perform the meta-analyses, STATISTICA version 13.1 software (StatSoft Inc., Tulsa, OK, USA) and MetaXL version 5.3 software (EpiGear International Pty Ltd., Wilston, Queensland, Australia) were used. A random-effects model was used in all analyses. The heterogeneity among the studies was evaluated, using both the chi-square test and the I-square statistic. The I-squared statistic was interpreted as follows: 0–40% as "might not be important"; 30–60% as "may represent moderate heterogeneity"; 50–90% as "may represent substantial heterogeneity"; 75–100% as "may represent considerable heterogeneity". The p-value < 0.05 and the confidence intervals (95% CI) were used to find statistically significant differences between the studied groups. In the case of overlapping confidence intervals, differences were considered statistically insignificant.

RESULTS

Search results

After the 22 selections of the initially accepted studies, a total of two studies were excluded. They
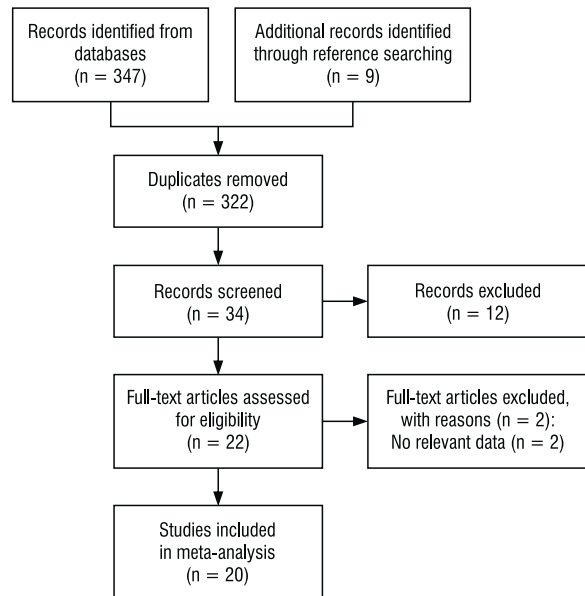
Figure 1. Flow diagram presenting process of collecting data included in this meta-analysis.

were disqualified due to the lack of relevant data. Finally, a total of 20 studies were included in this meta-analysis. According to the PRISMA guidelines, an overall data collection process is presented in Figure 1. In addition, the characteristics of all the submitted studies are collected in Table 1 [1, 2, 7, 8, 10, 13, 18, 20, 21, 24–27, 29, 32, 37, 39, 41, 46, 47].

Prevalence of divided zygoma on the sides

A total of 49,734 zygomatic bones were analysed in relation to the prevalence of DZ. Furthermore, 14,324 left and 14,324 right zygomatic bones were analysed. The pooled prevalence of any DZ was 1.69% (95% CI: 0.73–3.01%). The pooled prevalence of any DZ on the left was shown to be 0.72% (95% CI: 0.28–1.36%) and on the right 0.98% (95% CI: 0.44–1.70%). Despite the general results, additional regional analyses were also enrolled. All the results mentioned above and the more detailed results are gathered in Table 2.

Prevalence of divided zygoma in skull

A total of 17,790 skulls were analysed concerning the prevalence of DZ. The pooled prevalence of any DZ was shown to be 1.36% (95% CI: 0.76–2.12%). Despite the general results, additional regional analyses were also enrolled. All the results mentioned above and the more detailed results are gathered in Table 2.

Table 1. Characteristics of the studies included in this meta-analysis

First author [reference]	Year	Continent	Country	Methodology	Number of ZB studied	Number of ZB with OJ
Anil et al. [1]	2000	Asia	Turkey	Cadaveric	2614	51
Bhargava et al. [2]	1960	Asia	India	Cadaveric	200	13
Dimowski [7]	2012	Europe	Serbia	Cadaveric	616	3
Ding [8]	1961	Asia	China	Cadaveric	1638	21
Gong and Du [10]	1965	Asia	China	Cadaveric	2036	10
Hanihara et al. [13]	1998	Multipopulational study		Cadaveric	19582	102
Hu et al. [18]	1985	Asia	China	Cadaveric	1600	11
Jeyasingh et al. [20]	1982	Asia	India	Cadaveric	1000	40
Jit [21]	1960	Asia	India	Cadaveric	200	5
Kozintsev et al. [24]	1999	Multipopulational study		Cadaveric	11202	777
Kundu et al. [25]	2016	Asia	India	Cadaveric	286	6
Li [26]	1985a	Asia	China	Cadaveric	400	9
Li [27]	1985b	Asia	China	Cadaveric	664	24
Mangalgiri et al. [29]	2015	Asia	India	Cadaveric	228	1
Nikolova et al. [32]	2017	Europe	Bulgaria	Cadaveric	2746	1
Pardoe [37]	1984	Australia	Australia	Cadaveric	2576*	1*
Soni and Khatri [39]	2016	Asia	India	Cadaveric	486	21
Wang and Dechow [41]	2016	Asia	China	Cadaveric	280	3
Yang [46]	1987	Asia	China	Cadaveric	1666	4
Zhang et al. [47]	2019	Asia	China	Cadaveric	2290	24

*Number of skulls studied and number of skulls with os japonicum; 2B — zygomatic bones; OJ — os japonicum

Table 2. Results established in this meta-analysis regarding the prevalence of the os japonicum (OJ) in each category

Source of data	Category	N	Prevalence	LCI	HCI	Q	I²
Results obtained analysing a number (n) of zygomatic bones	**OJ prevalence**						
	Overall	49734	1.69%	0.73%	3.01%	1380.41	98.70
	In Asian population	28143	2.07%	1.07%	3.38%	657.53	97.41
	In European population	10212	0.96%	0.00%	3.52%	316.26	98.74
	In South and North American populations	2796	1.00%	0.00%	5.16%	64.77	96.91
	Prevalence of OJ occurring on the left side						
	Overall	14324	0.72%	0.28%	1.36%	47.57	83.18
	In Asian population	6546	1.13%	0.77%	1.57%	7.79	35.83
	In European population	3104	0.18%	0.00%	0.54%	7.47	59.82
	Prevalence of OJ occurring on the right side						
	Overall	14324	0.98%	0.44%	1.70%	49.02	83.68
	In Asian population	6533	1.49%	1.00%	2.07%	9.90	49.52
	In European population	3094	0.27%	0.04%	0.66%	5.47	45.13
Results obtained analysing a number (n) of skulls	**OJ prevalence**						
	Overall	17790	1.36%	0.76%	2.12%	130.43	89.27
	In Asian population	7689	2.11%	1.34%	3.04%	47.46	76.82
	In Australian and Oceanian populations	4591	0.07%	0.01%	0.18%	1.72	0.00
	In European population	3232	0.27%	0.05%	0.64%	5.37	44.16

LCI — lower confidence interval; HCI — higher confidence interval; Q — Cochran's Q

Table 3. Results of the prevalence of the os japonicum (OJ) in each sex

Category	N	Prevalence	LCI	HCI	Q	I²
Females						
OJ overall in women	1414	1.08%	0.00%	4.02%	12.06	75.13
OJ on the left side in women	705	1.25%	0.00%	3.64%	5.33	43.73
OJ on the right side in women	709	1.37%	0.00%	4.26%	6.37	52.91
Males						
OJ overall in men	1084	0.87%	0.00%	2.50%	30.53	90.17
OJ on the left side in men	857	2.02%	1.17%	3.08%	2.95	0.00
OJ on the right side in men	855	2.08%	0.00%	5.63%	7.75	61.27

LCI — lower confidence interval; HCI — higher confidence interval; Q — Cochran's Q

Table 4. Results of this meta-analysis regarding the number of divisions of zygomatic bone and the symmetricity of occurrence of the os japonicum (OJ)

Category	N	Prevalence	LCI	HCI	Q	I²
Number of divisions of the zygomatic bone in OJ						
Overall prevalence of bipartite zygomatic bone	271	95.08%	88.75%	99.06%	28.03	57.19
Overall prevalence of tripartite zygomatic bone		2.77%	0.75%	5.82%	14.62	17.90
Prevalence of bipartite zygomatic bone in Asian population	165	93.69%	86.33%	98.52%	16.91	46.78
Prevalence of tripartite zygomatic bone in Asian population		4.70%	1.95%	8.48%	6.28	0.00
Symmetricity of occurrence of the OJ						
Overall prevalence of OJ occurring bilaterally	46	60.18%	46.27%	73.34%	6.17	0.00
Overall prevalence of OJ occurring unilaterally		39.82%	26.66%	53.73%	6.17	0.00
Prevalence of OJ occurring bilaterally in Asian population	42	63.98%	49.32%	77.47%	2.89	0.00
Prevalence of OJ occurring unilaterally in Asian population		36.02%	22.53%	50.68%	2.89	0.00

LCI — lower confidence interval; HCI — higher confidence interval; Q — Cochran's Q

Divided zygoma prevalence according to the gender

Analysis of the prevalence of DZ according to sex and side was performed on a total of 1,414 zygomatic bones of the female group and 1,084 zygomatic bones of the men's group. The zygomatic bones were divided into two subgroups: the left and right side. The pooled prevalence for each group was 1.08% (95% CI: 0.00–4.02%) for the women and 0.87% (95% CI: 0.00–2.50%) for the men's group. Despite the general results, additional analyses were also enrolled in the left and right subgroups. All the results mentioned above and the more detailed results are gathered in Table 3.

Divisions of zygomatic bone

An analysis of the number of divisions of the zygomatic bone (Fig. 2) in DZ was performed on a total of 271 zygomatic bones. Bipartite zygomatic bone was found to be the most common, with a prevalence of 95.08% (95% CI: 88.75–99.06%). On the other

hand, tripartite zygomatic bone was found, with a prevalence of 2.77% (95% CI: 0.75–5.82%). Despite the general results, additional regional analyses were also enrolled. All the results mentioned above and the more detailed results are gathered in Table 4.

Symmetricity of divided zygoma

An analysis of the symmetry of the occurrence of DZ was performed on a total of 46 DZ. The bilaterally DZ was found to be the most common, with a prevalence of 60.18% (95% CI: 46.27–73.34%). However, unilateral DZ was found, with a prevalence of 39.82% (95% CI: 26.66–53.73%). Despite the general results, additional regional analyses were also enrolled. All the results mentioned above and the more detailed results are gathered in Table 4.

DISCUSSION

The prevalence of DZ has been extensively discussed in the literature. The DZ was first described in 1779 by Sandifort as a single case report [19]. In
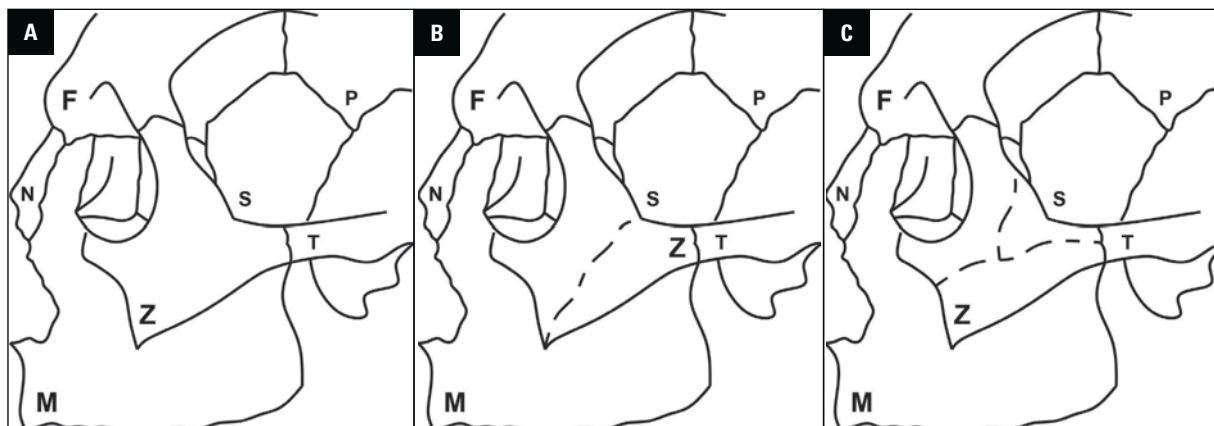
Figure 2. Illustrations of the single, bipartite and tripartite zygomatic bone; **A.** Single zygomatic bone; **B.** Bipartite zygomatic bone (os japonicum/ /divided zygoma); **C.** Tripartite zygomatic bone (os japonicum/divided zygoma); Z — zygomatic bone; M — maxilla; N — nasal bone; F — frontal bone; S — sphenoid bone; P — parietal bone; T — temporal bone.

the 19th and 20th centuries, some researchers had examined the DZ [12, 23]. Hilgendorf [17] was the first author to give the name 'os japonicum' for DZ due to his research. In his study, two DZ were found in 11 Japanese skulls. However, this synonym was not well received by everyone because of its occurrence in other populations, especially in a study conducted by Martin and Saller [30], where it was pointed out that the prevalence of DZ in the Japanese population is too low to consider that this structure has a Japanese trait [12, 30]. Despite this controversy, many researchers still use the name 'os japonicum' for this structure [2, 15, 20, 37, 40]. Although, in 1998, a Japanese researcher, Hanihara et al. [13] made a huge analysis of DZ prevalence around the world. After this examination, they concluded that the trait of DZ is not specified for Japanese but for the East Asian population. The os zygomaticum bipartitum was also called "os ainonicum" by Belz [see 33], a German pathologist. However, Koganei [23] found that no individuals who had a complete division of the zygomatic bone in the skulls of Hokkaido (homeland of the Ainu people) and Hanihara et al. [13] confirmed that Asian people have a higher frequency of DZ than Ainu people. In 1984, Pardoe [37], who was the only one who made the exploration in Australia, stated that searching for a complete OJ is essentially fruitless since only one DZ was found in that region [37]. In addition, other geographic regions, except Asian populations, have small elucidated data by the authors up to the present times. Some researchers collected their data from the skulls from the old days, such as: Kozintsev et al. [24], who used skulls from the bronze age to find the posterior trace of the OJ,

or Anil et al. [1], who found DZ among Anatolian skulls from the 18th century, and Wang and Dechow [41] and Zhang et al. [47], who described many DZs in museums collections and archaeological sites. The majority of the studies investigating the DZ focused purely on the prevalence of this structure, rather than its morphometric properties [41].

There has been a lot of controversy regarding the prevalence of DZ in many different geographical groups. The DZ was previously described as a Japanese trait, which caused the name 'os japonicum'; however, not all authors agreed with this statement. Some researchers argued that DZ seems to be an East Asian trait [13]. The results of the present meta-analysis show that there is no statistically significant difference between the overall population and the Asian population group ($p > 0.05$). Moreover, other region groups (Europe, North and South America, and Australia and Oceania) have similar statistical results. This score applies to both the prevalence of DZ in the skull and single zygomatic bone. Therefore, a change in the nomenclature of the DZ seems redundant. Wang and Dechow [41] claimed that the prevalence of DZ in Rhesus macae is significantly lower than in humans, especially in East Asia and South Africa. Some researchers have also seen no evidence of the occurrence in Homo Sapiens, Homo erectus, Australopithecus, and other fossil hominids of DZ traits [19, 48]. The results of DZ lateralisation show that the right side of the zygomatic bone appears to be more affected by DZ than the left side (0.98% for the right side and 0.72% for the left side). The DZ was prevalent more often in the female group (1.08%). In both sexual

groups, the right side was more frequent than the left side; however, all the above results did not show any statistical significance (p > 0.05). Similarly, Anil et al. [1] did not observe any differences in gender and side preferences in the cadaveric and radiograph groups. Zhang also reported that the existence of bipartite or tripartite zygomatic bones was not related to gender, age, or side [47].

The divisions of the zygomatic bone depend on many sutures that form during prenatal time. Hauser and De Stefano [15] categorized the sutures on the zygomatic bone into four subgroups for bipartite zygomatic bone and into two for tripartite zygoma: type I, simple horizontal inferior; type II, simple oblique lateral; type III, simple horizontal superior; type IV, simple oblique medial; type V, horizontal inferior + oblique medial; type VI, horizontal superior + oblique lateral. The same criteria could be used in radiological findings [1]. Anil et al. [1] observed that type I and IV were significantly frequent. This classification was not included in the present meta-analysis because hardly any authors used this division in their studies. Some researchers observed that the horizontal division could be complete or incomplete [1, 37]. Interestingly, there is a high frequency of a vestigial (incomplete) transverse zygomatic suture in the zygomatic bone, mainly in the posterolateral part of the zygoma in human populations worldwide (10–25%) [9, 14, 36]. The bipartite zygomatic bone is much more common than the tripartite zygomatic bone (p < 0.05). However, there are no statistically geographical traits of the bipartite zygoma. The bilateral symmetry of the DZ is often that of the unilateral one (60.18%), but there are no statistically significant results (p > 0.05). The probable explanations for this situation could be the small amount of studies on this subject; data are obtained from a small number of sources, and therefore, the data is homogeneous ($I^2 = 0.00$).

Knowledge about the existence of DZ, its prevalence, symmetry, sexual dimorphism, and lateralisation in different populations could be of great importance in neurosurgery and reconstructive procedures. This knowledge can be especially important in patients with facial trauma, particularly fractures of the buccal surface of the zygomatic bone shaft, as the zygomatic bone is the most prominent part of the facial skeleton [25, 39]. After zygomaticomaxillary complex fracture all patients have performed the three-dimensional (3D) analysis of the degree of recovery of malar asymmetry [3]. This 3D image is essential before reconstruction operation and the DZ could be seen in the frontal view, which could be misunderstanding. It is crucial to not confuse potential fracture lines with the sutures, which divide the zygomatic bone, for a correct diagnosis. Furthermore, the DZ is also a clinically important structure for the plastic or maxillofacial surgeon during the osteotomy operation, which is used in patients with deformed viscerocranium, malocclusion, speech defects, or nasal defects. The said procedure is usually focused on the nasal bone and nasal septum to improve the patient's respiration and aesthetics. In both aspects, having knowledge that the zygomaticofacial vessels and nerves pass through the zygomaticofacial foramen, could be clinically significant to prevent undesirable complications [25].

Limitations of the study

This study is not without limitations and is burdened with potential bias, as the results of this meta-analysis are only as accurate as the results from the submitted studies. A potential morphometry dimorphism in the anatomical features of the DZ was not established due to the lack of data. Analogically, no relation was enrolled with respect to the other structures surrounding the zygomatic bone statistics.

CONCLUSIONS

In conclusion, the authors of the present study believe that this study can be considered an up-to-date meta-analysis regarding the prevalence, divisions, and symmetricity of the DZ. The most common type of DZ is the bilaterally DZ bone (60.18%). The data provided by the present study may be useful for doctors to recognise the DZ from potential fractures and during zygomatic bone osteotomy. Detailed anatomical knowledge of the midfacial region can prevent surgical complications when operating in this area.

Conflict of interest: None declared

REFERENCES

1. Anil A, Peker T, Turgut HB, et al. Incidence of os japonicum in Anatolian dry skulls and plain cranium radiographs of modern Anatolian population. J Craniomaxillofac Surg. 2000; 28(4): 217–223, doi: 10.1054/jcms.2000.0142, indexed in Pubmed: 11110153.
2. Bhargava KN, Garg TC, Bhargava SN. Incidence of Os japonicum (bipartite zygomatic bone) in Madya Pradesh skulls. J Anat Soc India. 1960; 9: 21–23.
3. Cho J, Kim Y, Choi Y. Three-dimensional analysis of facial asymmetry after zygomaticomaxillary complex fracture

reduction: a retrospective analysis of 101 East Asian patients. Arch Craniofac Surg. 2021; 22(3): 148–153, doi: 10.7181/acfs.2021.00241, indexed in Pubmed: 34225406.

4. Covington DS, Wainwright DJ, Teichgraeber JF, et al. Changing patterns in the epidemiology and treatment of zygoma fractures: 10-year review. J Trauma. 1994; 37(2): 243–248, doi: 10.1097/00005373-199408000-00016, indexed in Pubmed: 8064924.

5. Cunningham DJ. Cunningham's text-book of anatomy. 8th Ed. Oxford University Press, London 1947.

6. D'Antoni AV, Tubbs RS, Patti AC, et al. The Critical Appraisal Tool for Anatomical Meta-analysis: A framework for critically appraising anatomical meta-analyses. Clin Anat. 2022; 35(3): 323–331, doi: 10.1002/ca.23833, indexed in Pubmed: 35015336.

7. Dimovski N. Os zygomaticum bipartitum na lobanjama sa srednjovekovnog nalazista manastiriste u Majdanu. Glasnik Antropoloskog drustva Srbije. 2012(47): 9–16, doi: 10.5937/gads1247009d.

8. Ding SH. Measurement and observation of Chinese orbit and design of several measuring tools. J Qingdao Med Coll. 1961; 02: 15–24.

9. Dodo Y. Non-Metrical Cranial Traits in the Hokkaido Ainu and the Northern Japanese of Recent Times. J Anthropol Soc Nippon. 1974; 82(1): 31–51, doi: 10.1537/ase1911.82.31.

10. Gong SQ, Du YL. The characteristic of Chinese zygoma. Acta Anat Sinica. 1965; 02: 223–233.

11. Grant JCB. A method of anatomy, descriptive and deductive. 5th Ed. Williams & Wilkins, Philadelphia 1952.

12. Gruber W. Vierter Nachtrag zum Vorkommen des zweigetheilten Jochbeines — Os zygomaticum bipartitum — beim Menschen. Arch Pathol Anatom Physiol Klin Med. 1877; 69(3-4): 382–383, doi: 10.1007/bf02326205.

13. Hanihara T, Ishida H, Dodo Y. Os zygomaticum bipartitum: frequency distribution in major human populations. J Anat. 1998; 192(4): 539–555, doi: 10.1046/j.1469-7580.1998.19240539.x, indexed in Pubmed: 9723981.

14. Hanihara T, Ishida H, Dodo Y. Characterization of biological diversity through analysis of discrete cranial traits. Am J Phys Anthropol. 2003; 121(3): 241–251, doi: 10.1002/ajpa.10233, indexed in Pubmed: 12772212.

15. Hauser G, de Stefano GF. Epigenetic variants of the human skull. E. Schweizerbart'sche Verlagsbuchhandlung, Stuttgart 1989.

16. Henry BM, Tomaszewski KA, Ramakrishnan PK, et al. Development of the anatomical quality assessment (AQUA) tool for the quality assessment of anatomical studies included in meta-analyses and systematic reviews. Clin Anat. 2017; 30(1): 6–13, doi: 10.1002/ca.22799, indexed in Pubmed: 27718281.

17. Hilgendorf F. Das Os japonicum betreffend. Archiv für pathologische Anatomie und Physiologie und für klinische Medicin. 1879; 78(1): 190–194, doi: 10.1007/bf01877952.

18. Hu XH, Li PZ, Zhen JG. Observation of the zygomatic morphology of Chinese. Acta Academiae Medicinae Jiangxi. 1985; 01: 11–15.

19. Hrdlicka A. New instances of complete division of the malar bone, with notes on incomplete division. Am Naturalist. 1902; 36(424): 273–294, doi: 10.1086/278119.

20. Jeyasingh P, Gupta CD, Arora AK, et al. Study of Os japonicum in Uttar Pradesh crania. Anat Anz. 1982; 152(1): 27–30, indexed in Pubmed: 7158785.

21. Jit I. J Anatomical Soc India. 1960; 9: 21–23.

22. Jones FW. Buchanan's manual of anatomy. 7th Ed. Bailliere, Tindall and Cox, London 1946.

23. Koganei Y. Suture of zygomatic bone. Zinruigaku Kenkyu. 1926; 16: 470–487.

24. Kozintsev A, Gromov AV, Moiseyev VG. Collateral relatives of American Indians among the Bronze Age populations of Siberia? Am J Phys Anthropol. 1999; 108(2): 193–204, doi: 10.1002/(sici)1096-8644(199902)108:2<193::aid-ajpa5>3.0.co;2-v.

25. Kundu B, Sarkar S, Sarkar T, et al. Incidence of bipartite zygomatic in East Indian population. Indian J Basic Applied Med Res. 2016; 5(4): 154–158.

26. Li YY. Observation on the Chinese zygomatic bone. Acta Anthropol Sin. 1985a; 03: 281–285.

27. Li YY. Observation of divided zygoma in Northwest Chinese. J Ningxia Med Coll. 1985b; 03: 27–30.

28. Mall F. On ossification centers in human embryos less than one hundred days old. Am J Anat. 1906; 5(4): 433–458, doi: 10.1002/aja.1000050403.

29. Mangalgiri A, Satpathy D, Bhojwani R. Study of Os Zygomaticum Bipartitum In Skulls of Central India. J Indian Acad Foren Med. 2015; 37(1): 59, doi: 10.5958/0974-0848.2015.00013.5.

30. Martin R, Saller K. Lehrbuch der Anthropologie, Band II. Gustav Fischer, Stuttgart 1959.

31. Morris H, Schaeffer JP. Morris' human anatomy: A complete systematic treatise. 11th Ed. Blakiston, Philadelphia 1953.

32. Nikolova S, Toneva D, Georgiev I. A case of bipartite zygomatic bone. Eur J Foren Sci. 2017; 4(4): 1, doi: 10.5455/ejfs.238160.

33. Ohnishi M. Bibliographie. Anthropol Anz. 1941; 18(4): 163–210.

34. Opperman LA. Cranial sutures as intramembranous bone growth sites. Dev Dyn. 2000; 219(4): 472–485, doi: 10.1002/1097-0177(2000)9999:9999<::AID-DVDY1073>3.0.CO;2-F, indexed in Pubmed: 11084647.

35. Ossenberg N. The influence of artificial cranial deformation on discontinuous morphological traits. Am J Phys Anthropol. 1970; 33(3): 357–371, doi: 10.1002/ajpa.1330330310.

36. Ossenberg NS. Brief communication: cranial nonmetric trait database on the internet. Am J Phys Anthropol. 2013; 152(4): 551–553, doi: 10.1002/ajpa.22377, indexed in Pubmed: 24122086.

37. Pardoe C. Prehistoric morphologic variation in Australia. The Australian National University, Canberra 1984.

38. Rice DP. Developmental anatomy of craniofacial sutures. Front Oral Biol. 2008; 12: 1–21, doi: 10.1159/000115028, indexed in Pubmed: 18391492.

39. Soni J, Khatri C. A study on variation of zygomatic bone in relation to bipartitism in Gujarat State. Int J Med Sci Public Health. 2016; 5(6): 1237, doi: 10.5455/ijmsph.2016.03022016393.

40. de Villiers H. The skull of the South African Negro. Witwatersrand University Press, Johannesburg 1968.

41. Wang Q, Dechow PC. Divided zygomatic bone in primates with implications of skull morphology and biomechanics. Anat Rec (Hoboken). 2016; 299(12): 1801–1829, doi: 10.1002/ar.23448, indexed in Pubmed: 27870346.

42. Wang Q, Smith AL, Strait DS, et al. The global impact of sutures assessed in a finite element model of a macaque cranium. Anat Rec (Hoboken). 2010; 293(9): 1477–1491, doi: 10.1002/ar.21203, indexed in Pubmed: 20652940.

43. Wang Q, Wood SA, Grosse IR, et al. The role of the sutures in biomechanical dynamic simulation of a macaque cranial finite element model: implications for the evolution of craniofacial form. Anat Rec (Hoboken). 2012; 295(2): 278–288, doi: 10.1002/ar.21532, indexed in Pubmed: 22190334.

44. Williams P, Warwick R, Dyson M. Gray's anatomy. 37th Ed. Churchill Livingstone, London 1993.

45. Woo JK. Notes on the ossification and growth of the human zygomatic bone. Scientia Sinica. 1956; 5(1): 133–135.

46. Yang YR. Observation on the Chinese zygoma. J Kunm Med Coll. 1987; 02: 33–39.

47. Zhang Q, Zhang Q, Yang S, et al. Divided zygoma in Holocene human populations from Northern China. Am J Hum Biol. 2019; 31(6): e23314, doi: 10.1002/ajhb.23314, indexed in Pubmed: 31456277.

48. Zimmermann A, Hassko A. Das Jochbein und das Os malare bipartitum des Orang-Utan. Anatom Anzeiger. 1930; 69: 1–11.

49. Zingg M, Laedrach K, Chen J, et al. Classification and treatment of zygomatic fractures: a review of 1,025 cases. J Oral Maxillofac Surg. 1992; 50(8): 778–790, doi: 10.1016/0278-2391(92)90266-3, indexed in Pubmed: 1634968.

50. Żytkowski A, Tubbs R, Iwanaga J, et al. Anatomical normality and variability: Historical perspective and methodological considerations. Transl Res Anat. 2021; 23: 100105, doi: 10.1016/j.tria.2020.100105.

V M
VIA MEDICA

REVIEW ARTICLE

The petroclinoid ligament: a meta-analysis of its morphometry and prevalence of mineralization with a review of the literature

D. Plutecki[1], P. Ostrowski[2], M. Bonczar[2], J. Iwanaga[3], J. Walocha[2], A. Pękala[2],
E. Szczepanek[2], R.S. Tubbs[3], M. Loukas[4], G. Wysiadecki[5], M. Koziej[2]

[1]Collegium Medicum, Jan Kochanowski University, Kielce, Poland
[2]Department of Anatomy, Jagiellonian University Medical College, Krakow, Poland
[3]Department of Neurosurgery, Tulane University School of Medicine, New Orleans, Louisiana, United States
[4]Department of Anatomical Sciences, St. George's University, Grenada, West Indies
[5]Department of Normal and Clinical Anatomy, Medical University of Lodz, Poland

Background: The petroclinoid ligament (PCL) is an important structure in the petroclival region. The anatomy of the PCL and its relationship with the surrounding structure is highly variable. The aim of this study was to estimate the morphometry, prevalence of mineralization, and anatomy of the PCL. To achieve this, the authors carried out a meta-analysis, including all studies that report extractable data on the PCL.

Materials and methods: Major online medical databases such as PubMed, Scopus, ScienceDirect, Web of Science, SciELO, BIOSIS, Current Content Connect, Korean Journal Database, and Russian Citation Index were searched to gather all studies regarding the anatomical characteristics, morphometry, and relationship with the anatomical surroundings of the PCL.

Results: A total of 25 studies were included in this meta-analysis. Data were gathered and analysed in eight categories: (1) mineralization of the PCL, (2) relationship of the abducens nerve with the PCL, (3) relationship of the dorsal meningeal artery with the PCL, (4) shape, number, and continuity of the PCL, (5) PCL anterior attachment, (6) PCL anterior attachment point on bone, (7) PCL posterior attachment point on bone, (8) morphometric features of the PCL.

Conclusions: In conclusion, the authors of the present study believe that this is the most accurate and up-to-date meta-analysis regarding the morphology and mineralization of the PCL. The data provided by the present study may be a useful tool for surgeons performing neurosurgical procedures, such as endoscopic transnasal surgeries. Detailed anatomical knowledge of the petroclival region can surely prevent surgical complications when operating in this area. (Folia Morphol 2023; 82, 3: 487–497)

Key words: petroclinoid ligament, Gruber ligament, petroclival region, mineralization, neurosurgery

Address for correspondence: Dr. M. Koziej, Department of Anatomy, Jagiellonian University Medical College, ul. Mikołaja Kopernika 12, 33–332 Kraków, Poland, tel: +48 888 202 628, e-mail: mateusz.koziej@gmail.com

INTRODUCTION

The petroclinoid ligament (PCL), also called the petrosphenoidal ligament (PSL), or Gruber's ligament (GL), is a fibrous structure in the petroclival region. It was first described in 1859 by Wenzel Leopold Gruber, a Russian physician and anatomist [7]. The PCL is usually described as a butterfly- or triangular-shaped structure that extends from the petrous tubercle of the petrous apex posteriorly and attaches to the posterior clinoid process anteriorly [1]. The PCL forms the superior portion of the Dorello canal (DC), which contains the abducens nerve (AN), the inferior petrosal sinus, and the dorsal meningeal artery (DMA) [29]. PCL and its close anatomical area are presented on Figures 1 and 2.

Ossification of the PCL have been described in the literature. The cause of ossification is usually said to be age-related. However, it has also been presented as a radiographic characteristic of basal cell carcinoma syndrome and systemic fluorosis [2]. Mineralization of ligaments can cause complications in surgical access, alter the appearance of important anatomical landmarks, or prevent mobilization of important structures during surgery [28].

Understanding the variability in the morphology and ossification of the PCL can be of great clinical significance when performing neurosurgical procedures in the petroclival region, such as endoscopic transnasal surgeries. The PCL has also been described as a useful landmark to locate the AN in tumour removal surgeries using the transnasal approach [27]. Therefore, the objective of the present study was to provide useful data on the morphometry, prevalence of calcifications, and anatomy of the PCL. To achieve this, a systematic search of the literature and a meta-analysis were performed. To the best knowledge of the authors, this is the first meta-analysis regarding the morphology and ossification of the PCL.

MATERIALS AND METHODS

Search strategy

Major online medical databases such as PubMed, Scopus, ScienceDirect, Web of Science, SciELO, BIOSIS, Current Content Connect, Korean Journal Database, and Russian Citation Index were searched to gather all studies on anatomical characteristics, morphometry, and relationships with surrounding structures of the PCL. The study collection ended in April 2022. In agreement with the Boolean technique, the following search terms were employed: (petroclinoid ligament)
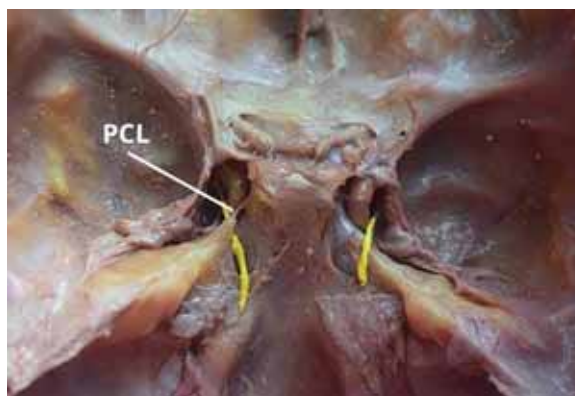
Figure 1. Petroclinoid ligament (PCL) and its close anatomical area.
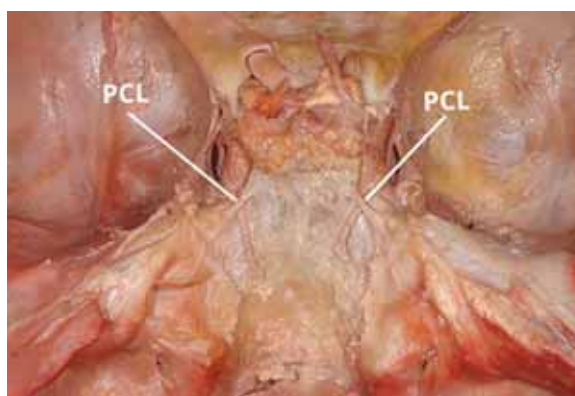
Figure 2. Petroclinoid ligament (PCL) and its close anatomical area.

OR (petroclinoid fold) OR (petrosphenoidal ligament) OR (Gruber's ligament) OR (paraclinoid region). The search terms were individually adapted to each database to minimise potential bias. Neither date, language, article type, nor text availability conditions were applied. An additional search was conducted through the references of the identified studies at the end of the search stage to ensure the accuracy of the process. During the study, the Preferred Reporting Items for Systematic Reviews and Meta-Analyses (PRISMA) guidelines were followed. Furthermore, the Critical Appraisal Tool for Anatomical Meta-analysis (CATAM) was used to provide the highest quality findings [3].

Eligibility assessment

The database search and the manual search identified a total of 518 studies that were initially evaluated by two independent reviewers. After removing duplicates and irrelevant records, a total of 145 articles were qualified for a full-text evaluation. To minimise potential bias and maintain accurate statistical meth-

odology, articles such as case reports, case series, conference reports, reviews, letters to editors, and studies that provided incomplete or irrelevant data were excluded. The inclusion criteria consisted of original studies with extractable numerical data regarding the topic of this study. Finally, a total of 25 studies were included in this meta-analysis. Additionally, the AQUA Tool which was specifically designed for anatomical meta-analyses was used to minimise the potential bias of included studies [8].

Data extraction

Data from qualified studies were extracted by two independent reviewers. Qualitative data, such as year of publication, country and continent of origin, data collection methodology and information on diseases in the studied groups, were collected. Quantitative data, such as sample size, numerical data on anatomical characteristics, morphometry, and relationship with the anatomical surroundings of the PCL were also gathered. Any discrepancies between studies, identified by the two reviewers, were resolved by contacting the authors of the original studies whenever possible or by consensus with a third reviewer.

Statistical analysis

To perform the meta-analyses, STATISTICA version 13.1 software (StatSoft Inc., Tulsa, OK, USA), MetaXL version 5.3 software (EpiGear International Pty Ltd., Wilston, Queensland, Australia), and Comprehensive Meta-analysis version 3.0 software (Biostat Inc., Englewood, NJ, USA) were used. A random-effects model was used in all analyses. The heterogeneity among the studies was evaluated, using both the Chi-squared test and the I-squared statistic [9]. The I-squared statistic was interpreted as follows: 0–40% as "might not be important"; 30–60% as "may represent moderate heterogeneity"; 50–90% as "may represent substantial heterogeneity"; 75–100% as "may represent considerable heterogeneity". P-value of < 0.05 and the confidence intervals (95% CI) were used to find statistically significant differences between the studied groups. In the case of overlapping confidence intervals, differences were considered statistically insignificant.

RESULTS

Search results

After the selection of the initially accepted 77 studies, a total of 52 studies were excluded. Most of
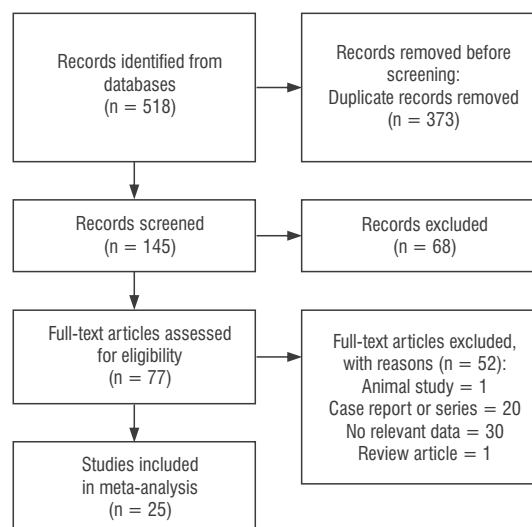
Figure 3. Flow diagram presenting process of collecting data included in this meta-analysis

them (n = 30) were disqualified due to the lack of relevant data. Twenty case reports from case series were excluded. Furthermore, two studies were excluded because they were a review article and an animal study. Eventually, a total of 25 studies were included in this meta-analysis [1, 2, 4–6, 10–16, 19–28, 32–34]. According to the PRISMA guidelines, an overall data collection process is presented in Figure 3. Additionally, the characteristics of all the submitted studies are collected in Table 1.

Mineralization of the PCL

A total of 5592 ligaments were analysed in relation to their mineralization process. Seven categories of data were established from the submitted studies: (1) subgroup in which the PCL mineralization process was not observed; (2) subgroup in which the PCL mineralization process was not observed; (3) subgroup in which complete mineralization of the PCL was observed; (4) subgroup of data collected from the studies in which the authors did not specify the degree of mineralization; however, any progress of mineralization was observed; (5) subgroup of patients in whom the mineralization process was observed bilaterally; (6) subgroup of patients in whom the mineralization process was observed unilaterally; (7) subgroup of patients in whom the other mineralization of head ligaments were observed. The pooled prevalence of any mineralization process was established to be 10.06% (95% CI: 5.61–15.27%). Despite the general results, additional regional and

Table 1. Characteristics of studies included in this meta-analysis

First author [reference]	Year	Region	Country	Type of study	Type of examination	Thickness slice [mm]
Ghorbanlou et al. [6]	2022	Asia	Iran	Radiological	CT	0.675
Kayaci et al. [14]	2021	Asia	Turkey	Cadaveric	–	–
Wysiadecki et al. [34]	2021	Europe	Poland	Cadaveric	–	–
Iwanaga et al. [13]	2020	North America	USA	Cadaveric	–	–
Touska et al. [28]	2019	Europe	UK	Radiological	CT	0.6
Bayrak et al. [1]	2019	Asia	Turkey	Radiological	CT	0.3
Kumar et al. [15]	2018	Asia	India	Cadaveric	–	–
Ozdede et al. [19]	2018	Asia	Turkey	Radiological	CT	0.4
Inal et al. [12]	2016	Asia	Turkey	Radiological	CT	0.67
Özgür and Esen [21]	2015	Asia	Turkey	Radiological	CT	0.5
Tomio et al. [27]	2015	Asia	Indonesia	Cadaveric	–	–
Wysiadecki et al. [33]	2015	Europe	Poland	Cadaveric	–	–
Ezer et al. [5]	2012	North America	USA	Cadaveric	–	–
Sedghizadeh et al. [24]	2012	North America	USA	Radiological	CT	–
Icke et al. [11]	2010	Asia	Turkey	Cadaveric	–	–
Ozer et al. [20]	2010	Asia	Turkey	Cadaveric	–	–
Liu et al. [16]	2009	Asia	China	Cadaveric	–	–
Skrzat et al. [25]	2007	Europe	Poland	Cadaveric	–	–
Cederberg et al. [2]	2003	North America	USA	Radiological	RTG	–
Iaconetta et al. [10]	2003	Europe	Germany	Cadaveric	–	–
Ozveren et al. [22]	2003	Asia	Turkey	Cadaveric	–	–
Destrieux et al. [4]	1997	Europe	France	Cadaveric	–	–
Umansky et al. [32]	1991	Asia	Israel	Cadaveric	–	–
Rzymski and Kosowicz [23]	1975	Europe	Poland	Radiological	RTG	–
Stanton and Wilkinson [26]	1949	Europe	UK	Radiological	RTG	–

CT — computed tomography; RTG — radiograph

methodological analyses were also enrolled. All the results mentioned above and the more detailed results are gathered in Table 2.

Relationship of the abducens nerve with the PCL

An analysis of the relationship between the PCL and the AN was established considering a total of 469 ligaments. The pooled prevalence for AN to run through the PCL was enrolled as 4.95% (95% CI: 0.00–17.03%). Despite the general results, additional regional analyses were also enrolled. All the results mentioned above and the more detailed results are gathered in Table 3.

Relationship of the dorsal meningeal artery with the PCL

The analysis of the relationship between the PCL and the DMA was established considering a total of

103 ligaments. A pooled prevalence for DMA to run below PCL was enrolled as 94.40% (95% CI: 83.15––100.00%). Despite the general results, additional regional analysis was also included. All the results mentioned above and the more detailed results are gathered in Table 4.

Shape, number, and continuity of the PCL

The analyses of shapes, number, and continuity of the PCL were performed on a total of 143 ligaments. Butterfly-shaped PCL was found to be the most common, with a prevalence of 79.59% (95% CI: 21.32–100.00%). A single PCL occurs much more frequently than a double one, with a prevalence of 93.09% (95% CI: 75.50–100.00%). Despite the general results, additional regional analysis was also included. All the results mentioned above and the more detailed results are gathered in Table 5.

Table 2. Statistical results of this meta-analysis regarding the mineralization of petroclinoid ligament in each category

Category	N	Pooled prevalence	LCI	HCI	Q	I²
Overall results	5592					
No mineralization		88.55%	80.16%	94.95%	1268.42	98.50
Partial mineralization		1.78%	0.23%	4.44%	520.65	96.35
Complete mineralization		2.20%	0.67%	4.49%	354.54	94.64
Any mineralization		10.06%	5.81%	15.27%	565.16	96.64
Bilateral		0.54%	0.10%	1.26%	113.22	83.22
Unilateral		0.75%	0.12%	1.80%	177.27	89.28
Other mineralizations of head ligaments		1.02%	0.03%	2.95%	412.96	95.40
Results gathered using radiological methods	5043					
No mineralization		78.58%	63.56%	90.63%	1171.33	99.23
Partial mineralization		3.07%	0.26%	8.06%	497.83	98.19
Complete mineralization		2.86%	0.52%	6.66%	335.77	97.32
Any mineralization		17.06%	9.69%	25.92%	504.64	98.22
Bilateral		0.44%	0.00%	1.43%	108.72	91.72
Unilateral		0.51%	0.00%	1.58%	167.25	94.62
Other mineralizations of head ligaments		1.61%	0.00%	4.48%	407.71	97.79
Results gathered from cadavers	549					
No mineralization		96.75%	94.37%	98.53%	14.13	36.31
Partial mineralization		0.55%	0.07%	1.38%	0.73	0.00
Complete mineralization		1.03%	0.23%	2.28%	10.78	16.49
Any mineralization		3.25%	1.47%	5.63%	14.13	36.31
Bilateral		0.40%	0.02%	1.15%	3.94	0.00
Unilateral		1.28%	0.48%	2.42%	7.10	0.00
Other mineralizations of head ligaments		0.57%	0.08%	1.42%	4.24	0.00
Results gathered in Asia	2681					
No mineralization		91.98%	85.59%	96.70%	188.14	95.22
Partial mineralization		1.13%	0.00%	3.14%	117.54	92.34
Complete mineralization		2.84%	0.00%	8.90%	304.29	97.04
Any mineralization		1.07%	0.05%	3.04%	79.56	88.69
Bilateral		0.30%	0.00%	0.93%	25.37	64.52
Unilateral		0.60%	0.00%	1.63%	55.29	83.72
Other mineralizations of head ligaments		0.20%	0.02%	0.53%	13.14	31.50
Results gathered in Europe	1623					
No mineralization		81.80%	55.28%	100.00%	678.82	99.12
Partial mineralization		2.36%	0.00%	7.05%	81.50	92.64
Complete mineralization		0.95%	0.35%	1.81%	9.10	34.04
Any mineralization		11.56%	2.83%	24.32%	194.88	96.92
Bilateral		0.84%	0.00%	3.29%	75.79	92.08
Unilateral		1.41%	0.00%	4.68%	89.35	93.28
Other mineralizations of head ligaments		1.11%	0.00%	3.36%	35.85	83.26
Results gathered in North America	1288					
No mineralization		88.14%	61.15%	100.00%	156.44	98.72
Partial mineralization		4.15%	0.00%	27.12%	197.06	98.99
Complete mineralization		3.46%	0.24%	9.23%	17.19	88.36
Any mineralization		11.86%	0.00%	38.85%	156.44	98.72
Bilateral		0.67%	0.00%	2.08%	6.54	69.40
Unilateral		0.39%	0.00%	1.76%	8.64	76.85
Other mineralizations of head ligaments		5.57%	0.00%	38.24%	285.69	99.30

LCI — lower confidence interval; HCI — higher confidence interval; Q — Cochran's Q

PCL general anterior attachment

An analysis of anterior PCL attachment was performed on a total of 330 ligaments. The studies included in this meta-analysis were not precise with regard to attachment. Therefore, the authors established four subcategories of data: (1) PCL attaches to a bone; (2) PCL attaches to the dura mater; (3) PCL attaches to a bone and the dura mater; and (4) PCL attached to a bone and a second bone. The most frequent anterior attachment was found to be PCL

Table 3. Statistical results of this meta-analysis regarding the relationship of the abducens nerve (AN) to the petroclinoid ligament (PCL) in each category

Category	N	Pooled prevalence	LCI	HCI	Q	I²
Overall results	469					
AN runs below the PCL		93.02%	79.67%	100.00%	288.75	95.50
AN runs above the PCL		1.57%	0.62%	2.92%	10.29	0.00
AN runs through the PCL		4.95%	0.00%	17.03%	300.24	95.67
Results gathered in Asia	274					
AN runs below the PCL		88.03%	55.49%	100.00%	270.68	97.41
AN runs above the PCL		1.16%	0.15%	2.90%	7.22	3.01
AN runs through the PCL		10.06%	0.00%	41.56%	277.49	97.48
Results gathered in Europe	152					
AN runs below the PCL		97.61%	94.46%	99.55%	1.79	0.00
AN runs above the PCL		2.39%	0.45%	5.54%	1.79	0.00
AN runs through the PCL		0.00%	0.00%	0.00%	0.00	0.00
Results gathered in North America	43					
AN runs below the PCL		98.96%	94.83%	100.00%	0.14	0.00
AN runs above the PCL		0.00%	0.00%	0.00%	0.00	0.00
AN runs through the PCL		0.00%	0.00%	0.00%	0.00	0.00

LCI — lower confidence interval; HCI — higher confidence interval; Q — Cochran's Q

Table 4. Statistical results of this meta-analysis regarding the relationship of the dorsal meningeal artery (DMA) to the petroclinoid ligament (PCL) in each category

Category	N	Pooled prevalence	LCI	HCI	Q	I²
Overall results	103					
DMA runs below the PCL		94.40%	83.15%	100.00%	8.71	65.56
DMA runs above the PCL		3.01%	0.00%	9.59%	7.33	59.06
Results gathered in Asia	30					
DMA runs below the PCL		90.80%	72.67%	100.00%	1.97	49.30
DMA runs above the PCL		9.20%	0.00%	27.33%	1.97	49.30

LCI — lower confidence interval; HCI — higher confidence interval; Q — Cochran's Q

attachment to the bone with a prevalence of 94.43% (95% CI: 85.60–100.00%). Despite the general results, additional regional analysis was also included. All the results mentioned above and the more detailed results are gathered in Table 6.

PCL anterior attachment point on the bone

Analysis of the anterior attachment point of the PCL on the bone was carried out in a total of 297 ligaments. The most common anterior attachment point was found to be in the posterior clinoid process with a prevalence of 72.95% (95% CI: 28.05–100.00%). Despite the general results, additional regional analysis was also included. All the results mentioned above and the more detailed results are gathered in Table 7.

PCL posterior attachment point on the bone

Analysis of the posterior attachment point of the PCL on the bone was carried out in a total of 297 ligaments. The most common posterior attachment point was found to be in the petrous apex with a prevalence of 86.00% (95% CI: 55.13–100.00%). Despite the general results, additional regional analysis was also included. All the results mentioned above and the more detailed results are gathered in Table 8.

Morphometric features of the PCL

From the submitted studies, a total of eight categories were established regarding the morphological characteristics of the PCL: (1) length; (2) left PCL length; (3) right PCL length; (4) width; (5) thickness;

Table 5. Statistical results of meta-analysis regarding the anatomical features, like shape, number and continuity of the petroclinoid ligament (PCL) in each category

Category	N	Pooled prevalence	LCI	HCI	Q	I²
Overall results	143					
Butterfly-shaped PCL		79.59%	21.32%	100.00%	175.71	97.72
Y-shaped PCL		4.12%	0.00%	14.95%	25.82	84.51
Triangular PCL		3.60%	0.00%	12.32%	19.63	79.63
Single PCL		93.09%	75.50%	100.00%	42.19	90.52
Double PCL		5.03%	1.03%	11.32%	7.12	43.85
Complete PCL		6.19%	0.00%	27.49%	60.03	93.34
Incomplete PCL		4.86%	0.00%	19.46%	37.88	89.44
Hypoplastic/Fragmented	5592	0.66%	0.16%	1.44%	113.55	83.27
Results gathered in Asia	70					
Butterfly-shaped PCL		92.90%	74.28%	100.00%	10.06	80.12
Y-shaped PCL		0.97%	0.00%	3.91%	0.20	0.00
Triangular PCL		7.10%	0.00%	25.72%	10.06	80.12
Single PCL		97.96%	94.02%	100.00%	1.94	0.00
Double PCL		7.61%	2.38%	15.12%	1.19	0.00
Complete PCL		12.81%	0.00%	61.07%	33.03	93.94
Incomplete PCL		9.84%	0.00%	42.39%	20.35	90.17
Hypoplastic/Fragmented	2681	8.02%	3.30%	14.41%	188.14	95.22

LCI — lower confidence interval; HCI — higher confidence interval; Q — Cochran's Q

Table 6. Statistical results of this meta-analysis regarding the anterior attachment of the petroclinoid ligament (PCL) in each category

Category	N	Pooled prevalence	LCI	HCI	Q	I²
General results	330					
PCL attaches to a bone		94.43%	85.60%	100.00%	76.79	88.28
PCL attaches to the dura mater		2.88%	0.55%	6.63%	20.43	55.95
PCL attaches to a bone and the dura mater		2.32%	0.00%	6.39%	36.10	75.07
PCL attaches to a bone and a bone		0.86%	0.10%	2.21%	5.45	0.00
Results gathered in Asia	219					
PCL attaches to a bone		99.24%	97.89%	100.00%	4.10	0.00
PCL attaches to the dura mater		0.76%	0.00%	2.11%	4.10	0.00
PCL attaches to a bone and the dura mater		0.00%	0.00%	0.00%	0.00	0.00
PCL attaches to a bone and a bone		0.00%	0.00%	0.00%	0.00	0.00
Results gathered in Europe	68					
PCL attaches to a bone		92.34%	84.65%	97.66%	0.82	0.00
PCL attaches to the dura mater		7.66%	2.34%	15.35%	0.82	0.00
PCL attaches to a bone and the dura mater		0.00%	0.00%	0.00%	0.00	0.00
PCL attaches to a bone and a bone		0.00%	0.00%	0.00%	0.00	0.00
Results gathered in North America	43					
PCL attaches to a bone		75.50%	0.00%	100.00%	15.94	93.73
PCL attaches to the dura mater		7.09%	0.00%	21.99%	1.53	34.62
PCL attaches to a bone and the dura mater		15.48%	0.00%	59.04%	6.99	85.69
PCL attaches to a bone and a bone		4.91%	0.16%	13.83%	0.46	0.00

LCI — lower confidence interval; HCI — higher confidence interval; Q — Cochran's Q

Table 7. Statistical results of this meta-analysis regarding the anterior attachment point of the petroclinoid ligament (PCL) on the bone in each category

Category	N	Pooled prevalence	LCI	HCI	Q	I²
Overall results	297					
On clivus		58.25%	7.68%	100.00%	528.14	98.49
Under posterior clinoid process		72.95%	28.05%	100.00%	426.46	98.12
On dorsum sellae		27.05%	0.00%	71.95%	426.46	98.12
Results gathered in Asia	219					
On clivus		52.44%	0.00%	100.00%	344.25	98.55
Under posterior clinoid process		90.01%	59.42%	100.00%	143.95	96.53
On dorsum sellae		25.10%	0.00%	72.15%	202.81	97.53
Results gathered in Europe	68					
On clivus		49.16%	0.00%	100.00%	130.96	99.24
Under posterior clinoid process		49.16%	0.00%	100.00%	130.96	99.24
On dorsum sellae		50.84%	0.00%	100.00%	130.96	99.24

LCI — lower confidence interval; HCI — higher confidence interval; Q — Cochran's Q

Table 8. Statistical results of this meta-analysis regarding the posterior attachment point of the petroclinoid ligament (PCL) on the bone in each category

Category	N	Pooled prevalence	LCI	HCI	Q	I²
Overall results	297					
On petrous apex		86.00%	55.13%	100.00%	291.71	97.26
On petrous ridge		4.75%	0.00%	14.07%	73.47	89.11
On petrous tubercle		6.07%	0.00%	27.10%	237.82	96.64
Results gathered in Asia	219					
On petrous apex		99.41%	98.20%	100.00%	0.74	0.00
On petrous ridge		0.00%	0.00%	0.00%	0.00	0.00
On petrous tubercle		0.00%	0.00%	0.00%	0.00	0.00
Results gathered in Europe	68					
On petrous apex		54.71%	0.00%	100.00%	110.94	99.10
On petrous ridge		0.71%	0.00%	3.41%	0.02	0.00
On petrous tubercle		45.29%	0.00%	100.00%	110.94	99.10

LCI — lower confidence interval; HCI — higher confidence interval; Q — Cochran's Q

(6) medial insertion; (7) lateral insertion and (8) midpoint. The results for each category are summarized in Table 9.

DISCUSSION

The morphology and variations of the PCL have been discussed extensively in the literature. The structure of the PCL has been described as being either butterfly- or triangular-shaped. Icke et al. [11] reported that 78% of PCLs were butterfly-shaped and 22% triangular. Iwanaga et al. [13] presented variations in PCL morphology in a study consisting of 36 sides of 18 fresh-frozen adult cadaveric heads. In the study, the shape of the PCL was described differently than that of a butterfly or a triangular shape. The PCL was categorized into three groups, which were, single-band type, Y-shaped type, and duplicated type. The single-band type was the most frequently observed type (58.1%). However, the results of the present meta-analysis show that the butterfly-shaped PCL is the most frequent type (79.59%).

There has been a lot of controversy with respect to the PCL attachment points, more specifically its anterior attachment point. The PCL was previously described as a ligament that extends from the posterior clinoid process anteriorly to its posterior attachment at the petrous tubercle of the petrous apex [11, 35]. However, a recent cadaveric study conducted

Table 9. Statistical result of meta-analysis regarding morphometrical features of petroclinoid ligament (PCL) in each category

Category	Mean	Standard error	Variance	Lower limit	Upper limit	Z-value	P-value
Length	11.05	1.00	1.00	9.09	13.01	11.06	0.00
Left PCL length	8.03	1.43	2.05	5.23	10.84	5.61	0.00
Right PCL length	8.01	1.53	2.34	5.01	11.01	5.24	0.00
Width	2.64	0.48	0.23	1.70	3.58	5.51	0.00
Thickness	0.74	0.22	0.05	0.31	1.18	3.34	0.00
Medial insertion	4.39	0.31	0.09	3.79	5.00	14.25	0.00
Lateral insertion	4.95	0.55	0.30	3.87	6.03	9.00	0.00
Midpoint	2.40	0.35	0.12	1.71	3.08	6.85	0.00

by Iwanaga et al. [13] states otherwise. In the study, the anterior attachment of the PCL was divided into two categories; PCL with an anterior attachment to the dura mater, or PCL with an anterior attachment to bone. When the PCL had an attachment to bone, the point of attachment was the lateral aspect of the upper clivus rather than the posterior clinoid process. However, the posterior attachment of the PCL was always at the petrous apex. Therefore, the authors of that study stated that the PCL should be described as the petroclival ligament because it represents this structure better and more accurately. The results of the present meta-analysis show that the most common anterior attachment of the PCL is the posterior clinoid process (72.95%), and the most frequently reported posterior attachment is the petrous apex (86.00%). Therefore, a change in the nomenclature of the PCL seems redundant.

The PCL forms the superior part of the DC. The DC was first described by Gruber in 1859 [7], as an osteofibrous canal at the apex of the petrous bone, containing the abducens nerve and the inferior petrosal sinus. Since then, numerous studies have been published on the morphology and clinical significance of DC. The AN has been described as a constant structure in the DC, with some studies reporting the nerve in 100% of the specimens [30, 32]. However, the present study shows that the prevalence of the AN going under the PCL (meaning inside the DC) is 93.02%. Tubbs et al. [30] presented an anatomical study on the DC and abducens nerve. In the study, a secondary tunnel was found within the DC that exclusively contained the abducens nerve. This structure limited the mobility of the AN, making it more susceptible to head trauma-induced injury. The DC also contains the DMA, which is said to supply the petroclival portion of the AN and the superior clival

dura, among others [17]. The data of this meta-analysis show that the DMA should be considered as a quite constant structure of the DC, with a prevalence of 94.40%.

The literature has been ambiguous regarding the nomenclature of the PCL. As mentioned above, some authors have used different terms when dealing with this structure. The other terms used for PCL include the Gruber ligament, the petrosphenoidal ligament, and the petroclival ligament [13]. Furthermore, it is crucial to understand that the PCL and posterior petroclinoid fold are two independent structures. The petroclinoid fold is a fold of the dura mater that extends between the anterior and posterior clinoid processes and the petrosal part of the temporal bone, and should not be referred to as a ligament [34]. Based on the results of the present meta-analysis, the PCL should be referred to as the petroclinoid ligament, because it represents this structure in the most precise way.

The PCL can undergo ossification causing changes in the anatomy of the base of the skull. The degree of ossification of PCL varies from being only partially ossified to being completely ossified, forming a bony bridge. Ossification can be unilateral or bilateral. The results of this meta-analysis show that the prevalence of ossification of PCL unilaterally is slightly higher (0.75%) than bilaterally (0.54%). Interestingly, the prevalence of complete PCL ossification was significantly higher in North America (3.46%) than in Europe (0.95%), even though the number of specimens in North America was lower by 335 PCLs. Although PCL ossification is said to be age-related, some studies have reported that it may also be a radiographic feature of basal cell carcinoma syndrome and systemic fluorosis [2].

Petroclinoid ligament ossification can increase the risk of AN injury. Tubbs et al. [31] reported that clini-

cians should consider ossification of PCL in patients with unexplained cases of AN palsy. In a radiological study conducted by Inal et al. [12] the calcification at the petroclival region was investigated using multiple slice computed tomography of the skull base. In the study, the clinical significance of PCL ossification was described. It was stated that if the PCL was ossified in patients with increased intracranial pressure syndrome, the pressure would not affect the AN passing under the PCL because the ligament would be hard and protect the nerve superiorly. Therefore, AN palsy would develop slower. On the contrary, the oculomotor nerve is superior to the PCL and DC. In the cases where PCL is ossified and lateral transtentorial herniation occurs, oculomotor nerve palsy would develop more rapidly.

Knowledge about the morphology of the PCL could be of great importance in neurosurgical procedures. Endoscopic transnasal surgeries are a good alternative for the treatment of skull base lesions. Tomio et al. [27] performed a cadaveric study in which they described the PCL as the most reliable landmark of the AN in the transnasal transclival view. They concluded that the PCL was a useful structure for locating the AN in tumour removal surgeries that use this approach. The PCL is also of significant clinical importance due to its proximity to the oculomotor nerve. During head trauma, downward displacement of the brain stem can result in damage to the pupillomotor fibres on the ventromedial surface of the oculomotor nerve, located on the PCL. This can lead to internal ophthalmoplegia [18].

Limitations of the study

This study is not without limitations and is burdened with potential bias, as the results of this meta-analysis may reflect anatomical variations of the Asian people, rather than of the global population. A potential sexual dimorphism in the anatomical features of the PCL was not established due to the lack of data. Analogically, no gender-related statistics were enrolled. Moreover, an analysis of morphometrical features of the PCL was not enrolled in relation to height of the subjects nor any other parameters due to lack of such information in primary studies.

CONCLUSIONS

In conclusion, the authors of the present study believe that this is the most accurate and up-to-date meta-analysis regarding the morphology and miner-

alization of the PCL. The most common attachment points of the PCL were the posterior clinoid process anteriorly (72.95%), and the petrous apex posteriorly (86.00%). The AN was most commonly found under the PCL, in the DC (93.02%), however, variations of the course of the AN fibres might occur. The data provided by the present study may be a useful tool for surgeons performing neurosurgical procedures, such as endoscopic transnasal surgeries. Detailed anatomical knowledge of the petroclival region can surely prevent surgical complications when operating in this area.

Conflict of interest: None declared

REFERENCES

1. Bayrak S, Göller Bulut D, Kurşun Çakmak EŞ, et al. Cone beam computed tomographic evaluation of intracranial physiologic calcifications. J Craniofac Surg. 2019; 30(2): 510–513, doi: 10.1097/SCS.0000000000004918, indexed in Pubmed: 30507878.
2. Cederberg RA, Benson BW, Nunn M, et al. Calcification of the interclinoid and petroclinoid ligaments of sella turcica: a radiographic study of the prevalence. Orthod Craniofac Res. 2003; 6(4): 227–232, doi: 10.1034/j.1600-0544.2003.00243.x, indexed in Pubmed: 14606526.
3. D'Antoni AV, Tubbs RS, Patti AC, et al. The critical appraisal tool for anatomical meta-analysis: a framework for critically appraising anatomical meta-analyses. Clin Anat. 2022; 35(3): 323–331, doi: 10.1002/ca.23833, indexed in Pubmed: 35015336.
4. Destrieux C, Velut S, Kakou MK, et al. A new concept in Dorello's canal microanatomy: the petroclival venous confluence. J Neurosurg. 1997; 87(1): 67–72, doi: 10.3171/jns.1997.87.1.0067, indexed in Pubmed: 9202267.
5. Ezer H, Banerjee AD, Thakur JD, et al. Dorello's canal for laymen: a lego-like presentation. J Neurol Surg B Skull Base. 2012; 73(3): 183–189, doi: 10.1055/s-0032-1311753, indexed in Pubmed: 23730547.
6. Ghorbanlou M, Moradi F, Mehdizadeh M. Frequency, shape, and estimated volume of intracranial physiologic calcification in different age groups investigated by brain computed tomography scan: a retrospective study. Anat Cell Biol. 2022; 55(1): 63–71, doi: 10.5115/acb.21.137, indexed in Pubmed: 34866062.
7. Gruber W. Anatomie des Keilbeins und Schlafenbeins. In: Richter HE, Winter A (eds.) Schmidt's Jahrbucher der Und Auslandischen. Gesammten Medicin, II, Anatomie und Physiologie 1859.
8. Henry BM, Tomaszewski KA, Ramakrishnan PK, et al. Development of the anatomical quality assessment (AQUA) tool for the quality assessment of anatomical studies included in meta-analyses and systematic reviews. Clin Anat. 2017; 30(1): 6–13, doi: 10.1002/ca.22799, indexed in Pubmed: 27718281.
9. Higgins JPT, Thomas J, Chandler J. et al. (eds). Cochrane Handbook for Systematic Reviews of Interventions. Wiley 2019.

10. Iaconetta G, Fusco M, Samii M. The sphenopetroclival venous gulf: a microanatomical study. J Neurosurg. 2003; 99(2): 366–375, doi: 10.3171/jns.2003.99.2.0366, indexed in Pubmed: 12924712.

11. Icke C, Ozer E, Arda N. Microanatomical characteristics of the petrosphenoidal ligament of Gruber. Turk Neurosurg. 2010; 20(3): 323–327, doi: 10.5137/1019-5149.JTN.2921-10.0, indexed in Pubmed: 20669104.

12. Inal M, Muluk NB, Burulday V, et al. Investigation of the calcification at the petroclival region through multi-slice computed tomography of the skull base. J Cranio-maxillofac Surg. 2016; 44(4): 347–352, doi: 10.1016/j.jcms.2016.01.018, indexed in Pubmed: 26922483.

13. Iwanaga J, Altafulla JJ, Gutierrez S, et al. The Petroclinoid Ligament: Its Morphometrics, Relationships, Variations, and Suggestion for New Terminology. J Neurol Surg B Skull Base. 2020; 81(6): 603–609, doi: 10.1055/s-0039-1692699, indexed in Pubmed: 33381363.

14. Kayacı S, Ozveren MF, Bas O, et al. Effect of clival bone growth on the localization of the abducens nerve at the petroclival region: a postmortem anatomical study. Surg Radiol Anat. 2021; 43(6): 953–959, doi: 10.1007/s00276-021-02691-z, indexed in Pubmed: 33687488.

15. Kumar A, Sehgal R, Roy TS. Ossified ligaments in relation to foramina and bony landmarks of the middle cranial fossa. J Anat Soc India. 2018; 67(1): 55–60, doi: 10.1016/j.jasi.2018.03.001.

16. Liu XD, Xu QW, Che XM, et al. Anatomy of the petrosphenoidal and petrolingual ligaments at the petrous apex. Clin Anat. 2009; 22(3): 302–306, doi: 10.1002/ca.20771, indexed in Pubmed: 19173250.

17. McCormack IG, Xu Lu, Nerva J, et al. Anatomy of the dorsal meningeal artery including its variations: application to skull base surgery and diagnostic and interventional imaging. World Neurosurg. 2021; 155: e41–e48, doi: 10.1016/j.wneu.2021.07.132, indexed in Pubmed: 34365050.

18. Nagaseki Y, Shimizu T, Kakizawa T, et al. Primary internal ophthalmoplegia due to head injury. Acta Neurochir. 1989; 97(3-4): 117–122, doi: 10.1007/BF01772821, indexed in Pubmed: 2718803.

19. Ozdede M, Kayadugun A, Ucok O, et al. The assessment of maxillofacial soft tissue and intracranial calcifications via cone-beam computed tomography. Curr Med Imag Rev. 2018; 14(5): 798–806, doi: 10.2174/1573405613666170428160219.

20. Ozer E, Icke C, Arda N. Microanatomical study of the intracranial abducens nerve: clinical interest and surgical perspective. Turk Neurosurg. 2010; 20(4): 449–456, doi: 10.5137/1019-5149.JTN.3303-10.1, indexed in Pubmed: 20963693.

21. Özgür A, Esen K. Ossification of the petrosphenoidal ligament: multidetector computed tomography findings of an unusual variation with a potential role in abducens nerve palsy. Jpn J Radiol. 2015; 33(5): 260–265, doi: 10.1007/s11604-015-0410-9, indexed in Pubmed: 25749833.

22. Ozveren MF, Sam B, Akdemir I, et al. Duplication of the abducens nerve at the petroclival region: an anatomic study. Neurosurgery. 2003; 52(3): 645–652, doi: 10.1227/01.neu.0000048186.18741.3c, indexed in Pubmed: 12590690.

23. Rzymski K, Kosowicz J. The skull in gonadal dysgenesis. A roentgenometric study. Clin Radiol. 1975; 26(3): 379–384, doi: 10.1016/s0009-9260(75)80082-1, indexed in Pubmed: 1201635.

24. Sedghizadeh PP, Nguyen M, Enciso R. Intracranial physiological calcifications evaluated with cone beam CT. Dentomaxillofac Radiol. 2012; 41(8): 675–678, doi: 10.1259/dmfr/33077422, indexed in Pubmed: 22842632.

25. Skrzat J, Walocha J, Jaworek JK, et al. The clinical significance of the petroclinoid ligament. Folia Morphol. 2007; 66(1): 39–43, indexed in Pubmed: 17533593.

26. Stanton JB, Wilkinson M. Familial calcification of the petrosphenoidal ligament. Lancet. 1949; 2(6582): 736–737, doi: 10.1016/s0140-6736(49)92258-8, indexed in Pubmed: 15390690.

27. Tomio R, Toda M, Sutiono AB, et al. Grüber's ligament as a useful landmark for the abducens nerve in the transnasal approach. J Neurosurg. 2015; 122(3): 499–503, doi: 10.3171/2014.10.JNS132437, indexed in Pubmed: 25380109.

28. Touska P, Hasso S, Oztek A, et al. Skull base ligamentous mineralisation: evaluation using computed tomography and a review of the clinical relevance. Insights Imaging. 2019; 10(1): 55, doi: 10.1186/s13244-019-0740-8, indexed in Pubmed: 31115710.

29. Tsitsopoulos PD, Tsonidis CA, Petsas GP, et al. Microsurgical study of the Dorello's canal. Skull Base Surg. 1996; 6(3): 181–185, doi: 10.1055/s-2008-1058643, indexed in Pubmed: 17170976.

30. Tubbs RS, Radcliff V, Shoja MM, et al. Dorello canal revisited: an observation that potentially explains the frequency of abducens nerve injury after head injury. World Neurosurg. 2012; 77(1): 119–121, doi: 10.1016/j.wneu.2011.03.046, indexed in Pubmed: 22130113.

31. Tubbs RS, Sharma A, Loukas M, et al. Ossification of the petrosphenoidal ligament: unusual variation with the potential for abducens nerve entrapment in Dorello's canal at the skull base. Surg Radiol Anat. 2014; 36(3): 303–305, doi: 10.1007/s00276-013-1171-8, indexed in Pubmed: 23877841.

32. Umansky F, Elidan J, Valarezo A. Dorello's canal: a microanatomical study. J Neurosurg. 1991; 75(2): 294–298, doi: 10.3171/jns.1991.75.2.0294, indexed in Pubmed: 2072168.

33. Wysiadecki G, Orkisz S, Gałązkiewicz-Stolarczyk M, et al. The abducens nerve: its topography and anatomical variations in intracranial course with clinical commentary. Folia Morphol. 2015; 74(2): 236–244, doi: 10.5603/FM.2015.0037, indexed in Pubmed: 26050813.

34. Wysiadecki G, Radek M, Tubbs RS, et al. Microsurgical anatomy of the inferomedial paraclival triangle: contents, topographical relationships and anatomical variations. Brain Sci. 2021; 11(5): 596, doi: 10.3390/brainsci11050596, indexed in Pubmed: 34064376.

35. Żytkowski A, Clarke E, Musiał A, et al. Atypical attachment of the petrosphenoidal (petroclival) ligament to the posterior genu of the cavernous internal carotid artery: case report. Transl Res Anat. 2022; 27: 100185, doi: 10.1016/j.tria.2022.100185.

VIA MEDICA

R E V I E W   A R T I C L E

Variations in extra-hepatic biliary tree morphology and morphometry: a narrative review of literature with focus on cystohepatic triangle

A. Priya[1], S.K. Ghosh[1], J.A. Walocha[2], A. Pasternak[2], J. Iwanaga[3–6], M. Loukas[7]

[1]Department of Anatomy, All India Institute of Medical Sciences, Phulwarisharif, Patna, India
[2]Department of Anatomy, Jagiellonian University, Krakow, Poland
[3]Department of Neurosurgery, Tulane Centre for Clinical Neurosciences, Tulane University School of Medicine, New Orleans, LA, United States
[4]Department of Neurology, Tulane Centre for Clinical Neurosciences, Tulane University School of Medicine, New Orleans, LA, United States
[5]Dental and Oral Medical Centre, Kurume University School of Medicine, Kurume, Fukuoka, Japan
[6]Division of Gross and Clinical Anatomy, Department of Anatomy, Kurume University School of Medicine, Kurume, Fukuoka, Japan
[7]Department of Anatomical Sciences, St. George's University, St. George's, Grenada, West Indies

The morphometry and morphology of the components of extrahepatic biliary tree show extensive variations. A beforehand recognition of these variations is very crucial to prevent unintended complications while performing surgeries in this region. This study was conducted to analyse the configuration of the extrahepatic biliary tree and its possible variations, as well as measure the components that limit the cystohepatic triangle. Articles were searched in major online indexed databases (Medline and PubMed, Scopus, Embase, CINAHL Plus, Web of Science and Google Scholar) using relevant key words. A total of 73 articles matched the search criteria of which 55 articles were identified for data extraction. The length of left and right hepatic duct in majority of studies was found to be > 10 mm. A wide range of diameters of hepatic ducts were observed between 5 and 43 mm. The average length of cystic duct is around 20 mm. The length and diameter of the common bile duct are 50–150 mm and 3–9 mm, respectively. The most frequently observed pattern of insertion of cystic duct into common hepatic duct is right lateral, rarely anterior, or posterior spiral insertion can present. The results of this study will provide a standard reference range which instead will help to differentiate the normal and pathological conditions. (Folia Morphol 2023; 82, 3: 498–506)

Key words: extrahepatic biliary tree, cystic duct, morphometry, morphology, cystohepatic triangle

Address for correspondence: Prof. A. Pasternak, Department of Anatomy, Jagiellonian University, ul. Kopernika 12, 31–034 Kraków, Poland, e-mail: artur.pasternak@uj.edu.pl

INTRODUCTION

The formation of extrahepatic bile duct is at the hepatic hilum (in proximity with the right end of porta hepatis) by union of left and right hepatic duct, to form common hepatic duct (Fig. 1). The normal length/diameter of left, right, and common hepatic duct is approximately 40 mm/4 mm, 30–40 mm//3–4 mm, and 60–80 mm/6 mm, respectively [21, 31]. Further, the lower end of cystic duct joins the right margin of common hepatic duct at an acute angle to form common bile duct (CBD; also known as Choledochal duct). The cystic duct usually measures 20 to 40 mm in length and the diameter of the cystic duct ranging from 1 to 5 mm [47, 52, 55]. Likewise, the length and diameter of CBD is generally varying between, 60 to 80 mm. The average external diameter is 9 mm (range 5–13 mm) and average internal diameter is 8 mm (range 4–12.5 mm) [56].

The evaluation of metrics of these ducts had begun in early 90's. At that point, the measurements were performed manually on autopsy specimens [15, 26]. In the course of time, several reports have attempted to measure these parameters by various techniques such as in cholangiograms [11, 32], vasculobiliary casts [12], sonographically [28], on computed tomography images [41], and recently magnetic resonance cholangiopancreatography (MRCP) [1, 14, 40] is being frequently used for these measurements. Eventually, it has been perceived that the dimensions of these ducts are highly variable as per available literature [1, 4, 7, 8, 11, 12, 14, 15, 26, 28, 31, 32, 40, 43, 44, 46, 48, 54, 57].

In addition, the union of cystic duct into common hepatic duct may have different configuration. The union can be right lateral, anterior spiral, posterior spiral, proximal, distal medial, distal lateral, or into the right hepatic duct. Based on this view, it has been classified [52]. This article attempts to review the existing literature on the variations of extrahepatic part of biliary tree to comprehend the possible cause and risk of post-operative complications of this region. According to the published studies the length and diameter of the extra hepatic biliary ducts may be correlated to the formation of bile duct stones, Mirizzi's syndrome, and bile duct cancer. This narrative review was undertaken to analyse the configuration of the extrahepatic biliary tree and its possible variations (morphological component), as well as collate the quantitative data regarding the components that limit the cystohepatic triangle (morphometric component).
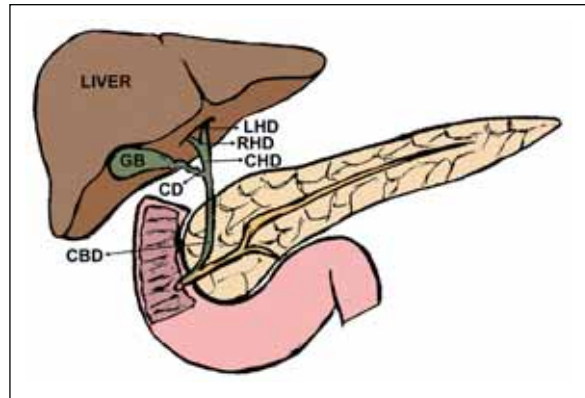

Figure 1. Illustration showing normal anatomical configuration of the components of extra-hepatic biliary tree; LHD — left hepatic duct; RHD — right hepatic duct; CHD — common hepatic duct; CD — cystic duct; CBD — common bile duct; GB — gall bladder.

Table 1. Inclusion and exclusion criteria used for literature search for the narrative review

Inclusion criteria

1. Full length original articles (peer reviewed and published) pertaining to morphology and morphometry of extrahepatic biliary tree
2. Studies reporting observational data relevant to the topic of study
3. Articles with information relevant to the study pertaining to any defined population
4. Articles published any time after inception of a database till conduction of literature search
5. Articles in English
6. Articles not in English but with available translations in English

Exclusion criteria

1. Pre-prints and non-peer-reviewed contents*
2. Case reports and short communications
3. Articles with limited information pertaining to the topic of study
4. Articles not in English and translation in English not available

*These were excluded as there could be possible changes in the data and the analysis thereof by the time it is published. This can have a confounding influence on data available from peer reviewed contents.

MATERIALS AND METHODS

Regarding the present study, narrative review was the preferred method as this approach was deemed as ideal to address the diverse aspects of the topic in terms of core concepts, published data, scientific resources and existing knowledge gaps [22]. Moreover, narrative review was found to be suitable in view of the fact that diverse methodologies were followed and taking into consideration the essentially descriptive nature of selected studies [18]. The literature search undertaken for this study was based on inclusion and exclusion criteria that were set after deciding the topic but before conducting literature search (Table 1).
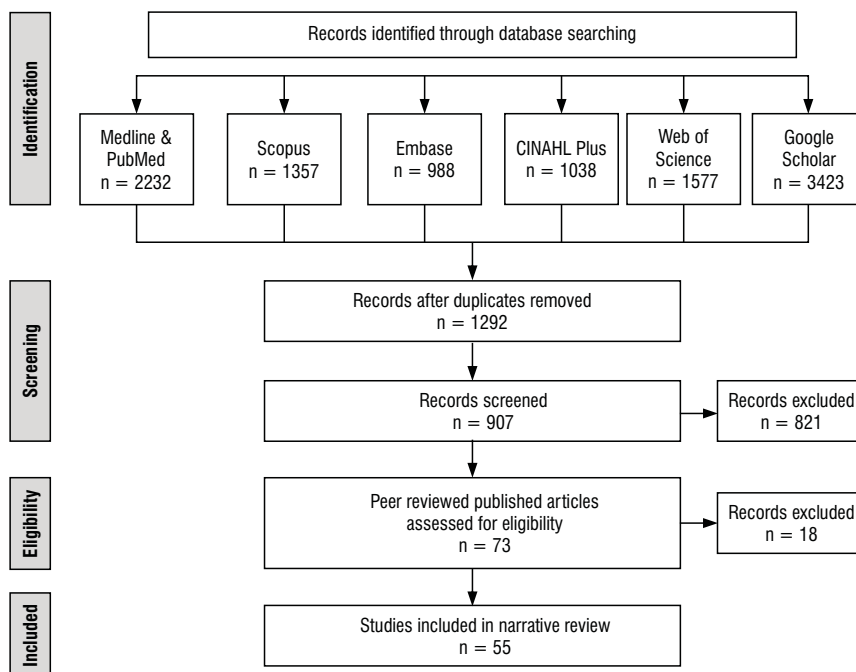
Figure 2. Flow chart depicting the literature search process for the present narrative review. The literature search was performed on the lines of searches for a narrative review, while incorporating the methodological rigour of a systematic review. The literature search process followed the best practice recommendations for preparing a narrative review by Ferrari [19] in order to mitigate risk of bias during selection of literature.

The study was conducted between May 2021 and January 2022. An extensive literature search was undertaken for this study from the following indexed databases:
— Medline and PubMed (United States National Library of Medicine, Bethesda, MD);
— Scopus (Elsevier, Amsterdam, The Netherlands);
— Embase (Ovid Technologies, Inc., New York, NY);
— CINAHL Plus (EBSCO Information Services, Ipswich, MA);
— Web of Science (Clarivate Analytics, Philadelphia, PA);
— Google Scholar (Google, Inc., Mountain View, CA).

The above databases were explored as all of them are multidisciplinary databases and provide access to a large volume of peer-reviewed scholarly research.

The literature search was based on key terms which were essentially key words from individual studies and mentioned at the time of indexation of particular research article. The key terms used for the present study were finalised during the course of literature search for finding articles relevant to the topic of present study. Accordingly, the following terms were used during literature search: "morphology of biliary tree"; "morphometry of biliary tree"; "morphology of extra-hepatic biliary tree"; "variations in anatomy of extra-hepatic biliary tree"; "morphology of bile duct";

"morphology of hepatic duct" and "morphology of cystic duct". Although the present study is a narrative review, but in order to mitigate the risk of bias in inclusion process, methodological rigour of a systematic review was incorporated in the literature search process. This was undertaken in accordance with the best practice recommendations for the preparation of a narrative review in clinical research [19]. A total of 55 published articles were identified as appropriate with regards to the topic of the present study (Fig. 2). After completion of literature search, the findings were compiled and final observations were prepared.

RESULTS

The anatomical variations of extrahepatic biliary duct have been documented since 3000 BC [36]. The surgical anatomy of this region gained importance with the emergence of cholecystectomy in 1882. In no area of the human body are the relationships as described in the text books of anatomy more misleading as to constancy than the region encompassing the extra-hepatic biliary ducts [25].

The variations in the morphometric components and configuration of extrahepatic biliary tree were analysed from available literature. The anatomy of the extrahepatic biliary tree is characterised with frequent aberrations [24]. In the present review it was noted with

Table 2. A chronological representation of variations in the morphometry of extrahepatic biliary tree in terms of length and diameter of left (LHD), right (RHD), and common (CHD) hepatic duct as reported in published literature

Authors [reference]	Sample size	Type of sample	Length [mm]			Diameter [mm]		
			LHD	RHD	CHD	LHD	RHD	CHD
Healey and Shroy [26]	100	Adult human livers	–	9	–	–	–	–
Dowdy et al. [15]	100	Autopsy specimens	10	8	20	3.4	4	8
Counaud [12]	110	Vasculobiliary casts	13.47	9	–	–	–	–
Kim et al. [32]	8194	Cholangiograms	–	–	–	–	–	Maximal diameter: 6.1 Mid-portion diameter: 5.3
Choi et al. [11]	300	Cholangiograms	–	12.8	–	–	–	–
Ayuso et al. [4]	25	Live liver specimens	–	< 10	–	3–4		–
Cachoeira et al. [8]	41	Cadaver	–	–	21.76	–	–	–
Deka et al. [14]	299	MRCP	7.83*	10.06*	22.05 ^	2.92*	2.59*	4.14 ^
Eftekhar et al. [16]	150	Cadaver	14.75	17.15	19.91	6.61	8.63	9.75
Awazli [3]	50	Human livers	–	–	25	–	–	–
Khatiwada et al. [31]	32	Liver specimens	20.77	10.48	–	ED = 2.54 ID = 1.37	ED = 3.37 ID = 2.1	–
Tellez et al. [54]	33	Blocks	12.6	10.3	28.6	3.1	4	4.6
Babu and Sharma [5]	100	Cadaver	15	13	29	15	16	43

*Length and diameter measured in 290 out of 299 samples only; ^ Length and diameter measured in 296 out of 299 samples only; MRCP — magnetic resonance cholangiopancreatography; ED — external diameter; ID — internal diameter

Table 3. A chronological representation of variations in the morphometry of extrahepatic biliary tree in terms of length and diameter of cystic duct as reported in published literature

Authors [reference]	Sample size	Type of sample	Cystic duct	
			Length [mm]	Diameter [mm]
Dowdy et al. [15]	100	Autopsy specimens	22	3
Cachoeira et al. [8]	41	Cadaver	19.11	–
Eftekhar et al. [16]	150	Cadaver	20.55	8.91
Rajguru and Dave [43]	100	Cadaver	2–62	2–8
Tellez et al. [54]	33	Blocks	27.8	3.3
Sangameswaran [46]	50	Cadaver	29	–

interest that there are significant variations in the range of length and diameter of hepatic, cystic, and CBD.

Furthermore, high frequency of aberration in the morphology (branching pattern) of the cystic duct was observed in published literature. Few authors have also classified it into various types based on the mode of insertion of the cystic duct into the common hepatic duct [6, 9, 23, 26, 37, 47].

Variations in morphometry of extrahepatic biliary ducts

Left, right, and common hepatic duct

The length and diameter of the right and left hepatic ducts constantly fluctuate. Frequently, the right hepatic duct is short, wide and more vertically aligned than the left hepatic duct [15, 31]. The mor-

phometry of hepatic ducts measured and evaluated in the previous studies has been tabulated (Table 2) [3–5, 8, 11, 12, 14–16, 26, 31, 32, 34].

Cystic duct

Few authors have found the cystic duct to be as short as 10 mm [38]. In, contrast to that the length of the cystic duct was observed to be > 40 mm in almost 25% cases [34]. The variances in length and diameter of cystic ducts are presented in (Table 3) [8, 15, 16, 34, 43, 46].

Common bile duct

Earlier, the deviation in size of CBD has been witnessed in different sample or imaging modalities as represented in (Table 4) [1, 2, 7, 12, 14, 15, 27, 28, 32–35,
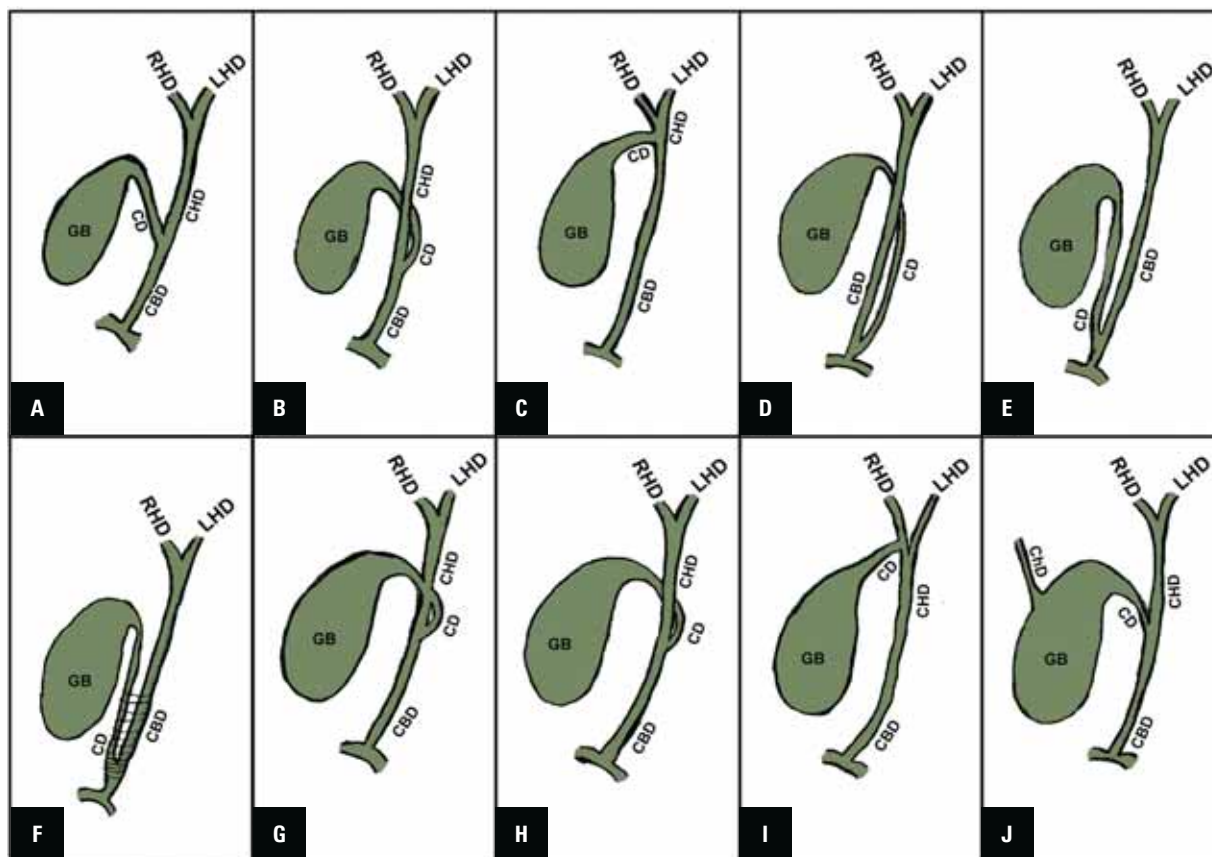
Figure 3. Illustration showing variations in the pattern of insertion of cystic duct as reported in available literature; **A.** Right lateral; **B.** Medial; **C.** Proximal; **D.** Low medial; **E.** Low lateral; **F.** Low lateral with common fibrous sheath; **G.** Anterior spiral; **H.** Posterior spiral; **I.** Into left hepatic duct; **J.** Cholecystohepatic duct; LHD — left hepatic duct; RHD — right hepatic duct; CHD — common hepatic duct; CD — cystic duct; CBD — common bile duct; GB — gall bladder.

40, 41, 44, 48, 57]. Additionally, the diameter of the CBD can range as high as 17 mm (average 8.85 mm) [20].

Classification of the morphology of cystic duct branching pattern

The entry of the cystic duct into the common hepatic duct has an inconsistent pattern. This pattern has been classified in different ways by various authors [6, 9, 23, 47, 52]. Cao et al. [9], 2019 gave a slightly unique classification in which the cystic duct represented three types of patterns (type I: right and angled up, type II: right and angled down, type III: angled up and left). Type I pattern was found to have great variation and could be further divided into three subtypes based on their mode of insertion: linear type, s type (s1, not surrounding CBD; s2, surrounding CBD), and α type (α1, forward α; α2, reverse α) by doing retrospective analysis of endoscopic trans papillary cannulation of the gallbladder. The schematic representation of various patterns of cystic duct insertion is shown in Figure 3.

DISCUSSION

The extra-hepatic biliary tract develops from the hepatic diverticulum (of foregut) at 4 weeks of intra-uterine life. Further, this diverticulum gives rise to pars hepatica and pars cystica. Hepatic ducts develop from pars hepatica and cystic duct develop from pars cystica. The stalk between the hepatic diverticulum and the foregut becomes the bile duct; its Y shaped bifurcation continues as right and left hepatic duct. Alteration in this normal phenomenon leads to developmental (morphological and morphometric) variants.

Morphometry of extrahepatic bile duct

The standard morphometric range plays significant role in differentiating between normal and pathological conditions. However, the exact morphometry of extrahepatic bile duct is still undetermined pertaining to the excessively varying dimensions observed by researchers in past.

Table 4. A chronological representation of variations in the morphometry of extrahepatic biliary tree in terms of length and diameter of common bile duct (CBD) as reported in published literature

Authors [reference]	Sample size	Type of sample	Common bile duct	
			Length [mm]	Diameter [mm]
Dowdy et al. [15]	100	Autopsy specimens	50	6.6
Couinand [12]			80–100	5–6
Mahour et al. [35]			–	6.21–8.39
Leslie [33]			9–58	5–17
Hollinshead [27]			90	–
Anson and McVay [2]			50–150	6–8
Horrow et al. [28]	258	Sonographic images	–	3.5
Kim et al. [32]	8194	Cholangiograms	–	Maximal diameter: 6.4 Mid-portion diameter: 5.5
Blidaru et al. [7]	172	Adults cadavers and human fetuses	72	5.25
Senturk et al. [48]	604	Patients	–	4.16
Deka et al. [14]	299	MRCP	5.1*	Diameter of CBD at upper end: 4.61 Diameter of CBD at lower end: 2.88
Peng et al. [40]	862	MRCP	–	4.13
Piyawong and Lekhavat [41]	277	CT images	–	4.65
Tellez et al. [54]	33	Blocks	CBD (supra duodenal): 15.5 CBD (retro duodenal): 29.3 CBD (intra pancreatic): 18.5	5.6
Worku et al. [57]	206	Sonographic images	–	3.64
Aljiffry et al. [1]	325	MRCP	–	7.57
Sah et al. [44]	30	Cadaver	46.92	6.50

*Length measured in 243 samples only, rest 56 was not measurable; CT — computed tomography; MRCP — magnetic resonance cholangiopancreatography

Left, right, and common hepatic ducts

The average length of the left and right hepatic duct is 17 mm and 9 mm [5], conforming to which, the length of left and right hepatic duct in majority of studies was found to be > 10 mm (Table 2). The length of common hepatic duct has been measured in various ways using cadavers, magnetic resonance imaging and MRCP. The length of common hepatic duct was seen to range from 19.1 to 36 mm [34]. The length of common hepatic duct was significantly long, i.e. 43 mm [14].

Cystic duct

The length of cystic duct often fluctuates from 10 to 50 mm (Table 3). An unusually long cystic duct [13, 30] may be associated with inflammatory changes and formation of calculi, resulting in persistent or recurrent biliary symptoms in affected patients. Too short cystic [3, 30, 34, 42, 47, 50] duct poses difficulty in clip occlusion during laparoscopic cholecystectomy.

Common bile duct

The size of the CBD helps to speculate about chances of biliary obstruction. With regard to this, an accurate CBD size reference range should exist [10]. A large number of published studies present the normal size of the CBD. However, an accurate range for CBD size is uncertain till date; therefore, a precise reference range for CBD size would help to distinguish obstructive from non-obstructive causes of jaundice [17]. The diameter of the CBD changes in response to various factors, such as, age, post-cholecystectomy, location of measurement, phase of respiration, and basal metabolic index. After analysing various studies we found the most common range of length was 50–100 mm and diameter to be 5–8 mm (Table 4).

Morphology of cystic duct
Pattern of cystic duct insertion into common hepatic duct

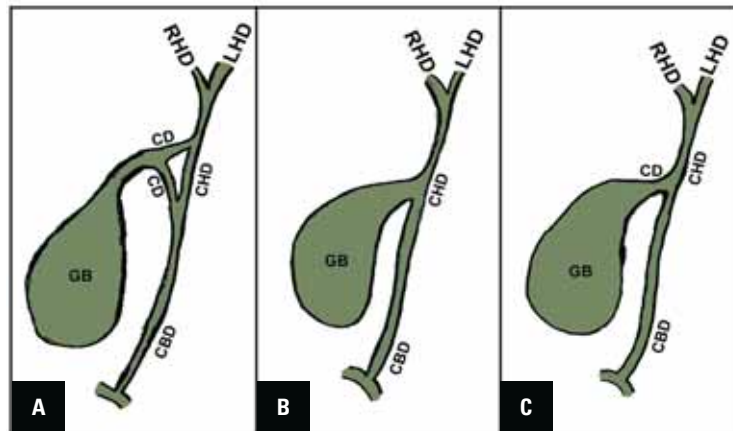Cystic duct anatomy was first described in 1654 by Francis Glisson. The mode of insertion of the cystic duct

Figure 4. Illustration showing variations in the morphology of cystic duct other than its pattern of insertion as reported in available literature; **A**. Bifurcation of cystic duct; **B**. Absent cystic duct; **C**. Short cystic duct; LHD — left hepatic duct; RHD — right hepatic duct; CHD — common hepatic duct; CD — cystic duct; CBD — common bile duct; GB — gall bladder.

in the common hepatic duct varies greatly. The pattern has been classified into several types: right lateral, medial, proximal, low medial, low lateral, low lateral with common fibrous sheath, anterior spiral, posterior spiral, into left hepatic duct (Fig. 3). The most common pattern observed is right lateral insertion [46, 50]. The proximal union of cystic duct with common hepatic duct resulting in short cystic duct [47]. Overlap of the cystic duct on the distal part of CBD is frequently seen with the low medial insertion [39, 55].

A cystic duct has parallel course (in cases of low medial or low lateral insertion). This long, parallel course sometimes is enclosed within a common fibrous sheath around the distal part of cystic duct and common hepatic duct. Therefore, it can be tricky during ligating the cystic duct in close proximity of common hepatic duct as there is risk of stricture formation in the latter post-cholecystectomy. The anterior and posterior spiral insertion may cause misperception during radiographic intervention such as MRCP. In rare situation, cystic duct enters into left hepatic duct [49, 50, 58]. Less commonly, cystic duct may drain into either ampulla of Vater or intraduodenally [46, 49, 55]. Cholecystohepatic duct (Fig. 3) can lead to post cholecystectomy biliary leak if unidentified pre-operatively.

Other variants of extrahepatic biliary duct

Accessory hepatic ducts, especially those arising from the right lobe, may join the common hepatic duct at its junction with the cystic duct or directly into the cystic duct (Fig. 4). Variable numbers of accessory hepatic ducts have been detected [51, 53]. There is high accidental probability of transection of this duct near its insertion into the cystic duct during

cholecystectomy [55]. Additionally, few other rare variants can be present such as bifurcation of cystic duct [45] before draining into common hepatic duct or absence of cystic duct [37, 50].

Limitations of the study

We concede that the present study is a narrative review and therefore has its limitations. Though we have tried to present a comprehensive data on this research topic, but we would imply on further evidence based meta-analysis which would be beneficial clinically.

CONCLUSIONS

Long cystic duct may be quiet baffling in cross-sectional imaging, which represents the parallel cystic duct and common hepatic duct as a septate cystic structure. Also, it can be cause of displacement of biliary stent. The usual diameter of cystic duct so as to differentiate it from pathological conditions such as dilatation due to passage of gall stone (as in Mirizzi syndrome). Calculus in the low medially inserting cystic duct at the ampulla of Vater may be confused for stones in the distal part of bile duct. Likewise, the other variant pattern should be known beforehand in order to prevent unmanageable unintended injury while operating. The bifurcation of cystic duct is often associated with morphological aberrations elsewhere and the condition is commonly referred to as VACTERL (vertebral defects, anal atresia, cardiac defects, tracheoesophageal fistula, renal anomalies, and limb abnormalities). Looking at the surge in laparoscopic cholecystectomies these variations in the extrahepatic biliary ducts can be dicey if the surgeons are not acquainted well before.

Acknowledgements

REFERENCES

1. Aljiffry M, Abbas M, Wazzan MAM, et al. Biliary anatomy and pancreatic duct variations: a cross-sectional study. Saudi J Gastroenterol. 2020 [Epub ahead of print]; 26(4): 188–193, doi: 10.4103/sjg.SJG_573_19, indexed in Pubmed: 32461381.

2. Anson B, Mcvay CB. Surgical anatomy. 5th ed. WB Saunders Co., Philadelphia 1971.

3. Awazli LG. Anatomical variations of extrahepatic biliary system. Iraqi J Med Sci. 2013; 11: 258–264.

4. Ayuso JR, Ayuso C, Bombuy E, et al. Preoperative evaluation of biliary anatomy in adult live liver donors with volumetric mangafodipir trisodium enhanced magnetic resonance cholangiography. Liver Transpl. 2004; 10(11): 1391–1397, doi: 10.1002/lt.20281, indexed in Pubmed: 15497156.

5. Babu CS, Sharma M. Biliary tract anatomy and its relationship with venous drainage. J Clin Exp Hepatol. 2014; 4(Suppl 1): S18–S26, doi: 10.1016/j.jceh.2013.05.002, indexed in Pubmed: 25755590.

6. Benson EA, Page RE. A practical reappraisal of the anatomy of the extrahepatic bile ducts and arteries. Br J Surg. 1976; 63(11): 853–860, doi: 10.1002/bjs.1800631105, indexed in Pubmed: 1000180.

7. Blidaru D, Blidaru M, Pop C, et al. The common bile duct: size, course, relations. Rom J Morphol Embryol. 2010; 51(1): 141–144, indexed in Pubmed: 20191134.

8. Cachoeira E, Rivas A, Gabrielli C. Anatomic variations of extrahepatic bile ducts and evaluation of the length of ducts composing the cystohepatic triangle. Int J Morphol. 2012; 30(1): 279–283, doi: 10.4067/s0717-95022012000100050.

9. Cao J, Ding X, Wu H, et al. Classification of the cystic duct patterns and endoscopic transpapillary cannulation of the gallbladder to prevent post-ERCP cholecystitis. BMC Gastroenterol. 2019; 19(1): 139, doi: 10.1186/s12876-019-1053-6, indexed in Pubmed: 31382888.

10. Chen D, Fei Z, Huang X, et al. Transcystic approach to laparoscopic common bile duct exploration. JSLS. 2014; 18(3), doi: 10.4293/JSLS.2014.00184, indexed in Pubmed: 25516702.

11. Choi JY, Kim MJ, Lee JM, et al. Hilar cholangiocarcinoma: role of preoperative imaging with sonography, MDCT, MRI, and direct cholangiography. AJR Am J Roentgenol. 2008; 191(5): 1448–1457, doi: 10.2214/AJR.07.3992, indexed in Pubmed: 18941084.

12. Couinaud C. Liver anatomy: portal (and suprahepatic) or biliary segmentation. Dig Surg. 1999; 16(6): 459–467, doi: 10.1159/000018770, indexed in Pubmed: 10805544.

13. Deenitchin GP, Yoshida J, Chijiiwa K, et al. Complex cystic duct is associated with cholelithiasis. HPB Surg. 1998; 11(1): 33–37, doi: 10.1155/1998/25781, indexed in Pubmed: 9830579.

14. Deka P, Islam M, Jindal D, et al. Analysis of biliary anatomy according to different classification systems. Indian J Gastroenterol. 2014; 33(1): 23–30, doi: 10.1007/s12664-013-0371-9, indexed in Pubmed: 24006122.

15. Dowdy GS, Waldron GW, Brown WG. Surgical anatomy of the pancreatobiliary ductal system. Observations. Arch Surg. 1962; 84: 229–246, doi: 10.1001/archsurg.1962.01300200077006, indexed in Pubmed: 13887616.

16. Eftekhar V, Shams AA, Jamalizade M. A study of the anatomic variations in extrahepatic bile ducts in 50 adults referred to Kerman forensic medicine organization. Anat Sci J. 2013; 10: 57–62.

17. Elgasim R, Abukonna A, Elgyoum A, et al. Measurement of the diameter of the common bile duct and pancreatic duct among healthy adult sudanese subjects using magnetic resonance cholangiopancreatography. Int J Biomed. 2020; 10(4): 392–396, doi: 10.21103/article10(4)_oa12.

18. El-Haddad J, Štrkalj G, Pather N. A global perspective on embryological and fetal collections: Where to from here? Anat Rec (Hoboken). 2022; 305(4): 869–885, doi: 10.1002/ar.24863, indexed in Pubmed: 35099840.

19. Ferrari R. Writing narrative style literature reviews. Med Writ. 2015; 24(4): 230–235, doi: 10.1179/2047480615z.000000000329.

20. Ferris DO, Vibert JC. The common bile duct: significance of its diameter. Ann Surg. 1959; 149(2): 249–251, doi: 10.1097/00000658-195902000-00011, indexed in Pubmed: 13627981.

21. Graham MF, Cooperberg PL, Cohen MM, et al. The size of the normal common hepatic duct following cholecystectomy: an ultrasonographic study. Radiology. 1980; 135(1): 137–139, doi: 10.1148/radiology.135.1.7360951, indexed in Pubmed: 7360951.

22. Gregory AT, Denniss AR. An introduction to writing narrative and systematic reviews: tasks, tips and traps for aspiring authors. Heart Lung Circ. 2018; 27(7): 893–898, doi: 10.1016/j.hlc.2018.03.027, indexed in Pubmed: 29857977.

23. Gündüz N, Doğan M, Alacagöz M, et al. Anatomical variations of cystic duct insertion and their relationship with choledocholithiasis: an MRCP study. Egypt J Radiol Nuclear Med. 2021; 52(1), doi: 10.1186/s43055-021-00579-x.

24. Hand B. Anatomy and function of the extrahepatic biliary system. Clin Gastroenterol. 1973; 2(1): 3–29, doi: 10.1016/s0300-5089(21)00331-x.

25. Hayes MA, Goldenberg IS, Bishop CC. The developmental basis for bile duct anomalies. Surg Gynecol Obstet. 1958; 107(4): 447–456, indexed in Pubmed: 13580794.

26. Healey JE, Schroy PC. Anatomy of the biliary ducts within the human liver; analysis of the prevailing pattern of branchings and the major variations of the biliary ducts. AMA Arch Surg. 1953; 66(5): 599–616, doi: 10.1001/archsurg.1953.01260030616008, indexed in Pubmed: 13039731.

27. Hollinshed WH. Anatomy for Surgeons. Vol. 2. 2nd ed. Harper and Row, New York 1971: 345–362.

28. Horrow MM, Horrow JC, Niakosari A, et al. Is age associated with size of adult extrahepatic bile duct: sonographic study. Radiology. 2001; 221(2): 411–414, doi: 10.1148/radiol.2212001700, indexed in Pubmed: 11687684.

29. Iwanaga J, Singh V, Ohtsuka A, et al. Acknowledging the use of human cadaveric tissues in research papers: Recommendations from anatomical journal editors. Clin Anat. 2021; 34(1): 2–4, doi: 10.1002/ca.23671, indexed in Pubmed: 32808702.

30. Khan AS, Shah Z. Anatomical variations of cystic duct encountered during open cholecystectomy. Kmuj. 2012; 4: 19–22.

31. Khatiwada S, Adhikari BN, Shakya S. Cadaveric study on the length and diameter of the hepatic ducts. Int J Health Sci Res. 2017; 7: 46–51.

32. Kim HJ, Kim MH, Lee SK, et al. Normal structure, variations, and anomalies of the pancreaticobiliary ducts of Koreans: a nationwide cooperative prospective study. Gastrointest Endosc. 2002; 55(7): 889–896, doi: 10.1067/mge.2002.124635, indexed in Pubmed: 12024146.

33. Leslie D. The width of the common bile duct. Surg Gynecol Obstet. 1968; 126(4): 761–764, indexed in Pubmed: 5643158.

34. Liechtenstein ME, Ivy AC. The function of the "valves" of Heister. Surgery. 1937; 1: 38–53.

35. Mahour GH, Wakim KG, Ferris DO. The common bile duct in man: its diameter and circumference. Ann Surg. 1967; 165(3): 415–419, doi: 10.1097/00000658-196703000-00011, indexed in Pubmed: 6019316.

36. Michels N. Blood supply and anatomy of the upper abdominal organs, with a descriptive atlas. Lippincott 1955.

37. Mortelé KJ, Ros PR. Anatomic variants of the biliary tree: MR cholangiographic findings and clinical applications. AJR Am J Roentgenol. 2001; 177(2): 389–394, doi: 10.2214/ajr.177.2.1770389, indexed in Pubmed: 11461869.

38. Nigam G, Lalwani R, Babu CSR, et al. Surgical anatomy of sub-hepatic biliary system. J Anat Soc India. 2014; 63(1): 48–51, doi: 10.1016/j.jasi.2014.05.001.

39. Pavlidis TE, Triantafyllou A, Psarras K, et al. Long, parallel cystic duct in laparoscopic cholecystectomy for acute cholecystitis: the role of magnetic resonance cholangiopancreatography. JSLS. 2008; 12(4): 407–409, indexed in Pubmed: 19275859.

40. Peng R, Zhang L, Zhang XM, et al. Common bile duct diameter in an asymptomatic population: A magnetic resonance imaging study. World J Radiol. 2015; 7(12): 501–508, doi: 10.4329/wjr.v7.i12.501, indexed in Pubmed: 26753065.

41. Piyawong W, Lekhavat V. Normal measurement of diameters of the common bile ducts in different aged groups. J Med Assoc Thai. 2016; 99(Suppl 4): S153–S158, indexed in Pubmed: 29926694.

42. Qamar N, Ishaque I, Ilyas A, et al. Identification of cystic duct variations in laparoscopic visual field. Pak J Surg. 2016; 32: 96–99.

43. Rajguru J, Dave M. The morphological aberrations of cystic duct and its clinical significance: a gross anatomical study. Int J Anat Res. 2018; 7: 2008–2013.

44. Sah SK, Pant H, Wang YX. Morphometric analysis of common bile duct: a cadaveric study. J Biomed Res Environmental Sci. 2021; 2(2): 064–068, doi: 10.37871/jbres1190.

45. Salih AM, Kakamad FH, Mohammed SH, et al. Double cystic duct, a review of literature with report of a new case. Int J Surg Case Rep. 2017; 38: 146–148, doi: 10.1016/j.ijscr.2017.07.027, indexed in Pubmed: 28759827.

46. Sangameswaran K. Variations of cystic duct and its clinical significance. Int J Anat Res. 2021; 9(4): 8120–8126, doi: 10.16965/ijar.2021.167.

47. Sarawagi R, Sundar S, Gupta SK, et al. Anatomical variations of cystic ducts in magnetic resonance cholangiopancreatography and clinical implications. Radiol Res Pract. 2016; 2016: 3021484, doi: 10.1155/2016/3021484, indexed in Pubmed: 27313891.

48. Senturk S, Miroglu TC, Bilici A, et al. Diameters of the common bile duct in adults and postcholecystectomy patients: a study with 64-slice CT. Eur J Radiol. 2012; 81(1): 39–42, doi: 10.1016/j.ejrad.2010.11.007, indexed in Pubmed: 21144686.

49. Shambhu Nath J, Omar S. Anatomical variation in extrahepatic biliary apparatus. Acad Anat Int. 2020; 6(2): 25–28, doi: 10.21276/aanat.2020.6.2.5.

50. Sirisha V, Udaya KP, Naveen K, et al. A study on the variations in cystic duct: clinical and embryological evaluation. Int J Anat Res. 2017; 5(3.2): 4308–4312, doi: 10.16965/ijar.2017.319.

51. Sobha DT, Krishna PH, Devi TS. The study of variations of extra-hepatic biliary apparatus. IOSR J Dent Med Sci. 2013; 5(5): 25–31, doi: 10.9790/0853-0552531.

52. Sureka B, Bansal K, Patidar Y, et al. Magnetic resonance cholangiographic evaluation of intrahepatic and extrahepatic bile duct variations. Indian J Radiol Imaging. 2016; 26(1): 22–32, doi: 10.4103/0971-3026.178283, indexed in Pubmed: 27081220.

53. Taourel P, Bret PM, Reinhold C, et al. Anatomic variants of the biliary tree: diagnosis with MR cholangiopancreatography. Radiology. 1996; 199(2): 521–527, doi: 10.1148/radiology.199.2.8668805, indexed in Pubmed: 8668805.

54. Tellez BS, Gomez EC, Porras PF, et al. Morphological expression of the extrahepatic bile duct. A study in a sample of Colombian mestizo population. Int Arch Med. 2018; 11, doi: 10.3823/2585.

55. Turner MA, Fulcher AS. The cystic duct: normal anatomy and disease processes. Radiographics. 2001; 21(1): 3–22, doi: 10.1148/radiographics.21.1.g01ja093, indexed in Pubmed: 11158640.

56. Vakili K, Pomfret EA. Biliary anatomy and embryology. Surg Clin North Am. 2008; 88(6): 1159–1174, doi: 10.1016/j.suc.2008.07.001, indexed in Pubmed: 18992589.

57. Worku MG, Enyew EF, Desita ZT, et al. Sonographic measurement of normal common bile duct diameter and associated factors at the University of Gondar comprehensive specialized hospital and selected private imaging center in Gondar town, North West Ethiopia. PLoS One. 2020; 15(1): e0227135, doi: 10.1371/journal.pone.0227135, indexed in Pubmed: 31971959.

58. Yamakawa T, Zhang T, Midorikawa Y, et al. A case of cystic duct drainage into the left intrahepatic duct and the importance of laparoscopic fundus-first cholecystectomy for prevention of bile duct injury. J Laparoendosc Adv Surg Tech A. 2007; 17(5): 662–665, doi: 10.1089/lap.2006.0240, indexed in Pubmed: 17907984.

REVIEW ARTICLE

The sternocleidomastoid muscle variations: a mini literature review

S. Silawal, G. Schulze-Tanzil

Institute of Anatomy and Cell Biology, Paracelsus Medical University, Nuremberg and Salzburg, General Hospital Nuremberg, Nuremberg, Germany

The sternocleidomastoid muscles (SCM) are prominent paired muscles of the neck connecting proximally the manubrium sterni and the clavicle to the mastoid process and the occipital bone distally. Following their points of attachment sternomastoid, sternooccipital, cleidomastoid and cleidooccipital portions of this muscle have been described. Altogether 23 case reports from year 2000 till 2020 with 29 subjects related to the SCM supernumerary variations were searched and analysed where parameters such as supernumerary proximal variation types (sternal vs. clavicular), insertional variation, unilaterality/bilaterality of the variation, study type, reported gender of the subjects and the country of research were extracted. The research shows that 48.3% of the subjects had bilateral presentation of SCM variations. If present unilaterally, three quarters of the cases were on the left side. The most frequent variation is located at the clavicular side of the proximal SCM head whereas isolated sternal sided proximal head variation or an insertional variation alone are very rare. Interestingly, with 96.6%, most of cases in the literature were discovered in cadavers during anatomical dissections. Male gender represented with 82.8% higher prevalence than females. The higher male prevalence in the body donor system, predominantly in the Asian continent could play a decisive role in the outcome as more than half of the reported cases stemmed from India in this period. Importantly, the knowledge of different anatomical variations of the SCM is highly relevant for surgical, clinical or radiological approaches in the neck. (Folia Morphol 2023; 82, 3: 507–512)

Key words: sternocleidomastoid, sternocervical, sternopharyngeal, trapezius, variation

INTRODUCTION

The sternocleidomastoid muscles (SCM) are prominent paired muscles of the neck connecting the sternum and the clavicle proximally to the mastoid process and the occipital bone distally [20]. Altogether, four different portions of the SCM, i.e. sternomastoid, sternooccipital, cleidomastoid and cleidooccipital, have been described [18]. The SCM blood supply is provided superiorly by the branches of the occipital artery and superior thyroid artery or direct branches of the external carotid artery or both and inferiorly by a branch arising from the suprascapular artery, the transverse cervical artery, the thyrocervical trunk or the superficial cervical artery [25]. The neural innervation of the SCM originates in the rostral portion of the brainstem nucleus of the accessory nerve

which receives input from both cerebral hemispheres whereas the neural branches to the cleidomastoid and trapezius muscles originate in the caudal portion of the brainstem nucleus and receive input only from the contralateral hemispheres [6]. In general, unilateral contraction of this muscle flexes the neck ipsilaterally and rotates the head so that the face is turned superiorly towards the contralateral side. Bilateral contraction helps to: (i) extend the neck at the atlantooccipital joints, (ii) flex cervical vertebrae that pulls chin towards the manubrium, or (iii) extend superior cervical vertebrae while flexing inferior vertebrae that thrusts the chin forward keeping the head levelled [30]. Also, a direct correspondence of the vestibular system with deep and superficial neck muscles such as SCM clarifies the importance of this muscle in movement and posture of the head and neck [9]. Furthermore, SCM is also part of the inspiratory muscles during deep respiration [30]. Any anomaly in the structure or/and physiology of this muscle could hence, result in respective functional limitation and alterations of the head or neck or even asymmetry in motion, in cases of unilateral variations.

From a developmental point of view, the muscles of the vertebrate neck generally comprise of the cucullaris and hypobranchial muscles along with the contribution of cephalic neural crest cells [8, 23, 24]. The cucullaris muscle is a gnathostome-specific muscle that is a homologue of sternocleidomastoid and trapezius muscles in mammals [23]. As suggested by the German anatomist Lubosch 1938, these two muscles are evolutionary derived from a single muscle that splits into two parts during amniote evolution [23]. A three-dimensional reconstruction technique in a human embryo showed the trapezius/SCM complex as a single cell condensation at estimated post-fertilisation age between 33 and 38 days which was later detected with separate identifiable muscles around 41 days [29]. The splitting of the embryological common trapezius/SCM complex can still be recognised as they share their innervation via the 11th cranial accessory nerve [10].

This process of separation of the common trapezius/SCM complex could result in different forms of SCM as well as trapezius variations. SCM variations are common where accessory branches from the clavicle or sternum connect to the normally existing SCM or separately either to the mastoid process or attach laterally to the superior nuchal line towards the trapezius muscle insertion [1, 2, 5, 7, 11, 12, 15, 17, 19, 27,

31–33, 35, 37, 41]. The variations at the insertional end of the muscle are less common in comparison to the occurrence of accessory proximal heads [7]. Depending upon the shape and courses of these additional muscular slips, neighbouring anatomical structures in the posterior triangle of the neck could be compromised. A clinical case report has also been reported where functional impairment with torticollis related to SCM variation was addressed in a male patient [27]. But also, a complete absence of the posterior triangle of neck on the left side of a 60-year-old Indian male cadaver was described in a case report where a unilateral separation of the trapezius/SCM complex failed to appear [44]. Hence, documentation of all these various anatomical variations of the SCM could be useful in clinical settings as well as surgical or radiological approaches in the neck.

METHODS

Studies related to the SCM supernumerary variations as well as embryological studies were achieved with Medline, Google Scholar as well as ResearchGate using mesh terms such as: sternocleidomastoid variations, sternocleidomastoid origin variation, sternocleidomastoid insertional variation. Supernumerary variation reports in proximal as well as distal attachment points of the SCM between year 2000 and 2020 have been included in this study. All reports with poor quality with no clear description of attachment points were excluded. Twenty nine subjects (individuals) in 23 research studies were analysed where parameters such as supernumerary proximal variation types (sternal vs. clavicular), insertional variation, unilaterality/ /bilateralism of the variation, study type as well as reported gender of the subjects and the country of research were extracted. Other variations, however, controversial in their affiliation to SCM variations, such as cleidocervical [46], cleidooccipital platysma [34], cleidohyoideus accessories [48] or recently described sternopharyngeal [43] muscles were not included in this survey.

RESULTS

The results from our small literature survey with altogether 23 case reports with 29 subjects has been illustrated in Table 1 [1–3, 5, 7, 11, 12, 15–17, 19, 22, 27, 28, 31–33, 35, 37, 38, 40, 41, 45]. Out of the total reported subjects, 86.2% presented with a muscular variation in the clavicular side of the SCM proximal head whereas 27.6% in the sternal side. However,

Table 1. List of the case reports with muscular variations of the sternocleidomastoid muscle

Publications	Proximal variation		Insertional variation	Unilateral		Bilateral	Cadaver report	Sex		Country
	Sternal	Clavicular		Left	Right			Male	Female	
Nayak et al., 2006 [32]	+							+		India (1)
Ramesh Rao et al., 2007 [37]		+				+	+	+		NP (1)
Cherian, Nayak, 2008 [5]		+		+			+	+		India (1)
Natsis et al., 2009 [31]	+	+				+	+	+		Greece (1)
Amorim Júnior et al., 2010 [1]		+	NP			+	+	+		Brazil (1)
Mehta et al., 2011 [28]		+		+			+	+		India (1)
Rani et al., 2011 [38]		+		+			+		+	India (1)
Raikos et al., 2012 [35]	+	+	#			+	+		+	NP (1)
Sirasanagandla et al., 2012 [45]		+			+		+	+		India (1)
Kaur et al., 2013 [17]	+	+			+		+	+		India (1)
Sabnis et al., 2013 [40]	+	+			+	+	++	+	+	India (2)
Kumar, George, 2014 [22]	+				+		+		+	India (1)
Saha et al., 2014 [41]		+++++		+++		++	+++++	+++++		India (5)
Kim et al., 2015 [19]	+	+				+	+	+		Korea (1)
Fulzele, Anil Kumar Reddy, 2015 [12]		+		+			+	+		India (1)
Anil et al., 2017 [2]		+				+	+	+		Turkey (1)
Arquez, 2017 [3]		++				++	++	++		Colombia (2)
Kaur et al., 2017 [16]		+		+			+	+		India (1)
Dupont et al., 2018 [7]			+			+	+	+		USA (1)
Mansoor, Rathore, 2018 [27]		+			+		+	+		Pakistan (1)
Oh et al., 2019 [33]		+				+	+		+	Korea (1)
Heo et al., 2020 [15]	+	+		+			+	+		Korea (1)
Fulmali et al., 2020 [11]		+		+			+	+		India (1)
	8/29 (27.6%)	25/29 (86.2%)	1/29 (3.5%)	10/29 (34.5%)	5/29 (17.2%)	14/29 (48.3%)	28/29 (96.6%)	24/29 (82.8%)	5/29 (17.2%)	

+ number of subjects; # cleidocervical variation; NP — not provided

509

isolated sternal head variation was reported only in 6.9% of the subjects. 20.7% presented with muscular variations in both clavicular as well as sternal ends of the SCM. Less than half of the analysed subjects (48.3%) showed a bilateral occurrence of a SCM variation. In case of a unilateral presentation, 66.7% out of 15 unilateral subjects were found on the left side of the SCM. Altogether, 96.6% of the SCM variations were discovered in anatomical dissection in cadavers. Furthermore, 82.8% of the subjects in the reported cases were male and 17.2% female. 58.6% of the case reports that were analysed in this study stemmed from India. Five case reports with six subjects were available from outside the Asian continent (Turkey included). Interestingly, there was 100% bilateral representation of the SCM variation in these cases. Also, all 6 reported subjects were male. Clavicular sided proximal variation was found in 83.3% of the cases whereas only a single report was available reporting an insertional variation.

DISCUSSION

A macroscopical study in an Indian population, SCM variations were reported in 27.8% of studied 18 cadavers [41]. Another similar small survey with 17 cadavers from Colombia showed 11.76% prevalence of SCM variations [3]. Focusing on the variation cases, we could show that clavicular sided variation of SCM is with around 3-fold more frequent in comparison to a sternal sided variation. Only a single report with an insertional variation was included in this review where a bilateral variant of the SCMs send one tendon to the mastoid and six distinct tendons along the lateral superior nuchal line to the midline [7]. A very low prevalence of this muscular insertional variation was seen in a Japanese statistical study of year 1968 where abnormal insertion of the SCM was found in 3.5% of Kyushu-Japanese male and 4.6% of the female from 354 bodies analysed [42]. Most case studies analysed in our survey, reported that the insertional attachments of the SCM were "normal", "as usual", "on the mastoid process", "lateral/near to the mastoid process" or "on the nuchal line". One of the limitations in most of the case reports where that even reported as normal insertional attachments, the manuscripts did not provide images showing the complete course of the SCM with clear depiction of the muscular insertion [2, 3, 5, 11, 12, 15–17, 19, 31–33, 35, 37, 38, 40, 41, 45]. Other insertional variations of SCM such as cleidocervical, cleidooccipital

platysma or the recently described sternopharyngeal variation of SCM have been described, however, they are discussed controversially in the literature as a subtype of a SCM variation [21, 26, 43, 46]. Since, this discussion is beyond the scope of this review, these variations have been excluded from our analysis.

Bilateral and unilateral presentation of the SCM variation was almost equally divided with 48.3% and 51.7% of the analysed subjects. If available unilaterally, there was a higher chance with 66.7% to be located on the left side of the neck. Discussing about the unilaterality, a clinical case of a young male patient was included in the study, where a right accessory unilateral clavicular head of SCM caused torticollis and limited the cervical range of motion in the patient [27]. This shows that besides unilateral agenesis of SCM or trapezius muscles, SCM variations can present a clinical image of congenital torticollis [4, 36, 47]. A different scenario was introduced before where a unilateral absence of the posterior triangle of the neck can also lead to access musculature on one side in comparison to other [44]. Even undiagnosed, many mild cases of such variations could limit certain range of cervical motion in affected people.

In our survey, 82.8% of the SCM variations were reported in males. There are two causes for this result. Either the variations in the embryological development is higher in males in comparison to females or simply the body donors for the dissections are dominantly males. In the above mentioned study from West Bengal, India with 18 cadavers, 3 out of 18 cadavers in anatomical dissections were female [41]. Likewise, the other study from Colombia also showed that from the 17 cadavers dissected, only 2 were female [3]. A lower female representation in the donor system of different countries can hence influence the statistics of variations in respect to gender-association. Cultural, religious, socioeconomic factors as well as specific research interests could exert great influence on the outcome of the results [14, 39]. 58.6% of the case reports that were analysed in this survey stemmed from India. Altogether 5 case reports with SCM variations from outside the Asian continent have been published since the year 2000. A heterogeneous collection of data from all parts of the world could probably provide a more representative picture. Likely the interest of reporting new anatomical case reports is not high enough today, where anatomical researches have more transitioned into cellular and molecular researches and macro-

scopical anatomy is underrepresented. On the other hand, a publication on case reports showed that there is still a big number of submitted case reports, but many are not published due to poor writing despite their academic worthiness [13]. Encouraging young students, investigators or clinicians and academics for publishing such case reports could support and improve practice of academic writing. In addition, the maintenance of practical dissection courses during early and late education of medical doctors opens the understanding for the multitude of variations possible, far away from the classical textbook knowledge — some of them indeed with practical clinical relevance. More data has to be documented for representative epidemiological researches. Finally, case reports can play a special role to inspire a possible association between an anatomical variation and developmental or genetical studies in the related area.

CONCLUSIONS

Analysing available case reports on the SCM variations we summarise that there is bilateral presentation in almost one in two SCM variations. If present unilaterally, three quarters of the cases are located on the left side. The most frequent variation is located at the clavicular side of the proximal SCM head whereas isolated sternal sided proximal head variation or an insertional variation alone are very rare. Interestingly, most of cases in the literature were discovered in male cadaver studies in anatomical dissections. This could be the result of higher male prevalence in the body donor system, predominantly in the Asian continent. Besides, reports of SCM variations from other clinical fields have to be encouraged to obtain a broader perspective in this field since knowledge of morphological variations are very relevant for clinical, surgical and radiological approaches into the neck.

Conflict of interest: None declared

REFERENCES

1. Amorim Junior AA, Lins CC, Cardoso APS, et al. Variation in clavicular origin of sternocleidomastoid muscle. Int J Morphol. 2010; 28(1): 97–98.
2. Anil A, Yasar YK, Anil F, et al. Variation of bilateral multi-headed sternocleidomastoid muscle. Gazi Med J. 2017; 28(1): 56–57, doi: 10.12996/gmj.2017.17.
3. Arquez HF. Muscular variation in the neck region with narrowing of the minor and major supraclavicular fossa. Int Arch Med. 2017; 10, doi: 10.3823/2478.
4. Chawla S, Tandon A, Meena G. Unilateral absence of sternocleidomastoid and ipsilateral trapezius presenting as congenital torticollis: a case of a rare entity. Cureus. 2021; 13(8): e17222, doi: 10.7759/cureus.17222, indexed in Pubmed: 34540449.
5. Cherian S, Nayak S. A rare case of unilateral third head of sternocleidomastoid muscle. Int J Morphol. 2008; 26(1), doi: 10.4067/s0717-95022008000100017.
6. De Toledo JC, David NJ. Innervation of the sterno-cleidomastoid and trapezius muscles by the accessory nucleus. J Neuroophthalmol. 2001; 21(3): 214–216, doi: 10.1097/00041327-200109000-00012, indexed in Pubmed: 11725190.
7. Dupont G, Iwanaga J, Altafulla JJ, et al. Bilateral sterno-cleidomastoid variant with six distinct insertions along the superior nuchal line. Anat Cell Biol. 2018; 51(4): 305–308, doi: 10.5115/acb.2018.51.4.305, indexed in Pubmed: 30637167.
8. Ericsson R, Knight R, Johanson Z. Evolution and development of the vertebrate neck. J Anat. 2013; 222(1): 67–78, doi: 10.1111/j.1469-7580.2012.01530.x, indexed in Pubmed: 22697305.
9. Forbes PA, Fice JB, Siegmund GP, et al. Electrical vestibular stimuli evoke robust muscle activity in deep and superficial neck muscles in humans. Front Neurol. 2018; 9: 535, doi: 10.3389/fneur.2018.00535, indexed in Pubmed: 30026725.
10. Fujita T. The smaller occipital nerve, its topographic relation to the trapezius-sternocleidomastoideus muscle system. Okajimas Folia Anat Japonica. 1959; 33(4): 217–224, doi: 10.2535/ofaj1936.33.4_217.
11. Fulmali D, Thute P, Keche H, et al. Variant sternocleidomastoid with extra clavicular head: a case report. J Evolution Med Dental Sci. 2020; 9(43): 3258–3260, doi: 10.14260/jemds/2020/715.
12. Fulzele RR, Anil Kumar Reddy Y. Accessory clavicular head of sternocleidomastoid muscle: a case report. Sch J Med Case Rep. 2015; 3(9B): 865–867.
13. Gopikrishna V. A report on case reports. J Conserv Dent. 2010; 13(4): 265–271, doi: 10.4103/0972-0707.73375, indexed in Pubmed: 21217956.
14. Habicht JL, Kiessling C, Winkelmann A. Bodies for anatomy education in medical schools: an overview of the sources of cadavers worldwide. Acad Med. 2018; 93(9): 1293–1300, doi: 10.1097/ACM.0000000000002227, indexed in Pubmed: 29561275.
15. Heo YR, Kim JW, Lee JH. Variation of the sternocleidomastoid muscle: a case report of three heads and an accessory head. Surg Radiol Anat. 2020; 42(6): 711–713, doi: 10.1007/s00276-019-02388-4, indexed in Pubmed: 31768700.
16. Kaur A, Sharma A, Sharma M. A case of unusual unilateral accessory clavicular head of sternocleidomastoid muscle. North States JJ Anat. 2017; 2(2): 25–28.
17. Kaur D, Jain M, Shukla L. Six heads of origin of sterno-cleidomastoid muscle: a rare case. Int J Med Update — EJOURNAL. 2013; 8: 62–64.
18. Kennedy E, Albert M, Nicholson H. The fascicular anatomy and peak force capabilities of the sternocleidomastoid muscle. Surg Radiol Anat. 2017; 39(6): 629–645, doi: 10.1007/s00276-016-1768-9, indexed in Pubmed: 27807639.
19. Kim SY, Jang HB, Kim J, et al. Bilateral four heads of the sternocleidomastoid muscle. Surg Radiol Anat. 2015;

37(7): 871–873, doi: 10.1007/s00276-014-1397-0, indexed in Pubmed: 25422097.

20. Kohan EJ, Wirth GA. Anatomy of the neck. Clin Plast Surg. 2014; 41(1): 1–6, doi: 10.1016/j.cps.2013.09.016, indexed in Pubmed: 24295343.

21. Kumar M, Sundaram SM, Fenn A, et al. Cleido-occipital platysma muscle: a rare variant of sternocleidomastoid muscle. Int J Anat Var. 2009; 2: 9–10.

22. Kumar V, George BM. A rare variation in the origin and insertion of sternocleidomastoid muscle: a case report. Int J Anat Var. 2014; 7: 17–18.

23. Kuratani S. Evolutionary developmental studies of cyclostomes and the origin of the vertebrate neck. Dev Growth Differ. 2008; 50(Suppl 1): S189–S194, doi: 10.1111/j.1440-169X.2008.00985.x, indexed in Pubmed: 18430164.

24. Kuratani S. Spatial distribution of postotic crest cells defines the head/trunk interface of the vertebrate body: embryological interpretation of peripheral nerve morphology and evolution of the vertebrate head. Anat Embryol (Berl). 1997; 195(1): 1–13, doi: 10.1007/s004290050020, indexed in Pubmed: 9006711.

25. Leclère FM, Vacher C, Benchaa T. Blood supply to the human sternocleidomastoid muscle and its clinical implications for mandible reconstruction. Laryngoscope. 2012; 122(11): 2402–2406, doi: 10.1002/lary.23430, indexed in Pubmed: 23007956.

26. Leon X, Maranillo E, Quer M, et al. Case report: cleido-cervical or levator claviculae muscle. A new embryological explanation as to its origin. J Anat. 1995; 187(Pt 2): 503–504, indexed in Pubmed: 7592015.

27. Mansoor SN, Rathore FA. Accessory clavicular sternocleidomastoid causing torticollis in an adult. Prog Rehabil Med. 2018; 3: 20180006, doi: 10.2490/prm.20180006, indexed in Pubmed: 32789231.

28. Mehta V, Arora J, Kumar A, et al. Bipartite clavicular attachment of the sternocleidomastoid muscle: a case report. Anat Cell Biol. 2012; 45(1): 66–69, doi: 10.5115/acb.2012.45.1.66, indexed in Pubmed: 22536555.

29. Mekonen HK, Hikspoors JP, Mommen G, et al. Development of the epaxial muscles in the human embryo. Clin Anat. 2016; 29(8): 1031–1045, doi: 10.1002/ca.22775, indexed in Pubmed: 27571325.

30. Moore KL, Dalley AF, Agur AMR. Clinically oriented anatomy. Wolters Kluwer Health/Lippincott Williams & Wilkins 2013.

31. Natsis K, Asouchidou I, Vasileiou M, et al. A rare case of bilateral supernumerary heads of sternocleidomastoid muscle and its clinical impact. Folia Morphol. 2009; 68(1): 52–54, indexed in Pubmed: 19384831.

32. Nayak SR, Krishnamurthy A, Kumar Sj M, et al. A rare case of bilateral sternocleidomastoid muscle variation. Morphologie. 2006; 90(291): 203–204, doi: 10.1016/s1286-0115(06)74507-6, indexed in Pubmed: 17432052.

33. Oh JS, Kim CE, Kim J, et al. Bilateral supernumerary clavicular heads of sternocleidomastoid muscle in a Korean female cadaver. Surg Radiol Anat. 2019; 41(6): 699–702, doi: 10.1007/s00276-019-02227-6, indexed in Pubmed: 30919044.

34. Rahman HA, Yamadori T. An anomalous cleido-occipitalis muscle. Acta Anat (Basel). 1994; 150(2): 156–158, doi: 10.1159/000313645, indexed in Pubmed: 7976196.

35. Raikos A, Paraskevas G, Triaridis S, et al. Bilateral supernumerary sternocleidomastoid heads with critical narrowing of the minor and major supraclavicular fossae: clinical and surgical implications. Int J Morphol. 2012; 30(3): 927–933, doi: 10.4067/s0717-95022012000300027.

36. Raman S, Takhtani D, Wallace EC. Congenital torticollis caused by unilateral absence of the sternocleidomastoid muscle. Pediatr Radiol. 2009; 39(1): 77–79, doi: 10.1007/s00247-008-1021-8, indexed in Pubmed: 18839164.

37. Ramesh Rao T, Vishnumaya G, Prakashchandra S, et al. Variation in the origin of sternocleidomastoid muscle: a case report. Int J Morphol. 2007; 25(3): 621–623, doi: 10.4067/s0717-95022007000300025.

38. Rani A, Kumar Srivastava A, Rani A, et al. Third head of sternocleidomastoid muscle. Int J Anat Var. 2011; 4: 204–206.

39. Rokade S, Bahetee B. Body donation in India: a review. Int J Res Med Sci. 2013; 1(3): 173, doi: 10.5455/2320-6012.ijrms20130814.

40. Sabnis A, Shaikh S, More R. Third head of sternocleidomastoid muscle. Nat J Clin Anat. 2020; 02(04): 218–220, doi: 10.1055/s-0039-3401721.

41. Saha A, Mandal S, Chakraborty S, et al. Morphological study of the attachment of sternocleidomastoid muscle. Singapore Med J. 2014; 55(1): 45–47, doi: 10.11622/smedj.2013215, indexed in Pubmed: 24241357.

42. Sato S. Statistical studies on the exceptional muscles of the Kyushu-Japanese. 2. The muscles of the neck. Kurume Med J. 1968; 15(2): 83–95, doi: 10.2739/kurumemedj.15.83, indexed in Pubmed: 5191620.

43. Silawal S, Morgan S, Ruecker L, et al. A unilateral sternopharyngeal branch of the sternocleidomastoid muscle in an aged Caucasian male: a unique cadaveric report. Folia Morphol. 2023; 82(2): 434–438, doi: 10.5603/FM.a2022.0016, indexed in Pubmed: 35187633.

44. Singh S, Chauhan P, Loh HK, et al. Absence of posterior triangle: clinical and embryological perspective. J Clin Diagn Res. 2017; 11(2): AD01–AD02, doi: 10.7860/JCDR/2017/23896.9176, indexed in Pubmed: 28384846.

45. Sirasanagandla S, Bhat K, Pamidi N, et al. Unusual third head of the sternocleidomastoid muscle from the investing layer of cervical fascia. Int J Morphol. 2012; 30(3): 783–785, doi: 10.4067/s0717-95022012000300001.

46. Tomo S, Toh H, Hirakawa T, et al. Case report: the cleido-cervical muscle with speculation as to its origin. J Anat. 1994; 184(Pt 1): 165–169, indexed in Pubmed: 8157489.

47. Vajramani A, Witham FM, Richards RH. Congenital unilateral absence of sternocleidomastoid and trapezius muscles: a case report and literature review. J Pediatr Orthop B. 2010; 19(5): 462–464, doi: 10.1097/BPB.0b013e32833ce404, indexed in Pubmed: 20647939.

48. Vorakulpipat C, Arayapisit T, Chunhabundit P, et al. The unilateral cleidohyoideus accessorius muscle in human: a case report. Mehidol Dent J. 2022; 42(1): 63–68, indexed in Pubmed: 255689.

VIA MEDICA

REVIEW ARTICLE

Cleidocervical muscle: a mini literature survey of a human muscle variation

S. Silawal, V. Franke, J. Wehrmann, G. Schulze-Tanzil

Institute of Anatomy and Cell Biology, Paracelsus Medical University, Nuremberg and Salzburg, General Hospital Nuremberg, Nuremberg, Germany

Cleidocervical muscles (CCM) or levator claviculae muscles in humans can be found as supernumerary unilaterally or bilaterally on the neck attached proximally to the clavicle and distally to the transverse process of cervical vertebrae at various levels. Altogether 20 case reports from year 1994 till present including 25 subjects related to CCM were found and analysed where parameters such as cervical insertion level, clavicular insertion at the middle vs. lateral third, unilateral vs. bilateral presence of the muscle, study type, reported gender of the subjects were extracted. Our literature survey shows that the prevalence of CCM in male and female was equally presented in radiological studies whereas almost 3-fold higher prevalence of males was found in cadaver reports. Since body donor system worldwide is male dominant, a 1:1 proportion of male and female in radiological studies could show more reality-based distribution of this muscle. Nevertheless, the presentation of this muscle was found in over 90% of the case reports unilaterally with higher left sided dominance. Even though the attachment points of CCM varied from case to case, the proximal attachment was found slightly more frequent on the middle third of the clavicle whereas the distal insertion was present more often on the superior cervical vertebrae than the lower ones. With prevalence of CCM in the population around 2.0–2.5%, the clinical, radiological and surgical relevance of this variation has to be highlighted to avoid potential misleading diagnostics in the neck. (Folia Morphol 2023; 82, 3: 513–518)

Key words: cleidocervical, levator claviculae, cleidoatlanticus, scalene muscles

INTRODUCTION

Cleidocervical muscles (CCM), also termed as levator claviculae muscles are vestigial muscles in humans which can be found unilaterally or bilaterally on the neck in around 2.0–2.5% of the population [7, 27, 34]. This muscle is attached proximally to the clavicle, runs upwards and crosses obliquely the posterior triangle of the neck before traversing underneath the sterno-cleidomastoid muscle to connect with the transverse process of the cervical vertebrae (Fig. 1). However, the proximal as well as distal points of their insertion can vary from case to case. For instance, both middle or lateral portions of the clavicle can serve as the attachment of the muscle proximally, whereas it can connect to the transverse process of cervical vertebrae at various levels distally. The muscle, when attached to the upmost cervical vertebra, the atlas, is termed as cleido-atlanticus muscle [12, 25]. On 28th April 1876, Grüber

Address for correspondence: Dr. S. Silawal, Institute of Anatomy and Cell Biology, Paracelsus Medical University, Salzburg and Nuremberg, Prof. Ernst Nathan Str. 1, 90419 Nuremberg, Germany, tel: +49 – (0)911-398-116771, fax: +49 – (0)911-398-6774, e-mail: sandeep.silawal@pmu.ac.at; sandeep.silawal@klinikum-nuernberg.de
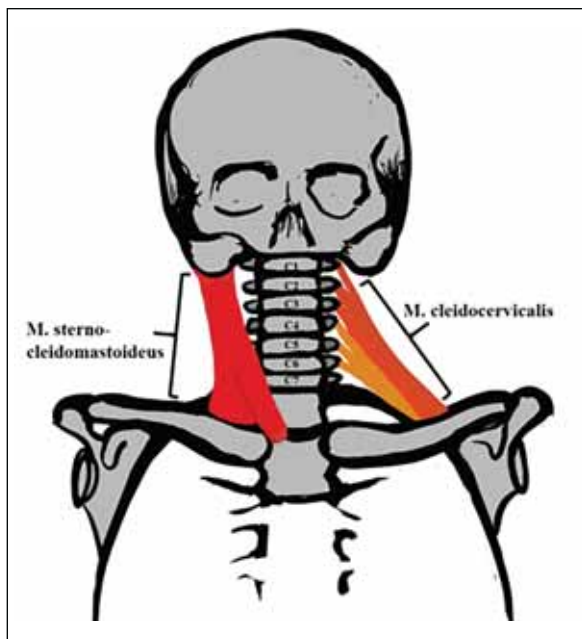
Figure 1. Schematic illustration of the cleidocervical muscle.

[15] dissected the cleidoepistrophicus muscle which connected the anterior tubercle of the transverse process of the axis with the clavicle on the right side of the neck in a male cadaver. Grüber [15] described this muscle as a long, broad and strong muscle slip innervated by the 3rd cervical spinal nerve. Odate et al. [22], reviewed different literatures that have suggested embryological muscle origins related to CCM such as the sternocleidomastoid muscle, trapezius muscle, the anterior scalene and the longus colli muscles. Following different literatures, affiliation to any one of the above origins is a controversial issue. In canines, CCM as well as cleidomastoid muscles are not any muscular variations but integral parts of the brachiocephalicus muscle group originating on the shoulder girdle and inserting on the fibrous raphe of the cranial half of the neck, the skull and on the mastoid process of the temporal bone, respectively [31]. In humans, this vestigial muscle is only found in rare cases, where the muscle is attached deep and medially to the cervical vertebra and extends laterally to the superficial clavicle, forming an irregular triangular space in the posterior triangle of the neck. Underneath this muscle blood vessels, nerves and lymphatics generally pass through to access communication between the upper extremity and the trunk. The presence of this muscle can be symptomatically silent, however, as a predictable result, symptomatic conditions such as thoracic outlet syndrome can be found as reported

in a case study where a 26-year-old male gymnast presented with pain on the right side of his neck, lateral side of right shoulder and right supraclavicular area while lifting heavy objects or arm elevation [3]. As known, a metastatic spread of cancer can lead to an enlargement of the left supraclavicular lymph node, known as the Virchow node [35]. To our context, left sided unilateral presence of this muscle for example could lead to misinterpretation in radiological images as a lymphadenopathy, especially in tumour patients [26, 28]. Therefore, understanding CCM anatomy, their clinical relevance can help radiologists, surgeons as well as clinicians to avoid possible confusion or unnecessary diagnostic measures.

MATERIALS AND METHODS

Literature research related to the CCM variations between year 1990 and 2019 as well as embryological studies were accessed with Medline, Google Scholar as well as ResearchGate using mesh terms such as: CCM variations, levator claviculae. Parameters such as muscular attachment points, unilaterality/bilaterality of the variation, study type as well as reported gender of the subjects were extracted.

Altogether 20 case reports from year 1994 till 2019 with 25 subjects were analysed in the survey. Some case reports were excluded from the analysis even though they would match according to the searching mesh terms. For example, a muscular variation originated from trapezius and inserted to the clavicle lateral to the sternocleidomastoid was unfortunately termed as levator claviculae muscle [23]. In terms of historic reports, more appropriate terminology for such variation would be cleidooccipital muscle [34]. Another case report by Bhatnagar and Smith (2021) [4] was also excluded from this analysis, since the superior attachment of this muscle was to the longus capitis muscle fascia rather than to the cervical vertebra itself.

RESULTS

The case reports that we have analysed for this study were based on cadaver research in anatomical dissections as well as on interpretation of radiological images, both 48%. Only a single case was reported as a surgery finding (Fig. 2A). In total subjects from all report types, this survey showed that presence of CCM was slightly more than double fold available in male in comparison to female gender (Fig. 2B). However, if only the radiological reports were considered
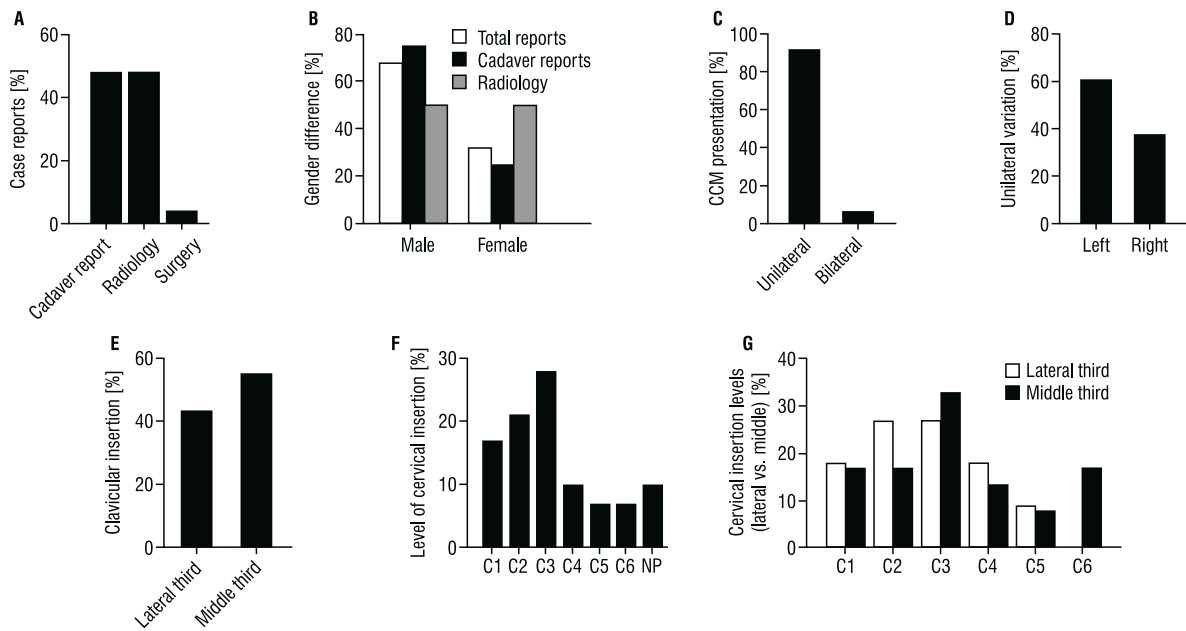
Figure 2. Graphical illustration of various parameters analysed in the literature review from the case reports listed in Table 1; CCM — cleido-cervical muscles; NP — not provided.

for the analysis, the distribution between male and female was equal, i.e. 1:1. In comparison, the cadaver reports showed discrepancy with 3-fold higher male prevalence compared to that in female. Interestingly, CCM was found in 92% of the cases unilaterally (Fig. 2C). However, when present unilaterally, the left sided presentation of the muscle was slightly more frequent than on the right side (Fig. 2D). The proximal attachment of the CCM was found in 56% of the cases on the middle third and 44% on the lateral third of the clavicle (Fig. 2E). Regarding the distal insertion, the attachment of CCM was found mostly at the C1–C3 vertebrae (Fig. 2F). The third cervical vertebra was reported in 28% of the cases as attachment site, followed by the axis with 21% and finally the atlas with 17%. C5 and C6 were the least involved vertebra where respectively 7% of the cases were reported. It has to be considered that in 10% of the case reports, proper description for distal attachments were not provided. If lateral and middle proximal insertions were analysed separately, it showed that the laterally inserted CCM were rather attached more frequently at C2–C3, both 27% whereas no attachment was found on C6 (Fig. 2G). On the other hand, CCM inserted proximally in the middle third of the clavicle showed their most frequent reported distal insertions with 36% at C3. In both of the cases with bilateral presentation, the distal insertions were superior levels of the cervical vertebrae. A tabular illustration for

the above results has been provided below (Table 1) [3, 5, 8, 10–14, 18–22, 24–29, 33].

DISCUSSION

Incidental anatomical findings can be identified in clinical practice during physical examinations, diagnostic imaging or surgical procedures. However, most of the incidental findings regarding anatomical variations are rather reported in cadaver studies [1, 32]. In our literature review, the reported cases were represented in cadaver studies as well as radiological findings equally with 48%, respectively (Fig. 2A). In a historic report of 1870, Wood and Sharpey [34] described CCM to the Royal Society which he discovered 5 years ago in 1864 bilaterally in 2 male subjects. In the same report, Wood and Sharpey [34] noted that CCM was found in altogether 4 males out of 131 (3.05%) and in 1 female out of 71 (1.4%) in a total number of 202 subjects with an average of ca. 2.5%. Hence, the distribution of CCM prevalence between male and female was about 2:1. More than a century later, Rubinstein et al. [27], showed in 1999 the prevalence of 2% in the population analysed using 300 computed tomography-scan images. However, the gender parameter was not considered in their analysis. Our literature review with altogether with 25 subjects displays a double fold prevalence of men in comparison to females of total case reports (Fig. 2B). This shows a very drastic

Table 1. Tabular illustration of case reports

Publications	Cervical insertion	Clavicular insertion	Unilateral		Bilateral	Cadaver report	Radiology	Surgery	Sex	
			Left	Right					Male	Female
Fasel et al., 1994 [10]	NP	L	+				+			+
Tomo et al., 1994 [33]	C6	M	+			+			+	
Leon et al., 1995 [19]	C2	M		+		+			+	
Rüdisüli, 1995 [28]	C3	L	+				+		+	
Rubinstein et al., 1999 [27]	C1–C3	L(5)/M(2)	++++	+	+		+++++		NP	
Ginsberg, Eicher, 1999 [14]	C3	M	+				+			+
Rosenheimer et al., 2000 [26]	C6	M		+			+			+
Ruiz Santiago et al., 2001 [29]	NP	M		+			+		+	
Koshy et al., 2005 [18]	C1–C2	L(2)			+	+			+	
Aydoğ et al., 2007 [3]	NP	M		+			+		+	
Capo, Spinner, 2007 [8]	C2	L	+			+			+	
Loukas et al., 2008 [20]	C3–C4	L	+			+			+	
Natsis et al., 2009 [21]	C3–C5	L		+		+			+	
Rodríguez-Vázquez et al., 2009 [25]	C1	M		+		+			+	
Fazliogullari et al., 2010 [11]	C3	M	+			+			+	
Feigl, Pixner, 2011 [12]	C1	M		+		+				+
Odate et al., 2012 [22]	C4	M	+			+				+
Raikos et al., 2012 [24]	C3	M	+			+				+
Billings, Sherrill, 2014 [5]	C5	M		+		+			+	
Ferreli et al., 2019 [13]	C2–C3	M	+					+	+	
Total			14	9	2	12	12	1	13	6

M — median third of a clavicle, L — lateral third of a clavicle; NP — not provided

difference in results depending on which reports was analysed for this study. The explanation could be that a drastic lower number of female cadavers are available for anatomical dissection in many parts of the world in comparison to their male counterparts [30]. In the second half of the 19th century, gender difference in the cadaver subjects reported by Wood and Sharpey [34] showed that almost two-third of the subjects were male. Hence, the distribution of the genders in the cadaveric studies can vary depending on the time period in which the studies were performed as well as socioeconomic, educational status of the donors in the society [2, 17]. A study from Ohio, United States, 1996 showed that even though the cadaveric donors to the donation programme were predominantly male (58%), a clear trend for increasing numbers of females were noted [9]. This clearly depicts the manner of dynamic changes in above mentioned aspects of our society. Analysing only the radiological reports however, there was an equal distribution between male and female prevalence of this muscle (Fig. 2B). The probable reason could be that the imaging diagnostics are not preferably performed more in males in comparison to females. Hence, we assume that radiological studies could show more reality-based distribution of this muscle at present time.

John Wood wrote that Professor W. Grüber in St. Petersburg, described CCM in year 1847 (Vier Abhandlungen, S. 22), where this muscle was attached from the transverse process of C2 to the middle portion of the clavicle [34]. Grüber [16] cited another right sided variation in a male reported by Kelch et al. in 1813 (Beitraege zur pathologischen Anatomie, Berlin, 1813,

xxiv. S. 32) which could possibly be the oldest record-ed description of this muscle. Other descriptions of this muscle by various authors in historic reports have been put together in a review by Odate et al. (2012) [22]. Our analysis comprises reports after 1990 until present day where unilateral CCM presentation was found in over 90% of the studies (Fig. 2C). A unilateral presence of the variance on the neck could probably provoke high attention in a clinical scenario where this muscle could be misinterpreted as pathological case such as lymphadenopathy, metastatic lymph nodes or neoplasms [13, 26]. Left sided presentation of CCM was slightly higher than on the ride side (Fig. 2D). Specially, the left sided CCM can be misread as an enlargement of the left supraclavicular Virchow node [35]. The proximal attachments of the muscle were described in all the case reports either on the lateral or on the middle third of the clavicle. But no report has been made so far describing their prox-imal attachment on the medial third. Slightly more reports with middle third insertion were available so far in comparison to the lateral one (Fig. 2E). However, concerning the cervical attachment C3 level had the highest reference in comparison to other cervical levels (Fig. 2F). In general, the superior cer-vical levels showed more regular distal attachment than to the inferior ones. Some case reports could not provide accurate cervical attachment level for the muscle, probably due to difficulty in the evaluation of the radiological images [3, 10, 29]. Obviously, an-atomical dissections are distinctly more convenient to evaluate the exact insertion points in comparison to radiological or surgical approaches. Figure 2G shows that CCM attached proximally on the lateral third of the clavicle are distally attached to the cervical vertebrae C1–C5 with maximum references to C2/C3 whereas the muscles with middle third attachment of the clavicle are distally attached to C1–C6 with maximum reference at C3. There could be a possible pattern to differentiate if lateral and middle third inserted muscles show their respective cervical inser-tion in higher and lower cervical levels, respectively. However, more cases have to be available to verify the result significantly. The proximal insertion of middle and anterior scalene in the first rib provides similar anatomy where the middle scalene muscle attaches more laterally on the rib compared to the anterior scalene muscle [6]. Also, comparing the points of dis-tal attachments middle, scalene muscle has broader distribution in the cervical levels in comparison to the anterior scalene muscle. Therefore, we propose the hypothesis that CCM attached laterally to the clavicle could be a variation derived from the middle scalene muscle whereas the medially attached CCM might derive from the anterior scalene muscle.

CONCLUSIONS

Our literature survey shows that the prevalence of CCM in male and female was equally presented in radiological studies whereas almost 3-fold higher prevalence of males in cadaver reports. The presenta-tion of this muscle was found in over 90% of the case reports unilaterally with higher left sided dominance. The proximal attachment was found slightly more frequent on the middle third of the clavicle whereas the distal insertion was available more often on the superior cervical vertebrae than the lower ones. The clinical, radiological as well as surgical relevance to this variation has to be highlighted to sensitise clini-cians or radiologists about the possible presence of CCM in order to avoid potential misleading diagnos-tics in the future.

Conflict of interest: None declared

REFERENCES

1. Alraddadi A. Literature review of anatomical variations: clinical significance, identification approach, and teaching strategies. Cureus. 2021; 13(4): e14451, doi: 10.7759/cureus.14451, indexed in Pubmed: 33996311.
2. Asad AL, Anteby M, Garip F. Who donates their bodies to science? The combined role of gender and migration status among California whole-body donors. Soc Sci Med. 2014; 106: 53–58, doi: 10.1016/j.socscimed.2014.01.041, indexed in Pubmed: 24534732.
3. Aydoğ ST, Ozçakar L, Demiryürek D, et al. An intervening thoracic outlet syndrome in a gymnast with levator clavic-ulae muscle. Clin J Sport Med. 2007; 17(4): 323–325, doi: 10.1097/JSM.0b013e3180321275, indexed in Pubmed: 17620791.
4. Bhatnagar K, Smith T. The anomalous human levator cla-viculae muscle: a case report. Ann Vasc Med Res. 2021; 8(1): 1125.
5. Billings HJ, Sherrill WC. A novel variant of the cleidocervica-lis muscle with clinical implications for nerve compression/entrapment. Surg Radiol Anat. 2015; 37(6): 697–699, doi: 10.1007/s00276-014-1384-5, indexed in Pubmed: 25326903.
6. Bordoni B, Varacallo M. Anatomy, head and neck, sterno-cleidomastoid muscle. StatPearls Publishing LLC, Treasure Island (FL) 2022.
7. Boyle E, Mahon V, Diogo R. Muscles lost in our adult pri-mate ancestors still imprint in us: on muscle evolution, de-velopment, variations, and pathologies. Curr Mol Biol Rep. 2020; 6(2): 32–50, doi: 10.1007/s40610-020-00128-x.

8. Capo JA, Spinner RJ. The levator claviculae muscle. Clin Anat. 2007; 20(8): 968–969, doi: 10.1002/ca.20439, indexed in Pubmed: 17149744.

9. Dluzen DE, Brammer CM, Bernard JC, et al. Survey of cadaveric donors to a body donation program: 1978–1993. Clin Anat. 1996; 9(3): 183–192, doi: 10.1002/(SICI)1098-2353(1996)9:3<183::AID-CA10>3.0.CO;2-N, indexed in Pubmed: 8740481.

10. Fasel J, Gailloud P, Terrier F. Three-dimensional reconstruction of a levator claviculae muscle. Surg Radiol Anat. 1994; 16(3): 303–305, doi: 10.1007/BF01627686, indexed in Pubmed: 7863417.

11. Fazliogullari Z, Cicekcibasi A, Dogan NU, et al. The levator claviculae muscle and unilateral third head of the sternocleidomastoid muscle: case report. Int J Morphol. 2010; 28(3): 929–932, doi: 10.4067/s0717-95022010000300043.

12. Feigl GC, Pixner T. The cleidoatlanticus muscle: a potential pitfall for the practice of ultrasound guided interscalene brachial plexus block. Surg Radiol Anat. 2011; 33(9): 823–825, doi: 10.1007/s00276-011-0820-z, indexed in Pubmed: 21590339.

13. Ferreli F, Mercante G, Spriano G. Levator claviculae muscle: anatomic variation found during neck dissection. Laryngoscope. 2019; 129(3): 634–636, doi: 10.1002/lary.27280, indexed in Pubmed: 30565677.

14. Ginsberg LE, Eicher SA. Levator claviculae muscle presenting as a neck mass: CT imaging. J Comput Assist Tomogr. 1999; 23(4): 538–539, doi: 10.1097/00004728-199907000-00009, indexed in Pubmed: 10433281.

15. Gruber W. Archiv fur Anatomie, Physiologie und Wissenschaftliche Medizin. Eichler 1876.

16. Gruber W. Vier Abhandlungen aus dem Gebiete der medicinisch-chirurgischen Anatomie. Förstner 1847.

17. Habicht JL, Kiessling C, Winkelmann A. Bodies for anatomy education in medical schools: an overview of the sources of cadavers worldwide. Acad Med. 2018; 93(9): 1293–1300, doi: 10.1097/ACM.0000000000002227, indexed in Pubmed: 29561275.

18. Koshy S, Rabi S, Indrasingh I. Supernumerary cleidocervicalis (levator claviculae) muscle: case report of its rare incidence with clinical and embryological significance. Eur J Anat. 2005; 9: 103–106.

19. Leon X, Maranillo E, Quer M, et al. Case report: cleidocervical or levator claviculae muscle. A new embryological explanation as to its origin. J Anat. 1995; 187(Pt 2): 503–504, indexed in Pubmed: 7592015.

20. Loukas M, Sullivan A, Tubbs RS, et al. Levator claviculae: a case report and review of the literature. Folia Morphol. 2008; 67(4): 307–310, indexed in Pubmed: 19085875.

21. Natsis K, Apostolidis S, Nikolaidou E, et al. Levator claviculae muscle: a case report. Cases J. 2009; 2: 6712, doi: 10.1186/1757-1626-2-6712, indexed in Pubmed: 19829849.

22. Odate T, Kawai M, Iio K, et al. Anatomy of the levator claviculae, with an overview and a literature survey. Anat Sci Int. 2012; 87(4): 203–211, doi: 10.1007/s12565-012-0148-8, indexed in Pubmed: 22923186.

23. O'Sullivan ST, Kay SP. An unusual variant of the levator claviculae muscle encountered in exploration of the brachial plexus. J Hand Surg Br. 1998; 23(1): 134–135, doi: 10.1016/s0266-7681(98)80247-7, indexed in Pubmed: 9571509.

24. Raikos A, Paraskevas G, Triaridis S, et al. Bilateral supernumerary sternocleidomastoid heads with critical narrowing of the minor and major supraclavicular fossae: clinical and surgical implications. Int J Morphol. 2012; 30(3): 927–933, doi: 10.4067/s0717-95022012000300027.

25. Rodríguez-Vázquez JF, Mérida-Velasco JR, Verdugo-López S, et al. Anatomical relationships of the cleidoatlanticus muscle. Interpretation about its origin. Anat Sci Int. 2009; 84(1-2): 47–52, doi: 10.1007/s12565-009-0018-1, indexed in Pubmed: 19224329.

26. Rosenheimer JL, Loewy J, Lozanoff S. Levator claviculae muscle discovered during physical examination for cervical lymphadenopathy. Clin Anat. 2000; 13(4): 298–301, doi: 10.1002/1098-2353(2000)13:4<298::AID-CA11>3.0.CO;2-Y, indexed in Pubmed: 10873223.

27. Rubinstein D, Escott EJ, Hendrick LL. The prevalence and CT appearance of the levator claviculae muscle: a normal variant not to be mistaken for an abnormality. Am J Neuroradiol. 1999; 20(4): 583–586, indexed in Pubmed: 10319965.

28. Rüdisüli T. Demonstration of a musculus levator claviculae. Surg Radiol Anat. 1995; 17(1): 85–87, doi: 10.1007/BF01629508, indexed in Pubmed: 7597574.

29. Ruiz Santiago F, López Milena G, Chamorro Santos C, et al. Levator claviculae muscle presenting as a hard clavicular mass: imaging study. Eur Radiol. 2001; 11(12): 2561–2563, doi: 10.1007/s003300100875, indexed in Pubmed: 11734959.

30. Saha A, Mandal S, Chakraborty S, et al. Morphological study of the attachment of sternocleidomastoid muscle. Singapore Med J. 2014; 55(1): 45–47, doi: 10.11622/smedj.2013215, indexed in Pubmed: 24241357.

31. Sharir A, Milgram J, Shahar R. Structural and functional anatomy of the neck musculature of the dog (Canis familiaris). J Anat. 2006; 208(3): 331–351, doi: 10.1111/j.1469-7580.2006.00533.x, indexed in Pubmed: 16533316.

32. Silawal S, Morgan S, Ruecker L, et al. A unilateral sternopharyngeal branch of the sternocleidomastoid muscle in an aged Caucasian male: a unique cadaveric report. Folia Morphol. 2023; 82(2): 434–438, doi: 10.5603/FM.a2022.0016, indexed in Pubmed: 35187633.

33. Tomo S, Toh H, Hirakawa T, et al. Case report: the cleidocervical muscle with speculation as to its origin. J Anat. 1994; 184(Pt 1): 165–169, indexed in Pubmed: 8157489.

34. Wood J, Sharpey W. VII. On a group of varieties of the muscles of the human neck, shoulder, and chest, with their transitional forms and homologies in the mammalia. Philosophical Transactions of the Royal Society of London. 1870; 160: 83–116, doi: 10.1098/rstl.1870.0007.

35. Zdilla MJ, Aldawood AM, Plata A, et al. Troisier sign and Virchow node: the anatomy and pathology of pulmonary adenocarcinoma metastasis to a supraclavicular lymph node. Autops Case Rep. 2019; 9(1): e2018053, doi: 10.4322/acr.2018.053, indexed in Pubmed: 30863728.

VM
VIA MEDICA

ORIGINAL ARTICLE

Lithium chloride promotes neural functional recovery after local cerebral ischaemia injury in rats through Wnt signalling pathway activation

Z. Junde[1], L. Tingting[1], Z. Lu[1], C. Shan[1], Y. Dan[1], Z. Yizhen[2]

[1]Department of Anatomy, School of Basic Medicine, Guizhou Medical University, Guiyang, China
[2]Nursing, Grade 2023, Guizhou Medical University, Guiyang, China

Background: Lithium chloride (LiCl) has a significant neuroprotective effect in cerebral ischaemia. However, to date, there is a paucity of evidence on the role of LiCl in neural restoration after brain ischaemia and the signalling pathways involved remain unclear.

Materials and methods: Therefore, to address this gap, the middle cerebral artery occlusion (MCAO) rat model was used to simulate human ischaemia stroke. Male Sprague-Dawley rats were given MCAO for 90 min followed by reperfusion, and Dickkopf-1 (DKK1, 5.0 μg/kg) was administered half an hour before MCAO. Rats were then treated with hypodermic injection of LiCl (2.0 mmol/kg) twice a day for 1 week. After treatment, cognitive impairment was assessed by the Morris water maze test. Neurological deficit score, 2,3,5-triphenyl tetrazolium chloride staining, brain water content, and histopathology were used to evaluate brain damage. Enzyme-linked immunosorbent assay was used to measure oxidative stress damage and inflammatory cytokines. Apoptosis of the hippocampal neurons was tested by western blot. The key factors of Wnt signalling pathway in the ischaemic penumbra were detected by immunofluorescence staining and quantitative real-time polymerase chain reaction.

Results: Current experimental results showed that LiCl treatment significantly improved the impaired spatial learning and memory ability, suppressed oxidative stress, inflammatory reaction, and neuron apoptosis accompanied by attenuating neuronal damage, which subsequently decreased the brain oedema, infarct volume and neurological deficit. Furthermore, the treatment of LiCl activated Wnt signalling pathway. Interestingly, the aforementioned effects of LiCl treatment were markedly reversed by administration of DKK1, an inhibitor of Wnt signalling pathway.

Conclusions: These results indicate that LiCl exhibits neuroprotective effects in focal cerebral ischaemia by Wnt signalling pathway activation, and it might have latent clinical application for the prevention and treatment of ischaemic stroke. (Folia Morphol 2023; 82, 3: 519–532)

Key words: lithium chloride, cerebral ischaemia, Wnt signalling pathway, neuroprotection, rats

Address for correspondence: Dr. Z. Junde, Department of Anatomy, School of Basic Medicine, Guizhou Medical University, Guiyang, 55005, China, e-mail: jdzhu73@126.com

INTRODUCTION

Stroke is a leading cause of disability and death in the United States and Great Britain, affecting 0.2% of the population each year [18]. It is reported that there are about 2.0 million stroke patients in China every year [8]. Strokes were classified as ischaemic and haemorrhagic, more than 75% of cases being ischaemic [25]. Although there have been significant clinical improvements in the treatment of ischaemic stroke, many patients remain severely disabled, effectiveness of treatment is finite [35]. Therefore, the search for potential new drug intervention targets is critical for treatment to reduce stroke-related brain injury.

At present, lithium chloride (LiCl; molecular weight 42.39) is widely used in the clinical treatment of affective disorders [31]. LiCl has recently been reported to play an unexpected neuroprotective role in animal models of various neurodegenerative diseases [5, 12]. For example, LiCl has been shown to activate the glycogen synthase kinase 3β (GSK-3β) related pathway and participate in the pathophysiological process of Alzheimer's disease; the overactivation and overexpression of GSK-3β lead to amyloid-β-induced neurotoxic damage, which can be normalised by lithium ion [6]. In a rat model of cerebral ischaemia, chronic LiCl treatment significantly reduced cerebral infarction volume and neurological deficits caused by permanent middle cerebral artery occlusion (MCAO) [13]. In addition, the neuroprotection of LiCl is associated with several signal transduction pathways in the nerve functional restoration after ischaemic stroke [11, 38]. Among these, the Wnt signalling pathway is associated with neuronal differentiation, development, and migration [1, 37]; the activation of Wnt signalling pathway can be induced by abnormal changes of key molecules in Wnt-3a, dishevelled-1 (Dvl-1), axis inhibition protein (Axin) and β-catenin [3]. However, few studies have investigated the neuroprotective mechanisms induced by LiCl post-conditioning via the Wnt signalling pathway. Based on these findings, we employed a rat model with MCAO to confirm the hypothesis that LiCl promotes neuroprotective effects after ischaemic stroke by activating the Wnt signalling pathway.

MATERIALS AND METHODS

Animals and ethics

For this study, 100 adult male Sprague-Dawley rats (4–5 months old, weighing 330–350 g) were purchased from the laboratory animal centre of Guizhou Medical University, P.R. China (clean grade, License No. SCXK [qian] 2018-0001). Rats were housed in a cage at humidity (50–70%), temperature (22–24°C) and a 12 h light/dark cycle. Moreover, water and food were supplied ad libitum during the period of the experiment. The study protocol was approved by the Experimental Animal Research Committee of Guizhou Medical University of China on March 3, 2021 (approval No. 2100034). During the study, all efforts were made to reduce animal suffering and reduce the number of rats. Furthermore, all animal protocols were conducted under the guidelines of the Ministry of Science and Technology of the People's Republic of China ([2006]398).

Animal model and experimental grouping

All rats were fed for 7 days before surgery to acclimatise to the environment. In this experiment, MCAO rat model was established according to slightly modified Zea-Longa's method [17]. Briefly, rats were anesthetised with pentobarbital sodium (50 mg/kg) and the skin of the neck was prepared and disinfected routinely. The right common carotid artery, external carotid artery, and internal carotid artery were exposed through a longitudinal incision of about 20 mm in the neck of rats, and the external carotid artery was ligated above the occipital artery. A longitudinal incision was made about 5.0 mm from the common carotid artery end. Nylon sutures with a diameter of 0.27 ± 0.03 mm were inserted along the internal carotid artery incision until slight resistance was felt, and the insertion depth was about 19.5 ± 0.5 mm. The artery was ligated at the distal part, clean the wound and suture the muscle and skin, disinfect the wound, and use local antibiotics to prevent infection. After 90 min of focal cerebral ischaemia, the nylon suture was withdrawn to form an ischaemia reperfusion injury. Sham-operated rats underwent the same procedure without the nylon suture. After surgery, which were maintained, the rats' body temperature of 37°C until recovery from anaesthesia. According to the principle of random block, rats were randomly divided into five groups (n = 20 for each group): sham operation (S) group, MCAO (M) group, MCAO + lithium (M+L) group, MCAO + Dickkopf-1 (DKK1) (M+D) group, and MCAO + lithium + DKK1 (M+L+D) group.

Drug administration

Lithium chloride (LiCl, Sigma-Aldrich, USA) was dissolved in 0.9% NaCl, and both the M+L group and

M+L+D group rats were then treated with LiCl twice a day at the dose of 2.0 mmol/kg for one consecutive week after MCAO operation according to formerly described [34]. The S group and M group rats simultaneously received equivalent volumes of normal saline injected. Both the M+D group and M+L+D group' rats were injected into the lateral ventricle of Dickkopf-1 (DKK1, 5.0 μg/kg, Rat DKK1 recombinant protein from R&D System from Minnesota of USA) before 30 min according to the previous description by He et al. [9]. In brief, the rats were anaesthetised with pentobarbital sodium by intraperitoneal injection, and then fixed into a brain stereotaxic instrument. According to the stereotactic brain atlas [21], longitudinal incision was made along the middle line of the parietal bone of rats, then haemostasis, periosteum incision was performed to expose the skull, and the right ventricle of rats was located (0.8 mm posterior to the bregma, 1.5 mm lateral to the midline, and 4.5 mm ventral from the skull surface), and a small hole with a diameter of 1.0 mm was drilled into the skull with a dental drill. A total of 2.5 μL (5.0 μg/kg) of DKK1 solution was subsequently injected over 5 min through a microsyringe into the rat right lateral ventricle. The needle was left in place for 5 min after the injection, and then removed, penicillin powder was sprayed over the incision, and the skin was sutured.

Cognitive function assessment

Cognitive deficits were tested by the Morris water maze (MWM) test based on formerly described [24] with modifications. The water maze apparatus (from Anhui Zhenghua Biological Instrument Equipment Co., LTD, China) consisted of a cylindrical stainless steel water tank with a diameter of 150.0 cm × a height of 60.0 cm, and filled with 22.5 ± 0.5℃. The water was becoming opaque through adding black ink. A platform with a diameter of 10.0 cm was submerged 2.0 cm below the water surface and placed at the midpoint of one quadrant. The general testing process has been described in detail elsewhere. Animals were placed into the tank, facing the wall of the pool, and were allowed to circumnavigate the pool in search of the platform for four trials (90 s per trial) at 9:00 am each day every day from days 1 to 5 after the LiCl treatment. Escape latency (second) was recorded using an on-line image video tracking system to indicate the learning results. After the last trial, the platform was removed from the pool and each rat received one 90 s swim probe trial. The number of crossing the platform and swimming time in the quadrant of the platform were recorded to indicate the memory results. A video camera was installed above the pool centre; all behaviours were recorded for following analyses. Data was automatically performed using the MWM image process system (Chengdu Tai Meng Technology, China).

Measurements of neurobehavioral scores, brain water content, and infarct volume

According to Longa scoring method [17], neurobehavioral scores were performed on rats after treatment. The scoring criteria of Longa scoring method: 0 points, no symptoms of neurological impairment; 1 point, one side of the forepaw cannot completely extend, slight neurological function defect; 2 points, one side of the forelimb fully flexed and turned in a circle, with moderate neurological impairment; at 3 points, the body of the rats was tilted toward the paralyzed side, with severe neurological impairment; 4 points, unable to walk spontaneously, conscious loss. After modelling, rats with neurobehavioural scores of 0, 4 and death were excluded, and the rats with neurobehavioural scores of 1–3 were judged as successful modelling.

Brain water content (BWC) was tested by the standard wet-dry ratio method as previously described [29]. Briefly, rats were sacrificed and then brain was quickly taken out and positioned on a dry aluminium foil. Then, wet weight was confirmed by immediately weighing the two hemisphere slices. Dry weight was obtained after dehydrating the samples for one day at 100℃. BWC was calculated as a percentage according to the following formula: (wet weight − dry weight) / wet weight × 100%.

After behavioural ability, rats from per group were optional, selected, and euthanised. The brain was immediately taken out and frozen at −20℃ for 30 min, then the olfactory bulb was removed, and the coronal surface was evenly sliced every 2.0 mm, the brain slices were put into 2.0% 2,3,5-triphenyl-tetrazolium chloride (TTC, Boster, China) for half-hour at 37℃ in the dark, and fixed with 4.0% paraformaldehyde (Leagene Biotechnology, China) overnight. In the result, normal brain tissue stained red, while the infarct area appears a pale grey colour. TTC-stained sections were taken a picture, and image processing software (Version 2.0.1, Bethesda, USA) was used to analyse the infarct size. The infarct percentage of normal volume was calculated as: infarct size (%) =

= (contralateral area − ipsilateral non-infarct area) /
/ contralateral area × 100%.

Enzyme-linked immunosorbent assay (ELISA)

After LiCl treatment, the rats were sacrificed and the hippocampus was quickly isolated from the brain. Half of the tissues were tested for oxidative stress, and the other half of the tissues were tested by ELISA and western blot. In brief, the hippocampus was cut into many pieces and then grinded in a homogenisation buffer at 4°C. According to the operating instruction (Boster, China), some brain tissue homogenates were used to detect the levels of oxidative stress markers, including superoxide dismutase (SOD), malondialdehyde (MDA), reactive oxygen species (ROS) and glutathione peroxidase (GSH-Px), to evaluate the degree of oxidative stress injury; the other part was used to detect changes in inflammatory response related factors including tumour necrosis factor alpha (TNF-α) and interleukin 6 (IL-6) by ELISA.

Pathological evaluation

Rats were anaesthetised by pentobarbital sodium, and perfused via the aorta with 0.1 M phosphate buffered saline (PBS, pH 7.4) for 10 min, followed by fixation by 4.0% paraformaldehyde (PBS, pH 7.4) for 10 min. The brain was quickly taken out and postfixed in 4.0% paraformaldehyde for 4 h, and then dehydrated all night through gradient sucrose solutions (10%, 20%, 30%, and 50%) until completely submerged. The dehydrated brain tissues were embedded in Tissue-Tek Optimal Cutting Temperature Compound (Sakura Finetek, Japan) under freezing conditions. Coronal sections with thickness of 8.0 μm were cut using a cryostat, and unbiased cell estimation was performed in the hippocampal CA1 region every 6 sections according to a systematic random sampling procedure. About 120~150 continuous sections were collected from hippocampus in every rat and used to Nissl staining and immunofluorescence.

Nissl staining

Slice was putted in 0.02% toluidine blue (Beyotime Biotechnology, China) for 15 min at indoor temperature, dehydrated twice by a graded ethyl alcohol (50%, 70%, 90%, 95%, and 100%), permeabilised with xylene, wet-placed onto glass slides, and quickly mounted using neutral resin. Nissl positive neuron from five slices of each rat was counted with a light microscope (Olympus, Japan). The mean value of Nissl positive neuron for every rat was gained as the number of neuron in the rats.

Immunofluorescent staining

In order to investigate the regulatory role of Wnt signalling pathway, β-catenin or Wnt-3a positive cell in the ischaemic hippocampus was detected by immunofluorescence staining. Brain section was incubated for half-hour in 2.0 M HCl to denature DNA, and the reaction was neutralised in 0.1 M boric acid for 15 min. Thereafter, brain section was rinsed in PBS containing 0.3% Triton for half an hour, preincubated in 10% normal goat serum for 2 h at indoor temperature, and incubated with monoclonal rabbit anti-Wnt-3a or anti-β-catenin (1:150; Boster Biotechnology, Wuhan, China) at 4°C overnight, and then incubated with Cy3-conjugated affinity purified goat anti-rabbit IgG (1:100; Sigma, St. Louis, MO, USA) in a humidified chamber for 1 h at 37°C. Anti-Wnt-3a or anti-β-catenin was used as cell-type specific markers in each brain section. The number of β-catenin or Wnt-3a positive cells was analysed by laser scanning confocal microscope analysis system (Olympus, Japan).

Western blot assay

Western blot analysis was performed on hippocampal tissue from the ischaemic hemisphere [4]. In brief, 100 mg brain tissue samples from the ischaemic hippocampus were isolated and homogenised in a radio immunoprecipitation analysis lysis buffer (Sigma, USA) containing a protease inhibitor. The protein concentration was measured by the bicinchoninic acid method (Sigma, USA). Proteins were isolated by 10% SDS-PAGE gel electrophoresis and then transferred to PVDF membranes. It was blocked in 5.0% skim milk and incubated with a primary antibody of Bcl-2 or Bax protein (1:100 dilution; Beyotime Biotechnology, China) one night at 4°C, then incubated with the peroxidase-conjugated rabbit anti-goat secondary antibodies IgG (1:200 dilution; Sigma) for 2 h at room temperature. This was probed for glyceraldehyde 3-phosphate dehydrogenase (GAPDH) for loading control. Immunoreactive protein was visualised by enhanced chemiluminescence and a western blotting detection system (BlotCycler, USA).

Quantitative polymerase chain reaction (q-PCR)

According to the manufacturer's instructions, Total RNA was extracted from rat hippocampal CA1 area with the TRIzol reagent (sigma, USA). And the

concentration of RNA was measured by an ultra-violet visible spectrophotometer (Beckman, USA). Vertibialiti® 96-Well Thermal Cycler instrument and cDNA Synthesis Reagents Kit (Super-Script™ III First-Strand Synthesis Super-Mix for q-PCR, USA) were applied to reverse transcription. Finally, the relative expression levels of Wnt-3a, Dvl-1, β-catenin, Axin-2, and GSK-3β were detected using a fluorescence quantitative PCR apparatus (Eco 48, Colpalmer Instruments, Shanghai, Co., LTD) and analysed by $2^{-\triangle\triangle Ct}$ method [28] and normalisation to GAPDH. Primer sequences used in this study were listed as follows: β-catenin (forward primer: 5'-GGGCGGCACCTTCCTACTTC-3', reverse primer: 5'-GACCTGGAAAACGCCATCAC-3'), Wnt-3a (forward primer: 5'-GACTATCCGGCAGTTGCGAAGT-3', reverse primer: 5'-CCACCCAGCCAC GAGACTCT-3'), Axin-2 (forward primer: 5'-CCTTGCCAAAA CGGAAT-ACGA AAGG-3', reverse primer: 5'-GG ACTTGCTCT-GACGCTCACTCT-3'), GSK-3β (forward primer: 5'-CCACCATCCTTATCCCTCCTCA -3', reverse primer: 5'-CGTTATTGGTCTGTCCACGGTCT -3'), and Dvl-1 (forward primer: 5'-CCTTCC ATCCAAATGTTGCCAGTA-3', reverse primer: 5'-GGGCAGC CTCATCACGGTTT-3').

Statistical analysis

The results represent the means ± standard errors and analysed by SPSS 20.0 software (SPSS Inc., Chicago, USA). Statistical analysis was performed using one-way analysis of variance (ANOVA) followed by Tukey test. Data with equal variance were compared intergroup by the least significant difference method; while data with unequal variances were compared between groups by Tamhane's T2 method. $P < 0.05$ was considered statistically significant. $P < 0.05$ was considered to indicate a statistically difference.

RESULTS

LiCl improved the cognitive deficits in rats with cerebral ischaemia-induced injury

Cognitive function was assessed with MWM test after LiCl treatment (Fig. 1). There is an evident increase in escape latency in rat's navigation test in the M group (F_{group} = 48.28, p < 0.05). In contrast, LiCl treatment clearly reduced the navigation test's escape latency (F_{group} = 51.37, p < 0.05, Fig. 1A). On the third day, the rat's path in the M+D group is complex, while rats in the M+L group find the platform easily (Fig. 1A, C). The swimming path of the rat of

each group on the fifth day is shown in Figure 1D. As shown in Figures 1B, 1C rats in the M+L group exhibited a shorter time in the target quadrant and a lower frequency of crossing the probe test platform than both the M group and the M+D group (F_{group} = 72.34, p < 0.05). These data collectively indicated that LiCl exerted beneficial effects on learning and memory.

LiCl promotes the recovery of neurological function in rats with cerebral ischaemia-induced injury

Neurological deficits were evaluated after LiCl treatment. The test analysis results are shown in Figure 2A. Because no neurological impairment occurred in the S group, the average neurological deficit score was 0, but the M group rats showed serious neurological deficit scores compared with the S group (F_{group} = 22.35, p < 0.05). Compared with the M group, the average neurological deficit scores were significantly reduced in both the M+L and the M+L+D groups, particularly in the M+L group (F_{group} = 65.37, p < 0.05). When pretreatment with the Wnt inhibitor DKK1 was performed, the neurological deficit scores of both the M+D group and the M+L+D group were clearly increased compared with those of both the S group and the M+L group (F_{group} = 47.28, p < 0.05), respectively. These results indicate that LiCl treatment clearly improved neurological impairment; nevertheless, the Wnt signalling inhibitor DKK1 restrained this neuroprotective effect.

LiCl attenuated cerebral oedema in rats with cerebral ischaemia-induced injury

Brain water content was used to assess brain oedema following LiCl treatment, as shown in Figure 2B. Compared with the S group, the BWC was clearly increased in the M group (F_{group} = 22.49, p < 0.05). After LiCl treatment, compared with the M group, the BWC was significantly decreased in both the M+L group and the M+L+D group (F_{group} = 76.53, p < 0.05), particularly in the M+L group (F_{group} = 85.26, p < 0.05). In addition, when the Wnt signal pathway inhibitor DKK1 was injected intracerebroventricularly, there were obvious differences in both the M+D group (F_{group} = 47.36, p < 0.05) and the M+L+D group (F_{group} = 42.16, p < 0.05). However, there were no significant changes in the contralateral hemisphere.
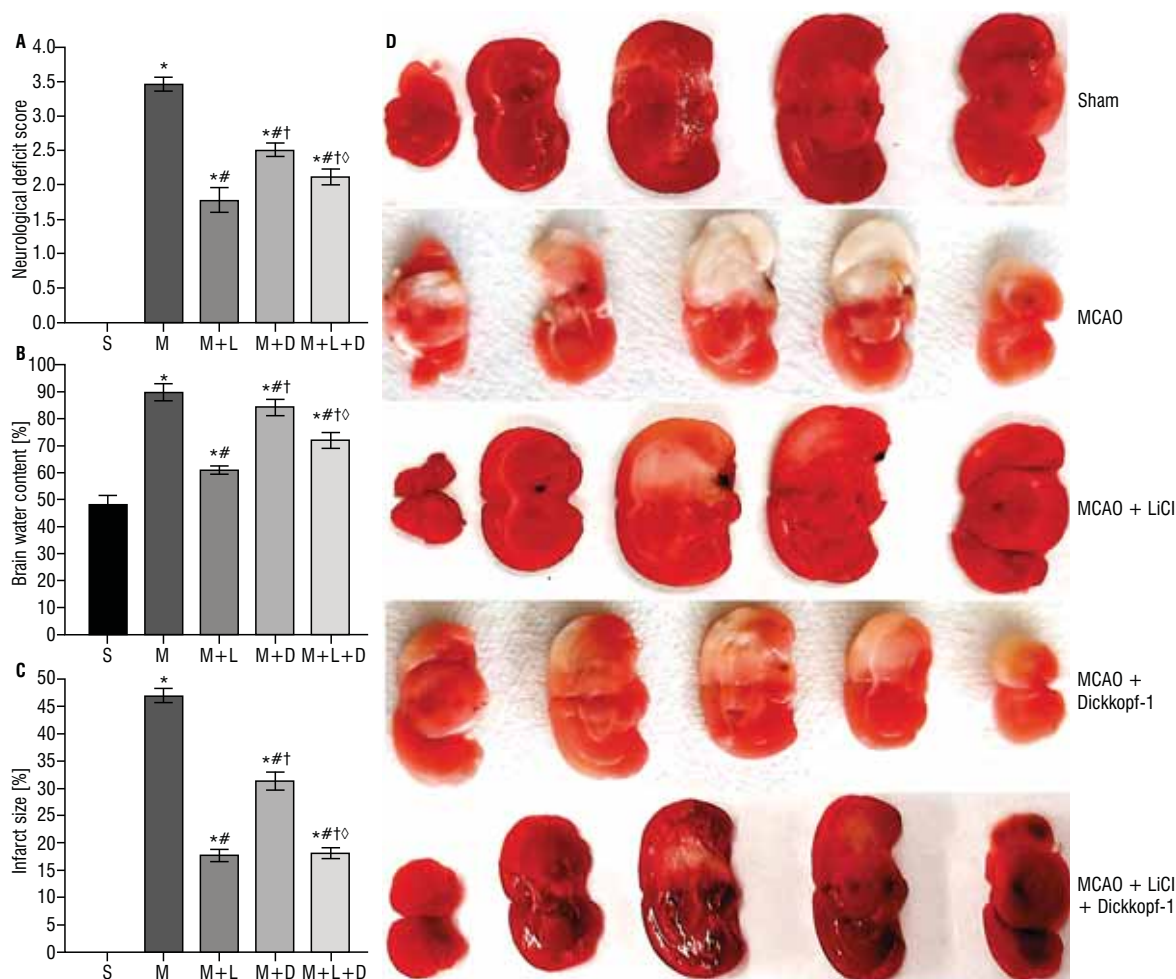
Figure 1. Effects of lithium chloride (LiCl) treatment on neurobehavioral ability in rats. Escape latency (**A**) and pathway (**D**) during platform trials, time spent in the target quadrant (**B**), and the number of crossings through the platform (**C**) in the probe test; S — sham; M — middle cerebral artery occlusion; L — lithium chloride; D — Dickkopf-1. The results are expressed as the mean ± standard error of 20 animals in each group and analysed by one-way ANOVA, followed by the Student–Newman–Keuls test; $^*p < 0.05$ vs. S group; $^\#p < 0.05$ vs. M group; $^\dagger p < 0.05$ vs. M+L group; $^\Diamond p < 0.05$ vs. M+D group; MCAO — middle cerebral artery occlusion.

LiCl reduced the infarct size in rats with cerebral ischaemia-induced injury

The area of cerebral infarction in MCAO-induced rats was determined by TTC staining (Fig. 2D). No infarct tissue was observed in the S group, and the infarct area (white) was very obvious in the M group. Extensive infarcts in the cortical and subcortical areas were observed in a series of brain sections, accounting for about half of the total infarcts in the cortical and subcortical areas (Fig. 2D). Compared with the M group and the M+D group, the infarct area of LiCl treated rats was significantly reduced ($F_{group} = 78.26$, $p < 0.05$). However, there were no significant differences in both the M+L group and M+L+D group after the Wnt signalling pathway suppressor DKK1 was administered ($F_{group} = 126.67$, $p > 0.05$, Fig. 2C).

LiCl relieved the oxidative stress damage in rats with cerebral ischaemia-induced injury

To evaluate the effects of LiCl on oxidative stress injury, the levels of MDA, SOD, GSH-Px, and ROS were measured (Fig. 3A, B). SOD and GSH-Px expression were significantly decreased in the M group compared with the S group ($F_{group} = 37.25$, $p < 0.05$; Fig. 3A, B). Compared to the S group, MAD and ROS expression were significantly increased in the M group ($F_{group} = 41.59$, $p < 0.05$; Fig. 3A, B). LiCl treatment resulted in a significant increase in the levels of MDA and ROS, and a remarkable decrease in the levels of SOD and GSH-Px in the brain tissues of rats, indicating a rise in oxidative stress in the rats with cerebral ischaemia. On the other hand, the Wnt signalling pathway inhibitor DKK1 attenuated LiCl antioxidant activity.
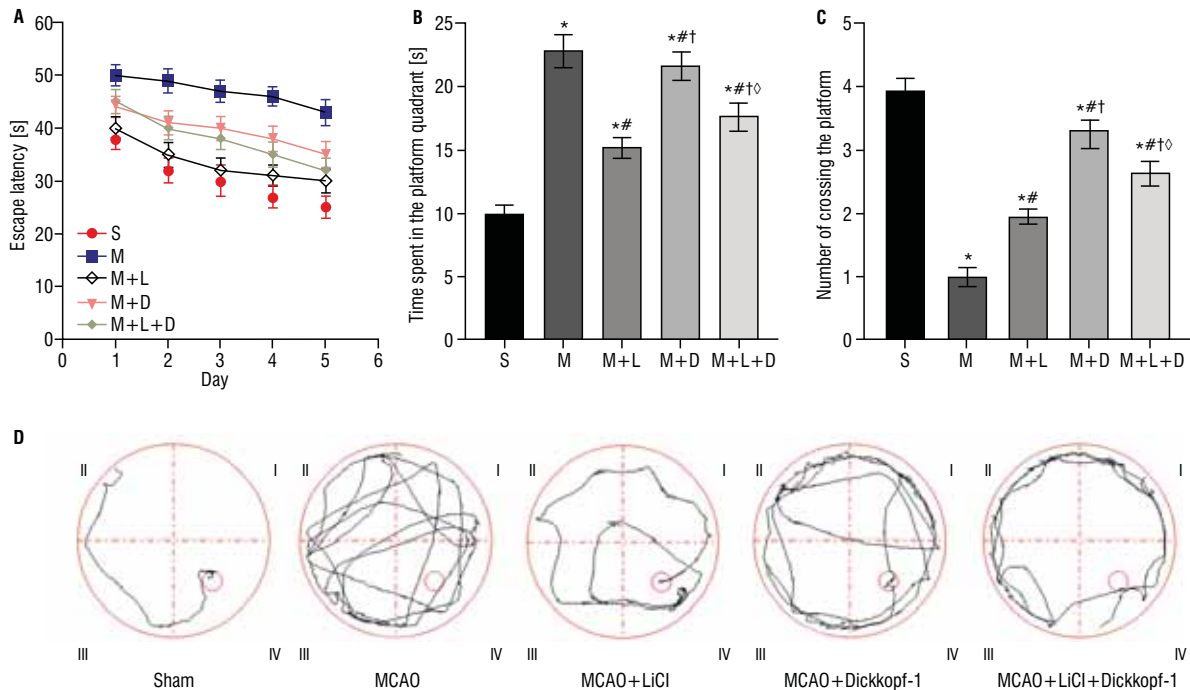
Figure 2. Neurological deficit scores of cerebral middle cerebral artery occlusion (MCAO) rats following lithium chloride (LiCl) treatment in the five groups (**A**, n = 20). Effect of lithium chloride treatment on brain water content (**B**, n = 5). Administration of lithium chloride reduced the infarct size (**C**, n = 5), Infarct size of the ischaemic cortex was measured, normalised to the contralateral cortex, and expressed as a percentage according to the following formula: Infarct size (%) = (contralateral area − ipsilateral non-infarct area) / contralateral area × 100%; **D.** Representative cerebral infarcts stained by a 2.0% 2,3,5-triphenyl tetrazolium chloride (TTC) solution. Normal brain tissue stained red by TTC staining; the infarct area appears a pale grey colour; S — sham; M — middle cerebral artery occlusion; L — lithium chloride; D — Dickkopf-1. The results are expressed as the mean ± standard error of those animals in each group and were analysed by one-way ANOVA, followed by the Student–Newman–Keuls test; *p < 0.05 vs. S group; #p < 0.05 vs. M group; †p < 0.05 vs. M+L group; ◊p < 0.05 vs. M+D group.

LiCl suppressed the inflammatory response in rats with cerebral ischaemia-induced injury

To investigate the anti-inflammatory effects of LiCl in cerebral ischaemia-induced rats, the TNF-α and IL-6 concentrations in the hippocampal CA1 region were investigated after the rats were sacrificed. The concentrations of TNF-α and IL-6 were significantly increased in the M group. However, after LiCl treatment, the proinflammatory factors TNF-α and IL-6 were significantly reduced (F_{group} = 51.68, p < 0.05; Fig. 3C). The Wnt signalling pathway inhibitor DKK1 reversed this protective effect.

LiCl against apoptosis in rats with cerebral ischaemia-induced injury

To further clarify the molecular mechanisms underlying the neuroprotective effect of LiCl, the analysis focused on two proteins involved in apoptotic death, Bcl-2 and Bax. Western blot assay revealed that after MCAO injury, Bcl-2 expression was significantly decreased in the M group compared to the S group (F_{group} = 74.23, p < 0.05; Fig. 3D, E). Treatment with

LiCl significantly suppressed this reduction in the expression level. In addition, Bax expression was significantly increased in the M group compared to the S group, and this was significantly prevented by treatment with LiCl (F_{group} = 67.86, p < 0.05; Fig. 3D, E). However, the Wnt signalling pathway inhibitor DKK1 only reversed the effects on Bcl-2 expression.

LiCl relieved the histopathological injury in rats with cerebral ischaemia-induced injury

Nissl staining was applied to measure the infarct volume after MCAO. Because Nissl bodies are unique structures in neurons [30], Nissl staining can be used to specifically stain the Nissl bodies for neuropathological evaluation. Nissl staining of the hippocampal CA1 area showed that there were four or five layers of pyramidal cells in the sham group (Fig. 4A). These neurons were arranged regularly and compactly with no obvious fracture of the Nissl body. After cerebral MCAO, the arrangement of neurons in the hippocampal CA1 region was disordered compared to the S group. The boundary was dim, and the cell band
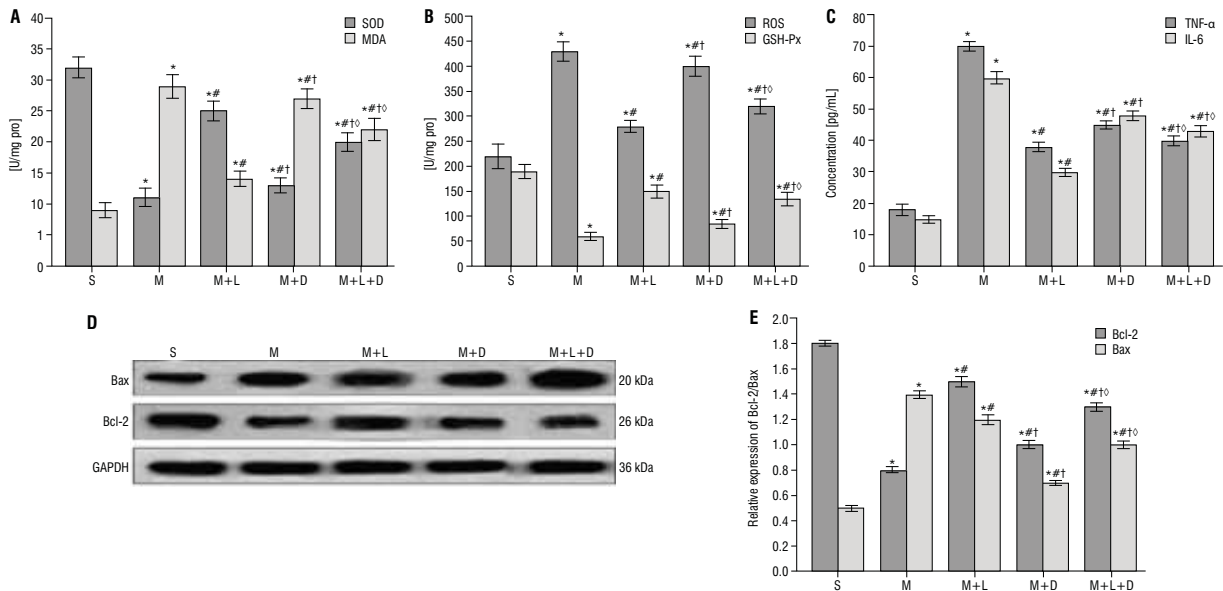
Figure 3. Effect of lithium chloride on oxidative stress damage, inflammatory cytokines, and apoptosis. The concentrations of malondialdehyde (MDA) and superoxide dismutase (SOD) (**A**), reactive oxygen species (ROS) and glutathione peroxidase (GSH-Px) (**B**), and interleukin 6 (IL-6) and tumour necrosis factor alpha (TNF-α) (**C**) in the cerebral tissues of treated rats were detected by ELISA. Bax and Bcl-2 protein expression in the hippocampus after cerebral ischaemia as analysed by western blot assay; **D**. Representative protein bands of Bax, Bcl-2, and glyceraldehyde 3-phosphate dehydrogenase (GAPDH) are shown; **E**. Representative relative optical densities of protein bands from the ischaemic penumbra are shown in the bar graphs. Expression was calculated as the ratio of the optical density of the target protein to that of GAPDH; S — sham; M — middle cerebral artery occlusion; L — lithium chloride; D — Dickkopf-1. The results are expressed as the mean ± standard error of 10 animals in each group and were analysed by one-way ANOVA followed by the Student–Newman–Keuls test; *$p < 0.05$ vs. S group; #$p < 0.05$ vs. M group; †$p < 0.05$ vs. M+L group; ◊$p < 0.05$ vs. M+D group.
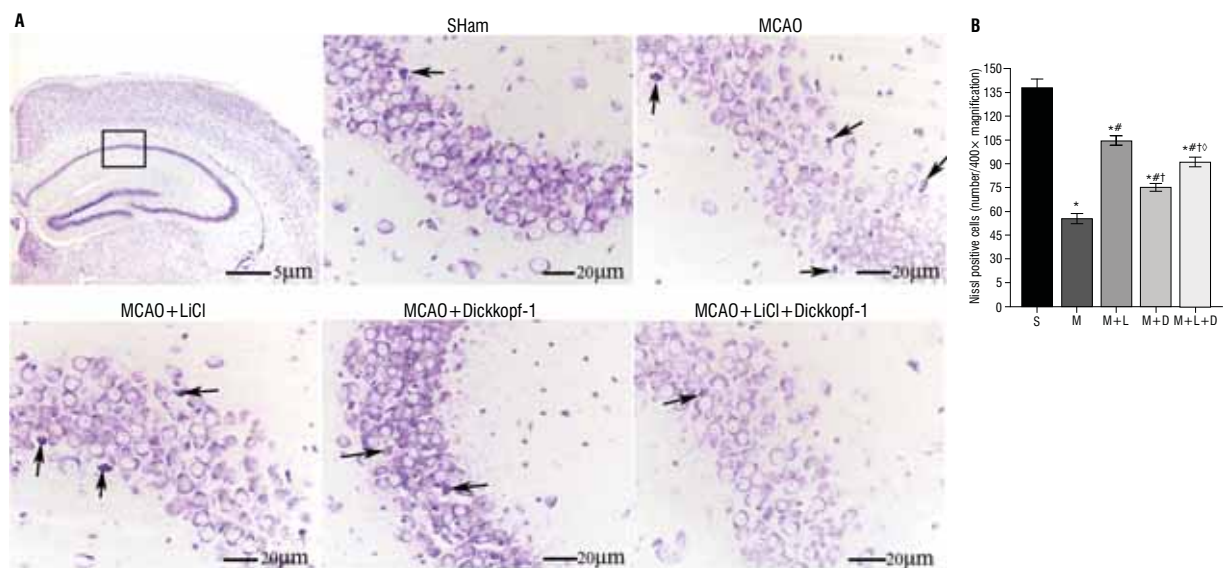
Figure 4. Representative brain sections of Nissl (cresyl violet) staining after brain ischaemia; **A**. Neurons in the hippocampal CA1 area. The box indicates the analysed region (Nissl staining, scale bar = 5.0 μm). In the sham group, the neurons were arranged regularly and the Nissl bodies in the cytoplasm were enriched; after cerebral middle cerebral artery occlusion (MCAO), the number of neurons was substantially reduced, and they were arranged in a disorderly manner. There was a reduction in the number of Nissl bodies in the cytoplasm (arrows indicate shrunken, darkened, damaged neurons). In rats given lithium chloride (LiCl) treatment, the number of neurons was increased and there were a greater number of Nissl bodies in the cytoplasm. When the Wnt signal pathway inhibitor Dickkopf-1 was injected intracerebroventricularly, many pyramidal cells were reduced in size and there were nuclear pyknosis and hyperchromatic nuclei. Scale bars = 20 μm; **B**. Quantitation of Nissl-positive cells; S — sham; M — middle cerebral artery occlusion; L — lithium chloride; D — Dickkopf-1. The results are expressed as the mean ± standard error of 5 animals in each group and were analysed by one-way ANOVA followed by the Student–Newman–Keuls test; *$p < 0.05$ vs. S group; #$p < 0.05$ vs. M group; †$p < 0.05$ vs. M+L group; ◊$p < 0.05$ vs. M+D group.
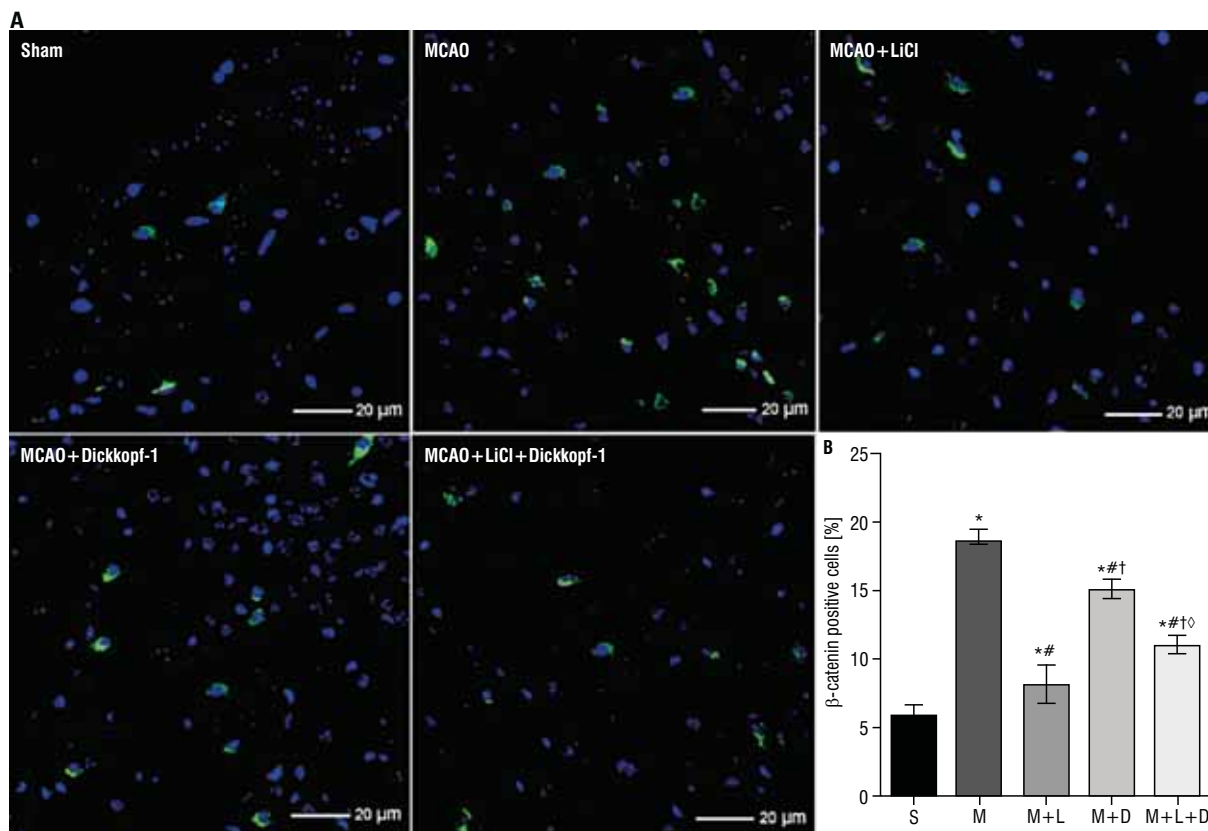
Figure 5. Effect of lithium chloride (LiCl) on β-catenin positive cells in rat parietal cortex; **A.** β-catenin positive cells were examined by immunofluorescence. β-catenin positive cells are labelled; these were mainly localized to the cytoplasm. Scale bars: 20 μm; **B.** Quantitation of β-catenin positive cells; S — Sham; M — middle cerebral artery occlusion; L — lithium chloride; D — Dickkopf-1. The results are expressed as the mean ± standard error of 5 animals in each group and were analysed by one-way ANOVA followed by the Student–Newman–Keuls test; *$p < 0.05$ vs. S group; #$p < 0.05$ vs. M group; †$p < 0.05$ vs. M+L group; ◊$p < 0.05$ vs. M+D group; MCAO — middle cerebral artery occlusion.

was irregular. There was a large reduction in the number of surviving cells and the Nissl body of many neurons was fragmented (F_{group} = 85.52, $p < 0.05$; Fig. 4A, B). In addition, these pathological changes in the hippocampal CA1 area of the M+L group were evidently reduced compared with the MCAO group; the M+L group exhibited almost normal morphology and structure of the pyramidal cells (F_{group} = 57.46, $p < 0.05$; Fig. 4A, B). Yet many pyramidal cells were reduced in size, with nuclear pyknosis and hyperchromatic nuclei in the M+L+D group ($p < 0.05$; Fig. 4A, B).

LiCl reduced β-catenin positive cells in rats with cerebral ischaemia-induced injury

Beta-catenin positive cells were examined by immunofluorescence. β-catenin protein immunofluorescent staining revealed intense green staining in the cytoplasm of neurons, particularly in the injured areas. The expression of the β-catenin protein in the rat pa-

rietal cortex is shown and quantified in Figure 5A, B. Compared with the small amount of expression in the S group, the expression of β-catenin positive cells was clearly increased in the M group (F_{group} = 54.43, $p < 0.05$). Treatment with LiCl significantly reduced the number of β-catenin positive cells compared to the M group (F_{group} = 60.27, $p < 0.05$). However, there was an obvious increase in the number of β-catenin positive cells in the M+L+D group compared to the M+L group (F_{group} = 64.37, $p < 0.05$).

LiCl activated the Wnt signalling pathway in rats with cerebral ischaemia-induced injury

To test the hypothesis that LiCl activates Wnt/ /β-catenin signalling, key proteins in the Wnt signalling pathway were evaluated by immunofluorescence and q-PCR after LiCl treatment, including Wnt-3a, Dvl-1, GSK-3β, β-catenin, and Axin-2. The expression levels of these indices reflect the activation of the relevant signalling pathway. The results indicated
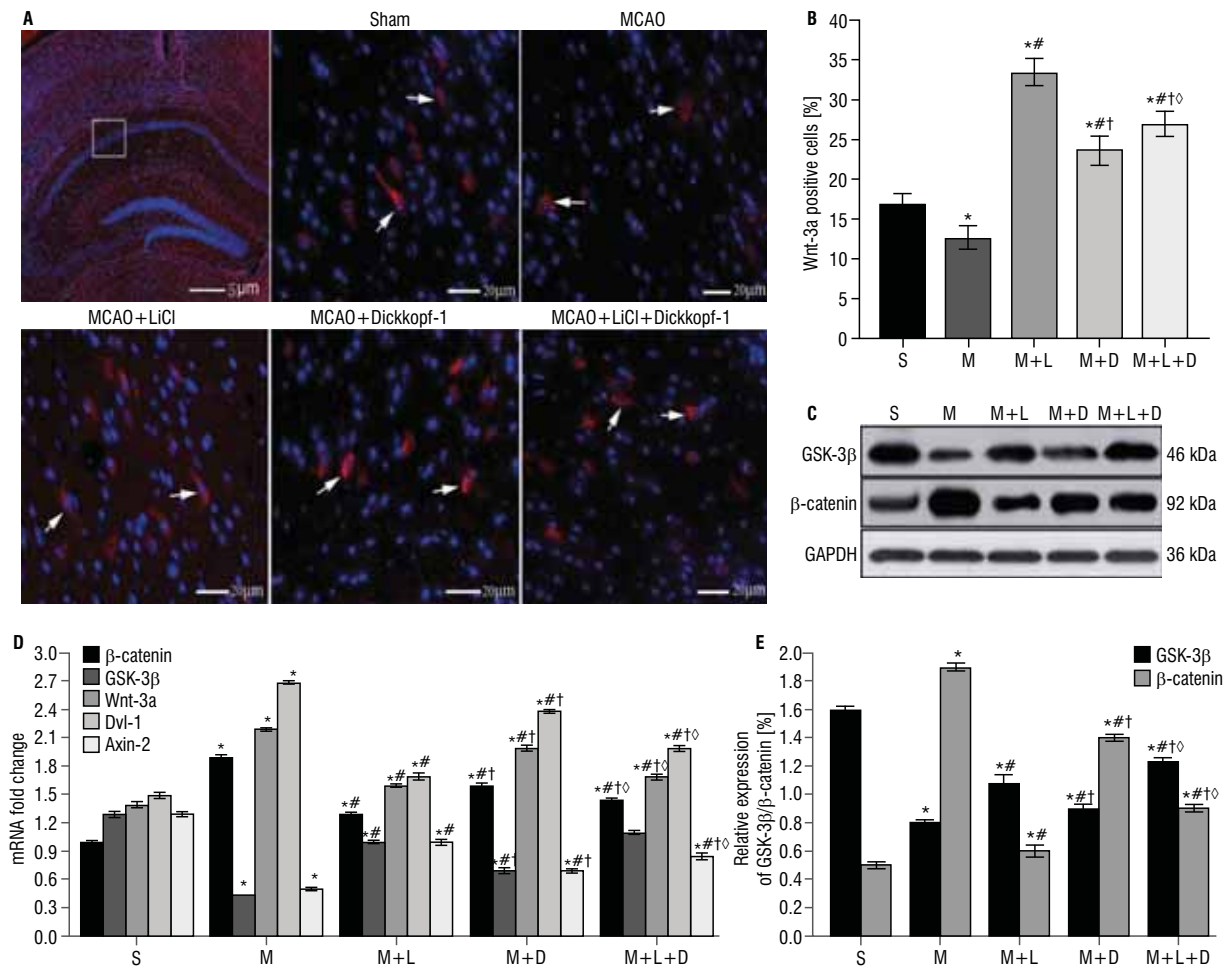
Figure 6. The key factors in the Wnt signalling pathway were examined by immunofluorescence staining and quantitative real-time polymerase chain reaction; **A.** Wnt-3a-positive cells are labelled; these were mainly localized in the cytoplasm. The red fluorescence indicates Wnt-3a and blue fluorescence indicates nuclei. The box indicates the analysed region (scale bars = 5.0 μm). Little positive staining was detected in the sham animals (arrows indicating Wnt-3a-positive neurons). Lithium chloride (LiCl) treatment promoted Wnt-3a-positive staining in the ischaemic penumbra; Wnt-3a-positive neurons were abundant in the CA1 region compared with the middle cerebral artery occlusion (MCAO) group. Scale bars = 20 μm; **B.** Quantitation of Wnt-3a-positive cells in the ischaemic penumbra is shown in the bar graph; **C.** Representative protein bands of glycogen synthase kinase 3β (GSK-3β), β-catenin, and glyceraldehyde 3-phosphate dehydrogenase (GAPDH) are shown, as determined by western blot assay. Expression was calculated as the ratio of the optical density of the target protein to that of GAPDH; **D.** Effects of lithium chloride on mRNA levels of Wnt-3a, β-catenin, dishevelled-1 (Dvl-1), GSK-3β, and axis inhibition protein 2 (Axin-2); **E.** Representative relative optical densities of protein bands from the ischaemic penumbra are shown in the bar graphs; S — sham; M — middle cerebral artery occlusion; L — lithium chloride; D — Dickkopf-1. The results are expressed as the mean ± standard error of 5 animals in each group and were analysed by one-way ANOVA followed by the Student–Newman–Keuls test; *p < 0.05 vs. S group; #p < 0.05 vs. M group; †p < 0.05 vs. M+L group; ◊p < 0.05 vs. M+D group.

that the expression of Wnt-3a-positive cells was increased in the rats in the LiCl-administered group compared with rats in the nondrug administration group, whereas the inhibitor DKK1 hindered this neuroprotective effect (F_{group} = 53.85, p < 0.05; Fig. 6A, B). Furthermore, the mRNA levels of Wnt-3a, β-catenin, and Dvl-1 in the M group were higher than those in the S group. By contrast, the mRNA levels of GSK-3β and Axin-2 were lower in the LiCl group than those in the M group (F_{group} = 63.87, p < 0.05; Fig. 6D). LiCl treatment significantly augmented GSK-3β

and Axin-2 mRNA expression and weakened Wnt-3a, β-catenin, and Dvl-1 mRNA expression compared to the M group (F_{group} = 71.52, p < 0.05; Fig. 6D). In the presence of DKK1 treatment, the mRNA expression levels of GSK-3β and Axin-2 were increased and the mRNA expression levels of Wnt-3a, β-catenin, and Dvl-1 were decreased compared to the M+L group (F_{group} = 73.82, p < 0.05; Fig. 6D). Thus, the Wnt signalling pathway blocker (DKK1) can inhibit the gene expression of Wnt-3a, Dvl-1, and β-catenin. Furthermore, the protein expression of GSK-3β and β-catenin, as

determined by western blot, confirmed that LiCl plays a neuroprotective role by activating the Wnt signalling pathway (F_{group} = 64.74, p < 0.05; Fig. 6C, E).

DISCUSSION

In this study, we apply the rat model with MCAO to simulate human ischaemia stroke. Administration of LiCl improved both impaired neurobehavioral ability and antioxidant capacity; it reduced the infarct volume, brain oedema, and inflammatory factors, which was corroborated by attenuated histopathologic changes. LiCl also increased the mRNA levels of Wnt-3a, β-catenin, and Dvl-1, and decreased the expression levels of mRNA of both GSK-3β and Axin-2 in ischaemic penumbra. However, these neuroprotective effects were reversed when pretreated with the Wnt signalling inhibitor DKK1.

Hippocampus is one of the most important brain areas relevant to learning and memory [15], some studies had found that the hippocampal CA1 area is particularly impressionable to ischaemic insult [15, 24]. Therefore, we choose neurons in the hippocampal CA1 area as the object of study. The MWM test is commonly used in the evaluation of cognitive function in rodents [24]. The training trial is applied to assess spatial or place learning, and the probe trials assess whether the animals remember the platform position. Current, experiment found that the S group rats quickly learned the platform location and rapidly arrived at the escape platform. On the contrary, the escape latency in the M group showed a significant increase, together with that of the distance travelled. The escape latency times after LiCl treatment showed an obvious decrease in both the M+L group and the M+L+D group, especially in the M+L group. Furthermore, a significant increase was noticed in the time going through the platform after LiCl treatment compared to the M group. However, a Wnt antagonist DKK1 suppressed the neuroprotective effects of LiCl treatment. These data demonstrated that LiCl improves impaired spatial learning and memory ability in MCAO rats.

The pathophysiology of stroke is related to many complex factors, including oxidative stress, injury, inflammatory response, and apoptosis. Oxidative stress is one of the mechanisms of cerebral ischaemia-reperfusion injury, and the production of ROS plays a major role in the early stage of cerebral ischaemia-reperfusion injury [16]. In the brain, intracellular antioxidants such as SOD, GSH-Px, and catalase can inhibit the

production of oxygen free radicals and protect brain tissue from the cytotoxicity of ROS at an early stage. In addition, excess ROS can lead to lipid peroxidation, producing MDA, 4-hydroxynonenal and acrolein [2]. MDA is also an important marker of oxidative stress, causing more serious oxidative stress damage by destroying lipids, enzymes, and nucleic acids in cell membranes or organelles. Current, data indicate that LiCl treatment resulted in a significant decrease in the levels of MDA and ROS, and a remarkable increase in the levels of SOD and GSH-Px; however, the Wnt inhibitor DKK1 attenuates LiCl antioxidant activity. At the same time, the inflammatory response, involving inflammatory cells and inflammatory mediators, is one of the causes of exacerbation of ischaemic brain injury [14]. The major cytokines associated with inflammation in ischaemic brain injury include IL-1, TNF-α, and IL-6, which have been observed to be upregulated in ischaemic brain injury [36]. Among various inflammatory factors, TNF-α is the main proinflammatory factor and participates in the pathophysiological process of ischaemic brain injury [10, 27]. IL-6, which is produced by monocytes, macrophages, and endothelial cells, and it appears rapidly in the early stages of ischaemic brain injury and increases rapidly [10]. The present study confirmed that IL-6 and TNF-α were induced by ischaemia; however, which was downregulated following LiCl treatment. These findings are consistent with previous studies [33, 34]. It has been reported that LiCl has a protective effect on apoptosis of damaged neurons in ischaemic brain injury [34]. In this process, activation of apoptotic genes and inactivation of antiapoptotic genes were observed. Ischaemia can downregulate Wnt signalling pathway and inhibit the transcription of many target genes including apoptotic genes Bcl-2 and Bax [26, 34]. Current studies have shown that LiCl upregulates the antiapoptotic Bcl-2 molecule and downregulates the proapoptotic Bcl-2 associated X protein (Bax). The molecular and cellular effects of lithium may be to inhibit n-methyl-D-aspartate receptor, up-regulate cellular protective Bcl-2, and down-regulate pro-apoptotic Bax [19].

The Wnt signalling pathway is well known for nervous system development and synapse formation [38], it is associated with neuronal differentiation and development and migration [1, 37]. To there exist of Wnt signals, β-catenin is able to translocate to the nucleus [7]. Signalling activating through the binding of a Wnt to a Frizzled family receptor, low-density

lipoprotein receptors interrelated with the protein 5/6 coreceptor to form a ternary cell surface complex. Thereafter, the β-catenin complex of destructed, which was constituted of GSK-3β and 2 folding proteins, and the axis inhibition protein, is then disintegrated by relevant to Disheveld protein [32]. Wnt signalling pathway activation also contributed to functional recovery and increased neuroprotective processes and neurogenesis after cerebral ischaemia [22]. Abnormal alterations to key molecules in the Wnt signalling pathway, including Wnt-3a, Axin-2, and β-catenin, induce Wnt signalling pathway activation. Wnt signalling pathway activation also contributed to functional recovery and increased neuroprotective processes and neurogenesis after cerebral ischaemia [32]. As an antagonist of the Wnt pathway, DKK1 prevents Wnt activation by binding to the Wnt receptor, leading to the activation of the Wnt/β-catenin signalling pathway [23]. Recent studies showed that DKK1 is potentially induced in the hippocampal CA1 area after global cerebral ischaemia, and administration of DKK1 antisense oligonucleotides protects the CA1 region against cerebral ischaemia-induced neuronal death [40]. In this study, to further examine the direct effects of the drug on the outcomes of ischaemic stroke, rats received an intracerebroventricular injection of the inhibitor DKK1 before LiCl treatment. We found that LiCl significantly decreased Wnt-3a-positive cells, increased β-catenin positive cells, and promoted neural functional recovery. It upregulated the mRNA expression levels of Wnt-3a, β-catenin, and Dvl-1, and downregulated the mRNA expression levels of GSK-3β and Axin-2. Nevertheless, those changes were reversed in the presence of DKK1. Our findings are consistent with previous studies [20, 39].These results indicated that the neuroprotection of LiCl may be related to the activation of Wnt signalling pathway.

Our research provides new clues to explain the role of Wnt signalling pathway regulation in causing ischaemic stroke. Nevertheless, there were several limitations for this study. First, although we finding that LiCl treatment provided strong protection against focal cerebral ischaemia, we did not insight which other cell signalling pathways were involved in its neuroprotective mechanism. Second, one dose of lithium was used in our study, and the therapeutic time windows were not explored. Third, only the chronic effects of LiCl for 1 week after stroke were studied, which need to be further explored.

CONCLUSIONS

In conclusion, our current studies show that LiCl has neuroprotective effects on focal cerebral ischaemia injury, and this study mimics the clinical interventions available in most ischaemic stroke patients. The mechanism by which LiCl promotes neural restoration involves on the Wnt signalling pathway activation. Therefore, we believe that LiCl may be an indispensable therapeutic agent for nerve repair after ischaemic brain injury.

Conflict of interest: None declared

REFERENCES

1. Ahn JiH, Choi JH, Park JHa, et al. Long-Term exercise improves memory deficits via restoration of myelin and microvessel damage, and enhancement of neurogenesis in the aged gerbil hippocampus after ischemic stroke. Neurorehabil Neural Repair. 2016; 30(9): 894–905, doi: 10.1177/1545968316638444, indexed in Pubmed: 27026692.

2. Ayala A, Muñoz MF, Argüelles S. Lipid peroxidation: production, metabolism, and signaling mechanisms of malondialdehyde and 4-hydroxy-2-nonenal. Oxid Med Cell Longev. 2014; 2014: 360438, doi: 10.1155/2014/360438, indexed in Pubmed: 24999379.

3. Bernkopf DB, Hadjihannas MV, Behrens J. Negative-feedback regulation of the Wnt pathway by conductin/axin2 involves insensitivity to upstream signalling. J Cell Sci. 2015; 128(1): 33–39, doi: 10.1242/jcs.159145, indexed in Pubmed: 25380820.

4. Choi KE, Hall CL, Sun JM, et al. A novel stroke therapy of pharmacologically induced hypothermia after focal cerebral ischemia in mice. FASEB J. 2012; 26(7): 2799––2810, doi: 10.1096/fj.11-201822, indexed in Pubmed: 22459147.

5. Ge W, Jakobsson E. Systems biology understanding of the effects of lithium on affective and neurodegenerative disorders. Front Neurosci. 2018; 12: 933, doi: 10.3389/fnins.2018.00933, indexed in Pubmed: 30618562.

6. Hampel H, Lista S, Mango D, et al. Lithium as a treatment for Alzheimer's disease: the systems pharmacology perspective. J Alzheimers Dis. 2019; 69(3): 615–629, doi: 10.3233/JAD-190197, indexed in Pubmed: 31156173.

7. Hao HP, Wen LB, Li JR, et al. LiCl inhibits PRRSV infection by enhancing Wnt/β-catenin pathway and suppressing inflammatory responses. Antiviral Res. 2015; 117: 99–109, doi: 10.1016/j.antiviral.2015.02.010, indexed in Pubmed: 25746333.

8. He L, Tang X, Song Y, et al. Prevalence of cardiovascular disease and risk factors in a rural district of Beijing, China:

a population-based survey of 58,308 residents. BMC Public Health. 2012; 12: 34, doi: 10.1186/1471-2458-12-34, indexed in Pubmed: 22248490.

9. He X, Mo Y, Geng W, et al. Role of Wnt/beta-catenin in the tolerance to focal cerebral ischemia induced by electroacupuncture pretreatment. Neurochem Int. 2016; 97: 124–132, doi: 10.1016/j.neuint.2016.03.011, indexed in Pubmed: 26994873.

10. Ibrahim RR, Amer RA, Abozeid AA, et al. Micro RNA 146a gene variant / TNF-alpha / IL-6 / IL-1 beta; A cross-link axis inbetween oxidative stress, endothelial dysfunction and neuro-inflammation in acute ischemic stroke and chronic schizophrenic patients. Arch Biochem Biophys. 2020; 679: 108193, doi: 10.1016/j.abb.2019.108193, indexed in Pubmed: 31738890.

11. Jiang TT, Zhang WY, Xiang XH, et al. [Lithium chloride arrests HK-2 cell cycle in G2 phase through AKT/GSK-3β signal pathway]. Nan Fang Yi Ke Da Xue Xue Bao. 2018; 38(5): 541–546, doi: 10.3969/j.issn.1673-4254.2018.05.06, indexed in Pubmed: 29891449.

12. Kerr F, Bjedov I, Sofola-Adesakin O. Molecular mechanisms of lithium action: switching the light on multiple targets for dementia using animal models. Front Mol Neurosci. 2018; 11: 297, doi: 10.3389/fnmol.2018.00297, indexed in Pubmed: 30210290.

13. Kim YR, van Meer MPA, Tejima E, et al. Functional MRI of delayed chronic lithium treatment in rat focal cerebral ischemia. Stroke. 2008; 39(2): 439–447, doi: 10.1161/STROKEAHA.107.492215, indexed in Pubmed: 18187690.

14. Le K, Song Z, Deng J, et al. Quercetin alleviates neonatal hypoxic-ischemic brain injury by inhibiting microglia-derived oxidative stress and TLR4-mediated inflammation. Inflamm Res. 2020; 69(12): 1201–1213, doi: 10.1007/s00011-020-01402-5, indexed in Pubmed: 32944799.

15. Lebedev IV, Bezryadnov DV, Deacon R, et al. The effect of a caudal hippocampus lesion on learning in a Morris water maze in Bank Voles (Clethrionomys glareolus). Biology Bulletin. 2013; 40(2): 179–186, doi: 10.1134/s1062359013020088.

16. Li X, Cheng S, Zhang X, et al. Corrigendum to "Progranulin protects against cerebral ischemia-reperfusion (I/R) injury by inhibiting necroptosis and oxidative stress" [Biochem. Biophys. Res. Commun. 521 (315) (2020) 569-576]. Biochem Biophys Res Commun. 2020; 525(3): 822, doi: 10.1016/j.bbrc.2020.03.001, indexed in Pubmed: 32171520.

17. Longa EZ, Weinstein PR, Carlson S, et al. Reversible middle cerebral artery occlusion without craniectomy in rats. Stroke. 1989; 20(1): 84–91, doi: 10.1161/01.str.20.1.84, indexed in Pubmed: 2643202.

18. Lu Y, Wang P, Zhou T, et al. Comparison of prevalence, awareness, treatment, and control of cardiovascular risk factors in China and the United States. J Am Heart Assoc. 2018; 7(3), doi: 10.1161/JAHA.117.007462, indexed in Pubmed: 29374046.

19. Ma J, Zhang GY. Lithium reduced N-methyl-D-aspartate receptor subunit 2A tyrosine phosphorylation and its interactions with Src and Fyn mediated by PSD-95 in rat hippocampus following cerebral ischemia. Neurosci Lett. 2003; 348(3): 185–189, doi: 10.1016/s0304-3940(03)00784-5, indexed in Pubmed: 12932824.

20. Mastroiacovo F, Busceti CL, Biagioni F, et al. Induction of the Wnt antagonist, Dickkopf-1, contributes to the development of neuronal death in models of brain focal ischemia. J Cereb Blood Flow Metab. 2009; 29(2): 264–276, doi: 10.1038/jcbfm.2008.111, indexed in Pubmed: 18827832.

21. Nowinski WL. Towards construction of an ideal stereotactic brain atlas. Acta Neurochir (Wien). 2008; 150(1): 1–13, doi: 10.1007/s00701-007-1270-6, indexed in Pubmed: 18030414.

22. Qiu CW, Liu ZY, Hou K, et al. Wip1 knockout inhibits neurogenesis by affecting the Wnt/beta-catenin signaling pathway in focal cerebral ischemia in mice. Exp Neurol. 2018; 309: 44–53, doi: 10.1016/j.expneurol.2018.07.011, indexed in Pubmed: 30048716.

23. Reinhold S, Blankesteijn W. Wnt/beta-catenin inhibitor Dickkopf 1. Arterioscler Thromb Vasc Biol. 2019; 39(2): 121–123, doi: 10.1161/atvbaha.118.312144.

24. Salimi Z, Khajehpour L, Moradpour F, et al. Nandrolone improve synaptic plasticity at the hippocampus CA1 area and spatial localization in the Morris water maze of male adolescent rats. Neurosci Res. 2020; 158: 21–29, doi: 10.1016/j.neures.2019.09.001, indexed in Pubmed: 31499080.

25. Shi ZY, Deng JX, Fu Su, et al. Protective effect of autophagy in neural ischemia and hypoxia: Negative regulation of the Wnt/β-catenin pathway. Int J Mol Med. 2017; 40(6): 1699–1708, doi: 10.3892/ijmm.2017.3158, indexed in Pubmed: 29039446.

26. Silva AK, Yi H, Hayes SH, et al. Lithium chloride regulates the proliferation of stem-like cells in retinoblastoma cell lines: a potential role for the canonical Wnt signaling pathway. Mol Vis. 2010; 16: 36–45, indexed in Pubmed: 20069066.

27. Silva B, Sousa L, Miranda A, et al. Memory deficit associated with increased brain proinflammatory cytokine levels and neurodegeneration in acute ischemic stroke. Arq Neuropsiquiatr. 2015; 73(8): 655–659, doi: 10.1590/0004-282X20150083, indexed in Pubmed: 26222355.

28. Song H, Mao W, Duan Z, et al. Selection and validation of reference genes for measuring gene expression in Toona ciliata under different experimental conditions by quantitative real-time PCR analysis. BMC Plant Biol. 2020; 20(1): 450, doi: 10.1186/s12870-020-02670-3, indexed in Pubmed: 33003996.

29. Symon L, Branston NM, Chikovani O. Ischemic brain edema following middle cerebral artery occlusion in baboons: relationship between regional cerebral water content and blood flow at 1 to 2 hours. Stroke. 1979; 10(2): 184–191, doi: 10.1161/01.str.10.2.184, indexed in Pubmed: 108819.

30. Tauchi M, Tejada de Rink MM, Fujioka H, et al. Targeted temperature management: peltier's element-based focal brain cooling protects penumbra neurons from progressive damage in experimental cerebral ischemia. Ther Hypothermia Temp Manag. 2018; 8(4): 225–233, doi: 10.1089/ther.2017.0055, indexed in Pubmed: 30199348.

31. Volkmann C, Bschor T, Köhler S. Lithium treatment over the lifespan in bipolar disorders. Front Psychiatry. 2020; 11: 377, doi: 10.3389/fpsyt.2020.00377, indexed in Pubmed: 32457664.

32. Wang Lu, Zhou J, Wang L, et al. The b' domain of protein disulfide isomerase cooperates with the a and a' domains

to functionally interact with platelets. J Thromb Haemost. 2019; 17(2): 371–382, doi: 10.1111/jth.14366, indexed in Pubmed: 30566278.

33. Wytrykowska A, Prosba-Mackiewicz M, Nyka WM. IL-1beta, TNF-alpha, and IL-6 levels in gingival fluid and serum of patients with ischemic stroke. J Oral Sci. 2016; 58(4): 509–513, doi: 10.2334/josnusd.16-0278, indexed in Pubmed: 28025434.

34. Xiao Y, Fan M, Jin W, et al. Lithium chloride ameliorated spatial cognitive impairment through activating mTOR phosphorylation and inhibiting excessive autophagy in the repeated cerebral ischemia-reperfusion mouse model. Exp Ther Med. 2020; 20(5): 109, doi: 10.3892/etm.2020.9237, indexed in Pubmed: 32989388.

35. Yang Z, Zhong L, Zhong S, et al. Hypoxia induces microglia autophagy and neural inflammation injury in focal cerebral ischemia model. Exp Mol Pathol. 2015; 98(2): 219–224, doi: 10.1016/j.yexmp.2015.02.003, indexed in Pubmed: 25666359.

36. Yi X, Xu C, Huang P, et al. 1-Trifluoromethoxyphenyl-3-(1-Propionylpiperidin-4-yl) urea protects the blood-brain barrier against ischemic injury by upregulating tight junction protein expression, mitigating apoptosis and inflammation and model. Front Pharmacol. 2020; 11: 1197, doi: 10.3389/fphar.2020.01197, indexed in Pubmed: 32848796.

37. Zeng Q, Long Z, Feng M, et al. Valproic acid stimulates hippocampal neurogenesis activating the Wnt/β-catenin signaling pathway in the APP/PS1/Nestin-GFP triple transgenic mouse model of Alzheimer's disease. Front Aging Neurosci. 2019; 11: 62, doi: 10.3389/fnagi.2019.00062, indexed in Pubmed: 30971911.

38. Zhang G, Ge M, Han Z, et al. Wnt/beta-catenin signaling pathway contributes to isoflurane postconditioning against cerebral ischemia-reperfusion injury and is possibly related to the transforming growth factorβ1/Smad3 signaling pathway. Biomed Pharmacother. 2019; 110: 420–430, doi: 10.1016/j.biopha.2018.11.143, indexed in Pubmed: 30530044.

39. Zhang QG, Wang R, Khan M, et al. Role of Dickkopf-1, an antagonist of the Wnt/beta-catenin signaling pathway, in estrogen-induced neuroprotection and attenuation of tau phosphorylation. J Neurosci. 2008; 28(34): 8430–8441, doi: 10.1523/JNEUROSCI.2752-08.2008, indexed in Pubmed: 18716201.

40. Zhu Z, Guo D, Zhong C, et al. Serum dkk-1 (Dickkopf-1) is a potential biomarker in the prediction of clinical outcomes among patients with acute ischemic stroke. Arterioscler Thromb Vasc Biol. 2019; 39(2): 285–293, doi: 10.1161/ATVBAHA.118.311960, indexed in Pubmed: 30580563.

V M
VIA MEDICA

ORIGINAL ARTICLE

Curcumin reduces blood-nerve barrier abnormalities and cytotoxicity to endothelial cells and pericytes induced by cisplatin

P. Kobutree, A. Tothonglor, A. Roumwong, D. Jindatip, S. Agthong

Department of Anatomy, Faculty of Medicine, Chulalongkorn University, Bangkok, Thailand

Background: Cisplatin is a platinum-based antineoplastic agent used to treat cancers of solid organs. Neuropathy is one of its major side effects, necessitating dose reduction or cessation. Previous studies suggested that cisplatin causes microvascular toxicity, including pericyte detachment. This study aimed to clarify whether these alterations occurred in the blood–nerve barrier (BNB) of capillaries after cisplatin treatment.

Materials and methods and Results: Electron microscopic analysis of rat sciatic nerves with cisplatin neuropathy showed increased frequency and severity of pericyte detachment. Moreover, the vascular basement membrane did not tightly encircle around the endothelial cells and pericytes. Cultured human umbilical vein endothelial cells and human brain vascular pericytes showed reduced viability, increased caspase-3 activity and enhanced oxidative stress following cisplatin treatment. In addition, cisplatin decreased transendothelial electrical resistance (TEER) and the expression of the tight junction proteins occludin and zonula occludens-1. Curcumin, a polyphenol found in the root of Curcuma longa, had favourable effects on cisplatin neuropathy in previous work. Therefore, curcumin was tested to determine whether it had any effect on these abnormalities. Curcumin alleviated pericyte detachment, cytotoxicity, oxidative stress, TEER reduction and tight junction protein expression.

Conclusions: These data indicate that cisplatin causes BNB disruption in the nerves and might result in neuropathy. Curcumin might improve neuropathy via the restoration of BNB. Whether alterations in the BNB occur and curcumin is effective in patients with cisplatin neuropathy remain to be investigated. (Folia Morphol 2023; 82, 3: 533–542)

Key words: capillaries, cisplatin, nerve, neuropathy

INTRODUCTION

Cisplatin is a chemotherapeutic agent for treating cancers of several solid organs [10]. One of its major side effects is peripheral neuropathy, often leading to dose reduction or cessation of chemotherapy. Sensory abnormalities were observed in both ani-mals and patients with cisplatin-induced neuropathy [5, 19, 30, 36]. Morphological analysis showed loss of spinal ganglion neurons with nuclear and nucleolar atrophy [2, 35]. In the sciatic nerve, degeneration and demyelination of nerve fibres have also been reported [3, 35]. To date, different agents targeting various

underlying mechanisms of cisplatin neuropathy have failed to show clinical efficacy [21, 32]. However, curcumin, a polyphenol found in the root of *Curcuma longa*, has demonstrated beneficial effects on cisplatin neuropathy [2]. This activity warrants further investigation of curcumin as a potential therapy.

Current evidence suggests that vascular dysfunction might play a role in cisplatin neuropathy. Arterial occlusion [20] and endothelial damage [9] were reported in patients receiving cisplatin. In cisplatin-treated rats, reduced nerve blood flow, a decreased number of vasa nervorum and endothelial apoptosis were observed [18]. Our previous study showed reduced density and detachment of pericytes in the nerve capillaries of rats with cisplatin neuropathy [17]. These abnormalities might be associated with an impaired blood–nerve barrier (BNB). This study aimed to confirm whether there were structural defects of BNB in rats treated with cisplatin. In addition, the direct effects of cisplatin on endothelial cells and pericytes were investigated in vitro. Moreover, we examined whether concomitant treatment with curcumin could alleviate the vascular toxicity of cisplatin.

MATERIALS AND METHODS

Tissue collection

The specimens used in this study were from a previous animal experiment [2]. Briefly, female Wistar rats were divided into three groups: control, cisplatin and cisplatin + curcumin (n = 8 each). Cisplatin (Cat. No. NDC 0069-0084-07, Pfizer, New York, NY, USA) 2 mg/kg was injected intraperitoneally twice a week for 5 consecutive weeks (20 mg/kg cumulative dose). During the 5-week administration of cisplatin, 200 mg/kg curcumin (Cat. No. 81025, Cayman Chemical, Ann Arbor, MI, USA) was concomitantly given by gavage to the cisplatin + curcumin group once daily. All animals were left untreated for 3 weeks until they were sacrificed. The rats were sacrificed by anaesthetic overdose and then transcardially perfused with normal saline followed by 4% paraformaldehyde (Cat. no. 818715, Merck Millipore, Darmstadt, Germany). L4 dorsal root ganglia and sciatic nerves were postfixed in 3% glutaraldehyde (Cat. No. 16220, EMS, Hatfield, PA, USA) and embedded in epoxy resin. The ganglia and left sciatic nerves were used for morphometric analysis, whereas right sciatic nerves were processed for electron microscopic examination.

The presence of neuropathy in the cisplatin group was confirmed by the hot plate test and nerve conduction study during the experiment and before sacrifice. Moreover, ganglion and nerve morphometry showed ultrastructural changes characteristic of experimental cisplatin-induced neuropathy [3, 5, 35, 36]. Curcumin significantly attenuated these abnormalities.

These specimens were from the previous study which showed thermal hypoalgesia in the 5th week and reduced sciatic motor nerve conduction velocity in the 5th and 8th weeks [2]. Moreover, ganglion morphometry showed nuclear and nucleolar atrophy including loss of neurons in the 8th week. Curcumin significantly attenuated these abnormalities.

Transmission electron microscopy

Ultrathin sections (70 nm thickness) of the sciatic nerves divided into the proximal and distal parts were stained with lead citrate and uranyl acetate. The morphology of pericytes and the vascular basement membrane (VBM) shared with endothelial cells was examined with a transmission electron microscope (JEM-1400PLUS; JEOL, Tokyo, Japan). In each rat, 20 capillaries were randomly chosen from serial sections of proximal and distal nerves. Each capillary was evaluated for the presence of pericyte detachment from endothelial cells and VBM, which was classified into two categories. In category 1, the pericyte was completely attached to the VBM and endothelial cell. In category 2, the pericyte had detached from the VBM and endothelial cell at least one point. Subsequently, the lengths of the farthest detachment between the pericytes and VBM were measured in the capillaries of category 2. The thickness of the VBM at the farthest detachment was also measured.

Cell culture

Human umbilical vein endothelial cells (HUVECs; Cat. No. #C-015-5C, Invitrogen, Waltham, MA, USA) and human brain vascular pericytes (HBVPs; Cat. No. 1200, ScienCell, Carlsbad, CA, USA) were grown according to manufacturers' protocols. Each experiment was performed in triplicate and repeated three times. HUVECs and HBVPs were divided into three groups: control, cisplatin, and cisplatin + curcumin. In the cisplatin and cisplatin + curcumin groups, HUVECs and HBVPs were incubated with 3 μg/mL and 1.5 μg//mL cisplatin (Cat. No. 1C 257/51, Korea United Pharm, Seoul, South Korea) for 24 hours, respectively. For curcumin treatment, the cells were co-incubated with 1 μg/mL curcumin (Cat. No. 81025, Cayman Chemical, Ann Arbor, MI, USA) for 24 hours. These doses were

chosen as the lowest concentrations to induce cytotoxicity in the HUVEC and HBVP in the pilot studies.

MTT assay

The MTT assay was used to evaluate the viability of HUVECs and HBVPs. The cells were seeded at 1×10^4 and 5×10^3 cells/well in 96-well plates and allowed to attach for 24 hours. The cells were then treated according to the experimental conditions for 24 hours. Finally, the cells were incubated with 100 μL MTT solution (Cat. No. M6494, Molecular Probes, Eugene, OR, USA) for 2 hours. Subsequently, purple formazan crystals were dissolved in 100 μL dimethyl sulfoxide. The absorbance was measured at 570 nm using a microplate reader (Multiskan GO 1510-02675; Thermo Fisher Scientific, Waltham, MA, USA). The percentage of cell viability was calculated from the absorbance of the sample divided by that of the negative control.

Caspase-3 assay

A caspase-3/CPP32 colorimetric assay kit (Cat. No. #K106-200, BioVision, Milpitas, CA, USA) was used to determine caspase-3 activity. Briefly, the cells were plated at 1×10^6 in the culture vessels. After treatments, the cells were harvested and resuspended in cell lysis buffer. The supernatant of each sample was collected, and the protein concentration was measured. Subsequently, the sample was diluted with cell lysis buffer to obtain a protein concentration of 1 μg/μL and transferred to a 96-well plate. Then, working reaction buffer and DEVD-pNA substrate were added. The plate was incubated at 37°C for 2 hours. Finally, the absorbance was measured at 405 nm using a microplate reader (Multiskan GO 1510-02675; Thermo Fisher Scientific, Waltham, MA, USA). The caspase-3 activity of treated cells was compared with that of controls.

ROS assay

Cells were seeded at 1×10^4 cells/well in 96-well black plates for 24 hours. Then, the cells were incubated with 2',7'-dichlorofluorescein diacetate (DCFH-DA; Cat. No. D688, Sigma-Aldrich, St. Louis, MO, USA) at 37°C for 30 minutes. After the cells were treated according to the experimental conditions, the level of DCF (T0) was measured using a fluorescence microplate reader (Varioskan Flash; Thermo Fisher Scientific, Waltham, MA, USA) at 480 and 535 nm for excitation and emission, respectively. Subsequently, the incuba-

tion was continued for 1 hour, and the level of DCF was measured again (T1). The relative production of reactive oxygen species (ROS) was calculated from the ratio of T1 to T0.

GSH/GSSG assay

The levels of oxidized (GSSG) and total glutathione were determined using a glutathione colorimetric detection kit (Cat. No. #9135, Promega, Madison, WI, USA). In brief, cells were plated at 1×10^6 cells//mL in a T-25 flask and treated according to the experimental conditions for 24 hours. The pellets were harvested and resuspended in cold 5% 5-sulfosalicylic acid (Cat. No. S2130, Sigma-Aldrich, St. Louis, MO, USA) and then incubated at 4°C for 10 minutes. The supernatant was mixed with the detection substrate and reaction mixture followed by incubation at room temperature for 20 minutes. Total glutathione was determined by measuring at 405 nm using a microplate reader (Multiskan GO 1510-02675, Thermo Fisher Scientific, Waltham, MA, USA). For GSSG detection, the sample and standard were pretreated with 2-vinylpyridine (Cat. No. 132292, Sigma-Aldrich, St. Louis, MO, USA). The level of reduced glutathione (GSH) was derived from subtraction of GSSG from total glutathione. Finally, the GSH/GSSG ratio was calculated.

Transendothelial electrical resistance (TEER) study

HUVECs were cultured in the upper chamber of a transwell insert (Cat. No. MCHT24H48, Merck, Kenilworth, NJ, USA), which was inserted into a 24-well plate at 1×10^4 cells/well. After 24 hours of treatments according to the experimental conditions, cell resistance (R) was measured using a Millicell electrical resistance apparatus (Millicell® ERS-2; Merck, Kenilworth, NJ, USA). The TEER value was calculated using the following formula: TEER value (Ωcm^2) = $= (R_{sample} - R_{blank}) \times$ membrane area (cm^2).

Western blot analysis

HUVECs were seeded at 2×10^6 cells/ml in a culture dish. After being treated according to experimental protocols for 24 hours, the cells were incubated on ice with lysis buffer (Cat. No. #9806, Cell Signaling, Danvers, MA, USA) containing 1 × protease inhibitor cocktail (Cat. No. #5871, Cell Signaling, Danvers, MA, USA) for 5 minutes. Subsequently, the cells were scraped and centrifuged, and the supernatant was collected. The protein concentration of the supernatant was determined using a PierceTM

BCA protein assay (Cat. No. 23227, Thermo Fisher Scientific, Waltham, MA, USA). The sample (1.5 µg/µL) was then mixed with the fluorescent dye (4:1 ratio) and denatured at 95°C for 5 minutes. The marker, sample, antibody diluent, primary antibody (1:200 β-actin [Cat. No. #4970, Cell Signaling, Danvers, MA, USA], 1:200 zonula occludens-1 [ZO-1; Cat. No. #PA5-28858, Invitrogen, Waltham, MA, USA], 1:200 zonula occludens-2 [ZO-2; Cat. No. #PA5-17155, Invitrogen, Waltham, MA, USA], 1:200 claudin-5 [Cat. No. #34-1600, Invitrogen, Waltham, MA, USA], 1:200 occludin [Cat. No. #PA5-20755, Invitrogen, Waltham, MA, USA]), rabbit secondary conjugate, streptavidin-HRP, and luminol peroxide (Cat. No. DM-001, ProteinSimple, Santa Clara, CA, USA) were added to the plate according to the manufacturer's protocol. Subsequently, separation and immunodetection were performed using a WES automated western blotting system (ProteinSimple; Santa Clara, CA, USA). The density of digital images was analysed using Compass software (ProteinSimple, Santa Clara, CA, USA). The expression of each protein was normalized to that of β-actin.

Statistical analysis

One-way ANOVA followed by Tukey's post-hoc test was used to compare the means of the above parameters between groups. The test was performed using SPSS for Windows version 23 (SPSS, Inc., Armonk, NY, USA). Differences were considered statistically significant when $p < 0.05$.

RESULTS

Ultrastructural analysis

Pericyte detachment from endothelial cells appeared to be more prominent in the nerve capillaries of the cisplatin-treated group than in the control group (Fig. 1). In contrast, detachment was less severe in the cisplatin + curcumin group. It was noted that the basement membrane did not tightly wrap around the endothelial cells and pericytes in the cisplatin-treated group (arrows in Fig. 1B) compared to the control and cisplatin + curcumin groups (arrows in Fig. 1A, C). No other pathological findings, such as the accumulation of lysosomes or vacuoles, were detected in the pericytes or endothelial cells in any group.

After morphometric analysis, the number of capillaries with detachment compared with that of total capillaries was significantly higher in the cisplatin group than in the control group (Fig. 2). Curcumin
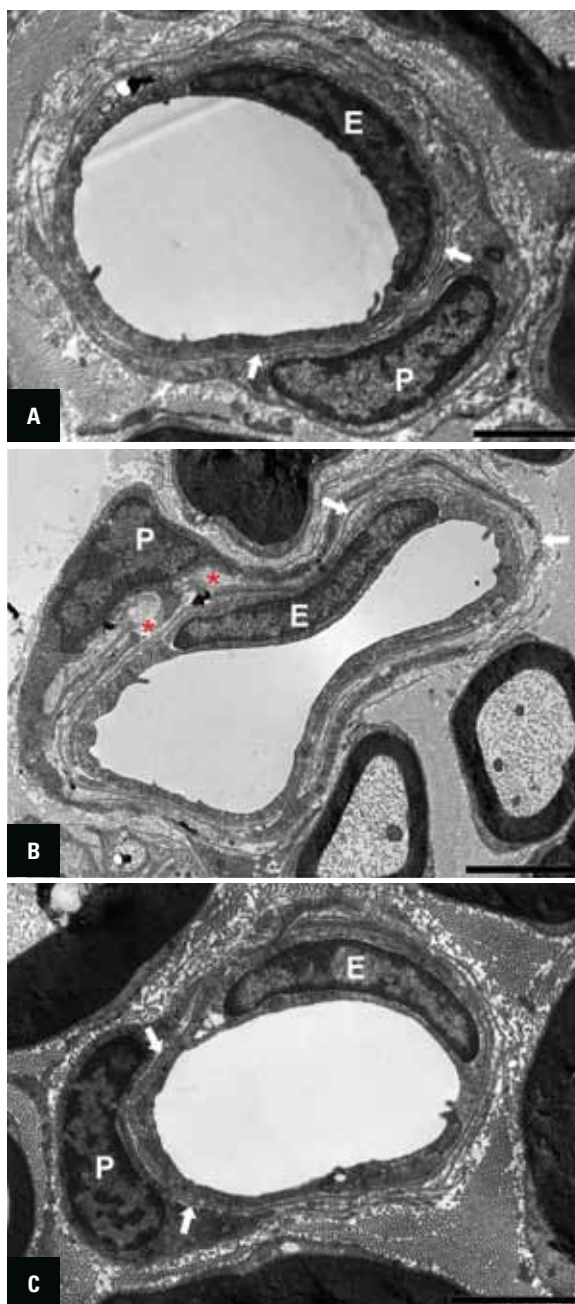

Figure 1. Representative electron microscopic images of capillaries in the sciatic nerves from the control (**A**), cisplatin (**B**), and cisplatin + curcumin (**C**) groups. Arrows indicate the basement membrane shared between the endothelial cell (E) and pericyte (P); *Pericyte detachment from the endothelial cell; scale bars: 1 µm.

treatment significantly reduced the ratio. In addition, the detachment distance was significantly longer in the cisplatin group than in the control group (Fig. 3). Treatment with curcumin significantly decreased the distance. Regarding the thickness of the basement membrane at the detachment site, there were no significant differences between groups (data not shown).
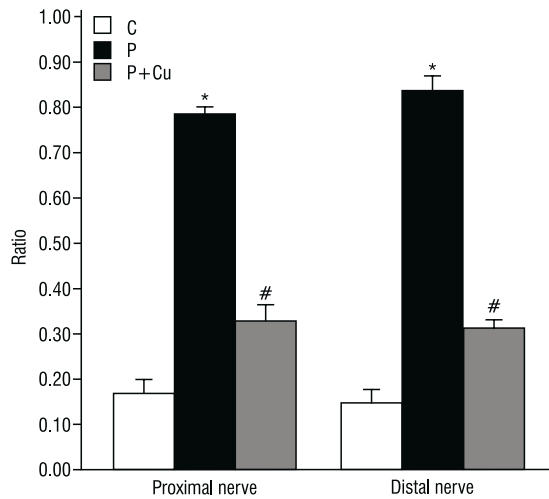
Figure 2. Ratio of the number of capillaries with pericyte detachment to the total number of capillaries in the proximal and distal parts of the sciatic nerve. The graph shows the means and standard error of the mean; C — control; P — cisplatin; P+Cu — cisplatin + curcumin; $*p < 0.001$ P vs. C; $\#p < 0.01$ P+Cu vs. C and $p < 0.001$ P+Cu vs. P.
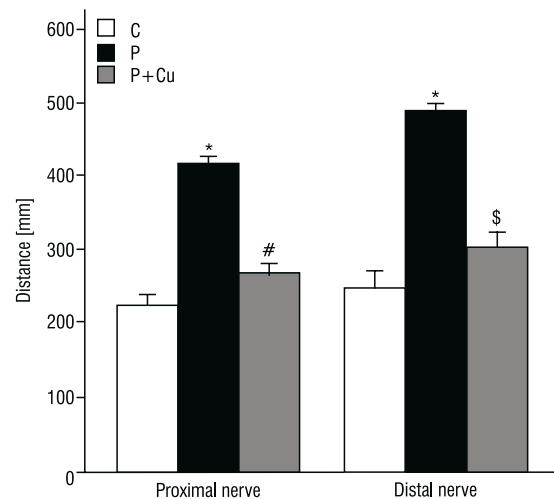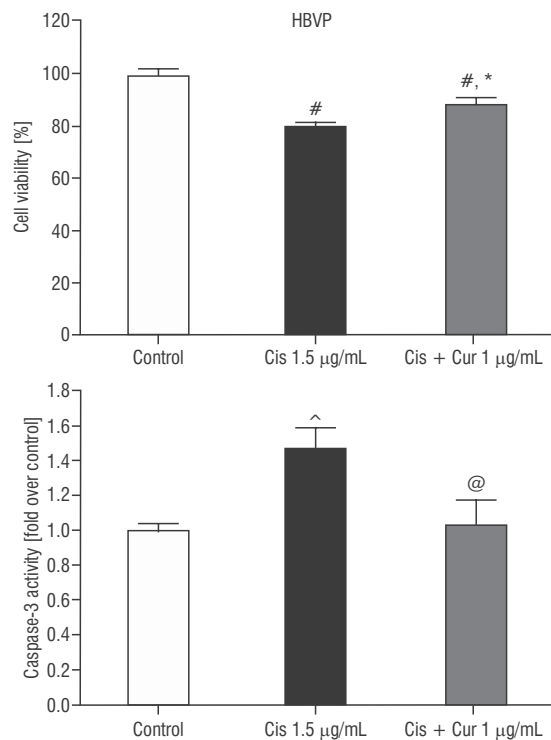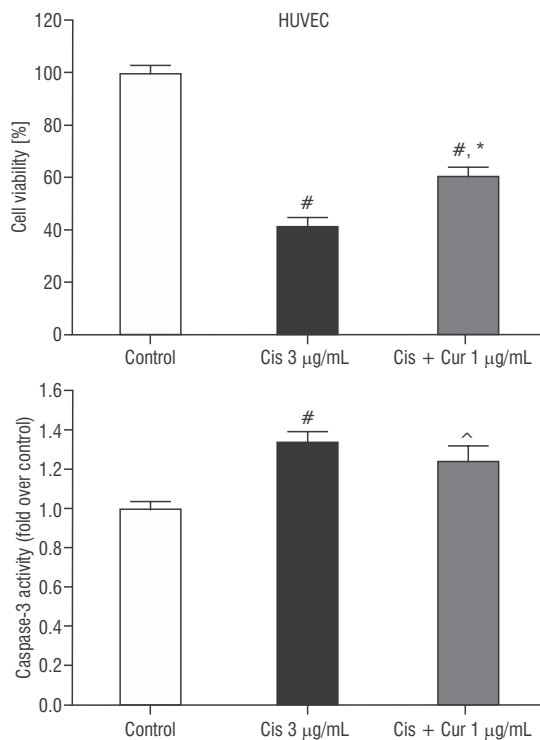

Figure 3. Distance at the widest detachment of pericytes in the proximal and distal parts of the sciatic nerve. The graph shows the means and standard error of the mean; C — control; P — cisplatin; P+Cu — cisplatin + curcumin; $*p < 0.001$ P vs. C; $\#p < 0.05$ P+Cu vs. C and $p < 0.001$ P+Cu vs. P; $\$p < 0.001$ P+Cu vs. P.

Figure 4. Cell viability and caspase-3 activity of human umbilical vein endothelial cells (HUVECs, left column) and human brain vascular pericytes (HBVPs, right column). The graphs show the means and standard error of the mean; Cis — cisplatin; Cur — curcumin; $\#p < 0.001$ vs. control; $*p < 0.01$ vs. Cis; $\hat{\ }p < 0.05$ vs. control; @$p < 0.05$ vs. Cis.

Cell viability and caspase-3 activity

The viability of HUVECs and HBVPs was significantly lower in the cisplatin group than in the control group (Fig. 4). In addition, caspase-3 activity was significantly elevated in the cisplatin group compared with the control group in both cell types. Curcumin treatment partially improved the viability of both cell types and caspase-3 activation in HUVECs. In HBVP, curcumin normalised caspase-3 activity.
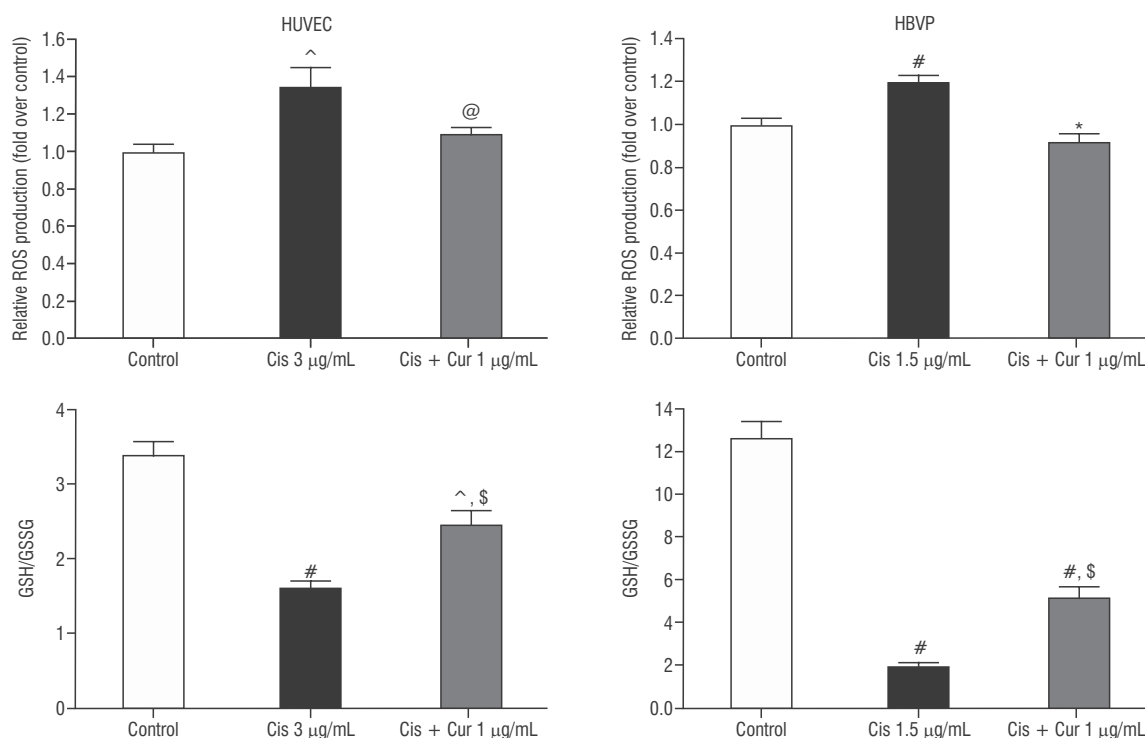
Figure 5. Reactive oxygen species (ROS) production and the ratio of reduced to oxidized glutathione (GSH/GSSG) in human umbilical vein endothelial cells (HUVECs, left column) and human brain vascular pericytes (HBVPs, right column). The graphs show the means and standard error of the mean; Cis — cisplatin; Cur — curcumin; ^p < 0.01 vs. control; #p < 0.001 vs. control; @p < 0.05 vs. Cis; $p < 0.01 vs. Cis; *p < 0.001 vs. Cis.

Oxidative stress parameters

Reactive oxygen species production was significantly increased after cisplatin exposure in HUVECs and HBVPs (Fig. 5). Consistently, the GSH/GSSG ratio was significantly decreased in the cisplatin group relative to the control group in both cell types. Curcumin treatment corrected the higher ROS production and partially elevated the GSH/GSSG ratio in both HUVECs and HBVPs.

Transendothelial electrical resistance

Cisplatin caused a significant reduction in the TEER value of HUVECs, and curcumin partially restored the resistance (Fig. 6).

Expression of tight junction proteins

The expression of occludin and ZO-2 in HUVECs was significantly decreased after cisplatin administration (Fig. 7). However, the expression of claudin-5 and ZO-1 was not significantly reduced. Following curcumin treatment, the expression of ZO-1 and ZO-2 was significantly upregulated compared with that in the cisplatin group. In addition, claudin-5 expression showed a tendency toward elevation in the cisplatin
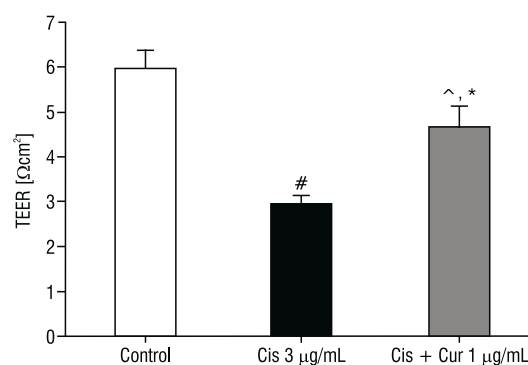

Figure 6. Transendothelial electrical resistance (TEER) of human umbilical vein endothelial cells. The graph shows the means and standard error of the mean; Cis — cisplatin; Cur — curcumin; #p < 0.001 vs. control; ^p < 0.05 vs. control; *p < 0.01 vs. Cis.

+ curcumin group. Curcumin had no significant effect on the downregulated expression of occludin caused by cisplatin.

DISCUSSION

A previous study suggested a higher incidence of pericyte detachment in the nerve capillaries of cisplatin-treated rats relative to controls [17]. With quantitative analysis, the present study confirmed
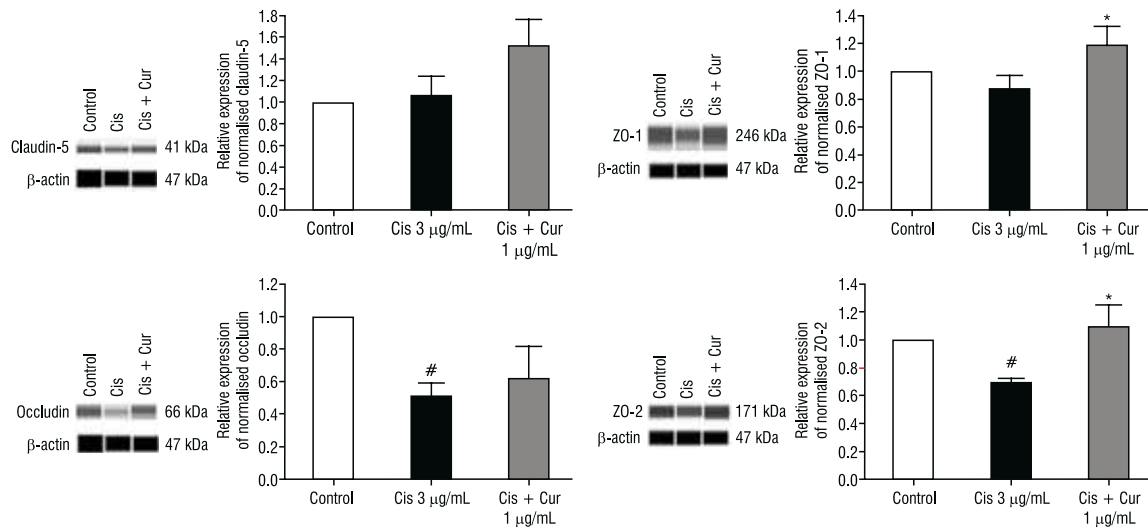
Figure 7. Protein expression of claudin-5, occludin, zonula occludens-1 (ZO-1) and zonula occludens-2 (ZO-2). Representative immunoblots are shown. The density of each protein was normalised to that of β-actin. The graphs show the means and standard error of the mean; Cis — cisplatin; Cur — curcumin; #$p < 0.05$ vs. control; *$p < 0.05$ vs. Cis.

that pericyte detachment occurred with higher frequency and severity in the cisplatin-treated than in the control rats. Pericyte detachment or migration has been observed in various conditions and organs. Increased pericyte migration was found in the brain after traumatic injury [11], in the retina of diabetic rats [29] and in the prolactinoma of the pituitary gland [16]. Although the consequences of pericyte detachment remain unclear, abnormalities in any component of the BNB likely result in barrier dysfunction. Since BNB maintains endoneurial homeostasis, its impairment is likely deleterious to nerve fibres and may lead to neuropathy [28]. This hypothesis is supported by a previous study showing that cisplatin-induced ototoxicity was associated with changes in cochlear endothelial cells and pericytes [37].

Our results showed that curcumin alleviated the pericyte detachment induced by cisplatin in the sciatic nerve. Curcumin, a polyphenol found in the root of *Curcuma longa*, has antioxidant, anti-inflammatory and neuroprotective properties [8, 15]. The mechanisms underlying pericyte detachment induced by cisplatin are still unclear. In vitro experiments on pericytes were performed to clarify this issue.

Using HUVEC and HBVP cultures, this study demonstrated that cisplatin reduced the viability of both cell types with activation of caspase-3. In addition, the production of ROS was increased, and reduced glutathione was decreased in the cells receiving cisplatin. Consistently, endothelial apoptosis and enhanced caspase-3 activity after cisplatin treatment

were reported [12, 13, 18, 26]. Oxaliplatin, another platinum-based antineoplastic drug, was also shown to activate caspase-3 and oxidative stress in a rat brain endothelial cell line [7]. All these data indicate that cisplatin induces oxidative stress, leading to caspase-3 activation and apoptosis in endothelial cells and pericytes.

Curcumin improved cell viability, reduced caspase-3 activity and attenuated oxidative stress in both HUVECs and HBVPs. This improvement might be due to the antioxidant property of curcumin [8, 15]. A previous study showed that curcumin ameliorated cisplatin-induced oxidative stress and neuronal death in the mouse optic nerve [27]. Another study demonstrated the favourable effects of curcumin on oxaliplatin-induced neuropathic pain via reduction of oxidative stress and inflammation [38]. Therefore, curcumin was effective against oxidative stress caused by cisplatin, leading to reduced cytotoxicity.

We also showed that the TEER value and expression of the tight junction proteins occludin and ZO-2 in HUVECs were reduced by cisplatin. Lower expression of tight junction proteins was also found in the stria vascularis of the cochlea in cisplatin-treated mice [37]. In oxaliplatin-induced endothelial cytotoxicity, fragmentation of ZO-1 immunostaining in the intercellular junction was observed [7]. The downregulation of endothelial tight junction proteins induced by cisplatin might arise from oxidative stress [31]. These tight junction proteins are crucial for BNB integrity. Perturbation in the expression or localisation

of these proteins is associated with BNB loosening and neuropathies [22]. Pericytes are also important for the normal functions of BNB [28]. Shimizu et al. [33] reported that pericytes controlled the expression of claudin-5 in endothelial cells through secretion of growth factors. In addition to claudin-5, nerve pericytes also express other important components of the BNB, such as fibronectin and collagen type IV [34]. Our results showed that cisplatin causes cytotoxicity and detachment of pericytes. Taken together, the findings show that cisplatin likely causes endothelial and pericyte cytotoxicity, resulting in decreased expression of tight junction proteins and barrier dysfunction. However, it remains to be proven whether these alterations in the BNB occur in patients with cisplatin neuropathy. Moreover, BNB integrity should be examined in neuropathies from other chemotherapeutic drugs or causes.

Curcumin alleviated the decreased TEER value and corrected the expression of ZO-2, including enhancement of ZO-1 expression above the control level. Combined with the above morphometric data, our results indicate that curcumin might attenuate pericyte detachment through the upregulation of endothelial tight junction proteins. Our previous study demonstrated the favourable effects of curcumin on functional and morphological changes associated with cisplatin neuropathy [2]. Curcumin also improved biochemical and histological alterations in the sciatic nerves of cisplatin-treated rats [3]. Therefore, when considering the results of this and previous studies, we propose that curcumin ameliorates cisplatin-induced oxidative stress and cytotoxicity in endothelial cells and pericytes, leading to restoration of tight junction proteins and BNB functions. Apart from chemotherapy-induced neuropathy, increasing evidence supports the beneficial effects of curcumin on neuropathies from various aetiologies [6]. However, whether curcumin can alleviate cisplatin-induced neuropathy in patients remains to be investigated.

Curcumin has several advantages. It is found in the turmeric spice made from the root of *Curcuma longa*, which has long been used in traditional medicine. Hence, it is relatively nontoxic and highly tolerable in humans [14]. In addition, curcumin can be administered concomitantly with chemotherapeutic agents without interfering with antitumor efficacy. On the contrary, several reports have confirmed the enhanced antitumor activity of cisplatin cotreated with curcumin [1, 23, 25]. However, the major lim-

itation is its poor absorption and bioavailability [4]. Novel methods are being developed to overcome this drawback of curcumin, including nanocarriers [24]. Collectively, the evidence shows that curcumin holds promise as a safe and effective therapeutic agent against cisplatin neuropathy.

CONCLUSIONS

This study demonstrated the favourable effects of curcumin on pericyte detachment induced by cisplatin in the capillaries of the sciatic nerve. In addition, in vitro experiments showed a reduction in the viability of endothelial cells and pericytes, TEER, and the expression of some tight junction proteins. These parameters were alleviated by curcumin. These data indicate that BNB disruption is a novel potential mechanism underlying cisplatin-induced neuropathy and that curcumin is effective against this abnormality. In the future, the BNB should be examined in neuropathies from other antineoplastic agents or causes, and drugs with beneficial effects on microvessels should be assessed as potential therapeutic agents.

Conflict of interest: None declared

REFERENCES

1. Abadi AJ, Mirzaei S, Mahabady MK, et al. Curcumin and its derivatives in cancer therapy: Potentiating antitumor activity of cisplatin and reducing side effects. Phytother Res. 2022; 36(1): 189–213, doi: 10.1002/ptr.7305, indexed in Pubmed: 34697839.
2. Agthong S, Kaewsema A, Charoensub T. Curcumin ameliorates functional and structural abnormalities in cisplatin-induced neuropathy. Exp Neurobiol. 2015; 24(2): 139–145, doi: 10.5607/en.2015.24.2.139, indexed in Pubmed: 26113793.
3. Al Moundhri MS, Al-Salam S, Al Mahrouqee A, et al. The effect of curcumin on oxaliplatin and cisplatin neurotoxicity

in rats: some behavioral, biochemical, and histopathologi-cal studies. J Med Toxicol. 2013; 9(1): 25–33, doi: 10.1007/s13181-012-0239-x, indexed in Pubmed: 22648527.

4. Anand P, Kunnumakkara AB, Newman RA, et al. Bioavail-ability of curcumin: problems and promises. Mol Pharm. 2007; 4(6): 807–818, doi: 10.1021/mp700113r, indexed in Pubmed: 17999464.

5. Authier N, Gillet JP, Fialip J, et al. An animal model of noci-ceptive peripheral neuropathy following repeated cisplatin injections. Exp Neurol. 2003; 182(1): 12–20, doi: 10.1016/s0014-4886(03)00003-7, indexed in Pubmed: 12821373.

6. Basu P, Maier C, Basu A. Effects of curcumin and its dif-ferent formulations in preclinical and clinical studies of peripheral neuropathic and postoperative pain: a com-prehensive review. Int J Mol Sci. 2021; 22(9): 4666, doi: 10.3390/ijms22094666, indexed in Pubmed: 33925121.

7. Branca JJ, Maresca M, Morucci G, et al. Oxaliplatin-induced blood brain barrier loosening: a new point of view on chemotherapy-induced neurotoxicity. Oncotarget. 2018; 9(34): 23426–23438, doi: 10.18632/oncotarget.25193, indexed in Pubmed: 29805744.

8. Cole GM, Teter B, Frautschy SA. Neuroprotective effects of curcumin. Adv Exp Med Biol. 2007; 595: 197–212, doi: 10.1007/978-0-387-46401-5_8, indexed in Pubmed: 17569212.

9. Dieckmann KP, Struss WJ, Budde U. Evidence for acute vascular toxicity of cisplatin-based chemotherapy in pa-tients with germ cell tumour. Anticancer Res. 2011; 31(12): 4501–4505, indexed in Pubmed: 22199322.

10. Dilruba S, Kalayda GV. Platinum-based drugs: past, present and future. Cancer Chemother Pharmacol. 2016; 77(6): 1103–1124, doi: 10.1007/s00280-016-2976-z, indexed in Pubmed: 26886018.

11. Dore-Duffy P, Owen C, Balabanov R, et al. Pericyte migra-tion from the vascular wall in response to traumatic brain injury. Microvasc Res. 2000; 60(1): 55–69, doi: 10.1006/mvre.2000.2244, indexed in Pubmed: 10873515.

12. Dursun B, He Z, Somerset H, et al. Caspases and calpain are independent mediators of cisplatin-induced endothelial cell necrosis. Am J Physiol Renal Physiol. 2006; 291(3): F578–F587, doi: 10.1152/ajprenal.00455.2005, indexed in Pubmed: 16622172.

13. Eguchi R, Fujimori Y, Ohta T, et al. Calpain is involved in cisplatin-induced endothelial injury in an in vitro three-dimensional blood vessel model. Int J Oncol. 2010; 37(5): 1289–1296, doi: 10.3892/ijo_00000780, indexed in Pubmed: 20878076.

14. Epstein J, Sanderson IR, Macdonald TT. Curcumin as a therapeutic agent: the evidence from in vitro, animal and human studies. Br J Nutr. 2010; 103(11): 1545–1557, doi: 10.1017/S0007114509993667, indexed in Pubmed: 20100380.

15. Hatcher H, Planalp R, Cho J, et al. Curcumin: from ancient medicine to current clinical trials. Cell Mol Life Sci. 2008; 65(11): 1631–1652, doi: 10.1007/s00018-008-7452-4, indexed in Pubmed: 18324353.

16. Jindatip D, Fujiwara K, Sarachana T, et al. Characteristics of pericytes in diethylstilbestrol (DES)-induced pituitary prolactinoma in rats. Med Mol Morphol. 2018; 51(3): 147–155, doi: 10.1007/s00795-018-0180-4, indexed in Pubmed: 29344720.

17. Jindatip D, Nopparat W, Kobutree P, et al. Pericyte loss and detachment in experimental cisplatin-induced neuropathy. Int J Morphol. 2019; 37(2): 509–514, doi: 10.4067/s0717-95022019000200509.

18. Kirchmair R, Walter DH, Ii M, et al. Antiangiogenesis medi-ates cisplatin-induced peripheral neuropathy: attenuation or reversal by local vascular endothelial growth factor gene therapy without augmenting tumor growth. Circulation. 2005; 111(20): 2662–2670, doi: 10.1161/CIRCULATIONA-HA.104.470849, indexed in Pubmed: 15897348.

19. Krarup-Hansen A, Helweg-Larsen S, Schmalbruch H, et al. Neuronal involvement in cisplatin neuropathy: prospective clinical and neurophysiological studies. Brain. 2007; 130(Pt 4): 1076–1088, doi: 10.1093/brain/awl356, indexed in Pubmed: 17301082.

20. Li SH, Chen WH, Tang Y, et al. Incidence of ischemic stroke post-chemotherapy: a retrospective review of 10,963 patients. Clin Neurol Neurosurg. 2006; 108(2): 150–156, doi: 10.1016/j.clineuro.2005.03.008, indexed in Pubmed: 16412836.

21. Liu YW, Liu CT, Su YL, et al. A narrative review of comple-mentary nutritional supplements for chemotherapy-in-duced peripheral neuropathy. Altern Ther Health Med. 2020; 26(4): 43–49, indexed in Pubmed: 31634876.

22. Maiuolo J, Gliozzi M, Musolino V, et al. The role of en-dothelial dysfunction in peripheral blood nerve barrier: molecular mechanisms and pathophysiological implica-tions. Int J Mol Sci. 2019; 20(12): 3022, doi: 10.3390/ijms20123022, indexed in Pubmed: 31226852.

23. Mendonça LM, da Silva Machado C, Teixeira CC, et al. Curcumin reduces cisplatin-induced neurotoxicity in NGF-differentiated PC12 cells. Neurotoxicology. 2013; 34: 205–211, doi: 10.1016/j.neuro.2012.09.011, indexed in Pubmed: 23036615.

24. Moballegh Nasery M, Abadi B, Poormoghadam D, et al. Curcumin delivery mediated by bio-based nanoparticles: a review. Molecules. 2020; 25(3): 689, doi: 10.3390/mol-ecules25030689, indexed in Pubmed: 32041140.

25. Notarbartolo M, Poma P, Perri D, et al. Antitumor effects of curcumin, alone or in combination with cisplatin or doxorubicin, on human hepatic cancer cells. Analysis of their possible relationship to changes in NF-kB activation levels and in IAP gene expression. Cancer Lett. 2005; 224(1): 53–65, doi: 10.1016/j.canlet.2004.10.051, indexed in Pubmed: 15911101.

26. Nuver J, De Haas EC, Van Zweeden M, et al. Vascular damage in testicular cancer patients: A study on en-dothelial activation by bleomycin and cisplatin in vitro. Oncology Reports. 2009; 23(1): 247–253, doi: 10.3892/or_00000630.

27. Özkaya D, Nazıroğlu M. Curcumin diminishes cispla-tin-induced apoptosis and mitochondrial oxidative stress through inhibition of TRPM2 channel signaling pathway in mouse optic nerve. J Recept Signal Transduct Res. 2020; 40(2): 97–108, doi: 10.1080/10799893.2020.1720240, indexed in Pubmed: 32019426.

28. Peltonen S, Alanne M, Peltonen J. Barriers of the peripheral nerve. Tissue Barriers. 2013; 1(3): e24956, doi: 10.4161/tisb.24956, indexed in Pubmed: 24665400.

29. Pfister F, Feng Y, vom Hagen F, et al. Pericyte migration: a novel mechanism of pericyte loss in experimental di-

abetic retinopathy. Diabetes. 2008; 57(9): 2495–2502, doi: 10.2337/db08-0325, indexed in Pubmed: 18559662.

30. Quasthoff S, Hartung HP. Chemotherapy-induced peripheral neuropathy. J Neurol. 2002; 249(1): 9–17, doi: 10.1007/pl00007853, indexed in Pubmed: 11954874.

31. Rao R. Oxidative stress-induced disruption of epithelial and endothelial tight junctions. Front Biosci. 2008; 13: 7210––7226, doi: 10.2741/3223, indexed in Pubmed: 18508729.

32. Santos NA, Ferreira RS, Santos AC. Overview of cisplatin-induced neurotoxicity and ototoxicity, and the protective agents. Food Chem Toxicol. 2020; 136: 111079, doi: 10.1016/j.fct.2019.111079, indexed in Pubmed: 31891754.

33. Shimizu F, Sano Y, Abe MA, et al. Peripheral nerve pericytes modify the blood-nerve barrier function and tight junctional molecules through the secretion of various soluble factors. J Cell Physiol. 2011; 226(1): 255–266, doi: 10.1002/jcp.22337, indexed in Pubmed: 20665675.

34. Shimizu F, Sano Y, Haruki H, et al. Advanced glycation end-products induce basement membrane hypertrophy in endoneurial microvessels and disrupt the blood-nerve barrier by stimulating the release of TGF-β and vascular endothelial growth factor (VEGF) by pericytes. Diabetologia. 2011; 54(6): 1517–1526, doi: 10.1007/s00125-011-2107-7, indexed in Pubmed: 21409414.

35. Wongtawatchai T, Agthong S, Kaewsema A, et al. Altered phosphorylation of mitogen-activated protein kinases in dorsal root ganglia and sciatic nerve of rats with cisplatin-induced neuropathy. Asian Biomed (Res Rev News). 2012; 6(3): 397–411.

36. Wongtawatchai T, Agthong S, Kaewsema A, et al. Sex-related differences in cisplatin-induced neuropathy in rats. J Med Assoc Thai. 2009; 92(11): 1485–1491, indexed in Pubmed: 19938741.

37. Zhang Na, Cai J, Xu L, et al. Cisplatin-Induced stria vascularis damage is associated with inflammation and fibrosis. Neural Plast. 2020; 2020: 8851525, doi: 10.1155/2020/8851525, indexed in Pubmed: 33029120.

38. Zhang X, Guan Z, Wang X, et al. Curcumin alleviates oxaliplatin-induced peripheral neuropathic pain through inhibiting oxidative stress-mediated activation of NF-κB and mitigating inflammation. Biol Pharm Bull. 2020; 43(2): 348–355, doi: 10.1248/bpb.b19-00862, indexed in Pubmed: 31776306.

ORIGINAL ARTICLE

Microanatomy of the central myelin portion and transitional zone of the oculomotor and abducens nerves

W. Quanchareonsap[1] , S. Jariyakosol[2] , S. Apinyawasisuk[2] , A. Roumwong[1] , V. Chentanez[1]

[1]Department of Anatomy, Faculty of Medicine, Chulalongkorn University, Bangkok, Thailand
[2]Department of Ophthalmology, Faculty of Medicine, Chulalongkorn University, Bangkok, Thailand

Background: The microanatomy of the central myelin portion and transitional zone of several cranial nerves including trigeminal, facial, vestibulocochlear, glossopharyngeal, and vagus nerves have been clearly demonstrated to provide information for neurovascular compression syndrome such as trigeminal neuralgia and hemifacial spasm. However, the study of oculomotor and abducens nerve is limited.

Materials and methods: Oculomotor and abducens nerves were harvested with a portion of brainstem and embedded in paraffin. Longitudinal and serial sections from ten of each cranial nerve were stained and a photomicrograph was taken to make the following observations and measurements: 1) patterns of central myelin portion, 2) length of central myelin portion, and 3) depth of central myelin-peripheral myelin transitional zone.

Results: For oculomotor nerve, the longest central myelin bundle was always seen on the first nerve bundle and that the length of central myelin decreased gradually. For abducens nerve, morphological patterns were classified into four types based on number of nerve rootlets emerging from the brainstem and number of nerve bundles in each rootlet. Length of central myelin portion was between 0.36–6.10 mm (2.75 ± 0.83 mm) and 0.13–5.01 mm (1.66 ± 1.39 mm) for oculomotor and abducens nerves, respectively. The oculomotor nerve transitional zone depth was 0.07–058 mm (0.23 ± 0.07 mm), while for abducens nerve, depth was 0.05–0.40 mm (0.16 ± 0.07 mm). Positive weak correlations between central myelin and depth of TZ were found in oculomotor nerve (r +0.310, p < 0.05) and abducens nerves (r +0.413, p < 0.05).

Conclusions: Detailed microanatomy of the central myelin and transitional zone might be beneficial for locating the site of compression in neurovascular conflicts at oculomotor and abducens nerves. (Folia Morphol 2023; 82, 3: 543–550)

Key words: abducens nerve, central myelin, oculomotor nerve, transitional zone, nerve compression syndrome

Address for correspondence: V. Chentanez, MD, PhD, Department of Anatomy, Faculty of Medicine, Chulalongkorn University, 1873 Rama IV Rd, Khwaeng Pathum Wan, Khet Pathum Wan, Bangkok, Thailand 10330, tel: +66860701084, e-mail: fmedvct@gmail.com

INTRODUCTION

Neurovascular compression syndrome is described as direct contact with mechanical irritation of cranial nerves by blood vessels [11]. Compression at the oculomotor and abducens nerves have been reported as a cause of ocular neuromyotonia (ONM) [10, 26, 28] and abducens nerve palsy (CN VI palsy) [2, 6, 7, 12, 13, 15, 16, 18, 19, 21, 30]. ONM is characterised by intermittent, tonic spasms of one or more extraocular muscles. Clinical presentations are strabismus and transient diplopia [23]. Its mechanism is unknown but it has been proposed to be related to neurovascular compression [10, 26, 28]. CN VI palsy is the most common ocular motor paralysis and presents with diplopia. It usually results from neoplasm, trauma, and microvascular ischaemia. It is very rare if vascular compression is considered as the cause [4]. Site of compression is reported variously for both diseases. A cranial nerve consists of central nervous system (CNS) and peripheral nervous system (PNS) segment connected by transitional zone (TZ) [24]. Glial cells in the CNS project distally making a well-defined dome-shaped TZ [22]. The PNS segment has been demonstrated to be more resistance to compression than CNS segment. The TZ is vulnerable since this junction contains both myelin sheaths in the central part produced by oligodendrocytes, and myelin sheaths in peripheral part which are produced by Schwann cells [3]. The difference in the origin of central and peripheral myelin explains the difference in molecular components which contributes to structural differences [1, 14]. The length of central glial segments vary between nerves and differs between each rootlet of the same nerve [25]. The microanatomy of the central myelin portion and TZ of several cranial nerves including trigeminal, facial, vestibulocochlear, glossopharyngeal, and vagus nerves have been clearly demonstrated [8, 9, 17, 20, 27]. However, there were only two previous studies reporting the central myelin portion of oculomotor and abducens nerves [22, 25]. Thus, more microanatomical knowledge of oculomotor nerve and abducens nerve is needed. This study aimed to determine the pattern of central myelin portion, length of central myelin, depth of TZ, and correlation between depth of TZ and length of central myelin of each nerve bundle.

MATERIALS AND METHODS

Twenty-nine oculomotor nerves and 53 abducens nerves were removed with a portion of brainstem attached from 46 embalmed cadaver brains. The specimens were further fixed in 10% neutral buffered formalin for 24 hours and embedded in paraffin. Each tissue block was longitudinally and serially sectioned into 5 μm thick sections. Only 10 specimens of each cranial nerve were included, the rest were excluded due to poor fixation and detachment of the cranial nerve from the brainstem. First section started where the nerve appeared and last section ended where the whole nerve disappeared. Sections with the nerve still connected to the brainstem were chosen under a light microscope for further staining with luxol fast blue for differentiation of central and peripheral myelin portions. Counterstain with haematoxylin and eosin was performed for better demonstration. Three to six sections with maximum extension of the central myelin from each nerve were chosen under a light microscope for measurement. Axiocam 506 colour microscope camera (Carl Zeiss, Jena, Germany) with a 5× microscope objective lens was used to take a photomicrograph via ZEN 3.3 (blue edition) and IMAGE-PRO plus programme version 6.0 was used for measurement. Patterns of central myelin portion, central myelin length, and depth of TZ were determined. This study was approved by the Faculty of Medicine, Chulalongkorn University IRB committee (IRB no. 712/64).

Determination of the length of central myelin portion (F) and depth of central myelin-peripheral myelin TZ (f) (Fig. 1)

On each photomicrograph (Fig. 1), 1) line A was drawn between the junction where nerve met the brainstem, 2) line F was drawn from the tip of the arch-shaped transitional zone continuing at the middle of the nerve bundles to line A, 3) line B was drawn between the junction where the central myelin met the peripheral myelin, 4) line f was drawn from the middle of line B to the tip of the arch-shaped TZ. In addition, the longest central myelin portion of each nerve was depicted. All measurements were executed 3 times by a single investigator to minimize intra- and inter-observer error.

Statistical analysis

Collected data were analysed with IBM SPSS version 22.0 (IBM Corp., Armonk, NY, USA). All distances were presented in mean and standard deviation. Pearson correlation coefficient, Spearman's rank correlation coefficient and scatter plot were used to de-
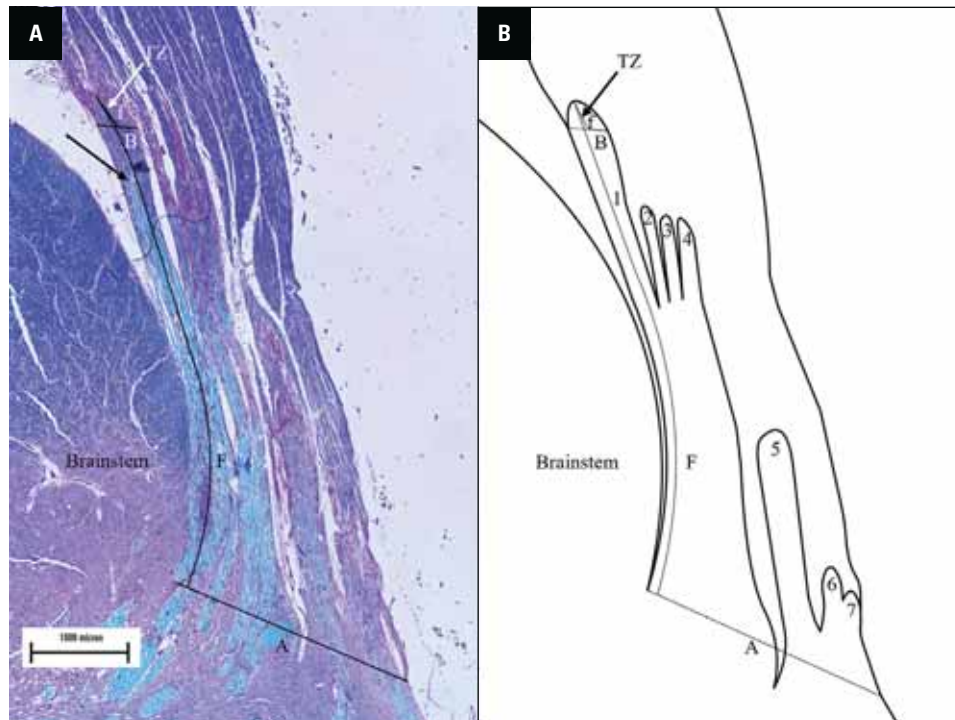
Figure 1. A. Photomicrograph of the oculomotor nerve stained with luxol fast blue demonstrates the longest central myelin seen at the first nerve bundle (black arrow) and then gradually decreased in length; **B.** Drawing demonstrating: A — a line drawn between junction where nerve met the brainstem; B — a line drawn between junction where central myelin met the peripheral myelin; F — length of central myelin of nerve bundle; f — depth of the transitional zone of the nerve bundle; TZ — transitional zone; 1, 2, 3, 4, 5, 6, 7 — order of the nerve bundle counted from the brainstem.

termine a correlation between depth of TZ and length of central myelin of each bundle. The significance level was set at a p-value of less than 0.05. Intra-observer reliability of each parameter was calculated.

RESULTS

Patterns of central myelin portion

Oculomotor nerve. The intramedullary rootlets of the oculomotor nerve united to form a single nerve trunk that emerged from the ventral surface of midbrain. The extension of central myelin length differs between nerve bundles. We observed that the longest central myelin bundle was always seen on the first nerve bundle and that the length of central myelin decreased gradually (Fig. 1). Number of nerve bundles in each observed section was between 5 to 7 (Table 1).

Abducens nerve. The intramedullary rootlets of abducens nerve emerged from the ventral surface of the pontomedullary junction separately as one to three nerve rootlets. The one with two or three nerve rootlets united to form a single nerve trunk. The number of nerve bundles in each observed section was 1, 3, 4, and 5 (Table 2). The longest central myelin nerve bundle was found between the first to the third

nerve bundle with a prevalence of 30%, 30%, and 40%, respectively. Based on number of nerve rootlets emerging from the brainstem and number of nerve bundles in each rootlet, we classified morphologies of abducens nerve into four types (Fig. 2) — type A: single nerve rootlet with one nerve bundle, type B: single nerve rootlet with more than one nerve bundle, type C: more than one nerve rootlet with one nerve bundle in each nerve rootlet, and type D: more than one nerve rootlet with the most caudal nerve rootlet having more than one nerve bundle.

Lengths of central myelin portion (F) and the longest central myelin portion (F*)

Oculomotor nerve. The mean length of central myelin portion (F) measured from the nerve bundles in each nerve was 2.75 ± 0.83 mm (Table 1). When the whole nerve was considered, 80% of oculomotor nerves had a mean F of more than 2.00 mm for each nerve (Table 1, Fig. 3A). The mean longest central myelin portion (F*) of each nerve was 4.29 ± 1.26 mm (Table 1).

Abducens nerve. The mean F was 1.66 ± 1.39 mm (Table 2). When the whole nerve was considered, types A and B tended to have a longer segment of F

Table 1. All measurements of oculomotor nerves

Oculomotor nerve	No. of nerve bundles	F* [mm]	F [mm]	f [mm]
Nerve 1	5	3.01	2.23 ± 0.75 (1.28–3.01)	0.16 ± 0.03 (0.13–0.20)
Nerve 2	6	3.22	2.24 ± 1.06 (0.64–3.22)	0.14 ± 0.04 (0.11–0.21)
Nerve 3	7	2.76	1.57 ± 0.97 (0.51–2.76)	0.19 ± 0.04 (0.13–0.23)
Nerve 4	7	5.11	3.33 ± 1.05 (2.14–5.11)	0.18 ± 0.06 (0.09–0.26)
Nerve 5	5	3.37	1.95 ± 0.96 (1.18–3.37)	0.34 ± 0.17 (0.19–0.58)
Nerve 6	6	6.10	3.99 ± 1.59 (2.12–6.10)	0.33 ± 0.11 (0.24–0.53)
Nerve 7	7	3.76	2.67 ± 0.91 (1.54–3.76)	0.27 ± 0.05 (0.20–0.32)
Nerve 8	6	5.21	3.78 ± 1.07 (2.33–5.21)	0.24 ± 0.13 (0.11–0.43)
Nerve 9	7	4.28	2.34 ± 1.57 (0.36–4.28)	0.20 ± 0.07 (0.09–0.28)
Nerve 10	7	6.10	3.44 ± 1.60 (1.92–6.10)	0.25 ± 0.14 (0.07–0.50)
Mean ± SD (range)		4.29 ± 1.26 (2.76–6.10)	2.75 ± 0.83 (0.36–6.10)	0.23 ± 0.07 (0.07–0.58)
Shrinkage correction (range)		3.31–7.32		0.08–0.70

F — length of central myelin; F* — longest central myelin; f — depth of transitional zone; SD — standard deviation

Table 2. All measurements of abducens nerves

Abducens nerve	No. of nerve bundles	Morphological pattern	F* [mm]	F [mm]	f [mm]
Nerve 1	1	A	2.00	2.00	0.14
Nerve 2	3	B	2.29	2.26 ± 0.03 (2.23–2.29)	0.21 ± 0.02 (0.20–0.24)
Nerve 3	3	B	5.01	4.76 ± 0.28 (4.46–5.01)	0.23 ± 0.02 (0.22–0.24)
Nerve 4	3	C	0.53	0.36 ± 0.21 (0.13–0.53)	0.13 ± 0.13 (0.05–0.27)
Nerve 5	5	B	3.01	2.80 ± 0.28 (2.31–3.01)	0.10 ± 0.05 (0.06–0.17)
Nerve 6	3	C	1.00	0.63 ± 0.33 (0.37–1.00)	0.17 ± 0.03 (0.15–0.20)
Nerve 7	4	D	1.73	0.35 ± 0.32 (1.03–1.73)	0.15 ± 0.06 (0.08–0.22)
Nerve 8	4	D	0.86	0.62 ± 0.23 (0.37–0.86)	0.10 ± 0.02 (0.08–0.13)
Nerve 9	3	B	2.03	1.56 ± 0.68 (0.79–2.03)	0.30 ± 0.10 (0.23–0.41)
Nerve 10	3	C	0.28	0.21 ± 0.06 (0.16–0.28)	0.07 ± 0.01 (0.06–0.07)
Mean ± SD (range)			1.88 ± 1.40 (0.28–5.01)	1.66 ± 1.39 (0.13–5.01)	0.16 ± 0.07 (0.05–0.40)
Shrinkage correction (range)			0.34–6.01		0.06–0.48

F — length of central myelin; F* — longest central myelin; f — depth of transitional zone; SD — standard deviation

than type C and D (Table 2, Fig. 3B). The mean longest central myelin portion (F*) of each nerve was 1.88 ± ± 1.40 mm (Table 2).

Depths of central myelin-peripheral myelin TZ (f)

The mean depth of TZ (f) of oculomotor nerve was 0.23 ± 0.07 mm (Table 1). For abducens nerve, mean f was 0.16 ± 0.07 mm (Table 2).

Correlation between depth of TZ and length of central myelin

We found a positive weak correlation between f and F in oculomotor nerve by Pearson's correlation coefficient (r +0.310, p < 0.05). While using Spearman's rank correlation coefficient, we found a positive weak correlation between f and F of each nerve bundle in abducens nerves (r +0.413, p < 0.05; Fig. 4).

Intra-observer intraclass correlation coefficient was 0.996 (0.992–1.000) for oculomotor nerve measurement and 0.998 (0.995–1.000) for abducens nerve measurement. The least intra-observer intraclass correlation coefficient among all parameters was 0.992.

DISCUSSION

The morphological pattern and number of nerve bundles of oculomotor and abducens nerves has never been described before. For oculomotor nerve,
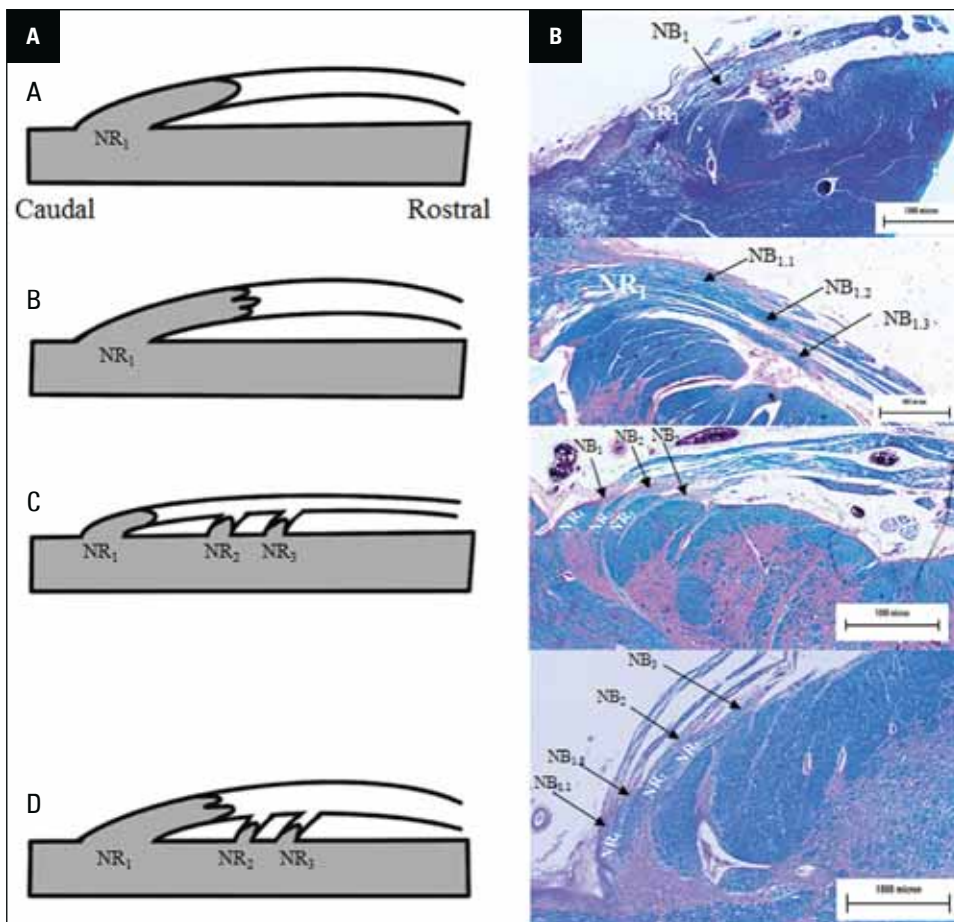
Figure 2. A. Schematic diagram demonstrates types of abducens nerve; **B.** Photomicrographs of abducens nerves stained with luxol fast blue demonstrate types of abducens nerve corresponding to the schematic diagram; A, B, C and D are types of abducens nerve; NR_1, NR_2, NR_3 — the first, second, and third nerve rootlet emerging from the ventral surface of brainstem; NB_1, NB_2, NB_3 — nerve bundle in the first, second and third nerve rootlets; $NB_{1.1}$, $NB_{1.2}$, $NB_{1.3}$ — number of nerve bundle in the first nerve rootlet.
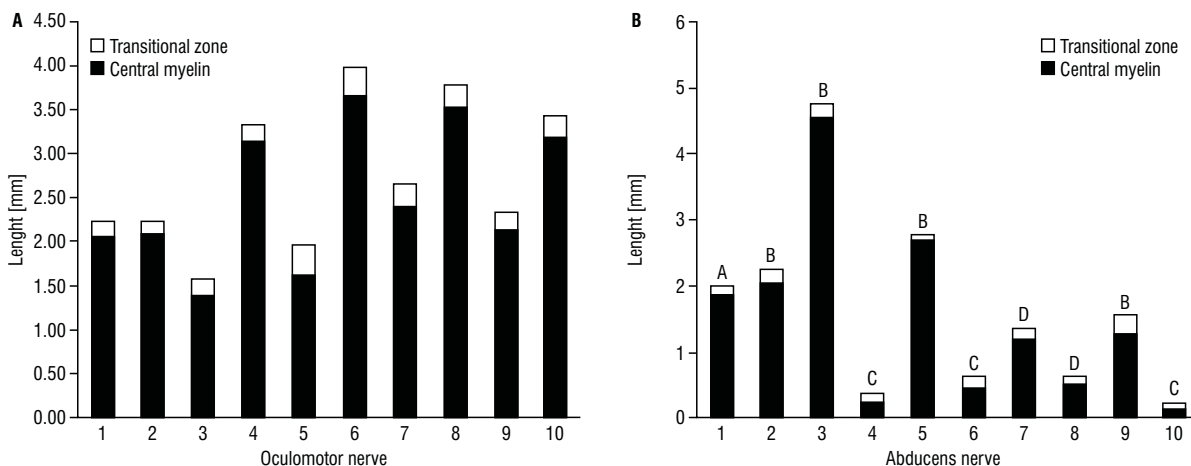

Figure 3. Bar graph showing mean value of central myelin portion (black) and depth of transitional zone (white) of 10 oculomotor (**A**) and 10 abducens nerves (**B**). Each bar represents each nerve. The letters A, B, C and D at the end of the graph of abducens nerves represent the morphology type of abducens nerves.

the longest central myelin was always seen on the first nerve bundle and the length of glial segment

decreased gradually. However, Fraher (1992) [5] who studied type of TZ in rats showed a similar central
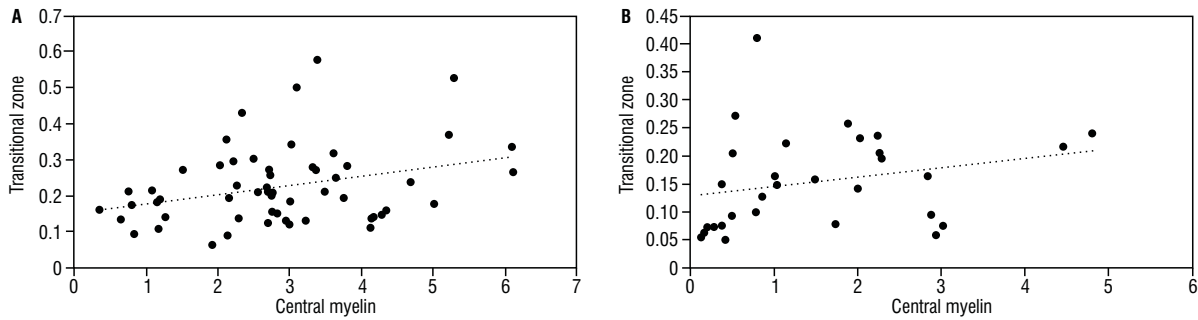
Figure 4. Scatter plot showing a correlation between central myelin portion and depth of transitional zone of each nerve bundle of oculomotor nerves (**A**) and abducens nerves (**B**).

myelin pattern and multiple nerve bundles in the schematic diagram of oculomotor nerves. For abducens nerve, the morphologies of the nerve bundle are classified into four types (A–D) based on the number of nerve rootlets and the number of nerve bundles. Fraher (1992) [5] also showed the same schematic diagram of abducens nerves having more nerve rootlets and one nerve bundle in each rootlet, similar to that found in the type C pattern in our study. Different positions of TZ could be explained by CNS and PNS tissue migration during development [5]. The morphological pattern of central myelin and appearance of TZ observed in this study were different from previous studies in other cranial nerves which always shows only one arch-shaped TZ [8, 9, 17, 20, 22, 25, 27]. Consequently, the measuring method in this study were designed to suit the pattern.

Skinner (1931) [22] is the first to demonstrate that length of glial part of oculomotor and abducens nerve from humans, dogs, cats, and rabbits were 1.2 and 0.5 mm, respectively. Tarlov (1937) [25] reported length of glial part of oculomotor and abducens nerve from humans were 0.6 and 0.5 mm, respectively. While our study found that lengths of central myelin are longer than previously reported for both cranial nerves. The oculomotor nerve had a greater length of central myelin when compared to abducens nerve in our study. This finding is consistent with Skinner [22] and Tarlov [25]. However, exact lengths cannot be compared because the definition of glial part was not mentioned and some nerve specimens were from animals. When the entire nerve was considered, most central myelin length of oculomotor nerves was between 2.00 and 4.00 mm (Fig. 3A). Furthermore, abducens nerve types A and B tend to have a longer segment of mean central myelin than types C and D (Fig. 3B). These findings could be

a benefit in neuroimaging interpretation. In cadaveric study, after specimens had been fixed, there were some shrinkages. Before applying in the clinical setting, this shrinkage must be taken into consideration. Estimated post fixation shrinkage has been reported up to 20% [29], therefore the corrected longest length of central myelin (F*) would be 3.31–7.32 mm for oculomotor nerve and 0.34–6.02 mm for abducens nerve (Tables 1, 2).

The depth of TZ would be 0.08–0.70 mm for oculomotor nerve and 0.06–0.48 mm for abducens nerve (Tables 1, 2) if considering post fixation shrinkage [29]. TZ started from 3.03 (1.65–4.39) and 1.79 (0.17–5.44) mm distal to where the cranial nerve exits the brainstem for oculomotor and abducens nerves, respectively. Knowing the starting point of TZ could be useful in the localisation of compressed sites in neuroimaging. Moreover, we found a positive weak correlation between the depth of transitional zone and length of central myelin of each nerve bundle in the oculomotor and abducens nerves which could imply that the greater the central myelin, the greater the transitional zone depth.

Limitations of the study

Our study had a few limitations. First, cranial nerves in this study were harvested from brain collection, so age, sex, underlying disease, and cause of death of the cadavers are unknown. Second, we could not analyse the difference between sides due to the small number of specimens. Third, our results cannot be compared to other studies because of different measurement method.

CONCLUSIONS

In conclusion, this study provides details of microanatomical knowledge of oculomotor and abducens

nerves. Knowing the length of the central myelin and depth of TZ would be helpful in the localisation of compressed sites in neuroimaging. Moreover, this might help to understand the aetiology of ONM and CN VI palsy from neurovascular compression.

Acknowledgements

Conflict of interest: None declared

REFERENCES

1. Bojrab D, Zhang B, Jiang H, et al. Expression of oligo-dendrocyte marker during peripheral-central transitional zone formation of the postnatal mouse cochlear nerve. Otolaryngol Head Neck Surg. 2017; 157(3): 488–492, doi: 10.1177/0194599817718806, indexed in Pubmed: 28695768.

2. De Ridder D, Menovsky T. Neurovascular compression of the abducent nerve causing abducent palsy treated by microvascular decompression. Case report. J Neurosurg. 2007; 107(6): 1231–1234, doi: 10.3171/JNS-07/12/1231, indexed in Pubmed: 18077964.

3. De Ridder D, Møller A, Verlooy J, et al. Is the root entry/exit zone important in microvascular compression syndromes? Neurosurgery. 2002; 51(2): 427–433, doi: 10.1097/00006123-200208000-00023, indexed in Pubmed: 12182781.

4. Elder C, Hainline C, Galetta SL, et al. Isolated abducens nerve palsy: update on evaluation and diagnosis. Curr Neurol Neurosci Rep. 2016; 16(8): 69, doi: 10.1007/s11910-016-0671-4, indexed in Pubmed: 27306521.

5. Fraher JP. The CNS-PNS transitional zone of the rat. Morphometric studies at cranial and spinal levels. Prog Neurobiol. 1992; 38(3): 261–316, doi: 10.1016/0301-0082(92)90022-7, indexed in Pubmed: 1546164.

6. Giray S, Pelit A, Kizilkilic O, et al. Isolated abducens nerve palsy caused by contralateral vertebral artery dolichoectasia. Neurol India. 2005; 53(2): 246–247, doi: 10.4103/0028-3886.16433, indexed in Pubmed: 16010080.

7. Goldenberg-Cohen N, Miller NR. Noninvasive neuroimaging of basilar artery dolichoectasia in a patient with an isolated abducens nerve paresis. Am J Ophthalmol. 2004; 137(2): 365–367, doi: 10.1016/S0002-9394(03)00898-5, indexed in Pubmed: 14962438.

8. Guclu B, Sindou M, Meyronet D, et al. Anatomical study of the central myelin portion and transitional zone of the vestibulocochlear nerve. Acta Neurochir (Wien). 2012; 154(12): 2277–2283, doi: 10.1007/s00701-012-1479-x, indexed in Pubmed: 22914910.

9. Guclu B, Sindou M, Meyronet D, et al. Cranial nerve vascular compression syndromes of the trigeminal, facial and vago-glossopharyngeal nerves: comparative anatomical study of the central myelin portion and transitional zone; correlations with incidences of corresponding hyperactive dysfunctional syndromes. Acta Neurochir (Wien). 2011; 153(12): 2365–2375, doi: 10.1007/s00701-011-1168-1, indexed in Pubmed: 21947457.

10. Inoue T, Hirai H, Shimizu T, et al. Ocular neuromyotonia treated by microvascular decompression: usefulness of preoperative 3D imaging: case report. J Neurosurg. 2012; 117(6): 1166–1169, doi: 10.3171/2012.9.JNS112361, indexed in Pubmed: 23020768.

11. Jannetta PJ. Neurovascular compression in cranial nerve and systemic disease. Ann Surg. 1980; 192(4): 518–525, doi: 10.1097/00000658-198010000-00010, indexed in Pubmed: 6968543.

12. Jeeva-Patel T, Margolin EA, Mandell D. Sixth cranial nerve palsy secondary to compression by dolichoectatic verte-brobasilar artery. BMJ Case Rep. 2020; 13(7), doi: 10.1136/bcr-2020-234949, indexed in Pubmed: 32636226.

13. Kato H, Nakajima M, Ohnaka Y, et al. Recurrent abducens nerve palsy associated with neurovascular compression. J Neurol Sci. 2010; 295(1-2): 135–136, doi: 10.1016/j.jns.2010.05.001, indexed in Pubmed: 20621803.

14. Kiernan J. Histochemistry of staining methods for normal and degenerating myelin in the central and peripheral nervous systems. J Histotechnol. 2013; 30(2): 87–106, doi: 10.1179/his.2007.30.2.87.

15. Madhugiri VS, Roopesh Kumar VR, Gopalakrishnan MS, et al. Cranial polyneuropathy associated with vertebrobasi-lar dolichoectasia. Clin Neurol Neurosurg. 2012; 114(7): 1059–1061, doi: 10.1016/j.clineuro.2012.02.002, indexed in Pubmed: 22386900.

16. Narai H, Manabe Y, Deguchi K, et al. Isolated abducens nerve palsy caused by vascular compression. Neurology. 2000; 55(3): 453–454, doi: 10.1212/wnl.55.3.453, indexed in Pubmed: 10932293.

17. Nomura K, Ryu H, Ohno K, et al. Wide distribution of central myelin segment along the facial nerve might explain hemifacial spasm with distal nerve compression. Clin Anat. 2021; 34(3): 405–410, doi: 10.1002/ca.23664, indexed in Pubmed: 32713009.

18. Ohhashi G, Irie K, Tani S, et al. [Isolated abducens nerve palsy caused by the compression of the basilar artery: a case report]. No To Shinkei. 2001; 53(1): 69–72, indexed in Pubmed: 11211735.

19. Ohtsuka K, Sone A, Igarashi Y, et al. Vascular compressive abducens nerve palsy disclosed by magnetic resonance imaging. Am J Ophthalmol. 1996; 122(3): 416–419, doi: 10.1016/s0002-9394(14)72068-9, indexed in Pubmed: 8794714.

20. Peker S, Kurtkaya O, Uzün I, et al. Microanatomy of the central myelin-peripheral myelin transition zone of the trigeminal nerve. Neurosurgery. 2006; 59(2): 354–359, doi: 10.1227/01.NEU.0000223501.27220.69, indexed in Pubmed: 16883175.

21. Pham T, Wesolowski J, Trobe JD. Sixth cranial nerve palsy and ipsilateral trigeminal neuralgia caused by verte-brobasilar dolichoectasia. Am J Ophthalmol Case Rep. 2018; 10: 229–232, doi: 10.1016/j.ajoc.2018.02.029, indexed in Pubmed: 29780939.

22. Skinner HA. Some histologic features of the cranial nerves. Arch Neurol Psychiatry. 1931; 25(2): 356, doi: 10.1001/archneurpsyc.1931.02230020144008.

23. Stockman AC, Dieltiëns M, Janssens H, et al. Ocular neuromyotonia: case reports and literature review. Strabismus. 2018; 26(3): 133–141, doi: 10.1080/09273972.2018.1467469, indexed in Pubmed: 29693497.

24. Tarlov IM. Structure of the nerve root.I. Nature of the junction between the central and the peripheral nervous system. Arch Neurol Psychiatry. 1937; 37(3): 555–583, doi: 10.1001/archneurpsyc.1937.02260150085005.

25. Tarlov IM. Structure of the nerve root. II. Differentiation of sensory from motor roots; observations on identification of function in roots of mixed cranial nerves. Arch Neurol Psychiatry. 1937; 37(6): 1338–1355, doi: 10.1001/archneurpsyc.1937.02260180118008.

26. Tilikete C, Vial C, Niederlaender M, et al. Idiopathic ocular neuromyotonia: a neurovascular compression syndrome? J Neurol Neurosurg Psychiatry. 2000; 69(5): 642–644, doi: 10.1136/jnnp.69.5.642, indexed in Pubmed: 11032618.

27. Tomii M, Onoue H, Yasue M, et al. Microscopic measurement of the facial nerve root exit zone from central glial myelin to peripheral Schwann cell myelin. J Neurosurg. 2003; 99(1): 121–124, doi: 10.3171/jns.2003.99.1.0121, indexed in Pubmed: 12854753.

28. Versino M, Colnaghi S, Todeschini A, et al. Ocular neuromyotonia with both tonic and paroxysmal components due to vascular compression. J Neurol. 2005; 252(2): 227–229, doi: 10.1007/s00415-005-0612-7, indexed in Pubmed: 15729532.

29. Yousry I, Moriggl B, Dieterich M, et al. MR anatomy of the proximal cisternal segment of the trochlear nerve: neurovascular relationships and landmarks. Radiology. 2002; 223(1): 31–38, doi: 10.1148/radiol.2231010612, indexed in Pubmed: 11930045.

30. Zhu Y, Thulborn K, Curnyn K, et al. Sixth cranial nerve palsy caused by compression from a dolichoectatic vertebral artery. J Neuroophthalmol. 2005; 25(2): 134–135, doi: 10.1097/01.wno.0000165319.75310.5a, indexed in Pubmed: 15937439.

ORIGINAL ARTICLE

Effects of liquid diet intake on nerve growth in salivary glands of growing rats

S. Takahashi, Y. Nakamichi, T. Yamamoto

Department of Oral Functional Anatomy, Hokkaido University Faculty of Dental Medicine, Sapporo, Japan

Background: The growth of parotid glands is inhibited by liquid diet intake during growing period, while that of submandibular glands is not affected. This study examined how liquid diet intake affects nerve growth in the parotid and submandibular glands of growing rats, because nerves are closely involved in the maintenance of salivary gland structure.

Materials and methods: Male Wistar rats were weaned at 21 days of age. Then, rats were fed a pellet diet and a liquid diet in the control group and experimental group, respectively. At 0, 2, 4, or 8 weeks, they were euthanised by isoflurane overdose, and parotid and submandibular glands were removed. The frozen sections were made and immuno-stained with anti-protein gene product 9.5 (PGP 9.5) antibody (general nerve marker), anti-tyrosine hydroxylase (TH) antibody (sympathetic nerve marker), or anti-neuronal nitric oxide synthase (nNOS) antibody (parasympathetic nerve marker).

Results: In control parotid glands, scattered punctate or short linear patterns of PGP 9.5-positive sites were observed at week 0. After 2 weeks, PGP 9.5-positive sites, some of which were arranged in long linear patterns, increased in number. There were some TH-positive sites at week 0. After 2 weeks, there were increasing numbers of TH-positive sites, often in long linear patterns. At week 0, there were very few nNOS-positive sites, and nNOS immunoreactivity increased over time. After week 4, they demonstrated linear patterns. In the experimental parotid glands, there were fewer PGP 9.5- and nNOS-positive sites than in control parotid glands at each time point, although TH immunoreactivity was similar between two groups at each time point. In control submandibular glands, few punctate exhibited PGP 9.5-positive site were observed at week 0. At week 4, PGP 9.5 immunoreaction increased and showed linear patterns. TH-positive sites demonstrated punctate or short linear patterns at week 0, and thereafter TH immunoreactivity increased and were arranged in long linear patterns. There were few nNOS-positive sites at week 0, and they gradually increased after week 4. The immunoreactivities of all antibodies in the experimental submandibular glands were similar to those in the control at each time point.

Conclusions: Parasympathetic nerve growth in rat parotid glands was inhibited by liquid diet intake during the growth period, while liquid diet intake did not affect parasympathetic nerve growth nor sympathetic nerve growth in rat submandibular glands. (Folia Morphol 2023; 82, 3: 551–557)

Key words: growth, liquid diet, nerve, salivary gland

Address for correspondence: Dr. S. Takahashi, Department of Oral Functional Anatomy, Hokkaido University Faculty of Dental Medicine, Kita 13, Nishi 7, Kita-ku, Sapporo, 060-8586, Japan, tel: +81 11 706 4218, fax: +81 11 706 4928, e-mail: tshigeru@den.hokudai.ac.jp

INTRODUCTION

Salivary glands are exocrine glands that secrete saliva, which helps to maintain the oral environment. Salivary gland function is controlled through innervation by autonomic, sympathetic, and parasympathetic nerves [19]. Generally, sympathetic nerve stimulation evokes protein-rich secretion, while parasympathetic nerve stimulation evokes large volumes of saliva [20]; however, there are some variations in these effects among salivary glands and species [21]. Because innervation is important for salivary gland function, the effects of nerve damage on salivary glands have been experimentally investigated. Salivary glands with excretory duct ligation including parasympathetic nerves weighed less and exhibited more parenchymal atrophy, compared with salivary glands that were subjected to excretory duct ligation excluding parasympathetic nerves [8, 9]. Furthermore, the weight of parasympathectomised salivary glands decreased [1, 2, 12, 22], and acinar cells became atrophic in parasympathectomised salivary glands [1, 22]. Although sympathectomy had an atrophic effect on salivary glands, it was much weaker than the atrophic effect of parasympathectomy [23, 24, 35]. Thus, autonomic nerves presumably play important roles in maintaining normal salivary gland structure; parasympathetic nerves may have a greater effect, compared with sympathetic nerves [6].

There is clinical interest in how the daily intake of soft foods, which is a characteristic of modern eating habits, affects the oral maxillofacial region. Therefore, many experimental studies have been conducted in which experimental animals were fed a liquid diet; the salivary glands of liquid diet-fed animals have also been examined. In these studies, biochemical analysis showed decreases in salivary amylase [7, 11, 14, 15, 27] and salivary protein [11] levels, as well as a decreased salivary flow rate [4, 10, 25]; these findings indicated reduced parotid gland function. Histological examinations revealed atrophic changes in parotid glands, such as reduction of gland weight [3, 4, 7, 11, 14–17, 25–27, 29], shrinkage of acinar cells [23, 25–27, 29], reduction of proliferative activity [29], and apoptotic death of acinar cells [5, 29]. However, many studies demonstrated that atrophic changes were minimal or absent in the submandibular glands of liquid diet-fed animals [3, 14, 16, 17, 26, 30].

There is a need to clarify the effects of successive intake of soft food during growth periods on salivary gland growth because children tend to prefer soft food, rather than hard food [37]. In a previous study, increases in parotid gland weight were smaller in rats that were continuously fed a liquid diet immediately after weaning, compared with rats that were fed a pellet diet [28]. In the parotid glands of rats that were continuously fed a liquid diet, acinar cells did not grow larger and proliferative activity was reduced during the growth period, demonstrating that parotid gland growth was strongly inhibited by liquid diet intake during the growth period [28]. In contrast, submandibular gland growth was not inhibited by liquid diet intake during the growth period [31]. These results indicated that the parotid and submandibular glands differed in their response to continuous intake of a liquid diet during the growth period. Because autonomic nerves are closely involved in the maintenance of salivary gland structure, as described above, it was speculated that salivary glands, particularly parotid glands, would be negatively affected in animals that were fed a liquid diet during the growth period.

The purpose of this study was to determine how liquid diet intake influenced nerve growth in salivary glands during the growth period. For this purpose, rats were fed a liquid diet beginning immediately after weaning; their parotid and submandibular glands were examined by immunohistochemical analysis with anti-protein gene product 9.5 (PGP 9.5) antibody (a marker of all nerves), anti-tyrosine hydroxylase (TH) antibody (a sympathetic nerve marker), and anti-neuronal nitric oxide synthase (nNOS) antibody (a parasympathetic nerve marker).

MATERIALS AND METHODS

Ethics and animal welfare

Animal experiments in this study were carried out in accordance with the Hokkaido University Guide for the Care and Use of Laboratory Animals; the experimental protocol was approved by the Hokkaido University Laboratory Animal Committee (approval no. 14-0108). During the experiment, animals were housed in a temperature-controlled room (approximately 22°C) with a 12-h light/dark cycle and free access to drinking water; they were weighed and visually observed to confirm health status. Statistical comparisons in body weight between the control and experimental groups at each time point were made using Mann-Whitney U test (Ystat2008, Igakutosho, Tokyo, Japan). $P < 0.05$ was considered significant.

Experimental procedures

Twenty-eight 12-day-old male Wistar rats and their mothers were obtained from CLEA Japan Inc. (Tokyo, Japan); the male rats were weaned at 21 days of age and divided into two groups. Each control rat was fed a pellet diet (25 g/day; Labo MR Standard, Nosan Corp., Yokohama, Japan) for 0, 2, 4, or 8 weeks (n = 4 at each time point); each experimental rat was fed a liquid diet (prepared daily by mixing 25 g of the pellet diet in powder form with 50 mL of water) for 2, 4, or 8 weeks (n = 4 at each time point). At the end of the experimental period, all animals were subjected to food deprivation for 12 h at night to synchronise the salivary gland status. They were then euthanised by isoflurane overdose; the parotid and submandibular glands were immediately removed. Extracted glands were embedded in Tissue Tek OCT compound (Miles Scientific, Naperville, IL, USA), frozen in liquid nitrogen, and stored at −80°C until preparation.

Immunohistochemical analysis

Fresh frozen sections were prepared using a cryostat and fixed with 4% paraformaldehyde in 0.1 M phosphate buffer (pH 7.4) for 5 min. After the sections had been washed with phosphate-buffered saline (PBS), they were incubated with the following primary antibodies overnight at 4°C: anti-PGP 9.5 rabbit monoclonal antibody (1:200; EPR4118, Abcam, Cambridge, UK) to detect all nerves, anti-TH rabbit polyclonal antibody (1:1000; AB152, Merck Millipore, Darmstadt, Germany) to detect sympathetic nerves, and anti-nNOS rabbit polyclonal antibody (1:100; Af480, Frontier Institute, Ishikari, Japan) to detect parasympathetic nerves. The sections were then incubated with biotinylated anti-rabbit goat polyclonal antibody (Histofine, Nichirei Bioscience, Tokyo, Japan) for 60 min at room temperature; subsequently, they were incubated with peroxidase-conjugated streptavidin (Histofine, Nichirei Bioscience) for 30 min at room temperature. Peroxidase activity was visualised using 3, 3'-diaminobenzidine; sections were lightly counterstained with Mayer's haematoxylin. After each incubation step above, sections were thoroughly washed with PBS.

Negative control sections were incubated in PBS without primary antibodies, then subjected to all other treatments as above.

RESULTS

Body weights of animals

Animals in both groups appeared healthy during the experimental period, and their body weights in-
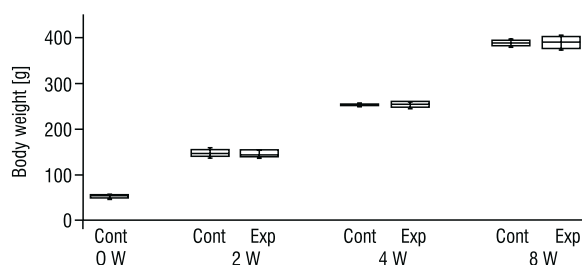

Figure 1. Box plot of body weights of the control (Cont) and experimental rats (Exp). There was no significant difference between two groups at each time point. Explanation of box plot: top of box, 75th percentile; bottom of box, 25th percentile; horizontal bar within box, median; upper whisker, maximum value; lower whisker, minimum value; W — week.

creased as normal. There was no significant difference in body weights between the control and experimental groups at every time point (Fig. 1).

Parotid glands

At week 0, thick nerve bundles in interlobular connective tissue exhibited PGP 9.5-positive sites. In glandular lobules, scattered punctate or short linear patterns of PGP 9.5-positive sites were observed (Fig. 2A). After 2 weeks of pellet diet intake, there were increasing numbers of PGP 9.5-positive sites around acini and ducts; some of these sites were arranged in long linear patterns (Fig. 2B). However, in the parotid glands of liquid diet-fed rats, there remained few PGP 9.5-positive sites at week 8 (Fig. 2C).

Furthermore, there were some TH-positive sites around acini in glandular lobules, as well as in thick nerve bundles in interlobular connective tissue, at week 0 (Fig. 2D). After 2 weeks of pellet diet intake, there were increasing numbers of TH-positive sites at the peripheries of acini and ducts, often in long linear patterns (Fig. 2E). TH immunoreactivity was similar between experimental and control groups at each time point (Fig. 2F).

At week 0, there were very few nNOS-positive sites in glandular lobules, most of which were punctate, although thick nerve bundles in interlobular connective tissues demonstrated extensive nNOS immunoreactivity (Fig. 2G). In control glands, nNOS immunoreactivity gradually increased. nNOS-positive sites were generally punctate at week 2, while they demonstrated linear patterns after week 4 (Fig. 2H). In experimental glands, nNOS immunoreactivity gradually increased. However, there were fewer nNOS-positive sites in experimental glands than in control glands at each time point; these sites mainly exhibited a punctate appearance (Fig. 2I).
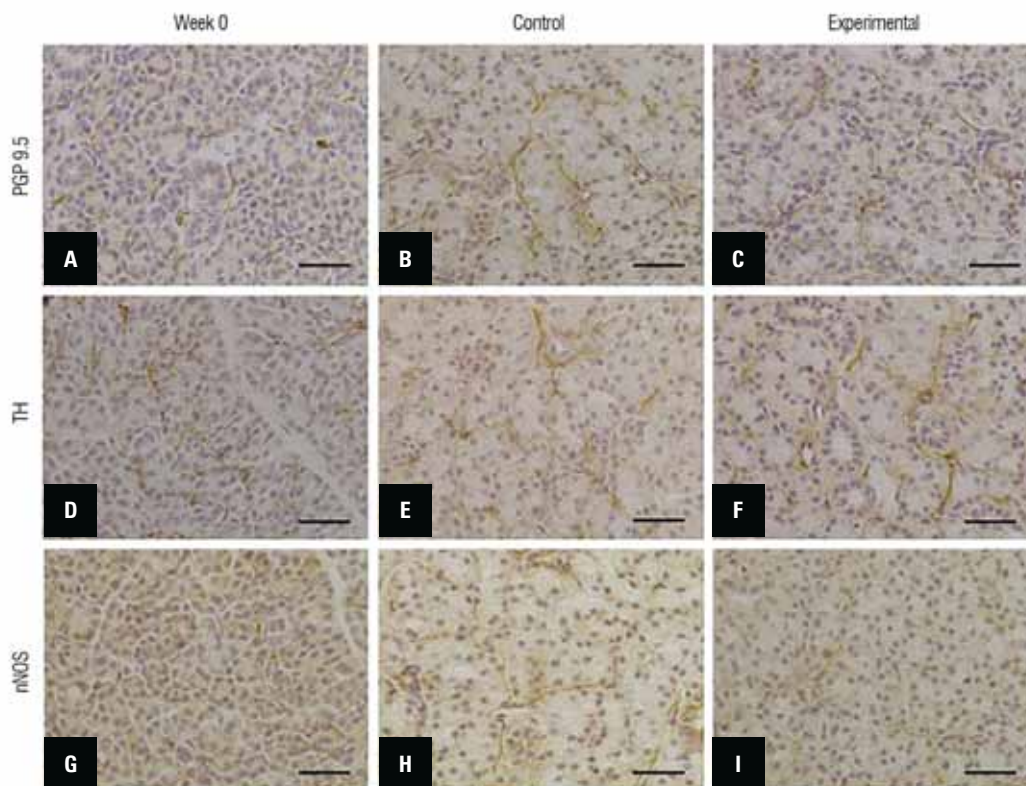
Figure 2. Immunohistochemical analyses of parotid glands to determine distributions of protein gene product 9.5 (PGP 9.5; **A–C**), tyrosine hydroxylase (TH; **D–F**), and neuronal nitric oxide synthase (nNOS; **G–I**). Normal parotid glands at week 0 (**A**, **D**, **G**); control parotid glands at week 8 (**B**, **H**) and week 4 (**E**); experimental parotid glands at week 8 (**C**, **I**) and week 4 (**F**). Scale bars = 30 μm. PGP 9.5 (**A**) and nNOS (**G**) immunoreactivities are minimal at week 0. Although PGP 9.5 and nNOS immunoreactivities both gradually increased in control glands (**B**, **H**), they remained minimal in experimental glands (**C**, **I**). TH immunoreactivity gradually increased in both control (**E**) and experimental glands (**F**), compared with parotid glands at week 0 (**D**).

Submandibular glands

At week 0, thick bundles of nerve fibres in interlobular connective tissue exhibited PGP 9.5-positive sites; few punctate exhibited PGP 9.5-positive sites were distributed around acini and ducts in glandular lobules (Fig. 3A). In control submandibular glands, PGP 9.5 immunoreactivity gradually increased around parenchymal tissue beginning at week 4; some PGP 9.5-positive sites demonstrated linear patterns (Fig. 3B). Immunoreactivity was similar between experimental and control groups at each time point (Fig. 3C).

Also at week 0, TH-positive sites were observed at the peripheries of acini and ducts, with a punctate or short linear appearance; they were also observed in thick nerve bundles in interlobular connective tissue (Fig. 3D). Thereafter, TH immunoreactivity gradually increased and TH-positive sites were present in long linear patterns (Fig. 3E). TH immunoreactivity was similar between experimental and control groups at each time point (Fig. 3F).

Finally, some thick nerve bundles in interlobular connective tissue exhibited nNOS immunoreactivity at week 0, while few nNOS-positive sites were present in glandular lobules (Fig. 3G). At week 2, nNOS immunoreactivity remained limited overall, although scattered punctate nNOS-positive sites were observed around acini and ducts in control glands. After week 4, nNOS immunoreactivity in glandular lobules gradually increased; some nNOS-positive sites demonstrated linear patterns (Fig. 3H). nNOS immunoreactivity was similar between experimental and control groups at each time point (Fig. 3I).

Analysis of negative control sections for all primary antibodies revealed no reactions.

DISCUSSION

Protein gene product 9.5 is a ubiquitin carboxyl--terminal hydrolase [36]. It was originally identified as a new brain-specific protein; it has since been used as a marker of all nerves [32]. TH is an enzyme involved in amino acid and neurotransmitter metabolism;
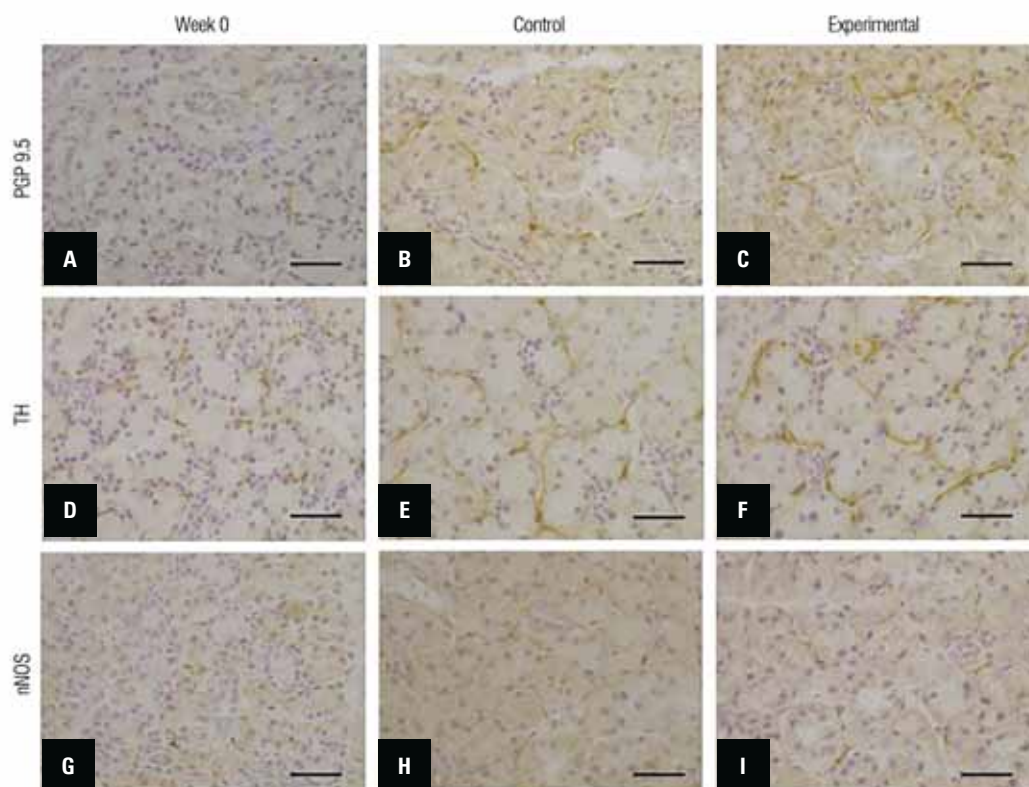
Figure 3. Immunohistochemical analyses of submandibular glands to determine distributions of protein gene product 9.5 (PGP 9.5; **A–C**), tyrosine hydroxylase (TH; **D–F**), and neuronal nitric oxide synthase (nNOS; **G–I**). Normal submandibular glands at week 0 (**A**, **D**, **G**); control submandibular glands at week 4 (**B**, **H**) and week 2 (**E**); experimental submandibular glands at week 4 (**C**, **I**) and week 2 (**F**). Scale bars = 30 μm. At week 0, all immunoreactivities were minimal (**A**, **D**, **G**). Immunoreactivities were similar between experimental glands (**B**, **E**, **H**) and control glands (**C**, **F**, **I**).

it is the rate-limiting enzyme in the synthesis of cate-cholamines (e.g. dopamine and noradrenaline) from tyrosine [18]. Therefore, TH can be used as a marker of sympathetic nerves [34]. Nitric oxide is formed from its precursor, L-arginine, by a family of nitric oxide synthases. nNOS is one of three nitric oxide synthase isoforms [33] and has been used as a para-sympathetic nerve marker in various tissues [13]. For these reasons, PGP 9.5, TH, and nNOS for immunohis-tochemical analyses of nerve distribution were used in this study. While comparisons can be performed between control and experimental glands that have been stained with the same antibody, it is difficult to compare glands that have been stained with different antibodies because the degree of immunoreactivity depends on each antibody's sensitivity.

In this study, PGP 9.5 and nNOS immunoreactivi-ties were lower in experimental parotid glands than in control parotid glands, suggesting that liquid diet intake during the growth period inhibits parasym-pathetic nerve growth in parotid glands. A previ-ous study [28] showed that liquid diet intake in the

growth period suppressed the proliferative activity of the parotid gland; it also suppressed increases in parotid gland weight and acinar cell size. Therefore, present results are consistent with the previous find-ing that liquid diet intake adversely affects parotid gland growth.

In contrast, nerve growth in submandibular glands was not affected by liquid diet intake during the growth period, as demonstrated by the absence of a difference between control and experimental submandibular glands in all immunohistochemical staining assays in this study. This is consistent with a previous report [31] that investigated gland weight, acinar cell size, and acinar cell proliferation in the submandibular glands of liquid diet-fed growing rats, confirming that submandibular gland growth is not affected by liquid diet intake. Thus, parotid glands are much more sensitive to liquid diet intake, compared with submandibular glands. This discrep-ancy might be related to differences in parasympa-thetic nerve system innervation of the two glands [30, 31]. The parasympathetic fibres of the parotid

glands arise from the inferior salivary nucleus and accompany the glossopharyngeal nerve, while the parasympathetic fibres of the submandibular glands arise from the superior salivary nucleus and accompany the facial nerve [38]. The expression of choline acetyltransferase, which is necessary for acetylcholine synthesis, is downregulated in the parotid glands of liquid diet-fed rats [3], suggesting suppression of the parasympathetic nerve system that is needed to maintain parotid gland structure. Thus, the parotid glands may exhibit degeneration. In contrast, the parasympathetic nerve system of the submandibular glands is unaffected by liquid diet intake. Our finding of a difference in parasympathetic nerve growth between parotid and submandibular glands might support the above theory that the different reactions to liquid diet intake are related to differences in parasympathetic nerve innervation between parotid and submandibular glands.

The previous study showed that liquid diet intake inhibited parotid gland growth by suppressing acinar cell enlargement and impeding acinar cell proliferation [28]; the present study showed that liquid diet intake inhibited parasympathetic nerve growth in parotid glands. The next question to address is whether the inhibition of parotid growth affects parasympathetic nerve growth in parotid glands, or whether the inhibition of parasympathetic nerve growth in parotid glands affects parotid growth. Although the present findings do not enable confirmation of either scenario, the inhibition of parasympathetic nerve growth might have a causative effect because parasympathetic nerves contribute to the maintenance of salivary gland morphology. Further studies are needed to investigate this sequence of events.

CONCLUSIONS

In conclusion, parasympathetic nerve growth in rat parotid glands was inhibited by liquid diet intake during the growth period, while liquid diet intake did not affect parasympathetic nerve growth nor sympathetic nerve growth in rat submandibular glands. Prudence is necessary to apply the conclusions obtained from rats to humans. However, they are considered to be a piece of evidence showing that the dietary habit requiring adequate mastication is important for healthy growth of the oral maxillofacial region. The conclusions of this study are significant in clinical dentistry to encourage patients to have the good dietary habit.

REFERENCES

1. Carpenter GH, Proctor GB, Garrett JR. Preganglionic parasympathectomy decreases salivary SIgA secretion rates from the rat submandibular gland. J Neuroimmunol. 2005; 160(1-2): 4–11, doi: 10.1016/j.jneuroim.2004.10.020, indexed in Pubmed: 15710452.
2. Chaparro O, Yu WH, Shaw PA. Isoproterenol-induced expression of the cystatin S gene in submandibular glands of parasympathectomized rats. Brain Res Mol Brain Res. 1998; 61(1-2): 136–146, doi: 10.1016/s0169-328x(98)00223-x, indexed in Pubmed: 9795188.
3. Eksrom J. Choline acethyltransferase and secretory responses of the rat's salivary glands after liquid diet. Q J Exp Physiol. 1973; 58(2): 171–179, indexed in Pubmed: 448796.
4. Ekström J, Templeton D. Difference in sensitivity of parotid glands brought about by disuse and overuse. Acta Physiol Scand. 1977; 101(3): 329–335, doi: 10.1111/j.1748-1716.1977.tb06014.x, indexed in Pubmed: 596206.
5. ElGhamrawy TA. The effect of liquid diet on the parotid gland and the protective role of L-carnitine: immunohistochemical and ultrastructural study. Folia Morphol. 2015; 74(1): 42–49, doi: 10.5603/FM.2015.0007, indexed in Pubmed: 25792394.
6. Garrett JR. Innervation of salivary glands: Neurohistological and functional aspects. In: Sreebny LM. The salivary system. CRC Press Inc., Boca Raton 1987: 69–93.
7. Hall HD, Schneyer CA. Salivary gland atrophy in rat induced by liquid diet. Proc Soc Exp Biol Med. 1964; 117: 789–793, doi: 10.3181/00379727-117-29699, indexed in Pubmed: 14244956.
8. Harrison JD, Fouad HM, Garrett JR. Variation in the response to ductal obstruction of feline submandibular and sublingual salivary glands and the importance of the innervation. J Oral Pathol Med. 2001; 30(1): 29–34, doi: 10.1034/j.1600-0714.2001.300105.x, indexed in Pubmed: 11140897.
9. Harrison JD, Garrett JR. Histological effects of ductal ligation of salivary glands of the cat. J Pathol. 1976; 118(4): 245–254, doi: 10.1002/path.1711180407, indexed in Pubmed: 1271136.
10. Ito K, Morikawa M, Inenaga K. The effect of food consistency and dehydration on reflex parotid and submandibular salivary secretion in conscious rats. Arch Oral Biol. 2001; 46(4): 353–363, doi: 10.1016/s0003-9969(00)00124-2, indexed in Pubmed: 11269869.
11. Johnson DA. Effect of a liquid diet on the protein composition of rat parotid saliva. J Nutr. 1982; 112(1): 175–181, doi: 10.1093/jn/112.1.175, indexed in Pubmed: 6172574.
12. Katsukawa H, Ninomiya Y, Funakoshi M. Effects of parasympathectomy on androgen responses of the rat submandibular gland. Arch Oral Biol. 1990; 35(4): 273–275,

doi: 10.1016/0003-9969(90)90042-9, indexed in Pubmed: 2198865.

13. Kiyokawa H, Katori Y, Cho KH, et al. Reconsideration of the autonomic cranial ganglia: an immunohistochemical study of mid-term human fetuses. Anat Rec (Hoboken). 2012; 295(1): 141–149, doi: 10.1002/ar.21516, indexed in Pubmed: 22095632.

14. Kurahashi M. The effect of dietary consistency and water content on the parotid glands of submandibular and sublingual duct-ligated rats. Arch Oral Biol. 2002; 47(5): 369–374, doi: 10.1016/s0003-9969(02)00015-8, indexed in Pubmed: 12015217.

15. Kurahashi M, Inomata K. Effects of dietary consistency and water content on parotid amylase secretion and gastric starch digestion in rats. Arch Oral Biol. 1999; 44(12): 1013–1019, doi: 10.1016/s0003-9969(99)00099-0, indexed in Pubmed: 10669079.

16. Månsson B, Ekman R, Håkanson R, et al. Neuropeptides and disuse of the rat parotid gland. Exp Physiol. 1990; 75(4): 597–599, doi: 10.1113/expphysiol.1990.sp003435, indexed in Pubmed: 1699560.

17. Månsson B, Nilsson BO, Ekström J. Effects of repeated infusions of substance P and vasoactive intestinal peptide on the weights of salivary glands subjected to atrophying influences in rats. Br J Pharmacol. 1990; 101(4): 853–858, doi: 10.1111/j.1476-5381.1990.tb14170.x, indexed in Pubmed: 1707705.

18. Moss PA, Davies KE, Boni C, et al. Linkage of tyrosine hydroxylase to four other markers on the short arm of chromosome 11. Nucleic Acids Res. 1986; 14(24): 9927–9932, doi: 10.1093/nar/14.24.9927, indexed in Pubmed: 2880337.

19. Pinkstaff CA. The cytology of salivary glands. Int Rev Cytol. 1980; 63: 141–261, doi: 10.1016/s0074-7696(08)61759-3, indexed in Pubmed: 395130.

20. Proctor GB. The physiology of salivary secretion. Periodontol 2000. 2016; 70(1): 11–25, doi: 10.1111/prd.12116, indexed in Pubmed: 26662479.

21. Proctor GB, Carpenter GH. Regulation of salivary gland function by autonomic nerves. Auton Neurosci. 2007; 133(1): 3–18, doi: 10.1016/j.autneu.2006.10.006, indexed in Pubmed: 17157080.

22. Schneyer CA, Hall HD. Amylase and electrolyte changes after postganglionic parasympathectomy of parotid gland. Am J Physiol. 1964; 207: 308–312, doi: 10.1152/ajplegacy.1964.207.2.308, indexed in Pubmed: 14205339.

23. Schneyer CA, Hall HD. Parasympathetic regulation of mitosis induced in rat parotid by dietary change. Am J Physiol. 1975; 229(6): 1614–1617, doi: 10.1152/ajplegacy.1975.229.6.1614, indexed in Pubmed: 1239958.

24. Schneyer CA, Hall HD. Neurally mediated increase in mitosis and DNA of rat parotid with increase in bulk of diet. Am J Physiol. 1976; 230(4): 911–915, doi: 10.1152/ajplegacy.1976.230.4.911, indexed in Pubmed: 1267023.

25. Scott J, Berry MR, Gunn DL, et al. The effects of a liquid diet on initial and sustained, stimulated parotid salivary secretion and on parotid structure in the rat. Arch Oral Biol. 1990; 35(7): 509–514, doi: 10.1016/0003-9969(90)90080-t, indexed in Pubmed: 2222254.

26. Scott J, Gunn DL. A comparative quantitative histological investigation of atrophic changes in the major salivary glands of liquid-fed rats. Arch Oral Biol. 1991; 36(11): 855–857, doi: 10.1016/0003-9969(91)90035-s, indexed in Pubmed: 1763982.

27. Sreebny LM, Johnson DA. Effect of food consistency and decreased food intake on rat parotid and pancreas. Am J Physiol. 1968; 215(2): 455–460, doi: 10.1152/ajplegacy.1968.215.2.455, indexed in Pubmed: 5665178.

28. Takahashi S, Uekita H, Kato T, et al. Growth of rat parotid glands is inhibited by liquid diet feeding. Tissue Cell. 2015; 47(3): 336–341, doi: 10.1016/j.tice.2015.04.003, indexed in Pubmed: 25956847.

29. Takahashi S, Uekita H, Kato T, et al. Involvement of apoptosis and proliferation of acinar cells in atrophy of rat parotid glands induced by liquid diet. J Mol Histol. 2012; 43(6): 761–766, doi: 10.1007/s10735-012-9442-y, indexed in Pubmed: 22918835.

30. Takahashi S, Uekita H, Kato T, et al. Immunohistochemical and ultrastructural investigation of acinar cells in submandibular and sublingual glands of rats fed a liquid diet. Tissue Cell. 2014; 46(2): 136–143, doi: 10.1016/j.tice.2014.01.001, indexed in Pubmed: 24553131.

31. Takahashi S, Uekita H, Taniwaki H, et al. Acinar cell response to liquid diet during rats' growth period differs in submandibular and sublingual glands from that in parotid glands. Tissue Cell. 2017; 49(2 Pt B): 275–284, doi: 10.1016/j.tice.2017.01.011, indexed in Pubmed: 28222888.

32. Thompson RJ, Doran JF, Jackson P, et al. PGP 9.5: a new marker for vertebrate neurons and neuroendocrine cells. Brain Res. 1983; 278(1-2): 224–228, doi: 10.1016/0006-8993(83)90241-x, indexed in Pubmed: 6640310.

33. Tsutsui M, Shimokawa H, Otsuji Y, et al. Pathophysiological relevance of NO signaling in the cardiovascular system: novel insight from mice lacking all NO synthases. Pharmacol Ther. 2010; 128(3): 499–508, doi: 10.1016/j.pharmthera.2010.08.010, indexed in Pubmed: 20826180.

34. Warburton AL, Santer RM. Decrease in synapsin I staining in the hypogastric ganglion of aged rats. Neurosci Lett. 1995; 194(3): 157–160, doi: 10.1016/0304-3940(95)11769-s, indexed in Pubmed: 7478227.

35. Wells H, Peronace AA. Functional hypertrophy and atrophy of the salivary glands of rats. Am J Physiol. 1967; 212(2): 247–251, doi: 10.1152/ajplegacy.1967.212.2.247, indexed in Pubmed: 6018002.

36. Wilkinson KD, Lee KM, Deshpande S, et al. The neuron-specific protein PGP 9.5 is a ubiquitin carboxyl-terminal hydrolase. Science. 1989; 246(4930): 670–673, doi: 10.1126/science.2530630, indexed in Pubmed: 2530630.

37. Yamanaka R, Akther R, Furuta M, et al. Relation of dietary preference to bite force and occlusal contact area in Japanese children. J Oral Rehabil. 2009; 36(8): 584–591, doi: 10.1111/j.1365-2842.2009.01971.x, indexed in Pubmed: 19548957.

38. Young JA, Lennep EWV. Gross anatomy. In The morphology of salivary glands. Academic Press Inc., London 1987: 8–21.

V M

VIA MEDICA

ORIGINAL ARTICLE

Duplicated superficial branch of the radial nerve and brachioradialis muscle belly: prevalence and significance

T. Herma[1] , J. Slezak[1, 2] , V. Baca[3] , D. Kachlik[1, 3]

[1]Department of Anatomy, Second Faculty of Medicine, Charles University, Prague, Czech Republic
[2]Department of Anatomy, Third Faculty of Medicine, Charles University, Prague, Czech Republic
[3]Department of Health Care Studies, College of Polytechnics Jihlava, Czech Republic

Background: The superficial branch of the radial nerve (SBRN) is a sensory nerve innervating the dorsoradial part of the hand. It originates in the cubital fossa, runs under the belly of the brachioradialis muscle (BM), emerges from underneath in the distal third of the forearm and continues in the subcutaneous tissue towards the hand. There exist several anatomical variations of its branching and course, including a rare variation of its duplication combined with a duplication of the brachioradialis muscle belly. The aim of this study was to find out the prevalence of this variation on a sample of cadaveric human bodies which has not been reported yet.

Materials and methods: We have carefully dissected 208 cadaveric upper limbs (Central European population). All cases of limbs containing the variation of a double SBRN and/or a double BM belly were measured and documented.

Results: We have identified 2 cases of a double SBRN combined with a double BM belly (0.96%). Both were present in the right forearm of a male donor and in both cases the nerve was impinged by muscle bundles connecting the 2 muscle bellies together. Moreover, we have encountered 1 case of a double SBRN without a double BM belly (0.48%), i.e. the total prevalence of a double SBRN was 1.44%.

Conclusions: The duplicated SBRN with the duplicated BM is a relatively rare anatomical variation that might cause complications while performing various surgical procedures in the forearm, moreover it might be a rare cause of Wartenberg's syndrome. (Folia Morphol 2023; 82, 3: 558–561)

Key words: **superficial branch, radial nerve, duplication, brachioradialis, variation, double**

INTRODUCTION

The superficial branch of the radial nerve (SBRN) is one of the two terminal branches of the radial nerve. It originates in the cubital fossa and continues distally along the forearm accompanying the radial vessels, covered by the belly of the brachioradialis muscle (BM). It leaves the lateral compartment of the forearm in the distal third of the forearm by penetrating the antebrachial fascia in a close relationship with the BM tendon, branches numerously and continues distally within the subcutaneous tissue over tendons surrounding the radial foveola (anatomical snuff box)

at the wrist, innervating the dorsolateral aspect of the hand and the lateral two and half fingers [3].

Although the above described course of the SBRN is well known, there are some anatomical variations — absence, aberration or connections with other sensory nerves of the upper limb — that may mislead clinicians or be a cause of iatrogenic damage to the nerve during various medical interventions over the forearm and hand (treatment of De Quervain's disease, extensor tendons rupture, surgery of wrist ganglia, etc.) [2].

In 2017, we have described an interesting anatomical variation of the SBRN and BM. The muscle had a duplicated belly (one of them was superficial, the other one deep) with one origin and one insertion. The SBRN was also duplicated, both branches originated in the cubital fossa and each of them ran underneath one of the muscle bellies — the proper SBRN underneath the deep belly and the accessory SBRN underneath the superficial one. The accessory nervous branch was impinged by two pairs of blood vessels and pierced through muscle bundles connecting the two bellies together [5].

A similar variation was indirectly described by Murphy and Blair in a patient with a Wartenberg's syndrome caused by impingement of an accessory nerve with the same anatomical course as the accessory SBRN in our case [8]. While this anatomical variation is of clinical significance and the anatomical literature on this topic is missing (either due to its rarity or neglect in the academic literature), we aimed to find out its prevalence in population.

MATERIALS AND METHODS

From 2017 to 2021 we have dissected 208 upper limbs (97 left and 111 right, 104 males and 104 females) of donor cadavers from the Central European population, fixed with classical formaldehyde embalming method. The SBRN was identified in each limb and carefully visualized in the whole extent from the cubital fossa to the level of the metacarpophalangeal joints. Each variation of either SBRN or BM muscle was identified, measured and documented.

Ethical statement

The protocol for the research project has been approved by the Ethics Commission of the Second Faculty of Medicine, Charles University (No. EK76/21) and it conforms to the provisions of the Declaration of Helsinki of 1975, as revised in 2000 and 2008.

RESULTS

We have identified 2 cases of a double SBRN combined with a double BM belly in a sample of 208 limbs (0.96%). Both were present in the right forearm of a male donor cadaver and in both cases the nerve was impinged by muscle bundles connecting the 2 muscle bellies together. The diameter of the trunk of the radial nerve in the cubital fossa was 3.5 mm in both cases. The diameter of SBRN was 1.5 mm and 1.7 mm, respectively, and the diameter of the accessory SBRN was 1 mm and 1.5 mm, respectively. In both cases, the SBRN and the accessory SBRN merged after certain extent in a common trunk for 17 mm and 11 mm, respectively, and then they separated again. The division of the common nerve trunk was 42 mm and 58 mm proximally from the styloid process of the radius, respectively. Then, the SBRN and accessory SBRN pierced the antebrachial fascia superficially into the subcutaneous layer and divided into terminal branches for the hand: in 1 case into 3 branches of the SBRN and 2 branches of the accessory SBRN, and in the other case into 3 branches of the SBRN and 1 branch of the accessory SBRN. In both cases, the SBRN innervated the skin of the thumb and the accessory SBRN innervated the dorsolateral aspect of the hand. In 1 case, the accessory SBRN innervated the superficial belly of the BM as well (Figs. 1, 2).

We have also encountered 1 case of a double SBRN without a double BM belly present in a left upper limb of a male donor cadaver. In this case the nerve branches were impinged neither by blood vessels nor by muscle bundles. The thinner accessory SBRN (diameter 1.2 mm) innervated the thumb with three branches and the thicker proper SBRN (diameter 3.5 mm) supplied the dorsal aspect of the hand with 2 branches. Both branches were interconnected by a 3-mm-thick interneural communication and the accessory SBRN was also connected to the lateral antebrachial cutaneous nerve via a 1-mm-thick communicating branch. The connection between the SBRN and the accessory SBRN was located 30 mm proximal to the styloid process of the radius and the connection between the accessory SBRN and the lateral antebrachial cutaneous nerve was situated 23 mm proximal to the styloid process of the radius (Fig. 3).

In our sample, the prevalence of a double SBRN combined with a double BM belly was 0.96% and the prevalence of a double SBRN without a double BM belly was 0.48%, i.e. the total prevalence of a double SBRN was 1.44%.

Figure 1. The accessory superficial branch of the radial nerve runs under the superficial belly of the brachioradialis muscle while innervating it. After emerging from underneath, the accessory superficial branch of the radial nerve merges with the superficial branch of the radial nerve into a common nerve trunk; ASBRN — accessory superficial branch of radial nerve; CT — common trunk; CV — cephalic vein; DBBM — deep belly of brachioradialis muscle; SBBM — superficial belly of brachioradialis muscle; SBRN — superficial branch of radial nerve.
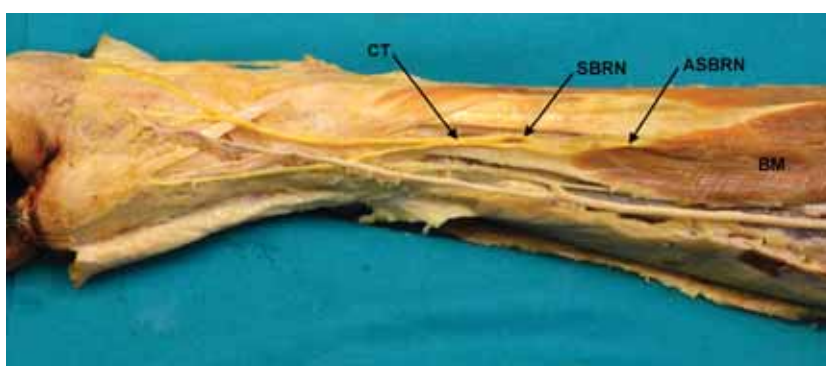
Figure 2. The superficial branch of the radial nerve and the accessory superficial branch of the radial nerve merge into a common trunk. The superficial branch of the radial nerve then innervates the dorsal aspect of the hand, while the accessory superficial branch of the radial nerve innervates the thumb; ASBRN — accessory superficial branch of radial nerve; BM — brachioradialis muscle; CT — common trunk; SBRN — superficial branch of radial nerve.
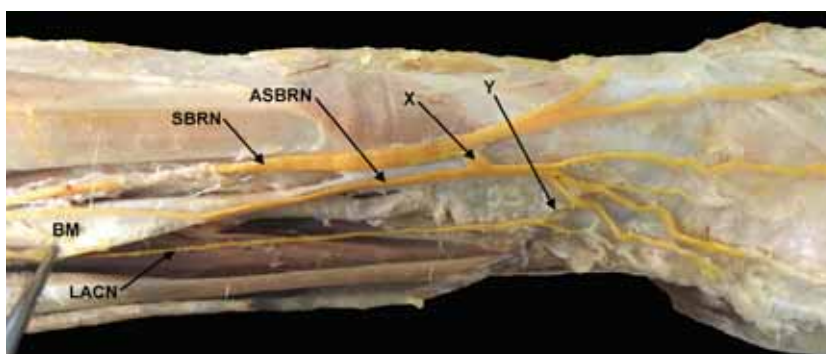
Figure 3. The superficial branch of the radial nerve and the accessory superficial branch are interconnected by a thick communicating branch. Moreover, there is a thin interconnection between the latter and the lateral antebrachial cutaneous nerve; ASBRN — accessory superficial branch of radial nerve; BM — brachioradialis muscle; LACN — lateral antebrachial cutaneous nerve; SBRN — superficial branch of radial nerve; X — thick communicating branch; Y — thin communicating branch.

DISCUSSION

We have found that the duplication of the SBRN and the BM is a rather rare variation in the Central European population with prevalence around 1%. It should be considered while performing surgeries in the forearm or in the differential diagnostics of paraesthesia and neural pain over the dorsolateral aspect of the hand. A similar variation of duplicated and aberrant SBRN was described recently by Patel et al. [9] as a potential complication of harvesting the radial fore-

arm free flap (but in their case, the SBRN was duplicated, 1 branch ran under the belly of a one-bellied BM and the other crossed it superficially) and another similar case of an accessory SBRN joining the main trunk of the nerve was described by Murphy and Blair as a cause of Wartenberg's syndrome in a patient [8].

All cases of the SBRN duplication were present in male donors. We presume that this finding is a bias due to a small number of the described cases rather than due to real difference between males and females.

There exist several variations of the SBRN described in literature — absence, duplication, aberrant course [1, 5, 7, 10, 12] and some of them may cause an impingement — such as the SBRN running in between two slips or piercing the tendon of the BM [11, 13, 14].

There have been also reported cases of absence and duplications of the BM, accessory long supinator muscle, brachioradialis brevis muscle, aberrant origins, aberrant insertions, tendon splits, divided or accessory bellies of the BM as well as variant innervation of the BM by the musculocutaneous nerve [3, 4, 6, 10–14].

CONCLUSIONS

To our best knowledge, nobody has reported the coincidence of the BM belly and the SBRN duplication before. We stated its prevalence in population with potential impingement sites: the prevalence of a double SBRN combined with a double BM belly is 0.96% and the total prevalence of a double SBRN is 1.44%. It might be a rare cause of Wartenberg's syndrome.

Conflict of interest: None declared

REFERENCES

1. Appleton AB. A case of abnormal distribution of the n. musculo-cutaneus, with complete absence of the ramus cutaneus n. radialis. J Anat Physiol. 1911; 46(Part 1): 89–94.
2. Auerbach DM, Collins ED, Kunkle KL, et al. The radial sensory nerve. An anatomic study. Clin Orthop Relat Res. 1994(308): 241–249, indexed in Pubmed: 7955689.
3. Doyle JR, Botte MJ. Surgical anatomy of the hand and upper extremity. Wolters Kluwer Health, Philadelphia 2015.
4. Gruber W. Über die Varietäten des Musculus brachioradialis. Bull Acad Imp Sci Saint-Petersbourg. 1868; 12: 259–269.
5. Herma T, Baca V, Yershov D, et al. A case of a duplicated superficial branch of radial nerve and a two-bellied brachioradialis muscle presenting a potential entrapment syndrome. Surg Radiol Anat. 2017; 39(4): 451–454, doi: 10.1007/s00276-016-1732-8, indexed in Pubmed: 27553247.
6. Kravarski M, Goerres GW, Antoniadis A, et al. Supernumerary brachioradialis - Anatomical variation with magnetic resonance imaging findings: A case report. World J Orthop. 2020; 11(9): 411–417, doi: 10.5312/wjo.v11.i9.411, indexed in Pubmed: 32999861.
7. Lindau RH, Wax MK. Abnormal anatomy of the superficial branch of the radial nerve. Head Neck. 2013; 35(9): E262–E263, doi: 10.1002/hed.23111, indexed in Pubmed: 22907933.
8. Murphy AD, Blair JW. An anatomical variant of the superficial branch of the radial nerve in Wartenberg's syndrome. J Hand Surg Eur Vol. 2012; 37(4): 365–366, doi: 10.1177/1753193411434907, indexed in Pubmed: 22275056.
9. Patel KB, Naik AN, Kang SY, et al. Aberrant superficial branch of the radial nerve-radial forearm free flap considerations. Plast Reconstr Surg Glob Open. 2019; 7(6): e2191, doi: 10.1097/GOX.0000000000002191, indexed in Pubmed: 31624666.
10. Spinner RJ, Spinner M. Superficial radial nerve compression at the elbow due to an accessory brachioradialis muscle: a case report. J Hand Surg Am. 1996; 21(3): 369–372, doi: 10.1016/S0363-5023(96)80346-7, indexed in Pubmed: 8724463.
11. Tryfonidis M, Jass GK, Charalambous CP, et al. Superficial branch of the radial nerve piercing the brachioradialis tendon to become subcutaneous: an anatomical variation with clinical relevance. Hand Surg. 2004; 9(2): 191–195, doi: 10.1142/s0218810404002224, indexed in Pubmed: 15810105.
12. Tubbs SR, Shoja MM, Loukas M. Bergman's comprehensive encyclopedia of human anatomic variation. Wiley-Blackwell, Hoboken 2016.
13. Turkof E, Puig S, Choi MS, et al. Superficial branch of the radial nerve emerging between two slips of a split brachioradialis muscle tendon: a variation of possible clinical relevance. Acta Anat (Basel). 1994; 150(3): 232–234, doi: 10.1159/000147624, indexed in Pubmed: 7817721.
14. Turkof E, Puig S, Choi SS, et al. The radial sensory nerve entrapped between the two slips of a split brachioradialis tendon: a rare aspect of Wartenberg's syndrome. J Hand Surg Am. 1995; 20(4): 676–678, doi: 10.1016/s0363-5023(05)80290-4, indexed in Pubmed: 7594301.

V M
VIA MEDICA

ORIGINAL ARTICLE

Investigation of anastomoses between coronary arteries in Akkaraman sheep by plastic injection and corrosion method

E. Yalman[1] , E. Unur[2] , H. Güler[2]

[1]*Department of Nursing, Faculty of Health Sciences, Yozgat Bozok University, Yozgat, Turkey*
[2]*Department of Anatomy, Faculty of Medicine, Erciyes University, Kayseri, Turkey*

Background: Since it is critical to understand the anatomy of the coronary arteries and the anastomoses between them in Akkaraman sheep, the coronary arteries will be examined using a plastic injection and corrosion technique.

Materials and methods: In our investigation, researchers used 20 Akkaraman sheep's hearts collected from slaughterhouses in and near Kayseri, and hearts from animals aged 2–3 years were included. The anatomy of the coronary arteries of the hearts was studied by plastic injection and corrosion method. The macroscopically examined patterns of the excised coronary arteries were photographed and recorded.

Results and Conclusions: This approach indicated arterial vascularisation of the heart in sheep, with a. coronaria dextra and a. coronaria sinistra developing from the commencement of the aorta. It was determined that a. coronaria sinistra, after leaving the initial part of the aorta, proceeds to the left and divides into two branches called r. interventricularis paraconalis and r. circumflexus sinister, forming a right angle between them, immediately after reaching the sulcus coronarius. Anastomosis of the branches of r. distalis atrii dextri with the branches of r. intermedius atrii dextri and r. ventriculi dextri; anastomosis of a thin branch separated from r. proximalis atrii sinistri with the branch of r. proximalis atrii dextri running in the initial part of the aorta; anastomosis of r. distalis atrii sinistri with r. intermedius atrii sinistri were detected. In one heart, the r. septalis protruded roughly 0.2 cm from the beginning of a. coronaria sinistra. (Folia Morphol 2023; 82, 3: 562–567)
Key words: anastomosis, anatomy, coronary artery, heart, sheep

INTRODUCTION

The heart is the most crucial basic building unit of the body, pumping blood and ensuring proper circulation. It is critical that the heart is in good health so that all organs may work effectively and systematically. Cardiovascular diseases are the leading cause of death worldwide and in Turkey (http://www.saglik.gov.tr, 2018). The first two causes of death related to heart disorders are ischaemic heart disease and cerebrovascular diseases [23].

Arteria (a.) coronaria dextra and a. coronaria sinistra emerge from the ascending aorta to supply the heart [1–3, 6, 7, 9, 14, 15, 18, 22, 24–26, 31, 33]. A. coronaria dextra originates from the level of the valvula semilunaris dextra at the initial level of the aorta [3, 9, 15]. A. coronaria dextra runs between

the truncus pulmonalis and the auricula dextra, then to the sulcus coronarius and back as the ramus (r.) circumflexus dexter [11, 18, 29, 30]. R. circumflexus dexter yields r. proximalis atrium dextri, r. intermedius atrii dextri and r. distalis atrium dextri for atrium dextrum, and r. coni arteriosi, r. proximalis ventriculi dextri, r. intermedius atrii dextri and r. distalis atrium dextri for ventriculus dexter, r. proximalis ventriculi dextri, r. marginis ventricularis dextri [9, 15, 21, 28, 32, 33].

Arteria coronaria sinistra is a branch of the aorta that begins slightly above the valvula semilunaris sinistra [9, 10, 29]. At the level of the sulcus coronarius, a. coronaria sinistra separates into r. circumflexus sinister and r. interventricularis paraconalis, making a right angle [5, 18, 20, 30, 32, 33]. The r. interventricularis paraconalis branches to the rr. septi interventriculares [12], r. coni arteriosi, r. collateralis sinister proximalis, and r. collateralis sinister distalis after its origin [11, 13, 18, 33]. Atria l branches of r. circumflexus sinister are r. proximalis atrii sinistri, r. intermedius atrii sinistri, and r. distalis atrii sinistri. Its ventricular branches are r. proximalis ventriculi sinistri, r. marginis ventricularis sinistri, and r. distalis venticuli sinistri [8, 11, 25, 30, 32, 33].

Polyester was employed in our study because it is abundant in the industry and inexpensive, and sheep's heart was used since it is accessible and one of the hearts closest to the human heart. Since it is critical to understand the anatomy of the coronary arteries and the anastomoses that connect them, it was decided to analyse the coronary arteries in Akkaraman sheep using a plastic injection and corrosion approach.

MATERIALS AND METHODS

This investigation was conducted in accordance with the principles of the "Ethics Committee," with 20 Akkaraman sheep's hearts procured from butchers or slaughterhouses in and around Kayseri. After the animals were slaughtered, the hearts and pericardia were removed from the thoracic cavity.

The hearts provided for the experiment were dissected in the laboratory for the plastic injection process. After the cannula was placed in the aorta, the solution was prevented from escaping between the cannula and the aorta by tying the periphery of the aorta with a thread. Vv. pulmonales were ligated. The polyester solution was prepared by adding 70% Polyester resin (Turkuaz Corolla Styrene Monomer TPY001), 30% Liquidizer (styrene), 2% Accelerator, 4% Freezer, Dye (Red dye) [4, 17].

After putting the prepared polyester solution into a 50 mL injector, it was injected into the aorta via the cannula inserted in the aorta until all of the coronary arteries were filled. During the injection, the periphery of the aorta was tied with a thread to prevent the solution from escaping between the cannula and the aorta. The hearts were stored at room temperature during 48–72 hours after the polyester injection to allow the polyester to harden in the artery. Following the solidification of the polyester, the hearts were immersed in 37.5% hydrochloric acid. Hearts were maintained in hydrochloric acid for a time interval of 48–72 hours. We observed that vascular integrity deteriorated in hearts that were kept in hydrochloric acid for a longer period of time. In this acid, the tissues were dissolved (corrosion). The collected materials were washed in tap water to remove any tissue remnants. As a result, the coronary artery mould was removed. Macroscopically, the patterns of the excised coronary arteries were analysed.

Ethical statement

It has been reported in writing by Erciyes University Animal Experiments Local Ethics Committee (20/045) that this study is not subject to HADYEK's permission.

RESULTS

The structure and anastomoses of the coronary arteries in 20 Akkaraman sheep aged 2–3 years and weighing 60–70 kg were studied. The arterial vascularisation of the heart in sheep was determined to be given by a. coronaria dextra and a. coronaria sinistra originating from the beginning of the aorta. An additional vessel was discovered at the ostium aortae level in one heart, originating between a. coronaria dextra and a. coronaria sinistra on the anterior surface of the aorta and supplying the anterior side of the left ventricle (the region where the sulcus interventricularis paraconalis is located). Based on the region it fed, this branch was named ramus septalis (Fig. 1).

Findings of arteria coronaria dextra

After exiting the aorta, a. coronaria dextra proceeded to the right and reached the sulcus coronarius, where it continued as r. circumflexus dexter in the subepicardial adipose tissue (Fig. 2). A. coronaria dextra was observed to give r. septalis to feed the septum interventriculare and r. coni arteriosi to feed the area where the conus arteriosus is located.

Figure 1. The branch that separates from the aorta (AO) between a. coronaria dextra (ACD) and a. coronaria sinistra (ACS); 1 — branch that separates from the aorta between a. coronaria dextra and a. coronaria sinistra (Ramus septalis).
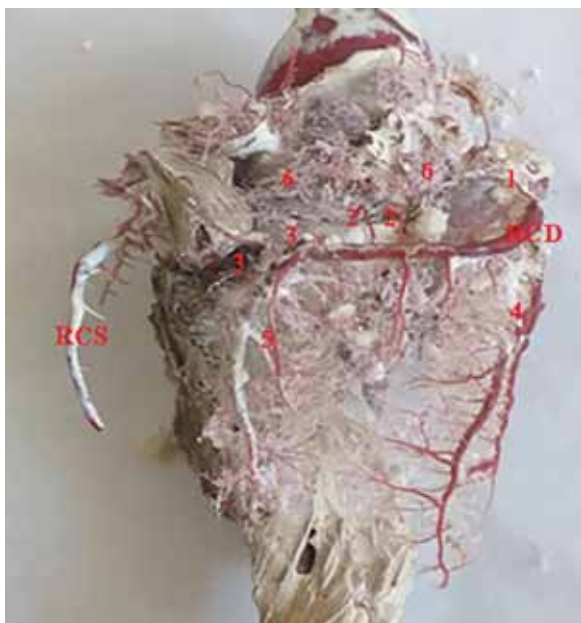

Figure 2. Ramus circumflexus dexter (RCD) is terminated by the formation of r. interventricularis subsinuosus; RCS — r. circumflexus sinister; 1 — r. proximalis atrii dextri; 2 — r. intermedius atrii dextri; 3 — r. distalis atrii dextri; 4 — r. marginis ventricularis dextri; 5 — r. distalis ventriculi dextri; 6 — r. intermedius atrii dextri anastomoses with r. proximalis atrii dextri and r. distalis atrii dextri.

The atrial dextrum was given the names r. proximalis atrii dextri, r. intermedius atrii dextri, and r. distalis atri dextri (Fig. 2). In 10 hearts, r. proximalis atrii dextri anastomoses with branches of r. intermedius atrii dextri, and a thin branch of it proceeds from the beginning of the aorta and anastomoses with a branch of r. proximalis atrii sinistri. The branches of r. intermedius atrii dextri that split before coming to margo venticularis dexter anastomoses with r. proximalis atri dexter, while the branches that divide after passing through margo ventricularis dexter anastomoses with r. distalis atri dexter (Fig. 2). It was determined that r. distalis atrii dextri was absent in one heart. The absence of this vessel was shown to be nourished by the r. ventriculi dextri, a branch of the r. interventricularis subsinuosus. The branches of r. distalis atrii dextri anastomose with those of r. intemedius atrii dextri and r. ventriculi dextri.

It was discovered that for ventriculus dexter, it gave r. proximalis ventriculi dextri, r. marginis ventricularis dextri, and r. distalis ventriculi dextri (Fig. 2). It was observed that r. proximalis ventriculi dextri dispersed in the middle and proximal regions of the ventriculus dexter and anastomose with the ventricular branches of the r. interventricularis paraconalis and the branches of the r. marginis ventricularis dextri. R. marginis ventricularis dextri was observed to anastomose with the branches provided by r. proximalis ventriculi dextri, r. distalis ventriculi dextri, and r. interventricularis paraconalis for ventriculus dexter. R. distalis ventriculi dextri anastomose with r. interventricularis paraconalis branches for ventriculus dexter.

Findings of arteria coronaria sinistra

After leaving the early segment of the aorta, a. coronaria sinistra proceeded to the left and reached the sulcus coronarius. It was discovered that 19 hearts split into two branches, r. interventricularis paraconalis and r. circumflexus sinister, immediately after reaching the sulcus coronarius, making a right angle between them. It divided into three branches in one heart, and the third branch, which emerged between the r. interventricularis paraconalis and the r. circumflexus sinister, was discovered to be the r. proximalis ventriculi sinistri (Fig. 3).

Ramus circumflexus sinister

The atrium sinistrum was given the titles r. proximalis atrii sinistri, r. intermedius atrii sinistri, and r. distalis atrii sinistri. In 2 hearts, a thin branch branching off from the r. proximalis atrii sinistri was found to anastomose with the branch of the r. proximalis atrii dextri running in the initial part of the
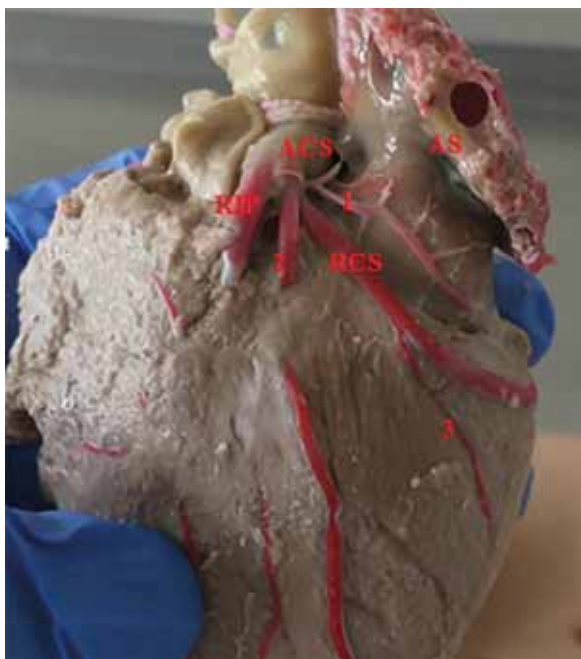
Figure 3. Division of a. coronaria sinistra (ACS) into three branches; AS — auricula sinistra; RCS — r. circumflexus sinister; RIP — r. interventricularis paraconalis; 1 — r. proximalis atrii sinistri; 2 — r. proximalis ventriculi sinistri; 3 — r. marginis ventricularis sinistri.

aorta. The r. intermedius atrii sinistri and r. distalis atrii sinistri were found to be absent in one heart, and the region it fed was identified to be nourished by the r. proximalis atrii sinistri (Fig. 3).

It was discovered that it was administered to the r. proximalis ventriculi sinistri, r. marginis ventricularis sinistri, and r. distalis ventriculi sinistri for ventriculus sinister. In one heart, a coronaria sinistra was found to be separated into 3 branches, with the third branch emerging between r. interventricularis paraconalis and r. circumflexus sinister being r. proximalis ventriculi sinistri. The r. proximalis ventriculi sinistri anastomosis with the r. marginis ventricularis sinistri and r. collateralis sinister proximalis was determined (Fig. 3). The r. distalis ventriculi sinistri anastomoses with the r. marginis ventricularis sinister and r. interventricularis subsinuosus. R. interventricularis subsinuosus gave a branch called r. ventriculi dextri about 0.3 cm from its beginning, and this branch anastomosed with r. distalis atri dextri. It was observed that 1 heart did not have r. distalis atrii dextri, and this region was fed by r. ventriculi dextri.

Ramus interventricularis paraconalis

It was determined that the r. coni arteriosi originating from the r. interventricularis paraconalis anas-

tomose with the terminal branches of the vein of the same name separated from a. coronaria dextra. In addition, r. collateralis sinister proximalis anastomoses with r. proximalis ventriculi sinistri, r. collateralis sinister distalis anastomose with r. proximalis ventriculi sinistri, branches given for ventriculus dexter r. proximalis ventriculi districuli deximalis and its branches for the ventriculus sinister were found to anastomose with the r. marginis ventricularis sinistri.

DISCUSSION AND CONCLUSIONS

Coronary artery diseases are common in humans and these vessels are frequently intervened. Sheep are used as a common model in translational research on vessels. Therefore, it is valuable to know the coronary artery anatomy of these animals. In our study, we benefited from coronary artery studies conducted in both sheep and humans.

According to Stankovic and Jesic (2004) [28], a third coronary artery can emerge from the aorta in humans [27]. An additional vessel was discovered at the level of the ostium aortae in our investigation, emerging between a. coronaria dextra and a. coronaria sinistra on the anterior surface of the aorta and feeding the anterior surface of the left ventricle (the region where the sulcus interventricularis paraconalis is located). This finding lends credence to the notion that differences in coronary arteries are widespread.

In our study, it was discovered that a coronaria dextra gave a thin branch on its dorsal surface at the beginning of one of the sheep bowls, and this branch rose on the anterior surface of the aorta. R. marginis ventricularis dextri was shown to anastomose with r. proximalis ventriculi dextri and r. distalis ventriculi dextri. For ventriculus dexter, r. distalis ventriculi dextri anastomoses with the branches provided by r. marginis ventricularis dextri and r. interventricularis paraconalis. These anastomoses have not been described in the literature.

In the human heart [20] and in the African sheep [16], a coronaria sinistra separates into three branches [19, 32]. In line with this discovery, it was revealed in our investigation that it was variably divided into three branches. There was anastomosis between the ramus interventricularis paraconalis and the ramus circumflexus sinister. We have encountered similar anatomical variations that have been seen before. Therefore, we used similar nomenclatures in the literature in our study, since we did not observe a different vessel finding for the first time.

A thin branch originating from the dorsal surface of 2 (10%) hearts was shown to rise above the aorta 0.2 cm following the beginning of a. coronaria sinistra. There was no such finding in the literature. It has been determined that r. distalis atrii sinistri anastomoses with r. intermedius atrii sinistri, which was not previously discovered in the literature.

As a consequence, the coronary arteries supplying the hearts of Akkaraman sheep were identified, as well as the anastomoses between them. This study, which determines the anastomoses connecting the coronary arteries of Akkaraman sheep, is expected to contribute to anatomical studies by filling a gap in the literature. From this point of view, the anastomoses of the branches of r. distalis atrii dextri with the branches of r. intermedius atrii dextri and r. ventriculi dextri, which have not been reported in the literature so far and were detected for the first time in sheep with our study, anastomoses of r. distalis ventriculi dextri with r. marginis ventricularis dextri and r. interventricularis paraconalis branches for ventriculus dexter, in 2 hearts, the anastomoses of a thin branch separated from the r. proximalis atrii sinistri with the branch of the r. proximalis atrii dextri running in the beginning of the aorta and the anastomoses of the r. distalis atrii sinistri with the r. intermedius atrii sinistri may contribute to the literature. Castration of coronary vessels can also help in model building for educational purposes. As a result, it has been determined that it may aid in better recognizing coronary anastomoses and progressing in the resolution of heart disorders.

Acknowledgements

Conflict of interest: None declared

REFERENCES

1. Akhtar S, Hossain F, Siddiqui M, et al. Morphology and Morphometrical studies on Semi lunar Heart valves of Indigenous Cattle (*Bos indicus*). Int J Nat Sci. 1970; 1(1): 7–11, doi: 10.3329/ijns.v1i1.8608.
2. Aksoy G, Karadağ H. Evcil kedi ve Beyaz Yeni Zelanda tavşanlarında kalp ve kalp arterıaları üzerinde anatomik bir çalışma. Vet Bil Derg. 2002; 18(1-2): 33–40.
3. Aksoy G, Özüdoğru Z, Özdemir D. A macroanatomic investigation of the coronary arteries and myocardial bridges in Awassi sheep. Eur J Vet Sci. 2018; 34(3): 171–177, doi: 10.15312/eurasianjvetsci.2018.192.
4. Aycan K, Bilge A. Plastik enjeksiyon ve korrozyon metodu ile vaskuler sistem anatomisinin araştırılması. Erciyes Ü Tıp Fak Derg. 1984; 6: 545–552.
5. Bhargava I, Beaver C. Observations on the arterial supply and venous drainage of the bovine hearth. Anat Anz. 1970; 126: 343–354.
6. Bhimalli S, Dixit D, Siddibhavi M, et al. A study of variations in coronary arterial system in cadaveric human heart. World J Sci Technol. 2011; 1(5): 30–35.
7. Bisaillon A. Anatomy of the heart in the North American Beaver (Castor Canadensis). Anat Anz. 1982: 381–391.
8. Boumzebra D, Solem JO, Nakeeb S, et al. The sheep as a model for coronary artery surgery experimention beating heart. J Tehran Heart Center. 2006: 11–15.
9. Büll ML, Martins MF. Study of the arterial coronary circulation in the dog (Canis familiaris). Rev Chil Anat. 2002; 20(2), doi: 10.4067/s0716-98682002000200001.
10. Doğruer A, Özmen E. Kıvırcık Koyunlarında Koroner Arterler Üzerine Makroanatomik Bir Çalışma. Atatürk Üniversitesi Veteriner Bilimleri Dergisi. 2012; 7(1): 35–45.
11. Döven O, Yurtdaş M, Çiçek D. Congenital absence of left circumflex coronary artery with superdominant right coronary artery. Anadolu Kardiyol Derg. 2006; 6: 208–209.
12. Dursun N. Veteriner Anatomi II. Ankara Üniversitesi Veteriner Fakültesi, Medisan Yayınevi, Ankara 2002: 186–198.
13. Dursun N, Türkmenoğlu İ. Kangal köpeklerinde septum interventricularenin arteriel vaskularizasyonu. Vet Bil Derg. 1996; 12: 141–144.
14. Dyce KM, Sack WO, Wensing CJG. Textbook of Veterinary Anatomy. WB Saunders Company 1996.
15. Frackowiak H, Jasiczak K, Pluta K, et al. Coronary arteries of the roe deer (Capreolus capreolus; Linnaeus 1758) heart. Pol J Vet Sci. 2007; 10(2): 105–108, indexed in Pubmed: 17882934.
16. Gomez FA, Cortés LS, Ballesteros LE. Morphological characterisation of the coronary arteries in African sheep (Ovis orientalis). Differential analysis with those of humans and other animal species. Folia Morphol. 2019; 78(1): 63–70, doi: 10.5603/FM.a2018.0054, indexed in Pubmed: 30009370.
17. Gürbüz İ. Tuj ve Hemşin koyunlarında kalp ve koroner damarlar üzerine karşılaştırmalı makroanatomik araştırmalar. Kafkas Üniversitesi Sağlık Bilimleri Enstitütü, Doktora Tezi, Kars, 2015.
18. Hassa O. Korozyon preparatlarının normal ve patolojik piyeslerin polyester bloka alma tekniği. Veteriner Fakültesi Dergisi. 1967; 14: 378–386.
19. Koizumi M, Kawai K, Honma S, et al. Anatomical study of a left single coronary artery with special reference to the various distribution patterns of bilateral coronary arteries. Ann Anat. 2000; 182(6): 549–557, doi: 10.1016/S0940-9602(00)80102-8, indexed in Pubmed: 11125806.
20. Kura GG, Poerschke RA, Tumelero RT, et al. Myocardial bridges and left coronary artery trifurcation: a case report. J Morphol Sci. 2013; 30: 209–211.
21. Miller M, Christensen G, Evans H. Anatomy of the dog. WB Saunders Company, Philadelphia, London 1965: 267–285.
22. Nickel RA, Schummer A, Seiferle E. The anatomy of the domestic animals the circulatory system. Verlag Paul Parey, Berlin, Hamburg 1981.
23. Nigri GR, Di Dio LJ, Baptista CA. Papillary muscles and tendinous cords of the right ventricle of the human heart:

morphological characteristics. Surg Radiol Anat. 2001; 23(1): 45–49, doi: 10.1007/s00276-001-0045-7, indexed in Pubmed: 11370142.

24. Öngen Z, Yılmaz Y. Aterosklerozun Patogenezi. Türkiye Klinikleri Dahili Tıp Bilimleri Dergisi Kardiyoloji. 2006; 2(7): 1–9.

25. Ozgel O, Haligur AC, Dursun N, et al. The macroanatomy of coronary arteries in donkeys (Equus asinus L.). Anat Histol Embryol. 2004; 33(5): 278–283, doi: 10.1111/j.1439-0264.2004.00548.x, indexed in Pubmed: 15352880.

26. Şahin F. Merinos Koyunlarında Septum Interventriculare'nin Arteriyal Vaskülarizasyonu. Balıkesir Üniversitesi Sağlık Bilimleri Enstitütü, Yüksek Lisans tezi, Balıkesir, 2016.

27. Schummer A, Wilkens H, Vollmerhaus B, Habermehl KH. The circulatory system, the skin and the cutaneus organs of the domestic mammals. Verlag Paul Parey, Berlin, Hamburg 1981.

28. Stankovic I, Jesic M. Morphometric characteristics of the conal coronary artery. McGill J Med. 2020; 8(1): 2–6, doi: 10.26443/mjm.v8i1.507.

29. Tecirlioğlu S, Dursun N, Uçar Y. Mandada kalp ve kalp arterialari üzerinde anatomik arastırmalar. Ankara Üniv Vet Fak Derg. 1977; 24: 361–374.

30. Teke B, Özüdoğru Z, Özdemir D, et al. Hasak Koyunlarında Kalp Kas Köprüleri ve Koroner Arterler. Bahri Dağdaş Hayvan Araştırmalar Dergisi. 2017; 6(1): 1–12.

31. Tıpırdamaz S. Akkaraman koyunları ve Kıl keçilerinde kalp ve kalp arteiaları üzerinde karsılastırmalı çalışmalar. Selçuk Veteriner Fakültesi Dergisi. 1987; 3: 179–191.

32. Veteriner Brüt Anatomik İsimlendirme Uluslararası Komitesi. Nomina Anatomica Veterineria (NAV), Beşinci baskı. Dünya Veteriner Anatomistleri Derneği, Hannover, Columbia, Gent, Sapporo, 2012.

33. Vladova D. Ventricular coronary pattern in the cat. Trakia J Sci. 2005; 3: 44–49.

VM
VIA MEDICA

O R I G I N A L   A R T I C L E

The petrosal artery and its variations: a comprehensive review and anatomical study with application to skull base surgery and neurointerventional procedures

A. Yu[1], G. Dupont[1], J.D. Nerva[2], S.N. Anadkat[3], A.V. D'Antoni[4, 5], A. Wang[6],
J. Iwanaga[6, 7], A.S. Dumont[6], R.S.Tubbs[3, 6–11]

[1]Tulane University School of Medicine, New Orleans, LA, United States
[2]Department of Neurosurgery, Medical College of Wisconsin, Milwaukee, WI, United States
[3]Department of Structural and Cellular Biology, Tulane University School of Medicine, New Orleans, LA, United States
[4]Physician Assistant Programme, Wagner College, Staten Island, New York, United States
[5]Division of Anatomy, Department of Radiology, Weill Cornell Medicine, New York, NY, United States
[6]Department of Neurosurgery, Tulane Centre for Clinical Neurosciences, Tulane University School of Medicine, New Orleans, LA, United States
[7]Department of Neurology, Tulane Centre for Clinical Neurosciences, Tulane University School of Medicine, New Orleans, LA, United States
[8]Department of Anatomical Sciences, St. George's University, St. George's, Grenada, West Indies
[9]Department of Surgery, Tulane University School of Medicine, New Orleans, LA, United States
[10]Department of Neurosurgery and Ochsner Neuroscience Institute, Ochsner Health System, New Orleans, LA, United States
[11]University of Queensland, Brisbane, Australia

Background: The petrosal artery supplies several structures at the skull base and is often the focus of various neurointerventional procedures. Therefore, knowledge of its anatomy and variations is important to surgeons and interventionalists.

Materials and methods: Twenty latex injected cadaveric heads (40 sides) underwent microsurgical dissection of the petrosal artery. Documentation of the course of the artery and its branches were made. Measurements of the petrosal artery's length and diameter were performed using microcallipers.

Results: A petrosal artery was identified on all sides. The mean length and diameter of the artery within the middle cranial fossa was 2.4 cm and 0.38 mm, respectively. Branches included the following: dural, ganglionic, V3 branches, branches extending through the foramen ovale, branches directly to the greater petrosal and lesser petrosal nerves, branches to the floor of the hiatus of the greater and lesser petrosal nerves, branch to the arcuate eminence, and superior tympanic artery. No statistically significant differences were noted between male and female specimens, but right-sided petrosal arteries were in general, larger in diameter than left sides.

Conclusions: A thorough anatomical knowledge of the petrosal artery and to its relationship to the facial nerve and other neurovascular structures is necessary to facilitate effective endovascular treatment and to preclude facial nerve complications. (Folia Morphol 2023; 82, 3: 568–579)

Key words: skull base, anatomy, surgery, neurosurgery, middle meningeal artery, meningioma

Address for correspondence: J. Iwanaga, DDS, PhD, Department of Neurosurgery, Tulane Centre for Clinical Neurosciences, 131 S. Robertson St. Suite 1300, New Orleans, LA 70112, United States, tel: 5049885565, fax: 5049885793, e-mail: iwanagajoeca@gmail.com
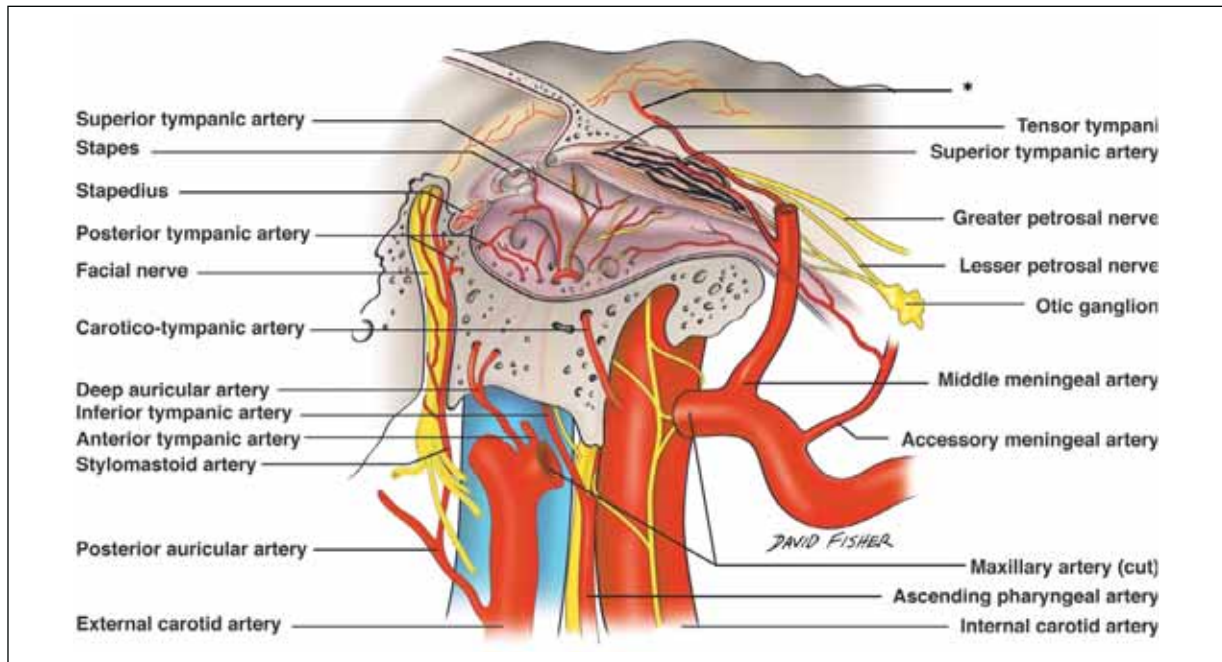
Figure 1. Schematic drawing of the left petrosal artery (*) (medial to lateral view) and its supply of the facial nerve. Also, note the surrounding blood vessels and their anastomoses.

INTRODUCTION

The petrosal artery (Figs. 1, 2), also known as the petrous branch of the middle meningeal artery (MMA) or the superficial petrosal artery, is an important supplier to the intrapetrous portion of the facial nerve (CN VII) and contributes to supplying several other structures near the floor of the middle cranial fossa [6]. Arising from the third branch of the first portion of the maxillary artery, the MMA is the dominant supplier to the meningeal arterial network in the cranial dura [32]. As it enters the foramen spinosum, its proximal intracranial segment gives off the petrosal and cavernous branches prior to its bifurcation into anterior and posterior divisions [3, 6, 28, 29, 32]. The textbook anatomy of the petrosal artery involves it entering the hiatus for the greater petrosal nerve to supply the facial nerve, geniculate ganglion, and tympanic cavity; however, it has more commonly been described as reaching this point by passing through the bone surrounding the tympanic segment of the facial nerve and the geniculate ganglion [6, 32, 33]. Together with the stylomastoid branch of the posterior auricular or occipital artery, the petrosal artery forms an anastomotic arterial arch supplying the geniculate ganglion, known as the facial nerve arterial arcade, the disturbance of which has several clinical consequences. Interruption of the petrosal artery during invasive extradural subtemporal approaches

to the middle cranial fossa, such as elevation of the dura or MMA embolisation, risks iatrogenic facial nerve palsy [6].

This paper describes an investigation of the artery through cadaveric dissection, and reviews the anatomical structure, its variations, and clinical significance of this important MMA branch. To facilitate effective results of endovascular treatment and to preclude iatrogenic injury, it is important during approaches to the middle cranial fossa to appreciate the variable anatomy of the petrosal artery and its relationship with the facial nerve and other neurovascular structures.

MATERIALS AND METHODS

Twenty latex injected cadaveric heads (40 sides) underwent microsurgical dissection of the petrosal artery. A surgical microscope (Zeiss, Germany) was used for all dissections. The specimens were 68–88 years old at death with a mean age at death of 71.5 years. Twelve specimens were male and eight were female. Documentation of the course of the artery and its branches were made. Measurements of the petrosal artery's length and diameter were performed using microcallipers (Mitutoyo, Japan). The diameters were measured at the take-off of the vessel from the MMA. Morphometric data were compared based on sides and sex. Descriptive and
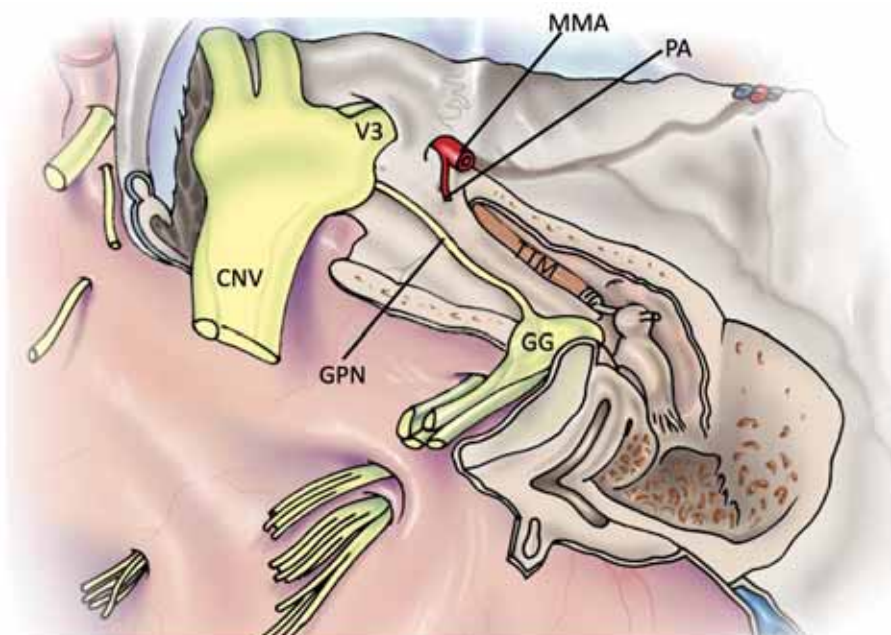
Figure 2. Schematic drawing of the right skull base and right petrosal artery (PA) and its origin from the middle meningeal artery (MMA). Note the relationships between the greater petrosal nerve (GPN), geniculate ganglion (GG), and mandibular nerve (V3). Also note the trigeminal nerve (CNV) and tensor tympani muscle (TTM).

inferential statistics were calculated using SPSS version XX (Armonk, NY).

RESULTS

A petrosal artery was identified on all sides (Figs. 3–8). The mean length of the artery within the middle cranial fossa was 2.4 cm (range 1.6–2.6 cm). The diameter of the petrosal artery ranged from 0.23 mm to 0.66 mm (mean 0.38 mm). Branches included the following: dural, ganglionic, V3 branches, branches extending through the foramen ovale, branches directly to the greater petrosal and lesser petrosal nerves, branches to the floor of the hiatus of the greater and lesser petrosal nerves, branch to the arcuate eminence, and superior tympanic artery. Some of these branches, especially branches to V3 were duplicated. The petrosal artery arose from below the foramen spinosum on two left and three right sides (12.5%). On 1 (2.5%) of these, the artery did not enter the middle cranial fossa but entered the skull through a more medial and unnamed aperture to then travel under a bony bridge (Fig. 7). Bony bridges covering the petrosal artery were found on 3 (7.5%) sides and these were found within 1.5 cm from the artery exit from the foramen spinosum. A superior tympanic artery arose from the petrosal artery on 3 (7.5%) sides. One left sided petrosal artery (2.5%) was found to form an arterial circle that gave off

dural branches and also branches to V3. No statistically significant differences were noted between male and female specimens, but right-sided petrosal arteries were in general, larger in diameter than left sides (p > 0.05).

DISCUSSION

We identified a petrosal artery on all sides. This artery commonly supplied the mandibular nerve and continued posteriorly parallel to the greater petrosal nerve. The mean length of the artery within the middle cranial fossa was 2.4 cm (range 1.6–2.6 cm). The diameter of the petrosal artery ranged from 0.23 mm to 0.66 mm (mean 0.38 mm). Branches included the following: dural, ganglionic, V3 branches, branches extending through the foramen ovale, branches directly to the greater petrosal and lesser petrosal nerves, branches to the floor of the hiatus of the greater and lesser petrosal nerves, branch to the arcuate eminence, and superior tympanic artery.

Anatomy

Normally, as the MMA enters through the foramen spinosum, it immediately gives off two branches prior to its split into anterior and posterior divisions: the petrosal branch laterally, and the cavernous branch to the trigeminal ganglion medially. The petrosal artery is the first intracranial branch of the MMA and
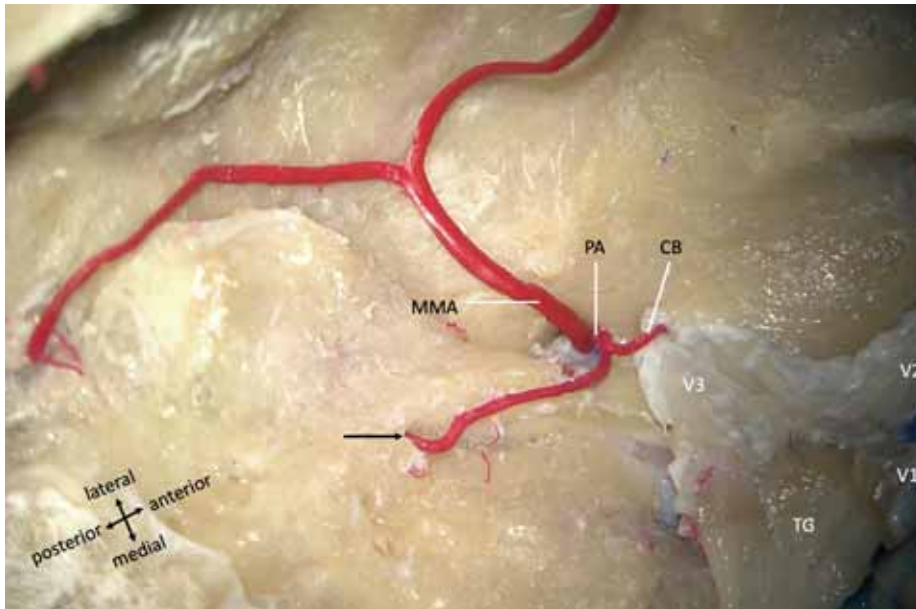
Figure 3. Cadaveric dissection of the left petrosal artery (PA). Note the cavernous branch (CB), middle meningeal artery (MMA), trigeminal ganglion (TG), and mandibular nerve (V3).
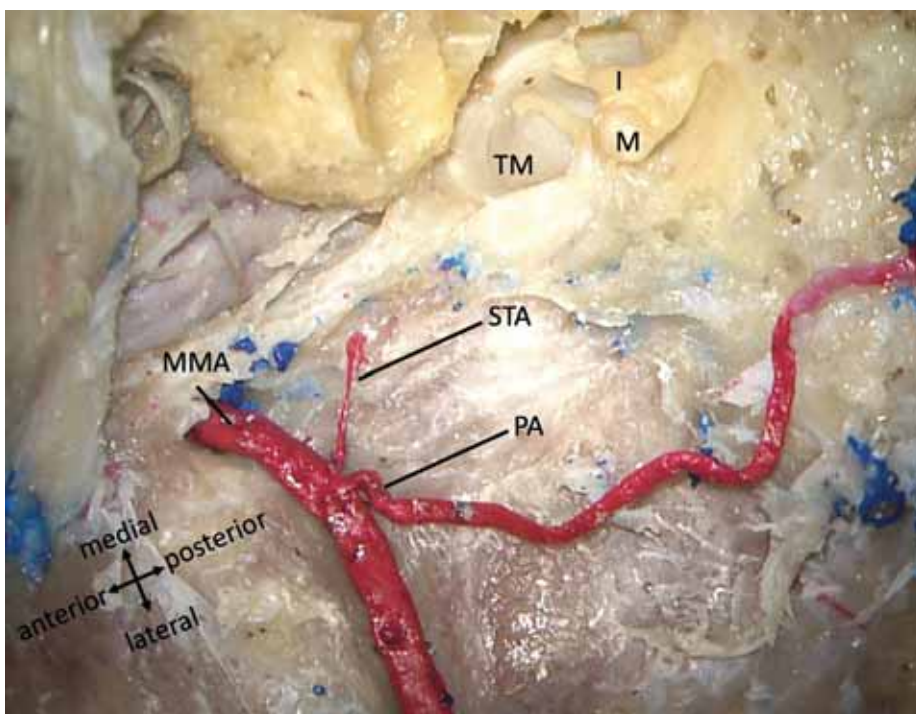
Figure 4. Right sided cadaver dissection illustrating a superior tympanic artery (STA) arising from the origin of the petrosal artery (PA) from the middle meningeal artery (MMA); I — incus; M — malleus; TM — tympanic membrane.

can originate slightly below or above the level of the foramen spinosum [6]. Craniotomy of the overlying temporal bone reveals that it usually arises from the first 10-mm intracranial segment of the MMA, or in some cases 15–20 mm above this level [6, 13]. It is commonly described as coursing posteriorly along the greater petrosal nerve, but it has been observed to run closer to the lesser petrosal nerve as seen in some of our cases (Fig. 5) [6]. The petrosal artery first enters the floor of the middle cranial fossa floor, where its
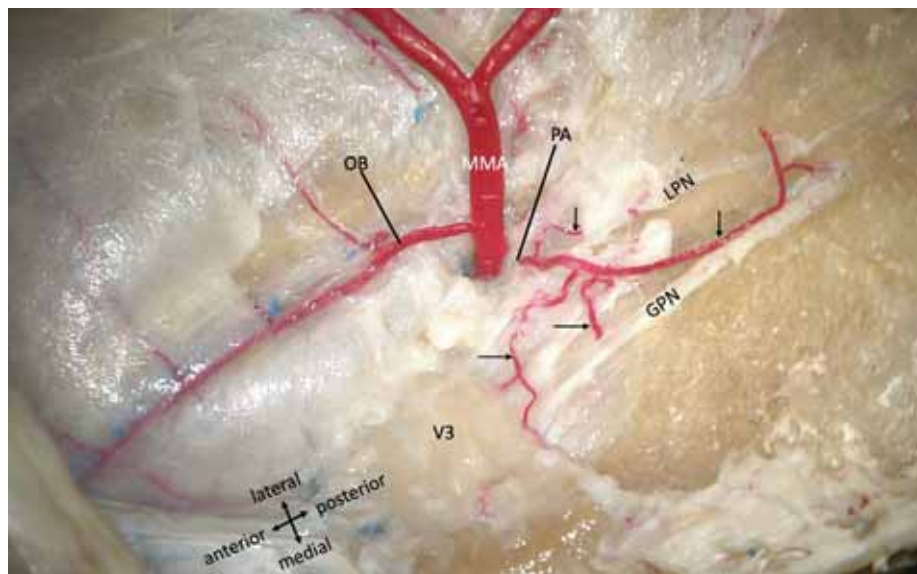
Figure 5. Right sided cadaver dissection noting the petrosal artery (PA), orbital branch (OB) of the middle meningeal artery (MMA), and greater (GPN) and lesser petrosal nerves (LPN). The vertical arrows show branches to the petrosal nerves and the horizontal arrows show branches to the mandibular nerve (V3) and the lesser petrosal nerve (LPN).
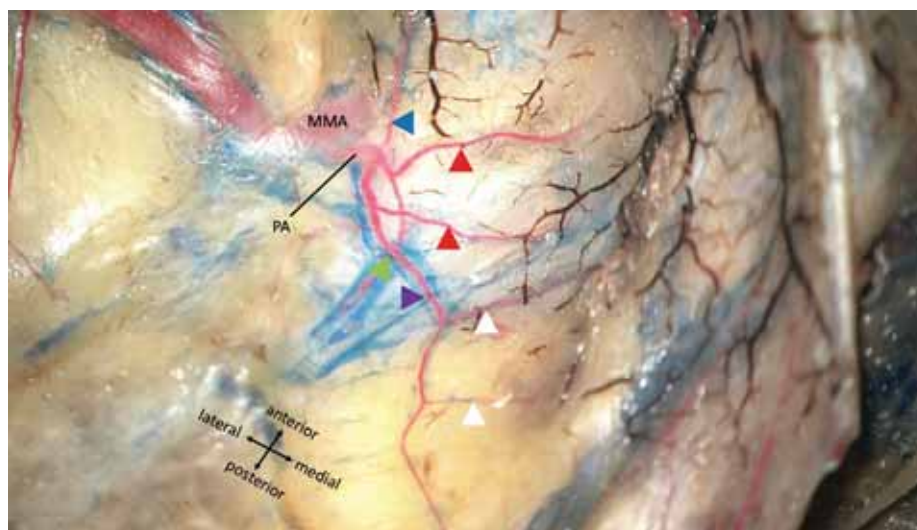
Figure 6. Left sided petrosal artery giving off an anterior dural branch (blue triangle) and then forming an arterial circle that ends (green triangle) to continue as a single petrosal artery (purple triangle) which gives off two medial dural branches (white triangles). Note the that the arterial circle gives two branches (red triangles) to the mandibular nerve (V3); MMA — middle meningeal artery; PA — petrosal artery.

distal portion is largely obscured, either partially or wholly, by the overlying bone of the middle cranial fossa floor [6]. Most commonly, it reaches the facial canal, also known as the fallopian canal, to supply the facial nerve by directly piercing the adjacent petrous part of the temporal bone surrounding the geniculate ganglion and the tympanic segment of the facial nerve. However, variations of this course will be detailed later [6]. Tiny branches to the neighbouring dura, as seen in our study, such as the dura over the posteromedial floor of the middle cranial fossa, and the petrous apex region, can also be given off before the petrosal artery enters the facial canal (Fig. 5) [17]. While travelling through this canal, it supplies the greater petrosal nerve [2].

The petrosal artery is usually the main supplier to the facial nerve crossing the middle cranial fossa floor and it provides other anastomosing branches in the region [6]. After entering the petrous part of the temporal bone laterally, it supplies the genicu-

Figure 7. Cadaveric example of a petrosal artery (PA) and middle meningeal artery (MMA) that arose from below the foramen spinosum and entered the floor of the middle cranial fossa through an unnamed aperture to then be 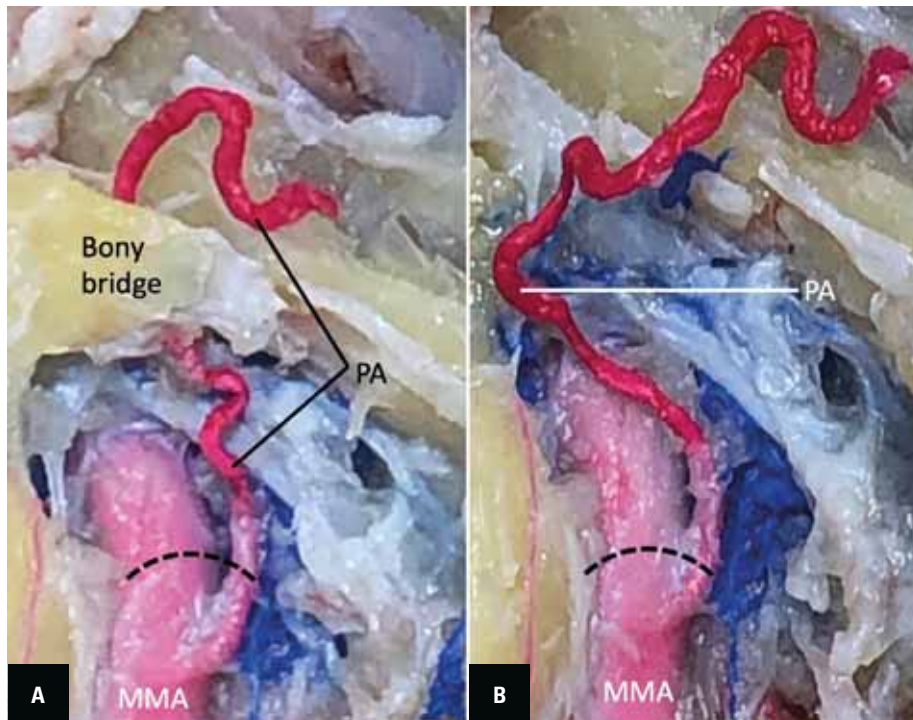covered by a bony bridge. The foramen spinosum (dotted lines) has been opened with adjacent bone to show the course of the petrosal artery; **A.** With the bony bridge; **B.** Following removal of the bony bridge.

late ganglion via small branches and subsequently supplies the tympanic segment of the facial nerve and the walls of the tympanic cavity [2]. At what can be considered an arterial crossroads between the external carotid, internal carotid, and vertebrobasilar systems, the petrosal artery is in position to participate in anastomoses with the anterior and posterior MMA divisions, accessory meningeal artery, carotid branch of the ascending pharyngeal artery, inferolateral trunk, and medial and lateral tentorial arteries [3, 6, 17]. Moreover, the stylomastoid branch of the posterior auricular artery anastomoses with the petrosal artery near the tympanic segment of the facial nerve via a tiny branch that enters the facial canal [9, 20]. Although no single artery supplies the entire facial nerve, the petrosal artery together with the stylomastoid branch is an important contributor to the facial nerve arterial arcade, an anastomotic loop supplying the intratemporal facial nerve and geniculate ganglion (Fig. 1) [30]. The petrosal artery alone supplies the pregeniculate part of the facial nerve [13]. Potentially, it can also participate in anastomoses with the meningohypophysial trunk, the recurrent meningeal artery of the ophthalmic artery, the mastoid branch of the occipital artery, and the

subarcuate artery [3, 17, 33]. Additionally, the stylomastoid branch, along with other collateral arteries including the inferolateral trunk of the cavernous internal carotid artery and labyrinthine arteries, can supply the facial nerve [30].

Among other anastomosing branches, the initial portion of the petrosal artery can give off a branch entering the middle ear. This is the superior tympanic artery, the petrosal remnant of the stapedial artery. The superior tympanic artery generally arises from the middle meningeal system but has been more specifically described as arising from the petrosal artery itself. Entering the middle ear adjacent to the lesser superficial petrosal nerve, it supplies the superior portion of the tympanic cavity and participates in a middle ear anastomosis with the caroticotympanic branch of the internal carotid artery, the inferior tympanic artery from the ascending pharyngeal artery, and the posterior tympanic artery from the occipital artery (Fig. 1) [3, 4, 14].

According to Lasjaunias et al. (1987) [14], the superior tympanic artery belongs to the petrosal artery, which divides initially into two branches, medial and lateral. The medial branch courses towards the cavernous sinus area. It provides some arterial con-
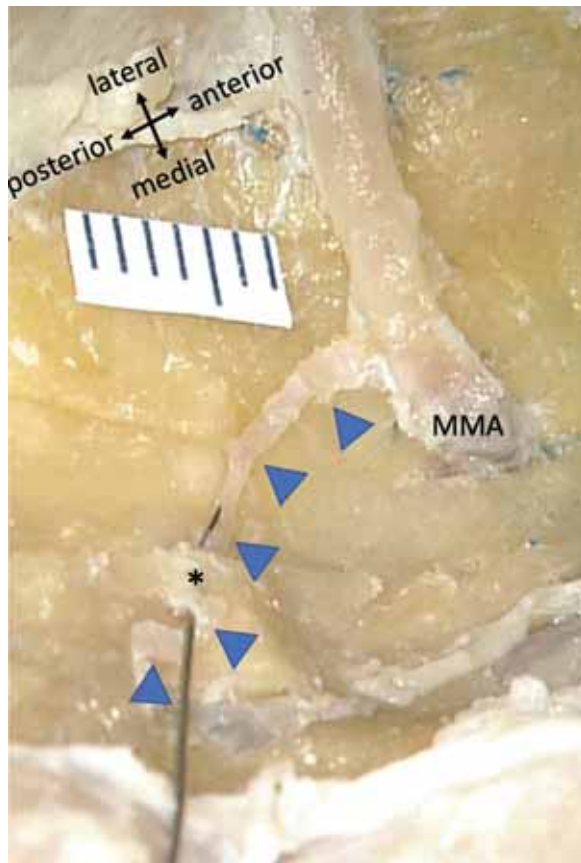
Figure 8. Left petrosal artery (blue triangles) with an intracranial origin from the middle meningeal artery (MMA) and then during its course in the floor of the middle cranial fossa, covered by a bridge of bone (*). Note that a small needle is inserted under the bony bridge.

tribution to the dura over the inferior wall of the cavernous sinus and anastomoses with the ascending pharyngeal branches in the temporal bone and with branches of the internal carotid artery [17, 28]. However, a superior tympanic artery arising from the petrosal artery was found in only 7.5% of sides in our cadaveric study. Sant'Anna et al. (2021) [26] report that this cavernous branch contributes to supplying the trigeminal ganglion, the mandibular nerve, and the dura surrounding the foramen ovale. The lateral branch also provides two additional smaller branches. One of these, the so-called basal tentorial branch, reaches the basal tentorial margin to distribute blood to the upper part of the cerebellopontine angle above the internal acoustic meatus [13–15]. The petrosal artery thus contributes to supplying blood to the medial portion of the tentorium cerebelli at its insertion along the petrous ridge, in addition to the walls of the superior petrosal sinus [3, 17]. At this level, it participates in the basal arcade of the tentorium cerebelli,

anastomosing medially with the lateral branch of the clivus and laterally with the basal tentorial branch of the petrosquamosal branch [13–15]. The other smaller branch of its lateral division, extending more posteriorly and superiorly, accompanies the greater petrosal nerve, often giving off small branches to supply it [14, 15]. It is via this nervous branch that the petrosal artery reaches the facial canal, contributing blood to the geniculate ganglion and facial nerve, anastomosing with the stylomastoid artery, and giving off the superior tympanic artery [14, 15]. While acknowledging it as a branch of the petrosal artery, some sources have stated that the superior tympanic artery is responsible for supplying the facial nerve and geniculate ganglion [4, 10].

Other descriptions of the branches of the intracranial MMA distinguish the petrosal and superior tympanic arteries as two distinct entities and this is supported by our study with the superior tympanic artery originating from the petrosal artery found only as a variation. According to one such description, the petrosal artery, upon giving off an anastomotic branch to the superior tympanic artery, divides into two primary branches [27]. The first of these supplies the geniculate ganglion and further divides into two smaller vessels, passing within the facial nerve territory to course either in the direction of the internal acoustic meatus or towards the periphery. The second main branch bypasses the geniculate ganglion and continues as a descending branch in an area between the facial nerve trunk and the facial canal. The petrosal artery then anastomoses with the stylomastoid artery in the upper third of the vertical segment of the facial canal [27]. The superior tympanic artery originates from the MMA separately from the petrosal artery and can either anastomose with the petrosal artery or travel into the facial canal accompanying the lesser petrosal nerve [3, 13].

Regardless of the inconsistencies in the literature, the evidence can be generally summarised as follows. The petrosal artery courses along the petrous apex posterolaterally, traverses within the facial canal, pierces the petrous bone, participates in several potential anastomoses, and gives off branches (varying in size and number) that provide arterial arborisation to several structures: the proximal tympanic (horizontal) segment of the facial nerve, the geniculate ganglion via the facial nerve arterial arcade, the maxillary and mandibular divisions of the trigeminal nerve, the medial portion of the tentorium cerebelli, and

the superior aspect of the tympanic cavity just distal to the geniculate ganglion via its superior tympanic branch [3, 6, 17].

Variations

The branch of the petrosal artery that traverses to supply the facial nerve is anatomically variable in respect of its dominance, course, branches, and origin. In nearly all cases (90%) studied by Lasjaunias et al. [15], the petrosal artery was consistently the dominant supply to the intrapetrous facial nerve territory. In the remaining 10%, the branch of the petrosal artery that reached the facial nerve supplied only the geniculate ganglion; the remaining portion of the facial nerve was supplied by the stylomastoid artery which arises from the posterior auricular artery. Paullus et al. (1977) [24] reported that the branch with the largest diameter of the petrosal artery travelled with the greater petrosal nerve in 92% of cases and with the lesser petrosal nerve in 8%. In the same study, the petrosal artery was noted in 46% to send branches to the trigeminal ganglion.

In 2008, El-Khouly et al. [6] examined the course of the petrosal artery as it travelled along the middle cranial fossa floor in 25 cadaveric specimens and described three distinct types of variation in its supply to the facial nerve. Of the 25 middle cranial fossae studied, the MMA was absent in one specimen; in four others, the branch of the petrosal artery to the facial nerve was absent although the MMA was intact. In patients lacking a branch of the petrosal artery to the facial nerve, the accessory meningeal artery or the stylomastoid artery from the posterior auricular artery, or a combination of the two, possibly contributes to supplying this nerve [29]. The labyrinthine artery has also been cited as a potential contributor to this arterial supply, joining the nerve at the cerebellopontine angle or the internal acoustic meatus [6]. The classification system of the petrosal artery supplying the facial nerve in the remaining middle cranial fossae (n = 20) is as follows:
— type A (65%): the petrosal artery travels through the bone near the geniculate ganglion and/or tympanic part of the facial nerve;
— type B (20%): the petrosal artery travels via the hiatus of the greater petrosal nerve to supply the facial nerve near the geniculate ganglion;
— type C (15%): two petrosal arteries, arising from either the MMA or a single petrosal artery, reach

the facial nerve. One of them pierces the bone adjacent to the geniculate ganglion, as in type A; the other enters the hiatus of the greater petrosal nerve, as in type B.

In type A, the petrosal artery was either exposed as it traversed the floor of the middle cranial fossa floor, or hidden, partially or completely, in the bone below this surface. Upon reaching the geniculate ganglion, the type A petrosal artery either sent a branch only to the ganglion and the tympanic part of the facial nerve, or divided into two arteries distal to its origin: a medial branch following along the ganglion and the greater petrosal nerve, and a lateral branch running along the tympanic segment of the facial nerve. The type B petrosal artery split into two branches near its origin, one artery traveling to the facial nerve and the other to the trigeminal nerve. El-Khouly et al. [6] thus reported the petrosal artery frequently giving rise to trigeminal ganglion branches, as mentioned previously. It is worth noting that the trigeminal branch is more likely to arise when the petrosal branches pass via the hiatus of the greater petrosal nerve, as opposed to passing through the bone surrounding the geniculate ganglion [6]. With type C arteries, in which the MMA gave off two petrosal arteries, one branch reaches the geniculate ganglion and the other the tympanic part of the facial nerve. In the alternative type C pattern, one petrosal artery divides into two arteries, one which reaches the Gasserian ganglion and the other reaches the tympanic part of the facial nerve.

Moreover, El-Khouly et al. (2008) [6] observed variations in the origin of the petrosal artery. In 17 (81%) of the specimens studied, the artery originated from the MMA above the foramen spinosum, an average of 5 mm distal to its intracranial end. In the remaining 19% it arose an average of 4 mm below this level, traversing the middle cranial fossa through the foramen spinosum or through a small adjacent opening. Jittapiromsak et al. (2009) [12] observed that the petrosal artery originated superior to the foramen spinosum in 50% of their specimens. Paullus et al. (1977) [24] described the petrosal artery arising distal to the foramen spinosum in 42% of specimens and proximal to it in 58%. Rarely, it arises from the internal carotid artery to give branches to the dura mater and subarcuate fossa [13]. It is duplicated in a small number of cases [13].

In our cadaveric study of the petrosal artery, variations were common. The petrosal artery arose from
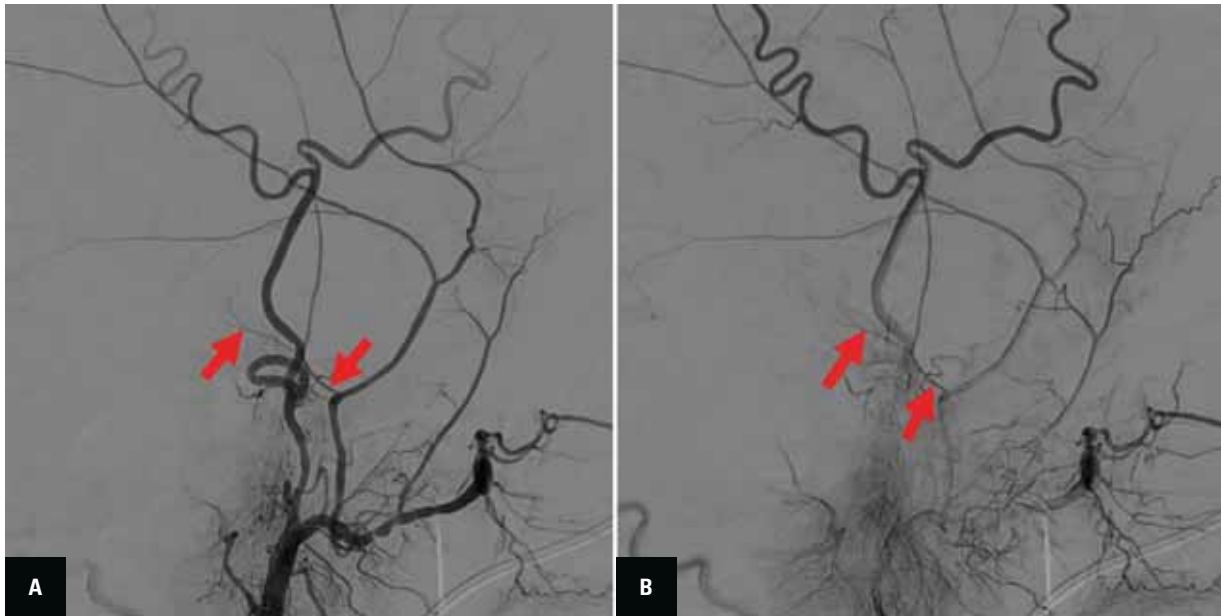
Figure 9. Lateral projection showing the left petrosal artery (red arrows) following external carotid artery angiogram; **A.** Arterial phase; **B.** Late arterial/capillary phase.

below the foramen spinosum on 12.5% of sides. On 1 (2.5%) of these, the artery did not enter the middle cranial fossa but entered the skull through a more medial and unnamed aperture to then travel under a bony bridge. Bony bridges covering the petrosal artery were found on 7.5% of sides. A superior tympanic artery arose from the petrosal artery on three sides. One left sided petrosal artery (2.5%) was found to form an arterial circle that gave off dural branches and also branches to V3.

Embryology

The foundations for cerebral blood flow are laid at the 1.3 mm embryonic stage by the pharyngeal arch arteries. The internal carotid artery pair begin their development at the 3 mm stage (day 24), formed by fusion of the third pharyngeal arch arteries [19, 23]. At the 4 mm stage, the internal carotid artery splits into two parts, the anterior providing major contributions to the circle of Willis, olfactory region, and optic region; the posterior persists as the posterior communicating artery [19, 22]. From 11 to 12 mm, the middle cerebral artery can be seen sprouting from the anterior communicating artery off the anterior part of the internal carotid artery. It is the major source of blood for the cerebral cortex, becoming more prominent at the 16–18 mm stage [22, 23].

After the early groundwork stages, intercarotid anastomosis formation peaks between the 20- and 40-mm stages, the 1st and 2nd pharyngeal arches forming the keystone stapedial artery [18]. The stapedial artery also gives off anterior (maxillofacial) and posterior (supraorbital) divisions, the former becoming the maxillary and mandibular arteries, the latter becoming the intracranial segment of the MMA while also carrying anastomosing branches to the ophthalmic artery (supraorbital branch of the MMA) [5]. The segment of the MMA outside of the skull is formed by fusion of the external carotid artery and maxillary artery. The stapedial artery begins to involute, leaving the remnant tympanic branch of the MMA. In some instances, the lacrimal artery can remain attached to the retroorbital branches of the stapedial artery. If these fail to regress, a lacrimal-MMA connection can form in addition to many other aberrant variations owing to the number of sprouting and regression events involved in forming the supra- and infra-orbital anastomoses with the MMA, and in anastomoses between the carotids [5].

Imaging

When the middle cranial fossa vasculature is examined, the petrosal artery (Fig. 9) should not be confused with the superior tympanic artery, which is either (a) occasionally another branch of the MMA closely related to the petrosal artery, or (b) a branch of the petrosal artery itself, as mentioned above [1, 8, 13, 20]. However, the petrosquamosal branch of

the MMA is most frequently mistaken for the petrosal artery on digital subtraction angiography imaging, especially in lateral view. These two arterial structures are difficult to distinguish by this technique owing to the superimposed projection of the petrosquamosal branch and the overlying dense petrous bone almost completely obscuring the course of the petrosal artery [29]. Frontal projections are far more useful for the purpose because the petrosal artery projects more superiorly in this view [29].

Clinical implications

The petrosal artery can be injured during invasive procedures such as extradural approaches to the middle cranial fossa floor, drilling of the middle cranial fossa, or MMA embolization, risking facial nerve palsy [6]. Elevation of the dura and drilling of the middle cranial fossa floor are most common during approaches to the internal acoustic meatus through the middle fossa and anterior petrosectomy. The risk of petrosal artery injury is greater with the former procedure since the latter is performed posterior to the greater petrosal nerve and medial to the internal acoustic meatus [6]. Drilling away bone anterosuperior to the geniculate ganglion and tympanic segment can pose a greater risk of petrosal artery injury since it most commonly traverses through that area. El-Khouly et al. [6] recommend intradural dissection around the foramen spinosum, splitting the dura mater into two parts, to avoid injury to the petrosal artery during elevation of the dura. However, Shibao et al. [30] contend on the basis of histological data that such a precaution could lead instead to venous plexus haemorrhage and make it far more difficult to identify the greater petrosal nerve.

In the literature, the origin of the petrosal artery varies. In some cases, it originates inferior to the level of the foramen spinosum, so interruption of the MMA at this level would not result in facial nerve ischaemia [6]. However, since it most often arises from the MMA distal to the foramen spinosum, certain procedures such as intraspinosal MMA ligation could pose a greater risk of facial nerve ischaemia, though a sufficient collateral arterial supply could prevent it [30]. Regardless, interruption of the MMA greater than 10 mm beyond the foramen spinosum would unlikely result in ischaemia to the facial nerve as the petrosal artery would already have originated [6]. Other risk factors of facial nerve palsy after extradural subtemporal procedures include direct intradural dissection and tension on the greater petrosal nerve [6, 30]. Although these latter cases could also be due to disruption of blood flow to the facial nerve, e.g. petrosal artery.

Since the MMA is a common pathway for endovascular embolisation to treat dural arteriovenous fistulas, meningiomas, and chronic subdural haematomas, embolisation of the intracranial MMA near the foramen spinosum carries an inherent risk of facial nerve palsy due to the petrosal artery [6, 8, 29]. MMA embolisation at a proximal position near the origin of the petrosal artery is particularly dangerous. The resulting facial nerve palsy is generally temporary, with symptoms resolving following the development of a collateral supply and steroid therapy [8]. In any case, certain precautions have been recommended when proximal embolisation of the MMA is necessary. The microcatheter should be advanced to a position beyond the point where the petrosal artery branches [29, 33]. As found in our study, bony bridges, might inhibit such microcatheter advancement. Embolic materials should be injected cautiously to avoid regurgitation into anastomosis points of the petrosal artery [33]. The consensus is that particles (depending on size) carry less risk of penetrating smaller anastomotic channels than liquid agents and should be used for precluding embolic complications involving cranial nerves [8, 29, 33]; certain calibrated particles used as embolic agents are too large in diameter to penetrate the vasa nervorum branches of the petrosal artery [31]. Non-adhesive liquid embolic agents such as the copolymer ethylene-vinyl alcohol can be difficult to control owing to their viscosity and lack of adhesion to vessel walls [16]. There are reports of complications with Onyx migration following endovascular treatment of dural arteriovenous fistulas, resulting in facial nerve palsy [16, 31]. Ischaemic injury related to the facial nerve can result from migration of Onyx or cyanoacrylate derivatives into the vasa nervorum branches of the petrosal artery and/or compression by the embolic agent [16]. For example, Onyx can reflux into the petrosal artery, which as previously mentioned is an important contributor to the facial nerve arcade, potentially leading to dysfunction of the facial and greater petrosal nerves. Thus, the severity and outcome of such injury depends largely on the permanence of the embolic agent used [16]. Onyx is a permanent embolic agent with a low recanalisation rate, so any facial nerve injuries it causes have a poorer prognosis than when

temporary agents are used [7]. Recommendations in the literature to minimise complications include a slower rate of Onyx injection, using detachable tip microcatheters, distal injection with wedged microcatheters, and using temporary embolic agents [2, 8, 21, 31].

Vascular disturbance to the facial nerve has been associated with Bell's palsy. Additionally, ischaemic events can result from compression of the arterial supply by oedema of the nerve in the facial canal. El-Khouly et al. [6] suggest that the arterial supplies to both the trigeminal nerves and facial nerves might be compromised. As mentioned in multiple reports, the petrosal artery sends branches to the trigeminal nerve. This could explain trigeminal nerve involvement in some cases of Bell's palsies if the petrosal artery suffers any disturbance. Pecket and Schattner (1982) [25] proposed that Bell's palsy is a diabetic mononeuropathy. Diabetic small vessel disease could affect the peripheral blood supply to the facial nerve through the stylomastoid artery and branches of the petrosal artery, embolisation of both arteries producing clinical outcomes comparable to Bell's palsy.

CONCLUSIONS

The petrosal artery is an important branch of the MMA and supplies the facial nerve. Along with cadaveric and angiographic data, this paper provides a comprehensive review of the anatomy of the petrosal artery and variations in its origin, dominance, anastomoses, and course. Particular emphasis has been placed on correlating its anatomical structure clinically. Recommendations in the literature to minimise iatrogenic injury to it have also been provided. Awareness of the petrosal artery is crucial for interventionalists and neurosurgeons when they consider the risk of interrupting it during invasive extradural subtemporal approaches to the floor of the middle cranial fossa and postoperative facial nerve palsy. A thorough anatomical knowledge of the petrosal artery and to its relationship to the facial nerve and other neurovascular structures is necessary to facilitate effective endovascular treatment and to preclude facial nerve complications.

Acknowledgements

REFERENCES

1. Baltsavias G, Kumar R, Valavanis A. The pharyngo-tympano-stapedial variant of the middle meningeal artery. A case report. Interv Neuroradiol. 2012; 18(3): 255–258, doi: 10.1177/159101991201800302, indexed in Pubmed: 22958762.

2. Bhatia KD, Kortman H, Lee H, et al. Facial nerve arterial arcade supply in dural arteriovenous fistulas: anatomy and treatment strategies. AJNR Am J Neuroradiol. 2020; 41(4): 687–692, doi: 10.3174/ajnr.A6449, indexed in Pubmed: 32193191.

3. Bonasia S, Smajda S, Ciccio G, et al. Middle meningeal artery: anatomy and variations. AJNR Am J Neuroradiol. 2020; 41(10): 1777–1785, doi: 10.3174/ajnr.A6739, indexed in Pubmed: 32883667.

4. Byrne JV. Tutorials in endovascular neurosurgery and interventional neuroradiology. 1st ed. Springer, Berlin Heidelberg 2012.

5. Dilenge D, Ascherl GF. Variations of the ophthalmic and middle meningeal arteries: relation to the embryonic stapedial artery. Am J Neuroradiol. 1980; 1(1): 45–54, indexed in Pubmed: 6779589.

6. El-Khouly H, Fernandez-Miranda J, Rhoton AL. Blood supply of the facial nerve in the middle fossa: the petrosal artery. Neurosurgery. 2008; 62(5 Suppl 2): ONS297–ONS303, doi: 10.1227/01.neu.0000326010.53821.a3, indexed in Pubmed: 18596507.

7. Gatto LA, Saurin F, Koppe GL, et al. Facial palsy after embolization of dural arteriovenous fistula: a case report and literature review. Surg Neurol Int. 2017; 8: 270, doi: 10.4103/sni.sni_428_16, indexed in Pubmed: 29204306.

8. Geibprasert S, Pongpech S, Armstrong D, et al. Dangerous extracranial-intracranial anastomoses and supply to the cranial nerves: vessels the neurointerventionalist needs to know. AJNR Am J Neuroradiol. 2009; 30(8): 1459–1468, doi: 10.3174/ajnr.A1500, indexed in Pubmed: 19279274.

9. Gray H. Anatomy, Descriptive and Applied, by Henry Gray. 18th ed., Thoroughly Rev. and Re-Edited with Additions, by Edward Anthony Spitzka … Illustrated with 1208 Engravings. Lea & Febiger, Philadelphia and New York 1910.

10. Harrigan MR, Deveikis JP. Handbook of cerebrovascular disease and neurointerventional technique. 3rd ed. Springer International Publishing 2018.

11. Iwanaga J, Singh V, Ohtsuka A, et al. Acknowledging the use of human cadaveric tissues in research papers: Recommendations from anatomical journal editors. Clin Anat. 2021; 34(1): 2–4, doi: 10.1002/ca.23671, indexed in Pubmed: 32808702.

12. Jittapiromsak P, Sabuncuoglu H, Deshmukh P, et al. Greater superficial petrosal nerve dissection: back to front or front to back? Neurosurgery. 2009; 64(5 Suppl 2): 253–258, doi: 10.1227/01.NEU.0000343522.79764.15, indexed in Pubmed: 19404106.

13. Krmpotic-Nemanic J, Draf W, Helms J. Surgical anatomy of head and neck. 1st ed. Springer-Verlag, Berlin Heidelberg 1988.
14. Lasjaunias P, Berenstein A. Surgical Neuroangiography: 1. Functional Anatomy of Craniofacial Arteries. 1st ed. Springer, Berlin Heidelberg 1987.
15. Lasjaunias P, Berenstein A, Brugge KG. Clinical vascular anatomy and variations. 2nd ed. Springer, Berlin Heidelberg 2001.
16. Lim EH, Mohd Khairi DM. Facial nerve palsy after transarterial embolization of dural arteriovenous fistula. Egypt J Ear Nose Throat Allied Sci. 2017; 18(2): 159–161, doi: 10.1016/j.ejenta.2016.11.002.
17. Martins C, Yasuda A, Campero A, et al. Microsurgical anatomy of the dural arteries. Operative Neurosurgery. 2005; 56(suppl_4): ONS-211–ONS-251, doi: 10.1227/01. neu.0000144823.94402.3d.
18. McLennan JE, Rosenbaum AE, Haughton VM. Internal carotid origins of the middle meningeal artery. Neuroradiology. 1974; 7(5): 265–275, indexed in Pubmed: 4413942.
19. Menshawi K, Mohr JP, Gutierrez J. A functional perspective on the embryology and anatomy of the cerebral blood supply. J Stroke. 2015; 17(2): 144–158, doi: 10.5853/jos.2015.17.2.144, indexed in Pubmed: 26060802.
20. Moonis G, Mani K, O'Malley J, et al. A venous cause for facial canal enlargement: multidetector row CT findings and histopathologic correlation. AJNR Am J Neuroradiol. 2011; 32(5): E83–E84, doi: 10.3174/ajnr.A2094, indexed in Pubmed: 20395388.
21. Odat H, Alawneh K, Al-Qudah M. Facial nerve paralysis after onyx embolization of a jugular paraganglioma: a case report with a long-term follow up. J Clin Med. 2018; 7(3): 48, doi: 10.3390/jcm7030048, indexed in Pubmed: 29518926.
22. Padget DH. The circle of Willis: its embryology and anatomy. Comstock Publishing, New York 1945.
23. Paget DH. The development of the cranial arteries in the human embryo. Contrib Embryol. 1948; 32: 205–262.

24. Paullus WS, Pait TG, Rhoton AI. Microsurgical exposure of the petrous portion of the carotid artery. J Neurosurg. 1977; 47(5): 713–726, doi: 10.3171/jns.1977.47.5.0713, indexed in Pubmed: 908935.
25. Pecket P, Schattner A. Concurrent Bell's palsy and diabetes mellitus: a diabetic mononeuropathy? J Neurol Neurosurg Psychiatry. 1982; 45(7): 652–655, doi: 10.1136/jnnp.45.7.652, indexed in Pubmed: 7119834.
26. Sant'Anna MAF, Luciano LL, Chaves PHS, et al. Anatomy of the middle meningeal artery. Arquivos Brasileiros de Neurocirurgia. 2021; 40(4): e339–e348, doi: 10.1055/s-0041-1733863.
27. Schuknecht HF. Pathology of the ear. 2nd ed. Lea & Febiger, Philadelphia 1993.
28. Shao YX, Xie X, Liang HS, et al. Microsurgical anatomy of the greater superficial petrosal nerve. World Neurosurg. 2012; 77(1): 172–182, doi: 10.1016/j.wneu.2011.06.035, indexed in Pubmed: 22120573.
29. Shapiro M, Walker M, Carroll KT, et al. Neuroanatomy of cranial dural vessels: implications for subdural hematoma embolization. J Neurointerv Surg. 2021; 13(5): 471–477, doi: 10.1136/neurintsurg-2020-016798, indexed in Pubmed: 33632880.
30. Shibao S, Borghei-Razavi H, Yoshida K. Intraspinosum middle meningeal artery ligation: a simple technique to control bleeding in the middle fossa during the anterior transpetrosal approach. Oper Neurosurg (Hagerstown). 2017; 13(2): 163–172, doi: 10.1093/ons/opw013, indexed in Pubmed: 28927220.
31. Shotar E, Premat K, Lenck S, et al. Middle meningeal artery embolization for chronic subdural hematoma. Case Med Res. 2019; 32(1): 57–67, doi: 10.31525/ct1-nct04065113, indexed in Pubmed: 33625552.
32. Stranding S. Gray's anatomy: the anatomical basis of clinical practice. 41st ed. Elsevier, New York 2016.
33. Tanoue S, Kiyosue H, Mori H, et al. Maxillary artery: functional and imaging anatomy for safe and effective transcatheter treatment. Radiographics. 2013; 33(7): e209–e224, doi: 10.1148/rg.337125173, indexed in Pubmed: 24224604.

VM VIA MEDICA

ORIGINAL ARTICLE

Unravelling the mystery of porta hepatis for surgical benefit

A. Saha[1], P. Srimani[2]

[1]Department of Anatomy, R.G. Kar Medical College, Kolkata, West Bengal, India
[2]Department of Anatomy, Calcutta National Medical College, Kolkata, West Bengal, India

Background: Hepatobilliary surgery is nowadays growing with increasing popularity throughout the world with advent of newer liver imaging modalities. Anticipating a wide range of morphological variations of porta hepatis (PH), a precise understanding is pertinent to preoperative diagnosis, operative procedure and post-operative outcome of hepatobiliary disease.
Materials and methods: Considering recent interest, present study was undertaken. One-hundred and ten isolated adult cadaveric livers of unknown age and sex were dissected to explore detail morphology and morphometry of PH.
Results: Classical picture of PH was observed in 20% liver. The standard representation of structures was highest in hepatic artery (59.1%) followed by portal vein (55.5%) and hepatic duct (51.8%). On the basis of structural distribution PH was described as 16 types. Maximum variable number was found in hepatic artery followed by portal vein and hepatic duct. In morphometric analysis, transverse diameter of PH was more than antero-posterior diameter, indicated that PH was slightly oval in transverse plane. Position of PH was more towards posterior and slightly right in inferior surface of liver.
Conclusions: Variations of portal anatomy regarding circulatory and biliary dynamics is worth knowing in successful planning of hepatobiliary surgeries with least complications. (Folia Morphol 2023; 82, 3: 580–586)

Key words: liver, porta hepatis, variation, morphology, morphometry

INTRODUCTION

Despite advancement in hepatic interventions, potential vascular complications might occur in hepatobilliary surgery due to topographical alteration with structural variability of porta hepatis (PH) or hepatic hilum resulting high degree of morbidity or even death [24]. In order to address the complications posed by variant vasculo-biliary system, detailed knowledge about portal anatomy assumes critical. Variations of biliary tree and hepatic arterial anatomy are reported more frequent than portal venous variants. Careful handling of such circulatory and biliary dynamics of liver is important during live donor liver transplantation. As surgical view is limited to delineate hepatic anatomy, introduction of minimally invasive methods also remains challenging for surgeons. Moreover, presence of aberrant components might be an obstacle during operation if over-looked. Unanticipated anatomical variations may cause increase in graft ischaemia time with associated risk of post-operative graft dysfunction and emphasizes need of additional anastomosis [3, 5, 11, 23].

Unfortunately, magnetic resonance cholangio-pancreatography (MRCP) study prior to any surgical intervention often fail to recognise all anomalies with certainty. Sensitivity of MRCP is only 74% in defining bile duct anomaly. Pre-treatment computed tomography failed to identify aberrant left hepatic artery in 31% cases [17, 27]. Therefore, accuracy and reliability of radiological analysis is still depending on anatomical references. Thus, present cadaveric study was attempted to revisit the vascular and biliary components of liver at PH updating the unusual configurations with an effort aimed at morphometry.

MATERIALS AND METHODS

One hundred and ten formalin fixed adult cadaveric livers of unknown age and sex without any pathological lesion were observed. Dissection of PH was done meticulously to observe number and position of portal vein (V), hepatic artery (A) and hepatic ducts (D). Specimens deviated from two divisions of portal vein, hepatic artery and hepatic duct were marked as variant and noted carefully with photographs. Different types of PH were categorised on the basis of morphology (number portal vein associated with number of hepatic artery and hepatic duct). For determination of morphometric data of PH and its exact position on inferior surface, following parameters were measured and mentioned in Figure 1 as follows:
— dimensions of PH:
  • transverse diameter ('a' — from left to right end of PH),
  • antero-posterior diameter ('b' — from anterior to posterior end of PH),
  • circumference ('c' — along the margin of non-peritoneal area with thread and finally thread length was calculated);
— measurements of inferior surface of liver for position of PH:
  • distance from left end of inferior surface of liver to left margin of PH — marked as "A",
  • distance from right end of inferior surface of liver to right margin of PH — marked as "B",
  • distance from postero-inferior border of liver to posterior margin of PH — marked as "C",
  • distance from inferior border of liver to anterior margin of PH — marked as "D".
All measurements were done thrice at the level of portal vein before its division by vernier calliper, measuring scale and thread and average of three
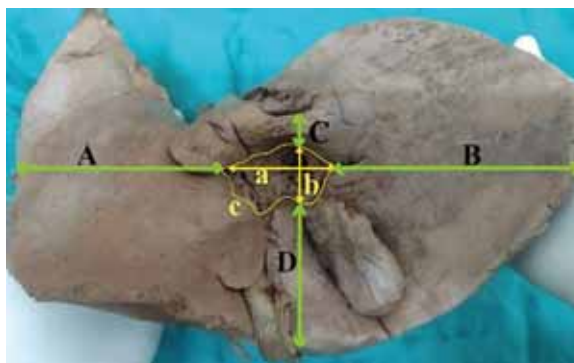

Figure 1. Morphometric measurements: a — transverse diameter of porta hepatis (PH); b — antero-posterior diameter of PH; c — circumference of PH; A — distance between left end of inferior surface and PH; B — distance between right end of inferior surface and PH; C — distance from postero-inferior border of liver to posterior margin of PH; D — distance from inferior border of liver to anterior margin of PH.

measurements were finally taken. Data were summarised by descriptive statistics and results were tabulated. All statistical calculations were performed using software SPSS version 23.

RESULTS

Standard morphology of PH was found in 20%. Rests 80% were variants in terms of numbers of either by portal vein or hepatic artery or hepatic duct or in combinations. Numeral normalcy was highest in hepatic artery followed by portal vein and hepatic duct. In all cases, arrangements of portal structures were ducts-arteries-veins from anterior to posterior. Detailed morphology of portal structures are depicted in Table 1 as follows:
— portal vein (V): conventional two divisions were present in 55.5% specimens. In the rest, vein was either single or three or four in numbers respectively;
— hepatic artery (A): usual presentation of two divisions was in 59.1% livers. In the rest, artery was variable with higher incidence in cases of single followed by three, four, five or six arteries respectively;
— hepatic duct (D): classical arrangement was in 51.8% cases. In the rest, PH represented with either single or with three ducts.

Figure 2 represents details about incidences of different morphological types of PH.

Sixteen types of PH were configured morphologically by numerical presence of structures in ascending order giving priority to vein, then artery and then duct. Thus, type 1 represented the minimum number

Table 1. Morphology and morphometry of portal structures

Portal structures, n (%)			Dimensions of porta hepatis [cm]	
Vein [V]	One	41 (37.3)	Transverse diameter	
	Two	61 (55.5)	Range	2.0–4.0
	Three	6 (5.5)	Mean ± SD	2.93 ± 0.51
	Four	2 (1.8)	95% CI: LL/UL	2.83/3.03
Artery [A]	One	21 (19.1)	Antero-posterior diameter	
	Two	65 (59.1)	Range	1.2–2.8
	Three	14 (12.7)	Mean ± SD	1.82 ± 0.38
	Four	6 (5.5)	95% CI: LL/UL	1.75/1.89
	Five	2 (1.8)	Circumference	
	Six	2 (1.8)	Range	4.8–11.5
Hepatic duct [D]	One	51 (46.4)	Mean ± SD	8.33 ± 1.63
	Two	57 (51.8)	95% CI: LL/UL	8.02/8.64
	Three	2 (1.8)		

CI — confidence interval; SD — standard deviation; LL — lower limit; UL — upper limit

Figure 2. Types 1–16 porta hepatis with incidences; V — portal vein; A — hepatic artery; D — hepatic duct.

Table 2. Comparison of portal structures between previous and present study

		Present study [%]	Sapna et al. [23] [%]	Gupta et al. [12] [%]	Neginhal and Kulkarni [20] [%]
Vein	One	37.3	50.8	84	26
	Two	55.5	44.1	12	72
	Three	5.5	5.1	4	–
	Four	1.8	–	–	2
Artery	One	19.1	20.3	4	8
	Two	59.1	55.9	32	56
	Three	12.7	15.3	36	26
	Four	5.5	8.5	25	8
	Five	1.8	–	4	2
	Six	1.8	–	–	–
Duct	One	46.4	79.7	76	100
	Two	51.8	16.9	20	–
	Three	1.8	3.4	4	–
Classical portal structures		20%	1.7%	0%	0%
Highest combination of portal structures		1V2A2D (23.6%)	1V2A1D (25.4%)	2A1V1D (32%)	2V2A1D (36%)

Table 3. Comparison of morphometry of porta hepatis between previous and present study

Studies	Transverse diameter [cm]	Antero-posterior diameter [cm]	Circumference [cm]
Sapna et al. [23]	4.825	2.433	–
Gupta et al. [12]	3.80 ± 1.03	1.79 ± 0.43	13.61 ± 1.92
Neginhal and Kulkarni [20]	3.17 ± 0.50	1.68 ± 0.36	10.46 ± 1.415
Present study	2.93 ± 0.51	1.82 ± 0.38	8.33 ± 1.63

Data are shown as mean ± standard deviation.

of portal vein with minimum number of hepatic artery and duct; whereas type 16 represented maximum number of portal vein with variable number of hepatic arteries and ducts. Type 3 (1V2A2D) was found as highest incidence followed by type 9 (2V2A2D) and type 7 (2V1A1D), respectively. In total 13.6% cases (type 1, 4, 6, 14) all of the three portal structures (vein, artery and ducts) were atypical in number. Maximum number of structures were noted as 9 (2V6A1D) in type 13. Absence of structures was not witnessed by present study.

Morphometry

Table 1 represents details about dimensions.
— Dimensions of PH: Morphometric data as transverse diameter (a) larger than antero-posterior diameter (b) indicated outline of PH was slightly oval in transverse plane.

— Measurements for position of PH: In left–right plane, length of "A" varied from 5.4 to 10.5 cm, with mean ± standard deviation (SD): 7.55 ± ± 1.36, whereas "B" varied from 5.2 to 11.6 cm, with mean ± SD: 7.35 ± 1.49. In antero-posterior plane, "C" and "D" ranged from 2 cm to 3.7 cm with mean ± SD: 2.76 ± 0.49 and 3.2 cm to 6.7 cm with mean ± SD: 4.87 ± 0.99, respectively. Schematic representation of morphometric measurements with position PH is shown in Figure 1.

Results of the present study with previous works have been compared in Tables 2 and 3 regarding morphology and morphometry of PH, respectively.

DISCUSSION

Highly variable vascular and biliary structures of the PH can impact clinical outcomes [3, 5, 9, 13]. In present study, arrangements of portal structures

were traditional in all livers as previously reported [12, 20, 23], but their number varied. Classical structures were seen in 20% cases in present study which was either missing or in a very low percentage (01.7%) in previous studies [12, 20, 23]. Rather authors [12, 20, 23] reported different "non-traditional" portal anatomy in higher percentages. We also found varied combinations of portal structures as 16 types. Type 3 represented as highest number (23.6% cases) which is in conflict with previous studies. In our study, maximum number of veins was 4, arteries were 6 and ducts were 3, which is discrepant with others by numbers and percentages. Vascular injury along with biliary tract trauma has a mortality of 50–75% for portal vein and 40–80% for hepatic artery. The most difficult part of management encountered in abdominal trauma is associated with PH injuries which have high potential for immediate or late mortality [25]. Thus, knowledge of prevalence of morphological variation is quite often helpful for surgical planning. So, it is imperative that the clinician working on this area must be well versed with the detail of anatomical knowledge and its variations.

Table 2 presents comparison of portal structures between present and previous studies.

Knowledge about portal vein variation is important in identifying the location of liver lesion as portal vein along with hepatic veins are used as landmarks in determining segmental anatomy of liver [11]. Transhepatic embolisation of portal vein is gaining acceptance as a method to induce contralateral liver hypertrophy in patients with small future remnant livers [16]. Absence of the right portal vein occurs in 16.5% of patients and is associated with trifurcation of the main vein to right anterior, posterior segmental veins and left portal vein. Absence of left portal vein occurs in 1% of patients. Portal vein trifurcation is a relative contraindication to liver transplantation using living donors as multiple anastomoses needed for right lobe graft transplantation [18]. In another study, incidence of overall variations of portal vein was as high as 27.4%; main portal vein branching variation was 21.5% and right portal vein variation was 3.9% [14]. In 51% of the liver, portal vein did not bifurcate before entering the liver [23]. We also found the same in 37.3% cases. On the other hand, portal vein bifurcation and trifurcation were in 83.3% and 15.2% cases [4]. We too noted three veins in 5.5% liver. Though most abdominal venous variations are asymptomatic, awareness about existence of these

variations decreases the complication rates in surgical procedures [5, 9].

While liver transplantation is often the best treatment option for end-stage acute or chronic hepatic disease, vascular complications following transplantation may hamper long-term success with an incidence rate as high as 9% [2, 7]. Furthermore donor selection is influence by arterial anatomy as liver grafts with multiple arteries are usually avoided [18]. Standard hepatic artery persists in 50–75% patients as previously reported [10, 13, 22, 26] but we found in 59.1% cases. Contrarily, variant anatomy has important implications in planning liver resections or placement of hepatic artery infusion catheters or pumps [10, 22, 26]. Multiple arteries (three-five) were reported in varied percentages by previous authors [12, 20, 23]. We also observed multiple arteries (maximum 6) in 21.8% liver.

Risk of bile duct variation is increased by presence of variant portal vein [26]. Normal biliary anatomy is thought to be present in 58% of the population [3, 19]. MRCP study shows an aberrant right hepatic duct in 4.8%, a right posterior hepatic duct in 5.7% and trifurcation of the duct in 0.8% of patients [8]. Kostov and Kobakov [15] found variation of hepatic ducts in 27.8% cases. Other authors reported the absence of right hepatic duct in 26% and absence of left hepatic duct in 2% of cases (Ohkubo et al., 2004 [21]). Single hepatic duct was observed in 100% cases by Neginhal and Kulkarni [20], 79.7% by Sapna et al. [23] and 76% cases by Gupta et al. [12]. However, our study found only 46.4% PH with single duct. Three ducts were seen in 3.4% and 4% by Sapna et al. [23] and Gupta et al. [12], respectively. Our study documented only 1.8% cases with 3 ducts. Accurate knowledge about such accessory hepatic ducts and also their position is important, especially during laparoscopic cholecystectomies, as incidence of bile duct injuries is as twice as high when compared with open cholecystectomies [6].

As majority of interventional procedures are made at the PH, which has a different location on the visceral surface of the liver, meticulous surgical technique and expertise are necessary to approach in a systematic way to obtain complete removal of tumour in peritoneal carcinomatosis. The centripetal approach from right side, left side and from anterior side is recommended to achieve a complete circumferential dissection [1]. Thus, a thorough assessment PH before initiation of dissection is needed. To describe

the location of the PH in respect of the borders of the visceral surface we performed detailed morphometric measurements which have not been reported yet. Regarding dimensions of porta (antero-posterior diameter, transverse diameter and circumference), our study is very close to Neginhal and Kulkarni [20] report, but quite different from others [12, 23]. Table 3 presents comparison of morphometry of PH between previous and present study.

CONCLUSIONS

Literature on anatomical knowledge of PH has not proved to be adequate to reduce the incidence of iatrogenic complications. Thus our main focus was to study portal anatomy as it guides surgical decision-making and impacts on outcomes. Variable portal structures were noted in 80% cases in this study. High incidence of variations helped us to come into a conclusion on anatomical classification of 16 types of PH depending on the number of structural pattern which may contribute additional benefit particularly in the field of portal surgery. Present study also found maximum 6 arteries in PH which differ from previous studies. Till now no anatomical morphometric study regarding position of PH has been reported as per our knowledge, which needs to be highlighted to achieve best possible results in surgical techniques in this challenging area of the abdomen.

Conflict of interest: None declared

REFERENCES

1. Aydin N, Sardi A, Milovanov V. Approach to the porta hepatis during cytoreductive surgery: technical considerations. Ann Surg Oncol. 2016; 23(2): 552–555, doi: 10.1245/s10434-015-4872-x, indexed in Pubmed: 26577121.
2. Caiado AH, Blasbalg R, Marcelino AS, et al. Complications of liver transplantation: multimodality imaging approach. Radiographics. 2007; 27(5): 1401–1417, doi: 10.1148/rg.275065129, indexed in Pubmed: 17848699.
3. Catalano OA, Singh AH, Uppot RN, et al. Vascular and biliary variants in the liver: implications for liver surgery. Radiographics. 2008; 28(2): 359–378, doi: 10.1148/rg.282075099, indexed in Pubmed: 18349445.
4. Chaib E. Absence of bifurcation of the portal vein. Surg Radiol Anat. 2009; 31(5): 389–392, doi: 10.1007/s00276-008-0413-7, indexed in Pubmed: 18795219.
5. Covey AM, Brody LA, Getrajdman GI, et al. Incidence, patterns, and clinical relevance of variant portal vein anatomy. Am J Roentgenol. 2004; 183(4): 1055–1064, doi: 10.2214/ajr.183.4.1831055, indexed in Pubmed: 15385304.
6. Devi KP. The study of variations of extra-hepatic biliary apparatus. IOSR J Dental Med Sci. 2013; 5(5): 25–31, doi: 10.9790/0853-0552531.
7. Duffy JP, Hong JC, Farmer DG, et al. Vascular complications of orthotopic liver transplantation: experience in more than 4,200 patients. J Am Coll Surg. 2009; 208(5): 896––903, doi: 10.1016/j.jamcollsurg.2008.12.032, indexed in Pubmed: 19476857.
8. Düşünceli E, Erden A, Erden I. [Anatomic variations of the bile ducts: MRCP findings]. Tani Girisim Radyol. 2004; 10(4): 296–303, indexed in Pubmed: 15611920.
9. Erbay N, Raptopoulos V, Pomfret EA, et al. Living donor liver transplantation in adults: vascular variants important in surgical planning for donors and recipients. Am J Roentgenol. 2003; 181(1): 109–114, doi: 10.2214/ajr.181.1.1810109, indexed in Pubmed: 12818839.
10. Fasel JH, Muster M, Gailloud P, et al. Duplicated hepatic artery: radiologic and surgical implications. Acta Anat (Basel). 1996; 157(2): 164–168, doi: 10.1159/000147878, indexed in Pubmed: 9142340.
11. Garg S, Kumar K, Sahni D, et al. Surgical anatomy of the vasculobiliary apparatus at the hepatic hilum as applied to liver transplantations and major liver resections. J Anat Soc India. 2018; 67(1): 61–69, doi: 10.1016/j.jasi.2018.02.002.
12. Gupta D, Sharma P, Gandotra A. Porta hepatis in normal liver. Int J Biomed Adv Res. 2017; 8(3): 121–125.
13. Hiatt JR, Gabbay J, Busuttil RW. Surgical anatomy of the hepatic arteries in 1000 cases. Ann Surg. 1994; 220(1): 50–52, doi: 10.1097/00000658-199407000-00008, indexed in Pubmed: 8024358.
14. Koç Z, Oğuzkurt L, Ulusan S. Portal vein variations: clinical implications and frequencies in routine abdominal multidetector CT. Diagn Interv Radiol. 2007; 13(2): 75–80, indexed in Pubmed: 17562511.
15. Kostov DV, Kobakov GL. Six rare biliary tract anatomic variations: implications for liver surgery. Eurasian J Med. 2011; 43(2): 67–72, doi: 10.5152/eajm.2011.16, indexed in Pubmed: 25610166.
16. Madoff DC, Hicks ME, Vauthey JN, et al. Transhepatic portal vein embolization: anatomy, indications, and technical considerations. Radiographics. 2002; 22(5): 1063–1076, doi: 10.1148/radiographics.22.5.g02se161063, indexed in Pubmed: 12235336.
17. McSweeney SE, Kim TK, Jang HJ, et al. Biliary anatomy in potential right hepatic lobe living donor liver transplantation (LDLT): the utility of CT cholangiography in the setting of inconclusive MRCP. Eur J Radiol. 2012; 81(1): 6–12, doi: 10.1016/j.ejrad.2010.10.013, indexed in Pubmed: 21041052.
18. Mortelé KJ, Cantisani V, Troisi R, et al. Preoperative liver donor evaluation: Imaging and pitfalls. Liver Transpl. 2003; 9(9): S6–14, doi: 10.1053/jlts.2003.50199, indexed in Pubmed: 12942472.
19. Mortelé KJ, Ros PR. Anatomic variants of the biliary tree: MR cholangiographic findings and clinical applications. Am J Roentgenol. 2001; 177(2): 389–394, doi: 10.2214/ajr.177.2.1770389, indexed in Pubmed: 11461869.
20. Neginhal DD, Kulkarni UK. Normal anatomy of porta hepatis: a cadaveric study. Nat J Clin Anat. 2019; 8(1): 22, doi: 10.1055/s-0039-1688545.
21. Ohkubo M, Nagino M, Kamiya J, et al. Surgical anatomy of the bile ducts at the hepatic hilum as applied to living donor liver transplantation. Ann Surg. 2004; 239(1): 82–86, doi: 10.1097/01.sla.0000102934.93029.89, indexed in Pubmed: 14685104.

22. Redman HC, Reuter SR. Angiographic demonstration of surgically important vascular variations. Surg Gynecol Obstet. 1969; 129(1): 33–39, indexed in Pubmed: 5790699.

23. Sapna M, Shetty SD, Nayak S. A study on the number and arrangement of the structures passing through the porta hepatis in south indian population. Int J Morphol. 2015; 33(1): 164–168, doi: 10.4067/s0717-95022015000100026.

24. Seco M, Donato P, Costa J, et al. Vascular liver anatomy and main variants: what the radiologist must know. JBR-BTR. 2010; 93(4): 215–223, doi: 10.5334/jbr-btr.319, indexed in Pubmed: 20957897.

25. Sheldon GF, Lim RC, Yee ES, et al. Management of injuries to the porta hepatis. Ann Surg. 1985; 202(5): 539–545, doi: 10.1097/00000658-198511000-00002, indexed in Pubmed: 4051602.

26. Suzuki T, Nakayasu A, Kawabe K, et al. Surgical significance of anatomic variations of the hepatic artery. Am J Surg. 1971; 122(4): 505–512, doi: 10.1016/0002-9610(71)90476-4, indexed in Pubmed: 5098656.

27. van den Hoven AF, Smits MLJ, de Keizer B, et al. Identifying aberrant hepatic arteries prior to intra-arterial radioembolization. Cardiovasc Intervent Radiol. 2014; 37(6): 1482–1493, doi: 10.1007/s00270-014-0845-x, indexed in Pubmed: 24469409.

VM

VIA MEDICA

ORIGINAL ARTICLE

Foramen magnum morphometry in children based on computed tomography examination

R. Wilk[1], M. Moroz[1], K. Zięba[2], W. Likus[1]

[1]Department of Anatomy, Faculty of Health Sciences in Katowice, Medical University of Silesia, Katowice, Poland
[2]Department of Forensic Medicine and Forensic Toxicology, Faculty of Medicine in Katowice, Medical University of Silesia, Katowice, Poland

Background: The foramen magnum is the largest opening at the base of the skull. The dimensions of the foramen magnum are of significant clinical importance because of the vital structures that pass through it. The aim of the study was the morphometric analysis of the foramen magnum in children based on head computed tomography (CT).
Materials and methods: The study was carried out on 84 CTs of the head of children aged 0–18 years; seven age groups were distinguished. The sagittal and transverse dimensions were measured to determine the growth rate, changes between groups, and differences in the foramen size by sex. Statistical analysis of changes was performed.
Results: The entire group's mean transverse and sagittal dimensions were 29.08 mm (standard deviation [SD] 3.4 mm) and 35.63 (SD 4.23) mm. By sex, the mean transverse dimension in girls was 28.53 (SD 3.25) mm, and in boys, 29.6 (SD 3.49) mm. The mean sagittal dimension was 35.15 (SD 3.76) mm in girls and 36.09 (SD 4.64) mm in boys. Both dimensions were higher for the male sex. A statistically significant increase in the foramen magnum size was demonstrated up to the age of 36 months in the following age groups; above that age, the increase was statistically insignificant.
Conclusions: The dimensions were similar to those described in adults a moderate dependence of the foramen magnum size on age was found. (Folia Morphol 2023; 82, 3: 587–595)
Key words: morphometry, foramen magnum, computed tomography, children

INTRODUCTION

The foramen magnum (FM) is surrounded by all parts of the occipital bone. It connects the posterior fossa with the vertebral canal allowing the correct relationship between the skull and the cervical spine. The FM research is the subject of interest to many biological sciences such as anatomy, anthropology, and forensic medicine [1, 10]. FM measurements are of great importance in skull base surgery and greatly facilitate the diagnosis of various diseases that develop in this area [6, 18]. In anthropology and forensics, the skull exhibits features of sexual variability and is used to determine gender with 80% accuracy [9, 20]. Anthropometric studies on FM concerning sex differences conducted on macerated skulls concluded that the transverse and sagittal dimensions of the FM in
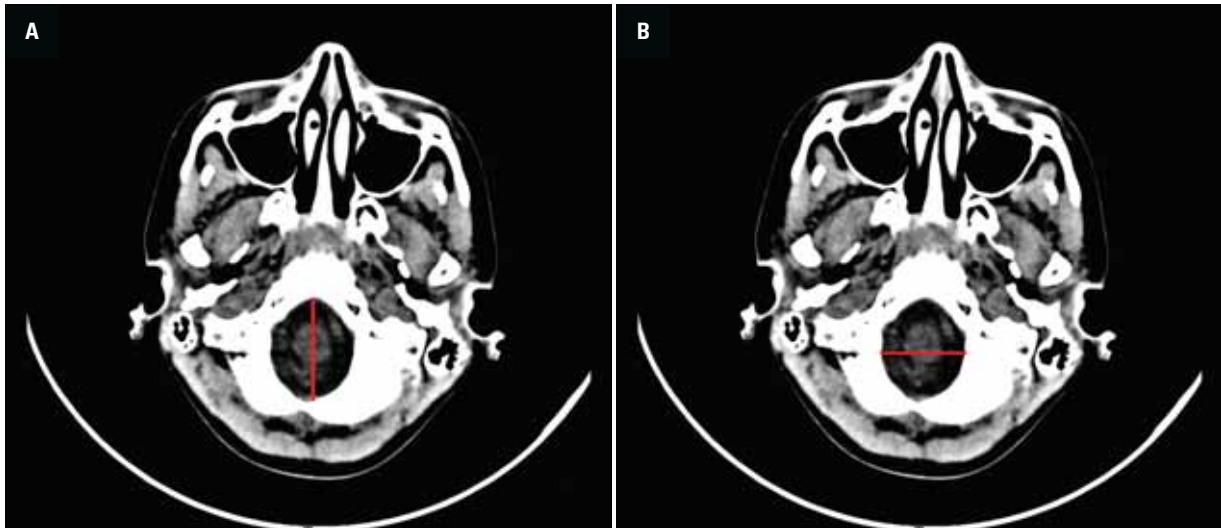
Figure 1. A. The sagittal dimension; **B.** The transverse dimension.

men were greater than in women [20]. Further studies in this field based on computed tomography (CT) and magnetic resonance imaging [15, 32] confirmed this correlation.

There is no precise data on FM dimensions change with age in children. Morphometric skull examinations in children are performed when the cranial development disorders are suspected or to assess the progress of the disease or treatment. The dimensions of FM are essential in many developmental malformations [6, 22] or skull deformities resulting from various diseases [3, 12, 18, 20]. In all these cases, the dimensions of the FM are altered, overlapping the developmental changes in FM size depending on the child's age. Therefore, it seems reasonable to determine the average dimensions of FM for individual age groups and depending on sex. The aim of the study was the morphometric analysis of FM in children of different ages based on CT examination to determine the growth rate of FM with age, based on sagittal and transverse dimensions and sex differences in each age group.

MATERIALS AND METHODS
Study group

A retrospective study was conducted on 84 (41 girls and 43 boys) selected head CT scans from patients diagnosed at the Independent Public Clinical Hospital No. 6 at the Medical University of Silesia in Katowice. The research material included CT images obtained from Polish Caucasian children aged 0 to 18 years referred for imaging examinations due to various medical reasons. Patients were defined as "without any changes" in the opinion of experienced radiologists. The exclusion criteria of the morphometric analysis were; incorrect patient positioning, artefacts (patient movement, blurred scan), detected trauma in the occipital bone area, and abnormal FM shape. The CT examinations were performed using Somatom Plus 4 CT scanner in spiral technique and the standard diagnostic protocol for head examination. Morphometric analysis and linear measurements of FM on CT images were performed using the Onis Dicom Viewer. The cross-sections of the head were carried out parallel to the Frankfurt plane at the level of the FM. The following were measured: the sagittal — basion — opisthon distance (APD) and transverse dimension in its highest width (TD) (Fig. 1) [15]. Statistical analysis was performed in Statistica 13.3 StatSoft PL. The patients were divided into age groups: 0–12 months, 12–36 months, 3–6 years, 6–9 years, 9–12 years, 12–15 years, and 15–18 years. The following variables were calculated for each group, depending on sex: the minimum and maximum of both FM dimensions, mean, standard deviation (SD), and median.

Additionally, the Pearson's correlation coefficients on the growth rate with age for both dimensions were calculated. To analyse the differences between adjacent age groups and by gender, the Student's t-test was calculated, assuming that $p < 0.05$ is statistically significant. Because this is a retrospective study, it does not require the consent of the Bioethics Committee.

Table 1. The results obtained for the sagittal and transverse dimensions of foramen magnum for the study group

Variable	N	Min [mm]	Max [mm]	Mean [mm]	Median	SD
Sagittal dimension	84	24.79	43.09	35.63	36.29	4.23
Transverse dimension	84	19.27	35.62	29.08	29.53	3.4

N — number of patients; Min — minimum; Max — maximum; SD — standard deviation

Table 2. Sagittal dimension and transverse dimension values of foramen magnum obtained in a particular age group

Age group	N	Min [mm]	Max [mm]	Mean [mm]	Median	SD	P
Sagittal dimension							
0–12 months	12	24.79	32.33	29.84	30.30	2.30	
12–36 months	12	27.21	37.85	33.76	34.86	3.41	< 0.01
3–6 years	12	29.46	41.61	34.84	33.95	3.79	0.47
6–9 years	12	32.38	42.51	36.72	35.70	3.82	0.24
9–12 years	12	30.72	42.9	38.32	38.45	3.25	0.28
12–15 years	12	33.74	43.09	38.74	38.48	3.24	0.75
15–18 years	12	32.74	39.83	37.19	37.65	2.16	0.18
Transverse dimension							
0–12 months	12	19.27	27.93	23.66	23.90	2.12	
12–36 months	12	24.76	32.37	28.16	27.99	2.57	< 0.01
3–6 years	12	23.36	33.46	29.26	29.41	3.13	0.36
6–9 years	12	26.43	34.64	30.04	29.51	2.20	0.49
9–12 years	12	27.51	33.78	31.03	31.65	2.43	0.31
12–15 years	12	25.24	35.62	30.90	31.19	2.51	0.9
15–18 years	12	27.28	35.08	30.49	30.17	2.33	0.68

N — number of patients; Min — minimum; Max — maximum; SD — standard deviation; P — statistical significance coefficient between adjacent age groups

RESULTS

The results obtained for the entire study group (n = 84) are presented in Table 1. The normal distribution of both dimensions was checked and confirmed. The mean value of both dimensions was statistically significantly higher in boys than in girls (Table 2). The mean values of both dimensions for the entire group and by gender are presented in Figure 2. The dimensions of the FM in individual age groups are presented in Table 3. Pearson's correlation coefficient for the sagittal dimension (APD) and for the transverse dimension (TD) with age was r = 0.59 and r = 0.56, respectively. Both coefficients indicated a moderate relationship between the size of FM dimensions and age. After determining the significance level for all age groups, only between groups of 0–12 months and 12–36 months, the changes for both the APD and TD were highly statistically significant (p < 0.01). The mean APD values in the individual age groups showed a slight increase with age up to 12 years. Only between groups of 12–15 years and 15–18
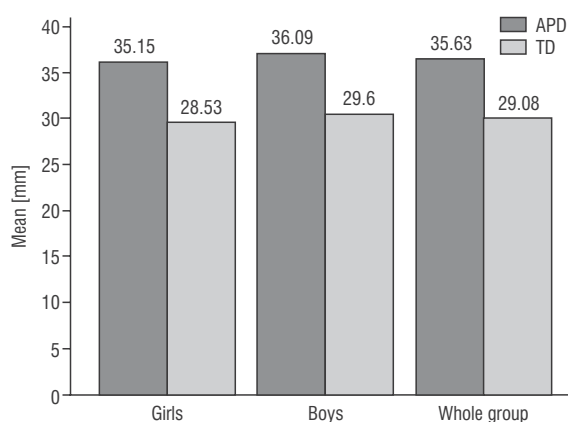
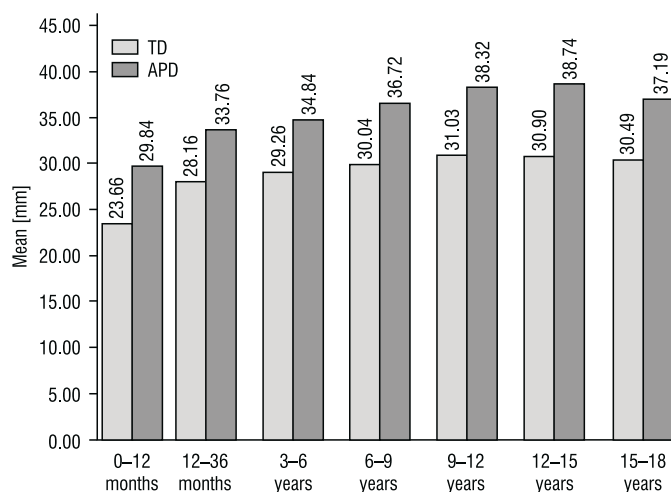**Figure 2.** Mean values of sagittal dimension (APD) and transverse dimension (TD) obtained for the whole group and by sex.

years, a decrease in the value of this dimension was observed (Fig. 3). In TD, an increase in the value of the dimension between individual age groups was observed up to the age of 12 years; however, these changes were not statistically significant, the changes between groups 9–12 years to 12–15 years and

Table 3. The results obtained for the sagittal and transverse dimensions of foramen magnum for the study group by sex

Variable	Sex	N	Min [mm]	Max [mm]	Mean [mm]	Median	SD
Sagittal dimension	Girls	41	28.17	42.9	35.15	35.42	3.76
	Boys	43	24.79	43.09	36.09	36.78	4.64
Transverse dimension	Girls	41	22.54	35.08	28.53	28.81	3.25
	Boys	43	19.27	35.62	29.6	30.06	3.49

N — number of patients; Min — minimum; Max — maximum; SD — standard deviation

Figure 3. Mean values of the sagittal (APD) and transverse dimension (TD) obtained for a particular age group.

12–15 years to 15–18 years groups show the decrease of the value (Fig. 3).

When comparing both FM dimensions obtained in individual age groups, an increase up to 12 years of age was noted; however, in older age groups, these values slightly decreased (Fig. 3). After analysing the descriptive statistics for the APD and TD for all age groups, the same groups were analysed by gender. In the analysis of changes in APD in individual age groups for girls, the increase in dimension was visible between the youngest 0–12 months group and 12–36 months group, as well as between 3–6 years and 6–9 years group; above this age the dimension remained at a similar level (Table 4). In boys, APD in the 0–12 months group was lower than in girls, and in the 12–36 months group, over the age of 3, the values for both sexes were similar; APD increase was visible up to the age of 12 years. In the oldest group, the mean APD values in girls and boys were identical (Table 4). The TD of the FM showed significantly lower values than APD in the corresponding age group. In girls, the increase in FM size was visible between the age groups of 0–12 months, 3–6 years, and 6–9 years, with the most significant changes between

those groups, then the FM size remained at a similar level (Table 5). Although there were some exceptions, the TD dimensions measured in boys in most study groups were higher than in girls. The most significant increase in the mean in TD was visible between the age groups of 0–12 months, 12–36 months, and 3–6 years; then, the size of the foramen did not change significantly. There were also the most significant changes in dimensions between the age groups. In the oldest age group of boys (15–18 years), there was a substantial decrease in the mean extent from 35.62 to 31.1 mm (Table 5).

The differences in the dimensions of the FM between the sexes were not significant, although noticeable in most age groups. APD was higher in boys than in girls (except for the 0–12 months group). The most significant difference was observed in the 12–15 years group (p < 0.02), and in the other groups, the differences were not statistically significant (p > 0.05) (Table 4). As in the case of APD, the differences in TD between girls and boys in individual age groups were noticeable but not significant. The most remarkable differences were observed in the 12–15 years group (p < 0.02) and the 3–6 years group (p < 0.05), in the

Table 4. Sagittal dimension values of the foramen magnum obtained by sex

Age group	Sex	n/%	Min [mm]	Max [mm]	Mean [mm]	Median	SD	P
0–12 months	Girls	6/50%	28.17	32.33	30.45	30.30	1.47	0.39
	Boys	6/50%	24.79	31.93	29.24	29.75	2.93	
12–36 months	Girls	3/25%	29.99	35.68	33.7	35.42	3.21	0.97
	Boys	9/75%	27.21	37.85	33.78	34.3	3.67	
3–6 years	Girls	5/41.7%	29.46	37.52	32.47	31.7	3.02	0.06
	Boys	7/58.3%	31.73	41.61	36.54	37.45	3.5	
6–9 years	Girls	7/58.3%	32.28	42.51	35.69	34.66	3.38	0.29
	Boys	5/41.7%	32.41	42.16	38.16	39.6	4.31	
9–12 years	Girls	6/50%	30.72	42.9	37.97	38.48	4.09	0.73
	Boys	6/50%	34.54	42.09	38.66	38.45	2.48	
12–15 years	Girls	6/50%	33.74	40.59	36.69	36.63	2.49	< 0.02
	Boys	6/50%	36.65	43.09	40.79	41.61	2.61	
15–18 years	Girls	8/66.7%	32.74	39.83	37.13	37.71	2.45	0.90
	Boys	4/33.3%	35.12	39.01	37.31	37.56	1.73	

n/% — number of patients/percent; Min — minimum; Max — maximum; SD — standard deviation; P — statistical significance coefficient

Table 5. Transverse dimension values of the foramen magnum obtained by sex

Age group	Sex	n/%	Min [mm]	Max [mm]	Mean [mm]	Median	SD	P
0–12 months	Girls	6/50%	22.54	24.62	23.78	23.9	0.82	0.86
	Boys	6/50%	19.27	27.93	23.54	23.47	3.03	
12–36 months	Girls	3/25%	24.76	27.37	26.12	26.23	1.31	0.12
	Boys	9/75%	25.09	32.37	28.85	29.62	2.57	
3–6 years	Girls	5/41.7%	23.36	30.91	27.2	27.06	3.16	< 0.05
	Boys	7/58.3%	27.7	33.46	30.74	31.45	2.28	
6–9 years	Girls	7/58.3%	27.4	34.64	30.16	29.55	2.27	0.83
	Boys	5/41.7%	26.43	32.31	29.87	29.44	2.33	
9–12 years	Girls	6/50%	27.51	33.78	29.89	28.62	2.7	0.11
	Boys	6/50%	29.51	33.75	32.17	32.21	1.6	
12–15 years	Girls	6/50%	25.24	31.65	29.3	29.7	2.18	< 0.02
	Boys	6/50%	30.99	35.62	32.5	31.82	1.73	
15–18 years	Girls	8/66.7%	27.28	35.08	30.8	30.03	2.66	0.55
	Boys	4/33.3%	27.53	31.1	29.88	30.45	1.63	

n/% — number of patients/percent; Min — minimum; Max — maximum; SD — standard deviation; P — statistical significance coefficient

other groups, the differences did not show statistical significance (p > 0.05) (Table 5).

DISCUSSION

The morphometry of the foramen magnum is of great clinical importance. The shape and size of FM are subject to changes in craniocervical region pathologies, which compresses the structures that pass through it and causes several undesirable symptoms [15]. Determining the dimensions of FM is vital in the case of many developmental defects [6, 22].

Knowing the dimensions of the FM is essential for diagnosing many diseases. Still, it is also invaluable in planning surgical interventions within the skull base, for example, in the case of craniovertebral stenosis or FM meningioma [3, 12]. The reduction in the size of the FM is found in patients with achondroplasia due to significantly lower skull base growth due to premature bone fusion [22]. In the case of patients with Chiari I and II malformations, the dimensions of FM were more significant than in the healthy population (mainly transverse) as a consequence of the

appearance of the cerebellar tonsil herniation and the displacement of brain structures toward the spinal canal and the deformation of FM as an effect of intracranial pressure [4, 6, 19]. In anthropology, morphometric studies help to determine the anthropometric differences between populations, such as ethnicity, sex, age, genetic factors, eating habits, and regional changes related to the living environment, which may influence the shape and size of bone structures [11] but also distinguish the norm from a pathological condition [33]. In the case of forensic examinations, the skeleton is often incomplete, making it challenging to identify sex, so the dimensions of FM and other features of the skull base can be used for this purpose [11]. Analysing the function of FM, Vinutha et al. [32] stated that no muscles influence changing its shape and size. The shape and size of FM are essential parameters in determining risk factors in patients with craniovertebral anomalies [21, 26], the normal range of its APD and TD is significant.

In most FM studies, the results came from the measurements taken in adults, both with macerated skulls and with imaging studies [10, 14, 32]. Research on children is rare and therefore presented results have additional value. The mean APD calculated for the entire study group of children was 35.63 (SD 4.23) mm. The mean TD was 29.08 (SD 3.4) mm, which indicates a certain disproportion between TD and APD which is similar to the observations made by selected other authors [5, 20].

Analysing the age groups, More et al. [14] compared two age groups of children: 0–9 years and 10–19 years group using CT examination. In the study cited, in the age group 0–9 years, the mean of APD was 36.00 (SD 6.93) mm, and TD was 27.85 (SD 0.64) mm. In the 10–19 years, both dimensions were 35.70 (SD 3.38) mm and 29.45 (SD 2.86) mm, respectively. By averaging the results obtained in our study for the group of 0–9 years, the APD was 33.79 (SD 4.15) mm, TD for the same group 27.78 (SD 3.5) mm. In the 10–18 years group, the values were 39.39 (SD 2.92) mm for APD and 30.81 (SD 2.37) mm for TD. Both studies show some discrepancies, especially in APD of the foramen magnum, caused most likely by the population differences (Indian population), sample size (250 CT examinations), and the measurement technique; in TD, the differences between both studies were slight. Our study group was divided into smaller age groups covering shorter periods of a child's development,

making it possible to analyse FM changes according to age.

The presented study showed a moderate dependence of the increase in FM's sagittal and transverse dimension with age (APD, r = 0.59; TD, r = 0.56). The research conducted by Samara et al. [23] found a weak negative linear correlation between the age of the subjects and both dimensions measured (APD, r = –0.15; TD, r = –0.14). In our work, slight changes were observed between adjacent age groups. However, most of these changes didn't show statistical significance (p > 0.05). Only for groups 0–12 months and 12–36 months the difference was highly statistically significant (p < 0.01), proving FM's rapid growth in this period.

The mean values of foramen magnum APD and TD presented in our work were similar to studies based on adults. In a survey by Radhika et al. [21] conducted on 150 macerated skulls of an adult Indian population, the mean APD was 35.30 (SD 2.7) mm, and the mean TD was 29.49 (SD 2.6) mm, which was close to the mean values of the entire study population obtained in our research. In similar studies conducted by Patel and Mehta [19] and Ganapathy et al. [7] on the Indian population of adults, the results were within one SD compared to the results of our work.

The study by Osunwoke et al. [17] showed results very close to ours in the skulls of the African population of adults, the same as Natsis et al. [16] in their studies conducted on the Greek people of adults and Pires et al. [20] in the Brazilian population. In the studies by Gruber et al. [8] carried out on the skulls of adults in the European population, the mean APD was 36.6 (SD 2.8) mm and the TD 31.1 (SD 2.7) mm, which were higher than the values obtained in our study, but still in the range of one SD. The results of Chethan et al. [5] obtained in the Turkish population in adults showed results slightly lower than those presented in our study, the same as Tubbs et al. [29] in the Caucasian population. At the same time, they didn't notice any significant differences in the dimensions of FM between different sexes. The study of Ulcay et al. [30] conducted in the Turkish population showed the mean APD at 35.81 mm and TD at 28.14 mm, which were similar to our results. Additionally, they suggested evaluating the shape of the FM predicted from the primary cranial index and measurements.

Based on the data presented above, it can be concluded that the results obtained by us in children

did not differ significantly from the results obtained by other authors in adults. In some cases, the FM dimensions of adults [5, 9, 25, 29, 30] were lower or higher than the mean values obtained by us in children. The differences from the presented data could be due to race differences, the measurement method used, or the sample size.

The increase of both measured dimensions in the present study was observed up to the age of 12, the changes were slight, and the most significant growth was visible up to the age of 3 and then slowed down. Shepur et al. [25] and Shmeltzer [24], in their study, stated that FM reaches its maximum size in early childhood, which is in line with our results if we take into consideration statistically significant changes; however, slight changes are still visible up to the age of 12 years. On the other hand, those studies confirmed that FM does not undergo significant secondary sexual changes during adolescence [24, 25] which is in line with our research. This may indicate that the size of FM increases to this age and then does not change; the same changes between individual age groups did not show statistically significant differences over the age of 3 years old.

In the case of the sex division in most analysed studies [5, 19], there was no certainty about the sex of the examined skulls, so they were studied together, or there were no sex differences in the FM dimensions described [5]. In our studies, taking gender into account, the mean APD value for girls was 35.15 (SD 3.76) mm, and for boys, it was slightly higher, reaching the value of 36.09 (SD 4.64) mm. The mean TD was lower for girls, 28.53 (SD 3.25) mm, while 29.6 (SD 3.49) mm for boys. Due to the lack of studies on children available in literature, the obtained results were compared, as before, with the results of adults. The results are similar to those obtained in our work, with differences within one SD from the mean. Manoel et al. [11], in the studies of Brazilian adult skulls, showed that APD in women was 35.1 (SD 3.3) mm and in men 35.7 (SD 2.9) mm, TD was in the range of 29.4 (SD 2.3) mm in women and 30.3 (SD 2.0) mm in men, obtained results were similar to our results. Samara et al. [23] and Moodley et al. [13] showed identical results. Studies by Shepur et al. [25], carried out in 150 adult skulls, presented results lower than ours obtained in children. Another study conducted by Murshed et al. [15] showed slightly higher results than the results obtained in our study. The results in women were lower but in men were higher than ours. Studies on

skulls in the Polish adult population by Tomaszewska et al. [28] also confirmed smaller dimensions of FM in women compared to men, which was consistent with the correct sex classification of skulls in 90% of cases.

The examination of the skulls based on CT also confirmed sexual dimorphism of FM in terms of both measured morphometric dimensions, confirming their higher values in men than in women. Burdan et al. [2], in a study based on CTs of Polish adults, noted statistically significant differences in the dimensions of APD and TD between women and men; however, their results were higher than the values obtained in the presented study. Results of Tellioglu et al. [27] based on CT of adults in the Turkish population also showed results that go along with ours in women and men for both dimensions measured. Uthman et al. [31] showed results lower than ours, obtained in the Arabic population of adults; however, the study by Ilgüy et al. [9] on the European population presented the results a little higher than ours both for women and men.

Considering the results of all the studies mentioned above, it can be concluded that the results obtained in this study and the data available in the literature are comparable. In adults, the shape of FM shows interpersonal changes, and its determination is difficult to assign to strict classification [27]. However, it should be noted that sex differences in FM dimensions and their shape should be considered when performing clinical and radiological diagnostics and during preparation for surgical procedures [15].

CONCLUSIONS

Based on the results obtained and data from the analysed literature, it has been shown that the FM has the shape of an oval, where the sagittal dimension is greater than the TD. Both the sagittal and the TDs of the FM correlate poorly with age, so age is not a criterion for determining the dimensions of FM above 12 months of age. There are visible differences in FM dimensions depending on gender; higher values of FM dimensions were found in men, both children and adults.

Conflict of interest: None declared

REFERENCES

1. Bagley CA, Pindrik JA, Bookland MJ, et al. Cervicomedullary decompression for foramen magnum stenosis in achondroplasia. J Neurosurg. 2006; 104(3 Suppl): 166–172, doi: 10.3171/ped.2006.104.3.166, indexed in Pubmed: 16572633.

2. Burdan F, Dworzanska A, Dworzanski W, et al. Foramen magnum: new and old anthropological data. Glob J Anthropol Res. 2014; 1(1): 25–34, doi: 10.15379/2410-2806.2014.01.01.05.

3. Campero A, Baldoncini M, Villalonga JF, et al. Transcondylar fossa approach for resection of anterolateral foramen magnum meningioma: 2-dimensional operative video. World Neurosurg. 2021; 154: 91–92, doi: 10.1016/j.wneu.2021.07.058, indexed in Pubmed: 34303002.

4. Carpenter K, Iwanaga J, Aysenne A, et al. An anatomical model for studying cerebellar tonsillar herniation related to raised intracranial pressure. Clin Anat. 2022; 35(2): 251–255, doi: 10.1002/ca.23827, indexed in Pubmed: 34913515.

5. Chethan P, Prakash KG, Murlimanju BV, et al. Morphological analysis and morphometry of the foramen magnum: an anatomical investigation. Turk Neurosurg. 2012; 22(4): 416–419, doi: 10.5137/1019-5149.JTN.4297-11.1, indexed in Pubmed: 22843456.

6. Furtado SV, Thakre DJ, Venkatesh PK, et al. Morphometric analysis of foramen magnum dimensions and intracranial volume in pediatric Chiari I malformation. Acta Neurochir (Wien). 2010; 152(2): 221–227, doi: 10.1007/s00701-009-0480-5, indexed in Pubmed: 19672553.

7. Ganapathy A, Sadeesh T, Rao S. Morphometric analysis of foramen magnum in adult human skulls and CT images. Int J Cur Res Rev. 2014; 6: 11–15.

8. Gruber P, Henneberg M, Böni T, et al. Variability of human foramen magnum size. Anat Rec (Hoboken). 2009; 292(11): 1713–1719, doi: 10.1002/ar.21005, indexed in Pubmed: 19777568.

9. İlgüy D, İlgüy M, Ersan N, et al. Measurements of the foramen magnum and mandible in relation to sex using CBCT. J Forensic Sci. 2014; 59(3): 601–605, doi: 10.1111/1556-4029.12376, indexed in Pubmed: 24588134.

10. Madadin M, Menezes RG, Al Saif HS, et al. Morphometric evaluation of the foramen magnum for sex determination: a study from Saudi Arabia. J Forensic Leg Med. 2017; 46: 66–71, doi: 10.1016/j.jflm.2017.01.001, indexed in Pubmed: 28157592.

11. Manoel C, Prado FB, Caria PHF, et al. Morphometric analysis of the foramen magnum in human skulls of Brazilian individuals: its relation to gender. Braz J Morphol Sci. 2009; 26(2): 104–108.

12. Meyer FB, Ebersold MJ, Reese DF. Benign tumors of the foramen magnum. J Neurosurg. 1984; 61(1): 136–142, doi: 10.3171/jns.1984.61.1.0136, indexed in Pubmed: 6726388.

13. Moodley M, Rennie C, Lazarus L, et al. The morphometry and morphology of the foramen magnum in age and sex determination within the south african black population utilizing computer tomography (CT) scans. Int J Morphol. 2019; 37(1): 251–257, doi: 10.4067/s0717-95022019000100251.

14. More CB, Saha N, Vijayvargiya R. Morphological analysis of foramen magnum for gender determination by using computed tomography. J Oral Med Oral Surg Oral Pathol Oral Radiol. 2015; 1(2): 51–56.

15. Murshed KA, Cicekcibasi AE, Tuncer I. Morphometric evaluation of the foramen magnum and variations in its shape: a study on computerized tomographic images of normal adults. Turk J Med Sci. 2003; 33: 301–306.

16. Natsis K, Piagkou M, Skotsimara G, et al. A morphometric anatomical and comparative study of the foramen magnum region in a Greek population. Surg Radiol Anat. 2013; 35(10): 925–934, doi: 10.1007/s00276-013-1119-z, indexed in Pubmed: 23620089.

17. Osunwoke E, Oladipo G, Gwunireama IU. Morphometric analysis of the foramen magnum and jugular foramen in adult skulls in southern Nigerian population. Am J Sci Ind Res. 2012; 3(6): 446–448, doi: 10.5251/ajsir.2012.3.6.446.448.

18. Ozcetin M, Arslan MT, Karapinar B. An achondroplastic case with stenosis of the foramen magnum, hydrocephaly, cortical atrophy, respiratory failure, and sympathetic dysfunction. Iran J Pediatr. 2012; 22(1): 121–124, indexed in Pubmed: 23056871.

19. Patel R, Mehta CD. Morphometric study of foramen magnum at the base of human skull in south gujarat. IOSR J Dental Med Sci. 2014; 13(6): 23–25, doi: 10.9790/0853-13642325.

20. Pires LAS, Teixeira AR, Leite TFO, et al. Morphometric aspects of the foramen magnum and the orbit in Brazilian dry skulls. Int J Med Res Health Sci. 2016; 5(4): 34–42.

21. Radhika PM, Shetty S, Prathap KJ, et al. Morphometric study of the foramen magnum in adult human skulls in Indian population. Asian J Med Clin Sci. 2014; 3: 68–72.

22. Ruiz-Garcia M, Tovar-Baudin A, Del Castillo-Ruiz V, et al. Early detection of neurological manifestations in achondroplasia. Childs Nerv Syst. 1997; 13(4): 208–213, doi: 10.1007/s003819770001, indexed in Pubmed: 9202856.

23. Samara O, Amarin J, Badran D, et al. Morphometric analysis of the foramen magnum. Int J Morphol. 2017; 35(4): 1270–1275, doi: 10.4067/s0717-95022017000401270.

24. Schmeltzer A, Babin E, Wenger JJ. Foramen magnum in children - measurement of the antero – posterior diameter on mid - sagittal pneumotomograms. Neuroradiology. 1971; 2: 162–163, doi: 10.1007/BF00335044, indexed in Pubmed: 5164217.

25. Shepur MP, Magi M, Nanjundappa B, et al. Morphometric analysis of foramen magnum. Int J Anat Res. 2014; 2(1): 249–255.

26. Smith WL, Pękala PA, Iwanaga J, et al. The forgotten intermediate condylar canal: anatomic study with application to skull base surgery. World Neurosurg. 2022; 161: e75–e79, doi: 10.1016/j.wneu.2022.01.028, indexed in Pubmed: 35033691.

27. Tellioglu AM, Durum Y, Gok M, et al. Suitability of foramen magnum measurements in sex determination and their clinical significance. Folia Morphol. 2018; 77(1): 99–104, doi: 10.5603/FM.a2017.0070, indexed in Pubmed: 28832085.

28. Tomaszewska A, Psonak D, Maślińska P, et al. Sex determination from fragmented human remains: hierarchy of the foramen magnum dimensions. Homo. 2020; 71(1): 9–17, doi: 10.1127/homo/2019/1139, indexed in Pubmed: 31651930.

29. Tubbs RS, Griessenauer CJ, Loukas M, et al. Morphometric analysis of the foramen magnum: an anatomic study. Neurosurgery. 2010; 66(2): 385–388, doi: 10.1227/01.NEU.0000363407.78399.BA, indexed in Pubmed: 20087140.

30. Ulcay T, Kamaşak B, Görgülü Ö, et al. A golden ratio for foramen magnum: an anatomical pilot study. Folia Morphol. 2022; 81(1): 220–226, doi: 10.5603/FM.a2021.0018, indexed in Pubmed: 33634836.

31. Uthman AT, Al-Rawi NH, Al-Timimi JF. Evaluation of foramen magnum in gender determination using helical CT scanning. Dentomaxillofac Radiol. 2012; 41(3): 197–202, doi: 10.1259/dmfr/21276789, indexed in Pubmed: 22116135.

32. Vinutha SP, Suresh V, Shubha R. Discriminant function analysis of foramen magnum variables in south indian population: a study of computerised tomographic images. Anat Res Int. 2018; 2018: 2056291, doi: 10.1155/2018/2056291, indexed in Pubmed: 30356386.

33. Żytkowski A, Tubbs R, Iwanaga J, et al. Anatomical normality and variability: Historical perspective and methodological considerations. Transl Res Anat. 2021; 23: 100105, doi: 10.1016/j.tria.2020.100105.

ORIGINAL ARTICLE

Morphological analysis of C2–C7 spinous process bifurcation in Chinese population: a study using three-dimensional reconstruction of computed tomography

Z. Feng, L. Liao, H. Yang, Y. Li

School of Traditional Chinese Medicine, Southern Medical University, Guangzhou, China

Background: This study aimed to investigate the anatomical morphology of the C2 to C7 spinous process (SP) bifurcation (SPB) in the Chinese population and reveal its potential clinical significance.

Materials and methods: Measurement parameters of the three-dimensional (3D) reconstructions of neck computed tomography scans (n = 92 scans) were retrospectively analysed. The 3D reconstruction and measurements were performed using Mimics Research 19.0 and 3-Matic Research 11.0. Two independent investigators reviewed all the data, including parameters such as the length and angle of the SPB. The effects of age and sex were also analysed.

Results: We identified four morphological types of SPB: fully bifid (n = 252, 45.65%), partially bifid (n = 65, 11.78%), non-bifid (n = 226, 40.94%) and unilateral branch (n = 9, 1.63%). The Kappa coefficients indicated good inter-observer reproducibility (0.776), and the intraclass correlation coefficients (ICC) values demonstrated excellent intra-rater reliability (ICC = 0.9, p < 0.0001) in the classification and measurement of SPB parameters. The percentage of general bifid SP was more than 70% in C2–5 and about 21% in C6, while all C7 SPs presented non-bifid. Morphology was symmetrical in bifid and partially bifid SP, while unilateral SP was not.

Conclusions: The classification system of SPB in this study proved consistent and reliable, despite the subjective bias. Identifying the cervical level by C6 bifurcation is unreliable, as nearly 80% of C6 SP is non-bifid. Our work provides an accurate and effective anatomical reference for SPB studies in the Chinese population.
(Folia Morphol 2023; 82, 3: 596–602)

Key words: cervical vertebra, spinous process, spinous process bifurcation, anatomy

INTRODUCTION

Previous research on cervical spinous process bifurcation (SPB) has focused on its application in archaeology, anthropology, and forensic medicine.

Nevertheless, little literature discussed its importance in clinical medicine [4, 8, 10, 14]. In clinical practice, the spinous process (SP) is generally used as an essential bony landmark for vertebral level determination,

either by palpation or during open operation. SP bifurcation could alter the practitioner's judgment in level determination [10]. Previous research describes cervical SPB as a morphological feature that can be easily identified in C2 to C6 vertebrae, while nearly all C7 presents no bifurcation [6, 11]. Few studies have reported a rare occurrence of truly bifid C7 and non-bifid C2 in SP [3, 6, 11, 14]. However, the incidence of bifurcation in the C3 to C6 SP varies according to gender, region, and race [14].

Additionally, morphology varies among different types of SPs [6, 11, 14]. According to Shore [14], Duray et al. [4], and Okuwa [13], the spinous process could be divided into fully bifid, partially bifid, and non-bifid types. To our best knowledge, very few articles described the quantification of SPB while most research determines morphological types by observation [6]. The incidence and quantification of SPB in the Chinese population have not been reported in detail. Thus, this study aimed to investigate the repeatability of the SP classification system and to describe the morphology of SPB by measurements.

MATERIALS AND METHODS

Materials

This retrospective study involved 92 cervical computed tomography (CT) scans of Chinese adults performed in Nanfang Hospital of Southern Medical University from January 2018 to December 2019. The inclusion criteria were: no cervical deformity, no fracture, and no history of neck surgery. The exclusion criteria: pathological conditions of the cervical spines, such as osteomyelitis, tuberculosis, severe osteoporosis, and bone tumour, were excluded. This study had approval from the institutional review board; the requirement for informed patient consent was waived. This study was compliant with the current regulations of our country. Ethical approval for this study was obtained

Table 1. Description of anatomical landmarks in specimen

Landmarks	Description
a	The apex of the right bifid branch
b	The deepest point of the bifid groove
c	The apex of the left bifid branch
d	The tip of the posterior tubercles of the left transverse process
e	The midpoint of line df (the transverse reference line)
f	The tip of the posterior tubercles of the right transverse process

from the Chinese Ethics Committee of Registering Clinical Trials (Reference number: ChiECRCT20210191).

Methods

The data for cervical spine CT scans were obtained in a DICOM format file and then transferred to Mimics 19.0 software to generate a three-dimensional (3D) reconstruction model of C2 to C7 vertebrae. The landmarks and parameters were defined in Tables 1 and 2. Measurements were conducted by 2 researchers independently using Mimics Research 19.0 and 3-Matic Research 11.0 software, including the length of bifid branches (left and right), angle α, angle β, angle γ, the distance between two branch tips, and the depth of the bifurcation (Fig. 1). Cervical SPB was divided into four categories: fully bifid, partially bifid, unilateral branch, and non-bifid. The unilateral branch is an unusual type of bifid SP that only has one branch and lacks another on the other side (Fig. 2).

Ethics approval and consent to participate

This study had approvals from the institutional review board. The requirement for informed patient consent was waived. This study was also compliant with the current regulations of our country.

Table 2. Measurement parameters of spinous process bifurcation

Parameters	Definition	Bifid	Partially bifid
The length of the left branch	Distance of bc	7.34 ± 2.37*	4.74 ± 1.42*
The length of the right branch	Distance of ba	7.56 ± 2.54*	4.74 ± 1.41*
The distance between two SPB tips	Distance of ac	10.87 ± 3.38*	8.56 ± 2.36*
The depth of bifurcation	h	4.77 ± 2.05*	1.84 ± 0.8*
The angle between two bifid SP branches	Angle α	96.91 ± 24.25*	132.66 ± 17.59*
The angle between the left branch and the transverse baseline	Angle β	81.66 ± 3.72#	83.38 ± 3.49#
The angle between the right branch and the transverse baseline	Angle γ	81.91 ± 3.71#	83.22 ± 3.79#

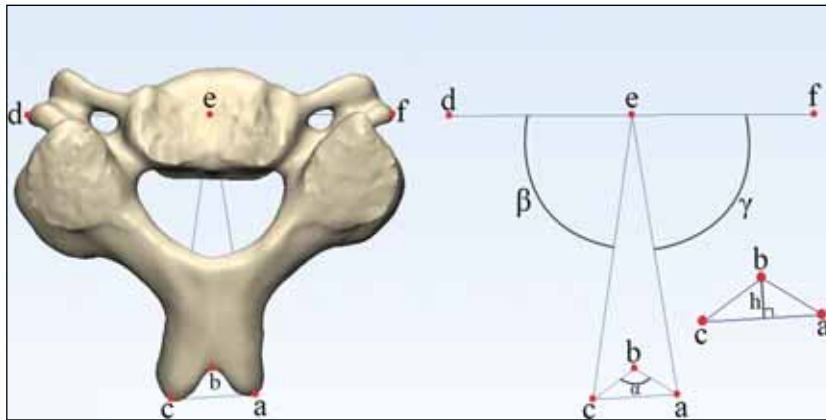*p < 0.001, using t-test; #p < 0.05, using t-test

Figure 1. Measurement of spinous process bifurcation; a — the apex of the right bifid branch; b — the deepest point of the bifid groove; c — the apex of the left bifid branch; d — the tip of the posterior tubercles of left transverse processes; e — the midpoint of the straight line df; f — the tip of the posterior tubercles of right transverse processes; ba — the length of the right branch; bc — the length of the left branch; ac — the distance between two spinous process bifurcation tips; h — the depth of bifurcation; α — the angle of two branches; β — the angle of deviation of the left branch; γ — the angle of deviation of the right branch.
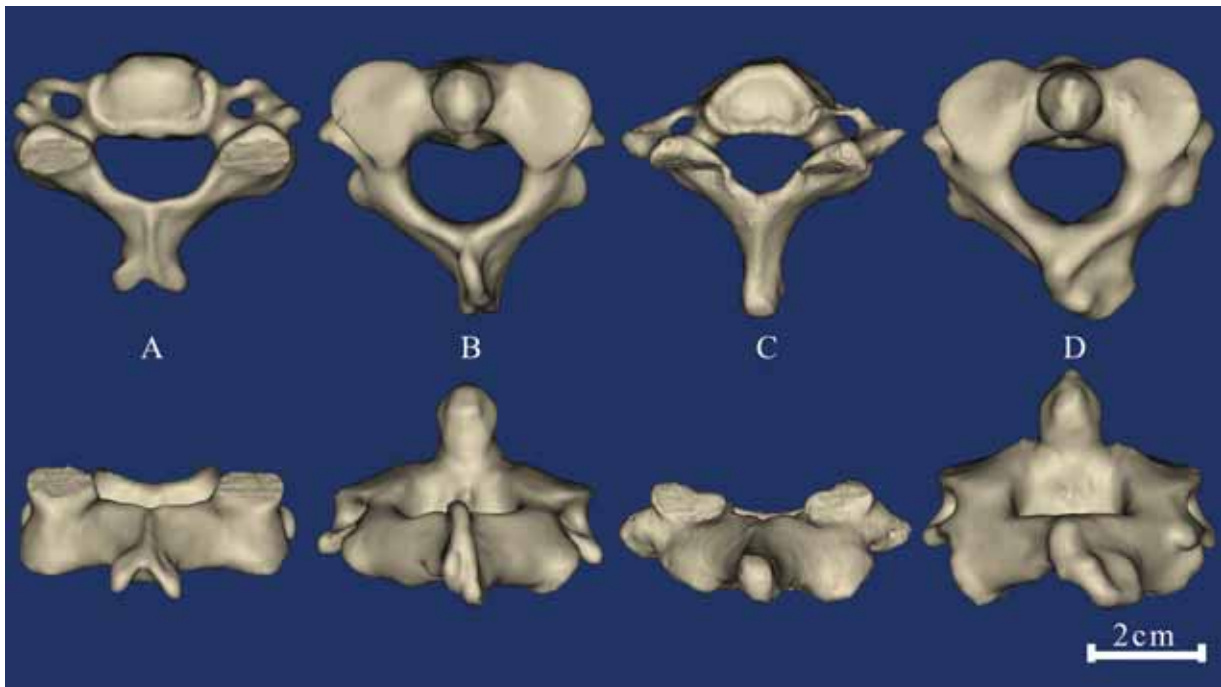

Figure 2. The superior view of cervical vertebra (the upper row) and posterior view of cervical vertebra (the lower row). Four types of spinous process: A — fully bifid; B — partially bifid; C — non-bifid; D — unilateral branch.

Statistical analysis

All statistical analyses were performed with the SPSS 20.0 software (IBM SPSS Statistics for Windows, IBM Corp, Armonk, New York). Qualitative data were expressed as percentages and quantitative data were expressed as mean ± standard deviation (SD). The consistency of the four SPB types was evaluated using the weighted kappa coefficient. To evaluate inter-observer reproducibility, Cohen's Kappa statistic was used to analyse the consistency of SPB types identification results of 2 investigators and intraclass correlation coefficients (ICC) were used to evaluate the inter-observer variability of measurements. Group differences of SPB types in gender were evaluated with Fisher's exact test of significance, and age differences among four SPB types were assessed with a Kruskal Wallis H test (multiple independent samples). Intergroup differences in parameters between

Table 3. Contingency table of classification of 552 spinous processes by two experimenters

		Experimenter A				Total
		Fully bifid	Partially bifid	Non-bifid	Unilateral branch	
Experimenter B	Fully bifid	244	40	0	0	284
	Partially bifid	2	28	31	0	61
	Non-bifid	0	0	198	1	199
	Unilateral branch	0	0	1	7	8
Total		246	68	230	8	552
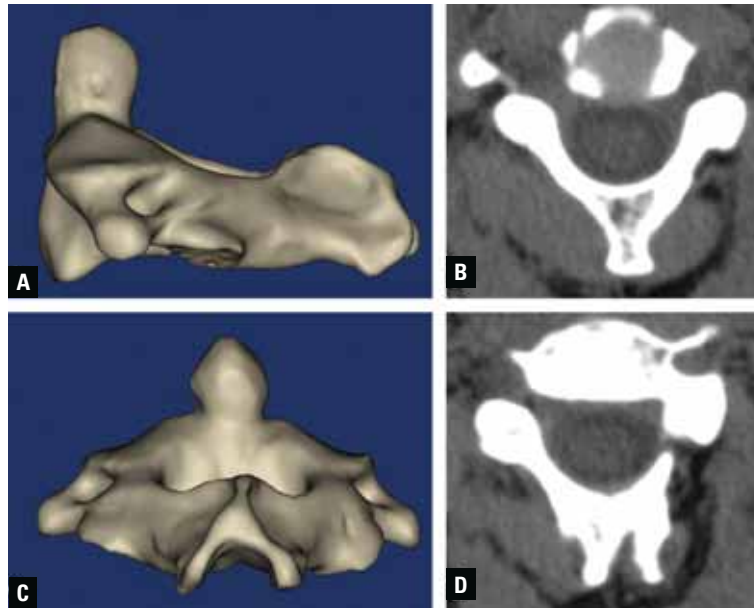
Figure 3. These four pictures are all from the same vertebra (C2). Different transverse slices of computed tomography scan presented different morphological types of spinous process bifurcation in C2. The lateral view (**A**) and posterior view (**C**) of three-dimensional reconstructed C2 vertebra; **B.** Non-bifid; **D.** Fully bifid.

RESULTS

Classification of spinous processes bifurcation

In this study, SPB was divided into four morphological types by two independent investigators, including fully bifid, partially bifid, non-bifid, and the unilateral branch. Results showed that the weighted kappa coefficient of inter-observer agreement on type judgment was 0.776 (p < 0.001), indicating strong consistency (Table 3). Each SP was considered a case (552 cases in total), and 2 investigators have made a consistent judgment on 477 cases, which means 75 cases were inconsistent. Inconsistent decisions were noted and further discussed by the 2 investigators. Observing the 3D reconstruction of all cervical vertebras in this study, it is found that the cervical SPB is located at the back of the spinous process (Fig. 3). There are different types of spinous process bifurcation in CT films at different levels of the same spinous process (Fig. 3).

The frequency of SPB morphological types according to age, sex and cervical level

This study enrolled 92 samples, including 42 (45.65%) females and 50 (54.35%) males. The overall age was 41 ± 9.5 years, ranging from 19 to 60. Fisher's exact tests showed sex differences among four SPB types are significant (p = 0.008). Men showed a slightly larger percentage of fully bifid type than women, while women had a slightly larger percentage of partially bifid type. The age differences between SPB types were compared by the Kruskal Wallis H test

The bifid group and the partially bifid group were evaluated by an independent sample t-test and paired t-test. Differences were considered statistically significant when p values were < 0.05.

Table 4. Frequency and percentage of spinous process bifurcation morphological types in age, sex and cervical level

Morphological types	Fully bifid	Partially bifid	Unilateral branch	Non-bifid	Total (cases)
Age (mean ± SD)	40.78 ± 9.55	40.15 ± 11.18	46.67 ± 6.87	40.31 ± 9.15	40.61 ± 9.61
Male (cases)	149 (49.67%)*	26 (8.67%)*	7 (2.33%)	118 (39.33%)	300
Female (cases)	103 (40.87%)*	39 (15.48%)*	2 (0.80%)	108 (42.86%)	252
C2 (cases)	85 (92.39%)	3 (3.26%)	4 (4.35%)	0	92
C3 (cases)	40 (43.47%)	26 (28.26%)	2 (2.17%)	24 (26.08%)	92
C4 (cases)	55 (59.78%)	15 (16.30%)	2 (2.17%)	20 (21.74%)	92
C5 (cases)	57 (61.96%)	16 (17.40%)	0	19 (20.65%)	92
C6 (cases)	15 (16.30%)	5 (5.43%)	1 (1.09%)	71 (77.17%)	92
C7 (cases)	0	0	0	92 (100%)	92
Total (cases)	252 (45.65%)	65 (11.78%)	9 (1.63%)	226 (40.94%)	552

Each of 92 samples has 6 cases corresponding to six cervical levels. *Fisher exact test (2×C) showed significant sex difference between fully bifid and partially bifid types ($p = 0.008 < 0.008333$, the α level was adjusted according to Bonferroni method, $\alpha = 0.008333$); SD — standard deviation

which showed no statistical significance (H = 3.358, p = 0.340).

The frequency and percentage of SPB morphological types are shown in Table 4. The number of cases in each type was as follows: fully bifid 252 (45.65%) cases, partially bifid 65 (11.78%) cases, unilateral branch 9 (1.63%) cases, and non-bifid 226 (40.94%) cases.

If we combine fully bifid and partially bifid types as general bifid the frequency of general bifid SP in overall 92 samples was as follows: 88 (95.65%) samples at C2, 66 (71.74%) samples at C3, 70 (76.09%) samples at C4, 73 (79.35%) samples at C5, 20 (21.74%) samples at C6. The percentage of general bifid SP in C2–5 was more than 70%. C7 spinous process was non-bifid in all cases while C2 did not present any non-bifid case (Table 4, Fig. 4). The frequency and percentage of SPB morphological types in age, sex, and cervical level are shown in Table 4.

The measurement of cervical SPB

In this experiment, SPB was divided into four categories. To be specific, measurements were only designed for fully bifid and partially bifid types (Table 3). The ICC value showed excellent inter-observer variability for measurements of two investigators (ICC > 0.85). The quantification of non-bifid and unilateral branch types was undone.

Results showed that the fully bifid type has greater branch length on both sides, greater distance between two SPB tips, and greater depth of bifurcation than those of the partially bifid type (p < 0.05). Whereas, the angle between two branches (angle α) and angle between the branches and the transverse baseline
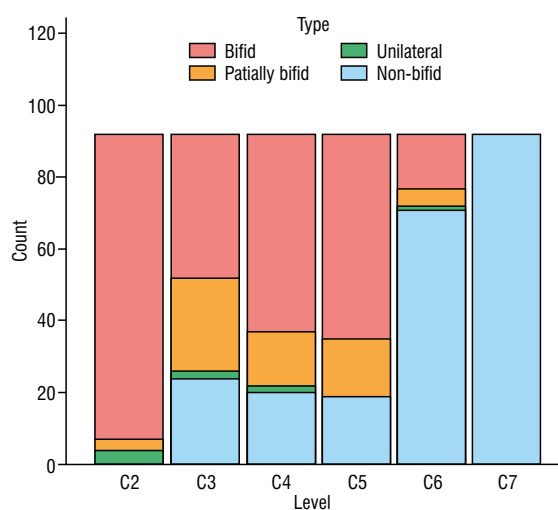

Figure 4. Counts of four spinous process bifurcation morphological types in six cervical levels.

(angle β and angle γ) were all smaller in fully bifid type than in partially bifid type (p < 0.05). In general, the morphology of SPB was characterized by two long branches with a sharp angle between them. In contrast, the partially bifid type presented two short branches with a larger angle in between (Table 3).

As for the symmetry of SPB, the paired t-test showed no statistical significance in the length and deflection angles (angle β and γ) between left and right sides in fully bifid and partially bifid types (p > 0.05). However, 9 cases of SP presented a unilateral branch, which was asymmetrical.

DISCUSSION

Previous studies commonly divide cervical SPB into three types: fully bifid, partially bifid, and non-bi-

fid [14]. According to Shore's criterion, any dorsal groove of SP deeper than 1 mm is defined as bifid [14]. Duray classified SPB as bifid, partially bifid, or non-bifid according to the following criteria: 1. Bifid: the SP includes clearly distinct cleft results in two elongate projects. The bifurcation must separate both the tubercles and part of the SP itself; 2. Partially Bifid: two distinct tubercles at the end of the SP are present. The SP itself is not bifurcated and no cleft is present; 3. Nonbifid: the end of the SP is rounded or flattened. A median groove may be present but two distinct tubercles are not present [4]. Cho's classification method of SPB is based on Duray's method [3]. Cho found that there are different types of SPB in CT films at different levels of the same SP, so he comprehensively judged the SPB types on multiple planes of the same SP. Singh B's specific description of SPB classification: partially bifid refers to two distinct tubes at the end of the SP are present and SP itself is not bifurcated and no cleft is present [15]. Fully bifid refers to the bifurcation that must separate both the tubercles and part of the SP itself [15]. Non-bifid refers to the end of the SP being rounded or flattened [15]. A specific description of SPB by Asvat: SP was classified as bifid (bifurcate and clear subtypes) and non-bifid (obtuse, pediculate, acinate, and clavate subtypes) [2]. However, Greiner believes that the classification of cervical SPB is relatively loose and has not reached a unified understanding [6, 14]. How deep, wide, and long should an SP be defined as bifurcation has not been determined [6, 14]. Most former researchers classify SPB only by subjective judgment [6].

In this study, we put forward a modified classification system of four SPB types based on previous literature. Criteria were as follows: 1. Non-bifid: the bifurcation depth of the spinous process is less than 1mm, or the end of the spinous process is rounded or flattened; 2. Partially bifid: the bifurcation depth of the spinous process is greater than 1 mm, but no distinct branches were observed; 3. Fully bifid: the bifurcation depth of the spinous process is greater than 1 mm, with distinct branches present; 4. Unilateral branch: not conforming to the above criteria, lacks SPB branch on one side. Due to the potential subjective bias in this classification system, we performed a test to evaluate the consistency of the two investigators in using this classification system. The weighted kappa coefficient was 0.776 (p < 0.001), which showed good repeatability and consistency.

This result demonstrated that this modified classification system is an ideal method despite subjective judgment exists.

Previous works studying SPB often chose materials such as dry cervical bone specimens, plain films, CT, and magnetic resonance imaging [3, 4, 6, 10, 11, 14]. Few used the reconstructed 3D model to study SPB. There were limitations with materials and methods in previous research. Dry bone specimens were often not reserved in sequence, and some may even lack data on gender and age. Plain films, CT, and magnetic resonance imaging slices failed to show the overall view of SPB. Cho also agreed that sectional images of SP were inadequate for analysis of SPB morphology [3]. As we mentioned above, there are different types of SPB morphology in CT films at different levels of the same SP [3]. This conclusion was intelligible under the 3D reconstruction model which clearly shows the complicated position of SP in the posterior vertebral region. Only a two-dimensional image is insufficient for SPB identification. Therefore, we suggest using the 3D reconstruction method for anatomical research in future SPB studies.

As described in many textbooks, SPB is a distinctive feature of the cervical vertebra compared to other spinal vertebras. However, cervical vertebrae are not always bifid [6]. In the studies of the European population, C3 and C6 are the most common cervical levels with SPB [14, 15]. According to Allbrook [1], SPB is most likely to occur in C2 and C5 levels. In our research, we came to the same conclusion. The occurrence rate of general bifurcation in the C2 and C5 levels was high (including fully bifid and partially bifid), which were 95.65% and 79.35%, respectively. In contrast, the C6 level had only a 21.74% occurrence rate of SP bifurcation, and C7 was all non-bifid. In addition, several studies have found gender differences between fully bifid and partially bifid. In the African population, fully bifid is more common in men than in women while partially bifid is on the contrary [4, 11]. This conclusion is consistent with our study of the Chinese population.

During open cervical operation, especially with the posterior cervical approach, it is often necessary to determine the cervical level with the most caudal level of SPB. However, there are arguments about the most caudal level of SPB, and some researchers suggest C5 [7, 16] and some suggest C6 [5]. According to our study, the occurrence rate of C5 and C6 SPB was 79.35% and 21.74%, respectively. Obviously, C5 is more likely to be the most caudal level of SPB

in the Chinese population. Nevertheless, more than one-fifth of individuals have a bifid SP at the C6 level. In other populations, some researchers even reported an occurrence of bifid C7, probably at a rate of 0.3% [3, 11]. In our study, all C7 SPs present non-bifid, which leaves us a mystery about the existence of bifid C7 in the Chinese population. Thus, the reliability of cervical level identification with the most caudal SPB still remains unclarified.

Spinous process is also an essential bony landmark in palpation of the cervical spine, commonly used by clinicians, manual therapists and chiropractic practitioners. In some theories, checking whether the SP is located in the posterior median position is a diagnosis procedure of cervical spine mal-alignment [10, 12]. Lewit [9] even advocated that the deviation of the SPs can be the source of neck pain. The direction of SP deviation is thus vital for the adjustment of spine alignment with manual therapy [10, 12]. However, we noticed that the asymmetry of bifurcation may have affected the results of SP palpation from the posterior neck region [6]. Few articles reported the symmetry of SPB [10]. Thus, the symmetry of SPB was analysed with quantitative parameters in our study. As described above, no significant difference was found in the angle between the two bifid branches and the angle between the branch and the transverse baseline on both sides. The results indicated that SPB was not likely to affect the results of palpation. However, the type of unilateral branch may have unknown effects on palpation. But then again, the accuracy and consistency of the palpation method are still questionable.

Limitations of the study

Our study has limitations. First, we only have 92 specimens for analysis, which means that some results in this study may not represent the entire population. Second, we only investigated the Chinese population but did not compare all results with different ethnic groups. Third, the study data are subject to the limitations and biases of retrospective analysis.

CONCLUSIONS

The classification system of SPB in this study proved consistent and reliable, despite the subjective bias. Identifying cervical level by C6 bifurcation is unreliable since nearly 80% of C6 SP is non-bifid. Our work provides an accurate and effective anatomical reference for SPB studies in the Chinese population.

REFERENCES

1. Allbrook DB. The East African vertebral column; a study in racial variability. Am J Phys Anthropol. 1955; 13(3): 489–513, doi: 10.1002/ajpa.1330130309, indexed in Pubmed: 13275582.
2. Asvat R. The configuration of cervical spinous processes in black and white South African skeletal samples. J Forensic Sci. 2012; 57(1): 176–181, doi: 10.1111/j.1556-4029.2011.01942.x, indexed in Pubmed: 22040199.
3. Cho W, Maeda T, Park Y, et al. The incidence of bifid C7 spinous processes. Global Spine J. 2012; 2(2): 99–104, doi: 10.1055/s-0032-1319776, indexed in Pubmed: 24353954.
4. Duray SM, Morter HB, Smith FJ. Morphological variation in cervical spinous processes: potential applications in the forensic identification of race from the skeleton. J Forensic Sci. 1999; 44(5): 937–944, indexed in Pubmed: 10486945.
5. Elaine NM. Human anatomy and physiology. 5th ed. Benjamin Cummings, San Fransisco 2001: 198–247.
6. Greiner TM. Shape analysis of the cervical spinous process. Clin Anat. 2017; 30(7): 894–900, doi: 10.1002/ca.22948, indexed in Pubmed: 28646520.
7. Hollinshead WH, Rosse C. Textbook of anatomy. 4th ed. Harper and Row Publishers, Philadelphia 1985: 285–307.
8. Jeong Y, Jeong G, Pergande S, et al. Generating a Vertebrae-based Method to Discriminate between Korean and U.S. White Male Casualties from the Korean War. J Forensic Sci. 2019; 64(6): 1776–1781, doi: 10.1111/1556-4029.14074, indexed in Pubmed: 31145480.
9. Lewit K. Deviation of the spinous processes. Br J Radiol. 1957; 30(351): 162–164, doi: 10.1259/0007-1285-30-351-162, indexed in Pubmed: 13404224.
10. Liao LQ, Li YK, Yuan F, et al. Morphological characteristics of the spinous process of axis: clinical implications for cervical spine manipulation. J Manipulative Physiol Ther. 2019; 42(1): 82–88, doi: 10.1016/j.jmpt.2018.05.002, indexed in Pubmed: 31054597.
11. Ludwisiak K, Podgórski M, Biernacka K, et al. Variation in the morphology of spinous processes in the cervical spine: An objective and parametric assessment based on CT study. PLoS One. 2019; 14(6): e0218885, doi: 10.1371/journal.pone.0218885, indexed in Pubmed: 31246998.
12. Maitland GD, Hengeveld E, Banks K, Matthew N. Maitland's Vertebral Manipulation. 8th ed. Elsevier, Philadelphia, PA 2014.
13. Okuwa T. Ueber die Arteria Mediana des Japaners. Kanazawaidai Kaibokyoshitsu Gyoseki. 1937; 27: 98–105.
14. Shore LR. A report on the spinous processes of the cervical vertebrae in the native races of south africa. J Anat. 1931; 65(Pt 4): 482–505, indexed in Pubmed: 17104343.
15. Singh B, Mishra G, Bhatnagar S, et al. Study of spinous process of typical cervical vertebrae and clinical significance. Int J Biomed Res. 2014; 5(9): 576, doi: 10.7439/ijbr.v5i9.779.
16. Yoshizawa E, Oiwa T. Comprehensive Textbook of Orthopaedic Operations. Vol. 8. Yamamuro T, Inoue S (eds.). Kanehara and CO., LTD, Tokyo 1993: 9–59.

VIA MEDICA

ORIGINAL ARTICLE

Morphological and morphometric features of sacral hiatus and its clinical significance in caudal epidural anaesthesia

E. Nastoulis[1] , D. Tsiptsios[1], P. Chloropoulou[2], V. Karapepera[1], V. Thomaidis[1], P. Pavlidis[3], A. Fiska[1]

[1]Department of Anatomy, School of Medicine, Democritus University of Thrace, Alexandroupolis, Greece
[2]Department of Anaesthesiology, School of Medicine, Democritus University of Thrace, Alexandroupolis, Greece
[3]Laboratory of Forensic Sciences, School of Medicine, Democritus University of Thrace, Alexandroupolis, Greece

Background: Caudal epidural block (CEB) failure or complications are not unheard even among experienced anaesthesiologists and are usually due to sacral hiatus (SH) anatomy variations. The aim of the present study is to observe, record and analyse important anatomical features of SH and correlate them with potential CEB limitations.

Materials and methods: The SH of 155 complete and undamaged Greek adult dry sacra of known sex were included in the study. Three non-metric (shape of SH and location of hiatal apex and base in relation to level of sacral/coccygeal vertebra) and five metric parameters (height of the SH, transverse width of the SH at the base, anteroposterior diameter of the SH at the level of its apex and the distance from the sacral apex and base to the upper border of S2 foramina) were evaluated.

Results: Inverted U (34.83%) and inverted V (26.45%) were the commonest shapes. Hiatal apex and base were most commonly related to the level of S4 (78.70%) and S5 vertebra (89.03%), respectively. Mean height, depth and inter-cornual distance were 19.05 ± 8.65 mm, 5.39 ± 1.84 mm and 12.41 ± 3.16 mm, respectively, whereas mean distance between the upper border of S2 foramen and the apex and base of the SH were 46.34 mm and 63.48 mm, respectively. Anatomical variations of SH that might be responsible for CEB failure, such as elongated SH, absence of SH, complete dorsal wall agenesis of sacral canal and narrowing (< 3 mm) at the apex of SH were found in 17.43% of sacra (male 10.94% and female 25.22%).

Conclusions: This study suggests a potential risk of failure of CEB in Greek patients, especially in females, which should be kept in mind while giving caudal epidural anaesthesia. (Folia Morphol 2023; 82, 3: 603–614)

Key words: **sacrum, sacral hiatus, anatomical variations, caudal epidural anaesthesia, Greece**

Address for correspondence: E. Nastoulis, MD, MSc, Forensic Pathologist, doctoral student, School of Medicine, Democritus University of Thrace, Dragana, 68100, Alexandroupolis, Evros Prefecture, Greece, tel: +30 6972524316, fax: +30 25513 53824, e-mail: nastevang@yahoo.gr

INTRODUCTION

The human sacrum constitutes a large triangular bone located at the base of vertebral column between the two hip bones that articulates with the fifth lumbar vertebra above and the coccyx below. Over the years, an abundance of sacral anatomical variations has been reported [29]. Embryologically, it is formed by the fusion of the five sacral vertebrae that is complete between the third or early fourth decade of life. Failure of fusion of the fifth, and occasionally the fourth, sacral vertebral laminae creates an opening on the posterior aspect of the lower end of the sacrum, known as sacral hiatus (SH). The remnants of the inferior articular processes of the fifth sacral segment extend downwards on both sides of the SH forming the two sacral cornua. These constitute its lateral margins and define important clinical landmarks during caudal epidural anaesthesia or block (caudal epidural block [CEB]) [1].

The dorsal surface of the fifth sacral and the coccygeal vertebrae and the deep posterior sacrococcygeal membrane connecting them, form the roof of the lower sacral canal. Down to the middle of S2 vertebra the sacral canal encompasses the termination of the dural sac containing the distal portion of the cauda equina and the internal filum terminale. Caudally, the fifth sacral and coccygeal spinal nerves formed within the sacral canal and exiting via the SH and the external filum terminale extending towards the dorsum of the coccyx are encountered. The sacral canal also contains the epidural venous plexus and is filled with adipose tissue that is subject to age-related decrease in density [41].

The application of local anaesthetic agents into the epidural space through the SH was first described by Fernard Cathelin and Jean-Athanase Sicard predating lumbar epidural block [8] and gained popularity by Hingson who implemented it on obstetrical cases [15, 37]. Caudal epidural anaesthesia produces sensory and motor blockade of the sacral roots and limited blockade of the autonomous nervous system. Thus, this type of anaesthesia has a wide variety of indications [15]. Most frequently it is used to provide anaesthesia in infants and children for surgery of the perineum, anus and rectum and for inguinal and femoral hernias [47]. In adults for surgery of the lumbar spine, cystoscopies, urethral and vaginal operations and for labour pain relief, although the latter has been superseded by lumbar epidural anaesthesia [17]. Additionally, it is useful in providing sympathetic block to patients suffering from acute vascular insufficiency of the lower extremities due to vascular spasm or occlusion. It can be used for any acute pelvic or leg pain, but most rewardingly in chronic pain due to diabetic neuropathy, post-herpetic pain, failed back syndrome, complex regional pain syndromes and for cancer pain management including peripheral neuropathy due to chemotherapy [10].

The technique of caudal epidural anaesthesia entails placing neonates and children in the lateral decubitus position, while for older children and adults the prone position is preferred [19, 39]. The SH can be located by palpating the sacral cornua, approximately at the level of the skin folds of the buttocks. After infiltrating with local anaesthetic, the epidural needle is inserted in the caudal canal by using the loss of resistance technique and its position is ascertained by fluoroscopy or ultrasound [3, 7]. After the correct placement of the needle is confirmed, a catheter is inserted to the desired depth. Special attention should be paid not to penetrate the cancellous bone of the sacrum and not to tear the dura if the needle is advanced more cephalad than the S2 level, as this level indicates the lowest extension of the dura. Complications of CEB can relate to unsuccessful technique, such as penetration of the dura, penetration, and injection of local anaesthetic agents into the soft bone of the sacrum (mainly in children), perforation of the rectum or even trauma to the baby's head in parturients, if the needle is placed too anteriorly [14]. In addition, complications can arise from the spread of the anaesthetic solutions and the development of systemic toxicity. This complication, although rare, seems to be more common in caudal epidural anaesthesia compared to lumbar epidural anaesthesia [9]. Infections such as meningitis, discitis or vertebral osteomyelitis are rare complications. Other complications such as epidural haematoma, dural puncture and post dural puncture headache, air embolism, back pain and broken or knotted catheters can occur after caudal anaesthesia, as with lumbar or thoracic epidural anaesthesia.

Caudal epidural block failure rate approximates 5–10% and is usually attributed to technical difficulties to accurately identify the SH due to its numerous anatomic and morphological variations. Thus, for optimal access into the sacral epidural space and successful, uncomplicated conduction of CEB, a thorough knowledge of the SH anatomical variations, as well as the

use of detailed anatomical landmarks to identify them, are required. To gain this knowledge, we conducted a descriptive osteological study in dry sacra of Greek adults, aiming to observe, record and analyse several metric and non-metric features of the SH.

MATERIALS AND METHODS

The aim of the present study is to observe, record and analyse important anatomical features of the SH in a Greek population. A total number of 155 dry sacra (82 male/73 female) were assessed in the study from the Third Cemetery of Athens, Greece, after formal consents and official permissions were obtained. Only bones that were fully ossified, dried, intact, with no fractures or other pathology were examined.

Three non-metric and five metric parameters were evaluated on these specimens.

Non-metric parameters

Non-metric parameters included:
— shape of SH;
— location of hiatal apex in relation to level of sacral vertebra;
— location of hiatal base in relation to level of sacral/ /coccygeal vertebra.

Metric parameters

Five anatomical measurements were performed by two authors (E.N. and V.T.) by using a vernier calliper accurate to 0.1 mm. Minor deviations were resolved by the lead anatomist of the Department (A.F.):
— (i) Height of the SH: measured from the apex to the midpoint of its base. Respective measurements were classified into six subgroups: 0–10 mm, 11–20 mm, 21–30 mm, 31–40 mm, 41–50 mm and > 51 mm (Fig. 1);
— (ii) Transverse width of the SH at the base (intercornual distance): measured between inner aspects of the inferior limit of the sacral cornua. Respective measurements were classified into four subgroups: 0–5 mm, 6–10 mm, 11–15 mm and > 16 mm (Fig. 1);
— (iii) Anteroposterior diameter (depth) of the SH at the level of its apex. Respective measurements were classified into four subgroups: 0–3 mm, 4–6 mm, 7–9 mm and > 9 mm (Fig. 2);
— (iv) Distance from the sacral apex to the upper border of S2 foramina (Fig. 1);
— (v) Distance from the base of SH to the upper border of S2 foramina (v = i + iv) (Fig. 1).
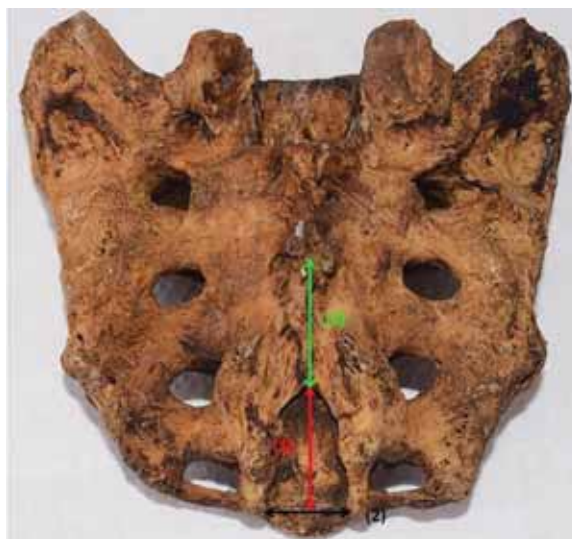

Figure 1. Metric parameters evaluated: 1 — height of sacral hiatus; 2 — transverse width of the sacral hiatus at the base (intercornual distance); 3 — distance from sacral apex to the upper border of S2 foramina; 4 (4 = 1 + 3) — distance from the base of sacral hiatus to the upper border of S2 foramina.

Figure 2. Anteroposterior diameter (depth) of the sacral hiatus at the level of its apex.

Statistical analysis

Data were expressed as mean, standard deviation), median and range. Analyses were performed using IBM SPSS Statistics 26.

RESULTS

With regards to the shape of SH nine types were recognised (Fig. 3), inverted U-shaped being the most commonly observed (34.83%) followed by inverted V (26.45%) and irregular (19.99%) (Table 1).

Considering hiatal apex and base location in relation to the level of sacral/coccygeal vertebra, it was detected that these were most often related to the
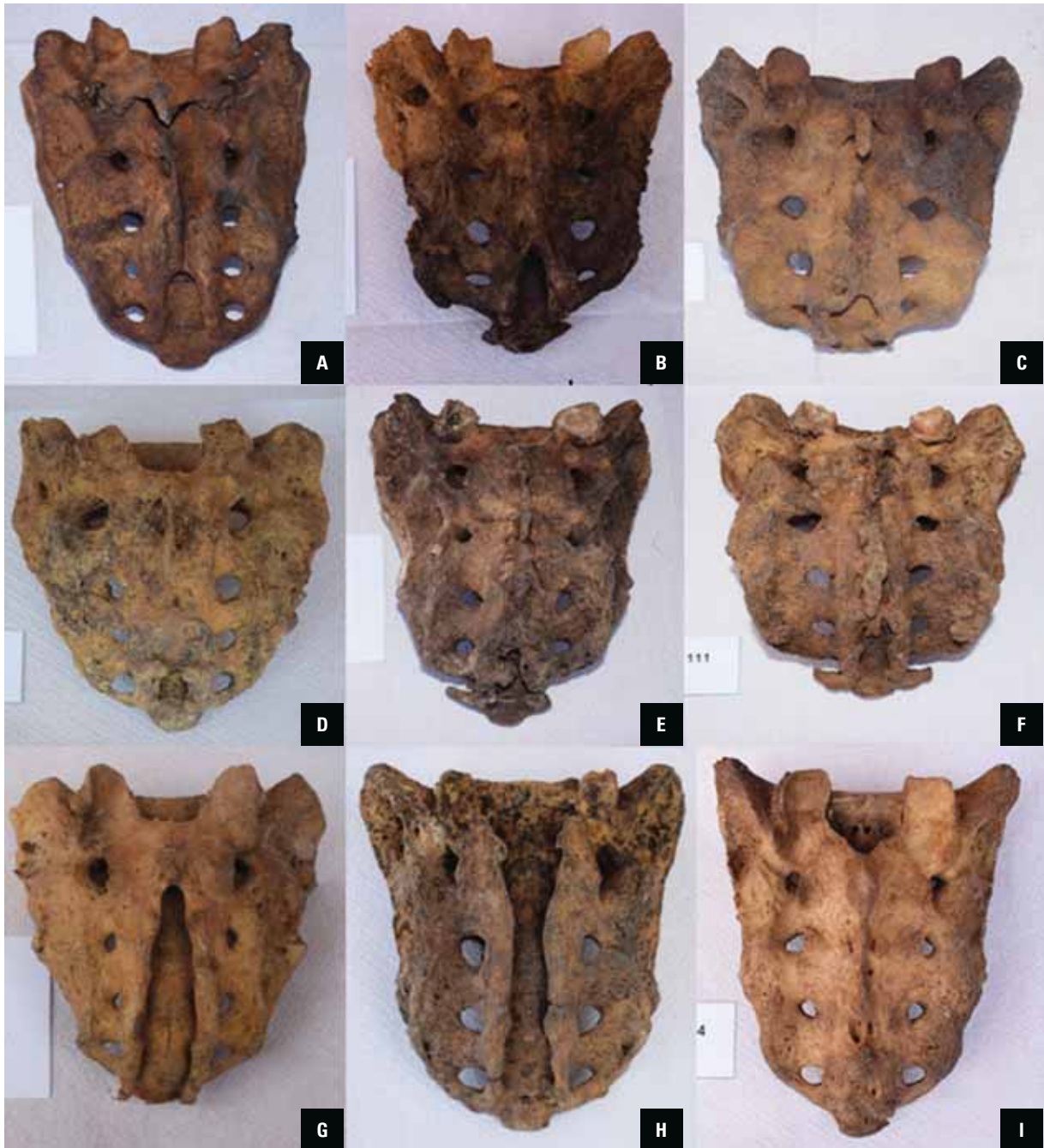
Figure 3. Observed sacral hiatus shapes: **A.** Inverted U; **B.** Inverted V; **C.** Irregular; **D.** Dumbbell; **E.** Bifid; **F.** M pattern; **G.** Elongated; **H.** Complete dorsal wall agenesis; **I.** Absence of sacral hiatus.

level of S4 (78.7%) and S5 (89.03%) vertebra, respectively (Tables 2, 3, Figs. 4, 5).

Furthermore, mean height of SH was 19.05 ± 8.65 mm (range: 1.57–58.91 mm) (Table 4), whereas most specimens exhibited respective heights between 11 and 20 mm (42.6%), followed by 21–30 mm (34.2%) and 0–10 mm (14.2%) (Table 5). Statistically significant differences between males (20.01 ± 9.37 mm) and females (17.8 ± 7.44 mm) were observed (p = 0.035) (Table 6).

Mean intercornual distance was 12.41 ± 3.16 (range: 3.32–20.09) (Table 4) and in most instances ranged between 11 and 15 mm (54.8%) followed by 6–10 mm (22.6%) and > 16 mm (21.9%) (Table 7). Statistically significant differences between males (12.87 ± 3.35 mm) and females (11.79 ± 2.79 mm) were not observed (p = 0.109) (Table 6).

Moreover, mean depth of the SH at the level of its apex was 5.39 ± 1.84 (1.22–12.12) (Table 4) and in

Table 1. Shape of sacral hiatus

Shape of sacral hiatus	Male		Female		Total	
	Number	Per cent	Number	Per cent	Number	Per cent
Inverted 'U'	30	36.58%	24	32.87%	54	34.83%
Inverted 'V'	22	26.82%	19	26.02%	41	26.45%
Irregular	17	20.73%	14	19.17%	31	19.99%
Elongated	1	1.21%	3	4.10%	4	2.58%
Dumbbell	6	7.31%	4	5.47%	10	6.45%
Bifid	2	2.43%	3	4.10%	5	3.22%
Pattern 'M'	0	0%	2	2.73%	2	1.29%
Complete dorsal wall agenesis	2	2.43%	1	1.36%	3	1.93%
Absence of sacral hiatus	2	2.43%	3	4.10%	5	3.22%
Total	82	100%	73	100%	155	100%

Table 2. Location of hiatal apex in relation to the level of sacral vertebra

Vertebral level	Male		Female		Total	
	Number	Per cent	Number	Per cent	Number	Per cent
S2	1	1.21%	1	1.36%	2	1.29%
S3	9	10.97%	8	10.95%	17	10.96%
S4	66	80.48%	56	76.71%	122	78.70%
S5	6	7.31%	8	10.95%	14	9.03%
Total	82	100%	73	100%	155	100%

Table 3. Location of hiatal base in relation to level of sacral/coccygeal vertebra

Vertebral level	Male		Female		Total	
	Number	Per cent	Number	Per cent	Number	Per cent
S4	1	1.21%	1	1.36%	2	1.29%
S5	74	90.24%	64	87.67%	138	89.03%
C1	7	8.53%	8	10.95%	15	9.67%
Total	82	100%	73	100%	155	100%

most instances ranged between 4 and 6 mm (55.5%) followed by 7–9 mm (32.3%) (Table 8). Statistically significant differences between males (5.62 ± 1.75 mm) and females (5.07 ± 1.93 mm) were not observed (p = 0.067) (Table 6).

Finally, mean distance from apex and from base of the SH to the upper border of S2 foramina were 46.34 ± 11.06 mm (range: 12.07–89.11) and 63.48 ± ± 8.25 mm (range: 48.47–90.65 mm), respectively (Table 4).

DISCUSSION

Based on the fact that SH constitutes the most important route for CEB, full understanding of its morphological and morphometrical variations across various population groups is of paramount importance in order to not only increase success rate, but also decrease complications' risks of CEB. In the present study, several metric and non-metric parameters of adult Greek dry sacra were evaluated.

As evidenced in Table 1, inverted U and inverted V were the most commonly observed SH shapes (34.83% and 26.45%, respectively). In keeping with our results, several researchers worldwide have also concluded that either inverted U or inverted V are the most prevalent SH shapes (Table 9) [2, 4–6, 13, 18, 21–24, 26–28, 30, 31, 33–36, 38, 42, 44–6]. Thus, these are considered as normal and provide enough

Figure 4. Level of sacral hiatus apex at S4.

Figure 5. Level of sacral hiatus base at S5.

Table 4. Evaluated morphometrical parameters of dry sacra

Parameters	Mean [mm]	Median [mm]	Standard deviation [mm]	Range [mm]
Height of sacral hiatus	19.05	18.8	8.65	1.57–58.91
Transverse width of sacral hiatus (intercornual distance)	12.41	12.71	3.16	3.32–20.09
Anteroposterior diameter (depth) of sacral hiatus at the level of its apex	5.39	5.48	1.84	1.22–12.12
Distance from sacral apex to the upper border of S2 foramina	46.34	45.87	11.06	12.07–89.11
Distance from the base of sacral hiatus to the upper border of S2 foramina	63.48	62.74	8.25	48.47–90.65

Table 5. Height of sacral hiatus from apex to midpoint of base

Height of sacral hiatus [mm]	Male		Female		Total	
	Number	Per cent	Number	Per cent	Number	Per cent
0–10	10	12.19%	12	16.43%	22	14.2%
11–20	36	43.90%	30	41.09%	66	42.6%
21–30	27	32.92%	26	35.61%	53	34.2%
31–40	7	8.53%	5	6.84%	12	7.7%
41–50	1	1.21%	0	0%	1	0.65%
> 51	1	1.21%	0	0%	1	0.65%
Total	82	100%	73	100%	155	100%

space for needle insertion during CEB. In contrast, alternate SH shapes, like irregular (observed in 19.99% of our cases), dumbbell (6.45%), bifid (3.22%) and "M" pattern (1.29%), may lead to CEB failure. The extreme case of absent (or closed) SH that may be caused by bony overgrowth and complete fusion of S4 and S5 laminae, thus precluding needle insertion into the caudal epidural space, was observed in 5 cases (3.22% — 2 males, 3 females). Furthermore, complete agenesis of the dorsal wall of the sacral

Table 6. Sexual dimorphism

Parameters [mm]	Sex	Mean [mm]	Median [mm]	SD [mm]	Range (mm)	P value (K-S test)	Normality	P value*
Height of SH	Male	20.01	19.02	9.37	1.57–58.91	0.2	Yes (t-test)	0.035
	Female	17.8	17.14	7.44	5.66–35.66			
Transverse width of SH (intercornual distance)	Male	12.87	13.29	3.35	3.32–20.09	0.2	Yes (t-test)	0.109
	Female	11.79	11.8	2.79	5.43–16.34			
Anteroposterior diameter (depth) of SH at the level of its apex	Male	5.62	5.61	1.75	1.38–12.12	0.2	Yes (t-test)	0.067
	Female	5.07	5.32	1.93	1.22–8.98			

*Differences among groups were considered statistically significant at p values of less than 0.05; SH — sacral hiatus; SD — standard deviation

Table 7. Transverse width of sacral hiatus (intercornual distance)

Transverse width [mm]	Male		Female		Total	
	Number	Per cent	Number	Per cent	Number	Per cent
0–5	1	1.21%	0	0%	1	0.65%
6–10	18	21.95%	17	23.28%	35	22.6%
11–15	44	53.65%	41	56.16%	85	54.8%
> 16	19	23.17%	15	20.54%	34	21.9%
Total	82	100%	73	100%	155	100%

Table 8. Anteroposterior diameter (depth) of sacral hiatus at the level of apex

Anteroposterior diameter [mm]	Male		Female		Total	
	Number	Per cent	Number	Per cent	Number	Per cent
0–3	4	4.87%	11	15.06%	15	9.7%
4–6	48	58.53%	38	52.05%	86	55.6%
7–9	27	32.92%	23	31.50%	50	32.2%
> 9	3	3.65%	1	1.36%	4	2.5%
Total	82	100%	73	100%	155	100%

canal was found in 3 cases (1.93% — 2 males, 1 female). This variation may also lead to CEB failure as bony landmarks are missing. Moreover, elongated SH was observed in 4 cases (2.58% — 1 male, 3 females). This variance may result in CEB complications as the closer the apex of SH to the dural sac is, the more likely it is for an unintentional dural puncture to happen.

Concerning hiatal apex location, in keeping with the majority of available studies this was most commonly related to the level of S4 vertebra (78.70%) and less frequently to the level of S3 (10.96%) or S5 (9.03%) vertebra (Table 2, Fig. 4). Nadeem [26] and Malarvani et al. [23] having evaluated dry sacra belonging to Caucasian Germans and Nepalis, re-

spectively, were the only ones to observe that hiatal apex location is most often related to the level of S3, and not S4, vertebra (Table 10) [2, 4–6, 13, 18, 23, 24, 26–28, 31, 33–35, 38, 42, 44–46]. Hiatal apex comprises an important bony landmark during CEB. However, in obese patients it may be hard to palpate. Exact knowledge of hiatal apex level is of paramount importance as this ensures dura safety during CEB. More specifically, the higher the hiatal apex is located, the shorter the distance between it and the dural sac termination is, thus increasing the risk of accidental dural puncture during CEB. In case dural puncture occurs and goes undetected, the entire volume of local anaesthetic will get injected into the subarachnoid space leading to total spinal anaesthesia [19, 43].

Table 9. Comparison between different studies regarding shapes of sacral hiatus

Author [reference]	Ethnicity/Race	Inverted "U"	Inverted "V"	Irregular	Dumbbell	Bifid
Kumar et al. [21]	India	46.53%	29.7%			
Nagar [27]	India	27%	41.5%	14.1%	13.3%	1.5%
Patel et al. [33]	India	49.3%	20%		4%	
Njihia et al. [30]	Kenya	16.7%	32.1%	19%	31%	
Seema et al. [38]	India	42.95 %	27.51%	16.10%	13.41%	
Suwanlikhid et al. [44]	Thailand	54.47%	19.57%	11.06%	2.13%	3.83%
Shewale et al. [42]	India	40.69%	32.35%	9.31%	5.89%	0.98%
Phalgunan, Baskaran [34]	India	35%	35%	28%		
Bhattacharya et al. [6]	India	65%	23%	12%		
Ukoha et al. [45]	Nigeria	48.2%	34.9%	4.8%	4.8%	4.8%
Nasr et al. [28]	Egypt	31.33%	38.66%	15.33%	12%	2.66%
Mayuri et al. [24]	India	42.37%	27.11%	16.1%	12.71%	1.69%
Rajeev et al. [35]	India	42.12%	35.43%	12.99%	4.00%	5.51%
Osunwoke et al. [31]	Nigeria	24.1%	33.1%	13%	9.3%	5.6%
Kamal et al. [18]	Bangladesh	38.00%	35.10%	15.20%	5.30%	0.60%
Nadeem [26]	Caucasians leaving in Germany	56%	14%	16%	10%	2%
Malarvani et al. [23]	Nepal	35%	32%	14%	3%	2%
Vasuki et al. [46]	India	36%	20%	33%	23%	3%
Laishram et al. [22]	India	39.35%	16.77%	24.51%	7.091%	
Saha et al. [36]	India	70.09%	14.53%	12.82%	0.85%	1.71%
Bagheri, Govsa [5]	Turkey	33.3%	19.45%	19.45%	6.9%	3.45%
Dhuria et al. [13]	India	35.22%	29.54%	14.77%		
Bagoji et al. [4]	India	42.02%	26.08%	7.24%	12.31%	5.07%
Abera et al. [2]	Ethiopia	37.7%	41%	4.9%	11.5%	3.3%

Abiding to the aforementioned mechanism, the risk of intrathecal injection of anaesthetic during CEB is high in case of dural sac termination caudally to the expected middle S2 level, as in 1–5% of humans it extends to S3 level or below, or in the presence of an incidental Tarlov cyst, a perineural cyst filled with cerebrospinal fluid that communicates with the dural sac and is usually found at or below S3 level [16, 41].

With regards to hiatal base location, in agreement with available literature (Table 10) this was most commonly related to the level of S5 vertebra (89.03%) (Table 3, Fig. 5). Moreover, the mean distance between the upper border of S2 foramen and the apex and base of the SH were 46.34 mm and 63.48 mm, respectively (Table 4). These findings signify the importance of advancing the needle only a few millimetres after penetrating the sacrococcygeal membrane in adults, in order to reduce the frequency of dural puncture during CEB.

Mean height of SH was 19.05 (range: 1.57–58.91) (Table 4), whereas heights < 20 mm were observed in 56.8% of dry sacra (Table 5). Our results approach respective measurements from Indian (Shewale et al. [42], Vasuki et al. [46]) and Ethiopian (Abera et al. [2]) dry sacra (Table 11) [2, 4, 11, 13, 24–28, 32, 34, 35, 38, 40, 42]. The longer the SH is, the shorter the sacral canal is, thus increasing the possibility of accidental dural puncture during CEB. In obese individuals, extreme fat deposition within the sacral canal makes elevating potential risk of CEB complications [2].

In our study, mean transverse width of the SH at the base (intercornual distance) was 12.41 mm (range: 3.32–20.09 mm) (Table 4), whereas most sacra (54.8%) exhibited respective distances between 11 and 15 mm (Table 7). Ours resemble measurements from Indian sacra confirmed by Nasr et al. [28], Shewale et al. [42] and Seema et al. [38] (Table 11).

Table 10. Comparison between different studies regarding the location of hiatal apex and base in relation to the level of sacral/coccygeal vertebra

Author [reference]	Ethnicity/Race	Location of hiatal apex in relation to level of sacral vertebra				Location of hiatal base in relation to level of sacral/ /coccygeal vertebra		
		S2	S3	S4	S5	S4	S5	C1
Nagar [27]	India	3.4%	37.3%	55.9%	3.4%	11.1%	72.6%	16.3%
Patel et al. [33]	India	0.66%	26.6%	53.3%	12.67%	10.67%	79.33%	
Seema et al. [38]	India	4.02%	35.57%	56.36%	4.02 %	13.42%	70.46%	16.10%
Suwanlikhid et al. [44]	Thailand	1.18%	16.2%	58.4%	15.01%	7.50%	71.14%	8.69%
Shewale et al. [42]	India	4%	15%	66%	14.5%	2%	82%	16%
Phalgunan, Baskaran [34]	India	7.1%	46%	46%				
Bhattacharya et al. [6]	India		5%	72%	23%			
Ukoha et al. [45]	Nigeria	2.04%	20.05%	69.9%	4.8%	2.4%	88%	7.2%
Nasr et al. [28]	Egypt	1.33%	14.66%	54.00%	27.33%	12%	70%	18%
Mayuri et al. [24]	India	4.23%	35.39%	56.77%	3.38%			
Rajeev et al. [35]	India	5.60%	17.71%	60.23%	16.53%	4.33%	75.19%	21.25%
Osunwoke et al. [31]	Nigeria	5.6%	20.4%	66.6%	7.4%	11.1%	59.3%	29.6%
Kamal et al. [18]	Bangladesh	4.70%	30.40%	60.20%	4.70%	0.60%	91.20%	8.20%
Nadeem [26]	Caucasians living in Germany	2%	62%	34%	2%	62%	24%	14%
Malarvani et al. [23]	Nepal	3%	42%	39%	13%	31%	54%	1%
Vasuki et al. [46]	India	3%	43%	48%	5%	16%	64%	20%
Bagheri, Govsa [5]	Turkey	1.15%	10.34%	71.11%	11.49%	2.3%	82.76%	8.05%
Dhuria et al. [13]	India	5.68%	21.59%	57.95%	9.09%		92.04%	7.95%
Bagoji et al. [4]	India	2.89%	26.81%	58.69%	6.52%	18.11%	70.28%	6.52%
Abera et al. [2]	Ethiopia	3.3%	26.2%	60.7	9.8%		78.7%	21.3%

Finally, mean depth of SH at the level of its apex was 5.39 mm (range 1.22–12.12 mm) (Table 4). Our findings were close to those reported by Abera et al. from Ethiopia [2] and Rajeev et al. from India [35] (Table 11). Anteroposterior diameter at the level of hiatal apex is clinically important, as in case it is < 3.7 mm, it is associated with technical difficulties while attempting to insert the needle into the caudal epidural space by blind technique [20]. However, under ultrasound guidance, such difficulties are encountered in case of depths < 1.6 mm [12]. It is noteworthy that in our study, anteroposterior diameters < 3 mm were observed in 15 (9.7%) of sacra (4 males, 11 females) (Table 8). Thus, in these patients it would have been difficult to advance a 22 G needle during CEB.

Due to the aforementioned anatomical variations, failure and complication rates when conventional blind technique for CEB is applied in adults are high even among experienced anaesthesiologists. According to the literature, fluoroscopy guided CEB has markedly increased CEB success rates. However, routine use of fluoroscopy is limited by radiation exposure, cost and special space requirements. On the other hand, ultrasound guided CEB does not face those limitations, being able to image accurately sacral anatomy and needle positioning in the caudal space, thus has risen in popularity since its introduction in 2003 [19].

CONCLUSIONS

The anatomy of the SH and caudal canal is highly variable, and thorough appreciation of this is critical to performing effective and safe CEBs. Despite its widespread use, the knowledge of extent of variability in this area remains limited even among experienced clinicians. In the present osteological study, all the anatomical variations of the SH reported in the international literature were found and recorded in the Greek population, in both sexes.

The variations of the SH that mainly might be responsible for CEB failure, such as elongated SH,

Table 11. Morphometric sacral hiatus (SH) measurements from various investigators worldwide

Author	Ethnicity/Race	Anteroposterior diameter (depth) of SH at the level of apex				Height of SH						Transverse width (intercornual distance) of SH at the level of base			
		0–3 mm	4–6 mm	7–9 mm	>9 mm	0 to 10 mm	11 to 20 mm	21 to 30 mm	31 to 40 mm	41 to 50 mm	>51 mm	0 to 5 mm	6 to 10 mm	11 to 15 mm	>15 mm
Nagar [27]	India	15.6%	64.2%	19.8%	0.4%	10.3%	35%	30.8%	17.1%	4.9%	1.9%				
Senoglou et al. [40]	Turkey						4.4%	35.6%	36.7%	20%	3.3%				
Seema et al. [38]	India	5.36%	71.81%	22.14%	0.67%	11.4%	34.8%	29.5%	16.7%	4.6%	2.6%	9.39%	30.20%	51.67%	8.72%
Shewale et al. [42]	India	7.5%	76%	16%	0.67%	5.5%	40%	37%	10.5%	5%	2%	1%	22%	56%	21%
Phalgunan, Baskaran [34]	India		57%	39%	3.5%										
Nasr et al. [28]	Egypt	18.66%	60.66%	20.66%		8%	36.6%	30%	16.6%	5.3%	3.3%	6%	33.33%	53.33%	7.33%
Rajeev et al. [35]	India	10.62%	79.13%	9.84%	0.4%	11.02%	31.10%	39.76%	12.16%	5.51%		15.35%	38.20%	6.92%	10.23%
Mayuri et al. [24]	India	5.08%	71.18%	22.03%	1.69%	11.01%	34.74%	29.66%	16.94%	4.23%	3.38%				
Chhabra [11]			50%	40%	10%	3.33%	30%	33.33%	30%	3.33%			10%	63.33%	26.67%
Nadeem [26]	India	5%	60%	30%	5%										
Mishra et al. [25]	India	23.86%	63.63%	12.51%		9.09%	44.31%	30.70%	14.77%	1.13%		1.14%	20.46%	57.95%	20.45%
Parashuram [32]	India	29.9%	68.1%	2.1%											
Vasuki et al. [46]	India					8%	42%	33%	6%	6%			9%	48%	43%
Dhuria et al. [13]	India	5.68%	47.72%	28.4%	10.22%	10.22%	15.9%	37.5%	25%	2.27%	5.68%		4.54%	30.68%	64.76%
Bagoji et al. [4]	India	4.34%	54.34%	25.36%	10.14%										
Abera et al. [2]	Ethiopia	8.2%	60.07%	31.1%		4.9%	45.9%	34.4%	13.1%	1.6%			19.7%	63.9%	14.8%

absence of SH, complete dorsal wall agenesis of the sacral canal, and narrowing (< 3 mm) at the apex of SH were recognized and found in significant percentage. This study notes a potential risk of failure of CEB in the Greek population, especially in females, which should be taken into consideration before the administration of caudal epidural anaesthesia and in the preoperative evaluation of patients.

In order to calculate the exact percentage that each anatomical variation causes complications during CEB, clinical studies (anaesthesiological– radiological) should be performed, where each time a complication occurs during anaesthesia the morphology and morphometry of the SH will be recorded.

Acknowledgements

Conflict of interest: None declared

REFERENCES

1. Aggarwal A, Aggarwal A, Harjeet SD. Morphometry of sacral hiatus and its clinical relevance in caudal epidural block. Surg Radiol Anat. 2009; 31(10): 793–800, doi: 10.1007/s00276-009-0529-4, indexed in Pubmed: 19578805.
2. Abera Z, Girma A, Bekele A, et al. Assessment of morphological and morphometrical variations of sacral hiatus in dry human sacrum in Ethiopia. Local Reg Anesth. 2021; 14: 25–32, doi: 10.2147/LRA.S277556, indexed in Pubmed: 33658843.
3. Adler AC, Belon CA, Guffey DM, et al. Real-time ultrasound improves accuracy of caudal block in children. Anesth Analg. 2020; 130(4): 1002–1007, doi: 10.1213/ANE.0000000000004067, indexed in Pubmed: 30829666.
4. Bagoji IB, Bharatha A, Prakash KG, et al. A morphometric and radiological study of sacral hiatus in human adult sacra and its clinical relevance in caudal epidural anaesthesia. Maedica (Bucur). 2020; 15(4): 468–476, doi: 10.26574/maedica.2020.15.4.468, indexed in Pubmed: 33603904.
5. Bagheri H, Govsa F. Anatomy of the sacral hiatus and its clinical relevance in caudal epidural block. Surg Radiol Anat. 2017; 39(9): 943–951, doi: 10.1007/s00276-017-1823-1, indexed in Pubmed: 28247084.
6. Bhattacharya S, Majumdar S, Chakraborty P, et al. A morphometric study of sacral hiatus for caudal epidural block among the population of West Bengal. IJBAMR. 2013; 7(2): 660–667.
7. Boretsky KR, Camelo C, Waisel DB, et al. Confirmation of success rate of landmark-based caudal blockade in children using ultrasound: a prospective analysis. Paediatr Anaesth. 2020; 30(6): 671–675, doi: 10.1111/pan.13865, indexed in Pubmed: 32267040.
8. Bromage PR. Epidural analgesia. WB Saunders 1978: 258–282.
9. Brown DL, Ransom DM, Hall JA, et al. Regional anesthesia and local anesthetic-induced systemic toxicity: seizure frequency and accompanying cardiovascular changes. Anesth Analg. 1995; 81(2): 321–328, doi: 10.1097/00000539-199508000-00020, indexed in Pubmed: 7618723.
10. Candido K, Stevens RA. Intrathecal neurolytic blocks for the relief of cancer pain. Best Pract Res Clin Anaesthesiol. 2003; 17(3): 407–428, doi: 10.1016/s1521-6896(03)00016-8, indexed in Pubmed: 14529011.
11. Chhabra N. An anatomical study of size and position of sacral hiatus, its importance in Caudal Epidural Block. Int J Health Sci Res. 2014; 4(12): 189–196.
12. Chen CP, Wong AM, Hsu CC, et al. Ultrasound as a screening tool for proceeding with caudal epidural injections. Arch Phys Med Rehabil. 2010; 91(3): 358–363, doi: 10.1016/j.apmr.2009.11.019, indexed in Pubmed: 20298824.
13. Dhuria R, Dave V, Ahuja M. Anatomical Variations and Clinical Correlations of Sacral Hiatus and Sacral Canal. J Med Acad. 2018; 1(2): 75–80, doi: 10.5005/jp-journals-10070-0016.
14. DiGiovanni AJ. Inadvertent intraosseous injection: a hazard of caudal anesthesia. Anesthesiology. 1971; 34(1): 92–94, doi: 10.1097/00000542-197101000-00025, indexed in Pubmed: 5540372.
15. Hatzic A. Textbook of regional anesthesia and acute pain management. Caudal anesthesia. McGrawHill Medical 2007: 269–283.
16. Joo J, Kim J, Lee J. The prevalence of anatomical variations that can cause inadvertent dural puncture when performing caudal block in Koreans: a study using magnetic resonance imaging. Anaesthesia. 2010; 65(1): 23–26, doi: 10.1111/j.1365-2044.2009.06168.x, indexed in Pubmed: 19922508.
17. Kakiuchi M, Abe K. Pre-incisional caudal epidural blockade and the relief of pain after lumbar spine operations. Int Orthop. 1997; 21(1): 62–66, doi: 10.1007/s002640050121, indexed in Pubmed: 9151189.
18. Kamal A, Ara S, Ashrafuzzaman Md, et al. Morphometry of sacral hiatus and its clinical relevance in caudal epidural block. J Dhaka Med Coll. 2015; 23(1): 31–36, doi: 10.3329/jdmc.v23i1.22690.
19. Kao SC, Lin CS. Caudal epidural block: an updated review of anatomy and techniques. Biomed Res Int. 2017; 2017: 9217145, doi: 10.1155/2017/9217145, indexed in Pubmed: 28337460.
20. Kim YH, Park HJ, Cho S, et al. Assessment of factors affecting the difficulty of caudal epidural injections in adults using ultrasound. Pain Res Manag. 2014; 19(5): 275–279, doi: 10.1155/2014/679128, indexed in Pubmed: 25111987.
21. Kumar V, Pandey SN, Bajpai RN, et al. Morphometrical study of sacral hiatus. J Anat Soc India. 1992; 41(1): 7–13.

22. Laishram D, Ghosh A, Shastri D. A study on the variations of sacrum and its clinical significance. IOSR-JDMS. 2016; 15(6): 08–14.

23. Malarvani T, Ganesh E, Nirmala P, et al. Study of sacral hiatus in dry human sacra in Nepal, Parsa Region. Int J Anat Res. 2015; 3(1): 848–855, doi: 10.16965/ijar.2014.527.

24. Mayuri J, Vijay G, Vasudha N, et al. Anatomical study of sacral hiatus in dry isolated sacra. J Res Med Den Sci. 2014; 2(2): 43, doi: 10.5455/jrmds.20142210.

25. Mishra M, Singh AK, Satyavathi P, et al. Sacral Hiatus Study in Dry Human Sacra. Janaki Med Coll J Med Sci. 2014; 2(1): 17–22, doi: 10.3126/jmcjms.v2i1.11391.

26. Nadeem G. Importance of knowing the level of sacral hiatus for caudal epidural anesthesia. J Morphol Sci. 2018; 31(01): 009–013, doi: 10.4322/jms.ao053913.

27. Nagar SK. A study of sacral hiatus in dry human sacra. J Anat Soc India. 2004; 53(2): 18–21.

28. Nasr A, Ali Y, ElSawy N. The sacral hiatus: an anatomic study on both cadaveric and dry bones. Trans Clin Bio. 2014; 2(1): 4, doi: 10.14259/tcb.v2i1.124.

29. Nastoulis E, Karakasi MV, Pavlidis P, et al. Anatomy and clinical significance of sacral variations: a systematic review. Folia Morphol. 2019; 78(4): 651–667, doi: 10.5603/FM.a2019.0040, indexed in Pubmed: 30949993.

30. Njihia BN, Awori KO, Gikenye G. Morphology of the sacral hiatus in an african population – implications for caudal epidural injections. Ann Afr Surg. 2011; 7(1), doi: 10.4314/aas.v7i1.67024.

31. Osunwoke EA, Oladipo GS, Alison TA, et al. A study of sacral hiatus in dry human sacra in Southern Nigeria. J Biol Agriculture Healthcare. 2014; 4(5): 43–48.

32. Parashuram R. Morphometrical study of sacral hiatus in dry human sacra. Int J Res Med Sci. 2015: 1726–1733, doi: 10.18203/2320-6012.ijrms20150260.

33. Patel ZK, Thummar B, Rathod SP, et al. Multi-centric morphometric study of dry human srum of Indian population in Gujarat region. NJIRM. 2011; 2: 31–35.

34. Phalgunan V, Baskaran S. Morphometric analysis of sacral hiatus and its clinical significance. Health Agenda. 2013; 1: 10–15.

35. Rajeev R, Surekha D, Medha A, et al. Variations in anatomical features of the sacral hiatus in Indian dry sacra. Int J Med Res Health Sci. 2014; 3(3): 634, doi: 10.5958/2319-5886.2014.00409.3.

36. Saha D, Bhattaracharya S, Uzzaman A, et al. Morphometric study of variations of sacral hiatus among West Bengal population and clinical implications. Ital J Anat Embryol. 2016: 165–171.

37. Sanghvi C, Dua A. Caudal Anesthesia. In: StatPearls [Internet]. Treasure Island (FL): StatPearls Publishing 2023 Jan. 2022 Sep 26.

38. Seema, Singh M, Mahajan A. An anatomical study of variations of sacral hiatus in sacra of north indian origin and its clinical significance. Int J Morphol. 2013; 31(1): 110–114, doi: 10.4067/s0717-95022013000100017.

39. Sekiguchi M, Yabuki S, Satoh K, et al. An anatomic study of the sacral hiatus: a basis for successful caudal epidural block. Clin J Pain. 2004; 20(1): 51–54, doi: 10.1097/00002508-200401000-00010, indexed in Pubmed: 14668657.

40. Senoglu N, Senoglu M, Oksuz H, et al. Landmarks of the sacral hiatus for caudal epidural block: an anatomical study. Br J Anaesth. 2005; 95(5): 692–695, doi: 10.1093/bja/aei236, indexed in Pubmed: 16155035.

41. Senoglu N, Senoglu M, Ozkan F, et al. The level of termination of the dural sac by MRI and its clinical relevance in caudal epidural block in adults. Surg Radiol Anat. 2013; 35(7): 579–584, doi: 10.1007/s00276-013-1108-2, indexed in Pubmed: 23515954.

42. Shewale S, Laeeque M, Kulkarni P, et al. Morphological and morphometrical study of sacral hiatus. IJRTSAT. 2013; 6(1): 48–52.

43. Shinde V, Bhusaraddi PS. A study of variations of sacral hiatus of dry human sacra in north interior Karnataka region. Nat J Clin Anat. 2019; 03(04): 215–219, doi: 10.1055/s-0039-3401772.

44. Suwanlikhid N, Lakchayapakorn K, Mahakkanukrauh P. The position and size of sacral size of sacral hiatus in Thai dry human sacra. Thammasat Med J. 2013; 13(3): 313–319.

45. Ukoha U, Okafor J, Anyabolu A, et al. Morphometric study of the sacral hiatus in Nigerian dry human sacral bones. Int J Med Res Heal Sci. 2014; 3(1): 115, doi: 10.5958/j.2319-5886.3.1.023.

46. Vasuki D, Nirmaladevi D, Hebzibah M, et al. Morphology of sacrum and its variations. IOSR-JDMS. 2016; 15(08): 129–142, doi: 10.9790/0853-150802129142.

47. Wiegele M, Marhofer P, Lönnqvist PA. Caudal epidural blocks in paediatric patients: a review and practical considerations. Br J Anaesth. 2019; 122(4): 509–517, doi: 10.1016/j.bja.2018.11.030, indexed in Pubmed: 30857607.

V M
VIA MEDICA

ORIGINAL ARTICLE

The occipital-vertebral anastomosis revisited

P. Ostrowski[1], M. Bonczar[1], A. del Carmen Yika[1], H. Czekańska[2], J. Batko[1], W. Wojciechowski[3],
S.K. Ghosh[4], J. Jaworek-Troć[1], K. Piątek-Koziej[1], A. Juszczak[1], T. Gładysz[1], D. Lusina[1],
J. Walocha[1], M. Koziej[1]

[1]Department of Anatomy, Jagiellonian University Medical College, Krakow, Poland
[2]Department of Anatomy, Medical University of Warsaw, Poland
[3]Department of Radiology, Jagiellonian University Medical College, Krakow, Poland
[4]Department of Anatomy, All India Institute of Medical Sciences, Patna, India

Background: The goal of the study was to provide relevant data about the location and prevalence of the occipital artery-vertebral artery (OA-VA) anastomosis in patients without visible occlusive disease, as well as to thoroughly discuss the clinical significance of these anastomotic channels. Furthermore, the morphometric properties of the OA and its branches were also analysed.

Materials and methods: A retrospective study was carried out to indicate anatomical variations, their prevalence, and morphometrical data on the OA and its branches. The study was performed on 55 randomly selected computed tomography angiographies (CTA) of the head and neck region. Each CTA result was analysed bilaterally. Thus, 110 results were originally assessed.

Results: The OA median maximal diameter was demonstrated at 4.85 mm (lower quartile [LQ]: 4.11; upper quartile [UQ]: 5.53) and the median maximal diameter of VA at 3.60 mm (LQ: 2.79; UQ: 4.38). The distances between OA and its branches were also measured giving a median result of 21.73, 30.29, 60.84, 34.88, 18.02, 55.16 mm for the lower and upper sternocleidomastoid branch, meningeal branch, mastoid branch, and descending branch, respectively. The median distance between OA and its first anastomosis was set to be 51.15 mm (LQ: 37.20; UQ: 60.10). Moreover, a set of additional measurements was carried out in order to create a three-dimensional anatomical heat-map of the occurrence of the OA-VA anastomosis.

Conclusions: Knowledge about the anatomy of the OA-VA anastomosis might be of immense importance to avoid potentially fatal complications during embolisation of the OA and its branches. (Folia Morphol 2023; 82, 3: 615–623)

Key words: occipital artery, anastomosis, anatomy, vertebral artery

INTRODUCTION

The occipital artery (OA) arises slightly above the level of the hyoid bone or facial artery, from the posterior side of the external carotid artery (ECA) [13]. It courses posteromedially and parallel to the attachment of the posterior belly of the digastric muscle in the occipital groove in the temporal bone. During its course, it gives off numerous branches. The upper and lower sternocleidomastoid branches are considered the main branches of the OA. However, other inconstant branches also arise from the OA, such as the auricular branch or the mastoid branch [12].

The amount of data concerning the prevalence of the occipital-vertebral (OA-VA) anastomosis is scarce in the available literature. The said anastomotic channel was first extensively described by Schechter in 1964 [16]. In the study, 1000 cerebral angiograms were analysed and the anastomosis was observed 8 times. Another study regarding this topic was conducted by Alvernia et al. [2] on 6 cadaveric heads. Microscopic anastomoses between the OA and the VA were present in 11 out of 12 hemispheres.

Knowledge about the OA-VA anastomosis is of immense importance during endovascular procedures. Vascular and neoplastic processes fed by the OA or its branches are embolised with increasing frequency due to the advancements in endovascular techniques and increased knowledge of the vascular anatomy. However, these procedures are associated with potentially disastrous complications, such as posterior circulation stroke [2, 17]. Understanding the variable anatomy of the OA and its branches might be of great importance when performing revascularisation procedures, such as the occipital artery-posterior inferior cerebellar artery (OA-PICA) bypass. The OA has been described as a great donor vessel for the revascularisation of the posterior fossa due to its satisfactory length, calibre match, and close proximity to the intracranial arteries in that region [3].

The goal of the study was to provide relevant data about the location and prevalence of the OA-VA anastomosis in patients without visible occlusive disease, as well as to thoroughly discuss the clinical significance of these anastomotic channels. Furthermore, the morphometric properties of the OA and its branches were also analysed. It is hoped that the present study can help physicians who perform endovascular and neurovascular procedures associated with the OA.

MATERIALS AND METHODS

Study group

A retrospective study was carried out to indicate anatomical variations, their prevalence, and morphometrical data on the OA and its branches. The study was performed on 55 randomly selected computed tomography (CT) angiographies (CTA) of the head and neck region. The CTAs were analysed in the Department of Radiology of Jagiellonian University Medical College, Krakow, Poland in May 2022. Each CTA result was analysed bilaterally. Thus, 110 results were originally assessed. Exclusion criteria were es-

tablished as follows: (1) head or/and neck trauma affecting the course of OA or/and its initial branches, (2) artifacts significantly preventing precise and accurate imaging or/and measurements, (3) unintelligible and low-quality images, and (4) significant deficit of filling the whole arterial system with contrast. Defects that met exclusion criteria but considered only one side of the CTA without affecting the clearance of the contralateral side, did not disqualify the entire CTA but only the damaged side. Finally, a total of 88 sides were analysed. Of the excluded, the majority (n = 14) was eliminated due to significant artifacts. The other 8 were low quality.

Results acquisition

All head and neck CTA were performed on a 128-slice scanner CT (Philips Ingenuity CT, Philips Healthcare). The main CT imaging parameters were as follows: collimation/increment: 0.625/0.3 mm; tube current: 120 mAs; field of view: 210 mm; matrix size: 512×512.

All of the patients received intravenous administration of contrast material at a dose of 1 mL/kg (standard dose). A non-ionic contrast medium (CM) containing 350 mg of iodine per mL was used (Jowersol 741 mg/mL, Optiray®, Guerbet, France). CT data acquisition was triggered using a real-time bolus-tracking technique (Philips Healthcare) with the region of interest placed in the ascending aorta. The CM was intravenously injected using a power injector at a flow rate of 5 mL/s, which was immediately followed by injecting 40 mL of saline solution at the same flow rate. Following injection of CM and saline, image acquisition was automatically started with a 2 s delay when the attenuation trigger value reached a threshold of 120 Hounsfield Units (HU). Scanning was performed in the caudocranial direction, while the CTA examination was started at the level of the aortic arch up to the circle of Willis.

The CTAs were analysed on a dedicated workstation in the Anatomical Department of Jagiellonian University Medical College, Krakow, Poland. To ensure the highest possible quality of the visualisations and measurements and minimise potential bias, Materialise Mimics Medical version 22.0 software (Materialise NV, Leuven, Belgium) software was used. Three-dimensional (3D) reconstructions of each scan were developed, employing a set of settings, severally adjusted to each scan. Due to the nature of the contrast study, the cut-off level was set at the lower

limit of normal, oscillating in the range of 25–80 HU. The range was individually adjusted to each OA after a visual investigation.

Evaluation and measurements

At the starting point of each calculating part, the authors ensured that OA, its branches, and close anatomical area were fully visualised. Moreover, each branch of OA was identified by following its course. The direction of the OA and a set of its branches with their arrangement were evaluated and descriptively noted. A set of measurements was enrolled by two independent researchers separately. The measurements executed on each OA are as follows: (1) OA's maximal diameter at its origin and at its ending, (2) OA's ostial area at its beginning and its ending. Additionally, all branches and anastomosis of each OA were identified and noted. Afterward, a set of measurements regarding the distances between each branch and/or anastomosis were enrolled. The ostial area and maximal diameter of each OA branch have been taken. Furthermore, the distance between OA and each branch was measured. Additionally, each OA was evaluated by respecting its course, its branches, and their pattern. The mean value has been established after obtaining the results of the research.

Ethical approval

The research protocol was submitted for assessment and approved by the Bioethical Committee of the Jagiellonian University, Krakow, Poland (1072.6120.51.2022). Further stages of the study were carried out in accordance with the approved guidelines.

Ethical concern

All procedures performed in studies involving human participants were in accordance with the ethical standards of the institutional and/or national research committee and with the 1964 Helsinki Declaration and its later amendments or comparable ethical standards. The material used for this research was obtained from a body donation programme.

Statistical analysis

Statistical analysis was performed with STATISTICA v13.1 (StatSoft Inc., Tulsa, OK, USA). The frequency and percentages presented qualitative features. The Shapiro-Wilk test was being used to establish the normal distribution. Quantitative characteristics were presented by medians and upper and lower quartiles (UQ, LQ), as well as means and standard deviation (SD), depending on the verified normality of the data. Statistical significance was defined as $p < 0.05$. U Mann-Whitney and Wilcoxon signed-rank tests were used to establish potential differences between groups. Spearman's rank correlation coefficient was used to determine possible correlations between the parameters.

RESULTS

A total of 88 OAs of 44 patients were analysed. Of these, 32 were from women (36.4%) and 56 from men (63.6%) in age from 17 to 82 years old (mean age: 48 years old, SD: 17.95). One of the criteria included in the study was the presence and absence of the occipital artery branches; lower sternocleidomastoid (LSCMB), upper sternocleidomastoid (USCMB), meningeal (MeB), mastoid (MaB), auricular (AB), and descending (DB) as well as the potential appearances of the anastomosis. LSCM branch was present in 11 (12.5%) of the cases, USCM in 12 (13.6%) of the cases, MeB in 9 (10.2%) of the cases, MaB in 4 (4.5%) of the cases, AB in 6 (6.8%) of the cases, and DB in 44 (50.0%) of the cases. Anastomoses were established in 11 (12.5%) occipital arteries. The detailed results are presented in Table 1. Illustration of the branches of the OA can be found on Figure 1. Illustration of a sample anastomosis of the OA can be found on Figure 2.

The OA median maximal diameter was demonstrated at 4.85 mm (LQ: 4.11; UQ: 5.53) and the median maximal diameter of VA at 3.60 mm (LQ: 2.79; UQ: 4.38). The distances between OA and its branches were also measured giving a median result of 21.73, 30.29, 60.84, 34.88, 18.02, 55.16 mm for the LSCMB, USCMB, MeB, MaB, and DB, respectively. The median distance between OA and its first anastomosis was set to be 51.15 mm (LQ: 37.20; UQ: 60.10). All the above-mentioned results and more detailed results are presented in Table 2.

To evaluate the sexual dimorphism in the morphometry and anatomical features of the OA results in each category were separated for each sex. There were no statistically significant differences ($p > 0.05$) in any of the studied groups. Detailed results concerning sex are gathered in Table 3.

Additionally, potential differences in the dimensions regarding the patients' side of the OA were analysed. There were no statistically significant dif-

Table 1. Qualitative results of the data analysis

Category	Number	Percentage
Patients' sex		
Female	32	36.4%
Male	56	63.6%
Initial direction of the OA		
Superior	32	76.2%
Posterior	8	19.0%
Interior	1	2.4%
Anterior	1	2.4%
Presence of the LSCMB		
Absent	77	87.5%
Present	11	12.5%
Presence of the USCMB		
Absent	76	86.4%
Present	12	13.6%
Presence of the MEB		
Absent	79	89.8%
Present	9	10.2%
Presence of the MAB		
Absent	84	95.5%
Present	4	4.5%
Presence of the AB		
Absent	82	93.2%
Present	6	6.8%
Presence of the DB		
Absent	44	50.0%
Present	44	50.0%
Presence of an anastomosis		
Absent	77	87.5%
Present	11	12.5%
Type of an anastomosis		
DB of the OA with VA	5	45.5%
USCMB of the OA with VA	3	27.3%
DB of the OA with deep cervical artery	3	27.3%

AB — auricular branch; DB — descending branch; LSCMB — lower sternocleidomastoid branch; MAB — mastoid branch; MEB — meningeal branch; OA — occipital artery; USCMB — upper sternocleidomastoid branch; VA — vertebral artery

Figure 1. Occipital artery and its branches; 1 — lower sterno-cleidomastoid branch; 2 — upper sternocleidomastoid branch; 3 — descending branch; 4 — mastoid branch; 5 — auricular branch; 6 — meningeal branch.
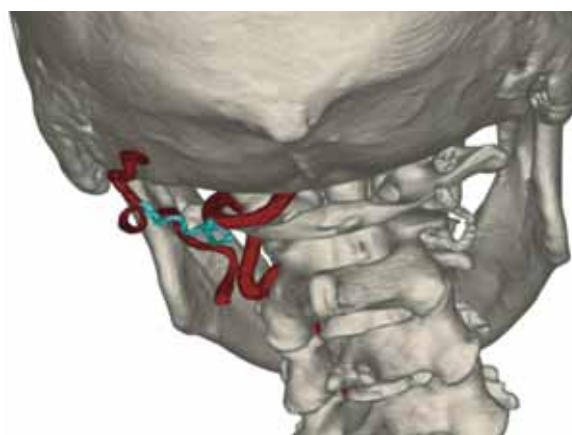
Figure 2. Sample anastomosis of the occipital artery.

ferences between measurements on the left and the right side. On the left, mean values of 4.79, 3.84, 75.08 mm (OA maximal diameter, VA maximal diameter, OA length, respectively), and on the right; 4.94, 3.51, 72.72 were established.

Moreover, possible correlations between the age of the patient and each dimension were analysed. The statistically significant associations between OA length and (1) distance between OA and USCMB (R = 0.59; p = 0.04), (2) distance between OA and MeB (R = 0.90; p = 0.001), (3) distance between OA and the DB (R = 0.75; p = 0.00) were obtained. The statistically significant correlation between the distance between OA and USCMB and the distance between OA and the DB was obtained. No association between age and any of the OAs morphology was found. The R values obtained in the correlation analysis between the groups can be found in Table 4.

Moreover, a set of additional measurements was carried out in order to create a 3D anatomical heat-map of the occurrence of the anastomosis of the OA. In order to create the heat-map, three points on each of the CTAs were localized: (1) internal occipital protuberance, (2) angle of the mandibula, and (3) condylar process. Out of those points, two triangles (on both sides) were established on each CTA. Furthermore, using geometrical transformations in order to maintain standardisation of the results, the

Table 2. Results of the measurements

Category	Median	LQ	HQ	Minimum	Maximum	Mean	SD
Overall results							
OA maximal diameter	4.85	4.11	5.53	2.69	9.32	4.86	1.07
VA maximal diameter	3.60	2.79	4.38	2.05	6.03	3.67	0.97
Distance between OA and LSCMB	21.73	10.40	28.65	5.95	31.61	20.24	9.02
Distance between OA and USCMB	30.29	24.15	39.48	12.10	49.16	31.37	11.13
Distance between OA and MEB	60.84	53.23	67.62	32.93	78.73	60.15	13.00
Distance between OA and MAB	34.88	21.30	52.51	16.75	61.12	36.91	19.70
Distance between OA and AB	18.02	17.37	21.49	10.40	26.60	18.65	5.33
Distance between OA and the DB	55.16	48.59	59.96	24.22	88.89	55.01	11.92
Distance between OA and its first anastomosis	51.15	37.20	60.10	35.78	63.70	50.74	10.32

AB — auricular branch; DB — descending branch; HQ — higher quartile; LQ — lower quartile; LSCMB — lower sternocleidomastoid branch; MAB — mastoid branch; MEB — meningeal branch; OA — occipital artery; SD — standard deviation; USCMB — upper sternocleidomastoid branch; VA — vertebral artery

Table 3. Results of the measurements regarding sex

Category	Sex	Median	LQ	HQ	Minimum	Maximum	Mean	SD	P
OA maximal diameter	Females	4.90	3.79	5.65	2.69	9.32	4.94	1.41	0.91
	Males	4.82	4.13	5.47	3.19	6.48	4.82	0.83	
VA maximal diameter	Females	3.74	2.67	4.43	2.05	6.03	3.75	1.19	0.98
	Males	3.58	2.93	4.38	2.32	5.67	3.63	0.82	
OA length	Females	75.81	69.75	82.60	45.86	96.56	75.63	11.39	0.26
	Males	70.52	64.02	85.38	45.36	95.42	72.92	13.09	
Distance between OA and LSCMB	Females	29.23	21.73	31.61	21.73	31.61	27.52	5.16	0.08
	Males	17.07	10.22	25.46	5.95	28.65	17.51	8.79	
Distance between OA and USCMB	Females	32.06	28.09	49.16	28.09	49.16	36.44	11.20	0.48
	Males	28.52	21.26	37.32	12.10	45.70	29.68	11.23	
Distance between OA and MEB	Females	63.08	56.80	72.03	52.75	78.73	64.41	10.87	0.73
	Males	60.84	53.23	67.62	32.93	69.11	56.75	14.73	
Distance between OA and MAB	Females	61.12	61.12	61.12	61.12	61.12	61.12	—	—
	Males	25.85	16.75	43.90	16.75	43.90	28.83	13.82	
Distance between OA and AB	Females	—	—	—	—	—	—	—	—
	Males	18.02	17.37	21.49	10.40	26.60	18.65	5.33	
Distance between OA and the DB	Females	57.15	51.81	61.22	46.64	88.89	59.57	11.99	0.18
	Males	54.89	44.76	57.90	24.22	81.41	52.88	11.46	
Distance between OA and its first anastomosis	Females	54.51	51.01	60.79	50.87	63.70	55.90	6.13	0.32
	Males	48.76	36.81	60.10	35.78	62.96	47.79	11.44	

AB — auricular branch; DB — descending branch; HQ — higher quartile; LQ — lower quartile; LSCMB — lower sternocleidomastoid branch; MAB — mastoid branch; MEB — meningeal branch; OA — occipital artery; SD — standard deviation; USCMB — upper sternocleidomastoid branch; VA — vertebral artery

positions of the anastomosis were applied to the illustrations. The heat maps are presented in Figure 3.

DISCUSSION

Mannie M. Schechter [16] was the first to extensively describe the prevalence of the OA-VA anastomosis in 1964. In the study, 1000 consecutive cerebral angiograms were reviewed, and the anastomosis was observed 8 times. However, in 2 of these patients, occlusive disease was present in the cervical portion of the vertebral arteries. These anastomotic channels can form as a result of disturbances in the haemodynamic balance between the external carotid and vertebral systems, such as in cases of stenotic disease. Howev-

Table 4. Table gathers the R values obtained in the correlation analysis between categories

Category	Age	OA maximal diameter	VA maximal diameter	OA length	Distance between OA and LSCMB	Distance between OA and USCMB	Distance between OA and MEB	Distance between OA and MAB	Distance between OA and AB	Distance between OA and the DB	Distance between OA and its first anastomosis
Age	1.00	−0.21	0.15	−0.07	0.09	−0.54	−0.38	−0.40	−0.03	0.01	−0.48
OA maximal diameter	−0.21	1.00	0.10	0.02	0.16	0.18	0.01	0.60	−0.31	−0.08	0.24
VA maximal diameter	0.15	0.10	1.00	0.04	−0.18	0.16	−0.61	−0.40	−0.20	−0.07	0.32
OA length	−0.07	0.02	0.04	1.00	0.16	0.59	0.90	0.80	0.80	0.75	0.58
Distance between OA and LSCMB	0.09	0.16	−0.18	0.16	1.00					0.30	
Distance between OA and USCMB	−0.54	0.18	0.16	0.59		1.00				0.88	
Distance between OA and MEB	−0.38	0.01	−0.61	0.90			1.00			0.50	
Distance between OA and MAB	−0.40	0.60	−0.40	0.80				1.00			
Distance between OA and AB	−0.03	−0.31	−0.20	0.80					1.00	0.40	
Distance between OA and the DB	0.01	−0.08	−0.07	0.75	0.30	0.88	0.50		0.40	1.00	
Distance between OA and its first anastomosis	−0.48	0.24	0.32	0.58							1.00

Highlighted in red are those in which the p value was smaller than 0.05; OA — occipital artery; VA — vertebral artery; LSCMB — lower sternocleidomastoid branch; USCMB — upper sternocleidomastoid branch; MEB — meningeal branch; MAB — mastoid branch; AB — auricular branch; DB — descending branch.

Figure 3. Heat maps of the occurrence of the anastomosis of the occipital artery.

er, these anastomoses can also occur in the absence of occlusive disease. Alvernia et al. [2] conducted a microanatomical study about the OA and the OA--VA anastomosis in the absence of occlusive disease. In the study, anastomotic vessels were observed in 11 out of the 12 specimens (91%), and they were characterised into three types. The most common type consisted of an anastomosis between the OA and the posterior radicular artery of the vertebral artery which was related to the dorsal root of C2.

Angiographically, these anastomotic channels are oftentimes not well visible because of their small calibre. The anastomoses may enlarge and become more functionally important under certain haemodynamic conditions. Therefore, in order to gather reliable data about the prevalence of the OA-VA anastomosis, cases where the patient suffered from visible occlusive disease were excluded. The result of the present study shows that the OA forms an anastomosis with another artery in 12.5% of the cases. The most common branch involved in the OA-VA anastomosis was the descending branch of the OA (45.5%); however, the USCM branch was also involved in this anastomosis (27.3%). Interestingly, the OA formed an anastomosis with the deep cervical artery, which is the branch of the costocervical trunk, in 27.3% of the cases (Fig. 4). The deep cervical artery may have a variable origin, originating either from the costo-cervical trunk or directly from the subclavian artery [4, 5, 14]. Nevertheless, these results show that the OA can form anastomoses between both the vertebral but also the subclavian systems. Our results show a higher prevalence of the OA-VA anastomoses than what Schechter presented [16], possibly because of the advancements in angiographic imaging. Alvernia et al. [2] presented a much higher frequency of the occurrence of the anastomotic channels; however, the said study was a microanatomical one, and the small
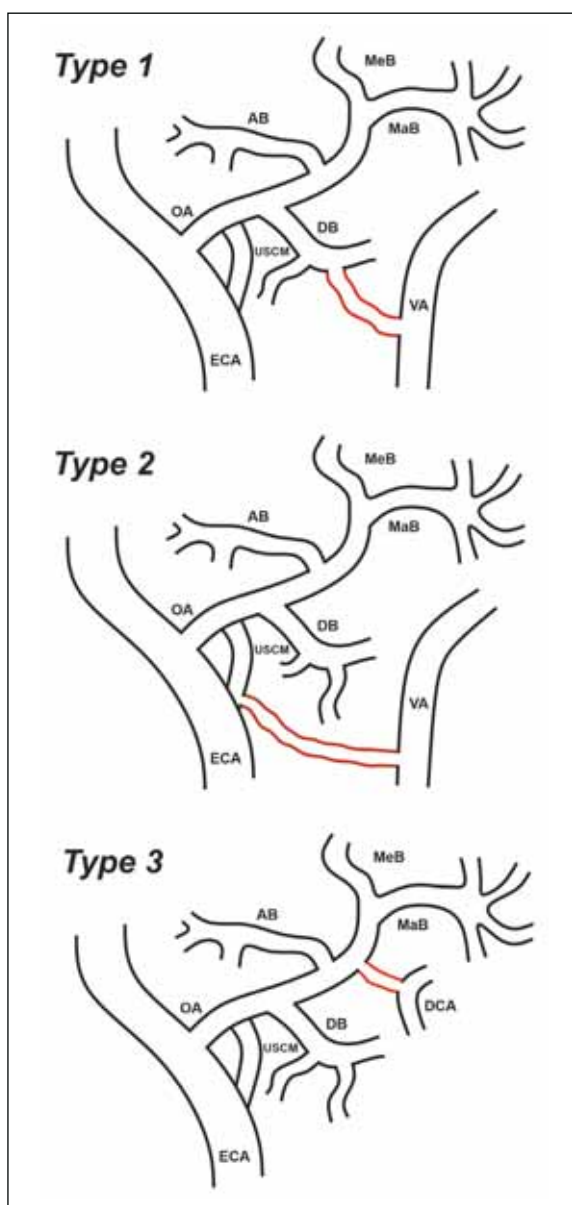
Figure 4. Three types of occipital-vertebral arterial anastomosis; AB — auricular branch; DB — descending branch; DCA — deep cervical artery; ECA — external carotid artery; MaB — mastoid branch; MeB — meningeal branch; OA — occipital artery; USCMB — upper sternocleidomastoid branch.

vessel calibre of the vessels forming the anastomosis would not be visible on CTA. Their small size can also raise questions about whether these microscopical anastomoses are as clinically significant as the ones that are well visible on CTA.

The OA-VA anastomotic channels are important to take into consideration because they can provide an additional route for the delivery of thrombolytic drugs in extreme cases of occlusive disease [2, 9]. Alvernia et al. [2] discussed a case where a patient with bilaterally occluded vertebral arteries and acute basilar artery syndrome could be treated because of the presence of the OA-VA anastomosis. Re-establishment of flow through the basilar artery was possible due to subselective catheterisation of the OA, which reconstituted the VA that it formed an anastomosis with. Subsequently, the thrombolytic agent could be delivered through the VA to the occluded basilar artery [2].

The importance of the OA-VA anastomosis was also highlighted by Milnerowicz et al. [11] in a case study about a 20-year-old patient who underwent adenotonsillectomy. The procedure itself went uncomplicated; however, the patient developed three episodes of significant bleeding from the left tonsillar bed. Therefore, the external carotid artery was ligated and the procedure had no complications. However, the patient came back with the same problem of recurrent bleeding. Selective arteriography of the left VA was performed and showed the presence of an OA-VA anastomosis with retrograde flow from the VA to the external carotid artery segment above the ligation. The trunk of the external carotid artery was then embolised through the anastomosis. Unfortunately, the patient became lethargic the next day. Subsequently, a head CT was performed and showed a hypodense area in the right thalamus corresponding to an ischaemic stroke.

Furthermore, Takeuchi et al. [18] stated that in patients who underwent external carotid artery ligation, the main collateral pathways to the external carotid artery were from the VA via the OA-VA anastomosis.

The morphological aspects of the OA were also analysed in the present study. This knowledge can be of great use in procedures associated with this artery, such as the OA-PICA bypass. The OA has been proven to be a reliable vessel for revascularisation procedures of the posterior cranial fossa because of its satisfactory length, calibre match, and close proximity to the intracranial arteries in that region. The present study shows that the mean diameter of the OA at its origin was 4.90 mm in females and 4.82 mm in males. These results are considerably higher than the results of other studies concerning this topic [2, 7, 8, 10]. The data presented in the current meta-analysis can also be of great use when performing reconstructive flaps. Scalp defects in the temporal and parietal regions are usually repaired using island flaps which are normally supplied by the superficial temporal vessels [19]. Knowledge about the anatomy of the OA might also come in handy when performing the OA fascial flap for ear reconstruction [1, 6, 15].

Furthermore, the OA provides significant blood supply to the dura of the posterior fossa through transosseous and transforaminal branches. In the present study, we referred to them as the meningeal branch (present in 10.2% of the cases) and the mastoid branch (present in 4.5% of the cases). These branches provide vascularity to the wall of the venous sinuses in this region. The presence of the said branches would explain why the OA is a usual feeding artery of dural arteriovenous fistulas.

Limitations of the study

The present study undoubtedly has some limitations. Although the size of the study group used in the current paper is the largest among imaging studies concerning the morphology of the OA and the OA-VA anastomosis, larger population-based research is still warranted to discern the true prevalence of its variants. Additionally, radiological imaging only allows one to evaluate haemodynamically efficient arteries. Therefore, this can be a relatively big source of bias when assessing anatomical variations of the OA, and other arterial entities.

CONCLUSIONS

In this study, the morphometric properties and variations of the OA were presented. Furthermore, the anastomotic channels between the OA and the VA were analysed and their potential clinical implications were discussed. Knowledge about the anatomy of the OA-VA anastomosis might be of immense importance to avoid potentially fatal complications during embolisation of the OA and its branches.

had no role in the study's design, data collection, or analysis, decision to publish, or preparation of the manuscript.

Conflict of interest: None declared

REFERENCES

1. Akeel M. Myomucosal island flap of the buccinator muscle: an anatomical study. Transl Res Anat. 2021; 22: 100091, doi: 10.1016/j.tria.2020.100091.

2. Alvernia JE, Fraser K, Lanzino G. The occipital artery: a microanatomical study. Neurosurgery. 2006; 58(1 Suppl): ONS114–22; discussion ONS114, doi: 10.1227/01. NEU.0000193519.00443.34, indexed in Pubmed: 16543868.

3. Benet A, Tabani H, Ding X, et al. The transperiosteal "inside-out" occipital artery harvesting technique. J Neurosurg. 2018; 130(1): 207–212, doi: 10.3171/2017.6.JNS17518, indexed in Pubmed: 29372878.

4. Bonczar M, Gabryszuk K, Ostrowski P, et al. The thoracoacromial trunk: a detailed analysis. Surg Radiol Anat. 2022; 44(10): 1329–1338, doi: 10.1007/s00276-022-03016-4, indexed in Pubmed: 36094609.

5. Bonczar M, Ostrowski P, Dziedzic M, et al. The costocervical trunk: A detailed review. Clin Anat. 2022; 35(8): 1130–1137, doi: 10.1002/ca.23929, indexed in Pubmed: 35796160.

6. Carvey M, Yang G, Hage R. Skin flaps: a novel approach to medical student instruction on integumentary arterial blood supply. Transl Res Anat. 2021; 23: 100104, doi: 10.1016/j.tria.2020.100104.

7. Di G, Fang X, Hu Q, et al. A microanatomical study of the far lateral approach. World Neurosurg. 2019; 127: e932–e942, doi: 10.1016/j.wneu.2019.04.004, indexed in Pubmed: 30995558.

8. Kawashima M, Rhoton AL, Tanriover N, et al. Microsurgical anatomy of cerebral revascularization. Part II: posterior circulation. J Neurosurg. 2005; 102(1): 132–147, doi: 10.3171/jns.2005.102.1.0132, indexed in Pubmed: 15658105.

9. Macchi C, Catini C. The anatomy and clinical importance of the collateral circles between the vertebral arteries and the cervical, costo-cervical, and occipital branches in 52 living subjects. Ital J Anat Embryol. 1993; 98(3): 153–163, indexed in Pubmed: 8185433.

10. de Magalhães RP, Ferraz AR, Brandão LG, et al. Osteogaleal pedicle flap of the occipital region for head and neck reconstruction: anatomic study. J Otolaryngol. 1998; 27(4): 195–199, indexed in Pubmed: 9711513.

11. Milnerowicz M, Garcarek J, Bladowska J, et al. Bilateral thalamic stroke after tonsillectomy in a patient with collateral extracranial anastomosis - case report. Pol J Radiol. 2019; 84: e126–e130, doi: 10.5114/pjr.2019.83004, indexed in Pubmed: 31019605.

12. Moore KL, Dalley AF, Agur A. Clinically oriented anatomy. 8th ed. Lippincott Williams and Wilkins 2017.

13. Ostrowski P, Bonczar M, Plutecki D, et al. The occipital artery: a meta-analysis of its anatomy with clinical correlations. Anat Sci Int. 2023; 98(1): 12–21, doi: 10.1007/s12565-022-00693-4, indexed in Pubmed: 36350498.

14. Ostrowski P, Bonczar M, Shafarenko K, et al. The thyrocervical trunk: an analysis of its morphology and variations. Anat Sci Int. 2023; 98(2): 240–248, doi: 10.1007/s12565-022-00692-5, indexed in Pubmed: 36350499.

15. Reinisch JF, van Hövell Tot Westerflier CV, Tahiri Y, et al. The occipital artery-based fascial flap for ear reconstruction. Plast Reconstr Surg. 2019; 143(3): 592e–601e, doi: 10.1097/PRS.0000000000005263, indexed in Pubmed: 30531625.

16. Schechter MM. The occipital-vertebral anastomosis. J Neurosurg. 1964; 21: 758–762, doi: 10.3171/jns.1964.21.9.0758, indexed in Pubmed: 14210007.

17. Spetzler RF, Modic M, Bonstelle C. Spontaneous opening of large occipital-vertebral artery anastomosis during embolization. Case report. J Neurosurg. 1980; 53(6): 849–850, doi: 10.3171/jns.1980.53.6.0849, indexed in Pubmed: 7441347.

18. Takeuchi Y, Numata T, Konno A, et al. Hemodynamic changes in the head and neck after ligation of the unilateral carotid arteries: a study using color Doppler imaging. Ann Otol Rhinol Laryngol. 1994; 103(1): 41–45, doi: 10.1177/000348949410300107, indexed in Pubmed: 7904812.

19. Tenna S, Brunetti B, Aveta A, et al. Scalp reconstruction with superficial temporal artery island flap: clinical experience on 30 consecutive cases. J Plast Reconstr Aesthet Surg. 2013; 66(5): 660–666, doi: 10.1016/j.bjps.2013.01.010, indexed in Pubmed: 23415876.

ORIGINAL ARTICLE

Mucous non-goblet cells in the small intestine of guinea pigs (*Cavia porcellus*): a histological and histochemical study

A. Chende[1], V. Miclăuș[2], A. Damian[1], C. Martonoș[1], V. Rus[2], M.-C. Matei-Lațiu[3],
C. Lațiu[4], A.F. Gal[2]

[1]Department of Anatomy, Faculty of Veterinary Medicine, University of Agricultural Sciences and Veterinary Medicine
Cluj-Napoca, Romania
[2]Department of Histology, Faculty of Veterinary Medicine, University of Agricultural Sciences and Veterinary Medicine
Cluj-Napoca, Romania
[3]Department of Physiology, Faculty of Veterinary Medicine, University of Agricultural Sciences and Veterinary Medicine
Cluj-Napoca, Romania
[4]Faculty of Animal Sciences, University of Agricultural Sciences and Veterinary Medicine Cluj-Napoca, Romania

Background: The covering and glandular epithelium of the small intestine in guinea pigs (Cavia porcellus) include some mucus-secreting cells. Goblet cells are specific cells for mucus secretion with a distinctive cup-like appearance due to the accumulation of mucin in the apical pole. The deep crypt secretory (DCS) cells were identified in a limited array of species and only recently were noticed in the large intestine in mice, guinea pigs, humans, monkeys, and pigs. Our study focuses on the microscopical and histochemical features of the DCS cells in the small intestine of guinea pigs.

Materials and methods: The samples from the small intestine were collected from five fully grown guinea pigs that were presented to the Hospital of the Faculty of Veterinary Medicine Cluj-Napoca (Romania) with severe lesions resulted from domestic activities. The collected tissue samples underwent fixation in 10% buffered formalin and were later processed by standard paraffin technique. Mucous substances were detected using the Periodic Acid-Schiff and Alcian-Blue histochemical stain methods.

Results: The intestinal samples of the guinea pigs assessed had a standard microanatomical structure. As regards the mucous-secreting cells from the small intestine, two cell types were identified, i.e. the goblet cells and DCS cells. DCS cells were only detected in the deep parts of the Lieberkühn glands from the jejunum and ileum, and were different morphologically and histochemically from the regular goblet cells.

Conclusions: Our study managed to describe for the first time in guinea pigs, the existence of DCS cells in the jejunum and ileum of the small intestine, but not in the duodenum. (Folia Morphol 2023; 82, 3: 624–632)

Key words: guinea pig, Lieberkühn glands, mucin, deep crypt secretory cells, goblet cells

INTRODUCTION

The epithelium of the intestinal villi, along with the lining epithelium of the Lieberkühn glands, is made predominantly of columnar cells. According to the classical histological sources, the cells of the glandular epithelium include the enterocytes, goblet cells, undifferentiated cells, enteroendocrine cells, and Paneth cells [5, 39]. The goblet cells are secreting mucin, a substance that reaches the surface of the intestinal epithelium to be laid as a well-represented layer [6]. This gel-like mucous coating consists mainly of heterogeneous glycoproteins [32]. The mucous layer of the gastrointestinal tract is responsible for lubrication facilitating the food passage, protection of the underlying surface epithelium from commensal microorganisms as well as the creation of a physical barrier against invading pathogens, toxins, and other environmental irritants [25]. Additionally, the mucous coat influences several cell signalling pathways that can modulate inflammatory responses, facilitate cell-cell interactions, together with the adjustment of cell proliferation, differentiation, and apoptosis [13, 38, 41].

The intestinal mucus is mainly made of a subset of glycoproteins called mucins, which play a central role in the physical protection and regulate the passage and concentration of ions, water, and other immune mediators (e.g. antimicrobial peptides or AMPs and immunoglobulin-A) [25]. So far, more than 20 genes responsible for mucin production were identified [9]. Based on their structural and functional features, mucins can be classified into gel-forming or trans-membrane types. The secreted gel-forming mucins include MUC2, MUC5AC, MUC5B, and MUC6, which are the principal components of the mucus layer and are responsible for viscoelastic properties [19]. MUC2 is the dominant gel-forming mucin in the intestine that contributes to the development of the mucus barrier. MUC5AC is usually present in the stomach, but can also be upregulated in the intestines during enteric infection [16]. MUC5B is usually expressed in low levels in the colon whereas MUC6 is typically expressed in the stomach and duodenum [42]. MUC7 is a secreted mucin detected in saliva and within the oral cavity [28]. Transmembrane mucins (e.g. MUC1, MUC3, MUC4, MUC13, and MUC17) are expressed on the apical poles of epithelial cells and induce the formation of the glycocalyx that acts as a defending coat between the elaborated mucins and the epithelial cells situated below [40]. However, the stomach and colon have a dual-layer of mucus that is made of polymeric sheets of highly glycosylated mucins, which can be classified into (a) the dense internal layer that is anchored to the subjacent epithelium and impermeable to bacteria, and (b) the external layer that is lightly attached to the dense underlying layer and can be penetrated by bacteria. As a comparison, the small intestine has only one layer of mucus with a loose appearance, which is penetrable by bacteria [13, 15].

Along with the goblet cells, that are present in all species, some authors mention the existence of another type of mucin-secretory cells in case of a limited range of species (e.g. humans, rabbits, rats, mice), located in the deep glandular area of the colon. Due to a vacuolated mucus-filled aspect of the cytoplasm in these cells, they were named "vacuolar cells" and considered precursors of the goblet cells [26, 27]. Accordingly, since "vacuolar cells" were noted in the bottom third of the glands in the ascending colon of rats, they were named "deep crypt secretory" (DCS) cells. A high number of DCS cells was noted at the level of the large intestine in mice and guinea pigs (*Cavia porcellus*), while in humans, monkeys, and pigs their number is significantly lower [1, 33].

Nowadays there is not a clear consensus on the terminology to be used on these cells. Currently, the terms "vacuolated cells", "non-goblet cells", "DCS cells" are used, but none of these seems to cover all features associated with these cells [23]. The most frequently used term, i.e. DCS cells, seems to prevail in the most recent literature [34].

The presence of such peculiar cells, i.e. DCS cells [34], was hinted for most of the species [2], but their limited number made them not clearly detectable. Some authors claim that these cells might be young goblet cells, but electron-microscopy studies on the nucleus, nucleolus, and cell organelles have demonstrated that DCS cells are different from goblet cells [2]. Furthermore, similar results were provided by histochemical reactions. Regarding the turnover rate, the literature mentions around 14 to 21 days in rats and mice [1, 2]. However, some recent reports sustain the equivalence of DCS cells to the Paneth cells from the mouse [34].

Paneth cells are secretory cells exclusively situated in the small intestine. They are situated at the base of intestinal crypts of Lieberkuhn and include numerous secretory granules that contain microbicidal proteins, such as alpha-defensins, lysozyme, C-type lectins, and

phospholipase A2. Practically, after recognition of microbial signals, Paneth cells discharge their granule contents in the intestinal lumen. Additionally, these cells play a fundamental role in the renewal of the epithelium of the small intestine. Paneth cells are located in crypts along with the multipotent stem cells, and by secreting some specific factors that sustain the proliferation of epithelial stem cells (e.g. EGF, WNt3, and the Notch ligand Dll4), they sustain the epithelial renewal [8, 18]. However, the DCS cells are positioned at bottom regions of colonic crypts and in the caecum [34]. They have a multivacuolated appearance of the cytoplasm with basally located oval nuclei [11]. According to Sasaki et al. (2016) [34], DCS cells support colonic stem cells by adjusting cellular differentiation and apoptosis along with stem cell localization. Basically, DCS cells represent the equivalents of Paneth cells in the colon crypts [34].

In the light of limited available data referring to DCS cells, our study focuses on the microscopical and histochemical features of the DCS cells in the small intestine of guinea pigs (*Cavia porcellus*).

MATERIALS AND METHODS

Biological material originates from 5 fully grown guinea pigs (*Cavia porcellus*), males, originating from the Hospital of the Faculty of Veterinary Medicine Cluj-Napoca (Romania). The biological material was harvested on a 10-month period of time (September 2018–June 2019) from casualties presented at the aforementioned Hospital, from individuals with severe lesions resulted from domestic activities (house accidents). In all utilized individuals, euthanasia was recommended as a humane method for relieving pain or distress that cannot be controlled by other means as recommended by American Veterinary Medical Association (AMVA) [4, 29].

After the anatomical identification of segments, fragments of duodenum, jejunum, and ileum were collected. Following necropsy examination, no pathological changes were identified in the digestive tract. For the histological investigation, several fragments from the small intestine were harvested (approximately 0.5 cm in length). The collected fragments underwent fixation in 10% buffered formalin for 3 days, followed by a progressive dehydration procedure (ethylic alcohol of 70%, 96%, and 100%) for 1 hour each stage. The clarification was made on 3 successive 1 hour-long 1-butanol baths and subsequentially embedded in the paraffin. For histological evaluation, 5 μm tissue sections were achieved using a Leica rotary microtome (RM2125, Germany) and stained later by Goldner's trichrome method [10].

The detection of mucous substances in the three regions of the small intestine was realized using the Periodic Acid-Schiff (PAS) and Alcian-Blue histochemical stain methods. Accordingly, the presence of neutral mucins was highlighted by the PAS method, whereas the acidic mucins were identified by Alcian-Blue stain, pH-2.5 [3, 24]. The histochemical reaction intensity was measured by grading from 0 (negative reaction) to two pluses (i.e. + faintly positive; ++ intensely positive).

The slides evaluation was performed with the aid of an Olympus BX-41 microscope (Olympus, Japan) attached to the Olympus E330 camera (Olympus, Japan).

The morphometric evaluation of the cells (DCS and Goblet cells) was performed using AmScope Version 4.8 software. The surface of the DCS cells was measured (μm^2) from the ileal and jejunal segments, while for the Goblet cells, their surface was assessed from all the three intestinal segments. The statistical analysis of the obtained results was performed with GraphPad Prism 8 and Microsoft Excel. An unpaired *t*-test, with p < 0.05 was used to compare the surfaces of the DCS cells between jejunal and ileal segments. ANOVA One-Way and Tukey's multiple comparisons tests were used for the assessment of Goblet cells surfaces from all the three analysed segments (duodenum, ileum, and jejunum).

RESULTS

Microscopically, typical goblet cells were clearly identified at the level of the surface and glandular epithelium of the Lieberkühn glands, in all segments of the small intestine (duodenum, jejunum, and ileum) collected from the guinea pig (*Cavia porcellus*) individuals (Fig. 1A). The identified goblet cells are similar in shape and size, and they exhibit some specific histological features, e.g. a large mucous droplet located mainly in the apical pole of the cell that induces cell distention in this region, and the placement of the nucleus towards the basal pole of the cells (cup-like appearance), region that is much narrower than the apical pole. The nucleus of the goblet cells is oval-shaped and located in the basal pole of the cell, and as compared to the basal membrane it has a perpendicular orientation. However, apart from the previously described goblet cells, morphologically different
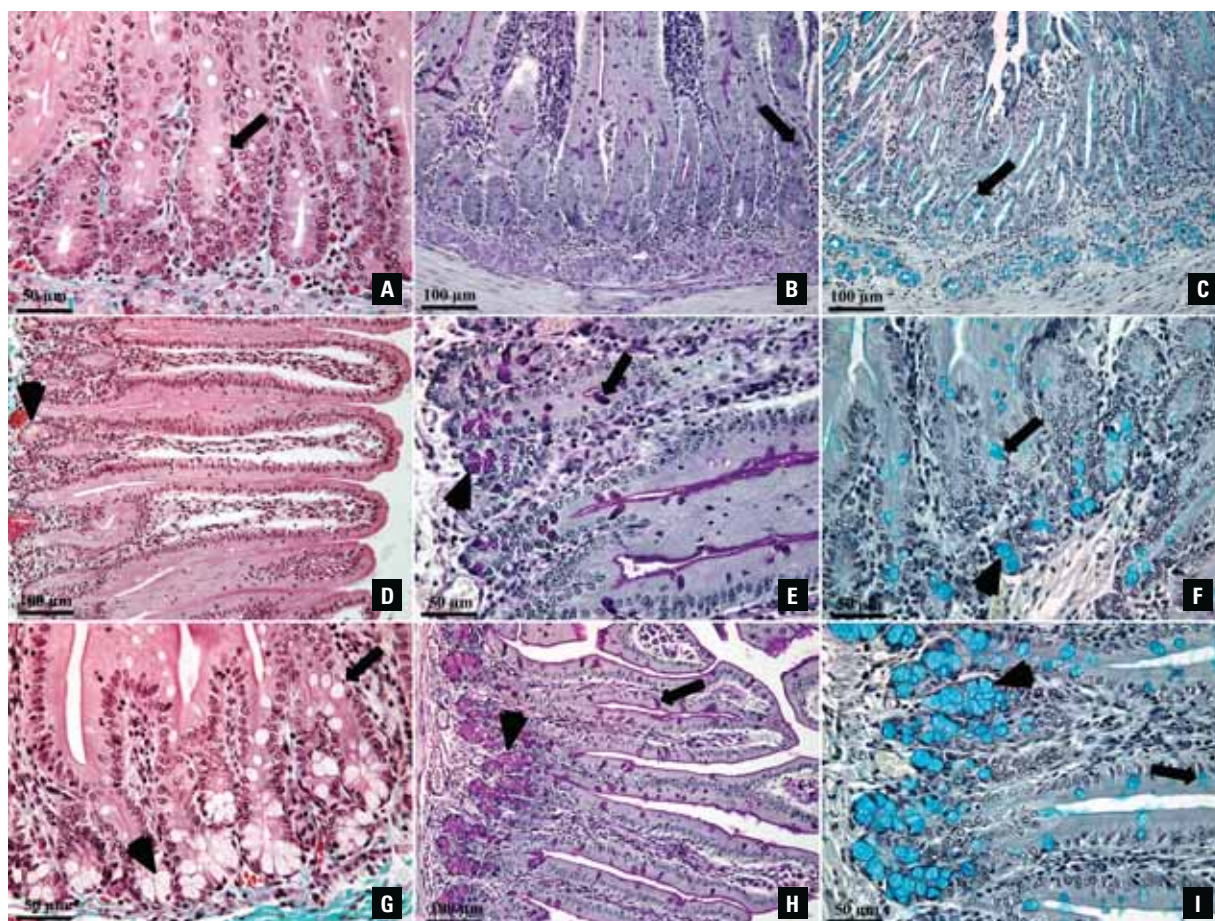
Figure 1. A. Duodenum (Goldner's trichrome stain): the only mucus-secreting cells in Lieberkühn glands are goblet cells with the specific cup-like appearance (black arrow); **B.** Duodenum (Periodic Acid-Schiff [PAS] stain): intensely PAS-positive (++) goblet cells (black arrow); **C.** Duodenum (Alcian-Blue stain): intensely Alcian-Blue-positive (++) goblet cells (black arrow); **D.** Jejunum (Goldner's trichrome stain): the presence of goblet cells and of non-goblet or deep crypt secretory (DCS) cells that have a multivacuolated or foamy cytoplasm (arrowhead), cells that are located in the deep part of the Lieberkühn glands; **E.** Jejunum (PAS stain): DCS cells (arrowhead) displaying a mild PAS-positive reaction (+) as compared to intensely PAS-positive (++) goblet cells (black arrow); **F.** Jejunum (Alcian-Blue stain): intensely Alcian-Blue--positive stain (++) for the both goblet (black arrow) and DCS cells (arrowhead); **G.** Ileum (Goldner's trichrome stain): the presence of the both goblet cells (black arrow) and DCS cells (arrowhead), the last ones in a higher number comparing to jejunum; **H.** Ileum (PAS stain): similar histochemical features as in the jejunum, i.e. mildly PAS-positive stain (+) for DCS cells (arrowhead) and a strong PAS reaction (++) of the goblet cells (black arrow); **I.** Ileum (Alcian-Blue stain): similarly with the jejunum, the both mucus secreting cells displayed a strong Alcian-Blue stain (black arrow — goblet cells, arrowhead — DCS cells).

mucus-secreting cells were identified but only in the jejunum and ileal segments of the small intestine. The so-called non-goblet cells were identified in groups in the bottom part of the Lieberkühn glands from the jejunum and ileum. Microanatomically, these cells are slightly different from goblet cells by their pyramidal shape, but significantly wider in the apical pole as compared to the goblet cells. Due to the presence of several uneven mucous droplets, the cytoplasm of non-goblet cells is multivacuolated, which confer a foamy aspect to the cytoplasm. In the non-goblet cells, the oval nucleus is pushed to the basal pole of the cell with a somehow parallel alignment with the subjacent basal membrane (Fig. 1D, G).

Histochemically, the goblet cells appear intensely PAS-positive (++) (Fig. 1B, E, H) and strongly Alcian-Blue positive (++) (Fig. 1C, F, I) in all intestinal segments (duodenum, ileum, jejunum). As a comparison, the non-goblet deep-crypt mucin-secreting cells from the jejunum and ileum displayed a mild PAS-positive reaction (+) and a strong reaction to Alcian-Blue (++) stain (Fig. 1B, C, E, F, H, I).

A total number of 60 glands (20 glands per intestinal segment) were analysed. In terms of cell counts, it can be observed that the proportion of goblet cells from the total number of cells is higher in ileal segments (13.13%) compared to the jejunum (8.13%) and duodenum (11.33%). Regarding DCS cells, their

Table 1. Descriptive statistics for cell count analysis

Segment		Descriptive statistics for cell count analysis						
		All cells	DCS cell count	Goblet cell count	Other type of cells	DCS cells [%]	Goblet cells [%]	Other type of cells [%]
Duodenum	Mean	51.15	0	5.6	45.55	**0.00%**	**11.33%**	88.67%
	SD	12.62	0	2.84	12.50			
	Min	32	0	3	27	0.00%	4.11%	75.00%
	Max	73	0	14	70	0.00%	25.00%	95.89%
	Range	41	0	11	43	0	0.208904	0.208904
Jejunum	Mean	33.63	3.74	2.89	27	**11.00%**	**8.13%**	80.87%
	SD	13.61	2.58	1.73	11.25			
	Min	11	0	0	10	0.00%	0.00%	65.63%
	Max	55	8	6	49	33.33%	13.04%	94.44%
	Range	44	8	6	39	0.33	0.13	0.29
Ileum	Mean	36.72	8.67	5.11	22.94	**24.93%**	**13.13%**	61.93%
	SD	8.66	2.30	2.72	6.42			
	Min	13	3	0	7	9.68%	0.00%	47.37%
	Max	49	13	10	33	46.15%	25.81%	78.57%
	Range	36	10	10	26	0.36	0.26	0.31

DCS — deep crypt secretory; SD — standard deviation; Min — minimal value; Max — maximal value

absence in the duodenal segment can be noted, while for the other two segments, their proportion is higher in the ileum (24.93%) as compared to the jejunal region (11.00%; Table 1).

Regarding the analysed surface of the cells in the three intestinal segments, it can be observed that the surface of the goblet cells is higher in the ileum (1162 $\pm$ 368.8 μm^2) as compared to the jejunum (932 $\pm$ 366.5 μm^2). The surface of goblet cells from the duodenum showed the smallest values compared to the other two analysed segments (825.7 $\pm$ 410.3 μm^2). The DCS cells surfaces follow the same pattern, having a bigger surface in the ileal segment (1829 $\pm$ 657.9 μm^2) vs. jejunal segment (936 $\pm$ 337.6 μm^2; Table 2). According to the obtained results, the differences between the surfaces of DCS cells in the ileum and jejunum are highly significant (p < 0.0001; Table 3, Fig. 2). The surface differences of goblet cells varied among the three segments, with a highly significant difference of the duodenal vs. ileal segments (p < 0.0001), significant differences of the jejunal vs. ileal segments (p < 0.001), and insignificant differences of the duodenal vs. jejunal segments (Fig. 3, Tables 4, 5).

DISCUSSION

Goblet cells are specific structures for the production and secretion of mucus. They received their name due to a distinctive goblet or cup-like appearance induced by the granular mucin that accumulates in the apical pole of the cell. Even if there is still incomplete information on the cell biology of goblet cells, it is evident that there are a number of types that function in diverse ways. The goblet cell from the small intestine (i.e. the ones adjacent to enterocytes) supply the bicarbonate for appropriate mucin unfolding [14]. In the large intestine, the goblet cell supplies bicarbonate by its own bestrophin-2 bicarbonate transporter [43]. The surface goblet cells from the inter-crypt region of the colon discharge the mucus continuously, whereas the goblet cells from the upper part of the colonic crypts secrete by fast compound exocytosis [20]. As observed, the goblet cells are more dissimilar and capable than have been earlier anticipated [6].

The intestinal samples of the guinea pigs (*Cavia porcellus*) assessed had a standard microanatomical structure, that includes mucosa, submucosa, muscularis externa, and serosa. As regards the mucous-secreting cells from the small intestine in guinea pigs (*Cavia porcellus*), two cell types were identified, i.e. the goblet cells and DCS cells. The goblet cells were identified in all the segments of the small intestine both in the covering the glandular epithelium, whereas DCS cells were only detected in the deep parts of the Lieberkühn glands from the jejunum and il-

Table 2. Descriptive statistics of measured cell surfaces

Intestinal segment	Descriptive statistics	Cell type	
		Goblet cells	DCS cells
		Cell surface [μm^2]	
Duodenum	Number of values	63	NA
	Minimum	263.8	NA
	Maximum	2039	NA
	Range	1775	NA
	Mean	825.7	NA
	SD	410.3	NA
	SEM	51.69	NA
	CV%	49.70%	NA
Jejunum	Number of values	64	71
	Minimum	326.4	253.7
	Maximum	1754	1630
	Range	1428	1376
	Mean	932	936
	SD	366.5	337.6
	SEM	45.81	40.06
	CV%	39.32%	36.06%
Ileum	Number of values	83	133
	Minimum	491.6	755.4
	Maximum	2093	4009
	Range	1601	3254
	Mean	1162	1829
	SD	368.8	657.9
	SEM	40.48	57.05
	CV%	31.73%	35.97%

DCS — deep crypt secretory; NA — not available; SD — standard deviation; CV% — coefficient of variation; SEM —standard error of the mean

Table 3. Comparison of deep crypt secretory cell surfaces from the jejunum and ileum, using two-tailed *t*-test

Unpaired *t*-test	
P value	< 0.0001
P value summary	≤ 0.0001
Significantly different (p < 0.05)?	Yes
One- or two-tailed p-value?	Two-tailed
t, df	t = 10.70, df = 202

Figure 2. Comparison of the surface of deep crypt secretory (DCS) cells between jejunal and ileal segments; I — ileum; J — jejunum; J-S cell — surface of the DCS cells from the jejunal segment; I-S cell — surface of the DCS cells from the ileal segment.
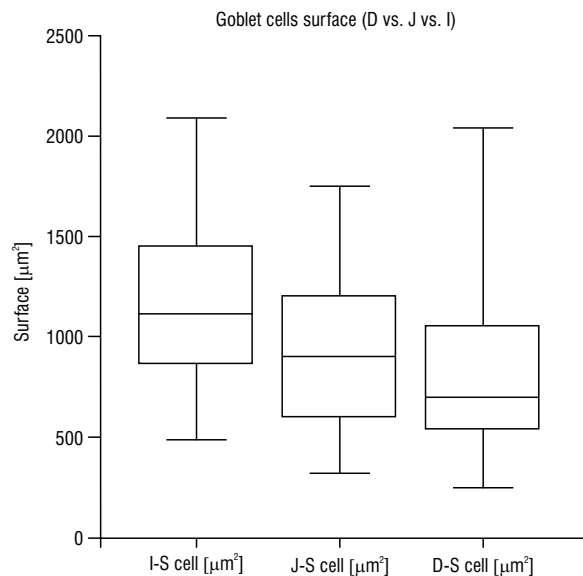
Figure 3. Comparison between the surface of goblet cells between duodenal, jejunal, and ileal segments; D — duodenum; I — ileum; J — jejunum; D-S cell — surface of the goblet cells from the duodenal segment; J-S cell — surface of the goblet cells from the jejunal segment; I-S cell — surface of the goblet cells from the ileal segment.

eum. The DCS cells are different morphologically and histochemically from the regular goblet cells. The non-goblet or DCS cells have higher dimensions than the typical goblet cells, somehow pyramidally shaped with the base against the basal membrane. On regular Goldner's trichrome stain, DCS cells present a vacuolated mucus-filled cytoplasm and a flattened nucleus, placed towards the basal membrane.

Similar cells (as concerns the shape, localization, and dimensions) were reported in some mammals in different regions of the large intestine. Accordingly, one of the first signallings of non-goblet cells

629

Table 4. Comparison of goblet cell surfaces from duodenal, jejunal, and ileal segments using Tukey's multiple comparison test

Tukey's multiple comparisons test	Mean diff.	95.00% CI of diff.	Significant?	Summary	Adjusted P value	
D-S cell μm^2 vs. J-S cell μm^2	−106.3	−266.0 to 53.30	No	NS	0.2599	A-B
D-S cell μm^2 vs. I-S cell μm^2	−336.5	−486.8 to −186.2	Yes	≤ 0.0001	< 0.0001	A-C
J-S cell μm^2 vs. I-S cell μm^2	−230.2	−379.8 to −80.55	Yes	≤ 0.01	0.001	B-C

CI — confidence interval; D — duodenum; J — jejunum; I — ileum; S — surface of the cell [μm^2]

Table 5. Comparison of goblet cell surfaces from duodenal, jejunal, and ileal segments using ANOVA One-Way

ANOVA summary	
F	15.08
P value	< 0.0001
P value summary	≤ 0.0001
Significant different among means (p < 0.05)?	Yes
R square	0.1271

was made in the deep region of the crypts from the rectum in humans, rabbit, mouse and rat, and they were named "vacuolated" cells [37]. Later, similar cells were described as non-goblet or DCS cells by Altmann (1983) [1] in the ascending colon of the rat, cells that were reported also by other more recent study [23]. However, we did not find any report to mention the presence of DCS cells in the small intestine in mammals, so it seems that our study is the first to report their presence in the small intestine in guinea pigs (*Cavia porcellus*).

The histochemical investigations performed in our study showed that the goblet cells displayed an intensely positive reaction to PAS and Alcian-Blue stains in all segments of the small intestine, in both superficial and deep glandular epithelium. This is a clear indicator of the fact the goblet cells are in charge of the synthesis of neutral and acidic mucins. However, the DCS cells identified in the deeper part of the jejunum and ileum in guinea pig (*Cavia porcellus*) displayed a mild PAS-positive reaction and a strong reaction to Alcian-Blue stain, implying the fact that these cells synthesize predominantly acidic mucins, and in a slightly lower amount the neutral mucin.

According to some other reports, in rats, DCS cells seem to be specialized for mucin production and capable to synthesize at least two distinctive mucin patterns [36]. The aforementioned authors stated the fact that the goblet cells located more superficial in the intestinal mucosa are in charge of sulfomucin secretion, whereas the mucus-secreting cells with a deeper location in the epithelium (i.e. DCS cells) are more likely associated with a sialomucin profile. Further histochemical investigations (e.g. PAS, Alcian-Blue stains) led to the conclusion that DCS cells are different from the typical goblet cells [33]. Electron-microscopy studies [30] confirmed the different mucin patterns as well as the fact that the DCS cells show a fine vacuolar material while the goblet cells have a much denser peculiar matrix with discrete secretory vesicles that fill most of the cellular cytoplasm. The presence of the rough endoplasmic reticulum and a developed Golgi apparatus suggests an intense glycoprotein secretory activity [17, 30, 39].

Goblet cells, as enterocytes, enteroendocrine cells, and Paneth cells of the gut mucosa derive from multipotent stem cells located at the base of crypts of Lieberkühn [12]. Due to the influence of the mucous layer on gastrointestinal inflammatory pathologies, the interest regarding gut-associated mucus is increasing in the last period. Frequently such pathological conditions go along with impaired goblet cell function along with dysregulated mucin biosynthesis, which triggers significant qualitative and quantitative changes [7, 25]. Inflammatory bowel disease is a group of disorders influenced by an inappropriate function of goblet cells, including their synthesized mucins. Inflammatory bowel disease is classified into Crohn's disease and ulcerative colitis [13]. These disorders are characterised by chronic inflammatory lesions in the gastrointestinal tract and are associated with obscure causes and poorly efficient therapies [21]. Some other morbid entities that evolve with alterations in gastrointestinal mucin production and function are represented by colorectal cancer and some bacterial and parasitic infections. The last ones are frequently associated with mucin dysfunction and inflammation of the gastrointestinal tract [25]. As regards the role of DCS cells, Sasaki et al (2016) [34] observed that ablation of Reg4+ DCS cells in the murine colon results in loss of stem cells from colonic crypts, a fact that disturbs gut homeostasis and colon organoid growth [34]. It is known that stem cells

fundamentally depend on their intricate microenvironment, otherwise known as niche (i.e. an anatomic place consisting of specialised cells that anchor stem cells and additionally offer physical protection and essential growth/maintenance signals). In the murine small intestine, an important part of the cellular niche for Lgr5+ stem cells is made by Paneth cells, which deliver molecules like Wnt3, EGF, and Notch ligands to preserve intestinal stem cells. Since the murine colon does not contain typical Paneth cells, the Reg4-DCS cells represent the colon equivalent of Paneth cells [34]. Accordingly, DCS cells support the organoid development of single Lgr5+ colon stem cells. As a fact, Reg4+ cells were also detected within colorectal tumoral lesions in humans [22, 31]. A connection between Reg4+ cells and Lgr5+ stem cells in mouse colon adenoma was observed, a fact that may suggest that Reg4+ cells in adenoma play a role as a niche for cancer stem cells [35].

CONCLUSIONS

Mucous cells, including goblet and non-goblet cells, along with their secretory product were underestimated for a long period of time. However, the latest findings changed this and situated these cells at the focal point for the understanding of intestinal mucosa biology and immunology. The intestinal mucosa possesses several types of mucous cells that can be outlined based on their position and microanatomy. Our study managed to describe for the first time in guinea pig (*Cavia porcellus*), the existence of formerly known vacuolated/non-goblet cells, or recently called DCS cells in the jejunum and ileum sections of the small intestine. Finally, the understanding of the full function of the mucous goblet and non-goblet cells will offer a further vision not only about gut homeostasis and organoid growth of the large intestine but some elucidation regarding the inflammatory bowel disease and the intricate biology of the niche for cancer stem cells that may reveal innovative therapeutic protocols for colorectal cancer.

Conflict of interest: None declared

REFERENCES

1. Altmann GG. Morphological observations on mucus-secreting nongoblet cells in the deep crypts of the rat ascending colon. Am J Anat. 1983; 167(1): 95–117, doi: 10.1002/aja.1001670109, indexed in Pubmed: 6869312.
2. Altman GG. Renewal of the intestinal epithelium: new aspects as indicated by recent ultrastructural observations. J Electron Microsc Tech. 1990; 16(1): 2–14, doi: 10.1002/jemt.1060160103, indexed in Pubmed: 1698949.
3. Alturkistani HA, Tashkandi FM, Mohammedsaleh ZM. Histological stains: a literature review and case study. Glob J Health Sci. 2015; 8(3): 72–79, doi: 10.5539/gjhs.v8n3p72, indexed in Pubmed: 26493433.
4. American Veterinary Medical Association. (2020). AVMA Guidelines for the Euthanasia of Animals: 2020 Edition. American Veterinary Medical Association. (2020).
5. Barker N, van de Wetering M, Clevers H. The intestinal stem cell. Genes Dev. 2008; 22(14): 1856–1864, doi: 10.1101/gad.1674008, indexed in Pubmed: 18628392.
6. Birchenough GMH, Johansson MEV, Gustafsson JK, et al. New developments in goblet cell mucus secretion and function. Mucosal Immunol. 2015; 8(4): 712–719, doi: 10.1038/mi.2015.32, indexed in Pubmed: 25872481.
7. Boltin D, Perets TT, Vilkin A, et al. Mucin function in inflammatory bowel disease: an update. J Clin Gastroenterol. 2013; 47(2): 106–111, doi: 10.1097/MCG.0b013e3182688e73, indexed in Pubmed: 23164684.
8. Chung HK, Xiao L, Jaladanki KC, et al. Regulation of paneth cell function by rna-binding proteins and noncoding rnas. Cells. 2021; 10(8), doi: 10.3390/cells10082107, indexed in Pubmed: 34440876.
9. Dharmani P, Srivastava V, Kissoon-Singh V, et al. Role of intestinal mucins in innate host defense mechanisms against pathogens. J Innate Immun. 2009; 1(2): 123–135, doi: 10.1159/000163037, indexed in Pubmed: 20375571.
10. Gabe M. Techniques Histologiques in French. Ch 9. Les colorations topographiques. Masson et Cie Editeurs, Paris, France 1968: 203–256.
11. Ghiurco F, Damian A, Martonos C, et al. First Report of Deep Crypt Secretory Cells in Ascending Colon in Chinchilla (Chinchilla lanigera): A Histological and Histochemical Study. Int J Morphol. 2021; 39(4): 1001–1005, doi: 10.4067/s0717-95022021000401001.
12. Gordon JI, Schmidt GH, Roth KA. Studies of intestinal stem cells using normal, chimeric, and transgenic mice. FASEB J. 1992; 6(12): 3039–3050, doi: 10.1096/fasebj.6.12.1521737, indexed in Pubmed: 1521737.
13. Grondin JA, Kwon YH, Far PM, et al. Mucins in intestinal mucosal defense and inflammation: learning from clinical and experimental studies. Front Immunol. 2020; 11: 2054, doi: 10.3389/fimmu.2020.02054, indexed in Pubmed: 33013869.
14. Gustafsson JK, Ermund A, Ambort D, et al. Bicarbonate and functional CFTR channel are required for proper mucin secretion and link cystic fibrosis with its mucus phenotype. J Exp Med. 2012; 209(7): 1263–1272, doi: 10.1084/jem.20120562, indexed in Pubmed: 22711878.
15. Hansson GC. Role of mucus layers in gut infection and inflammation. Curr Opin Microbiol. 2012; 15(1): 57–62, doi: 10.1016/j.mib.2011.11.002, indexed in Pubmed: 22177113.
16. Hasnain SZ, Evans CM, Roy M, et al. Muc5ac: a critical component mediating the rejection of enteric nematodes. J Exp Med. 2011; 208(5): 893–900, doi: 10.1084/jem.20102057, indexed in Pubmed: 21502330.
17. Hiraishi H, Terano A, Ota S, et al. Oxygen metabolites stimulate mucous glycoprotein secretion from cultured rat gastric mucous cells. Am J Physiol. 1991; 261(4 Pt 1):

G662–G668, doi: 10.1152/ajpgi.1991.261.4.G662, indexed in Pubmed: 1928352.

18. Hooper LV. Epithelial cell contributions to intestinal immunity. Adv Immunol. 2015; 126: 129–172, doi: 10.1016/bs.ai.2014.11.003, indexed in Pubmed: 25727289.

19. Johansson MEV, Hansson GC. Immunological aspects of intestinal mucus and mucins. Nat Rev Immunol. 2016; 16(10): 639–649, doi: 10.1038/nri.2016.88, indexed in Pubmed: 27498766.

20. Johansson MEV. Fast renewal of the distal colonic mucus layers by the surface goblet cells as measured by in vivo labeling of mucin glycoproteins. PLoS One. 2012; 7(7): e41009, doi: 10.1371/journal.pone.0041009, indexed in Pubmed: 22815896.

21. Kaplan GG. The global burden of IBD: from 2015 to 2025. Nat Rev Gastroenterol Hepatol. 2015; 12(12): 720–727, doi: 10.1038/nrgastro.2015.150, indexed in Pubmed: 26323879.

22. Kaprio T, Hagström J, Mustonen H, et al. REG4 independently predicts better prognosis in non-mucinous colorectal cancer. PLoS One. 2014; 9(10): e109600, doi: 10.1371/journal.pone.0109600, indexed in Pubmed: 25295732.

23. Karam SM. Lineage commitment and maturation of epithelial cells in the gut. Front Biosci. 1999; 4: D286–D298, doi: 10.2741/karam, indexed in Pubmed: 10077541.

24. Kiernan J. Staining theory. Histological and Histochemical Methods. Scion, UK 2008: 67–104.

25. Kim JJ, Khan WI. Goblet cells and mucins: role in innate defense in enteric infections. Pathogens. 2013; 2(1): 55–70, doi: 10.3390/pathogens2010055, indexed in Pubmed: 25436881.

26. Kim YS, Ho SB. Intestinal goblet cells and mucins in health and disease: recent insights and progress. Curr Gastroenterol Rep. 2010; 12(5): 319–330, doi: 10.1007/s11894-010-0131-2, indexed in Pubmed: 20703838.

27. Kober O. The role of mucus in the cross talk between gut bacteria and the host. Doctoral dissertation, University of East Anglia 2013.

28. Linden SK, Sutton P, Karlsson NG, et al. Mucins in the mucosal barrier to infection. Mucosal Immunol. 2008; 1(3): 183–197, doi: 10.1038/mi.2008.5, indexed in Pubmed: 19079178.

29. Mobius G. Ethical and legal questions regarding the killing of animals to avoid considerable pain and suffering. DTW. Deutsche Tierarztliche Wochenschrift. 1994; 101(9): 372–376.

30. Neutra M, Leblond CP. Synthesis of the carbohydrate of mucus in the golgi complex as shown by electron microscope radioautography of goblet cells from rats injected with glucose-H3. J Cell Biol. 1966; 30(1): 119–136, doi: 10.1083/jcb.30.1.119, indexed in Pubmed: 5966171.

31. Rafa L, Dessein AF, Devisme L, et al. REG4 acts as a mitogenic, motility and pro-invasive factor for colon cancer cells. Int J Oncol. 2010; 36(3): 689–698, doi: 10.3892/ijo_00000544, indexed in Pubmed: 20126989.

32. Rieger J, Drewes B, Hünigen H, et al. Mucosubstances in the porcine gastrointestinal tract: Fixation, staining and quantification. Eur J Histochem. 2019; 63(2), doi: 10.4081/ejh.2019.3030, indexed in Pubmed: 31232013.

33. Rodney DP, Altmann GG. Mucus-composition of the colonic goblet and DCS cells as shown by staining with periodic Schiff and alcian blue. Anat Rec. 1986: 214–225.

34. Sasaki N, Sachs N, Wiebrands K, et al. Reg4+ deep crypt secretory cells function as epithelial niche for Lgr5+ stem cells in colon. Proc Natl Acad Sci U S A. 2016; 113(37): E5399–E5407, doi: 10.1073/pnas.1607327113, indexed in Pubmed: 27573849.

35. Schepers AG, Snippert HJ, Stange DE, et al. Lineage tracing reveals Lgr5+ stem cell activity in mouse intestinal adenomas. Science. 2012; 337(6095): 730–735, doi: 10.1126/science.1224676, indexed in Pubmed: 22855427.

36. Shamsuddin AK, Trump BF. Colon epithelium. II. In vivo studies of colon carcinogenesis. Light microscopic, histochemical, and ultrastructural studies of histogenesis of azoxymethane-induced colon carcinomas in Fischer 344 rats. J National Cancer Institute. 1981; 66(2): 389–401, indexed in Pubmed: 6935486.

37. Sheahan DG, Jervis HR. Comparative histochemistry of gastrointestinal mucosubstances. Am J Anat. 1976; 146(2): 103–131, doi: 10.1002/aja.1001460202, indexed in Pubmed: 821330.

38. Singh PK, Hollingsworth MA. Cell surface-associated mucins in signal transduction. Trends Cell Biol. 2006; 16(9): 467–476, doi: 10.1016/j.tcb.2006.07.006, indexed in Pubmed: 16904320.

39. Specian RD, Oliver MG. Functional biology of intestinal goblet cells. Am J Physiol. 1991; 260(2 Pt 1): C183–C193, doi: 10.1152/ajpcell.1991.260.2.C183, indexed in Pubmed: 1996606.

40. Tailford LE, Crost EH, Kavanaugh D, et al. Mucin glycan foraging in the human gut microbiome. Front Genet. 2015; 6: 81, doi: 10.3389/fgene.2015.00081, indexed in Pubmed: 25852737.

41. van Putten JPM, Strijbis K. Transmembrane mucins: signaling receptors at the intersection of inflammation and cancer. J Innate Immun. 2017; 9(3): 281–299, doi: 10.1159/000453594, indexed in Pubmed: 28052300.

42. Walsh MD, Clendenning M, Williamson E, et al. Expression of MUC2, MUC5AC, MUC5B, and MUC6 mucins in colorectal cancers and their association with the CpG island methylator phenotype. Mod Pathol. 2013; 26(12): 1642–1656, doi: 10.1038/modpathol.2013.101, indexed in Pubmed: 23807779.

43. Yu K, Lujan R, Marmorstein A, et al. Bestrophin-2 mediates bicarbonate transport by goblet cells in mouse colon. J Clin Invest. 2010; 120(5): 1722–1735, doi: 10.1172/JCI41129, indexed in Pubmed: 20407206.

Gallic acid treatment protects intestinal tissue against ischaemia-reperfusion

C. Durgun[1], E. Deveci[2]

[1]Division of General Surgery, Memorial Dicle Hospital, Diyarbakır, Turkey
[2]Department of Histology and Embryology, Faculty of Medicine, Dicle University, Diyarbakır, Turkey

Background: This study aimed to investigate the protective effects of gallic acid (GA) in the rat intestine against ischaemia-reperfusion (IR) injury.

Materials and methods: Thirty male Wistar albino rats with a mean weight of 200–250 g were used. Animals were categorized into the sham, IR, and IR+GA groups. Ischaemia of the intestine was induced for 3 h by occluding the superior mesenteric artery (SMA) and then left for 3 h of reperfusion. In the IR+GA group, after ischaemia induction, 50 mg/kg GA was orally administered to the animals. Blood samples were collected for biochemical assays. Intestinal tissues were excised for histopathologic and immunohistochemical processing.

Results: Malondialdehyde (MDA) levels were increased, and catalase (CAT) and glutathione (GSH) levels were decreased in the IR group compared to the sham group. After GA treatment, MDA levels decreased and CAT and GSH levels increased in the GA-treated group compared to the IR group. In the sham group, normal intestinal histology was observed. In the IR group, the villi structures were completely degenerated. In the IR+GA group, histology was improved after GA treatment. In the sham group, the caspase-3 reaction was generally negative in the epithelium and glands. In the IR group, the caspase-3 reaction increased in apoptotic bodies and inflammatory cells. The caspase-3 reaction was negative in goblet cells and the epithelium. A moderate caspase-3 reaction was observed in the IR+GA group. The beclin-1 reaction was negative in epithelial cells and goblet cells in villi in the sham group. In the IR group, the beclin-1 reaction was positive in the degenerated villi. An intense beclin-1 reaction was also observed in some inflammatory cells. After GA treatment, the beclin-1 reaction was positive in a few cells. In general, moderate beclin-1 positivity was observed.

Conclusions: Gallic acid, with its antioxidative effect, inhibited the apoptotic pathway (caspase-3) through beclin-1 regulation. (Folia Morphol 2023; 82, 3: 633–640)

Key words: ischaemia-reperfusion, gallic acid, caspase-3, beclin-1

INTRODUCTION

Intestinal ischaemia-reperfusion (IR) injury is an event in which blood flow to the intestines is reduced and then restored to the ischaemic tissue [9].

Intestinal IR injury leads to severe local and systemic inflammation followed by damage to surrounding distant organs. Thus, the intestinal mucosal barrier is disrupted, and the organ is damaged. If this dam-

age continues for a long time and is left untreated, the life of the animal may be endangered. Mortality rates vary between 60% and 80% in patients with acute intestinal IR; thus, new treatment strategies are needed for intestinal IR [7, 23].

Gallic acid (GA; 3,4,5-trihydroxybenzoic acid) is a polyhydroxy phenolic compound, and structurally related compounds are widely found in fruits and plants. GA esters have diverse uses in industry, including as antioxidants in food, in cosmetics, and in the pharmaceutical industry. GA is a source material for inks, paints, and colour developers. Studies have shown that these compounds are potential therapeutics, with anti-cancer and antimicrobial properties [10, 14]. GA was found to possess anti-inflammatory activity. Scavenging of superoxide anions, inhibition of myeloperoxidase release and activity, and interference with the assembly of active NADPH-oxidase may be the mechanisms underlying the inhibition of inflammatory process by GA [10].

Caspases are cysteine proteases that are involved in cell death. They play very important roles in embryonic development and cell homeostasis. Caspase-3, on the other hand, belongs to the effector caspase group and causes apoptotic cell morphology by degrading relevant proteins in the cell that will undergo apoptosis [16]. Beclin-1 is a multidomain protein involved in autophagy mechanisms and membrane trafficking. It can also bind to B-cell lymphoma 2 to regulate apoptosis. Beclin-1 plays roles in tumorigenesis, neurodegeneration, and other diseases. The expression of beclin-1 is affected by many other factors [13, 21]. Immunohistochemistry is a laboratory method used to detect the localization of specific antigens.

In this study, we aimed to investigate the effect of GA in rat intestinal tissue against ischaemia and reperfusion with immunohistochemical and biochemical techniques.

MATERIALS AND METHODS

Animals

All experimental protocols were conducted according to the National Institutes of Health Guidelines for the Care and Use of Laboratory Animals. The study was approved by a local ethics committee. Thirty male Wistar albino rats with a mean weight of 200–250 g were used. They were housed in an air-conditioned room with a 12 h/12 h light/dark cycle and constant temperature (23 ± 2°C) and relative humidity (65–70%).

Surgical procedure

All rats were fasted 12 h before the experiment. The rats were anaesthetized with an intramuscular injection of ketamine (50 mg/kg; Ketalar, Parke Davis, Turkey) and xylazine (10 mg/kg; Rompun, Bayer AG, Germany) under aseptic conditions. The abdominal region was shaved, and a 2–3-cm abdominal midline incision was made. In the intestinal IR injury model, the superior mesenteric artery (SMA) was carefully blocked with a nontraumatic microvascular clamp. At the end of the ischaemic period, the clamp was removed, and the mesenteric artery was released.

Sham group: — animals were laparotomized without SMA occlusion.

IR group: — 3-h ischaemia was induced by SMA occlusion. The intestine was then reperfused for 3 h.

IR+GA group — after the IR procedure, 50 mg/kg GA was orally administered to the rats for 14 days.

At the end of the experiment, all animals were sacrificed. The jejunum tissues of all groups were removed, divided into two equal pieces, and stored under suitable conditions for biochemical and histopathological investigations.

Biochemical analyses

Blood samples were collected in tubes with a gel separator and centrifuged for 5 min at 1550 g. The supernatant plasma was removed and placed in polypropylene plastic tubes. The tubes were labelled with the appropriate sample name and type. Samples were stored at −80°C for the determination of the malondialdehyde (MDA), glutathione (GSH), and catalase (CAT) levels. MDA levels were determined using the double heating method of Draper and Hadley [3]. MDA values were expressed as nanomoles per gram (nmol/g) of wet tissue. The GSH activity was measured by the method of Paglia and Valentine [15]. CAT values were measured by the method of Zhang et al. [25].

Histopathological analysis

Intestinal sections were obtained for histopathological analysis and fixed in 10% buffered formalin, dehydrated in ethanol (50% to 100%), purified in xylene, and embedded in paraffin. Sections (4–5 mm thickness) were cut and stained with haematoxylin and eosin. The sections were studied to assess the pathological changes in the gingiva tissue [4].

Immunohistochemical analysis

Formaldehyde-fixed tissue was embedded in paraffin wax for further immunohistochemical examination. Sections were deparaffinized in xylene and passed through a descending alcohol series. The antigen retrieval process was performed in citrate buffer solution (pH 6.0) for 15 min in a microwave oven at 700 W. Sections were allowed to cool at room temperature for 30 min and washed twice in phosphate buffered saline (PBS) for 5 min. Endogenous peroxidase blockage was performed in a 3% hydrogen peroxide solution for 7 min. The washed samples were incubated in Ultra V block (catalogue no. TA-015UB, Thermo Fisher, USA) for 8 min. Blocking solution was removed from the sections, which were then incubated overnight at 4°C with primary antibodies against caspase-3, (catalogue no. ab4051, Abcam, USA) and beclin-1 (catalogue no. 207612, Abcam, USA). After washing the sections in PBS, secondary antibody (TP-015-BN, Thermo Fischer, US) was applied for 20 min. The sections were washed in PBS for 2 × 5 min and then exposed to streptavidin-peroxidase (TS-015-HR, Thermo Fisher, USA) for 20 min. Sections washed with PBS were allowed to react with DAB (TA-001-HCX, Thermo Fischer, US) chromogen. Counterstaining with haematoxylin and eosin was performed, and after washing, the preparations were mounted. Sections were examined under a light microscope (Zeiss Imager A2, Germany) [24].

The quantification of histological and immunohistochemical parameters was performed blindly by two expert pathologists. The H-score (HS) was used to assess the outcomes of immunohistochemical staining. $HS = \Sigma(1 + i) \times pi$, where "i" indicates the staining intensity (0 = no expression, 1 = light, 2 = medium, 3 = dense, and 4 = very dense) and "pi" indicates the percentage of staining intensity [19]. Results were presented as median (minimum–maximum) and statistical analysis was conducted.

Statistical analysis

Data were analysed using IBM SPSS 25.0 software (IBM, Armonk, New York, USA). The Shapiro–Wilk test was used for data distribution analysis. The Kruskal––Wallis test was used for multiple comparisons, and the Mann–Whitney U test was used for within-group comparisons. $P < 0.05$ was considered statistically significant.

RESULTS

The statistical analysis of biochemical and histochemical parameters is shown in Table 1. MDA levels, histological scores of inflammation, dilatation, and caspase-3 and beclin-1 expression were higher in the IR group than the sham group. CAT and GSH levels and histological scores of epithelialisation were significantly lower in the IR group than the sham group. After GA treatment, MDA levels, histological scores of inflammation, dilatation, and caspase-3 and beclin-1 expression decreased in the GA-treated group compared to the IR group, and this decrease was statistically significant (Fig. 1A, C). Similarly, CAT and GSH levels and histological scores of epithelialisation statistically significantly increased in the IR+GA group compared to the IR group (Fig. 1B).

Haematoxylin and eosin findings

In the sham group, the transversal section showed that that the villi structures of the intestine were regularly preserved, the goblet cells were regularly located in the epithelium, the prismatic appearance of the intestinal epithelial cells was smooth, and the connective tissue cells were freely distributed in the lamina propria in the lower parts. The muscle layer had a normal structure and the fibres extending from the lamina muscularis mucosal layer to the lamina propria were also in a smooth course. Vascular lumens were regular and endothelial cells were smooth (Fig. 2A). In the IR group, the villi structures completely disappeared. Intense inflammation and cell infiltration was present between the muscle cells. Degeneration of goblet cells was found, and significant desquamation was observed in the intestinal epithelium. Degenerative and apoptotic changes were observed in the intestinal glands. Deterioration of the vascular structure and increased inflammation were observed. Mild hyperplasia was also observed in the muscles (Fig. 2B). In the IR+GA group, the villi structures were found to be arranged in the form of leaves parallel to the lumen in the transversal section of the intestine, but desquamative cell debris was found at the ends. Cell degeneration was evident at the tip. Improvement was observed in goblet cells. Inflammatory cells in the lamina propria region showed a solitary distribution but did not increase much. The vascular structure was regular, and there were no degenerative changes in the endothelial cells. The muscle layer was smooth and circular (Fig. 2C).

Caspase-3 immunostaining findings

In the sham group, although the villi structures were significantly preserved, the caspase-3 reaction was generally negative in the epithelium and glands.

635

Table 1. Biochemical and histological parameters of the sham, IR, and IR+GA groups

Parameters	Groups	N	Median (minimum–maximum)	Mean rank	P-value
Malondialdehyde	Sham	10	22.05 (14.98–46.28)	6.00	< 0.001*
	IR	10	48.57 (24.68–64.51)	20.50	0.04**
	IR+GA	10	36.58 (25.16–50.36)	15.75	
Glutathione	Sham	10	1.63 (1.42–1.76)	20.30	< 0.001*
	IR	10	0.42 (0.13–1.18))	5.50	< 0.001**
	IR+GA	10	1.38 (1.19–1.88)	20.50	
Catalase	Sham	10	8.02 (5.47–8.63)	25.50	< 0.001*
	IR	10	4.11 (2.08–4.98)	7.00	< 0.001**
	IR+GA	10	6.48 (4.83–7.33)	15.50	
Epithelialization	Sham	10	2.00 (1.00–3.00)	29.75	< 0.001*
	IR	10	0.50 (0.00–3.00)	8.00	< 0.001**
	IR+GA	10	2.00 (1.00–3.00)	20.00	
Inflammation	Sham	10	0.00 (0.00–1.00)	6.50	< 0.001*
	IR	10	2.50 (2.00–3.00)	23.50	< 0.001**
	IR+GA	10	1.00 (1.00–3.00)	16.50	
Dilatation	Sham	10	0.00 (0.00–1.00)	6.50	< 0.001*
	IR	10	2.00 (2.00–3.00)	22.50	< 0.001**
	IR+GA	10	1.00 (1.00–3.00)	14.75	
Caspase-3 expression	Sham	10	0.00 (0.00–1.00)	6.50	< 0.001*
	IR	10	2.00 (2.00–3.00)	24.00	< 0.001**
	IR+GA	10	1.00 (1.00–3.00)	16.00	
Beclin-1 expression	Sham	10	0.00 (0.00–1.00)	6.50	< 0.001*
	IR	10	2.00 (2.00–3.00)	24.00	< 0.001**
	IR+GA	10	1.00 (1.00–3.00)	14.50	

*Sham vs. IR; **IR vs. IR+GA; IR — ischaemia-reperfusion; GA — gallic acid; n — number of animals

The caspase-3 reaction was found to be positive in some spilled parts but could be considered normal, and there was no apoptotic process. Additionally, towards the lamina propria and submucosa layer, some macrophage cells were concentrated, especially around the vessel, and showed positivity. A slight caspase-3 reaction was also observed in the endothelial cells (Fig. 2D). In the IR group, the integrity of the villi was completely lost. Breaks were also very evident in the underlying gland cells. In particular, the caspase-3 reaction started to show significant positivity in the squamous cells in this direction. A significantly higher number of apoptotic areas were found, and intermediate inflammatory cells were also evaluated as positive for caspase-3. Significant degenerative changes in the muscles were found with caspase-3 positivity (Fig. 2E). In the IR+GA group, the caspase-3 reaction was clearly negative, especially in goblet cells and prismatic cells. Again, a moderate caspase-3 reaction was observed in some of the gland cells, while the caspase-3 reaction was widely evaluated as negative in the connective tissue cells in the lamina propria. The caspase-3 reaction was positive in some cells in the submucosal region. In general, the apoptotic process was found to be weakened or decreased (Fig. 2F).

Beclin-1 immunostaining findings

In the sham group, the beclin-1 reaction was observed to be negative, especially in epithelial cells and goblet cells in the villi structures. Expression was also found to be negative in the underlying gland epithelium and goblet cells. Occasionally, the beclin-1 reaction was found to be positive in some macrophages and inflammatory cells and in the lamina propria. The beclin-1 reaction was negative in the muscle layer, but moderate beclin-1 positivity was observed in some submucosal regions, especially
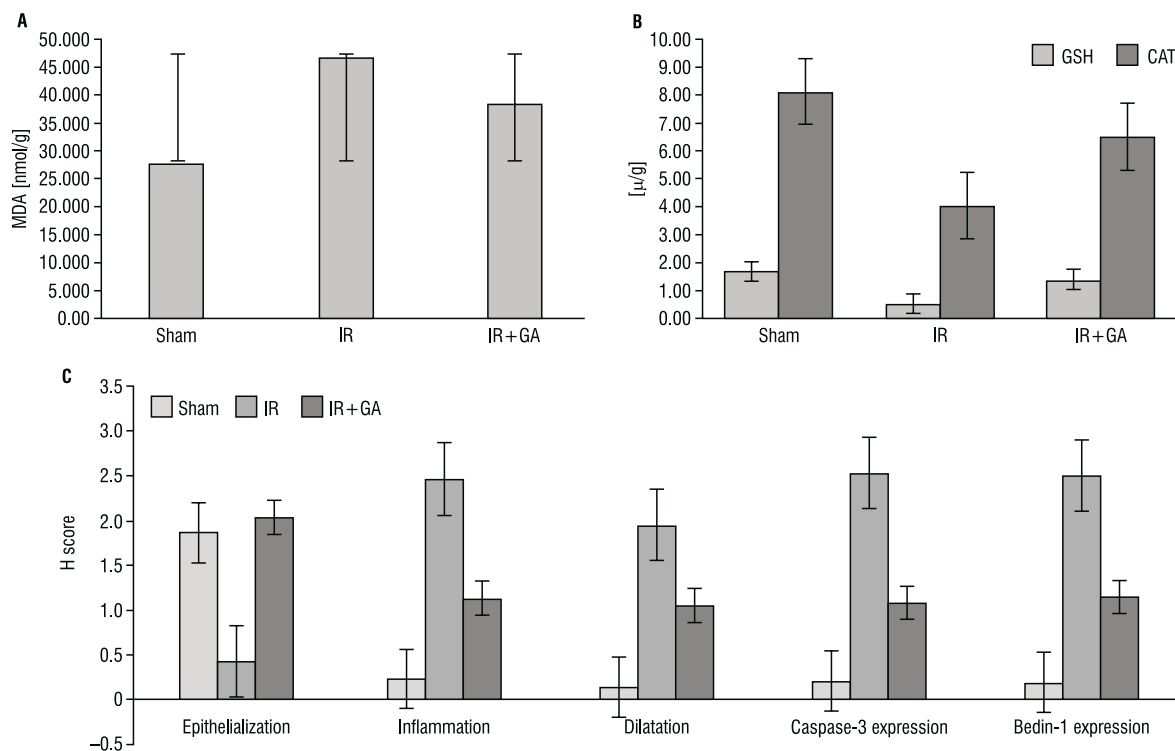
Figure 1. Graphical illustration of malondialdehyde (MDA) (**A**), glutathione (GSH), and catalase (CAT) levels (**B**), epithelialization, inflammation, dilatation, and caspase-3 and beclin-1 expression (**C**); IR — ischaemia-reperfusion; GA — gallic acid.
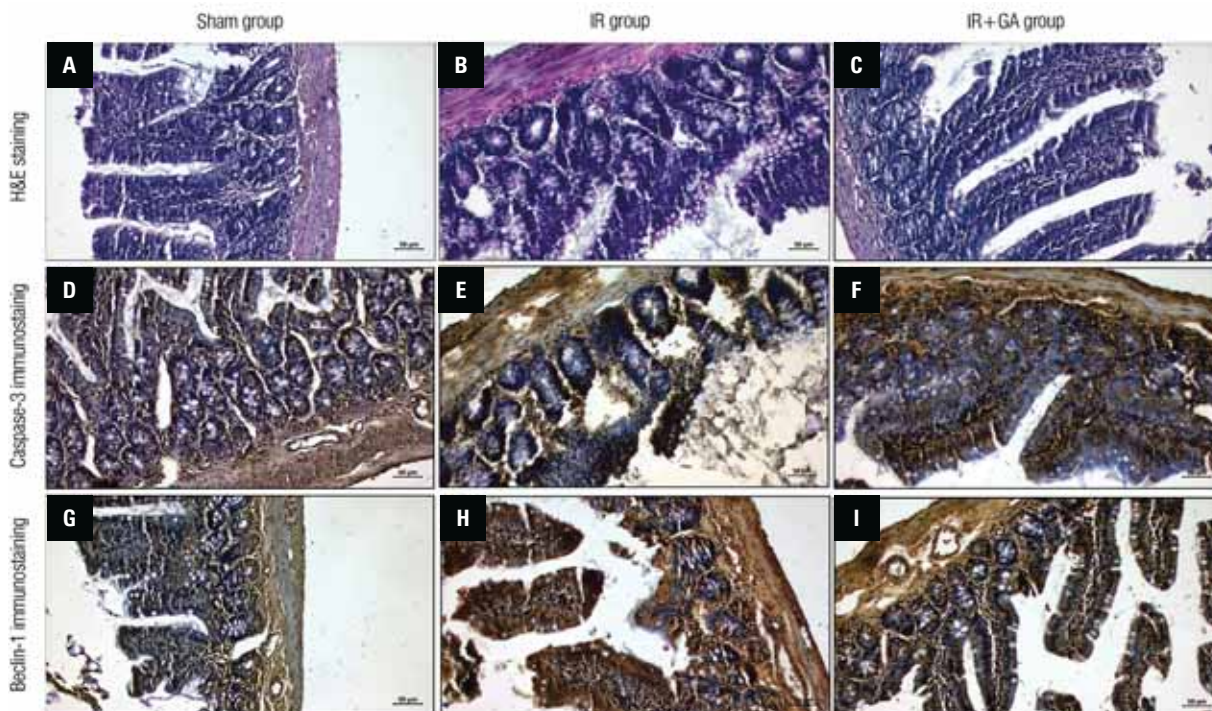
Figure 2. Haematoxylin and eosin (H&E) staining of intestinal tissue sham group (**A**), IR group (**B**), IR+GA group (**C**); bar: 50 μm, magnification: 20×. Caspase-3 immunostaining of intestinal tissue sham group (**D**), IR group (**F**), IR+GA group (**G**), bar: 50 μm, magnification: 20×. Beclin-1 immunostaining of intestinal tissue sham group (**G**), IR group (**H**), IR+GA group (**I**); bar: 50 μm, magnification: 20×; IR — ischaemia-reperfusion; GA — gallic acid.

around the vessel (Fig. 2G). In the IR group, with the deterioration of the villi structures, the beclin-1 reaction was positive, especially at the ends of the ruptured parts. An intense beclin-1 reaction was also observed in some inflammatory cells in the lamina propria. The beclin-1 reaction was found to be positive in degenerative gland cells close to the basement membrane and was also detected in inflammatory cells and vascular endothelium close to the muscle layer and submucosa region (Fig. 2H). In the IR+GA group, the villi structure was preserved, and beclin-1 expression was negative, especially in goblet cells. With the decrease in inflammatory structures, the beclin-1 reaction was positive in a small number of cells. Particularly, moderate beclin-1 positivity was observed in the vascular endothelium. Along with the preservation of the cell structure in some glands, the beclin-1 reaction was observed to be positive in the cells that were degenerative from time to time. In general, moderate beclin-1 positivity was noted (Fig. 2I).

DISCUSSION

Ischaemia causes the insufficient delivery of oxygen and other metabolites by the circulation to the tissues, leading to cell death and organ failure. Reperfusing the ischaemic tissue may sometimes cause more harm than ischaemia itself. During IR injury, the production of reactive oxygen species increases. MDA is an indicator of lipid peroxidation in tissues, and high levels of MDA are related to oxidative damage. The cell scavenges these harmful molecules using antioxidant enzymes such as superoxide dismutase, GSH, and CAT. During intestinal IR, the oxidant/antioxidant balance may change. Ji et al. [6] studied the effects of intestinal IR on MDA and myeloperoxidase levels and found that MDA and myeloperoxidase levels increased in the IR group. Similarly, Chen et al. [1] studied MDA, SOD, and GSH levels in intestinal IR injury and found that MDA levels increased in the IR group compared to the sham group, while SOD and GSH levels were lower in the IR group than in the sham group. The statistical analysis of biochemical and histochemical parameters in our study is shown in Table 1. MDA levels, histological scores of inflammation, dilatation, and caspase-3 and beclin-1 expression were higher in the IR group than the sham group. CAT and GSH levels and histological scores of epithelialisation were significantly lower in the IR group than the sham group. After GA treatment, MDA levels, histological

scores of inflammation, dilatation, and caspase-3 and beclin-1 expression decreased in the GA-treated group compared to the IR group in a statistically significant manner. Similarly, CAT and GSH levels and histological scores of epithelialisation statistically significantly increased in the IR+GA group compared to the IR group.

After reperfusion, some cellular functions may be regained; however, reperfusion may cause more cellular damage. These changes affect the histology of intestinal tissue. Çimen et al. [2] induced intestinal IR in rats and showed that IR injury caused polymorphonuclear leukocyte infiltration, oedema, haemorrhage, vascular dilatation, and congestion in the IR group. Terzi et al. [20] induced 60 min/60 min IR injury in the rat intestine and observed pathologies including desquamation in the epithelial layers, haemorrhage, and oedema in the IR group [20]. In our study, in the sham group, the villi structures of the intestine were regularly preserved, the goblet cells were regularly located in the epithelium, and the muscle layer had a normal structure (Fig. 2A). In the IR group, the villi structures completely disappeared, and intense inflammation and cell infiltration was observed between the muscle cells. Goblet cells were degenerated, and significant desquamation was observed in the intestinal epithelium (Fig. 2B). In the IR+GA group, the villi structures were arranged as normal, cell degeneration was decreased, goblet cells improved, inflammatory cells were decreased, and the vascular structure was regular (Fig. 2C).

Caspases are cysteine proteases that are involved in cell death. They play very important roles in embryonic development and cell homeostasis. Caspase-3, on the other hand, belongs to the effector caspase group and causes apoptotic cell morphology by degrading relevant proteins in the cell that will undergo apoptosis. Li et al. [11] reported that caspase-3 plays the most important role in the apoptotic process and that caspase-9 has similar properties to caspase-3. Kim et al. [8] studied cardiac IR and showed that oligonucleosomal deoxyribonucleic acid fragments were formed with the activation of caspase-3, and the cell entered an irreversible pathway with the appearance of apoptotic bodies. Zhang et al. [26] showed that caspase-3 messenger ribonucleic acid expression increased after IR injury in the rat lung. In our study, in the sham group, the caspase-3 reaction was generally negative in the epithelium and glands

and in other layers (Fig. 2D). In the IR group, the caspase-3 reaction increased in the apoptotic areas and intermediate inflammatory cells. Muscles showed caspase-3 positivity (Fig. 2E), while the caspase-3 reaction was negative in goblet cells and the epithelium. A moderate caspase-3 reaction was observed in some of the gland cells, while the caspase-3 reaction was largely negative in connective tissue cells in the lamina propria (Fig. 2F).

Autophagy is the lysosomal degradation of cell substances, which is key for maintaining cell homeostasis. Beclin-1 is a protein that regulates both apoptosis and autophagy. During IR, beclin-1 expression is affected by many factors. Shi et al. [17] showed that beclin-1 expression was especially upregulated during the reperfusion stage in myocardial IR injury. Luo et al. [12] found that beclin-1 was overexpressed during cerebral IR injury and thus protected against neuronal death. Beclin-1 was also shown to protect against myocardial IR by regulating caspase-4 expression [18]. In our study, the beclin-1 reaction was negative in epithelial cells and goblet cells in the villi structures. The beclin-1 reaction was also negative in the muscle layer (Fig. 2G). The beclin-1 reaction was positive mainly in the ruptured villi. An intense beclin-1 reaction was also observed in some inflammatory cells and degenerative gland cells (Fig. 2H). The beclin-1 reaction was positive in a small number of cells. In general, moderate beclin-1 positivity was noted (Fig. 2I).

Limitations of the study

There are limited clinical studies on the relationship between GA and beclin-1 regulation at the apoptotic level. Huang et al. [5] suggested that exposure to the GA-derived compound methyl gallate inhibits hepatocellular carcinoma proliferation both in vitro and in vivo. They also reported increased methyl gallate-induced cytotoxicity in hepatocellular carcinoma cells to block autophagy. Based on their findings, it has been suggested that methyl gallate may act as a powerful therapeutic for human hepatocellular carcinoma patients [5]. Similarly, cells treated with propyl gallate, a derivative of GA, induced cell apoptosis, suggesting that it may be a new candidate for hepatocellular carcinoma therapy. The authors showed that propyl gallate inhibits hepatocellular carcinoma cell proliferation through enhanced reactive oxygen species production and autophagy activation [22].

CONCLUSIONS

Ischaemia-reperfusion caused cell degeneration, which activated a signal in the basal membrane accelerating the apoptotic process. Regulation of beclin-1 was disrupted, and caspase-3 was activated. GA reduced oxidative stress with its antioxidative effect and slowed down the apoptotic process mediated through the cell basal membrane with impaired beclin-1 regulation. In addition, GA, which has an antioxidative effect in the IR model induced by SMA, has been experimentally shown to inhibit the apoptotic pathway (caspase-3) through beclin-1 regulation for the first time. In this respect, more experimental studies are needed.

Conflict of interest: None declared

REFERENCES

1. Chen R, Zhang YY, Lan JN, et al. Ischemic postconditioning alleviates intestinal ischemia-reperfusion injury by enhancing autophagy and suppressing oxidative stress through the Akt/GSK-3 β/Nrf2 pathway in mice. Oxid Med Cell Longev. 2020; 2020: 6954764, doi: 10.1155/2020/6954764, indexed in Pubmed: 32256957.
2. Çimen FK, Çimen O, Altuner D, et al. Effect of rutin on experimentally induced small intestinal ischemia reperfusion injury in rats: A biochemical and histopathological evaluation. J Surg Med. 2021; 5(1): 26–30, doi: 10.28982/josam.858237.
3. Draper HH, Hadley M. Malondialdehyde determination as index of lipid peroxidation. Methods Enzymol. 1990; 186: 421–431, doi: 10.1016/0076-6879(90)86135-i.
4. Durgun C, Aşir F. Effect of ellagic acid on damage caused by hepatic ischemia reperfusion in rats. Eur Rev Med Pharmacol Sci. 2022; 26(22): 8209–8215, doi: 10.26355/eurrev_202211_30352, indexed in Pubmed: 36459004.
5. Huang CY, Chang YJ, Wei PL, et al. Methyl gallate, gallic acid-derived compound, inhibit cell proliferation through increasing ROS production and apoptosis in hepatocellular carcinoma cells. PLoS One. 2021; 16(3): e0248521, doi: 10.1371/journal.pone.0248521, indexed in Pubmed: 33725002.
6. Ji YY, Wang ZD, Wang SF, et al. Ischemic preconditioning ameliorates intestinal injury induced by ischemia-reperfusion in rats. World J Gastroenterol. 2015; 21(26): 8081–8088, doi: 10.3748/wjg.v21.i26.8081, indexed in Pubmed: 26185379.
7. Kassahun WT, Schulz T, Richter O, et al. Unchanged high mortality rates from acute occlusive intestinal ischemia: six year review. Langenbecks Arch Surg. 2008; 393(2): 163–171, doi: 10.1007/s00423-007-0263-5, indexed in Pubmed: 18172675.
8. Kim GT, Chun YS, Park JW, et al. Role of apoptosis-inducing factor in myocardial cell death by ischemia-reperfusion. Biochem Biophys Res Commun. 2003; 309(3): 619–624, doi: 10.1016/j.bbrc.2003.08.045, indexed in Pubmed: 12963035.

9. Klempnauer J, Grothues F, Bektas H, et al. Long-term results after surgery for acute mesenteric ischemia. Surgery. 1997; 121(3): 239–243, doi: 10.1016/s0039-6060(97)90351-2, indexed in Pubmed: 9068664.

10. Kroes BH, van den Berg AJ, Quarles van Ufford HC, et al. Anti-inflammatory activity of gallic acid. Planta Med. 1992; 58(6): 499–504, doi: 10.1055/s-2006-961535, indexed in Pubmed: 1336604.

11. Li M, Ona VO, Chen M, et al. Functional role and therapeutic implications of neuronal caspase-1 and -3 in a mouse model of traumatic spinal cord injury. Neuroscience. 2000; 99(2): 333–342, doi: 10.1016/s0306-4522(00)00173-1, indexed in Pubmed: 10938439.

12. Luo H, Huang D, Tang X, et al. Beclin 1 exerts protective effects against cerebral ischemiareperfusion injury by promoting DNA damage repair through a nonautophagydependent regulatory mechanism. Int J Mol Med. 2022; 49(5), doi: 10.3892/ijmm.2022.5117, indexed in Pubmed: 35266018.

13. Menon MB, Dhamija S. Beclin 1 phosphorylation: at the center of autophagy regulation. Front Cell Dev Biol. 2018; 6: 137, doi: 10.3389/fcell.2018.00137, indexed in Pubmed: 30370269.

14. Ow YY, Stupans I. Gallic acid and gallic acid derivatives: effects on drug metabolizing enzymes. Curr Drug Metab. 2003; 4(3): 241–248, doi: 10.2174/1389200033489479, indexed in Pubmed: 12769668.

15. Paglia DE, Valentine WN. Studies on the quantitative and qualitative characterization of erythrocyte glutathione peroxidase. J Lab Clin Med. 1967; 70(1): 158–169, indexed in Pubmed: 6066618.

16. Porter AG, Jänicke RU. Emerging roles of caspase-3 in apoptosis. Cell Death Differ. 1999; 6(2): 99–104, doi: 10.1038/sj.cdd.4400476, indexed in Pubmed: 10200555.

17. Shi B, Ma M, Zheng Y, et al. mTOR and beclin 1: Two key autophagy-related molecules and their roles in myocardial ischemia/reperfusion injury. J Cell Physiol. 2019; 234(8): 12562–12568, doi: 10.1002/jcp.28125, indexed in Pubmed: 30618070.

18. Sun W, Lu H, Dong S, et al. Beclin1 controls caspase-4 inflammsome activation and pyroptosis in mouse myocardial reperfusion-induced microvascular injury. Cell Commun Signal. 2021; 19(1): 107, doi: 10.1186/s12964-021-00786-z, indexed in Pubmed: 34732218.

19. Taş F, Erdemci F, Aşır F, et al. Histopathological examination of the placenta after delivery in pregnant women with COVID-19. J Health Sci Med. 2022; 5(3): 868–874, doi: 10.32322/jhsm.1100731.

20. Terzi A, Coban S, Yildiz F, et al. Protective effects of Nigella sativa on intestinal ischemia-reperfusion injury in rats. J Invest Surg. 2010; 23(1): 21–27, doi: 10.3109/08941930903469375, indexed in Pubmed: 20233001.

21. Tran S, Fairlie WD, Lee EF. BECLIN1: protein structure, function and regulation. Cells. 2021; 10(6): 1522, doi: 10.3390/cells10061522, indexed in Pubmed: 34204202.

22. Wei PL, Huang CY, Chang YJ. Propyl gallate inhibits hepatocellular carcinoma cell growth through the induction of ROS and the activation of autophagy. PLoS One. 2019; 14(1): e0210513, doi: 10.1371/journal.pone.0210513, indexed in Pubmed: 30653551.

23. Wilcox MG, Howard TJ, Plaskon LA, et al. Current theories of pathogenesis and treatment of nonocclusive mesenteric ischemia. Dig Dis Sci. 1995; 40(4): 709–716, doi: 10.1007/BF02064966, indexed in Pubmed: 7720458.

24. Yaris M, Deveci E. Prophylactic Effect of Potentilla fulgens on Renal Ischemia-Reperfusion Injury in Rats. Int J Morphol. 2021; 39(1): 116–122, doi: 10.4067/s0717-95022021000100116.

25. Zhang C, Chen K, Wang J, et al. Protective effects of crocetin against radiation-induced injury in intestinal epithelial cells. Biomed Res Int. 2020; 2020: 2906053, doi: 10.1155/2020/2906053, indexed in Pubmed: 32964024.

26. Zhang Z, Shen H, Qin Hd, et al. [Protective effect of N-acetylcysteine against pneumocyte apoptosis during ischemia/reperfusion injury of lung in rats]. Zhongguo Wei Zhong Bing Ji Jiu Yi Xue. 2012; 24(2): 111–115, indexed in Pubmed: 22316545.

V M

VIA MEDICA

ORIGINAL ARTICLE

Anti-inflammatory, anti-apoptotic, and antioxidant effects of obestatin on the colonic mucosa following acetic acid–induced colitis

Y.H. Elhassan

Department of Anatomy, College of Medicine, Taibah University, Madinah, Saudi Arabia

Background: Cellular inflammatory processes, fibrogenesis, and apoptosis are the most characteristic pathologic features of colonic injury and colitis in human and experimental animals. Obestatin, a peptide derived from proghrelin, is reported to have significant protective and curative actions on many gastrointestinal tract inflammatory diseases, including ulcerative colitis. However, its exact protective mechanisms and the associated histopathological changes, are still in need of deeper exploration. This study explores the effect of obestatin on the course of acetic acid (AA)-induced colitis as an antifibrotic, anti-inflammatory, and anti-apoptotic agent in relation to associated tissue stress parameters.

Materials and methods: A total of 40 healthy male albino Wistar rats weighing 200–250 g were recruited in this study. The rats were classified into four groups (10 rats each); group I: control, group II: obestatin only treated (16 nmol/kg), group III: colitis induced group (AA 1 mL of 3.5% (v/v), and group IV: AA-induced colitis + obestatin for 14 days. Colonic samples were examined after staining haematoxylin and eosin, Alcian blue, Masson trichrome. The expression of proliferating cell nuclear antigen (PCNA), nuclear factor kappa B (NFkB), and caspase-3 was estimated after immunohistochemical staining. Oxidative stress parameters, antioxidant enzymes, tissue myeloperoxidase (MPO) activity, ghrelin, and fibrogenesis markers were identified by immunoassay and colorimetric techniques.

Results: Colonic mucosa of group IV exhibited mucosal healing and regeneration of the surface epithelium with the restoration of the goblet cells' function together with a decline in PCNA, NFkB, and caspase-3 immunoreactivity in comparison to group III. This was accompanied by a reduction of the expression of fibrosis markers, hydroxyproline and fibronectin. In addition, tissue antioxidant status was significantly improved with a marked reduction of tissue MPO. Ghrelin level was significantly increased in comparison to group III. Group IV exhibited significant reduction in the levels of oxidative stress markers, malondialdehyde, total oxidant status with a marked increase in the activity of antioxidant enzymes, superoxide dismutase, catalase, and total cellular total antioxidant capacity.

Address for correspondence: Dr. Y.H. Elhassan, Ass. Prof., Department of Anatomy, College of Medicine, Taibah University, Madinah, Saudi Arabia, tel: +966 (14) 8483250, fax: +966 (14) 8484811, mob: 0966569737966, e-mail: yhassanresearch@hotmail.com; yasiranatomy2@hotmail.com; yhassan@taibahu.edu.sa

Conclusions: The concomitant treatment of obestatin inhibits the development of AA-induced colitis. The data signify that it has both curative and protective effects via antifibrotic, antioxidant, and anti-inflammatory activities. (Folia Morphol 2023; 82, 3: 641–655)

Key words: ghrelin, ulcerative colitis, oxidative stress, colon histopathology, apoptosis

INTRODUCTION

Ulcerative colitis (UC) is a common inflammatory bowel disease (IBD) mediated by an autoimmune process that significantly leads to extensive mucosal disruption and ulceration [42]. Despite innumerable research in the field of IBD, the exact aetiology of UC is still unclear, and their pathogenesis is complex, requiring the co-existence of environmental and genetic factors. However, research has suggested that both UC and Crohn's disease result from an abnormal immunological response to microflora present in the digestive system [39]. Untreated UC may proceed to colorectal cancer, life-threatening respiratory and/ or circulatory complications [16]. The severity of the disease is associated with the extent of colonic barrier disruption with subsequent exposure of the mucosa and submucosa to proinflammatory and environmental factors [45, 46, 49, 58]. These factors can directly or indirectly activate local mesenchymal cells, such as fibroblasts, myofibroblasts, and smooth muscle cells, for the expression of increasing amounts of extracellular matrix components (ECM) such as collagens or fibronectins. These proceedings eventually end in fibrosis, goblet cell inhibition, and disruption of the colonic wall histological building [38, 45, 52]. In addition, the associated imbalance between tissue matrix-metalloproteinases, which degrade ECM, and tissue inhibitors of metalloproteinases, which inhibit ECM degradation, adds to the alteration of the colonic wall construction [38].

The serious complications of UC and the lack of presence of proper drug therapy necessitates more scientific trials to choose and/or discover alternative drug candidates with improved tolerability, minimum side effects, and more safety for the treatment of this disease. There are numerous methods to ameliorate the signs and symptoms of IBD, but there is no method to permanently cure this disease [2]. This leads to a search for new therapeutic strategies.

Obestatin is reported in many studies to possess protective and therapeutic effects on gastrointestinal tract inflammatory diseases [10, 11, 14]. Chemically, obestatin is a ghrelin-associated peptide formed of a 23-amino acid peptide derived from the post-translational processing of the preproghrelin gene [61]. Biologically, obestatin was identified in several organs such as the stomach, endocrine pancreas, adipose tissue, the lung, liver, skeletal muscle, mammary glands, and the male reproductive system [23, 26, 40]. Nevertheless, the stomach comprises the major source of circulating obestatin [13, 23].

In experimental models, administration of obestatin exhibited numerous therapeutic effects mediated through activation of receptors like the G-protein-coupled receptor [60] and the glucagon-like peptide 1 receptor in adipocytes and pancreatic beta cells [24, 25]. The main reported effects were suppression of the motility of the gastrointestinal tract, inhibition of cellular oxidative stress induced by molecular H_2O_2 [57], and regulation of the secretion of insulin [24, 25]. Accordingly, obestatin was considered a promising therapeutic agent in managing many clinical syndromes [27, 35, 62], particularly those related to the digestive system [47, 57]. Moreover, the role of obestatin in augmenting the healing of gastric ulcers via increasing both blood flow in gastric mucosa and cell proliferation has been reported [17]. Inflammatory bowel disease is another example with the advantage of using the ratio of obestatin to ghrelin in the serum as a corresponding marker for monitoring the severity of the accompanying inflammatory process [2, 30].

Experimentally development of colitis and related gastric complications induced by acetic acid [39] or dextran sodium sulfate [43] were significantly suppressed following administration of obestatin. Even though these studies proved the therapeutic effect of obestatin, the exact protective mechanisms, and the associated histopathological changes, are still in need of deeper exploration.

From the aforementioned studies relating to the pathogenesis of UC and the proposed therapeutic effect of obestatin, this study aims to explore the

biological roles of obestatin as an antifibrotic, anti-inflammatory, and antioxidant agent on a murine model of acetic acid (AA)-induced colitis, and to investigate whether this action is associated with changes in the expressions of proliferating cell nuclear antigen (PCNA), nuclear factor kappa B (NFkB), and caspase-3, and further to explore the concomitant changes in the levels of oxidative stress parameters, antioxidant enzymes, tissue myeloperoxidase (MPO) activities. The expressions of ghrelin and fibrogenic markers like collagen and fibronectins in mucosal tissues of control and in AA-induced colitis rats are also pursued.

MATERIALS AND METHODS

A total of 40 healthy male albino Wistar rats weighing 200–250 g were obtained from the Animal breeding unit at (Taibah University). All the study steps were strictly designed and followed by the Ethical Committee of Taibah University Research Board and were in line with the National Institutes of Health (NIH) guidelines for the care and use of laboratory animals (NIH Publication 85-23 Rev. 1985).

All animals were kept in cages at room temperature under a 12 h light-dark cycle. Prior to induction of colitis, the animals were fasted for 16 h with free access to water through ad libitum. Then, the animals were provided with normal basal diets containing 21.1% of protein, 5.1% of fat, 60.0% of carbohydrates, 3.9% of fibre, 7.9% of minerals, and 2.0% of vitamins.

The rats were randomly categorized into four groups (10 rats each). Group I (control) was treated with saline, group II (treated with obestatin only), group III (AA-induced colitis), and group IV (AA-induced colitis + obestatin). Starting 24 h before the rectal enema, the rats were treated with intraperitoneally (i.p.) saline (groups I, II and III) or obestatin (group IV) twice per day for 4 consecutive days. Rat obestatin (Yanaihara Institute, Shizuoka, Japan) was given at dose of 16 nmol/kg [14, 17, 39].

After pentobarbital (30 mg/kg i.p.) anaesthesia, 1 mL of 3.5% (v/v) AA diluted in saline was used to induce colitis in groups III and IV by a rectal enema using a polyethylene catheter containing AA solution inserted into the rectum at 4.5 cm from the anus. Rats were kept in a vertical position during installation and for 1 min after installation to avoid solution leakage. Animals of groups I and II received 0.5 mL of saline 0.9% by the same procedure.

Fourteen days after the induction of colitis, rats were again anesthetized with pentobarbital (30 mg//kg i.p.) and sacrificed to collect the serum and colon tissue samples from all groups for biochemical and histopathological investigations. After excision of the colon, it was examined thoroughly for microscopic, immunohistochemical, and biochemical examinations.

The colon samples were fixed in 10% buffered formaldehyde and embedded in paraffin. Paraffin sections were processed and stained with haematoxylin and eosin, Alcain blue, and Masson trichrome stains according to the standard methodology. The stained sections were examined under a light microscope (Nikon Eclipse E600W, Japan), and the represented areas were photographed.

The haematoxylin and eosin-stained sections were further examined by the pathologist, uninformed about the treatment given. The grading of colonic damage (ulceration, inflammation, depth of the lesion, and fibrosis) and the number of goblet cells were determined using a scale of Vilaseca as described in detail previously [37, 54]. The standard techniques of staining of caspase-3, PCNA, and NFkB were followed as provided by the instructors [1, 18, 59].

The homogenates of colonic tissue were subjected to the estimation of oxidative stress antioxidant system markers, including malondialdehyde (MDA), total oxidant status (TOS), superoxide dismutase (SOD), catalase (CAT), and total antioxidant capacity (TAC) levels as previously analysed [19, 50]. Tissue MPO activity was identified in colonic tissue samples by colorimetric assays as previously reported in the literature [61]. The amount of MPO present in tissue samples that caused a change in absorbance measured at 460 nm for 3 min referred to one unit of MPO enzyme activity [28]. Ghrelin concentrations were estimated in the homogenates of the colonic tissue samples using commercially available EIA assay kits (Phoenix Pharmaceuticals, Burlingame, CA) as fully characterised in previous work by Ghomraoui et al. [22]. Hydroxyproline was estimated in acidified colonic tissues by adding 5 mL of 6N HCl for 3 h at 130°C, as reported previously in 1963 by Bergman and Loxley [6]. For assessment of fibronectin, a glass homogenizer was used to homogenize colonic tissues with 5–10 mL of ice-cold phosphate buffered saline (0.01 mol/L, pH 7.0–7.2). An ultrasonic cell disrupter was applied to the resulting suspension to destroy hard cell wall compartments for future extraction. Then,

centrifugation of the homogenates for 5 min at 5000 g and the residue was used using an immunoassay ELISA kit (ABIN1874233, Atlanta, GA30338, USA) at a wavelength of 450 nm on a spectrophotometer. The fibronectin concentration was then determined by comparing the optical density of the samples to the standard curve as described by Attallah et al. [4].

Statistical analysis

All data were expressed as mean ± standard deviations (SD). The results obtained were statistically analysed by GraphPad Prism (version 7). In addition, a one-way ANOVA test followed by Tukey's post hoc analysis was applied to compare and identify the significance between groups. The statistical significance was assigned at a p-value < 0.05.

RESULTS

In groups, I and II, tissue sections of rats exhibited normal colonic structure with intact colonic mucosa and numerous goblet cells on the surface epithelium and crypts (Fig. 1A, B). Notable pathological changes present in group III involved all colonic laminae (epithelial, propria, muscularis mucosae, and the submucosa). These laminae could not be distinguished from each other due to extensive inflammatory cell infiltration and ulceration (Fig. 1C). In addition to severe goblet cell depletion, an absence of crypts was evident. Treatment with obestatin in group IV did not completely alleviate the lesions but just restricted them (Fig. 1D). The mucosa retained its unharmed appearance with active goblet cells detected on the surface and the crypt's epithelium.

The mucous secretions of the goblet cells in groups I and II stained Alcian blue stain demonstrated numerous deeply stained goblet cells lining the crypts and an intact film of mucus on the surface epithelium (Fig. 2A, B). On the other hand, group III shows nearly absent goblet cells and mucous, as evidenced by an extreme reduction in the intensity of Alcian blue stain. Group IV revealed few goblet cells and restored the intensity of the stain, particularly on the surface (Fig. 2C, D).

Masson trichrome stain of groups I and II detect minimal bluish stained collagen fibres in the lamina propria, muscularis mucosae, and the submucosa (Fig. 3A, B). Group III, on the other hand, showed increased expression of fibrosis in all colonic laminae (Fig. 3C). Group IV still shows extensive collagen fibres expression (Fig. 3D).

The immunohistochemical examination of PCNA of the mucosa of the colon of group I exhibited weak brown cytoplasmic positive immunoreaction in the epithelium and few cells in the lamina propria (Fig. 4A). the picture was more or less the same in group II (Fig. 4B). Group III exhibited marked increased immunoreactivity in both epithelial cells and cells of lamina propria (Fig. 4C). On the other hand, sections in the colonic mucosa of group IV demonstrated a decrease in positive immunoreaction compared to groups III (Fig. 4D).

NFkB immune staining of the group I demonstrated scanty brownish cytoplasmic positive immunoreaction in both the surface epithelium and the cells of lamina propria (Fig. 5A). Group II showed a similar presentation (Fig. 5B). Whereas sections of group III disclosed widespread marked immunoreactivity in all layers of colonic mucosa (Fig. 5C), while colonic mucosa of group IV displayed a limited presentation of the immunoreactivity to the mucosa and nearly absent reaction in the lamina propria (Fig. 5D).

Caspase 3 expression in the colon mucosal area showed a nearly absent reaction in both groups I and II (Fig. 6A, B). Group III showed a strong and diffuse reaction in all layers of the colonic mucosa (Fig. 6C). Group IV shows very weak reactivity in comparison (Fig. 6D).

The grading of colonic injury and a number of goblet cells was scored in Table 1. The results showed that normal rats treated with saline or obestatin showed no mucosal damage. However, rats with colitis induced by AA (group III) showed significant mucosal damage and remarkably decreased goblet cells number compared to control or obestatin-treated rats (group I and II). Group IV, on the other hand, showed a significant improvement in the colon mucosal damage score compared to group III rats. Additionally, the number of goblet cells was significantly increased in group IV compared with group III.

The expression levels of MDA, TOS, and the activity of SOD, CAT, and TAC in tissue samples of group I and rats of the experimental groups are tabulated (Table 2). In groups I and II, the results showed no significant effect. However, group III showed a significant reduction in the concentration of MDA, TOS, and an increase in the activity of SOD, CAT, and TAC, respectively. In group III, AA induced a significant increase in the levels of MDA, TOS and a reduction in the activity of SOD, CAT, and TAC compared to groups I and II. In rats with colitis treated with obestatin (group IV), there was a significant (p < 0.003) reduction in the levels of MDA,
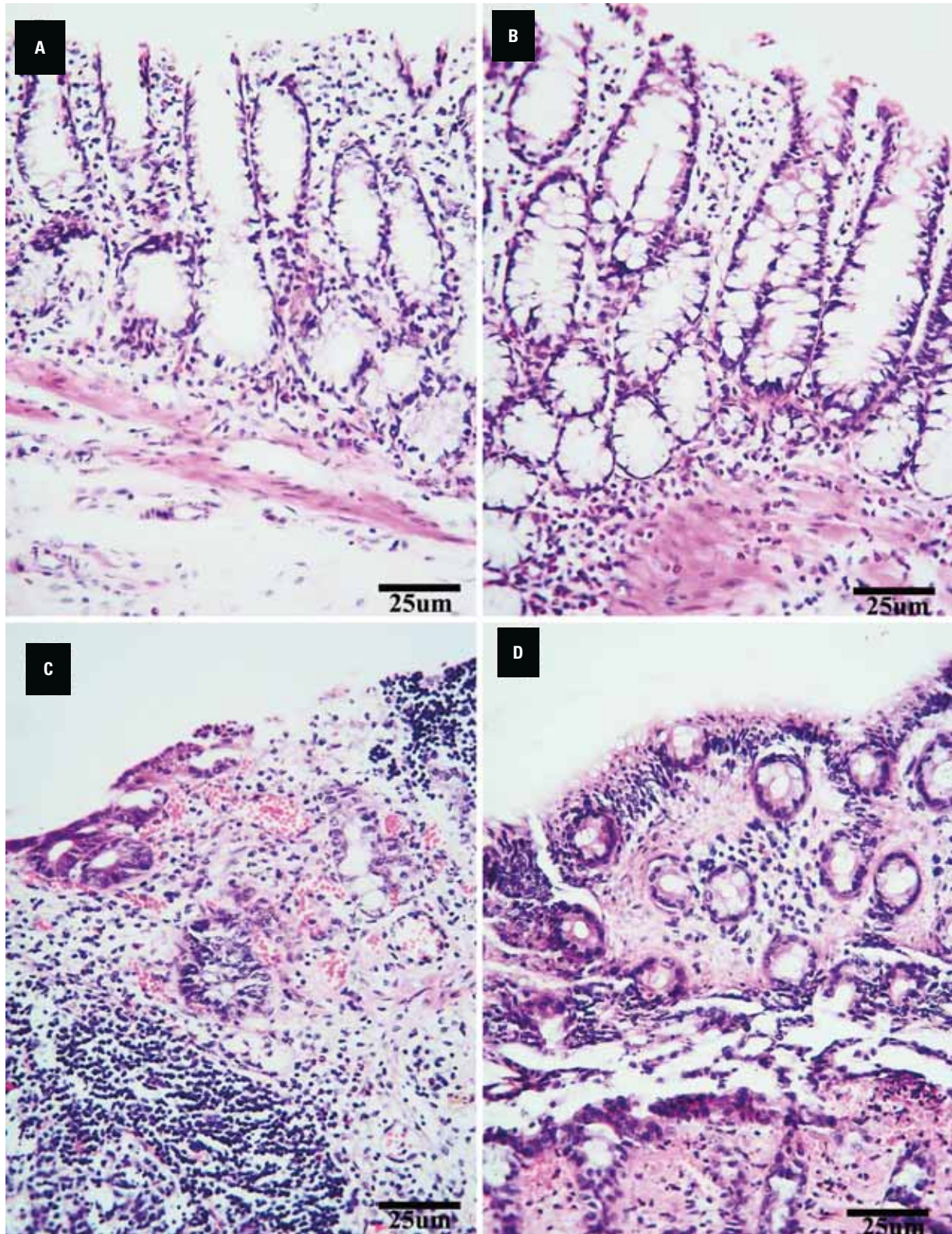
Figure 1. Tissue sections of rats in group I and II stained with haematoxylin and eosin exhibited normal colonic structure with intact colonic mucosa and numerous goblet cells on the surface epithelium and crypts (**A**, **B**); **C.** Group III shows marked pathological changes in all colonic laminae which appears barely differentiated. The mucosa shows focal ulceration with complete absence of the goblet cells. The muscularis mucosae are not evident and the submucosa is infiltrated by extensive inflammatory cell infiltration. Group IV shows areas of limited ulceration, inflammatory cell infiltration and loss of crypts alternating with areas of intact mucosa with goblet cells and crypts revival (**D**).
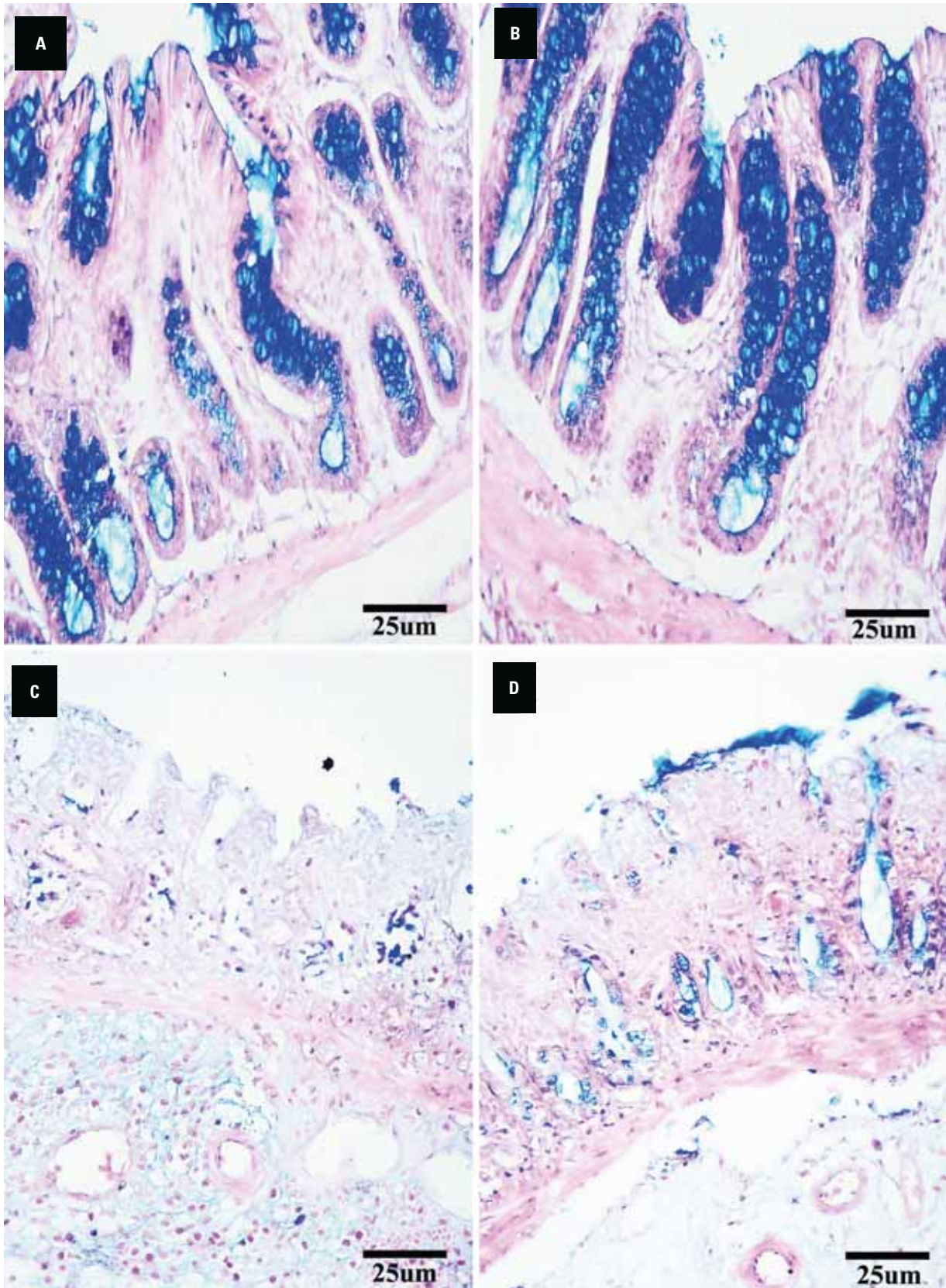
Figure 2. The mucous secretions of the goblet cells in groups I and II stained Alcian blue demonstrated numerous deeply blue stained goblet cells lining the crypts and intact film of mucus on the surface epithelium (**A**, **B**); **C.** Group III shows nearly absent goblet cells and mucous in addition to extreme reduction in the intensity of the stain; **D.** Group IV revealed few goblet cells and restored intact film of mucus on the surface epithelium.
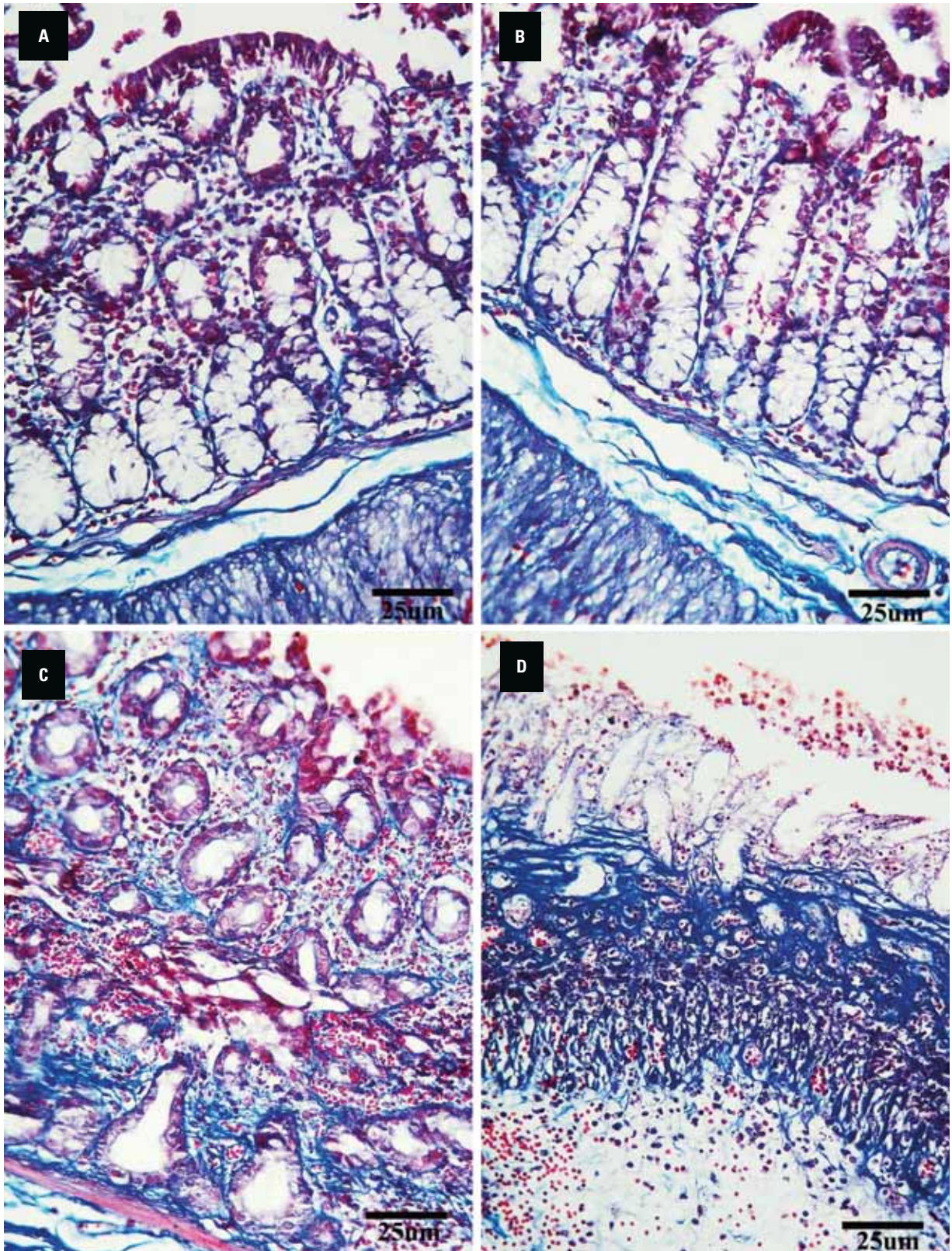
Figure 3. Masson trichrome stain of groups I and II. Minimal bluish stained collagen fibres can be detected in the lamina propria, muscularis mucosae, and the submucosa (**A**, **B**); **C.** Group III shows increased expression of bluish stained collagen fibres in all colonic laminae; **D.** Group IV show extensive collagen fibres expression in the submucosa and limited fibres in the mucosa.
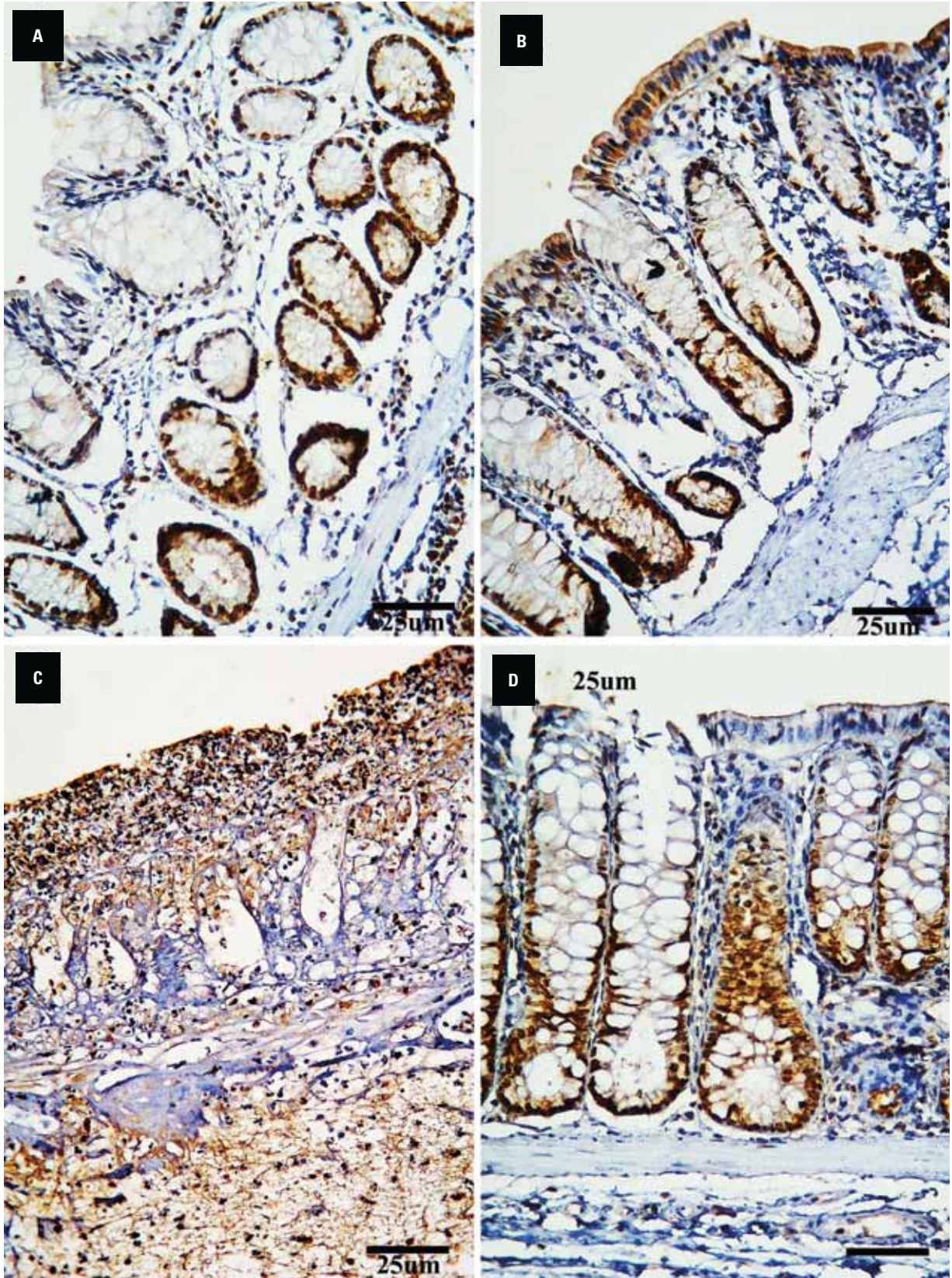
Figure 4. The immunohistochemical examination of proliferating cell nuclear antigen of the mucosa of the colon of group I demonstrates weak brown cytoplasmic positive immunoreaction in the epithelium and few cells in the lamina propria (**A**). The picture is more or less the same in group II (**B**). Group III shows marked increased immunoreactivity in both epithelial cells and cells of lamina propria (**C**). Group IV reveals decrease in positive immunoreaction (**D**).
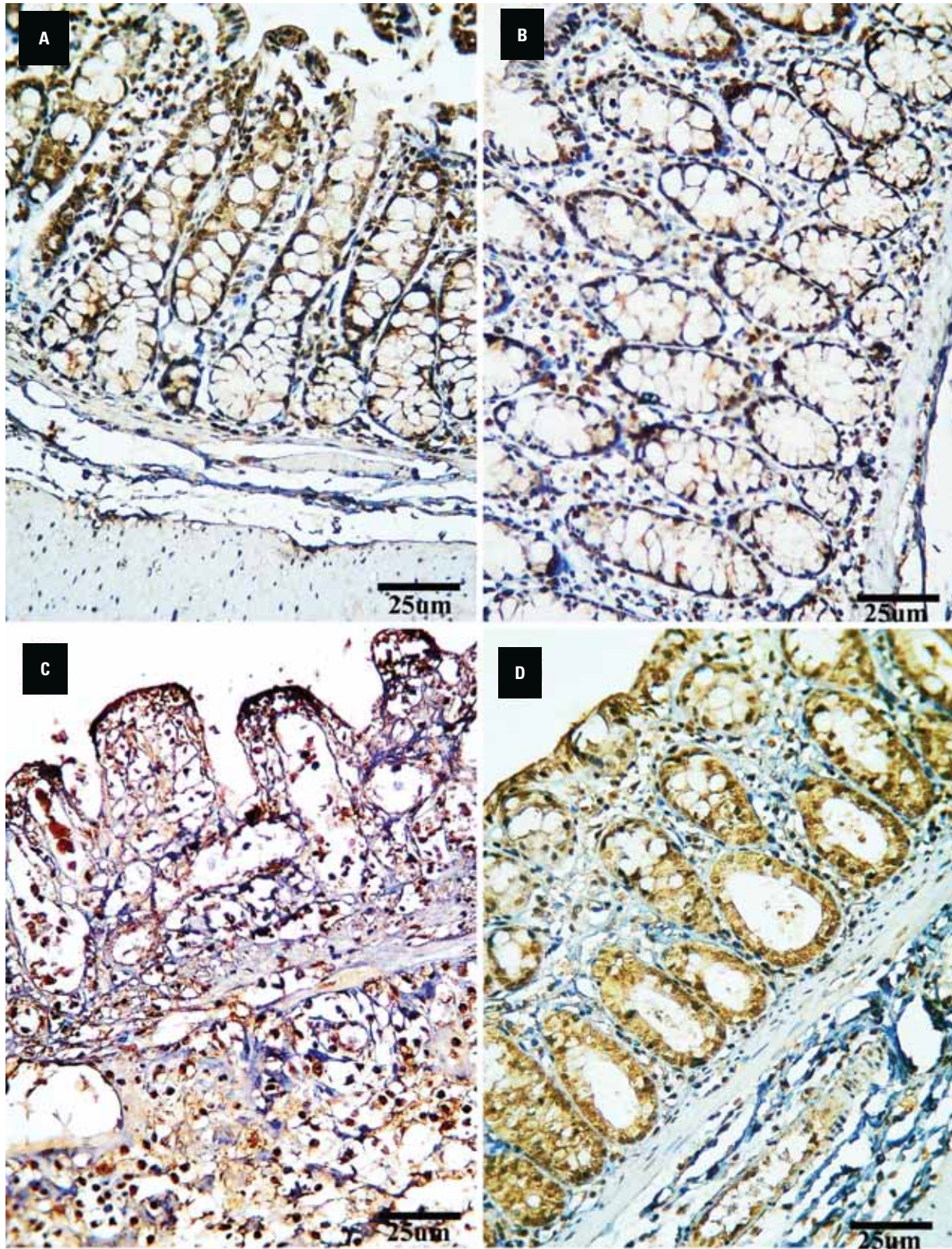
Figure 5. Nuclear factor kappa B immune staining of the group I show scanty brownish cytoplasmic positive immunoreaction in both the surface epithelium and the cells of lamina propria (**A**). Group II showed a more or less similar presentation in the mucosal crypts (**B**). Group III displays widespread marked immunoreactivity in all layers of colonic mucosa (**C**), while colonic mucosa of group IV presents a limited appearance of the immunoreactivity to the mucosa and nearly absent reaction in the lamina propria (**D**).
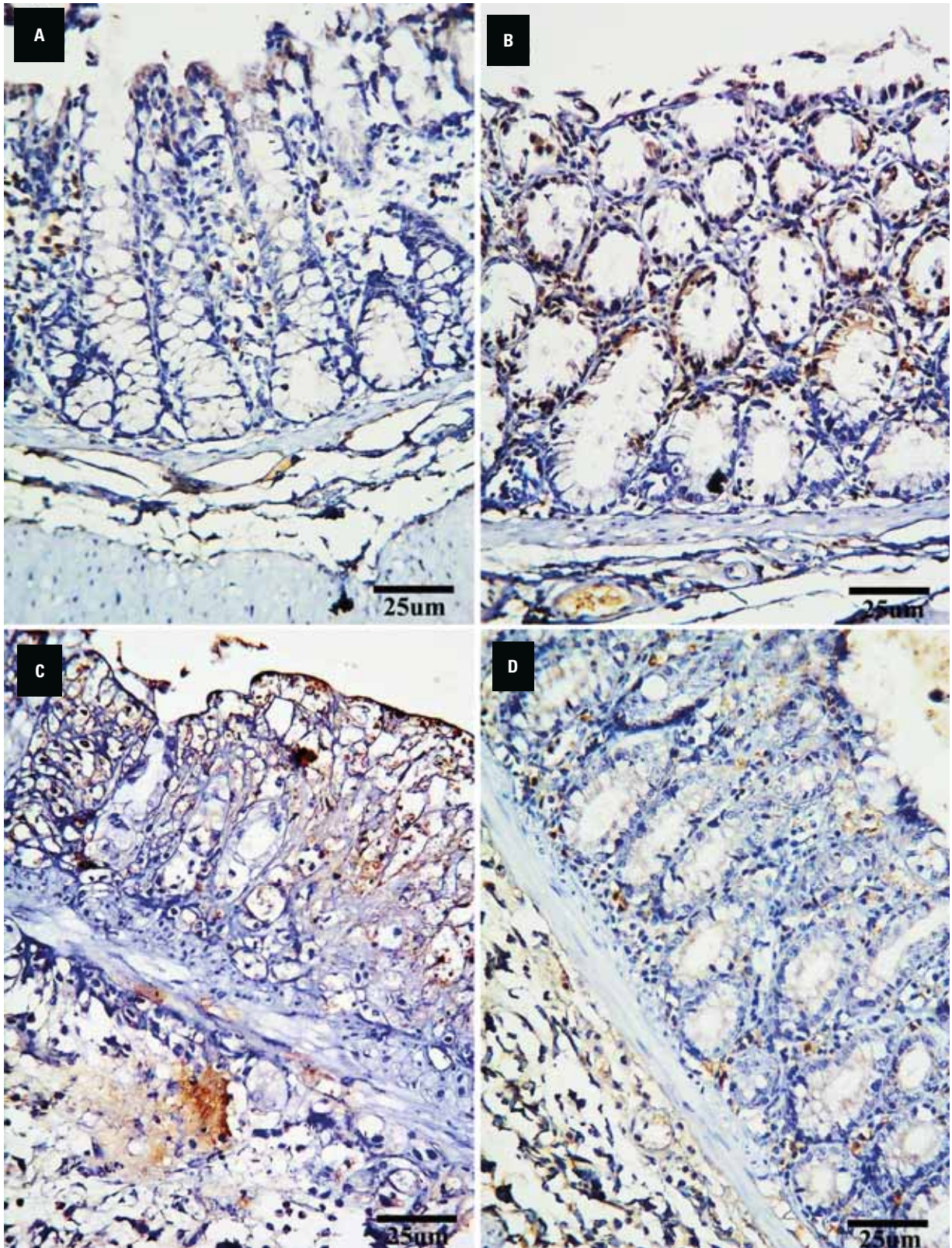
Figure 6. Caspase-3 expression in the colon mucosa showing nearly absent reaction in both groups I and II (**A, B**). Group III shows strong and diffuse reaction in all layers of the colonic mucosa (**C**). Group IV on the other hand shows very weak reactivity (**D**).

Table 1. Colonic injury grades and number of goblet cells among the study groups observed 14 days after induction of colitis

Groups	I	II	III	IV
Microscopic grade	0.89 ± 0.2	0.92 ± 0.1	13.6 ± 1.8[a]	5.3 ± 2.6[b]
Goblet cell	51.3 ± 12.5	50.9 ± 11.9	18.7 ± 12.3[a]	42.8 ± 15.2[b]

Mean ± standard deviation; n = 10 in each group of animals; [a]$p < 0.01$ (group III vs. group I), [b]$p < 0.001$ (group III vs. group II)

Table 2. Comparison of tissue oxidant-antioxidant parameters among the study groups (n = 10)

Groups	I	II	III	IV
MDA [nmol/g]	4.1 ± 0.46	3.52 ± 0.38[a]	7.5 ± 2.8[b]	3.6 ± 1.3[c]
TOS [μmol/g]	1.86 ± 1.2	1.76 ± 1.5[a]	4.8 ± 12.3[b]	2.8 ± 1.4[c]
SOD [U/mg protein]	2.4 ± 0.98	2.8 ± 0.91[a]	0.51 ± 04[b]	3.6 ± 1.9[c]
CAT [k/g protein]	1.8 ± 0.65	1.9 ± 0.84[a]	0.36 ± 0.45[b]	1.6 ± 1.1[c]
TAC [mmol/L]	2.1 ± 0.48	2.8 ± 0.25[a]	0.45 ± 0.25[b]	2.3 ± 1.4[c]

Mean ± standard deviation; n = 10 in each group of animals; [a]$p < 0.01$ (group II vs. group I); [b]$p < 0.001$ (group III vs. group II/group I); [c]$p < 0.003$ (group IV vs. group III);
MDA — malondialdehyde; TOS — total oxidant status; SOD — superoxide dismutase; CAT — catalase; TAC — total antioxidant capacity
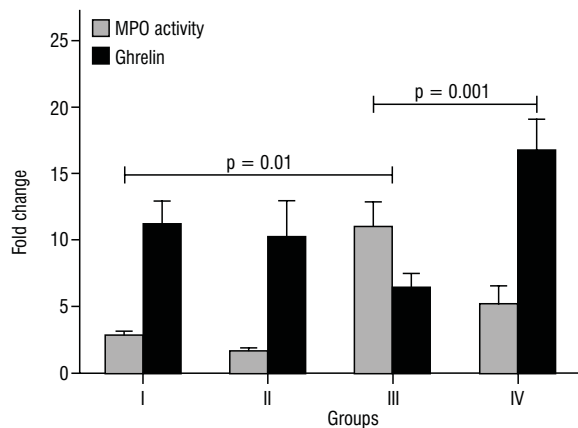
Figure 7. Levels of myeloperoxidase (MPO) and ghrelin activity in colonic mucosa of rats in control and experimental groups. In rats with colitis (group III), significant increase in the activity of tissue MPO with a reduction in the levels of tissue ghrelin were observed ($p < 0.01$). Group IV presents a significant reduction in the activity of MPO with an elevation in the levels of tissue ghrelin ($p < 0.001$) following the treatment with obestatin. The results expressed as mean ± standard deviation (SD); n = 10 in each group of animals; $p < 0.01$ when compared with group I; $p < 0.001$ when compared with group I or II and III, respectively.
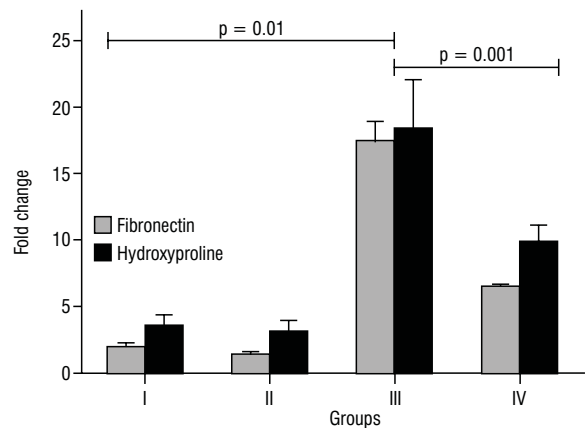
Figure 8. The expression of fibrotic markers (fibronectin and hydroxyproline) in control and experimental groups. Rats treated of group III shows significant increase in the expression levels of fibronectin and hydroxyproline compared to control group ($p < 0.01$). However, group IV shows a significant reduction in the expression of both fibronectin and hydroxyproline compared to group III ($p < 0.001$). The results expressed as mean ± standard deviation; n = 10 in each group of animals; $p < 0.01$ when compared with group I or II; $p < 0.001$ when compared with group III.

TOS with more increased in the activity of antioxidant enzymes, SOD, CAT, and total cellular TAC.

The expression levels of tissue ghrelin and MPO is shown in Figure 7. A significant increase in the tissue activity of MPO and a decrease in ghrelin levels in group III rats compared to control rats treated with saline only. In AA-induced colitis rats treated with obestatin (group IV), a significant reduction in the activity of MPO with an elevation in the levels of tissue ghrelin. A significant increase in the expression

levels of fibronectin and hydroxyproline as markers of fibrosis (Fig. 8) was noted in group III compared to groups I and II. However, when treated with obestatin compared to group III, rats of group IV exhibited a significantly reduced expression of both fibronectin and hydroxyproline.

DISCUSSION

The current study results established the curative and protective effect of i.p. obestatin on the histo-

pathological structure of the colon and the mucosal inflammatory and cellular antioxidant levels.

The model of colitis induced by AA investigates common colon diseases such as IBD as it induces a similar picture of inflammation together with ulceration [55]. The models of AA-induced colitis inject the acid with the tip of the catheter positioned at variable distances (from 1.2 [36] to 8 cm [44]) proximal to the anus verge. In this study, an intermediate depth of catheter insertion at 4.5 cm from the anus verge was chosen.

The curative outcome of obestatin was confirmed on the histopathological level as obestatin significantly amended the lesions grades, ulcerations, inflammatory cell infiltrations, and the loss of crypts induced by AA. The number of the goblet cells was significantly increased, and goblet cells were redetected with increased mucous secretions on the surface and crypt epithelium as evidenced by Alcian blue stain when compared with the AA-induce UC as likewise reported [31]. Obestatin significantly reduced colitis by increasing blood leukocytes and mucosal concentration of proinflammatory markers and leading to reduced histological signs of colonic damage [53]. These results also showed that obestatin improved the mucosal blood flow in the colon and decreased the local and systemic inflammatory processes.

As a marker of cell proliferation, PCNA immune stain was markedly increased in AA-induced colitis and decreased with obestatin. Similar results were reported [53]. In NFkB immune stain as a marker of coordination of chronic inflammatory condition of the colon also reported a marked increase in the AA-induced colitis and an apparent decrease in NFkB immunoreactivity with the use of obestatin indicating tissue induced anti-inflammatory effect [5]. At the same time, the indicator of apoptosis, caspase-3, was also markedly decreased in the obestatin treated group after induction of UC compared to the AA-induced colitis group. This indicator was helpful in a study on the heart proving the protection of the cardiac muscles with prior use of obestatin [3].

The administration of obestatin improved antioxidant status, reduced inflammation, increased the expression levels of tissue ghrelin, and reduced the activity of tissue MPO. At the same time, this curative effect was proved in AA-induced colitis, whereas fibrosis markers, inflammatory MPO markers, and oxidant markers such as MDA, TOS were significantly reduced, and the antioxidant enzymes SOD, CAT, and

total TAC were significantly increased. The objective antifibrotic impact of obestatin was proven in our study by the marked inhibited expression of Masson trichrome stain in the treated group compared to the AA-UC group. These results are in line with others who reported that obestatin displayed preventive and therapeutic effects on acute pancreatitis [9–11], chronic gastric ulcers [17], and some models of colitis [39].

Oxidative stress is an important component of mucosal injury pathogenesis [32] which activates cellular apoptosis [21, 51], as evidenced in our study by the increased expression of caspase-3 as a marker of apoptosis. In contrast, deregulation or excessive apoptosis disrupts equilibrium and manifests variable clinical presentations [41, 48]. That is why most studies have focused on proposed treatment modalities with antioxidant and anti-inflammatory properties.

Colonic injury in this study was detected in the AA-colitis model with a significant increase in oxidative stress markers and histopathological changes. Oxidative stress is the key factor of AA-associated UC, where the overload of oxygen-free radicals induces disruption and apoptosis [15]. In addition, AA significantly augmented the reduction in the level of the antioxidant enzyme. Similarly, a decrease in the activity of tissue SOD, CAT, and the total cellular TAC was reported in rats with AA-colitis [20]. The inhibition of lipid peroxidation and improvement of cellular antioxidant status is one of the anti-inflammatory actions of obestatin and ghrelin as previously described [29, 34].

Ghrelin, an alternative product of preproghrelin, also had a therapeutic effect on the gastrointestinal tract [56]. It has a protective effect on gastrointestinal mucosa against damage caused by harmful factors [8, 29, 33] and potentially inhibits colitis development. Ghrelin has a protective effect on gastrointestinal mucosa against damage caused by harmful factors [7, 56] and potentially inhibits the development of colitis. Tissue ghrelin levels were identified to confirm the protective effect of obestatin against AA-UC and confirmed a significantly increased tissue ghrelin level in concomitant to the previously reported protective effect of ghrelin on gastrointestinal mucosa against damage with harmful factors [7, 29, 33].

In our study, the expression of tissue MPO was reported to be directly proportional to the number of inflammatory cell infiltration [12, 43]. It was suggested that obestatin inhibits polymorphonuclear cell recruitment during the progression of chronic colitis.

Obestatin decreased tissue MPO levels significantly in rats with AA-colitis in the current study. At the same time, the histopathological examination reported that the inflammatory cell infiltration was markedly reduced. Accordingly, our results with others provided further evidence that obestatin exhibits anti-inflammatory actions and confirmed its curative, protection, and healing properties in this model.

Limitations of the study

We used Wistar rats as they are good models when studying colitis. However, some of the causes behind controversy may be the animal or species-related difference and this is one of the study limitations. Moreover, the effect related to multiple doses and long term use of acetic acid and obestatin may cause differences in results. Furthermore, the sex difference in the inflammatory response may be cause controversial results. We used male animals because although females have higher innate and adaptive immune responses than males, this contributes to increased susceptibility to inflammatory and autoimmune diseases in females compared with males. So it is recommended to repeat the experiment with multiple doses of drugs and with different animals and species with different sex.

Clinical applications

We recommend the use of obestatin in management of colitis through its anti-inflammatory, antioxidant, antiapoptotic and antifibrotic effect with regulation of regeneration of colic mucosa.

CONCLUSIONS

The current study concludes that pretreatment with obestatin at a dose of 16 nmol/kg inhibits the development of acetic acid-induced colitis. This effect significantly proceeded via a reduction in cellular inflammatory and overproduction of both cellular fibrosis and oxidative stress markers with a potential improvement of antioxidant status of the colonic cells. These data recommended that obestatin was independent anti-inflammatory, antioxidant, and antifibrotic against AA-induced colitis.

Conflict of interest: None declared

REFERENCES

1. Al-Henhena N, Ying RP, Ismail S, et al. Chemopreventive efficacy of Andrographis paniculata on azoxymethane-in-duced aberrant colon crypt foci in vivo. PLoS One. 2014; 9(11): e111118, doi: 10.1371/journal.pone.0111118, indexed in Pubmed: 25390042.

2. Alexandridis E, Zisimopoulos A, Liratzopoulos N, et al. Kouklakis GJIbd. Obestatin/ghrelin ratio: a new activity index in inflammatory bowel diseases. Inflamm Bowel Dis. 2009; 15(10): 1557–1561.

3. Alloatti G, Arnoletti E, Bassino E, et al. Obestatin affords cardioprotection to the ischemic-reperfused isolated rat heart and inhibits apoptosis in cultures of similarly stressed cardiomyocytes. Am J Physiol Heart Circ Physiol. 2010; 299(2): H470–H481, doi: 10.1152/ajpheart.00800.2009, indexed in Pubmed: 20525876.

4. Attallah A, Abdallah S, Attallah A, et al. Diagnostic value of fibronectin discriminant score for predicting liver fibrosis stages in chronic hepatitis C virus patients. Ann Hepatol. 2013; 12(1): 44–53, doi: 10.1016/s1665-2681(19)31384-5.

5. Beck EA, Currey MC, Small CM. Cresko WAJGG, Genomes, Genetics. QTL mapping of intestinal neutrophil variation in threespine stickleback reveals possible gene targets connecting intestinal inflammation and systemic health. G3 (Bethesda). 2020; 10(2): 613–622.

6. Bergman I, Loxley RJ. Two improved and simplified methods for the spectrophotometric determination of hydroxyproline. Analytical Chemistry. 1963; 35(12): 1961–1965.

7. Brzozowski T, Konturek PC, Drozdowicz D, et al. Role of central and peripheral ghrelin in the mechanism of gastric mucosal defence. Inflammopharmacology. 2005; 13(1-3): 45–62, doi: 10.1163/156856005774423971, indexed in Pubmed: 16259727.

8. Brzozowski T, Konturek P, Sliwowski Z, et al. Neural aspects of ghrelin-induced gastroprotection against mucosal injury induced by noxious agents. J Physiol Pharmacol. 2006; 57(Suppl 6): 63–76.

9. Bukowczan J, Cieszkowski J, Warzecha Z, et al. Therapeutic effect of obestatin in the course of cerulein-induced acute pancreatitis. Pancreas. 2016; 45(5): 700–706, doi: 10.1097/MPA.0000000000000517, indexed in Pubmed: 26474436.

10. Bukowczan J, Warzecha Z, Ceranowicz P, et al. Obestatin accelerates the recovery in the course of ischemia/reperfusion-induced acute pancreatitis in rats. PLOS ONE. 2015; 10(7): e0134380, doi: 10.1371/journal.pone.0134380, indexed in Pubmed: 26226277.

11. Bukowczan J, Warzecha Z, Ceranowicz P, et al. Pretreatment with obestatin reduces the severity of ischemia/reperfusion-induced acute pancreatitis in rats. Eur J Pharmacol. 2015; 760: 113–121, doi: 10.1016/j.ejphar.2015.04.016, indexed in Pubmed: 25912801.

12. Ceranowicz P, Warzecha Z, Dembinski A, et al. Pretreatment with obestatin inhibits the development of cerulein-induced pancreatitis. J Physiol Pharmacol. 2009; 60(3): 95–101, indexed in Pubmed: 19826187.

13. Ceranowicz P, Warzecha Z, Cieszkowski J, et al. Essential role of growth hormone and IGF-1 in therapeutic effect of ghrelin in the course of acetic acid-induced colitis. Int J Mol Scie. 2017; 18(6): 1118, doi: 10.3390/ijms18061118, indexed in Pubmed: 28538694.

14. Ceranowicz P, Warzecha Z, Dembinski A. Peptidyl hormones of endocrine cells origin in the gut — Their discov-

ery and physiological relevance. J Physiol Pharmacol. 2015; 66(1): 11–27, indexed in Pubmed: 25716961.

15. Cetinkaya A, Bulbuloglu E, Kurutas EB, et al. Beneficial effects of N-acetylcysteine on acetic acid-induced colitis in rats. Tohoku J Exp Med. 2005; 206(2): 131–139, doi: 10.1620/tjem.206.131, indexed in Pubmed: 15888969.

16. Chu TPC, Moran GW, Card TR. The pattern of underlying cause of death in patients with inflammatory bowel disease in england: a record linkage study. J Crohns Colitis. 2017; 11(5): 578–585, doi: 10.1093/ecco-jcc/jjw192, indexed in Pubmed: 28453767.

17. Dembiński A, Warzecha Z, Ceranowicz P, et al. Administration of obestatin accelerates the healing of chronic gastric ulcers in rats. Med Sci Monit. 2011; 17(8): BR196–BR200, doi: 10.12659/msm.881897, indexed in Pubmed: 21804455.

18. Ercan G, Yigitturk G, Erbas O. Therapeutic effect of adenosine on experimentally induced acute ulcerative colitis model in rats1. Acta Cir Bras. 2020; 34(12): e201901204, doi: 10.1590/s0102-865020190120000004, indexed in Pubmed: 32074166.

19. Erel O. A novel automated method to measure total antioxidant response against potent free radical reactions. Clin Biochem. 2004; 37(2): 112–119, doi: 10.1016/j.clinbiochem.2003.10.014, indexed in Pubmed: 14725941.

20. Flora G, Gupta D, Tiwari A. Toxicity of lead: a review with recent updates. Inter Toxicol. 2012; 5(2): 47–58, doi: 10.2478/v10102-012-0009-2.

21. Franco R, Sánchez-Olea R, Reyes-Reyes EM, et al. Environmental toxicity, oxidative stress and apoptosis: ménage à trois. Mutat Res. 2009; 674(1-2): 3–22, doi: 10.1016/j.mrgentox.2008.11.012, indexed in Pubmed: 19114126.

22. Ghomraoui FA, Alotaibi ST, Alharthi MA, et al. Plasma ghrelin and leptin in patients with inflammatory bowel disease and its association with nutritional status. Saudi J Gastroenterol. 2017; 23(3): 199–205, doi: 10.4103/sjg.SJG_575_16, indexed in Pubmed: 28611344.

23. Granata R, Baragli A, Settanni F, et al. Unraveling the role of the ghrelin gene peptides in the endocrine pancreas. J Mol Endocrinol. 2010; 45(3): 107–118, doi: 10.1677/JME-10-0019, indexed in Pubmed: 20595321.

24. Granata R, Gallo D, Luque RM, et al. Obestatin regulates adipocyte function and protects against diet-induced insulin resistance and inflammation. FASEB J. 2012; 26(8): 3393–3411, doi: 10.1096/fj.11-201343, indexed in Pubmed: 22601779.

25. Granata R, Settanni F, Gallo D, et al. Obestatin promotes survival of pancreatic beta-cells and human islets and induces expression of genes involved in the regulation of beta-cell mass and function. Diabetes. 2008; 57(4): 967–979, doi: 10.2337/db07-1104, indexed in Pubmed: 18162507.

26. Gurriarán-Rodríguez U, Santos-Zas I, Al-Massadi O, et al. The obestatin/GPR39 system is up-regulated by muscle injury and functions as an autocrine regenerative system. J Biol Chem. 2012; 287(45): 38379–38389, doi: 10.1074/jbc.M112.374926, indexed in Pubmed: 22992743.

27. Harsch I, Koebnick C, Tasi A, et al. Ghrelin and obestatin levels in type 2 diabetic patients with and without delayed gastric emptying. Dig Dis Sci. 2008; 54(10): 2161–2166, doi: 10.1007/s10620-008-0622-2, indexed in Pubmed: 19082715.

28. Hillegass LM, Griswold DE, Brickson B, et al. Assessment of myeloperoxidase activity in whole rat kidney. J Pharmacol Methods. 1990; 24(4): 285–295, doi: 10.1016/0160-5402(90)90013-b, indexed in Pubmed: 1963456.

29. İşeri S, Şener G, Yüksel M, et al. Ghrelin against alendronate-induced gastric damage in rats. J Endocrinol. 2005; 187(3): 399–406, doi: 10.1677/joe.1.06432, indexed in Pubmed: 16423819.

30. Jung JY, Jeong JiB, Kim JiW, et al. Circulating ghrelin levels and obestatin/ghrelin ratio as a marker of activity in ulcerative colitis. Intest Res. 2015; 13(1): 68–73, doi: 10.5217/ir.2015.13.1.68, indexed in Pubmed: 25691845.

31. Kaur K, Saxena A, Larsen B, et al. Mucus mediated protection against acute colitis in adiponectin deficient mice. J Inflamm (Lond). 2015; 12: 35, doi: 10.1186/s12950-015-0079-y, indexed in Pubmed: 25949213.

32. Kim YJ, Kim EH, Hahm KB. Oxidative stress in inflammation-based gastrointestinal tract diseases: challenges and opportunities. J Gastroenterol Hepatol. 2012; 27(6): 1004–1010, doi: 10.1111/j.1440-1746.2012.07108.x, indexed in Pubmed: 22413852.

33. Konturek PC, Brzozowski T, Walter B, et al. Ghrelin-induced gastroprotection against ischemia-reperfusion injury involves an activation of sensory afferent nerves and hyperemia mediated by nitric oxide. Eur J Pharmacol. 2006; 536(1-2): 171–181, doi: 10.1016/j.ejphar.2006.02.032, indexed in Pubmed: 16581065.

34. Kwiecien S, Jasnos K, Magierowski M, et al. Lipid peroxidation, reactive oxygen species and antioxidative factors in the pathogenesis of gastric mucosal lesions and mechanism of protection against oxidative stress-induced gastric injury. J Physiol Pharmacol. 2014; 65(5): 613–622, indexed in Pubmed: 25371520.

35. Liu W, Yue H, Zhang J, et al. Effects of plasma ghrelin, obestatin, and ghrelin/obestatin ratio on blood pressure circadian rhythms in patients with obstructive sleep apnea syndrome. Chin Med J. 2014; 127(5): 850–855, indexed in Pubmed: 24571875.

36. MacPherson BR, Pfeiffer CJ. Experimental production of diffuse colitis in rats. Digestion. 1978; 17(2): 135–150, doi: 10.1159/000198104, indexed in Pubmed: 627326.

37. Maduzia D, Matuszyk A, Ceranowicz D, et al. The influence of pretreatment with ghrelin on the development of acetic-acid-induced colitis in rats. J Physiol Pharmacol. 2015; 66(6): 875–885, indexed in Pubmed: 26769837.

38. Matsuno K, Adachi Y, Yamamoto H, et al. The expression of matrix metalloproteinase matrilysin indicates the degree of inflammation in ulcerative colitis. J Gastroenterol. 2003; 38(4): 348–354, doi: 10.1007/s005350300062, indexed in Pubmed: 12743774.

39. Matuszyk A, Ceranowicz P, Warzecha Z, et al. The influence of ghrelin on the development of dextran sodium sulfate-induced colitis in rats. Biomed Res Int. 2015; 2015(6): 718314–885, doi: 10.1155/2015/718314, indexed in Pubmed: 26713317.

40. Moretti E, Vindigni C, Tripodi SA, et al. Immunolocalisation of ghrelin and obestatin in human testis, seminal vesicles, prostate and spermatozoa. Andrologia. 2013; 46(9): 979–985, doi: 10.1111/and.12183, indexed in Pubmed: 24147986.

41. Myers B, Martin J, Dempsey D, et al. Acute experimental colitis decreases colonic circular smooth muscle contractility in rats. Am J Physiol. 1997; 273(4): G928–G936, doi: 10.1152/ajpgi.1997.273.4.g928, indexed in Pubmed: 9357837.

42. Niu X, Zhang H, Li W, et al. Protective effect of cavidine on acetic acid-induced murine colitis via regulating antioxidant, cytokine profile and NF-κB signal transduction pathways. Chem Biol Interact. 2015; 239: 34–45, doi: 10.1016/j.cbi.2015.06.026, indexed in Pubmed: 26102009.

43. Pamukcu O, Kumral ZN, Ercan F, et al. Anti-inflammatory effect of obestatin and ghrelin in dextran sulfate sodium-induced colitis in rats. J Pediatr Gastroenterol Nutr. 2013; 57(2): 211–218, doi: 10.1097/MPG.0b013e318294711e, indexed in Pubmed: 23549326.

44. Randhawa PK, Singh K, Singh N, et al. A review on chemical-induced inflammatory bowel disease models in rodents. Korean J Physiol Pharmacol. 2014; 18(4): 279–288, doi: 10.4196/kjpp.2014.18.4.279, indexed in Pubmed: 25177159.

45. Rieder F, Fiocchi C. Intestinal fibrosis in inflammatory bowel disease: Current knowledge and future perspectives. J Crohns Colitis. 2008; 2(4): 279–290, doi: 10.1016/j.crohns.2008.05.009, indexed in Pubmed: 21172225.

46. Scales BS, Huffnagle GB. The microbiome in wound repair and tissue fibrosis. J Pathol. 2013; 229(2): 323–331, doi: 10.1002/path.4118, indexed in Pubmed: 23042513.

47. Słupecka M, Woliński J, Herman AP, et al. [Biological role of obestatin in physiology and pathophysiology]. Med Wieku Rozwoj. 2012; 16(1): 47–52, indexed in Pubmed: 22516773.

48. Souza HSP, Tortori CJA, Castelo-Branco MTL, et al. Apoptosis in the intestinal mucosa of patients with inflammatory bowel disease: evidence of altered expression of FasL and perforin cytotoxic pathways. Int J Colorectal Dis. 2005; 20(3): 277–286, doi: 10.1007/s00384-004-0639-8, indexed in Pubmed: 15503066.

49. Sponheim J, Pollheimer J, Olsen T, et al. Inflammatory bowel disease-associated interleukin-33 is preferentially expressed in ulceration-associated myofibroblasts. Am J Pathol. 2010; 177(6): 2804–2815, doi: 10.2353/ajpath.2010.100378, indexed in Pubmed: 21037074.

50. Sun Y, Oberley LW, Li Y. A simple method for clinical assay of superoxide dismutase. Clin Chem. 1988; 34(3): 497–500, doi: 10.1093/clinchem/34.3.497.

51. Thompson CB. Apoptosis in the pathogenesis and treatment of disease. Science. 1995; 267(5203): 1456–1462, doi: 10.1126/science.7878464, indexed in Pubmed: 7878464.

52. Vaalamo M, Karjalainen-Lindsberg M-L, Puolakkainen P, et al. Distinct expression profiles of stromelysin-2 (MMP-10), collagenase-3 (MMP-13), macrophage metalloelastase (MMP-12), and tissue inhibitor of metalloproteinases-3 (TIMP-3) in intestinal ulcerations. Am J Pathol. 1998; 152(4): 1005–1014.

53. van den Toren SJ, van Grieken A, Mulder WC, et al. School Absenteeism, Health-Related Quality of Life [HRQOL] and Happiness among Young Adults Aged 16-26 Years. Int J Environ Res Public Health. 2019; 16(18), doi: 10.3390/ijerph16183321, indexed in Pubmed: 31505862.

54. Vilaseca J, Salas A, Guarner F, et al. Dietary fish oil reduces progression of chronic inflammatory lesions in a rat model of granulomatous colitis. Gut. 1990; 31(5): 539–544, doi: 10.1136/gut.31.5.539, indexed in Pubmed: 2161781.

55. Vishwakarma N, Ganeshpurkar A, Pandey V, et al. Mesalazine-probiotics beads for acetic acid experimental colitis: formulation and characterization of a promising new therapeutic strategy for ulcerative colitis. Drug Deliv. 2015; 22(1): 94–99, doi: 10.3109/10717544.2013.872711, indexed in Pubmed: 24491122.

56. Warzecha Z, Dembinski A. Protective and therapeutic effects of ghrelin in the gut. Curr Med Chem. 2012; 19(1): 118–125, doi: 10.2174/092986712803414051.

57. Xing Y-X, Yang L, Kuang HY. Function of obestatin in the digestive system. Nutrition. 2017; 34: 21–28, doi: 10.1016/j.nut.2016.08.009, indexed in Pubmed: 28063509.

58. Yamagata M, Mikami T, Tsuruta T, et al. Submucosal fibrosis and basic-fibroblast growth factor-positive neutrophils correlate with colonic stenosis in cases of ulcerative colitis. Digestion. 2011; 84(1): 12–21, doi: 10.1159/000320773, indexed in Pubmed: 21304240.

59. Zedan W, Mourad MI, El-Aziz S, et al. Evaluation of caspase 3 as a target for apoptosis induced via chemotherapy in rats. Int J Adv Res. 2015; 3: 1591–1601.

60. Zhang JV, Jahr H, Luo CW, et al. Obestatin induction of early-response gene expression in gastrointestinal and adipose tissues and the mediatory role of G protein-coupled receptor, GPR39. Mol Endocrinol. 2008; 22(6): 1464–1475, doi: 10.1210/me.2007-0569, indexed in Pubmed: 18337590.

61. Zhang JV, Ren PG, Avsian-Kretchmer O, et al. Obestatin, a peptide encoded by the ghrelin gene, opposes ghrelin's effects on food intake. Science. 2005; 310(5750): 996–999, doi: 10.1126/science.1117255, indexed in Pubmed: 16284174.

62. Zhang N, Yuan C, Li Ze, et al. Meta-analysis of the relationship between obestatin and ghrelin levels and the ghrelin//obestatin ratio with respect to obesity. Am J Med Sci. 2011; 341(1): 48–55, doi: 10.1097/MAJ.0b013e3181ec41ed, indexed in Pubmed: 21139496.

VIA MEDICA

ORIGINAL ARTICLE

Potential therapeutic role of microvesicles derived from mesenchymal stem cells and platelet-rich plasma in murine burn wound healing: scar regulation and antioxidant mechanism

R.A. Imam[1] , M.M. Amer[2]

[1]Department of Anatomy and Embryology, Faculty of Medicine, Cairo University, Cairo, Egypt
[2]Anatomy and Embryology Department, Faculty of Medicine, Ain Shams University, Egypt

Background: Microvesicles (MVs) derived from mesenchymal stem cells exhibited an emerging promising therapy in many animal model diseases. Post-burn scars represent one of the significant challenges in wound healing processes. The present study investigated the possible role of MVs derived from mesenchymal stem cells vs. platelet-rich plasma (PRP) in murine burn wound healing.

Materials and methods: Wistar rats (n = 40) were assigned into four equal groups (control, burn, burn + PRP, burn + MVs). Small-sized burns were induced, morphologically followed for 3 weeks, then rats were sacrificed and skin lesions were analysed biochemically and immunohistochemically.

Results: Both MVs and PRP modulated the burn healing process with better results in the MVs group than in PRP. MVs significantly ($p < 0.05$) accelerated burn wound size healing and dramatically modulated tissue interleukin (IL)-10, IL-6, and hyaluronidase. Both MVs and PRP significantly downregulated gene expression of miRNA203 and alpha smooth muscle actin and immunoblotting analysis of matrix metalloproteinases 3 and transforming growth factor beta compared with the burn group. The immune-staining intensity of tumour necrosis factor alpha was dramatically reversed in the MVs group compared with the burn group, whereas that of connective tissue growth factor, collagen I and III was significantly reduced in both groups. The antioxidant Nrf2 immune-staining intensity had been dramatically enhanced particularly in MVs.

Conclusions: Microvesicles derived from mesenchymal stem cells and PRP may improve burn wound healing via regulating scar formation and antioxidant mechanism. (Folia Morphol 2023; 82, 3: 656–667)

Key words: microvesicles, stem cells, platelet-rich plasma, burn, miRNA203, rats

---

Address for correspondence: Dr. R.A. Imam, Department of Anatomy and Embryology, Faculty of Medicine, Cairo University, Cairo, Egypt,
tel: +2001006114696; e-mail: redaabdelnasser@cu.edu.eg; abdelnasserreada@gmail.com

INTRODUCTION

Scarring of the skin following burns and traumatic surgery forms a major load on healthcare. The children suffer a lot from long-term functional and psychological problems as a result of scars [14]. Stem cell therapy evolved in the last years to exosomes and microvesicles (MVs) treatment paradigm which exhibited emerging promising modalities [15]. Exosomes or MVs are small secretory organelles with single membranes and enormous amounts of proteins, lipids, nucleic acids, and carbohydrate conjugates. They are capable of extracellular matrix remodelling and signalling as well as molecules delivering to other cells with preferable usage over stem cells due to stability, easy storage, and dosage control, non-rejection by the immune system [1, 2]. Extracellular vesicles are the principal mediators of stem cells' paracrine effects. They are plentiful with large numbers of miRNAs and act as transferral agents of miRNAs to recipient cells, where they can modulate the gene expression of recipient cells [22]. Platelet-rich plasma (PRP) has been widely used in post-burn disfiguring aesthetics with proven efficacy and tolerability. PRP is regarded as "tissue sealants" owing to their favourable effects on wound healing mediated by high levels of granular growth factors ready to be secreted [8]. Targeting the transforming growth factor beta (TGF-β) pathway is a still promising goal for wound scarring modulation in animals, although this matter is debated in human studies debated. In contrast, connective tissue growth factor (CTGF) pathway blocking agents for scar formation produced highly encouraging results in phase II clinical trials in human studies [14]. Fetal wounds possess the beverage of being scarless owing to large amounts of hyaluronic acid and an elevated ratio of collagen type III to type I [19]. The role of miRNA203 in the process of wound repair had been investigated. It was demonstrated that after 3 and 5 days from skin wound induction the GTPase Ran (a pro-proliferative factor) and Raph1 (a pro-migratory factor) are putative direct miR-203 targets whose expression could be essential wound for skin homeostasis and re-epithelialisation [18]. The present study investigated the possible role of MVs derived from mesenchymal stem cells and PRP in murine burn wound healing regarding inflammatory markers (interleukin [IL]-6, IL-10, tumour necrosis factor alpha [TNF-α]), scar regulating parameters (matrix metalloproteinases 3 [MMP-3], TGF-β, CTGF, hyaluronic acid, type I and III collagen), antioxidant marker (Nrf2), and involvement of miRNA203.

MATERIALS AND METHODS

Animals

This study was approved by CU-IACUC under the number CU-III-F-31-21 following all ethics of animal research studies. Forty adult Wistar rats weighing 170–220 g were housed in the animal house of the faculty of medicine, Cairo University, in isolated cages under standard temperature and light, fed ad libitum. Four groups of rats (n = 10) were utilized in this study; control, burn group, burn + PRP, burn + MVs.

Burn induction

After the removal of rats' skin hair by epilating cream, the skin of the dorsum of rats was sterilised with alcohol, and the tip of a tuning fork was applied to the skin for 20 s after being put in boiling water for 15 s [9]. Anaesthesia with ketamine (Ketamax, India) and xylazine (Xylaject, Adwia, Egypt) was done to rats just before burn induction and on the 7th and 14th day to obtain proper images of the skin burn wounds. Ceftriaxone (100 mg/kg IM, Rocephin, Roche) and buprenorphine were injected into rats to obtain antibiosis and analgesia, respectively for the 1st 5 days [17]. Burn size was assessed by ImageJ software from the captured images on the 1st, 7th, 14th, and 21st days.

PRP preparation

Blood of the PRP animal group (III) was aspirated from a retro-orbital vein and underwent double centrifugation, the 1st at 160 G for 20 min, the 2nd at 400 G for 15 min [7] using Beckman centrifuge (USA). 0.5 mL of PRP was obtained and injected locally into each rat of this group.

Microvesicles preparation

Mesenchymal stem cells (MSC) were obtained from bones of rats similar to that described by Zaki et al. 2018 [23]. Cultured cells were counted and their viability was confirmed by trypan blue, whereas their proliferation was verified using the MTT (3-[4,5-dimethylthiazol-2-yl]-2.5-diphenyl tetrazolium bromide) cell proliferation kit (Thermo Fisher Scientific, USA) as manufacturer's protocol. A flow cytometer (FACS Caliber, BD Bioscience USA) was used to delineate BM-MSCs cells which exhibited a negative reaction for CD34 (haematopoietic) and a strong positive reaction for CD90 and CD105 (MSC specific markers) (Fig. 1). MVs were obtained from supernatants of MSCs cultured overnight in RPMI deprived of fetal calf serum. The supernatants were centrifuged at 10,000 g for 20 min
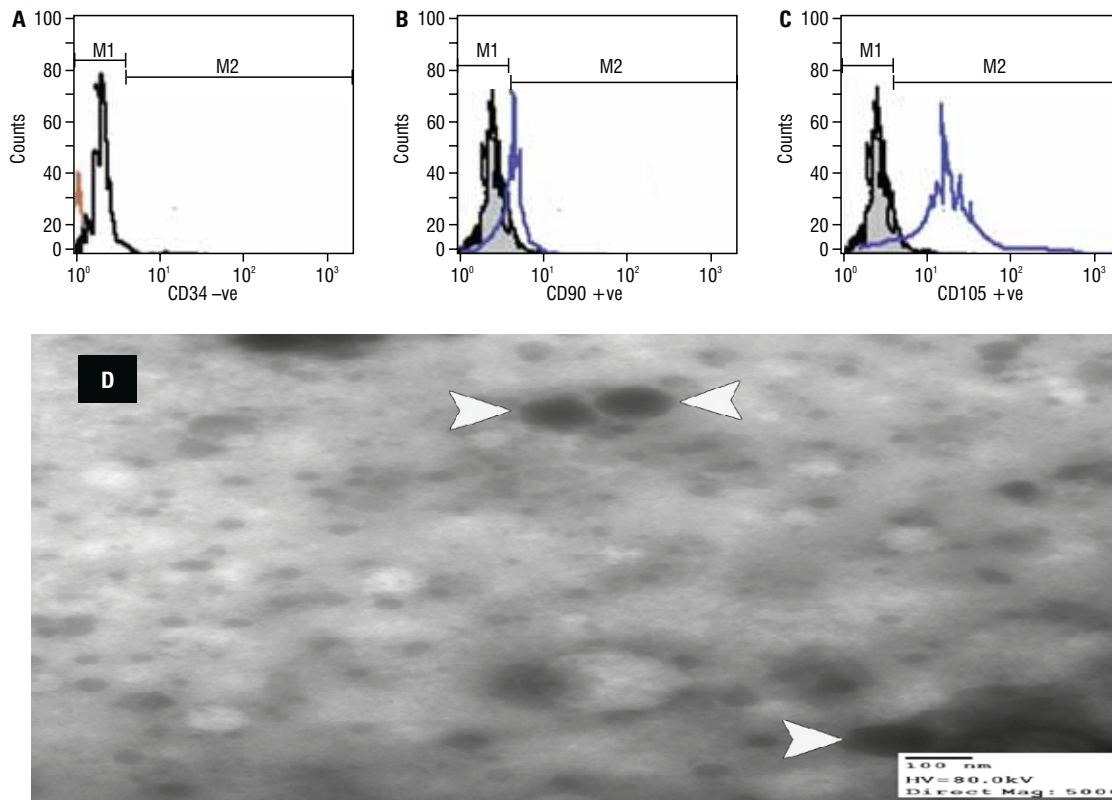
Figure 1. The flow cytometry of bone marrow derived-mesenchymal stem cells (MSCs) is showing negative (–ve) reaction to CD34 (**A**), whereas positive (+ve) reaction to CD90 (**B**) and CD105 (**C**); **D.** Electron microscope picture of MSCs-derived microvesicles (arrowheads).

to remove their debris, then centrifuged at 100,000 g (Beckman Coulter Optima L-90K Ultracentrifuge) for 1 h at 4°C, washed in serum-free medium 199 containing N-2-hydroxyethyl piperazine-N'-2-ethane sulfonic acid (HEPES) 25 mM (Sigma) and subjected to repeated ultracentrifugation in the same conditions [4]. Obtained MVs were fixed with 2.5% glutaraldehyde for 2 h for demonstration by transmission electron microscopy (TEM) then ultra-centrifuged and suspended in 100 μL HSA. A 20 μL volume of MVs was loaded onto a formvar/carbon-coated grid, stained with 3% aqueous phosphotungstic acid for 1 min, and examined under TEM (Joel Jem 1400, Germany) [6]. TEM displayed their spheroid morphology and confirmed their size (Fig. 1). After preparation, they were injected locally into the burn site at a dosage of 800 μg (RNA concentration) MVs suspended in 1 mL phosphate buffered saline [12].

Biochemical tests

Measurement of hyaluronic acid IL-10 and IL-6. Skin samples from different groups were subjected to measurement of hyaluronic acid IL-10 and IL-6 by ELISA technique with kits supplied from MyBioSource (USA).

Real-time reverse transcription polymerase chain reaction (PCR) for alpha smooth muscle actin (αSMA) and miRNA203. Extracting total RNA from tissue homogenates was performed by the RNeasy purification reagent (Qiagen). cDNA was generated by using high capacity cDNA Reverse Transcription Kit (Fermentas). Quantitative PCR amplification was done using SYBR Green I. The endogen for αSMA RNA was beta-actin, the forward primer was 5'-GACGT-ACAACTGGTATTGTG-3' and reverse 5'-TCAGGATCT-TCATGAGGTAG-3'. For miRNA203 detection, RNA extraction was performed according to the manufacturer's protocol by acidic phenol/chloroform extraction (peqGOLD RNAPure; PEQLAB Biotechnologie), then RNA was subjected to DNase treatment (Ambion), reverse transcribed. The endogen for miRNA203 was SnU6RNA and the forward primmer for miRNA203 was 5'-CGGTAGTCTGATACTGTAA-3' and the reverse primer was 5'-GTGCTCCGAAGGGGGGT-3'. The αSMA RNA and miRNA203 expressions were analysed with the ABI Prism® 7500 detection system (Applied Biosystems) according to the 2-ΔΔCt method.

Western blot analysis. Skin tissue homogenates protein extracts were prepared via the BioRad

system. A Bradford assay followed by loading on a polyacrylamide gel. Electrophoresed proteins on SDS-PAGE were transferred to a Hybond™ nylon membrane (GE Healthcare) and β-actin was applied as a housekeeping protein, then incubated in an antibody solution containing the anti-MMP-3 antibody (Abcam, USA). Detects a band of approximately 50 kDa and anti-β-actin antibody (Abcam, USA) separately, followed by incubation in HRP-conjugated 2ry antibody solution. Data analysis by Totallab analysis software (Ver.1.0.1) using a Gel documentation system (Geldoc-it, UVP, England). The same was done for the detection of TGF-β (Santa Cruz, USA) with the results were expressed using the image analysis software to read the band intensity by protein normalisation by β-actin on the ChemiDoc MP imager.

Histological and immunohistochemical examination [16]

Skin sections were prepared and stained with haematoxylin and eosin (H&E) as well as Masson's trichrome. Deparaffinised sections underwent immunohistochemical study by antigen retrieval, H_2O_2 blocking, incubation with the following 1ry antibodies; collagen I and III (Abcam, USA, rabbit, polyclonal, dilution 1/100), TNF-α (Santa Cruz, USA, rabbit, polyclonal, dilution, 1/100), CTGF and Nrf2 (Invitrogen, USA, rabbit, polyclonal, dilution 1/100). The slides were then incubated for 30 min at room temperature with anti-rabbit IgG secondary antibodies (Envision + system HRP; Dako) to be visualised with diaminobenzidine commercial kits and finally counterstained with May's haematoxylin. The slides were imaged with a Leica DFC camera attached to the microscope except that of TNF-α were imaged with a Leica ICC 50 microscope.

Histomorphometric measurements

The intensity of trichrome stain and that of immune stains (CTGF, TNF-α, collagen I and III, and Nrf2) were measured using ImageJ software (NIH, USA) and sent to statistical analysis.

Statistical analysis

All gathered data (biochemical, Western blotting (WB), PCR, and intensity of different stains) were analysed using GraphPad version 8, two-way ANOVA was used to analyse burn wound size followed by Tukey's test. One-way ANOVA was performed on all other tests followed by a post-hoc Tukey's test.

RESULTS

Microvesicles morphologically accelerate burn wound healing

Microvesicles significantly decreased burn wound size after 2 weeks from burn induction compared with burn and burn + PRP groups. After 3 weeks, the MVs group showed a significant decline in burn wound size as compared with the burn group (II) (Fig. 2).

Microvesicles and PRP modulate ELISA levels of IL-10, IL-6, and hyaluronic acid in burn wounds

Burn had significantly elevated IL-6 and hyaluronic acid, whereas decreased IL-10 in skin tissue compared with the control. MVs and PRP significantly alleviated levels of IL-6 and hyaluronic acid, whereas MVs significantly upregulated IL-10 in burn tissue compared with the burn group (II) with significantly favourable results in the MVs group as compared with PRP (Fig. 3).

Microvesicles and PRP attenuate PCR levels of α-SMA and miRNA203 burn wound

Microvesicles and PRP significantly attenuate PCR levels of α-SMA and miRNA203 in burn tissue as compared with the burn group (II) with significantly better results in the MVs group as compared with PRP (Fig. 3).

Microvesicles and PRP mitigate WB levels of TGF-β and MMP-3 in burn wounds

Microvesicles and PRP significantly attenuate WB levels of TGF-β and MMP-3 in burn tissue as compared with the burn group (II) (Fig. 4).

Histological results

Via H&E staining (Fig. 5), the skin of the control animals showed normal epidermal and dermal layers, whereas the skin of burned animals displayed complete epithelial necrosis with the formation of scab, with still signs of inflammation and haemorrhage, and without any signs of epithelisation. The skin of PRP-treated animals showed marked epithelisation and granulation tissues formation with still collagenous matrix, still the presence of blood capillaries, and marked proliferation of collagen fibrous tissues. The skin of MVs treated animals exhibited complete epithelial layer formation, decreased number of inflammatory cells, and marked noticeable remodelling of collagen fibrous tissues. Via Masson's Trichrome staining (Fig. 6), the skin of the control animals ex-

A

Burn 1st day

Burn 1st week   Burn + PRP 1st week   Burn + MVs 1st week

Burn 2nd week   Burn + PRP 2nd week   Burn + MVs 2nd week

Burn 3rd week   Burn + PRP 3rd week   Burn + MVs 3rd week

B
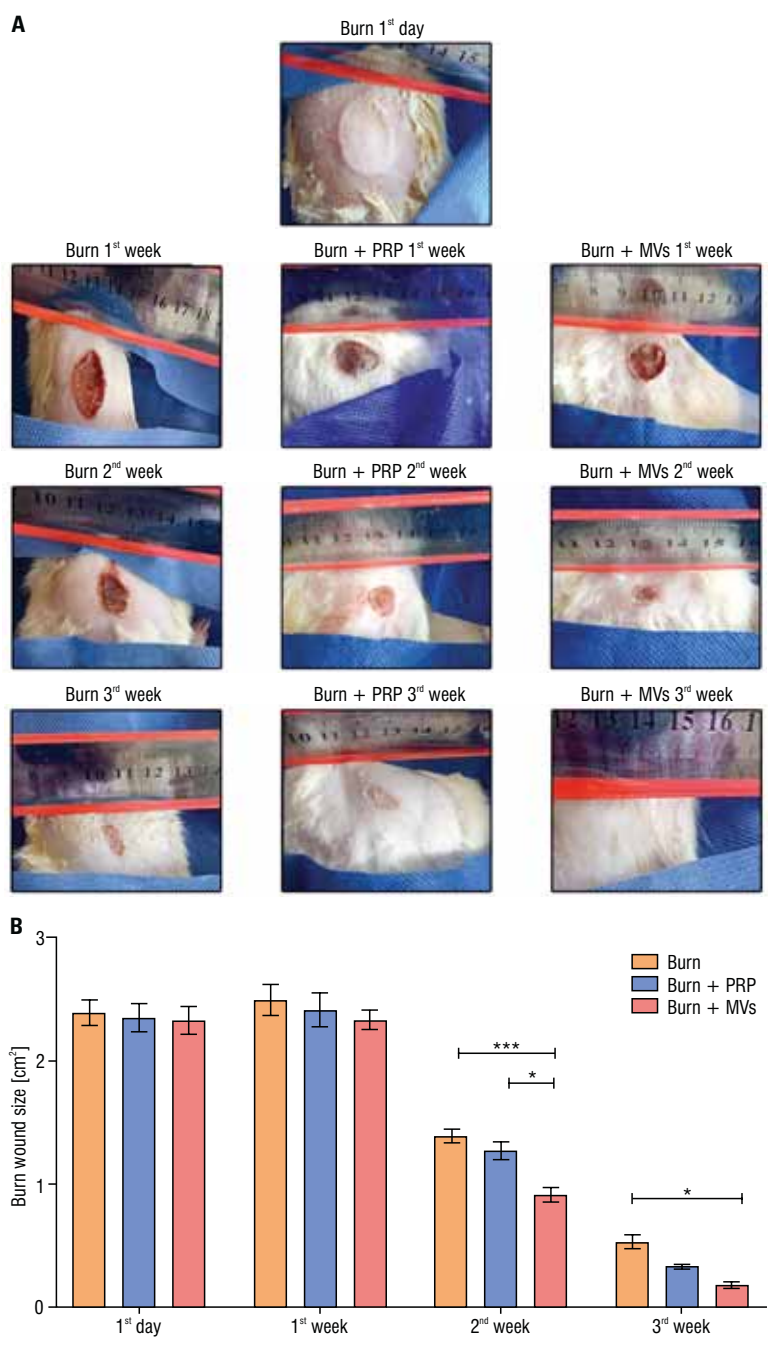
Figure 2. A. Burn images at 1st day, 1st, 2nd, and 3rd weeks from burn induction showing accelerated burn wound healing, particularly in microvesicles (MVs) treated rats. **B.** The graph shows a significant decrease in burn wound size in platelet-rich plasma (PRP) and MVs groups compared to the burn group after 2 weeks from burn induction, whereas only a significant decrease in MVs compared to the burn group after 3 weeks; number of animals = 10 in each group; *$p < 0.05$, ***$p < 0.0001$.

hibited normal collagen bundles within the dermal layer, whereas the skin of burned animals showed a marked reduction of fibrous connective tissues. The skin of PRP-treated animals showed marked proliferation of collagen fibrous tissues, whereas the skin of burned animals treated with MVs displayed marked remodelling and maturation of collagen fibrous tissues. Histomorphometric data revealed a dramatic reduction in the intensity of Trichrome stains in the burn group (II), whereas a significant elevation was recorded in both treated groups particularly MVs treated one (Fig. 3).

Immunohistochemical results

Microvesicles and PRP downregulate CTGF immune expression in burn wounds. Burn increased
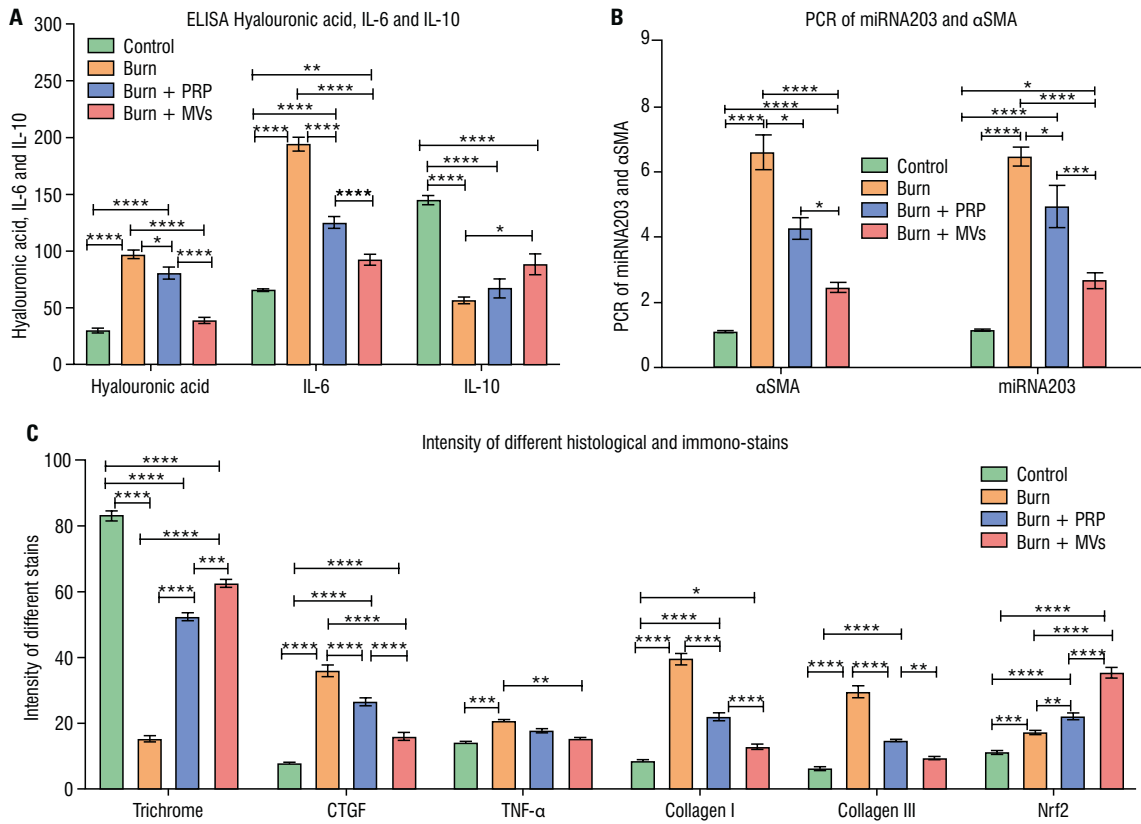
Figure 3. Bar charts of ELISA levels of hyaluronic acid, interleukin 6 (Il-6) and interleukin 10 (IL-10) (**A**), polymerase chain reaction (PCR) levels of alpha smooth muscle actin (αSMA) and miRNA203 (**B**), and intensity of different histological and immune stains (Trichrome, CTGF, TNF-α, collagen I and III, and Nrf2) (**C**); n = 10 for each group; *when p < 0.05, **when p < 0.01, ***when p < 0.001, ****when p < 0.0001 (error bar = standard error of the mean).

the CTGF immune expression in group II, whereas in MVs and PRP treated groups, CTGF was markedly reduced (Fig. 7). Morphometrically, MVs, and PRP significantly downregulated CTGF immuno-staining intensity in burn tissue as compared with the burn group (II) with significantly more downregulation in the MVs group as compared with PRP (Fig. 3).

Microvesicles ameliorate the inflammatory cytokine TNF-α immune expression. Burn increased the TNF-α immune expression in group II, whereas PRP partially reduced it. in MVs, it was markedly reduced (Fig. 8). Histomorphometrically, MVs significantly ameliorated TNF-α immuno-staining intensity in burn wounds compared with the burn group (II) (Fig. 3).

Microvesicles modulate collagen I and III depositions in burn wounds. MVs and PRP (particularly the MVs) decreased collagen I and III depositions in burn wounds (Fig. 9). Via histomorphometric analysis, a significant decline in the immuno-staining intensity of collagen I and III was recorded in the MVs and PRP groups compared with the burn group with

significantly favourable results in MVs than the PRP group (Fig. 3).

Microvesicles and PRP enhance the antioxidant Nrf2 immune expression in burn tissue. MVs and PRP increased the Nrf2 in the burn, particularly in the MVs group (Fig. 10). Via histomorphometric analysis, Nrf2 immune expression was dramatically enhanced especially in the MVs group (Fig. 3).

DISCUSSION

Microvesicles and PRP considerably accelerate burn wound healing and improved the parameters involved in little scar formation in the present work. Previously, Xiao et al. (2016) [21] reported that human umbilical cord mesenchymal stem cells (hcMSC)-derived exosomes downregulated inflammatory reaction in severely burned rat model via reducing the inflammatory cytokine TNF-α levels and increasing IL-10 levels. Recently, adipose-derived MSC exosomes proved to regulate collagen remodelling to counteract scar hyperplasia which changes the aesthetic

A

B
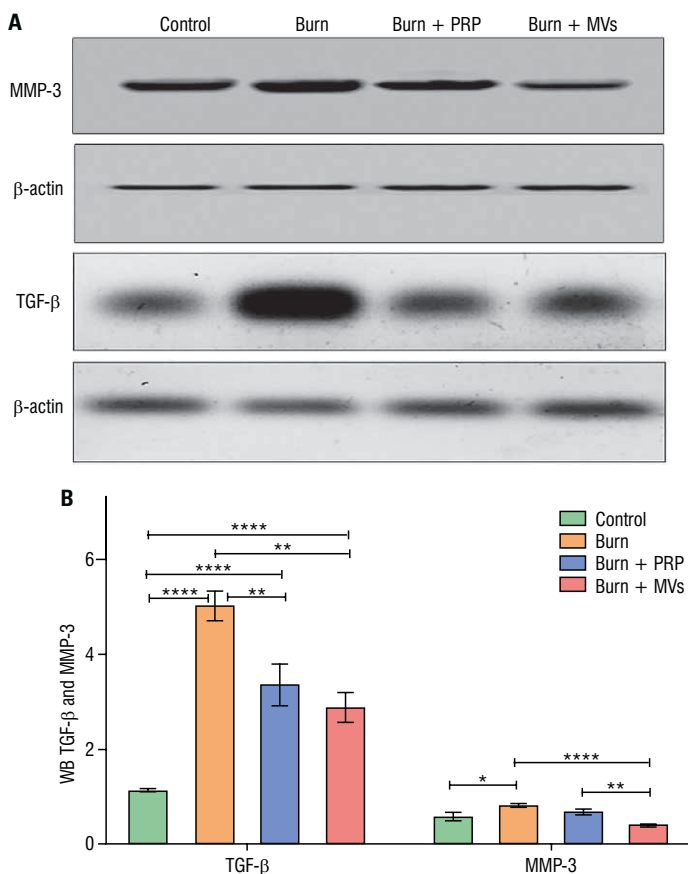
Figure 4. A. Western blotting (WB) analysis of matrix metalloproteinases 3 (MMP-3) and transforming growth factor beta (TGF-β) in skin tissues among different groups with β-actin as a housekeeping protein. Both proteins are overexpressed in the burn group, whereas exhibited a decreased expression in platelet-rich plasma (PRP) and microvesicles (MVs) treated groups. **B.** The graph shows the WB results among different groups; n = 10 for each group; *when p < 0.05; **when p < 0.01; ***when p < 0.001; ****when p < 0.0001 (error bar = standard error of the mean).

appearance and impairs organ function [1]. MVs significantly decreased the burn wound size after 3 weeks from burn induction compared with the burn group (II) and PRP group (III). Despite limited available data regarding the impact of MVs on burn wound size, it was reported that at any time point from 1st to 4th week from burn induction, adipose-derived stem cells-significantly decreased burn wound size with more hair growth when compared to the control group [5], supporting the results of the present work. PRP failed to change the burn wound size significantly in this work, conversely, PRP was proved to attenuate burn wound size 14 days from burn induction in diabetic rats [8]. This might be attributed to the larger burn wound size and induction of diabetes in the latter study. MVs dramatically attenuated IL-6 and immunohistochemical expression of TNF-α, whereas increased IL-10 in burn tissue elucidating the anti-inflammatory and immune-modulatory mechanism of these MVs. In accordance, ADSCs-EXOs were reported to mitigate in-vitro interferon-α secretion, with the resultant deactivation of T cells proposing a presumable immunosuppressive role [3]. In addition, ADSCs-EXOs were evidenced to comprise immunoregulatory proteins such as TNF-α,

macrophage colony-stimulating factor, and retinol binding protein-4 [10]. Briefly, An et al. 2021 [1], recently concluded that exosomes upregulate early inflammation, thereby accelerating wound healing. Interestingly, MVs considerably modulated some scar regulating parameters (hyaluronic acid, αSMA, TGF-β, MMP-3, and immunohistochemical CTGF) in burn tissue associated with modulation of the collagen I and III immune expression in the present work elucidating a presumable action of these MVs towards a scarless burn wound healing. Supporting these findings, ADSCs-EXOs upregulated the MMP-3 expression in skin dermal fibroblasts enhancing the remodelling of extracellular matrix, and ameliorating scaring [20]. ADSCs-EXOs also might regulate fibroblast differentiation and gene expression, enhancing the reconstruction of the extracellular matrix, thus preventing scar proliferation [1]. Fetal wounds heal without scar because of higher amounts of hyaluronic acid, higher extracellular matrix production by fibroblast, and the absence of myofibroblast [15, 14]. Although the ratio of type III to type I collagen is higher in the fetal wound than in the adult, collagen III is the main type of collagen in pathologic scar hyperplasia [14]. MVs decreased the immune expression
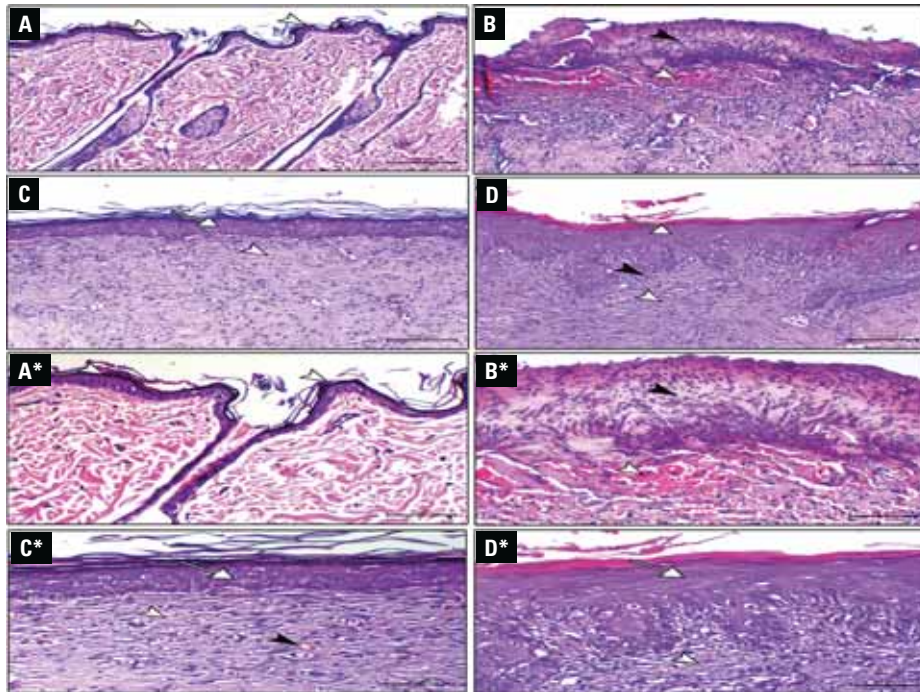
Figure 5. A, A*. Skin of control animal showing normal epidermal and dermal layers (arrowheads indicate normal stratified squamous epithelium with keratin covering); **B, B*.** Skin of burned animal showing complete epithelial necrosis with formation of scab (black arrowhead), with still signs of inflammation and haemorrhage (white arrowhead), and without any signs of epithelization; **C, C*.** Platelet-rich plasma treated group shows marked epithelisation (arrow) and granulation tissues formation with still collagenous matrix (white arrowhead), still the presence of blood capillaries (black arrowhead), and marked proliferation of collagen fibrous tissues (white arrowhead); **D, D*.** With microvesicles treated group shows complete epithelial layer formation (arrow), decreased number of inflammatory cells (black arrowhead), and marked noticeable remodelling of collagen fibrous tissues (white arrowhead), haematoxylin and eosin stain, $\times 100$, bar $= 100\,\mu$m, $\times 200$, bar $= 50\,\mu$m.
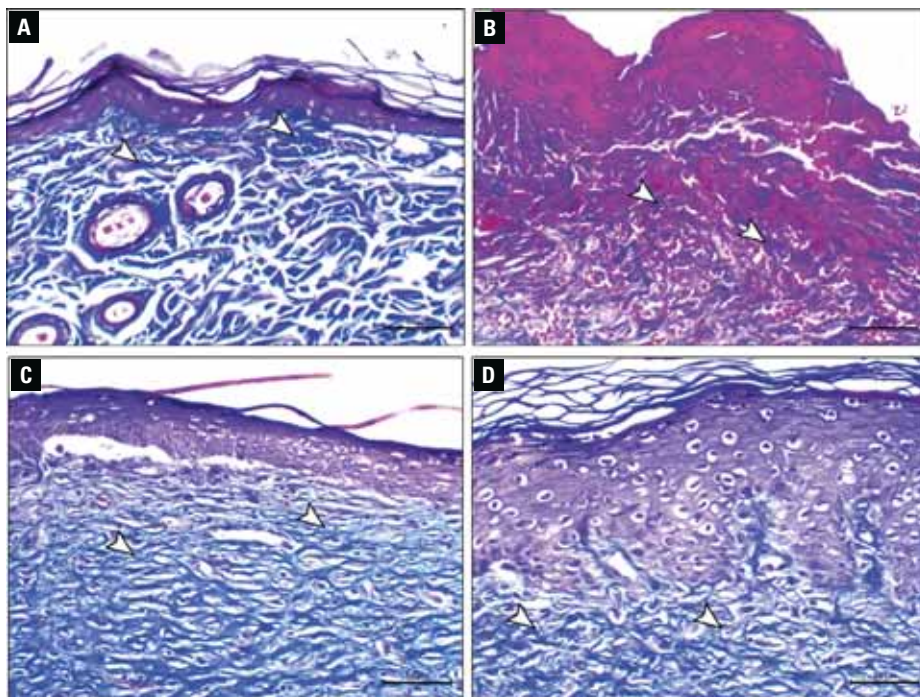
Figure 6. A. The skin of the control animal shows normal collagen bundles within the dermal layer (arrowheads); **B.** Skin of burned animal showing marked reduction of fibrous connective tissues (arrowheads); **C.** Platelet-rich plasma treated group shows marked proliferation of collagen fibrous tissues (arrowheads); **D.** Microvesicles treated group shows marked remodelling and maturation of collagen fibrous tissues (arrowheads), Masson's Trichrome stain, $\times 200$, bar $= 50\,\mu$m.
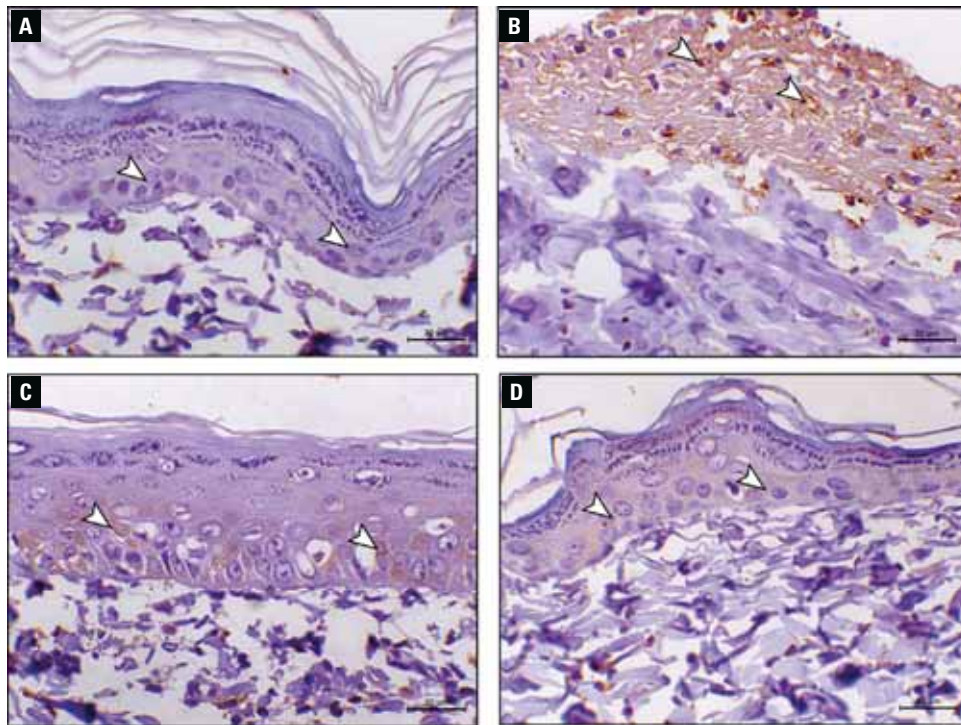
Figure 7. Connective tissue growth factor (CTGF) immuno-expression in different groups; **A.** Skin of the control animal shows a mild expression of CTGF within the epidermal epithelium (arrowheads), whereas burn group (II) (**B**) shows marked expression; **C.** Platelet-rich plasma treated group displays a declined expression of CTGF within the epidermal covering; **D.** Burn group treated with microvesicles shows a marked decrease in the expression; CTGF ×400, bar = 20 μm.
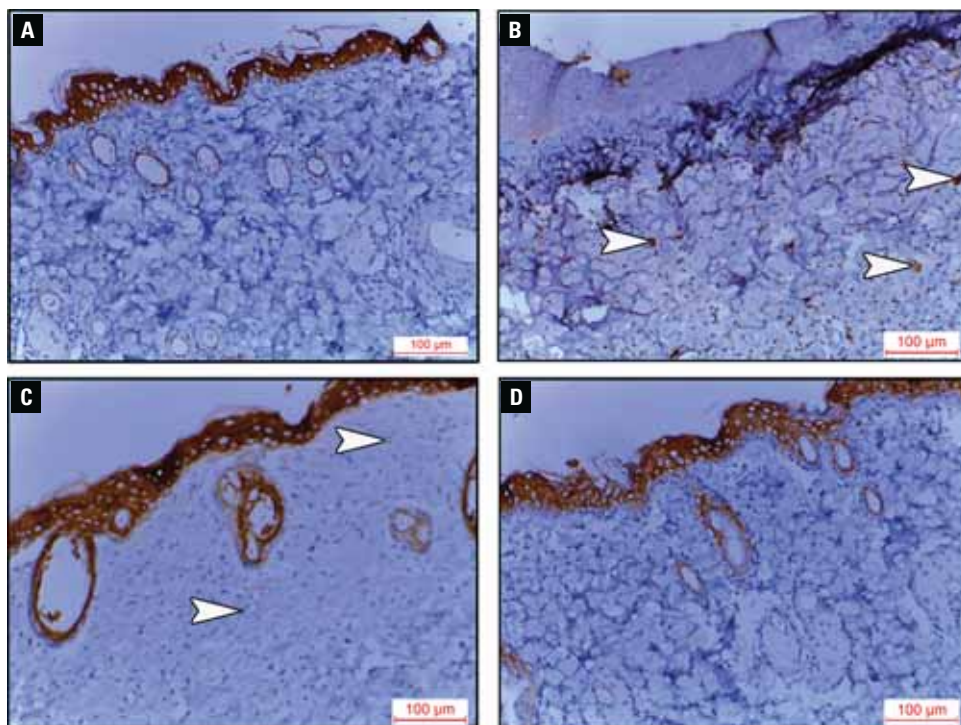
Figure 8. Tumour necrosis factor alpha (TNF-α) immuno-expression in different groups; **A.** Skin of the control animal shows minimal expression within the dermis, whereas the burn group II (**B**) is showing increased expression; **C.** Platelet-rich plasma treated group shows a declined dermal TNF-α immune expression compared to the burn group; **D.** Microvesicles treated group exhibits normal expression; TNF-α ×200, bar = 100 μm.
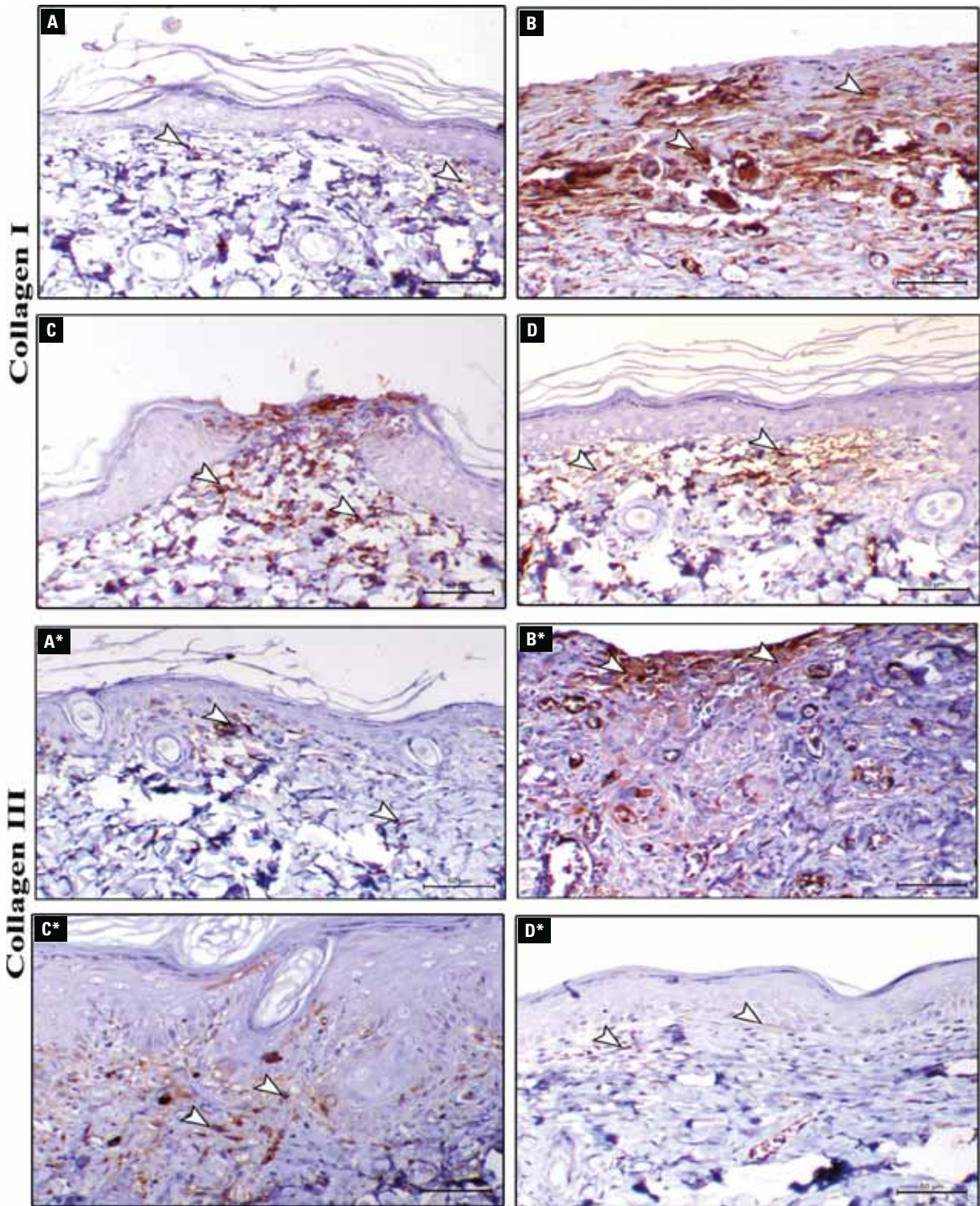
Figure 9. Collagen I and III among different groups; **A.** The skin of the control animal displays a mild expression of collagen I within the dermal fibrous tissues (arrowheads), whereas burn group II (**B**) displays a marked expression; **C.** Platelet-rich plasma (PRP) treated group displays a decrease in the expression of collagen I within the dermal fibrous tissues (arrowheads); **D.** Microvesicles (MVs) treated group displays a marked decrease in its expression; **A*.** The skin of the control animal shows a mild expression of collagen III within the dermal fibrous tissues (arrowheads). In contrast the burn group (**B***) displays a marked collagen III expression; **C*.** PRP treated group shows a decrease in the expression of collagen III within the dermal fibrous tissues (arrowheads); **D*.** MVs treated group displays a marked decrease in collagen III expression (collagen I and III immunohistochemistry, bar = 20 μm).
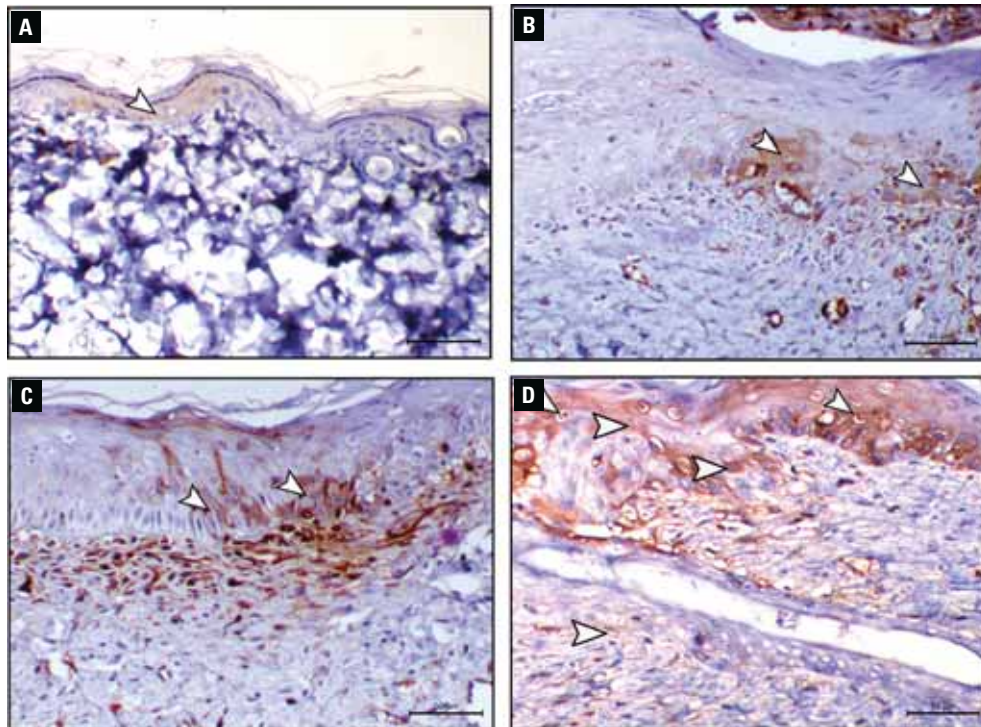
Figure 10. A. The skin of the control animal displays a mild expression of Nrf2 within the dermal fibrous tissues (arrowheads), whereas burned animal group II (**B**) displays a marked expression; **C.** Platelet-rich plasma treated group displays a decrease in the expression of Nrf2; **D.** Microvesicles-treated group displays a marked decrease in expression; Nrf2 ×200, bar = 20 μm.

of collagen I and III in burn wounds in this work, more studies on the effect of MVs on collagen deposition and their association with scar proliferation still deserve further work. MVs and PRP had attenuated TGF-β in burn wounds in this work, TGF-β action is not restricted to scar formation after injury but shares in the development of fibrosis in the lung, liver, and kidneys that follows chronic inflammation [11]. TGF-β blocking agents were clinically tried for scar prevention with disappointing results, whereas clinical trials with CTGF blocking drugs are encouraging [11]. Accordingly, MVs might provide hope for scarless burn wounds as they considerably modulated CTGF expression in this work. Down-regulation of miRNA203 in MVs and PRP groups in this work elucidate the involvement of miRNA203 in the process of burn wound repair. It was demonstrated that after 3 and 5 days from skin wound induction the GTPase Ran (a pro-proliferative factor) and Raph1 (a pro-migratory factor) are putative direct miR-203 targets whose expression could be essential for skin wound homeostasis and re-epithelialisation [18]. Limited available knowledge about miRNA203 after 3 weeks from burn induction and future works are still warranted. MVs and PRP dramatically enhanced the antioxidant

Nrf2 immune expression in this work elucidating the mechanistic beyond their role in burn wound healing. Agreeing with this finding, ADSCs-EXOs overexpressing the antioxidant receptors (Nrf2), had noticeably accelerated the healing of diabetic foot ulcers [13]. From the previous findings, we could conclude that MVs and PRP may improve burn wound healing via controlling scar regulation parameters, antioxidant role, and miRNA203 recruitment.

CONCLUSIONS

Microvesicles derived from mesenchymal stem cells and PRP may improve burn wound healing via regulating scar formation and antioxidant mechanism.

Conflict of interest: None declared

REFERENCES

1. An Y, Lin S, Tan X, et al. Exosomes from adipose-derived stem cells and application to skin wound healing. Cell Proliferation. 2021; 54(3), doi: 10.1111/cpr.12993.
2. Baglio SR, Pegtel DM, Baldini N. Mesenchymal stem cell secreted vesicles provide novel opportunities in (stem) cell-free therapy. Front Physiol. 2012; 3: 359, doi: 10.3389/fphys.2012.00359, indexed in Pubmed: 22973239.

3. Blazquez R, Sanchez-Margallo FM, de la Rosa O, et al. Immunomodulatory Potential of Human Adipose Mesenchymal Stem Cells Derived Exosomes on in vitro Stimulated T Cells. Front Immunol. 2014; 5: 556, doi: 10.3389/fimmu.2014.00556, indexed in Pubmed: 25414703.

4. Bruno S, Grange C, Deregibus MC, et al. Mesenchymal stem cell-derived microvesicles protect against acute tubular injury. J Am Soc Nephrol. 2009; 20(5): 1053–1067, doi: 10.1681/ASN.2008070798, indexed in Pubmed: 19389847.

5. Feng CJ, Lin CH, Tsai CH, et al. Adipose-derived stem cells-induced burn wound healing and regeneration of skin appendages in a novel skin island rat model. J Chin Med Assoc. 2019; 82(8): 635–642, doi: 10.1097/JCMA.0000000000000134, indexed in Pubmed: 31259836.

6. Gatti S, Bruno S, Deregibus MC, et al. Microvesicles derived from human adult mesenchymal stem cells protect against ischaemia-reperfusion-induced acute and chronic kidney injury. Nephrol Dial Transplant. 2011; 26(5): 1474–1483, doi: 10.1093/ndt/gfr015, indexed in Pubmed: 21324974.

7. Hosni Ahmed H, Rashed LA, Mahfouz S, et al. Can mesenchymal stem cells pretreated with platelet-rich plasma modulate tissue remodeling in a rat with burned skin? Biochem Cell Biol. 2017; 95(5): 537–548, doi: 10.1139/bcb-2016-0224, indexed in Pubmed: 28314112.

8. Hosseini Mansoub N, Gürdal M, Karadadaş E, et al. The role of PRP and adipose tissue-derived keratinocytes on burn wound healing in diabetic rats. Bioimpacts. 2018; 8(1): 5–12, doi: 10.15171/bi.2018.02, indexed in Pubmed: 29713597.

9. Imam RA, Rizk AAE. Efficacy of erythropoietin-pretreated mesenchymal stem cells in murine burn wound healing: possible in vivo transdifferentiation into keratinocytes. Folia Morphol. 2019; 78(4): 798–808, doi: 10.5603/FM.a2019.0038, indexed in Pubmed: 30949996.

10. Kranendonk MEG, Visseren FLJ, van Balkom BWM, et al. Human adipocyte extracellular vesicles in reciprocal signaling between adipocytes and macrophages. Obesity (Silver Spring). 2014; 22(5): 1296–1308, doi: 10.1002/oby.20679, indexed in Pubmed: 24339422.

11. Kumar V, Abbas AB, Aster JC. Inflammation and Repair. Chapter 3. In: Kumar V, Abbas AB (eds.) Robbins Basic Pathology. 10th ed. Elsevier 2018: 57–96.

12. Li X, Liu L, Yang J, et al. Exosome derived from human umbilical cord mesenchymal stem cell mediates MiR-181c attenuating burn-induced excessive inflammation. EBioMedicine. 2016; 8: 72–82, doi: 10.1016/j.ebiom.2016.04.030, indexed in Pubmed: 27428420.

13. Li X, Xie X, Lian W, et al. Exosomes from adipose-derived stem cells overexpressing Nrf2 accelerate cutaneous wound healing by promoting vascularization in a diabetic foot ulcer rat model. Exp Mol Med. 2018; 50(4): 1–14, doi: 10.1038/s12276-018-0058-5, indexed in Pubmed: 29651102.

14. Marshall CD, Hu MS, Leavitt T, et al. Cutaneous scarring: basic science, current treatments, and future directions. Adv Wound Care (New Rochelle). 2018; 7(2): 29–45, doi: 10.1089/wound.2016.0696, indexed in Pubmed: 29392092.

15. Ren S, Chen J, Duscher D, et al. Microvesicles from human adipose stem cells promote wound healing by optimizing cellular functions via AKT and ERK signaling pathways. Stem Cell Res Ther. 2019; 10(1): 47, doi: 10.1186/s13287-019-1152-x, indexed in Pubmed: 30704535.

16. Sanderson S, Wild G, Cull AM. et al.. Immunohistochemical and immunofluorescent techniques. In: Suvarna SK, Layton C, Bancroft JD (eds.) Bancroft's Theory and Practice of Histological Techniques. 8th Edition. Elsevier Limited 2019: 337–394.

17. Vinish M, Cui W, Stafford E, et al. Dendritic cells modulate burn wound healing by enhancing early proliferation. Wound Repair Regen. 2016; 24(1): 6–13, doi: 10.1111/wrr.12388, indexed in Pubmed: 26609910.

18. Viticchiè G, Lena AM, Cianfarani F, et al. MicroRNA-203 contributes to skin re-epithelialization. Cell Death Dis. 2012; 3(11): e435, doi: 10.1038/cddis.2012.174, indexed in Pubmed: 23190607.

19. Walmsley GG, Maan ZN, Wong VW, et al. Scarless wound healing: chasing the holy grail. Plast Reconstr Surg. 2015; 135(3): 907–917, doi: 10.1097/PRS.0000000000000972, indexed in Pubmed: 25719706.

20. Wang Lu, Hu Li, Zhou X, et al. Exosomes secreted by human adipose mesenchymal stem cells promote scarless cutaneous repair by regulating extracellular matrix remodelling. Sci Rep. 2017; 7(1): 13321, doi: 10.1038/s41598-017-12919-x, indexed in Pubmed: 29042658.

21. Xiao Li, Lingying L, Jing Y, et al. Exosome derived from human umbilical cord mesenchymal stem cell mediates MiR-181c attenuating burn-induced excessive inflammation. EBioMedicine. 2016; 8: 72–82, doi: 10.1016/j.ebiom.2016.04.030, indexed in Pubmed: 27428420.

22. Yan Y, Wu R, Bo Y, et al. Induced pluripotent stem cells-derived microvesicles accelerate deep second-degree burn wound healing in mice through miR-16-5p-mediated promotion of keratinocytes migration. Theranostics. 2020; 10(22): 9970–9983, doi: 10.7150/thno.46639, indexed in Pubmed: 32929328.

23. Zaki SM, Algaleel WA, Imam RA, et al. Mesenchymal stem cells pretreated with platelet-rich plasma modulate doxorubicin-induced cardiotoxicity. Hum Exp Toxicol. 2019; 38(7): 857–874, doi: 10.1177/0960327119842613, indexed in Pubmed: 30991846.

VM VIA MEDICA

ORIGINAL ARTICLE

Protective effect of liriodendrin against liver ischaemia/reperfusion injury in mice via modulating oxidative stress, inflammation and nuclear factor kappa B/toll-like receptor 4 pathway

Z.Y. Yu[1], G. Cheng[2, 3, 4]

[1]Department of General Surgery, Panjin Central Hospital, Panjin, Liaoning Province, China
[2]Department of Intensive Care Unit, The People's Hospital of Shimen County, Changde, Hunan Province, China
[3]Department of Clinical Medicine, Yiyang Medical College, Yiyang, Hunan Province, China
[4]Changsha Medical University, Changsha, Hunan Province, China

Background: The aim of the present study was to investigate the protective effect and mechanism of liriodendrin (LDN) is a lignan diglucoside in hepatic ischaemia//reperfusion (I/R) injury.

Materials and methods: The liver I/R was established in male C57BL/6 mice. The effect of LDN is initially investigated on hepatic I/R injury via estimating histopathology of liver. The level of metabolic enzymes alanine aminotransferase (ALT), aspartate aminotransferase (AST) and alkaline phosphatase (ALP) was studied along with apoptosis of mouse hepatocytes via TUNEL and flow cytometry analysis. The effect of LDN was investigated on oxidative stress biomarkers (glutathione [GSH] content, malondialdehyde [MDA] and superoxide dismutase [SOD] activities) and pro-inflammatory cytokines (tumour necrosis factor alpha [TNF-α], interleukin [IL]-1β and IL-6). Western blot study was also conducted to elucidate the effect of LDN on toll-like receptor 4/nuclear factor kappa B (TLR4/NF-κB).

Results: Liriodendrin alleviates liver I/R injury, as manifested by decreased plasma ALT, AST and ALP with improvement in liver necrotic area. LDN also reduces apoptosis of mouse hepatocytes with reduction of oxidative stress and generation of pro-inflammatory cytokines. It significantly reduces the expression of TLR4 and NF-κB.

Conclusions: The study demonstrated that LDN reduces liver injury and prevented apoptosis of hepatocytes following I/R injury. In addition, LDN also reduces oxidative stress, inflammation, and TLR4/NF-κB in I/R injured mice. (Folia Morphol 2023; 82, 3: 668–676)

Key words: liriodendrin, liver ischaemia/reperfusion injury, apoptosis, inflammation

Address for correspondence: Dr. G. Cheng, Department of Intensive Care Unit, The People's Hospital of Shimen County, Changde, Hunan Province, China, e-mail: kongk1976@sina.com

INTRODUCTION

Liver ischaemia and reperfusion injury has been the topic of intense study during the last decades since it is implicated in many clinical scenarios, including haemorrhagic shock and resuscitation, trauma, liver resections [8]. It can seriously impair liver function, even producing irreversible damage, which causes a cascade of multiple organ dysfunction [1, 12]. Among the causes that affect liver, ischaemic/reperfusion (IR) injury is major cause resulting from the alteration in the blood flow with instant oxygen deficiency of cells. Although the nature of I/R injury has been studied extensively, the mechanisms by which organ damage occurs are unclear [27]. Various studies have shown oxidative stress is a main causative factor for the hepatic I/R injury. It is originated due to excessive production of reactive oxygen species (ROS) which hinder cellular redox status and innervate to hepatocyte necrosis. Furthermore, in response to stress, Kupffer–Browicz cells also mediate hepatocyte injury via the production of pro-inflammatory cytokines which further aggravate the injury [36, 39]. However, the current treatment options to manage this condition are merely supportive in nature. Thus, it is more imperative to identify novel agent which provides therapeutic support to hepatic I/R injury.

Plant-based drugs have been providing therapeutic benefit to the mankind since the ancient days. Modern science has also shown the significant benefit of plant-based drugs in many ailments, such as, cancer, diabetes, cardiovascular diseases, and so on [4]. These plant-based drugs have strong free radical scavenging and anti-inflammatory properties. Considering the importance of oxidative stress and inflammation in the hepatic I/R injury, the plant-based drugs have shown great benefit than conventional therapy and provide the impetus for the search of novel agents from the plant origin [33].

Liriodendrin (LDN) is a lignan diglucoside obtained from the inner bark of Yellow Poplar (*Liriodendron tulipifera L.*). Various studies have enumerated the pharmacological activity LDN in various *in-vitro* and *in-vivo* models [9]. It possesses anti-inflammatory, anti-nociceptive [13], anti-arrhythmic [9], hypoglycaemic [37], and inhibitory activity on HepG-2 cells [26], resisting glutamate-induced PC12 cell damage [10], increasing of heat shock factor 1 expression [22]. It also reduces sciatic endometriosis-associated pain [11].

However, despite its strong anti-oxidant and anti-inflammatory properties, none of the study has reported the effect of LDN on hepatic I/R injury. Hence, the present investigation is an attempt to study the pharmacological effect of LDN in hepatic I/R injury.

MATERIALS AND METHODS

Chemical

The LDN study was obtained from Sigma Aldrich, USA. The reagents and solvents used were procured from the Sigma Aldrich, USA and used without further purification unless otherwise stated.

Animals

Male C57BL/6 mice weighing 18–22 g (6–8 weeks) were after obtaining from the institutional animal house was housed under a controlled temperature and humidity, in strict hygienic condition. The mice were allowed to acclimatise with laboratory conditions and were supplied with food and water *ad-libitum* in alternate day and night cycle of 12 h. The study has been approved by Institutional Animal Ethical Committee for Biomedical Experiments of Changsha Medical University, China.

Establishment of the liver I/R model

A 70% liver ischaemia model was established following a previously described method [16, 17]. Briefly, ketamine (70 mg/kg body weight) and xylazine (5 mg/kg body weight) were used to anaesthetize the animals intraperitoneally, and abdominal cavity was exposed by creating the median incision in the upper abdomen. The middle lobe and the right lobe of the liver were separated, followed by the separation of the left lobe and the caudate lobe. The hepatic left artery, portal vein, and bile duct running together for about 0.5 cm, and then splitting into their respective lobe was observed. By slightly separating the posterior hepatic vein from anterior wall, hepatic artery, portal vein, and bile duct was clamped using non-invasive small blood vessel clamp in the common running section without separating them individually. After blocking the running for 60 min, the establishment of nearly 70% of the liver with ischaemia was achieved. Evidence of ischaemia was based on visualizing the pale blanching of the ischaemic lobes. The right lobe and caudate lobe of liver blood flow were not blocked to avoid gastrointestinal congestion. After 1 h of ischaemia, the clamp was removed, and reperfusion was performed. The sham group underwent the same procedure, but without clamping blood vessels. Blood and liver

tissue samples were collected at the end of the reperfusion for further analysis.

Drug treatment protocol

The mice were randomly divided into five groups (10 mice in each group): group 1: sham, group 2: I/R, group 3: LDN (5 mg/kg) + IR, group 4: LDN (10 mg//kg) + IR, group 5: LDN (20 mg/kg) + IR.

The LDN was dissolved in dimethyl sulfoxide and then diluted with normal saline. The final concentration of dimethyl sulfoxide (DMSO) was 0.4%. The LDN treated groups were gavaged with LDN for 1 week before the experiment. The sham and I/R groups received an equivalent volume of saline containing 0.4% DMSO.

Biochemical assessments

The alanine aminotransferase (ALT), aspartate aminotransferase (AST), and alkaline phosphatase (ALP) levels in mouse plasma were measured using commercial kits (JianCheng Bioengineering Institute, Nanjing, China) according to manufacturer's instructions.

Haematoxylin and eosin staining

Liver tissues were fixed in 10% formaldehyde solution for 24 h and embedded in paraffin. The tissue was cut into 5-μm sections and stained with haematoxylin and eosin (Servicebio, Wuhan, China). The images were photographed using a light microscope (Olympus, Tokyo, Japan).

TUNEL staining

Terminal deoxynucleotidyl transferase dUTP nick end labelling (TUNEL) staining was performed using an in-situ apoptosis detection kit (Servicebio, Wuhan, China), according to the manufacturer's instructions. The paraffin-embedded tissue was cut into 5-μm sections and stained with TUNEL reagents at room temperature for 1 h in the dark. DAPI (Servicebio, Wuhan, China) was used to stain the nucleus at room temperature for 10 min, followed by the addition of an anti-fluorescence quenching solution (Servicebio, Wuhan, China). Images were captured using a fluorescence microscope (Olympus, Tokyo, Japan).

Annexin V/PI assay

Primary hepatocyte isolation and culture were performed as previously described [38]. The apoptosis in hepatocytes was recorded by using Annexin V-FITC and PI (BioVision, Mountain View, CA, USA)

staining as per the manufacturer instruction and analysed with a flow cytometer (BD FACS Canto™; BD Biosciences).

Estimation of oxidative stress biomarkers

The level of antioxidant biomarkers glutathione (GSH) content, malondialdehyde (MDA) and superoxide dismutase (SOD) activities were estimated using commercial kits (Nanjing Jiancheng Bioengineering Institute, Nanjing, China) as per the manufacturer's instructions.

Enzyme-linked immunosorbent assay (ELISA)

The determination of tumour necrosis factor alpha (TNF-α), interleukin (IL)-1β and IL-6 were performed using commercially available ELISA kits (Thermo Fisher Scientific) as per the manufacturer's instructions.

Western blot analysis

The isolated proteins were subjected to sodium dodecyl sulphate polyacrylamide electrophoresis and transferred onto nitrocellulose membranes (Merck Millipore, Billerica, MA, USA). The membranes were blocked and incubated overnight at 4°C with primary antibodies, followed by incubation with appropriate secondary antibodies. Antibody binding was detected with ECL chemiluminescence reagents (Sigma-Aldrich, St. Louis, MO, USA).

Statistical analysis

The data were articulated as mean ± standard error of mean (SEM). Statistical analysis was executed using ANOVA pursued by Bonferroni *post hoc* multiple comparison test using GraphPad Prism 5.0 (California, USA). The p value < 0.05 was measured as statistically significant.

RESULTS

LDN reduces hepatic I/R injury

The level of ALT, AST and ALP were studied in the different treated-experimental subjects and results were presented in Figure 1B–D, respectively. The histopathology of liver was also studied to determine the degree of injury in the liver and effect of LDN (Fig. 1A). As shown in Figure 1, the plasma levels of ALT, AST and ALP were found to be increased in I/R injury model group as compared to sham, which is further found in agreement with the liver injury of I/R group. The liver injury was found to be reduced significantly with considerable improvement in plas-
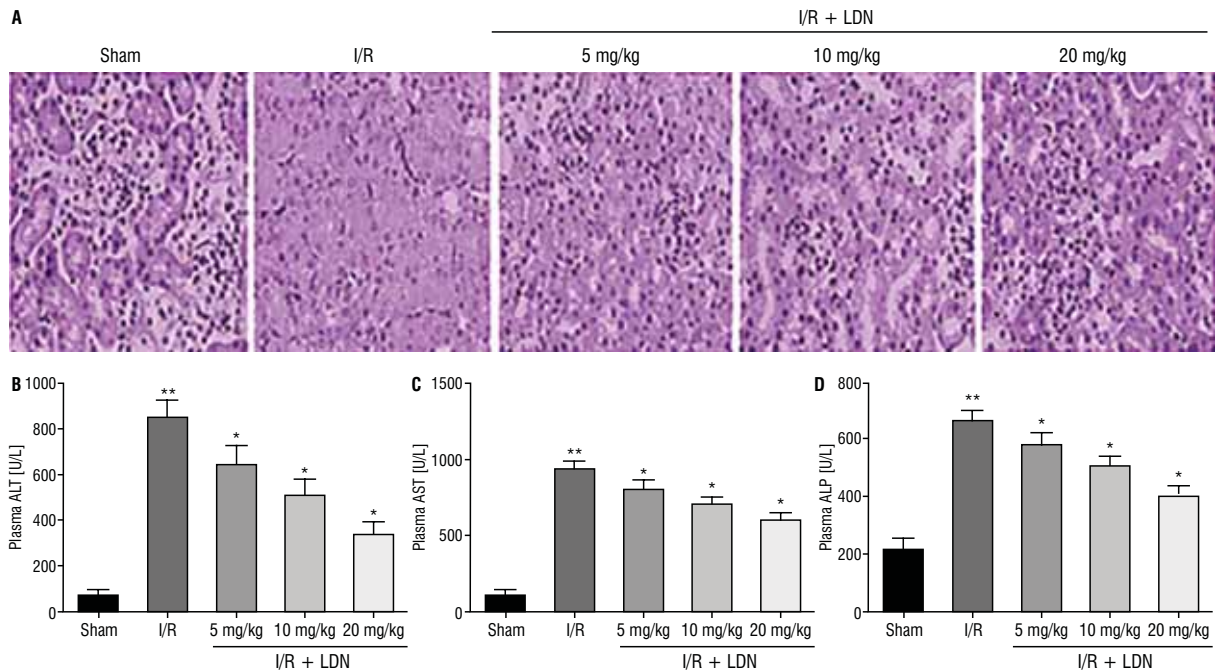
Figure 1. Liriodendrin (LDN) reduces hepatic ischaemia/reperfusion (I/R) injury histopathology of liver sections (**A**), plasma level of alanine aminotransferase (ALT) (**B**), aspartate aminotransferase (AST) (**C**), and alkaline phosphatase (ALP) (**D**). Values represent the mean ± standard error of mean; **p < 0.05 vs. sham; *p < 0.05 vs. I/R, one-way analysis of variance (ANOVA) followed by Bonferroni post hoc test.
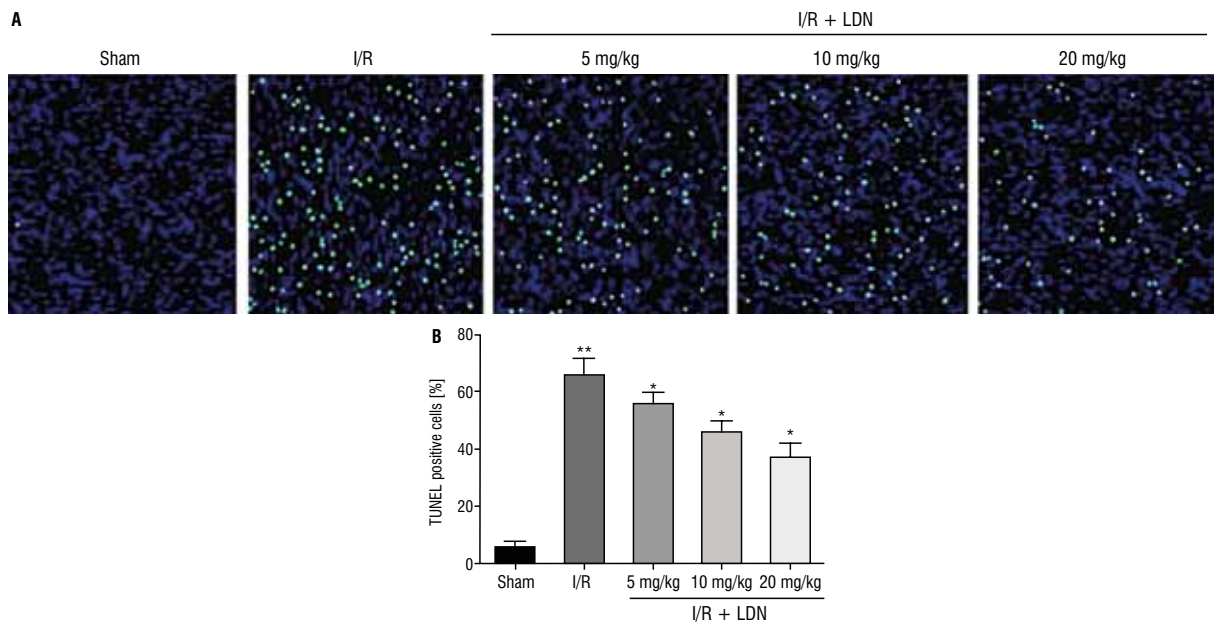
Figure 2. Liriodendrin (LDN) reduces apoptosis of hepatocytes after hepatic ischaemia/reperfusion (I/R) injury. Representative TUNEL staining of hepatocyte apoptosis (**A**) and quantification of TUNEL(+) cells (**B**). Values represent the mean ± standard error of mean; **p < 0.05 vs. sham; *p < 0.05 vs. I/R, one-way analysis of variance (ANOVA) followed by Bonferroni post hoc test.

ma levels of ALT, AST and ALP in LDN treated group in comparison to I/R injury. These results propose that LDN can effectively mitigate the liver injury and provide protective effect against I/R injury.

LDN reduces hepatocyte apoptosis

As shown in Figure 2, TUNEL positive cells were found significantly increased in I/R injury group as compared to sham. However, the LDN-treated group

671
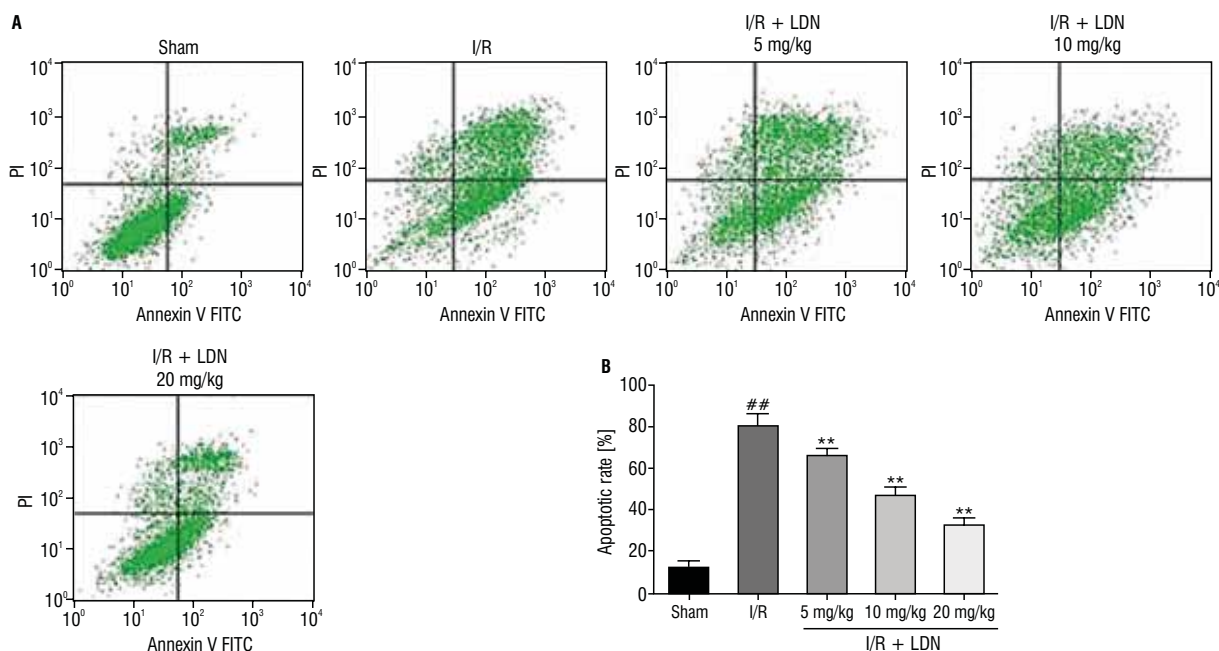
Figure 3. Liriodendrin (LDN) reduces apoptosis of hepatocytes following the hepatic ischaemia/reperfusion (I/R) injury by flow cytometry (**A**), representative bar-graph of apoptotic rate (**B**). Values represent the mean ± standard error of mean; ##p < 0.05 vs. sham; **p < 0.05 vs. I/R, one-way analysis of variance (ANOVA) followed by Bonferroni post hoc test; PI — propidium iodide; Annexin V FITC — annexin V conjugated with fluorescein isothiocyante.
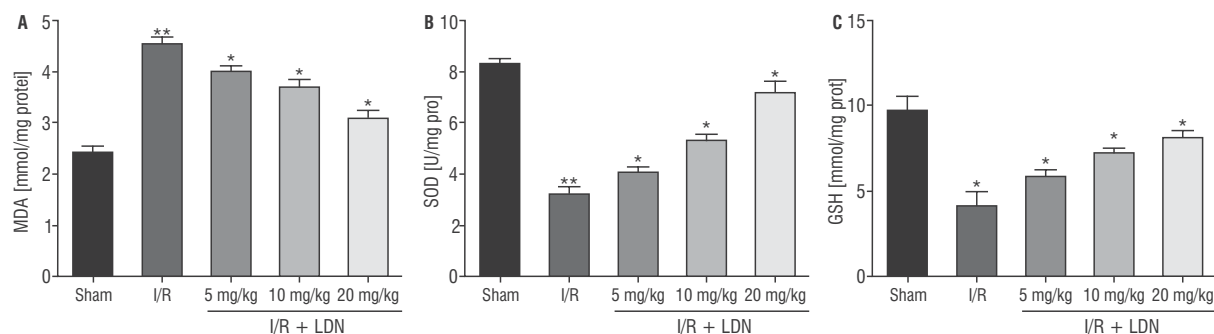
Figure 4. Liriodendrin (LDN) inhibits oxidative stress after hepatic ischaemia/reperfusion (I/R) injury. Expression of malondialdehyde (MDA) (**A**), superoxide dismutase (SOD) (**B**), and glutathione (GSH) (**C**). Values represent the mean ± standard error of mean; **p < 0.05 vs. sham; *p < 0.05 vs. I/R, one-way analysis of variance (ANOVA) followed by Bonferroni post hoc test.

showed dose-dependent reduction of TUNEL positive cells as compared to I//R injury group. In flow cytometry analysis (Fig. 3), similar results were obtained where LDN treated group significantly reduces apoptosis (Fig. 3). These results suggest that LDN provides significant protective effect against I/R injury in mice possibly due to inhibition of hepatocyte apoptosis.

LDN reduces oxidative stress

As shown in Figure 4, following I/R injury, the level of MDA was found elevated with reduction in SOD and GSH as compared to sham. However, in LDN treated experimental subject the level of these studied biomarker were restored near to normal in a significant way in dose-dependent manner. These results suggest that LDN significantly reduces oxidative stress following the I/R injury.

LDN reduces hepatic inflammation

The level of tested cytokines TNF-α, IL-1β, and IL-6 were found significantly elevated in I/R injury group as compared to sham. However, in LDN treated group, the levels of these cytokines were found significantly reduced as compared to I/R group (Fig. 5).
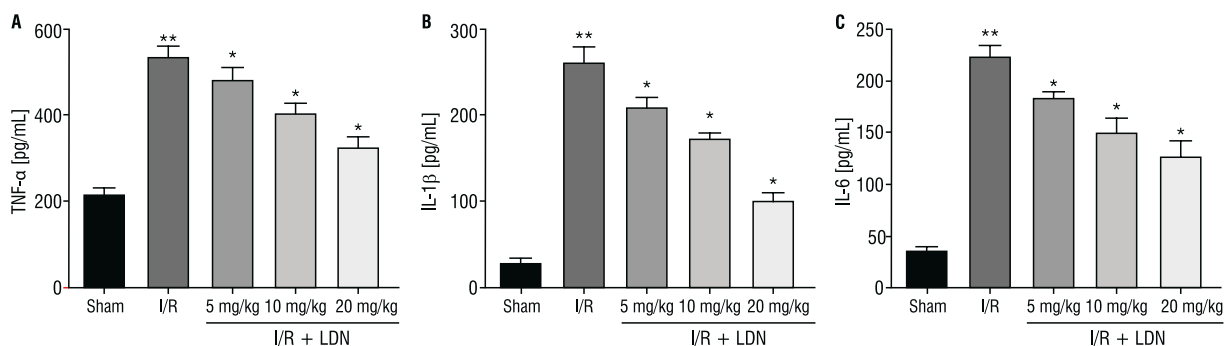
Figure 5. Effect of liriodendrin (LDN) on various cytokines tumour necrosis factor alpha (TNF-α) (**A**), interleukin (IL)-1β (**B**), and IL-6 (**C**). Values represent the mean $\pm$ standard error of mean; **p $<$ 0.05 vs. sham; *p $<$ 0.05 vs. ischaemia/reperfusion (I/R), one-way analysis of variance (ANOVA) followed by Bonferroni post hoc test.
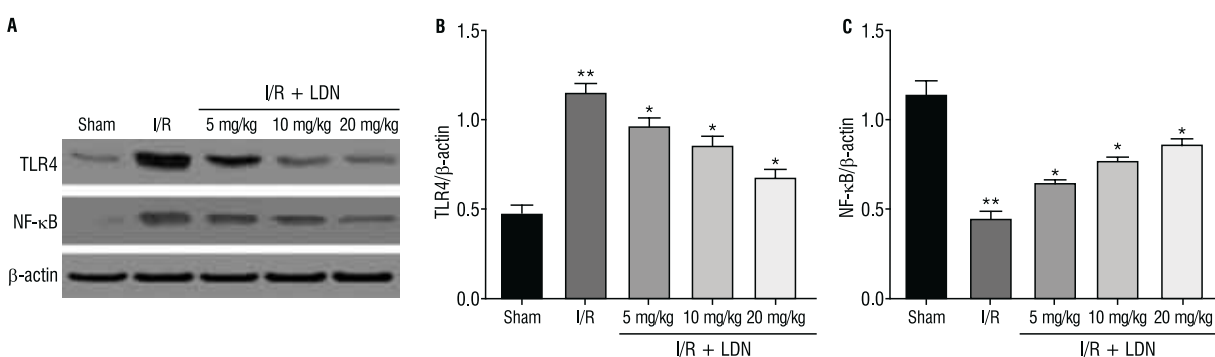
Figure 6. Effect of liriodendrin (LDN) on the toll-like receptor 4/nuclear factor kappa B (TLR4/NF-κB) by Western blot analysis (**A**), representative quantitative bar-graph for TLR4 (**B**), and NF-κB (**C**). Values represent the mean $\pm$ standard error of mean. **p $<$ 0.05 vs. sham; *p $<$ 0.05 vs. ischaemia/reperfusion (I/R), one-way analysis of variance (ANOVA) followed by Bonferroni post hoc test.

LDN inhibited TLR4/NF-κB

As shown in Figure 6, the level of both toll-like receptor 4/nuclear factor kappa B (TLR4/NF-κB) was found significantly elevated after I/R injury in experimental subjects as compared to sham. However, LDN causes dose-dependent reduction of these tested biomarkers in treated group as compared to I/R group.

DISCUSSION

Ischaemia causes metabolic changes in hepatocytes, especially in mitochondria. After reintroduction of oxygen to ischaemic tissues, toxic ROS are released from mitochondria, mainly as the main causes of I/R injury [8]. Studies have shown that hepatic I/R injury is a multifactorial process [7]. This has put selective pressure for the discovery and development of novel agent which acts via multiple pathways to provide protective effect against I/R injury. Towards this, various natural products have shown tremendous success against hepatic I/R injury, such as hesperidin [16], methyl eugenol [32], galangin [17], curcumin [5],

etc. Impressed by the above studies and excellent anti-oxidant and anti-inflammatory effect of LDN, for the first time, we have evaluated the effect of LDN in live I/R injury. Results of the present study showed that I/R induced acute kidney injury led to liver injury, which manifested itself as elevated levels of AST, ALT, and ALP as well as increased oxidative stress (MDA rise), diminished total antioxidant capacity (SOD, and GSH decline), increased expression of TLR4/NF-κB. The animals were healthy throughout the study and did not observe any mortality in them in the whole experimental protocol.

In the current study, we have found that I/R injury provoke acute hepatic injury which results in elevation of various hepatic enzymes such as, AST, ALT, and ALP. Both aminotransferases (ALT, and AST) are highly concentrated in the liver, and any an increase in serum levels is, therefore, more specific for liver damage [1]. ALP is an enzyme that transports metabolites across cell membranes. Studies have shown that these biomarkers are considered as key parameter depicting

the state of liver and their elevated levels greatly correlate with liver damage [3].

Reperfusion injury can cause liver dysfunction after cold storage and warm ischaemia [18]. Recently it has been suggested that more than 50% of hepatocytes and sinusoidal endothelial cells are undergoing apoptosis during the first 24 h of reperfusion [35]. Thus, apoptosis is the main determinant in both acute and chronic graft rejection [34]. Therefore we have studied the effect of LDN via TUNEL and flow-cytometry analysis on the apoptosis of hepatocytes in I/R injury mice. The results of the study suggested that LDN significantly reduces the apoptosis of hepatocytes. Studies have shown that compounds inhibiting apoptosis in I/R injury have significant benefit against the disease and have less changes of late allograft rejection (Acubine, and others).

A considerable number of experimental studies have indicated that I/R-induced liver injury occurs in a biphasic manner [15]. Data obtained by several different research groups suggest that in both early and late phases of reperfusion injury, oxidative stress is one of the main pathogenic mechanisms [20, 24, 30, 31]. SOD and GSH-Px are important antioxidants, and MDA is a product of lipid peroxidation. Thus, these compounds are important indicators of oxidative stress. After liver I/R injury, SOD, GSH-Px activities and cell activity decreased significantly, and MDA content was found to be increased significantly [6, 29]. In current study, LDN treatment provides a significant reduction of oxidative stress damage in the I/R injury model.

Data from murine models have indicated that liver I/R injury has hypoxic cellular stress and inflammation-mediated injury components [14, 19, 20, 31, 40]. Local circulatory damage first induces endogenous reactive oxygen species production causing hepatocyte death. This cellular damage initiates the second phase by recruiting and activating innate immune cells at the site of injury [25]. Thus, activated Kupffer cells secrete TNF-α, IL-1β, IL-6 cytokines, which is an indicator of both oxidative stress and inflammatory reaction [15]. In the present study, I/R group showed significantly higher level of these cytokines than sham group. According to the results, LDN significantly reduces the elevated levels of these cytokines in dose-dependent manner showing LDN have good anti-inflammatory effect. In order to understand the mechanism behind the protective effect of LDN, lastly, we have examined the effect of LDN on the expression of TLR4/NF-κB [21,

28]. The TLR4/NF-κB signalling pathway is a classic pathway that mediates inflammation and plays an important role in ischaemic injury of the heart, brain, liver, lung, and other important organs [2]. During liver I/R injury, ROS promote expression of the early response transcription factor IRF-1, enhance activity of histone acetyl transferase, and promotes acetylation of HMGB1. Acetylated HMGB1 is transferred from intracellular to extracellular environments, binds to TLR4 and RAGE, activates the nuclear transcription factor NF-κB P65, inhibits IκB-α kinase activity, and mediates the release of inflammatory factors TNF-α and IL-1β [23]. Results of the study suggested that was able to reduce the inflammatory response caused by liver ischaemia and reperfusion injury by inhibiting the expression of both TLR4 and NF-κB. Moreover, the current study has some limitations, first, the sample size is very low; second, other mice/rat species and different animal models may also be used to completely characterise the benefit of LDN; third, pharmacokinetic and metabolic assessment were need to be performed; fourth, the study does not provide any idea about the effect of LDN on the entry of Ca^{2+} ion, which is responsible for the progression of I/R injury; fifth, the specific mechanism through which LDN regulates mitochondria injury mediated apoptosis remains unclear and further research is needed.

CONCLUSIONS

Present study demonstrated the LDN significantly ameliorate the liver I/R injury in *in-vivo* experiment. Results suggested that LDN reduces liver injury and prevented apoptosis of hepatocytes following I/R injury. In addition, LDN also reduces oxidative stress, inflammation, and TLR4/NF-κB in I/R injured mice.

Conflict of interest: None declared

REFERENCES

1. Agrawal S, Dhiman RK, Limdi JK. Evaluation of abnormal liver function tests. Postgrad Med J. 2016; 92(1086): 223–234, doi: 10.1136/postgradmedj-2015-133715, indexed in Pubmed: 26842972.
2. Arumugam TV, Okun E, Tang SC, et al. Toll-like receptors in ischemia-reperfusion injury. Shock. 2009; 32(1): 4–16, doi: 10.1097/SHK.0b013e318193e333, indexed in Pubmed: 19008778.

3. Badrick T, Turner P. Review and recommendations for the component tests in the liver function test profile. Indian J Clin Biochem. 2016; 31(1): 21–29, doi: 10.1007/s12291-015-0493-1, indexed in Pubmed: 26855484.

4. Balunas MJ, Kinghorn AD. Drug discovery from medicinal plants. Life Sci. 2005; 78(5): 431–441, doi: 10.1016/j.lfs.2005.09.012, indexed in Pubmed: 16198377.

5. Bavarsad K, Riahi MM, Saadat S, et al. Protective effects of curcumin against ischemia-reperfusion injury in the liver. Pharmacol Res. 2019; 141: 53–62, doi: 10.1016/j.phrs.2018.12.014, indexed in Pubmed: 30562571.

6. Birben E, Sahiner UM, Sackesen C, et al. Oxidative stress and antioxidant defense. World Allergy Organ J. 2012; 5(1): 9–19, doi: 10.1097/WOX.0b013e3182439613, indexed in Pubmed: 23268465.

7. Czigány Z, Turóczi Z, Bulhardt O, et al. [Remote ischemic conditioning: short-term effects on rat liver ischemic-reperfusion injury]. Orv Hetil. 2012; 153(40): 1579–1587, doi: 10.1556/OH.2012.29469, indexed in Pubmed: 23022881.

8. Datta G, Fuller BJ, Davidson BR. Molecular mechanisms of liver ischemia reperfusion injury: insights from transgenic knockout models. World J Gastroenterol. 2013; 19(11): 1683–1698, doi: 10.3748/wjg.v19.i11.1683, indexed in Pubmed: 23555157.

9. Feng C, Li BG, Gao XP, et al. A new triterpene and an antiarrhythmic liriodendrin from Pittosporum brevicalyx. Arch Pharm Res. 2010; 33(12): 1927–1932, doi: 10.1007/s12272-010-1206-1, indexed in Pubmed: 21191756.

10. Gan M, Zhang Y, Lin S, et al. Glycosides from the root of Iodes cirrhosa. J Nat Prod. 2008; 71(4): 647–654, doi: 10.1021/np7007329, indexed in Pubmed: 18327912.

11. Gong J, Xue L, Wei M, et al. Liriodendrin alleviates sciatic endometriosis-associated pain in rats via suppressing inflammatory response and regulating the signaling pathway of PI3K/Akt/mToR. Arch Med Sci. 2021, doi: 10.5114/aoms/143423.

12. Han SJ, Lee HT. Mechanisms and therapeutic targets of ischemic acute kidney injury. Kidney Res Clin Pract. 2019; 38(4): 427–440, doi: 10.23876/j.krcp.19.062, indexed in Pubmed: 31537053.

13. Jung HJ, Park HJ, Kim RG, et al. In vivo anti-inflammatory and antinociceptive effects of liriodendrin isolated from the stem bark of Acanthopanax senticosus. Planta Med. 2003; 69(7): 610–616, doi: 10.1055/s-2003-41127, indexed in Pubmed: 12898415.

14. Kudoh K, Uchinami H, Yoshioka M, et al. Nrf2 activation protects the liver from ischemia/reperfusion injury in mice. Ann Surg. 2014; 260(1): 118–127, doi: 10.1097/SLA.0000000000000287, indexed in Pubmed: 24368646.

15. Li J, Li RJ, Lv GY, et al. The mechanisms and strategies to protect from hepatic ischemia-reperfusion injury. Eur Rev Med Pharmacol Sci. 2015; 19(11): 2036–2047.

16. Li S, Qin Q, Luo D, et al. Hesperidin ameliorates liver ischemia/reperfusion injury via activation of the Akt pathway. Mol Med Rep. 2020; 22(6): 4519–4530, doi: 10.3892/mmr.2020.11561, indexed in Pubmed: 33174025.

17. Li Y, Tong L, Zhang J, et al. Galangin alleviates liver ischemia-reperfusion injury in a rat model by mediating the PI3K/AKT pathway. Cell Physiol Biochem. 2018; 51(3): 1354–1363, doi: 10.1159/000495553, indexed in Pubmed: 30481779.

18. Ligeret H, Brault A, Vallerand D, et al. Antioxidant and mitochondrial protective effects of silibinin in cold preservation-warm reperfusion liver injury. J Ethnopharmacol. 2008; 115(3): 507–514, doi: 10.1016/j.jep.2007.10.024, indexed in Pubmed: 18061382.

19. Lin J, Huang HF, Yang SK, et al. The effect of Ginsenoside Rg1 in hepatic ischemia reperfusion (I/R) injury ameliorates ischemia-reperfusion-induced liver injury by inhibiting apoptosis. Biomed Pharmacother. 2020; 129: 110398, doi: 10.1016/j.biopha.2020.110398, indexed in Pubmed: 32603889.

20. Liu H, Fan J, Zhang W, et al. OTUD4 alleviates hepatic ischemia-reperfusion injury by suppressing the K63-linked ubiquitination of TRAF6. Biochem Biophys Res Commun. 2020; 523(4): 924–930, doi: 10.1016/j.bbrc.2019.12.114, indexed in Pubmed: 31964525.

21. Masih A, Agnihotri AK, Srivastava JK, et al. Discovery of novel pyrazole derivatives as a potent anti-inflammatory agent in RAW264.7 cells via inhibition of NF-κB for possible benefit against SARS-CoV-2. J Biochem Mol Toxicol. 2021; 35(3): e22656, doi: 10.1002/jbt.22656, indexed in Pubmed: 33094891.

22. Nam JW, Kim SY, Yoon T, et al. Heat shock factor 1 inducers from the bark of Eucommia ulmoides as cytoprotective agents. Chem Biodivers. 2013; 10(7): 1322–1327, doi: 10.1002/cbdv.201200401, indexed in Pubmed: 23847077.

23. Neumann M, Naumann M. Beyond IkappaBs: alternative regulation of NF-kappaB activity. FASEB J. 2007; 21(11): 2642–2654, doi: 10.1096/fj.06-7615rev, indexed in Pubmed: 17431096.

24. Pan Y, Yu S, Wang J, et al. N-acetyl-L-tryptophan attenuates hepatic ischemia-reperfusion injury via regulating TLR4/NLRP3 signaling pathway in rats. PeerJ. 2021; 9: e11909, doi: 10.7717/peerj.11909, indexed in Pubmed: 34434653.

25. Rampes S, Ma D. Hepatic ischemia-reperfusion injury in liver transplant setting: mechanisms and protective strategies. J Biomed Res. 2019; 33(4): 221–234, doi: 10.7555/JBR.32.20180087, indexed in Pubmed: 32383437.

26. Ran XK, Wang XT, Liu PP, et al. Cytotoxic constituents from the leaves of Broussonetia papyrifera. Chin J Nat Med. 2013; 11(3): 269–273, doi: 10.1016/S1875-5364(13)60027-8, indexed in Pubmed: 23725840.

27. U PR, M MU, Videla L. Mecanismos moleculares en el daño por isquemia-reperfusión hepática y en el preacondicionamiento isquémico. Revista Médica de Chile. 2005; 133(4), doi: 10.4067/s0034-98872005000400012.

28. Srivastava J, Awatade N, Bhat H, et al. Pharmacological evaluation of hybrid thiazolidin-4-one-1,3,5-triazines for NF-κB, biofilm and CFTR activity. RSC Advances. 2015; 5(108): 88710–88718, doi: 10.1039/c5ra09250g.

29. Storz G, Imlay JA. Oxidative stress. Curr Opin Microbiol. 1999; 2(2): 188–194, doi: 10.1016/s1369-5274(99)80033-2, indexed in Pubmed: 10322176.

30. Tüfek A, Tokgöz O, Aliosmanoglu I, et al. The protective effects of dexmedetomidine on the liver and remote organs against hepatic ischemia reperfusion injury in rats. Int J Surg. 2013; 11(1): 96–100, doi: 10.1016/j.ijsu.2012.12.003, indexed in Pubmed: 23261946.

31. Wang J, Yu S, Li J, et al. Protective role of N-acetyl-l-tryptophan against hepatic ischemia-reperfusion injury via the RIP2/caspase-1/IL-1β signaling pathway. Pharm Biol. 2019;

57(1): 385–391, doi: 10.1080/13880209.2019.1617750, indexed in Pubmed: 31184936.

32. Wang M, Zhang Ji, Zhang J, et al. Methyl eugenol attenuates liver ischemia reperfusion injury via activating PI3K//Akt signaling. Int Immunopharmacol. 2021; 99: 108023, doi: 10.1016/j.intimp.2021.108023, indexed in Pubmed: 34358859.

33. Wang S, Hu Y, Liu T. Plant distribution and pharmacological activity of flavonoids. Trad Med Res. 2019; 4(5): 269–287, doi: 10.53388/tmr20190824131.

34. Wu QR. Wang YG. Apoptosis and ischemia-reperfusion injury following liver transplantation. J Clin Rehab Tissue Eng Res. 2011; 15(18): 3371–3375.

35. Xue S, He W, Zeng X, et al. Hypothermic machine perfusion attenuates ischemia/reperfusion injury against rat livers donated after cardiac death by activating the Keap1/Nrf2ARE signaling pathway. Mol Med Rep. 2018; 18(1): 815–826, doi: 10.3892/mmr.2018.9065, indexed in Pubmed: 29845199.

36. Yang G, Yang Yu, Li Y, et al. Remote liver ischaemic preconditioning protects rat brain against cerebral ischaemia-reperfusion injury by activation of an AKT-dependent pathway. Exp Physiol. 2020; 105(5): 852–863, doi: 10.1113/EP088394, indexed in Pubmed: 32134522.

37. Yang Y, Tang Z, Wei Y. Hypoglycemic effects of active constituents extracted from the stem bark of Kalopanax septemlobus (Thunb.) Koidz. in Guangxi. Med J Wuhan Uni. 2008; 29(6): 759–762.

38. Yang Yi, Wang P, Zhang C, et al. Hepatocyte-derived MANF alleviates hepatic ischaemia-reperfusion injury via regulating endoplasmic reticulum stress-induced apoptosis in mice. Liver Int. 2021; 41(3): 623–639, doi: 10.1111/liv.14697, indexed in Pubmed: 33064897.

39. Yoon SY, Kim CY, Han HJ, et al. Protective effect of ischemic postconditioning against hepatic ischemic reperfusion injury in rat liver. Ann Surg Treat Res. 2015; 88(5): 241–245, doi: 10.4174/astr.2015.88.5.241, indexed in Pubmed: 25960986.

40. Yu Q, Chen S, Tang H, et al. Veratric acid alleviates liver ischemia/reperfusion injury by activating the Nrf2 signaling pathway. Int Immunopharmacol. 2021; 101(Pt B): 108294, doi: 10.1016/j.intimp.2021.108294, indexed in Pubmed: 34749250.

ORIGINAL ARTICLE

Morphological study of the anatomical variations of anterior belly of digastric muscle in Brazilian cadavers

D.J. Gross[1], A.C. Rossi[1], B.C. Ferreira-Pileggi[1], L.N.O. Watanabe[1], P.R. Botacin[2], F.B. Prado[1], A.R. Freire[1]

[1]Department of Biosciences, Anatomy Division, Piracicaba Dental School, University of Campinas, Piracicaba, São Paulo, Brazil
[2]Basic Sciences Department, Araçatuba Dental School, Paulista State University – UNESP, Araçatuba, São Paulo, Brazil

Background: Cases of variations in anterior belly of the digastric muscle must be carefully identified to avoid misinterpretations and assist in the correct surgical or aesthetic procedure and help in the teaching of anatomy. The aim of this study was to describe the anatomical variations of anterior belly of digastric muscle in Brazilian cadavers.

Materials and methods: Thirty-one human heads were selected, from adult cadavers (18–80 years, 29 males and 2 females). The morphology of the anterior belly of the digastric muscle was observed, identifying the possible anatomical variations that were characterised and classified according to the amount of muscle bellies, fibre direction and place of origin and insertion. The morphometric measurements were performed using a digital calliper. To analyse the data obtained, photographic documentation, anatomical description and individual morphometric description of each muscle belly were performed. The incidence of anatomical variation was obtained in percentage (%).

Results: The anatomical variation of the anterior belly of the digastric muscle was present in 6 cadavers (19.31%; 1 female and 5 male). All anatomical variations presented an accessory belly to the anterior belly. However, these accessory bellies were configured differently in the location, direction of muscle fibres and in their dimensions (length and width).

Conclusions: The gross anatomy of the anterior belly of the digastric muscle and their variations is important to assist in surgical procedures, pathological or diagnostic function. In addition, asymmetrical variations in the submental region must be carefully identified to avoid misinterpretations. (Folia Morphol 2023; 82, 3: 677–682)

Key words: anatomy, digastric muscle, anatomical variations, morphology

Address for correspondence: Prof. A.R. Freire, PhD, Researcher, Department of Biosciences, Anatomy Division, Piracicaba Dental School, University of Campinas, Piracicaba, São Paulo, Brazil, Av. Limeira, 901-Areião, Piracicaba – SP, Brazil 13.414-903, tel: +55 19 21065721, e-mail: alerfreire@gmail.com

INTRODUCTION

The digastric muscle (DM) is in the submental region and is a muscle that has two bellies, called the anterior belly and the posterior belly, separated by an intermediate tendon, which forms an anchorage in the hyoid bone. Its origin is characterised by the attachment of the posterior belly to the mastoid notch, at the base of the skull, and its insertion is in the digastric fossa, at the base of the mandible in the chin region. Because they have different embryological origins, DM bellies have different innervation and vascularization, and the anterior belly is innervated by the mylohyoid nerve, a branch of the mandibular nerve. The submental artery and vein, branches of the facial artery and vein, are responsible for its vascularisation [2]. The anterior belly lies superficial to the mylohyoid muscle [6] and its function is to elevate the hyoid bone when the infrahyoid muscles are relaxed and to lower the mandible when the hyoid bone is fixed [13].

The DM shows great variability in size, shape, and number. These variations mainly involve the anterior belly of the muscle and the number of anterior bellies or the presence of accessory bundles originating from a common tendon or the intermediate tendon [4, 9]. The anterior belly variations can be unilateral or bilateral and more rarely being symmetrical, extending to the mandible or the mylohyoid muscle or even crossing the midline to the opposite mylohyoid or the opposite digastric fossa [3].

Digastric muscle variability is of paramount importance during mobilisation of the platysma myocutaneous flap in reconstructive procedures [15]. In-depth knowledge of the typical and variable anatomy of the anterior bellies is of paramount importance due to muscle use after facial nerve paralysis and submental artery flap procedures [16]. In addition, the anterior belly is used as a reference point when identifying the lingual nerve or submandibular gland duct [12].

The submental and submandibular areas are very well vascularised, and knowledge of their muscle abnormalities is essential when a myocutaneous flap is mobilised in reconstructive plastic surgery. Vascular variations can coexist and, to maintain and increase the viability of the flap, the branching pattern of the vessels must be well preserved intraoperatively [10]. Thus, cases of variations in this region must be carefully identified to avoid misinterpretations and assist in the correct surgical or aesthetic procedure and help in the teaching of anatomy.

The aim of this study was to describe the anatomical variations of anterior belly of DM in Brazilian cadavers.

MATERIALS AND METHODS

Ethics approval

The research was analysed and approved by the Committee of Research Ethics of the University of Campinas (Protocol number CEP-FOP-UNICAMP-CAAE 59065622.6.0000.5418).

Sample

Thirty-one human heads belonging to the Laboratory of Anatomy of the Piracicaba Dental School from University of Campinas (FOP-UNICAMP) were selected for the study. The heads were from adult cadavers, selected at random, ranging in age from 18 to 80 years and of both sexes (29 males and 2 females).

The inclusion criteria were as follows: cadaveric specimens from adult individuals with preserved anatomical structures in the submental region, especially the suprahyoid muscles, among which the DM is included. The exclusion criteria were that cadaveric specimens that do not show the preservation of the suprahyoid muscles in the submental region, or that present any pathology that have the presence of a foreign body in the submental region, interfering with the anatomy of the suprahyoid muscles, were excluded.

Calibration

Initially, an anatomical study of the submental region was performed to identify the anatomy of the suprahyoid muscles and adjacent anatomical structures. After this study, the examiner identified the anterior belly of the DM and calibrated the measurements to be performed using a digital calliper (Mituyo®).

Evaluation of the morphology and the morphometry of the anterior belly of the DM

The morphology of the anterior belly of the DM was observed, identifying the possible anatomical variations that were characterised and classified according to the amount of muscle bellies, fibre direction and place of origin and insertion.

The morphometric measurements were performed using a digital calliper (Mituyo®), in which the measurements of the width (mm) and length (mm) of the anterior belly were obtained to add to the morphological descriptions.

Data analysis

To analyse the data obtained, photographic documentation, anatomical description and individual morphometric description of each muscle belly were performed. The incidence of anatomical variation was obtained in percentage (%).

RESULTS

Of the 31 cadavers evaluated, the anatomical variation of the anterior belly of the DM was present in 6 (19.31%; 1 female and 5 male). All anatomical variations presented an accessory belly to the anterior belly of the DM. However, these accessory bellies were configured differently in the location, direction of muscle fibres and in their dimensions (length and width). Anatomical variations are described below. The occurrence of each type can be seen in Figure 1.

Figure 1A and B show anatomical variation of the anterior belly of the DM with the appearance of a unilateral accessory minor belly, in which its muscle fibres originate from the intermediate tendon of the DM and are obliquely directed to insert into the mylohyoid muscle raphe together with mylohyoid muscle fibres. In the total of variations found, 3 heads presented this configuration. In the heads that were found in this configuration, the accessory belly (1a) on the left side (Fig. 1A) had a length equal to 26.36 mm and a width equal to 6 mm. As for the main bellies, the DM anterior belly on the right side had a length of 52.62 mm and a width of 16.22 mm. And the DM anterior belly on the left side had a length equal to 54.27 mm and width equal to 20.94 mm. In Figure 1B, the accessory belly (1a) was located on the right side, with a length equal to 26.70 mm and width equal to 12.47 mm. As for the main bellies, the DM anterior belly on the right side had a length equal to 43.43 mm and a width equal to 11.42 mm. And the DM anterior belly on the left side had a length equal to 33.35 mm and width equal to 15.08 mm.

In Figure 1C, a more complex configuration can be seen, in which the variation occurred bilaterally. The accessory bellies in this configuration originate in the intermediate tendon of the DM and their fibres are directed obliquely across the midsagittal plane until they reach their point of insertion at the base of the mandible on the opposite side in an extension of the digastric fossa. Both accessory bellies are superficial in relation to the mylohyoid muscle. The accessory belly 1a has a length equal to 48.16 mm and a width

equal to 12.54 mm. And the accessory belly 1b has a length equal to 39.16 mm and a width equal to 8.63 mm. As for the main bellies, the DM anterior belly on the right side had a length equal to 40.23 mm and a width equal to 14.26 mm. And the DM anterior belly on the left side had a length equal to 41.16 mm and width equal to 16.11 mm.

In Figure 1D, the variation was presented with the presence of accessory bellies on the right and left sides. Muscle fibres originate from the intermediate tendon of the DM and insert into the extension of the digastric fossa ipsilaterally. However, a small number of fibres can be observed originating from the intermediate tendon on the opposite side, crossing the midline in a similar way to that found in item C of Figure 1. The accessory bellies are found superficially to the mylohyoid muscle. The accessory belly 1a is 26.53 mm long and 6.92 mm wide. And the accessory belly 1b has a length equal to 23.49 mm and a width equal to 4.99 mm. As for the main bellies, the DM anterior belly on the right side had a length equal to 30.17 mm and a width equal to 11.58 mm. And the DM anterior belly on the left side had a length equal to 35.68 mm and a width equal to 8.96 mm.

Considering the variations found, the configuration found in item E of Figure 1 was the most complex. In this situation, the variation appeared bilaterally, with different accessory bellies on each side. In addition, the main anterior belly on the left side also showed an anatomical variation.

On the left side, the main anterior belly originates from the intermediate tendon, but its fibres are directed obliquely to insert into the base of the mandible, right in the midsagittal plane. In addition, part of its fibres has insertion in the mylohyoid muscle raphe. The accessory belly on the left, at its origin, presents fibres together with the main anterior belly. However, when approaching the midsagittal plane, the group of fibres separates to insert into the mylohyoid muscle raphe. Thus, the accessory belly on the left is located posterior to the main anterior belly. On the right side, the main anterior belly did not show variation as on the left side. The accessory belly presented a different configuration from the other variations that were found. Its fibres originate in the intermediate tendon and are directed anteriorly to insert into the digastric fossa together with the main anterior belly. This accessory belly is located laterally in relation to the main anterior belly and is separated from it by
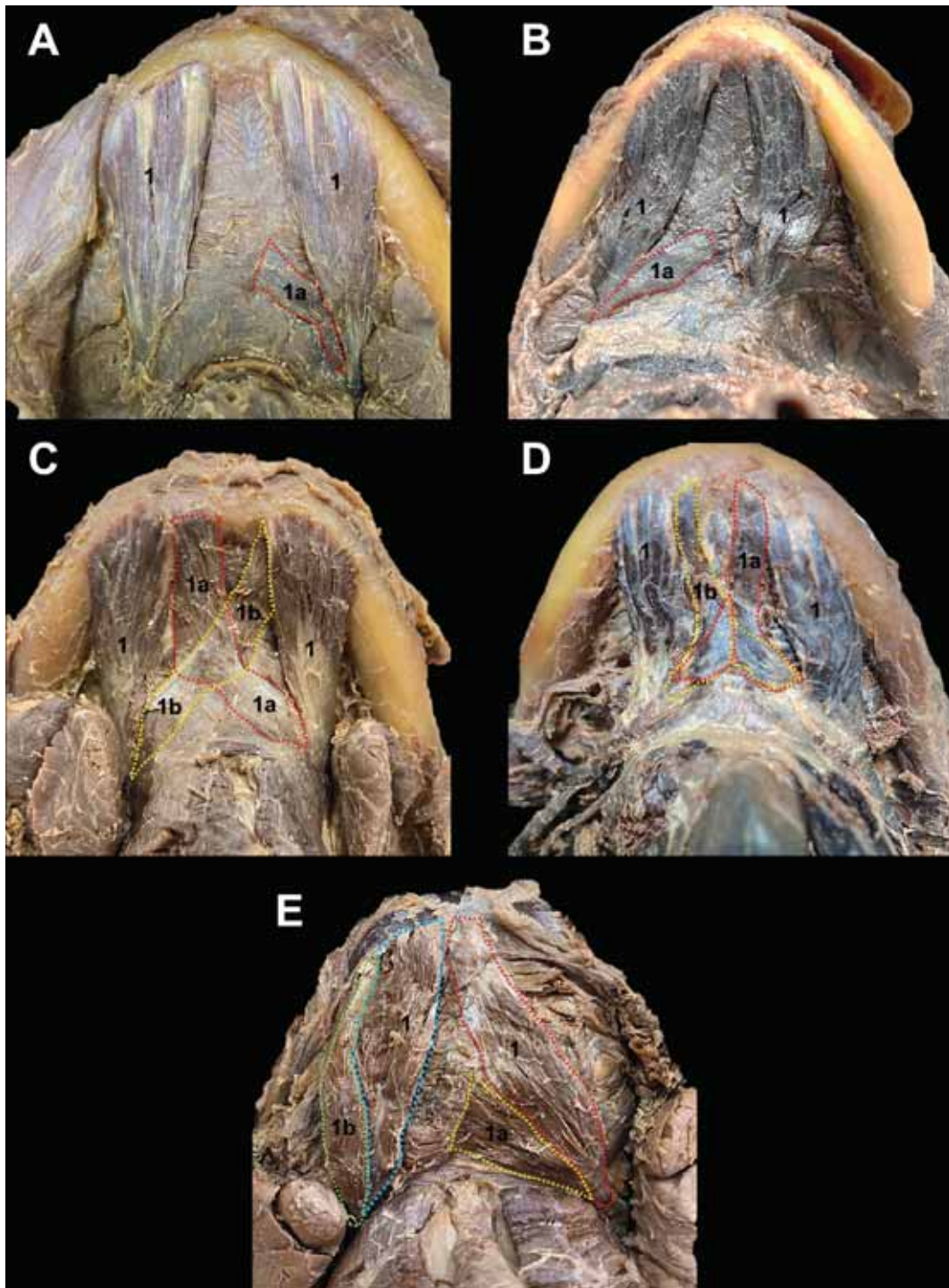
Figure 1. Submental region with emphasis on the location of the anatomical variation of the anterior bellies of digastric muscle. Different colours delimit the belly area; 1 — main anterior belly; lowercase letters — accessory bellies.

a fascia. It is also observed that at its insertion, the accessory belly on this side had a longer tendon in relation to the main anterior belly.

In item E of Figure 1, the anterior belly 1a had a length equal to 24.79 mm and width equal to 12.94 mm. And the anterior belly 1b had a length

equal to 33.03 mm and width equal to 12.94 mm. As for the main bellies, the DM anterior belly on the right side (blue) had a length equal to 34.02 mm and a width equal to 14.13 mm. And the MD anterior belly on the left side (red) had a length equal to 40.94 mm and width equal to 12.20 mm.

DISCUSSION

Digastric muscle variability is of paramount importance during mobilisation of the platysma myocutaneous flap in reconstructive procedures [15]. In-depth knowledge of the typical and variable anatomy of the anterior bellies is of paramount importance due to muscle use after facial nerve paralysis and submental artery flap procedures [16]. In addition, the anterior belly is used as a reference point when identifying the lingual nerve or submandibular gland duct [12].

The knowledge of the anatomical variations of the anterior belly of the DM is also necessary for professionals who perform conservative and surgical treatments in the submental region, as well as in teaching the anatomy of this structure. Therefore, knowing the anatomical variations can facilitate diagnosis and prevent possible complications during surgical procedures [13].

The variations may also be responsible for aesthetic alterations in the submental region. For example, a bulky anterior belly of the digastric muscle can contribute to an unsightly contour of the neck by giving a bulge in the submental area. By removing a good portion of the anterior belly muscle (i.e. making the anterior belly thinner), the bulge in the submental area can be minimised, thus giving the patient a better contour of the neck [5].

Regarding the variations found, ethnicity as the most frequent factor in the occurrence of these variations. Literary data show a higher prevalence of these variations in the Asian population, especially the Japanese. While in the general population a rate of 31.4% was found, in the Asian population the rate was 51.7% for the occurrence of anatomical variation of the DM [1].

Another factor responsible for variations, such as bilateral duplication of the anterior belly, may be the embryological origin, which is explained by a deficiency in the differentiation of the mesoderm of the first pharyngeal arch on both sides or by abnormal migration of the cells of the pharyngeal arch neural crest. In relation to the crossing of muscle fibres in the midline, it may be due to the proximity of the pharyngeal arches [8].

The DM is an important muscle in the neck, which pulls the mandible down to open the mouth and elevates the hyoid bone for stabilisation during swallowing and is also involved in chewing and speaking. In the functional aspect, the changes may affect some DM functions. For example, in crossed anterior bellies, the difficulty of opening the mouth is suggestive. Probably, the crossing of the bellies makes it difficult for the mandible to be moved downwards.

In the supernumerary bundles, due to their proximity to the anterior belly of the digastric and mylohyoid muscles, additional force is likely to be provided to these muscles during mastication [14]. In the case of the additional belly or unilateral accessory, an imbalance can occur when elevating the hyoid bone or lowering the mandible [11]. These unilateral or bilateral muscle bundles or slips may occur because of a phylogenetic reduction of the DM or an unusual development of ontogenetic material [3].

Notably, knowing the variations found, clinicians and surgeons can make use of and must be very careful in interpreting radiographs and computed tomography scans, as the variations may appear like soft tissue masses, especially in the unilateral type [13].

CONCLUSIONS

The gross anatomy of the anterior belly of the DM and their variations is important to assist in surgical procedures, pathological or diagnostic function. In addition, asymmetrical variations in the submental region must be carefully identified to avoid misinterpretations.

REFERENCES

1. Arayapisit T, Vorakulpipat C, Srimaneekarn N, et al. Anatomical variations of the anterior belly of the digastric muscle in Thai cadavers: a cross-sectional study. J Int Soc Prev Community Dent. 2022; 12(2): 171–177, doi: 10.4103/jispcd.JISPCD_188_21, indexed in Pubmed: 35462749.
2. Aszmann OC, Ebmer JM, Dellon AL. The anatomic basis for the innervated mylohyoid/digastric flap in facial reanimation. Plast Reconstr Surg. 1998; 102(2): 369–372, doi: 10.1097/00006534-199808000-00010, indexed in Pubmed: 9703071.

3. Atamaz Pinar Y, Govsa F, Bilge O. The anatomical features and surgical usage of the submental artery. Surg Radiol Anat. 2005; 27(3): 201–205, doi: 10.1007/s00276-005-0317-8, indexed in Pubmed: 16003485.

4. Celik HH, Aldur MM, Ozdemir B, et al. Abnormal digastric muscle with unilateral quadrification of the anterior belly. Clin Anat. 2002; 15(1): 32–34, doi: 10.1002/ca.1088, indexed in Pubmed: 11835541.

5. Connell BF, Shamoun JM. The significance of digastric muscle contouring for rejuvenation of the submental area of the face. Plast Reconstr Surg. 1997; 99(6): 1586–1590, indexed in Pubmed: 9145126.

6. Hollinshead WH. The Jaws, Palate and Tongue, In: Anatomy for Surgeons. Vol. 1, 3rd print, A Hoeber – Harper Book, New York 1961: 340–400.

7. Iwanaga J, Singh V, Ohtsuka A, et al. Acknowledging the use of human cadaveric tissues in research papers: Recommendations from anatomical journal editors. Clin Anat. 2021; 34(1): 2–4, doi: 10.1002/ca.23671, indexed in Pubmed: 32808702.

8. Kim SD, Loukas M. Anatomy and variations of digastric muscle. Anat Cell Biol. 2019; 52(1): 1–11, doi: 10.5115/acb.2019.52.1.1, indexed in Pubmed: 30984445.

9. Mangalagiri AS, Razvi MR. Variations in the anterior belly of digastric. Int J Health Sci (Qassim). 2009; 3: 257–262.

10. Natsis K, Piagkou M, Lazaridis N, et al. Asymmetry of the accessory anterior digastric muscle bellies: the clinical significance in facial and neck surgery. Cureus. 2020; 12(2): e7148, doi: 10.7759/cureus.7148, indexed in Pubmed: 32257693.

11. Netter FH. Neck. In: Hansen JT, Benninger B, Brueckner JK, Carmichael SW, Granger NA, Tubbs RS (eds.). Atlas of Human Anatomy. 5th ed. Elsevier, Philadelphia 2011: 26–34.

12. Norton MR. Bilateral accessory digastric muscles. Br J Oral Maxillofac Surg. 1991; 29(3): 167–168, doi: 10.1016/0266-4356(91)90030-9, indexed in Pubmed: 1873284.

13. Reyes G, Contreras C, Ramírez LM, et al. The digastric muscle's anterior accessory belly: case report. Med Oral Patol Oral Cir Bucal. 2007; 12(5): E341–E343, indexed in Pubmed: 17767094.

14. Sowman PF, Flavel SC, McShane CL, et al. Asymmetric activation of motor cortex controlling human anterior digastric muscles during speech and target-directed jaw movements. J Neurophysiol. 2009; 102(1): 159–166, doi: 10.1152/jn.90894.2008, indexed in Pubmed: 19420123.

15. Turan-Ozdemir S, Oygucu IH, Kafa IM. Bilateral abnormal anterior bellies of digastric muscles. Anat Sci Int. 2004; 79(2): 95–97, doi: 10.1111/j.1447-073x.2004.00065.x, indexed in Pubmed: 15218629.

16. Uzun A, Aluclu A, Kavakli A. Bilateral accessory anterior bellies of the digastric muscle and review of the literature. Auris Nasus Larynx. 2001; 28(2): 181–183, doi: 10.1016/s0385-8146(00)00100-0, indexed in Pubmed: 11240328.

ORIGINAL ARTICLE

VIA MEDICA

Expression and distribution of erythropoietin, vascular endothelial growth factor (VEGF) and VEGF receptor 2 in small intestine of yaks at different ages

Y. Zhou[1#], T. Zhang[1#], Y.Y. Zhang[1, 2, 3], J. Xu[1], M. Li[1], Q. Zhang[4], Z. Qiao[2, 3], K. Yang[1, 2, 3]

[1]Life Science and Engineering College, Northwest Minzu University, Lanzhou, P.R. China
[2]Key Laboratory of Biotechnology and Bioengineering of State Ethnic Affairs Commission, Biomedical Research Centre, Northwest Minzu University, Lanzhou, P.R. China
[3]Gansu Tech Innovation Centre of Animal Cell, Biomedical Research Centre, Northwest Minzu University, Lanzhou, P.R. China
[4]Laboratory of Animal Anatomy and Tissue Embryology, Department of Basic Veterinary Medicine, Faculty of Veterinary Medicine, Gansu Agricultural University, Lanzhou, P.R. China

Background: This study aimed to detect the expression and distribution of vascular endothelial growth factor (VEGF), VEGF receptor 2 (VEGFR-2), and erythropoietin (EPO) proteins in small intestinal tissues of 50-day-old, newborn, and adult yaks. The results provide basic data for the study of the relationship between adaptability and age of plateau yak.

Materials and methods: Small intestine tissues from healthy adult, 50-day-old, and newborn yak were collected and embedded in paraffin sections. Histological features were observed by haematoxylin and eosin staining. The expression of VEGF, VEGFR-2, and EPO proteins were detected by immunohistochemical staining.

Results: Immunohistochemical results showed that of the expression VEGF, VEGFR-2, and EPO were detected in the small intestinal villi of yaks at all ages. The EPO expression level in the jejunum and duodenal villous epithelial cells of newborn yaks was significantly higher than that of 50-day-old and adult yaks. The EPO expression level in ileum villous epithelial cells of 50-day-old yaks was significantly higher than that of newborn and adult yaks. VEGF expression in newborn yak ileum and jejunum epithelial cells of the intestinal villus were significantly higher than in the 50-day-old and adult. In the 50-day-old yaks, the duodenal intestinal villus epithelial cells expression levels were higher than in the adult and newborn yaks. The expression level of VEGFR-2 in the ileum, jejunum and duodenal villous epithelial cells of 50-day-old yak was significantly higher than in that of adult and newborn yak.

Conclusions: The expression and distribution characteristics of EPO, VEGF, and VEGFR-2 in yak intestinal tissues of different ages indicate that these proteins may be involved in the physiological regulation of yak intestines in hypoxic environments. It may be an important regulatory protein in yak adaptation to a high altitude and low oxygen environment. (Folia Morphol 2023; 82, 3: 683–695)

Key words: yak, intestine, growth, protein expression

Address for correspondence: Dr. K. Yang, Ass. Prof., College of Life Science and Engineering, Northwest Minzu University, Lanzhou, 730030, P.R. China, tel: +86 18153622395, e-mail: onionyk@qq.com

#Equaly contributing

INTRODUCTION

Yak (scientific name: Bos mutus or Bos grunniens, English name: Wild yak) is an herbivorous ruminant belonging to the Bovidae family. It is a rare cattle species native to the Qinghai-Tibet Plateau in China and its adjacent alpine and subalpine regions. Yak can adapt to the cold climate and, except for human beings, is the mammal living at the highest altitude in the world. It is distributed in areas higher than 3000 m above sea level. As all-round livestock, yak is an extremely valuable genetic pool and has social and economic significance to human beings that cannot be ignored. There are nearly 16 million yaks globally, of which 15 million are found in China. Hypoxia is a key factor affecting the survival of organisms in such an environment and plays an important role in kidney injury, pulmonary hypertension, and other organ diseases [5]. The ability of mammalian cells to adapt to high altitude and low oxygen environments is an evolutionary change that may result in considerable physiological changes related to animal viability. This has been demonstrated by some native species living in the region, including Tibetan antelope, gazelle, and yak [19]. The Tibetan Plateau, the highest plateau in the world, is known for its hypoxic environment.

Erythropoietin (EPO) is a key regulator of erythropoiesis, and its continuous production is necessary to maintain daily erythropoiesis [15]. EPO and EPO receptors (EPORs) are widely expressed in the brain, peripheral nerves, heart, kidney, skeletal muscle, bone marrow, endothelial cells, and intestinal tissues [2]. Exogenous EPO improves intestinal motility in vivo through its powerful antioxidant and inflammatory decomposition properties [2]. Hypoxia-inducible transcription factors (HIFs) induce the expression of EPO. EPO is then released into the blood and binds to EPORs on erythrocyte progenitor cells in the bone marrow, triggering erythropoiesis and leading to tissue hypoxia compensation [3]. In addition, HIF-EPO pathway deregulation mediates disorders that affect altitude adaptation. Strict regulation of erythropoietin production leads to the clearance of red blood cells and normalization of haemoglobin elevation after descent, which is a typical observation of long-term adaptation to high-altitude residents and high-altitude areas [6]. Vascular endothelial growth factor (VEGF) is a downstream target gene induced by HIF activation and plays an important role in cell adaptation to hypoxia [3]. Hypoxia also promotes VEGF expression, which has been found in many organs [3, 10]. The kidney is susceptible to hypoxia, and angiogenesis is affected under hypoxia. VEGF enhances vascular permeability, stimulates angiogenesis, and promotes blood delivery to hypoxic sites, thereby reducing tissue damage. Vascular endothelial growth factor receptor 2 (VEGFR-2) is a VEGF receptor, and many of the VEGF biological activities in endothelial cells are mediated by the tyrosine kinase receptors VEGFR-2 [13] and VEGFR-1. The binding of VEGF to the extracellular domain of these receptors results in dimerisation and phosphorylation of the tyrosine kinase domain [7]. Despite its lower affinity for ligands, VEGFR-2 is responsible for most of the biological behaviour of VEGF due to its higher ability in signal transduction [4]. The oxygen concentration in granulosa cells affects VEGF gene expression in granulosa cells [14]. Similarly, cells cultured at low oxygen concentrations, such as mouse mesenchymal cells, human trophoblast cells, and umbilical endothelial cells, produce more VEGF [12] and show higher mRNA expression of VEGF ligands and their receptors [9].

Erythropoietin can promote angiogenesis by upregulating the expression of VEGF, thereby promoting the repair of brain tissue injury and improving cardiac function and myocardial ischaemia and hypoxia, thereby decreasing the expression of HIF, which provides a certain experimental and theoretical basis for the clinical treatment of chronic myocardial infarction. The effect of EPO therapy on wound healing is attributed to EPO-mediated stimulation of cell proliferation and angiogenesis and is associated with the increased expression of VEGF, endothelial nitric oxide synthase, and inducible nitric oxide synthase. EPO and VEGF have significant genetic and functional homology, suggesting that the two cytokines play similar roles in bone repair. In addition, it has been reported that EPO can stimulate tissue regeneration after skin injury and myocardial infarction through the VEGF-dependent pathway [17]. This suggests that EPO stimulates early angiogenesis through the VEGF-dependent pathway. On the other hand, EPO has a significant inhibitory effect on the accumulation of anti-VEGF antibodies. Studies have found that increasing VEGF in fetal bovine serum medium is not sufficient to induce increased activity of EPO, highlighting the importance of VEGF in the role of epithelial cells erythropoietin. The relationship between EPO and VEGF is particularly important during

normal neovascularisation and in patients treated with recombinant human erythropoietin (rhEPO) [1]. Yang et al. [20] also confirmed that rhEPO has a significant protective effect on blood-brain barrier leakage, reduces blood-brain barrier permeability, and alleviates brain oedema, usually caused by focal ischaemia in the acute stage after injury. VEGFR-1 and VEGFR-2 were significantly decreased after rhEPO treatment on day three after injury compared to VEGF upregulation. Prevention of EPO-mediated damage after ischaemia may involve endothelial cell storage, preservation of microvascular integrity, and downregulation of VEGFR-1 and VEGFR-2. EPO induces neovascularisation through expression and upregulation of VEGF/VEGFR-2, an essential growth factor and potent angiogenic factor for vascular endothelial cells.

Yak is a native species of China, mainly distributed in the plateau and its adjacent areas where the atmospheric oxygen pressure is only 53–62% of that at sea level [19]. Cattle have been domesticated for more than 4000 years and have been well adapted to hypoxia conditions through natural selection [19], making them a perfect model for studying the mechanisms related to hypoxia. In this study, the expression and distribution characteristics of EPO, VEGF and VEGFR-2 in the small intestine of yaks of three different ages in high altitude areas were analysed using an immunohistochemical method. The research results will also provide basic information for understanding the stress response mechanism in high altitude hypoxic environment.

MATERIALS AND METHODS

Animal ethics

The study was approved by the State Forestry Administration, and all procedures were performed in compliance with guidelines for the care and use of laboratory animals adopted by the Ministry of Science and Technology of the People's Republic of China.

Materials

Wild adult, newborn, and 50-day-old yaks were collected in Hezuo City (Gansu Province, China) at an altitude of around 3000 m. Animals were euthanized with pentobarbital sodium (200 mg/kg, IV) at local slaughterhouses, complying with local regulations. Small intestine samples were collected and preserved in 4% paraformaldehyde for tissue fixation immediately after euthanasia.

Haematoxylin and eosin staining detection

Fully fixed samples were embedded in paraffin and the tissue blocks then were sliced into 5 μm sections for subsequent processes. Haematoxylin and eosin staining was used to observe the histological features of the samples.

Immunohistochemistry detection

Immunohistochemical staining was carried out based on Histostain TM-Plus Kits (Bioss, China, SP-0023). Briefly, tissue sections were deparaffinized in xylene and rehydrated in different concentration gradient of alcohol. After being rinsed in phosphate buffered saline (PBS) buffer, sections were autoclaved (15 min in a microwave oven) in 0.01 M sodium citrate buffer (pH 6.0) for antigen retrieval. The endogenous peroxidase was inactivated using 3% hydrogen peroxide at 37ºC for 10 min. The sections were then incubated with anti-EPO polyclonal antibody, anti-VEGF polyclonal antibody, anti-VEGFR-2 polyclonal antibody (Bioss, China, 1:200 dilution, bs-20398R, bs-1447R, bs-1665R and bs-0565R) at 4ºC overnight in a humid chamber. Antibody binding was coloured with DAB Substrate kit (Solarbio, China, DA1010) and tissue sections were counterstained with haematoxylin. All washing steps in-between were done in PBS. To assess the specificity of the immunolabelling, negative control slides were created using the bovine serum albumin as the primary antibody while all other steps and conditions.

Statistical analysis

Images of the stained tissue sections were observed and captured by a light microscope (Olympus CX31, Tokyo, Japan).

Image-Pro Plus (Version 6.0, Media Cybernetics, Inc.: Bethesda, MD, USA) was used to quantify the positive results of expression of VEGF, VEGFR-2 and EPO. The measurement parameters included sum area and sum integrated optical density. SPSS software (Version 19.0, SPSS Inc., Chicago, USA) was used to analyse the statistical significance.

RESULTS

Histological observation

The intestinal wall of yak consists of mucosa, submucosa, muscularis and serosal layers. The lamina propria of the mucosa extends into the lumen and is covered by intestinal epithelial cells to form intestinal villi (Figs. 1, 2A–I). Duodenal and intestinal villi are densely distributed, short and thick, in the shape of
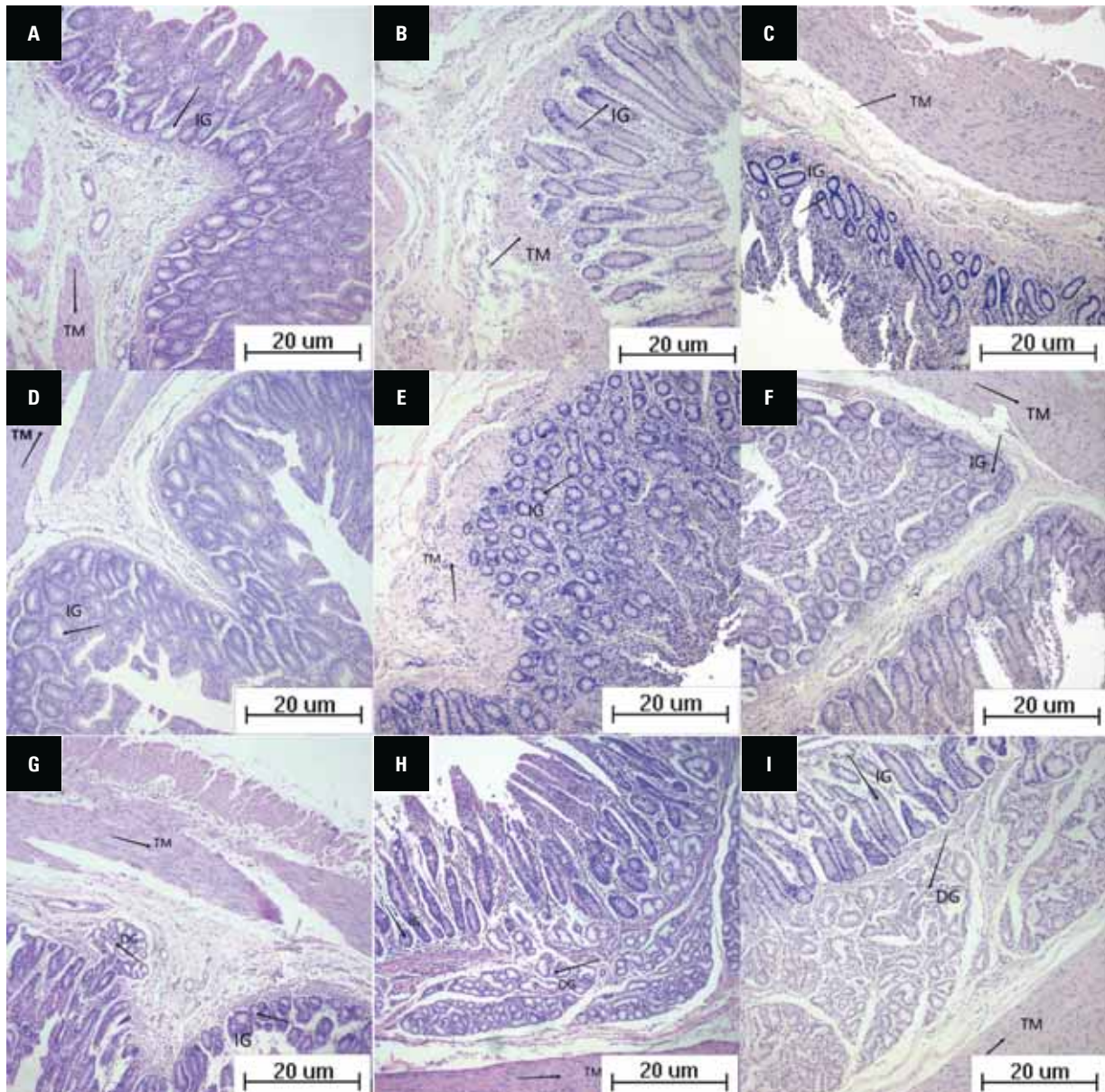
Figure 1. Histological observations of yak small intestine (100×); **A.** Newborn ileum; **B.** 50-day-old ileum; **C.** Adult ileum; **D.** Newborn jejunum; **E.** 50-day-old jejunum; **F.** Adult jejunum; **G.** Newborn duodenum; **H.** 50-day-old duodenum; **I.** Adult duodenum; IG — intestinal gland; DG — duodenal gland; TM — tunica muscularis; IGC — intraepithelial goblet cell.

a comb; jejunum villi are sparse and foliate; and ileum villi are dense and finger-like. There are many mall intestinal glands in the lamina propria of the duodenum, jejunum, and ileum. Duodenal glands are seen in the submucosa of the duodenum, isolated lymph nodes are occasionally seen in the submucosa of the jejunum, and numerous clustered lymph nodes are seen in the submucosa of the ileum. There were some differences in the small intestine morphology in yaks at different developmental stages.

The results showed that the intestinal wall of yaks was composed of the mucosa, submucosa, muscularis, and outer membrane. The mucosa was composed of villi, lamina propria, and mucosal muscularis. Intestinal mucosa formed a large number of intestinal villi, protruding into the intestinal lumen. There were some differences in the small intestine morphology in yaks at different developmental stages.

Compared with the jejunum and ileum, the duodenal villi of newborn yaks were leaf-like and sparsely distributed. The columnar cells of the small intestinal villi are distributed in a single layer, and the nuclei, which are closely arranged in the base of the epithelial cells of the small intestinal villi, are oval or round.
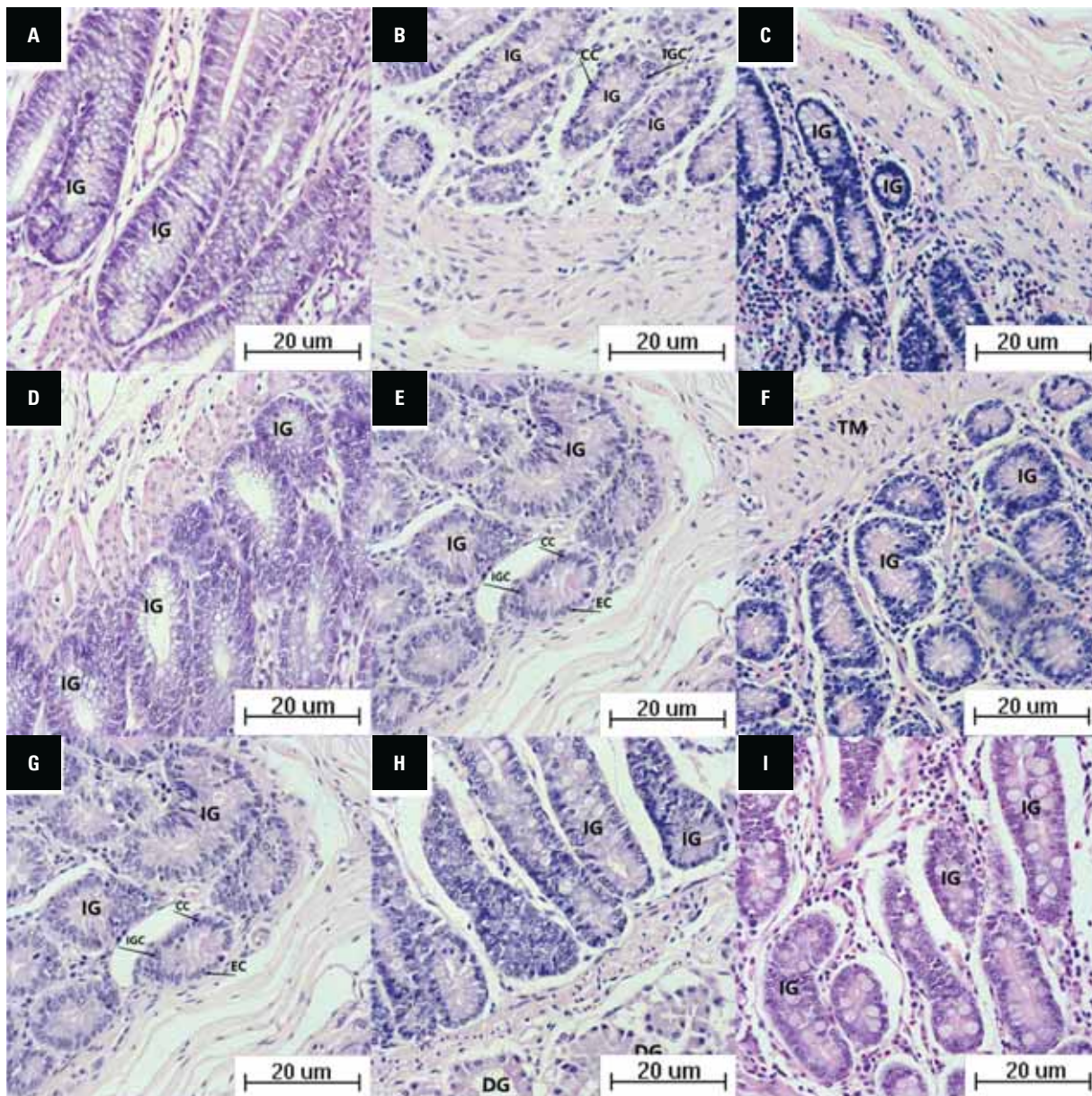
Figure 2. Histological observations of yak small intestine (400×); **A**. Newborn ileum; **B**. 50-day-old ileum; **C**. Adult ileum; **D**. Newborn jejunum; **E**. 50-day-old jejunum; **F**. Adult jejunum; **G**. Newborn duodenum; **H**. 50-day-old duodenum; **I**. Adult duodenum; IG — intestinal gland; DG — duodenal gland; TM — tunica muscularis; IGC — intraepithelial goblet cell.

There are goblet cells and scattered lymphocytes between the epithelial cells. A few of the villi appear on the surface of the folds, similar to the cerebral furrows. Scattered lymphocytes were seen in the lamina propria in the central villi of the small intestine, but no aggregative lymphoid nodule was formed. Many intestinal glands were distributed in the lamina propria of the mucosa, and a small number of duodenal glands were distributed in the submucosa (Figs. 1, 2A, D, G). The jejunum villi of newborn yaks are rod-shaped, slender, and dense. The ileum and jejunum villi of newborn yaks are similar in shape but

shorter in length and sparsely arranged. The columnar cells at the top of the small intestine's villi contained a large number of vacuolar structures, and the nucleus was located at the base of the cells. The columnar cells in the villi from the centre downward had no vacuolar structures in the cytoplasm. Many intestinal glands and lymphoid aggregates were distributed in the lamina propria of the mucosa, and the lymphoid aggregates were dark and round or oval in shape (Figs. 1, 2A, D, G).

The columnar cells in the villi of the small intestine of 50-day-old yak were arranged neatly, and the cell

Table 1. Average integrated optical density values of vascular endothelial growth factor (VEGF), VEGF receptor 2 (VEGFR-2), and erythropoietin (EPO) in small intestine of newborn yak, 50-day-old yak and adult yak (mean ± standard deviation)

Species	EPO	VEGF	VEGFR-2
Newborn yak	0.1076000 ± 0.074607774	0.130878 ± 0.1016521	0.00020000 ± 0.000327872
50-day-old yak	0.3320444 ± 0.039606651	0.056822 ± 0.0199790	0.02978889 ± 0.009988549
Adult yak	0.03253444 ± 0.01572786	0.043800 ± 0.0310143	0.00427300 ± 0.004416746

structure was normal. The width of duodenal villi decreased, and the morphology of jejunum and ileum villi did not change significantly. The villi length the small intestine decreased compared with that at birth. Many intestinal glands were distributed in the lamina propria of the small intestine, and the number of duodenal glands in the submucosa of the duodenum increased significantly compared with that at birth. The number and volume of lymphoid aggregates in the ileum are significantly increased and enlarged, oval or long-oval, and deeply stained, accounting for approximately 1/2 of the thickness of the wall of the ileum (Figs. 1, 2B, E, G). The villi morphology in the jejunum and ileum of adult yak had noticeable changes. The nuclear volume of villi columnar cells in the jejunum and ileum decreased obviously, and the cytoplasm was darker. The length of lymph aggregation in the ileum increased, accounting for approximately 3/4 of the wall thickness (Figs. 1, 2C, F, I).

Immunohistochemical localizations

Expression of VEGF, VEGFR-2, and EPO were detected in the small intestine of 50-day-old yaks in the positive control group (Figs. 3B, E, H; 4B, E, H; 5B, E, H, 6A–I). Immunohistochemical results showed that EPO was highly expressed in the ileum and villous epithelial cells in 50-day-old yaks, but showed lower expression in newborns and adults. In newborn yak jejunum intestines and a strong positive expression in intestinal villus epithelial cells, and intestinal villus epithelial cells in adult yak's jejunum intestines positive expression, 50 days of age in yak and jejunum was weakly positive expression in intestinal villus epithelial cells, the newborn yak duodenal glands and a strong positive expression in intestinal villus epithelial cells. Expression was high in the duodenal glands and intestinal villus epithelial cells of adult yak, but lower in those of 50-day-old yak. VEGF was highly expressed in the ileo-intestinal glands and villous epithelial cells of newborn yaks, and lower in those cells in 50-day-old and adult yaks.

It was highly expressed in the jejunal intestinal glands and villous epithelial cells of newborn yaks, and weakly positive in jejunal intestinal glands and villous epithelial cells of 50-day-old and adult yaks. It was highly expressed in duodenal glands and intestinal villus epithelial cells of 50-day-old yaks, lower in those cells in adult yaks as well as in newborn yaks. VEGFR-2 was strongly positive in duodenal gland and intestinal villi epithelial cells, strongly positive in adult yak and jejunum ileum adenoma positive in intestinal villi epithelial cells, weakly positive in newborn yak and jejunum gland, and weakly positive in duodenal gland and intestinal villi epithelial cells of adult yak. No expression was detected in the ileal intestinal glands and intestinal villus epithelial cells, or in the duodenal glands and intestinal villus epithelial cells of newborn yaks.

Optical density analysis

Results of average integrated optical density (Table 1) showed that the immunostaining intensity of VEGF was the highest in ileum of newborn yaks, followed by ileum of 50-day-old yaks and adult yaks ($p < 0.05$, Figs. 3, 6). The immunostaining intensity of VEGFR-2 was the highest in ileum of yaks at 50 days of age, followed by adult ileum and newborn ileum ($p < 0.05$, Figs. 4, 6). The immunostaining intensity of EPO was the highest in ileum of 50-day-old yaks, followed by ileum of newborn yaks and ileum of adult yaks ($p < 0.05$, Figs. 5, 6).

DISSCUSSION

Oxygen is an important substrate for aerobic organisms to maintain metabolism and physiological functions. As a result, vertebrates evolved complex respiratory and cardiovascular systems to ensure an optimal oxygen supply to each cell. Hypoxia is a biological limiting factor in most mammals and can lead to various organ diseases, such as kidney damage and pulmonary hypertension [18]. The ability of mammals living in anoxic environments, such as the Tibetan
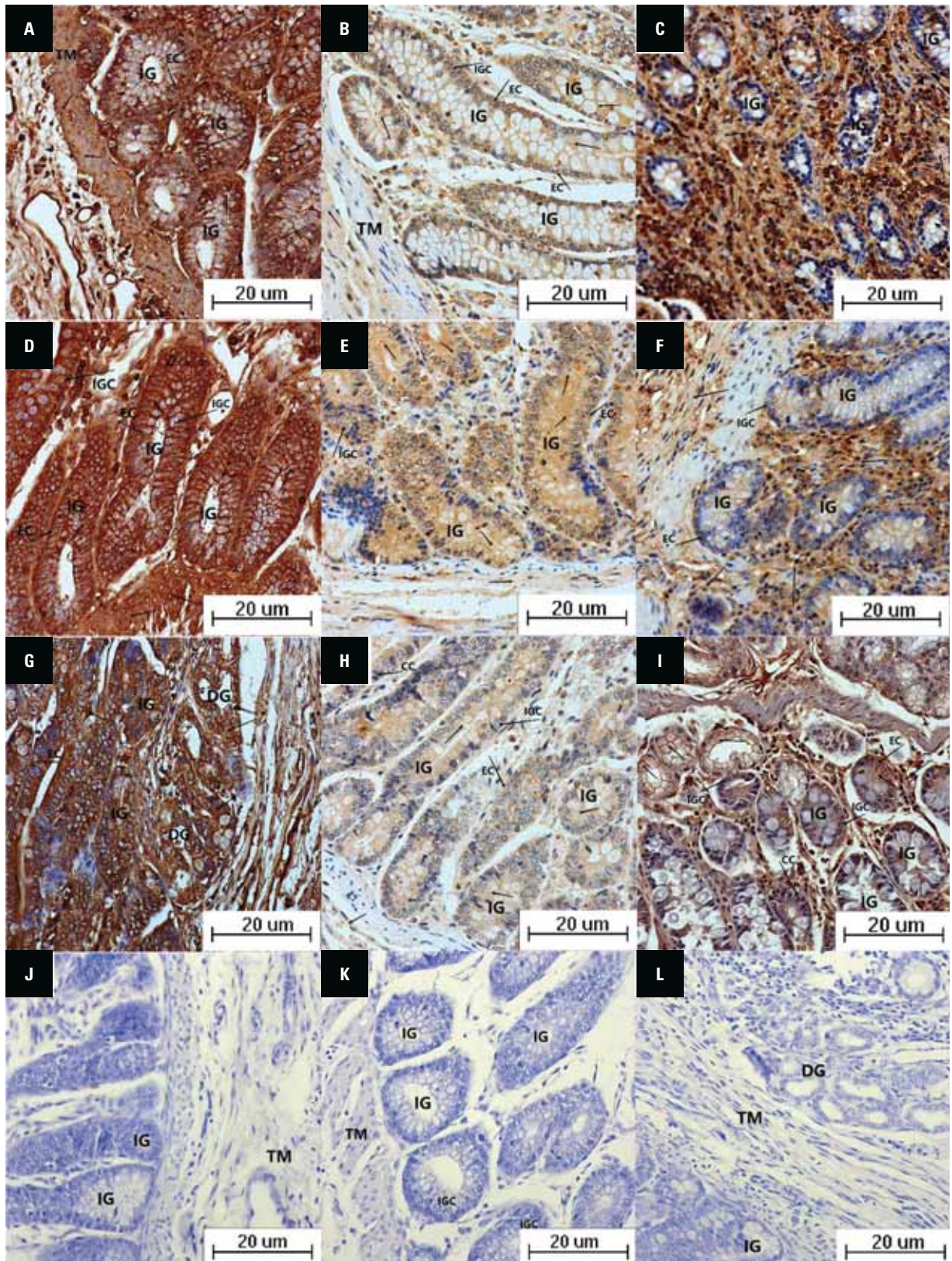
Figure 3. Representative endothelial growth factor (VEGF) immunostaining images. Immunohistochemical results for VEGF in the ileum; **A**, **B**, **C.** VEGF immunostaining for newborn ileum 50-day-old ileum and adult ileum, respectively; **D**, **E**, **F.** VEGF immunostaining for newborn jejunum, 50-day-old jejunum and adult jejunum, respectively; **G**, **H**, **I.** VEGF immunostaining for newborn duodenum, 50-day-old duodenum and adult duodenum, respectively; **J**, **K**, **L.** Negative immunohistochemical expression results for the ileum, jejunum, and duodenum; IG — intestinal gland; DG — duodenal gland; TM — tunica muscularis; IGC — intraepithelial goblet cell; CC — columnar cell; EC — endocrine cell; black arrows — positive expression.

689
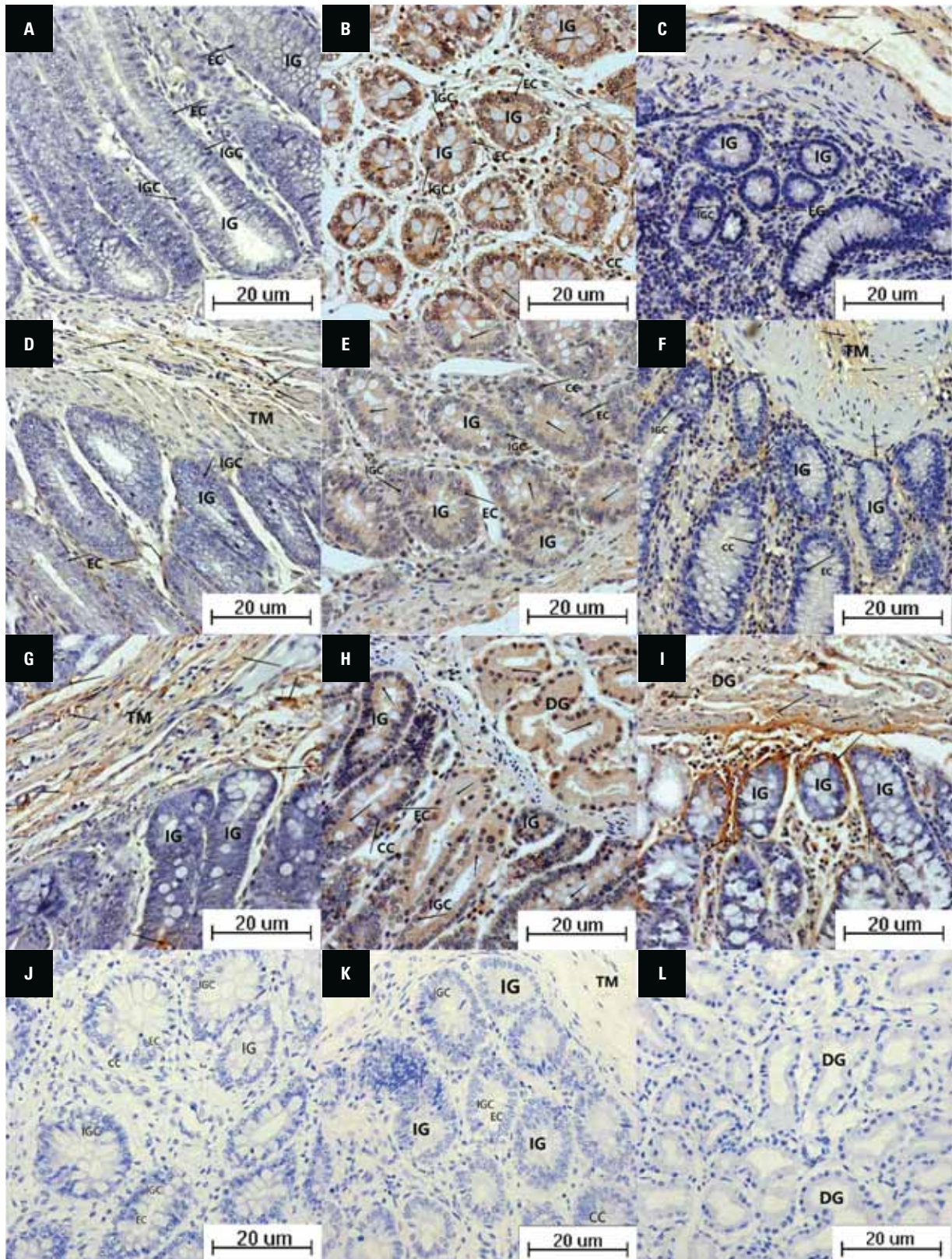
Figure 4. Representative endothelial growth factor receptor 2 (VEGFR-2) immunostaining images. Immunohistochemical results for VEGFR-2 in the ileum; **A**, **B**, **C**. VEGFR-2 immunostaining for newborn ileum 50-day-old ileum and adult ileum, respectively; **D**, **E**, **F**. VEGFR-2 immunostaining for newborn jejunum, 50-day-old jejunum and adult jejunum, respectively; **G**, **H**, **I**. VEGFR-2 immunostaining for newborn duodenum, 50-day-old duodenum and adult duodenum, respectively; **J**, **K**, **L**. Negative immunohistochemical expression results for the ileum, jejunum, and duodenum; IG — intestinal gland; DG — duodenal gland; TM — tunica muscularis; IGC — intraepithelial goblet cell; CC — columnar cell; EC — endocrine cell; black arrows — positive expression.
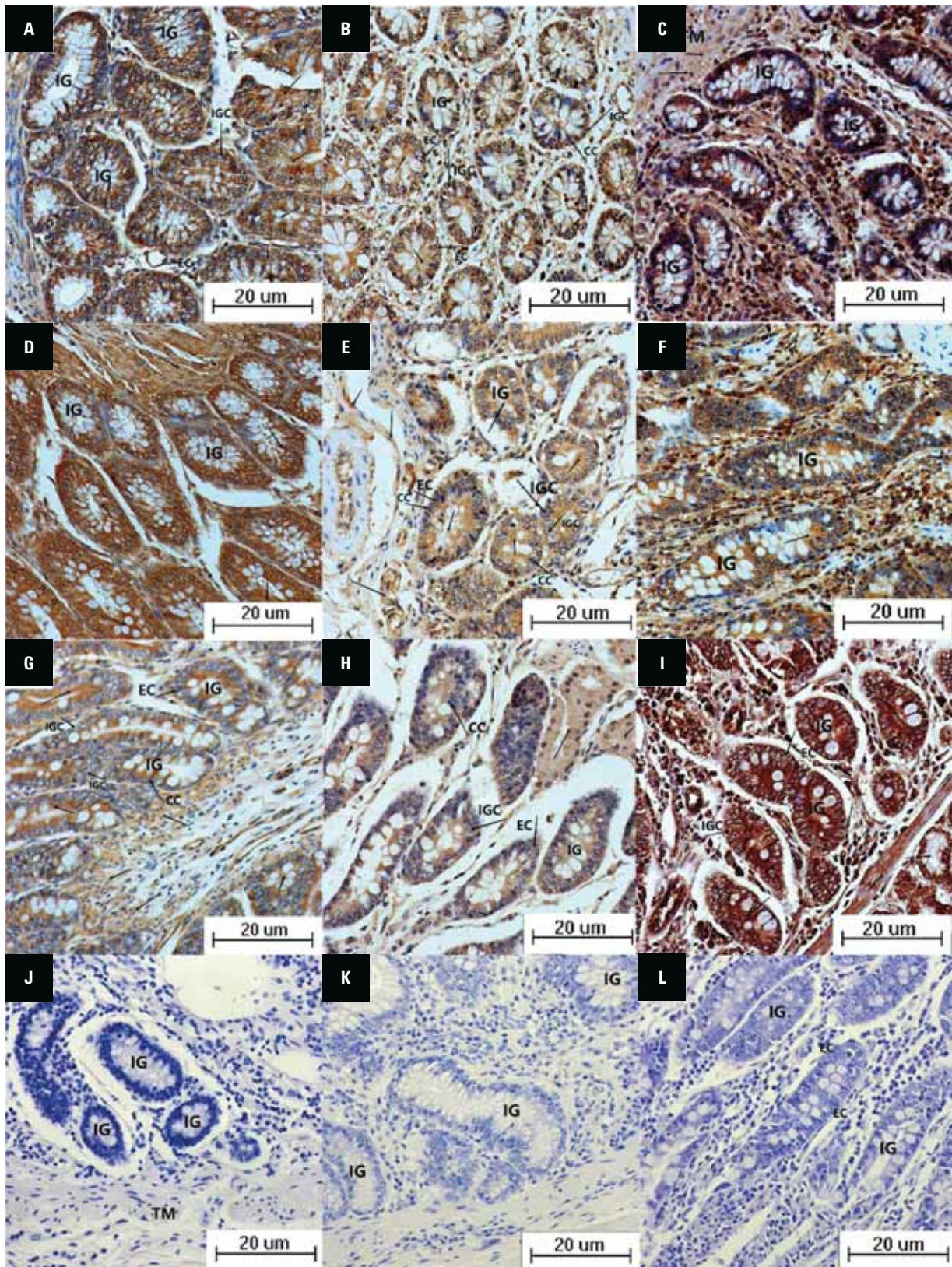
Figure 5. Representative erythropoietin (EPO) immunostaining images; **A, B, C.** EPO immunostaining for newborn ileum 50-day-old ileum and adult ileum, respectively; **D, E, F.** EPO immunostaining for newborn jejunum, 50-day-old jejunum and adult jejunum, respectively; **G, H, I.** EPO immunostaining for newborn duodenum, 50-day-old duodenum and adult duodenum, respectively; **J, K, L.** Negative immunohistochemical expression results for the ileum, jejunum, and duodenum; IG — intestinal gland; DG — duodenal gland; TM — tunica muscularis; IGC — intraepithelial goblet cell; CC — columnar cell; EC — endocrine cell; black arrows — positive expression.
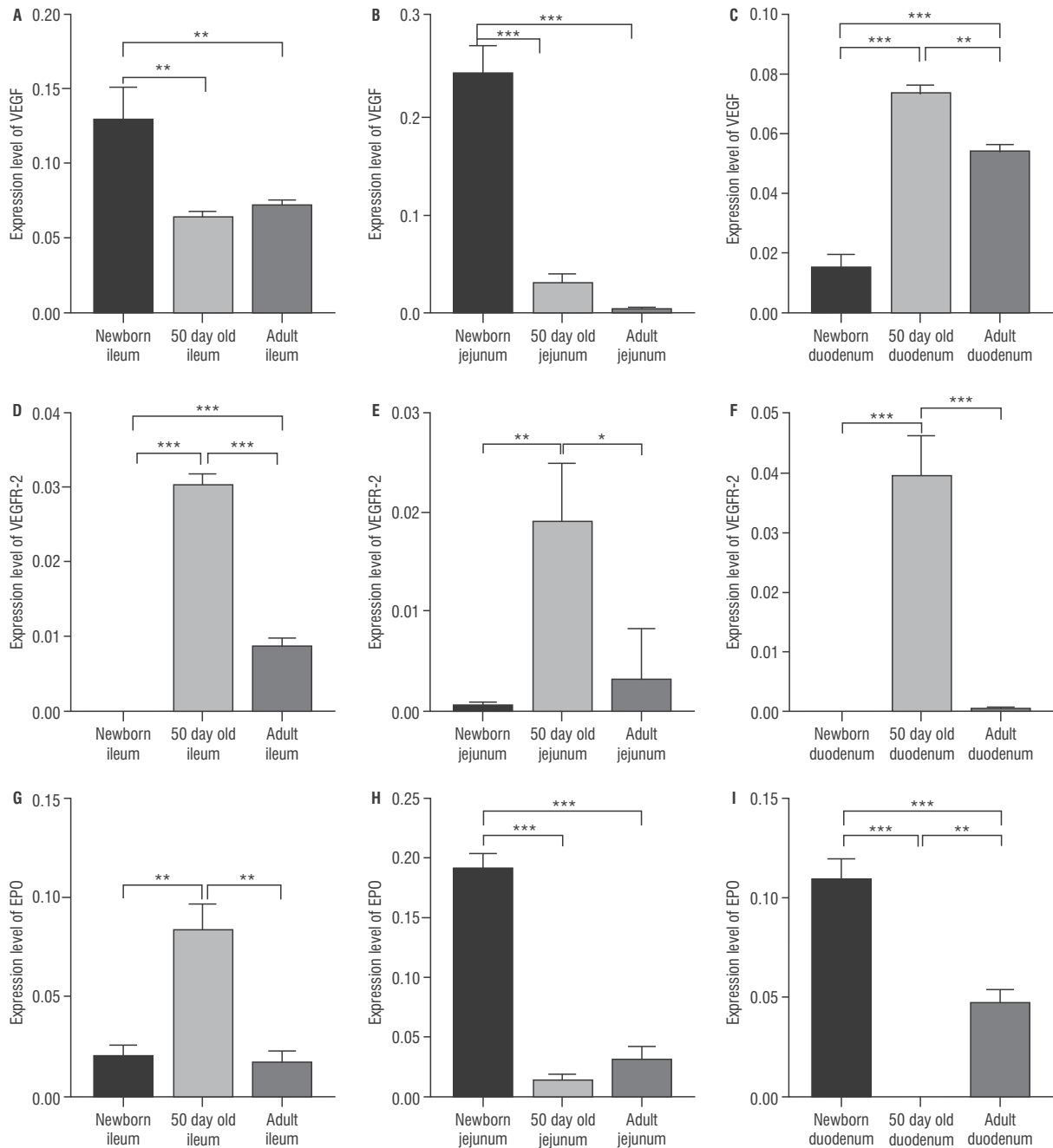
Figure 6. Comparison of the integrated optical density values for vascular endothelial growth factor (VEGF), VEGF receptor 2 (VEGFR-2), and erythropoietin (EPO) among the studied samples; **A, B, C.** One way ANOVA of VEGF in ileum, jejunum and duodenum at different ages; **D, E, F.** One-way ANOVA of VEGFR-2 in ileum, jejunum and duodenum at different ages; **G, H, I.** One-way ANOVA of EPO in ileum, jejunum and duodenum at different ages. Data was analysed using one-way ANOVA. The values are shown as the mean ± standard deviation; * and *** indicate significant differences of $p < 0.05$ and $p < 0.0001$, respectively; **represents a significant difference.

Plateau, to maintain homeostasis depends heavily on proper respiratory regulation and blood pressure. At the same time, hypoxic conditions can activate cellular sensing mechanisms, focusing on restoring oxygen to hypoxic areas to maintain cell viability [8]. The small intestine, especially its epithelial cells, is susceptible to hypoxia. Intestinal epithelium plays an important role

in nutrient absorption and nonpathogenic antigen tolerance, and is regulated by oxygen supply. In recent years, it has been increasingly recognized that tissue oxygen metabolism is the key to maintaining intestinal intraepithelial homeostasis. The unique oxygen tolerance of normal intestinal epithelium may be an adaptive adjustment to extremely low oxygenation

levels. Hypoxic responses play a vital role in various biological processes in the body and are the pathogenesis of various diseases such as gastrointestinal diseases, tumours, and cardiovascular diseases. Nutrient absorption takes place mainly through small intestinal villi, and its morphology plays a great role in nutrient absorption and utilisation. Studies have shown that when the height of small intestinal villi decreases or the shape changes, it will affect the number of absorbing cells in the villi per unit area, thus affecting the digestion and absorption area, reducing the function of digestion and absorption, and seriously affecting the growth and development of animals. In this study, EPO, VEGF and VEGFR-2 showed was highly expressed in yak. Intestinal villous epithelial cells and intestinal glands.

Erythropoietin is a glycoprotein cytokine that plays a role in the proliferation, differentiation, and maturation of erythrocyte progenitors. EPO and its receptors are widely distributed in different tissues of an infant's intestines, suggesting that EPO may play a role in gastrointestinal development. Previous studies have shown that recombinant EPO can reduce the inflammatory response, autophagy and apoptosis, and limit intestinal mucosal necrosis, thereby improving necrotizing enterocolitis damage. EPO production is induced under conditions of anaemia and hypoxia to control red blood cell production and is necessary for the maintenance of normal blood oxygen concentrations [10]. The small intestine tissue sections indicated that EPO was highly expressed in the intestinal glands, duodenal glands, and intestinal villus epithelial cells. The expression intensity in neonatal yaks ileum was higher than that in adult ileum and 50-day-old yaks ileum. The expression intensity in the jejunum of newborn yak was higher than that in the jejunum of 50-day-old yaks and higher than that in the jejunum of adult yaks. The expression intensity in 50-day-old yaks duodenum was higher than that in adult yaks duodenum and higher than that in newborn yaks duodenum. The expression level in ileal glands and villous epithelial cells of 50-day-old yaks was higher than that in adult yaks and higher than that in newborn yaks. Hypoxia stimulates the expression of EPO, further increasing red blood cells, enhancing oxygen supply capacity, and promoting angiogenesis and reconstruction. EPO is an important protein that enables yak, and other plateau animals, adapt to the low oxygen environment at high altitude VEGF and VEGFR-2 play key roles in angiogenesis

and cell proliferation. VEGF can promote blood flow by promoting the formation of blood vessels in hypoxic areas, thus alleviating tissue damage caused by hypoxia [19]. In endothelial cells, much of the bioactivity of VEGF is mediated by VEGFR-2 [10]. After soft tissue injury, strong expression of VEGF can interact with platelet-derived growth factor or basic fibroblast growth factor to promote the rapid generation of mature vascular networks, and the expression of VEGF increases from the angiogenesis stage. It was observed that VEGF and VEGFR-2 were mainly expressed in the intestinal glands, duodenal glands, and intestinal villus epithelial cells in small intestine tissue sections. The expression of VEGF in the ileum and jejunum of newborn yaks was significantly higher than in adult yaks and 50 days of age. The expression of VEGFR-2 in the small intestine of 50-day-old yaks was significantly higher than in that of newborn and adult yaks. These results suggest that VEGF and VEGFR-2 play important roles in the effects of hypoxia on the small intestine of yaks of different ages. Vascular endothelial growth factor A (VEGF-A) and its receptor (VEGFR-2) are the major signalling pathways involved in tumour angiogenesis. Previous studies have shown that increased VEGFR-2 expression is associated with differentiation, metastasis/recurrence, and poor prognosis in colon cancer samples [16]. These findings suggest that VEGFR-2 is functional on the surface of endothelial cells and that VEGFR-2 has potential as an anti-angiogenic cancer therapy molecule.

Erythropoietin mediates neurovascular remodelling and neurobehaviuoral recovery in traumatic brain injury rats by increasing intracerebral VEGF expression and VEGFR-2 phosphorylation. Yang et al. [20] demonstrated that VEGF-A activates EPOR and enhances VEGFR-2-mediated retinal angiogenesis in an oxygen-induced retinopathy rat model. Nakano et al. [11] demonstrated that EPO upregulation of the VEGF/VEGFR-2 system plays an important role in the mobilisation of epithelial cells in ischaemic tissues. They showed that vascular EPOR and EPO promote postischaemic angiogenesis by increasing VEGF secretion in ischaemic muscle, mobilisation of epithelial cells, and recruitment of bone-marrow pro-angiogenic cells to ischaemic tissue [11]. This study found that when the expression level of EPO increased in the ileum and jejunum of yaks, the expression level of VEGF also increased. This confirmed that EPO regulates the formation of blood vessels in

the yaks' intestinal tissue through the VEGF/VEGFR-2 pathway, enabling yaks to adapt to the hypoxic and cold environment at high altitude.

In our study, VEGF, VEGFR-2, and EPO were mainly expressed in the small intestinal villi of yaks of different ages, reflecting the adaptation of plateau yaks to the cold and anoxic environment (Fig. 6). Combined with previous studies, this study suggests that EPO, VEGF, and VEGFR-2 may be involved in the protection, structural maintenance, and function regulation of the small intestine in yaks of different ages in hypoxic environments.

CONCLUSIONS

The results showed that the expression and distribution characteristics of VEGF, VEGFR-2, and EPO in the small intestine of yaks of different ages might be related to physiological regulation in hypoxic environments. Therefore, they are considered important potential regulatory proteins of yak adaptation. However, the underlying molecular mechanisms remain unclear. This study is a preliminary experiment, and the regulation mechanism requires further investigation. This study also provides basic data from a comparative study of the small intestine of yaks of different ages in high altitude areas.

In our study, the expression intensity of VEGF in ileum and jejunum of newborn yaks was higher than that in ileum and jejunum, ileum and intestinal glands and villous epithelial cells of 50-day-old yaks and adults. The expression level in duodenal glands and intestinal villus epithelial cells of 50-day-old yaks was much higher than that in adult yaks and higher than that in newborn yaks. These results suggest that VEGF and VEGFR-2 play important roles in the effects of hypoxia on the small intestine of yaks of different ages. The expression intensity of VEGFR-2 in intestinal glands, villous epithelial cells and duodenal glands of 50-day-old yaks was much higher than that in adult and newborn yaks. These results suggest that VEGF and VEGFR-2 play important roles in reducing the effects of high altitude and low oxygen environment on the yak small intestine.

In our study, VEGF, VEGFR-2, and EPO were mainly expressed in the small intestinal villi of yaks of different ages which reflecting the adaptation of plateau yaks to the cold and hypoxic environment.

Research shows that the small intestine is anoxic sensitive organ; the oxygen level in the blood and the oxygen concentration that diffuses into the organ play a vital role in maintaining the metabolism of intestinal mucosa epithelial cells. Hypoxic conditions can result in serious damage of the intestinal mucosa epithelium.

Conflict of interest: None declared

REFERENCES

1. Alvarez Arroyo MV, Castilla MA, González Pacheco FR, et al. Role of vascular endothelial growth factor on erythropoietin-related endothelial cell proliferation. J Am Soc Nephrol. 1998; 9(11): 1998–2004, doi: 10.1681/ASN.V9111998, indexed in Pubmed: 9808085.

2. Elfar W, Gurjar AA, Talukder MA, et al. Erythropoietin promotes functional recovery in a mouse model of postoperative ileus. Neurogastroenterol Motil. 2021; 33(2): e14049, doi: 10.1111/nmo.14049, indexed in Pubmed: 33368893.

3. Haase VH. Regulation of erythropoiesis by hypoxia-inducible factors. Blood Rev. 2013; 27(1): 41–53, doi: 10.1016/j.blre.2012.12.003, indexed in Pubmed: 23291219.

4. Hernández-Morales J, Hernández-Coronado CG, Guzmán A, et al. Hypoxia up-regulates VEGF ligand and downregulates VEGF soluble receptor mRNA expression in bovine granulosa cells in vitro. Theriogenology. 2021; 165: 76–83, doi: 10.1016/j.theriogenology.2021.02.006, indexed in Pubmed: 33640589.

5. Honda T, Hirakawa Y, Nangaku M. The role of oxidative stress and hypoxia in renal disease. Kidney Res Clin Pract. 2019; 38(4): 414–426, doi: 10.23876/j.krcp.19.063, indexed in Pubmed: 31558011.

6. Klein M, Kaestner L, Bogdanova AY, et al. Absence of neocytolysis in humans returning from a 3-week high-altitude sojourn. Acta Physiol (Oxf). 2021; 232(3): e13647, doi: 10.1111/apha.13647, indexed in Pubmed: 33729672.

7. Koch S, Claesson-Welsh L. Signal transduction by vascular endothelial growth factor receptors. Cold Spring Harb Perspect Med. 2012; 2(7): a006502, doi: 10.1101/cshperspect.a006502, indexed in Pubmed: 22762016.

8. Labrousse-Arias D, Castillo-González R, Rogers NM, et al. HIF-2α-mediated induction of pulmonary thrombospondin-1 contributes to hypoxia-driven vascular remodelling and vasoconstriction. Cardiovasc Res. 2016; 109(1): 115–130, doi: 10.1093/cvr/cvv243, indexed in Pubmed: 26503986.

9. Munaut C, Lorquet S, Pequeux C, et al. Hypoxia is responsible for soluble vascular endothelial growth factor receptor-1 (VEGFR-1) but not for soluble endoglin induction in villous trophoblast. Hum Reprod. 2008; 23(6): 1407–1415, doi: 10.1093/humrep/den114, indexed in Pubmed: 18413304.

10. Murphy JF, Fitzgerald DJ. Vascular endothelial growth factor induces cyclooxygenase-dependent proliferation of endothelial cells via the VEGF-2 receptor. FASEB J. 2001; 15(9): 1667–1669, doi: 10.1096/fj.00-0757fje, indexed in Pubmed: 11427521.

11. Nakano M, Satoh K, Fukumoto Y, et al. Important role of erythropoietin receptor to promote VEGF expression and angiogenesis in peripheral ischemia in mice. Circ Res. 2007; 100(5): 662–669, doi: 10.1161/01.RES.0000260179.43672.fe, indexed in Pubmed: 17293480.

12. Page P, DeJong J, Bandstra A, et al. Effect of serum and oxygen con-centration on gene expression and secretion of paracrine factors by mesen-chymal stem cells. Int J Cell Biol. 2014; 2014: 601063, doi: 10.1155/2014/601063, indexed in Pubmed: 25614742.

13. Park SY, Jeong KJ, Lee J, et al. Hypoxia enhances LPA-induced HIF-1alpha and VEGF expression: their inhibition by resveratrol. Cancer Lett. 2007; 258(1): 63–69, doi: 10.1016/j.canlet.2007.08.011, indexed in Pubmed: 17919812.

14. Shiratsuki S, Hara T, Munakata Y, et al. Low oxygen level increases proliferation and metabolic changes in bovine granulosa cells. Mol Cell Endocrinol. 2016; 437: 75–85,

doi: 10.1016/j.mce.2016.08.010, indexed in Pubmed: 27519633.

15. Tomc J, Debeljak N. Molecular insights into the oxygen-sensing pathway and erythropoietin expression regulation in erythropoiesis. Int J Mol Sci. 2021; 22(13), doi: 10.3390/ijms22137074, indexed in Pubmed: 34209205.

16. Tong Q, Zheng L, Lin Li, et al. VEGF is upregulated by hypoxia-induced mitogenic factor via the PI-3K/Akt-NF-kappaB signaling pathway. Respir Res. 2006; 7(1): 37, doi: 10.1186/1465-9921-7-37, indexed in Pubmed: 16512910.

17. Westenbrink BD, Ruifrok WPT, Voors AA, et al. Vascular endothelial growth factor is crucial for erythropoietin-induced improvement of cardiac function in heart failure. Cardiovasc Res. 2010; 87(1): 30–39, doi: 10.1093/cvr/cvq041, indexed in Pubmed: 20139114.

18. Will DH, Hicks JL, Card CS, et al. Inherited susceptibility of cattle to high-altitude pulmonary hypertension. J Appl Physiol. 1975; 38(3): 491–494, doi: 10.1152/jappl.1975.38.3.491, indexed in Pubmed: 238929.

19. Yang K, Zhang Z, Li Y, et al. Expression and distribution of HIF-1α, HIF-2α, VEGF, VEGFR-2 and HIMF in the kidneys of Tibetan sheep, plain sheep and goat. Folia Morphol. 2020; 79(4): 748–755, doi: 10.5603/FM.a2020.0011, indexed in Pubmed: 32020576.

20. Yang Z, Wang H, Jiang Y, et al. VEGFA activates erythropoietin receptor and enhances VEGFR2-mediated pathological angiogenesis. Am J Pathol. 2014; 184(4): 1230–1239, doi: 10.1016/j.ajpath.2013.12.023, indexed in Pubmed: 24630601.

Anatomical identification of supraseptal posterior ethmoid cells and its significance for endoscopic sinus surgery

J. Liu[1] , Y. Wang[1], Z. Yan[2], Y. Yang[3]

[1]Department of Otorhinolaryngology Head and Neck Surgery, Beijing Chaoyang Hospital, Capital Medical University, Beijing, P.R. China
[2]Department of Otorhinolaryngology, Beijing University of Chinese Medicine Affiliated Dongzhimen Hospital, Beijing, P.R. China
[3]Department of Otolaryngology, Beijing Hospital, National Centre of Gerontology, Institute of Geriatric Medicine, Chinese Academy of Medical Sciences, Beijing, P.R. China

Background: To investigate the anatomical imaging characteristics of supraseptal posterior ethmoid cells (SPEC).

Materials and methods: Paranasal sinus computed tomography scans of 153 inpatients from February 2019 to September 2021 were reviewed, and the anatomical characteristics of SPEC in the scans were collected.

Results: Supraseptal posterior ethmoid cells are posterior ethmoid (PE) cells extending medially and superiorly to the posterior superior of the nasal septum and into the sphenoid body but not close to the optic canal. The SPEC, Onodi cell, and sphenoidal sinus (SS) may appear in the posterior superior of the nasal septum, but the occurrence rate of the SPEC (5.88%; 9/153 cases) was significantly lower than that of the SS (22.88%) and Onodi cell (21.57%). The anterior SPEC is adjacent to the cribriform plate, the perpendicular plate of the ethmoid bone and the posterior ethmoidal artery (PEA). The posterior SPEC is adjacent to the SS and PE (6/9 cases), the SS and Onodi cell (2/9 cases) or the PE only (1/9 cases).

Conclusions: The SPEC is a rare pneumatization that occurs in the posterior superior area of the nasal septum. Care should be taken to protect the skull base, cribriform plate and PEA when opening the SPEC during endoscopic sinus surgery. (Folia Morphol 2023; 82, 3: 696–703)

Key words: ethmoid sinus, posterior ethmoid cell, sphenoid sinus, anatomic variation, endoscopic sinus surgery, tomography, X-ray computed

INTRODUCTION

Pneumatization of the nasal septum has aroused great interest from scholars in recent years [4, 12, 13, 16]. Pneumatization of the anterior nasal septum mainly originates from the frontal recess and crista galli, then extending to the perpendicular plate of the ethmoid bone (PPE), which is known as the sinus septi nasi [13]. Furthermore, ethmoid cells can expand to the posterior superior of the nasal septum [4, 16].

The cell in the posterior nasal septum has been reported and focused on because of the pneumatization observed in the computed tomography (CT) coronal plane that occurs in the superior or middle area of the posterior nasal septum [12, 13]. In fact, the so-called air cell in the middle of the posterior nasal septum is essentially pneumatization of the sphenoid rostrum; it is found on the coronal plane and is not an independent air cell [13]. A similar situation can also occur above the posterior nasal septum, with the sphenoid sinus (SS) extending anteriorly and superiorly on one side; it appears in the coronal plane rather than as an independent air cell. In addition, posterior ethmoid (PE) cells extend to the SS to form the superolateral type (Onodi cell), inferolateral type (Jinfeng cell) and whole lateral type of sphenoethmoidal cells [7, 9]. Some sphenoethmoidal cells can also expand anteriorly and medially, being displayed in the coronal plane [16]. Hence, there are many originations of the cell in the posterior superior of the nasal septum, which need to be carefully identified.

In the present study, the cell we focused on and described is an independent air cell that is formed by pneumatization expansion of the PE cells to the posterior superior of the nasal septum but is not adjacent to the optic canal, which is called a supraseptal posterior ethmoid cell (SPEC). This retrospective analysis of the anatomical features of the SPEC in CT scans is intended to help surgeons open it safely during endoscopic sinus surgery (ESS) because of its important anatomical location [16].

MATERIALS AND METHODS

Study design

We conducted a retrospective analysis of paranasal sinus CT scans obtained from adult inpatients seen in our hospital from February 2019 to September 2021. All of these patients underwent a routine paranasal sinus CT scan because of sinus disease or nasal septum deviation and to confirm the clinical symptoms or determine diagnosis. CT scans were also intended to obtain accurate anatomy before ESS [15].

Each CT scan was performed in the Radiological Department, Beijing Chaoyang Hospital, Capital Medical University. A total of 153 patients were included, and their CT images were reviewed and analysed. Some of these CT data have been used in a previous study [8]. The collection of these CT data was approved by the Ethics Committee of Capital Medical University affiliated with Beijing Chaoyang Hospital. The study was also conducted in accordance with the Helsinki Declaration.

The enrolment criteria were as follows: 1) no history of head or sinus injury; 2) no history of sinonasal surgery or septoplasty; 3) clear PE, nasal septum and SS anatomical structures; and 4) age older than 18 years. Cases were excluded if CT findings of sinonasal disease (e.g., neoplasm, fungal sinusitis, osteofibroma, fibrous dysplasia or chronic rhinosinusitis) involving the PE or SS occurred [9].

CT examination and analysis

The CT scanning range spanned from the superior margin of the frontal sinuses to the inferior margin of the maxillary alveolar process. A GE Lightspeed 64-slice spiral CT (USA) system was used with a bone imaging algorithm. CT scans were obtained at a section thickness of 0.625 mm and an interval of 0.5 mm. The following parameters of acquisition were used: 120 kV, 320 mA, collimation 40 × 0.6 mm, tube rotation 1 s, matrix size 512 × 512, and reconstruction thickness 3 mm [7, 9].

The GE system was used to obtain multiplanar reconstructions using three anatomical planes. The standard plane of coronal reconstruction requires being perpendicular to the hard palate to minimise the effect of the reconstruction plane on the observations (Fig. 1). An indicator line of reconstruction is shown in Figure 1, and this reconstruction was designed to avoid the excessive forward or backward inclination of the reconstruction plane to affect the appearance of the cell on the coronal plane.

GE Centricity Enterprise Web 3 software (GE Medical Systems) was used for viewing and measuring. Continuous observation was performed by sliding the computer mouse. The posterior nasal septum and its adjacent SS and PE were the main structures that were observed.

Identification of the SPEC

Definition of the SPEC. Below the sphenoid planum, the PE was expanded above the posterior nasal septum but was not adjacent to the optic nerve. We referred to this cell as the SPEC (Figs. 2–4).

Determination of the SPEC. On the midsagittal plane, the posterior edge of the hard palate serves as the posterior boundary of the nasal septum. Before the posterior edge, if the PE could be seen at the top of the posterior nasal septum in the coronal
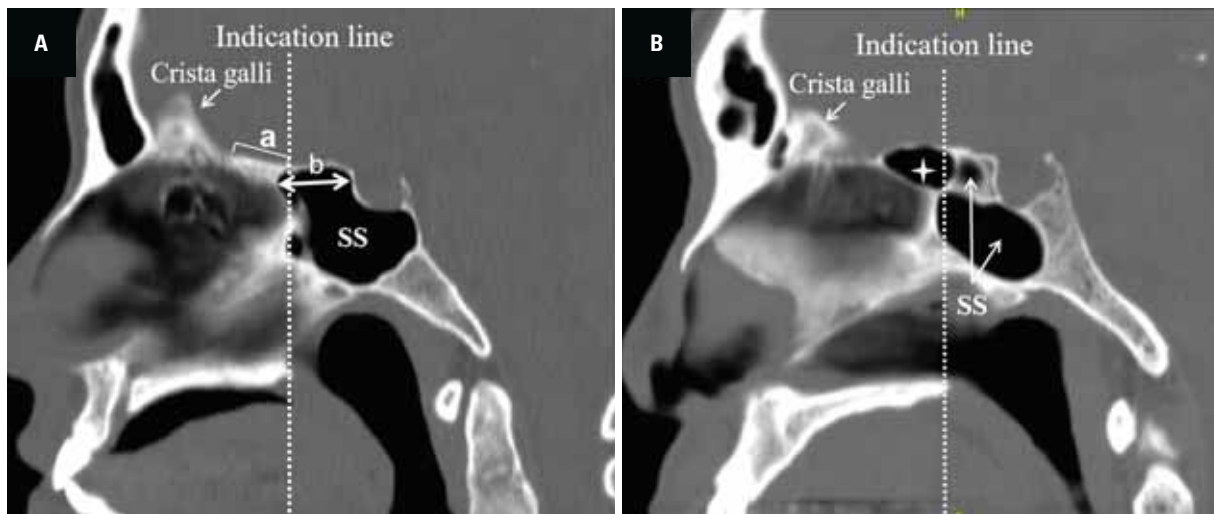
Figure 1. The location line of the coronal reconstruction of the computed tomography scan (the indication line in the midsagittal plane); **A.** The area a is the sphenoid bone under the sphenoid planum, which is a potential area for the pneumatization and expansion of the air cell. Line 'b' indicates the range of the anterior extension of the sphenoidal sinus (SS); **B.** The asterisk refers to the supraseptal posterior ethmoid cells displayed in the midsagittal plane, and this pneumatization position is area 'a' of panel A (panel B were obtained from the patient presented in Figure 2).

Figure 2. The location of the supraseptal posterior ethmoid cells (SPEC) in the coronal and axial plane of the computed tomography (CT) images. A series of coronal CT scans (**A–C**) showing that a cell (indicated by the arrow) lies to the posterior superior area of the nasal septum. An axial CT scan of the top-down series (**D–F**) showing the SPEC (indicated by the star) located between the two sphenoidal sinus (SS) and the perpendicular plate of the ethmoid bone. The SPEC is connected to the left posterior ethmoid and drains into it; PEA — posterior ethmoidal artery.

plane, this PE was identified as an SPEC (Figs. 2–4). As observed on consecutive sections in all three planes (axial, coronal and sagittal), if the posterior superior cell of the nasal septum was an Onodi cell or/and the SS, it was identified and excluded (Figs. 5–7). SPEC identification was performed by one otolaryngolo-gist (L.J.), and cases of SPEC were confirmed by two otolaryngologists working together (L.J. and W.Y.).

Determination of the Onodi cell

The Onodi cell is the most posterior ethmoid air cell that pneumatizes superolateral, superior, or lat-

Figure 3. The axial plane of computed tomography scan shows the adjacent structure of the supraseptal posterior ethmoid cells (SPEC) (indicated by the solid triangle). Panel **A** shows the posterior portion of the SPEC adjacent to the posterior ethmoid (PE), panels **B–D** show that the posterior portion of the SPEC is adjacent to the sphenoidal sinus (SS). In addition, the SPEC can be adjacent to the PE or Onodi cell on both sides (**B**, **C**) or on one side (**D**).
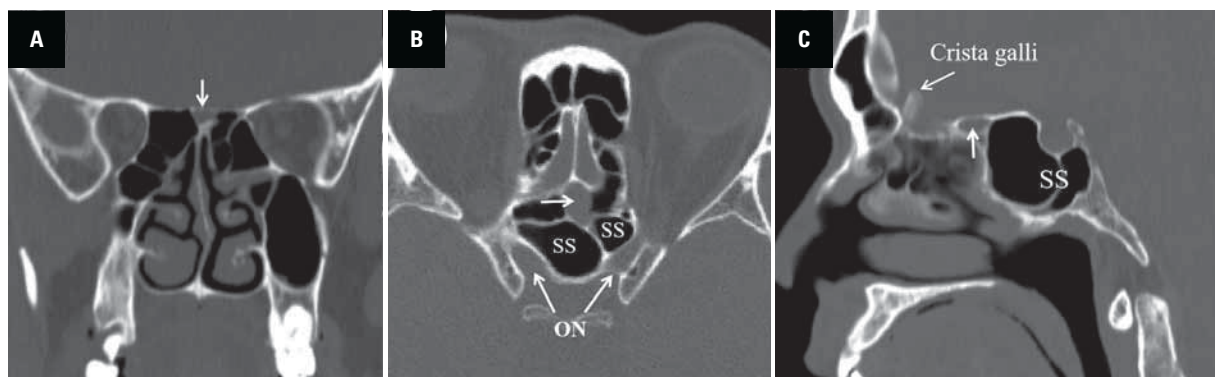
Figure 4. Axial, coronal and sagittal planes (**A–C**) show isolated opacities within the supraseptal posterior ethmoid cells (indicated by the arrow); SS — sphenoidal sinus; ON — optic nerve.

eral to the SS and surrounds the optic canal; it penetrates into the anterior clinoid process (Fig. 5) [9, 11].

Statistical analysis

Data regarding patient age are presented as the mean ± standard deviation. Descriptive statistics were determined using SPSS (version 17.0, SPSS, Inc., USA). Incidence rates of the SPEC were calculated to two decimal places. The difference in incidence for the posterior superior cells of the nasal septum (SPEC, Onodi cell and SS) was calculated and evaluated by the chi-squared test. Differenc-
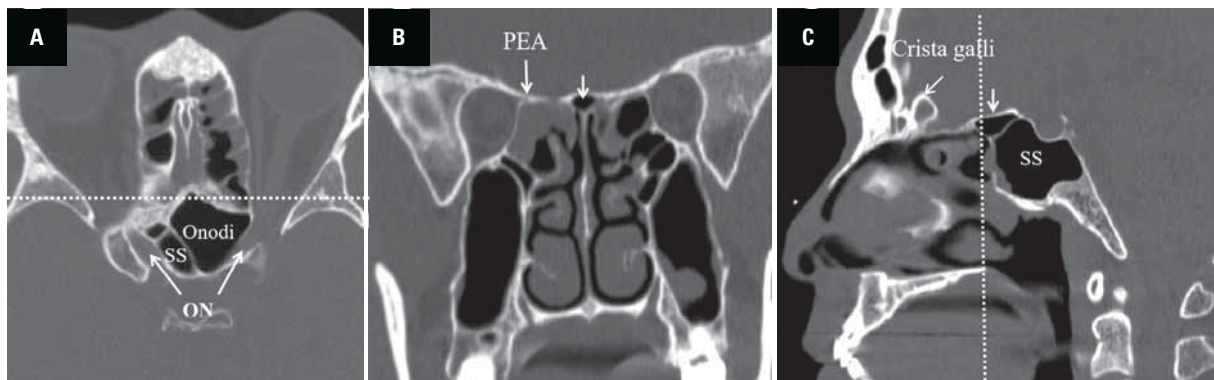
Figure 5. Anterior expansion of the left Onodi cell; panel **A** shows the anterior expansion of the left Onodi cell between the posterior-superior nasal septum and the sphenoid planum. It looks like a supraseptal posterior ethmoid cells in the coronal plane (indicated by the arrow in panels **B** and **C**). The white lines in panels **A** and **C** indicate the reconstruction position in the coronal plane (**B**). In the sagittal plane (**C**), the Onodi cell occupies the entire region under the sphenoid planum at the midline position; PEA — posterior ethmoidal artery; SS — sphenoidal sinus; ON — optic nerve.
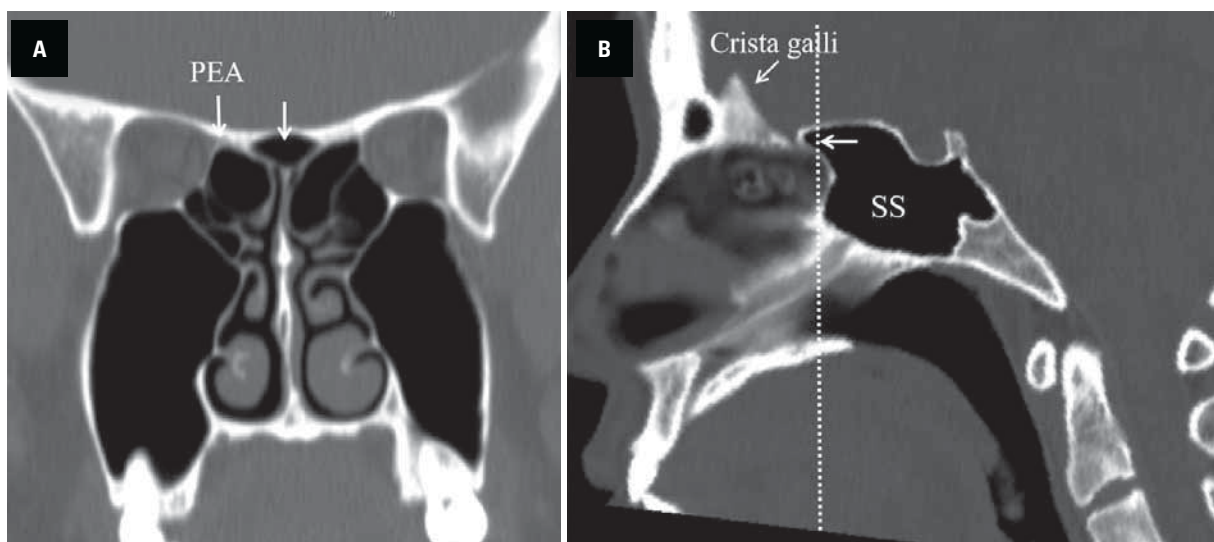
Figure 6. Anterior superior expansion of the sphenoidal sinus (SS). The SS extends anteriorly and superiorly (indicated by the arrow in panels **A** and **B**), filling the entire sphenoid planum (**B**). It looks like a supraseptal posterior ethmoid cells appears in the coronal plane (indicated by the arrow) (**A**); PEA — posterior ethmoidal artery.

es with a p < 0.05 were accepted as statistically significant.

RESULTS

General characteristics of the SPEC

The paranasal sinus CT images of 153 patients ranging in age from 18 to 80 years (mean 42.53 ± ± 13.51 years) were reviewed and analysed. Of them, 102 were males and 51 females. If the origination of air cells was not distinguished, the air cells could be seen in the posterior superior of the nasal septum in 50.33% of the patients (77/153 cases) on the coronal plane CT scan. However, most of the posterior supe-

rior cells of the nasal septum that were displayed on the coronal plane originated from the anterior and superior pneumatization of the Onodi cell (21.57%; 33/153 cases) and the SS (22.88%; 35/153 cases) under the sphenoid planum. The occurrence rates of the SS and Onodi cell were significantly higher than those of the SPEC (5.88%, 9/153 cases) ($\chi^2 =$ = 15.896; p = 0.000; $\chi^2 = 17.944$; p = 0.000) (Table 1). The SPEC observed originated from the left PE (Figs. 2–4). The incidence of the SPEC in females was 7.84% (4/51 cases), slightly higher than that in males (4.90%, 5/102 cases), though the difference was not significant ($\chi^2 = 0.133$; p = 0.716).
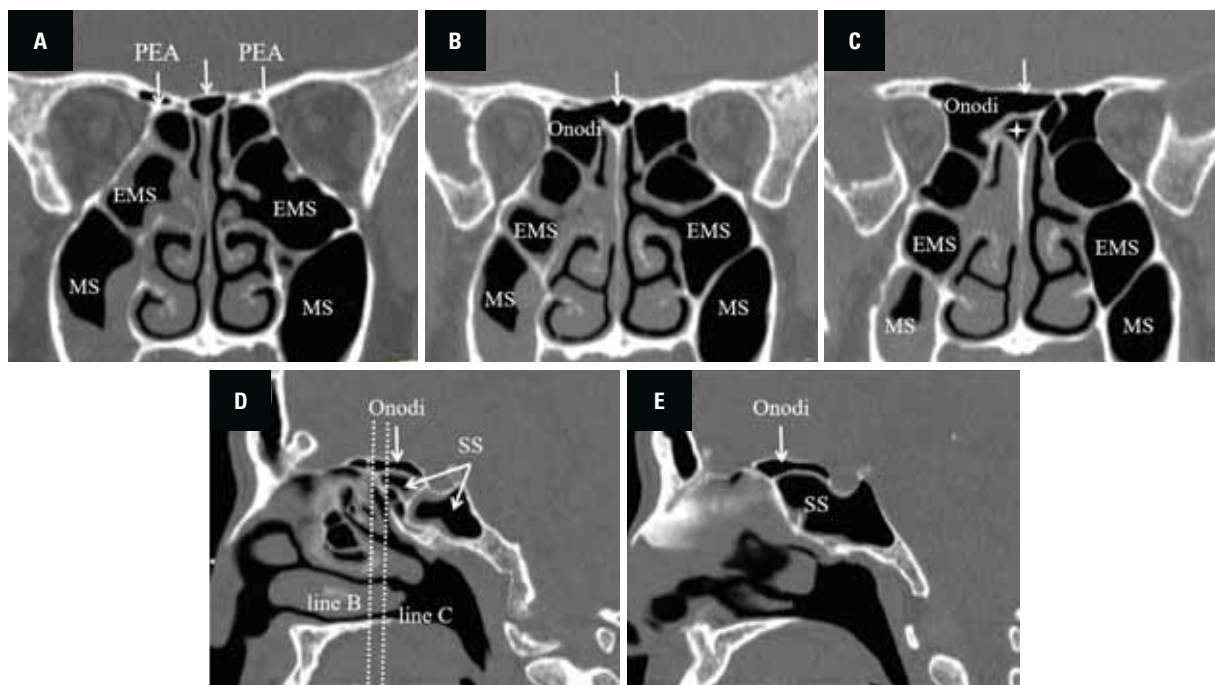
Figure 7. Anterior expansion of the Onodi cell and sphenoidal sinus (SS) simultaneously. A series of coronal computed tomography scans show that a rare variant, the Onodi cell (**A–C**), is above the SS (indicated by star); both cells extend to the posterior-superior nasal septum simultaneously (**D, E**). Two cells from two different sources appear in the coronal plane and look like supraseptal posterior ethmoid cells (**C**). The two lines in panel **D** indicate the section reconstruction position in the coronal plane (**B, C**); EMS — ethmomaxillary sinus; MS — maxillary sinus; PEA — posterior ethmoidal artery.

Table 1. Characteristics of the supraseptal posterior ethmoid cells (SPEC) and differences from the Onodi cell and sphenoidal sinus (SS)

Type	Characteristics	Incidence			
		N	Right	Left	Total sides (%)
SPEC	The cell is limited to the central position under the sphenoid planum and is not close to the optic canal	153	0	9	9 (5.88%)
Onodi cell	The cell extends superolateral to the SS and is attached to the optic canal	153	16	17	33 (21.57%)
SS	The cell is connected to the SS	153	18	17	35 (22.88%)

Imaging anatomy of the SPEC

The SPEC is defined when the PE extends medially and superiorly to the posterior superior of the nasal septum but does not further extend to the SS. Therefore, the SPEC only forms an air cell in the centre of the sphenoid planum (Figs. 2–4). The SPEC is located below the sphenoid planum and is the highest cell at the anterior skull base, slightly higher than the cribriform plate.

The midsagittal plane shows that the SPEC is not pneumatization of the PPE but is due to expansion of the PE in the sphenoid body (Figs. 1B, 2, 4). Therefore, the SPEC is not limited by the nasal septum, and it reaches and crosses the midline (Fig. 2). However, the anterior SPEC is adjacent to the cribri-

form plate and the upper part of the PPE, and the anterior expansion of the SPEC is limited by the PPE. Inferior expansion of the SPEC is also limited by the sphenoid bone.

Cells on the posterior and surrounding regions of the SPEC show large variation. The SPEC can be adjacent to the SS and PE (6/9 cases), the SS and Onodi cell (2/9 cases) or the PE only (1/9 cases) (Figs. 2–4). The SPEC is not close to the optic canal and can be distinguished from the Onodi cell (Fig. 3).

The SPEC is relatively small. In the midsagittal position, the range of the anterior posterior diameter was between 3.59–14.62 mm (8.60 ± 3.15 mm), and the height was between 2.72–14.36 mm (6.44 ± ± 3.53 mm).

Differences among the SPEC, Onodi cell and SS

The Onodi cell extends to one side of the SS and close to the ipsilateral optic canal. When the Onodi cell extends anteriorly, it will be displayed on the coronal plane, similar to the SPEC (Fig. 5). The SS can extend anteriorly and superiorly, which is also similar to the SPEC (Fig. 6), but it is easy to distinguish from the SPEC (Table 1). Interestingly, in a few cases, the Onodi cell and SS extended to the middle line together, with stacking of the cells at the middle line. In such cases, the Onodi cell was above, and the SS was below (Fig. 7).

The relationship between the SPEC and the posterior ethmoidal artery

The anterior SPEC is adjacent to the posterior ethmoidal artery (PEA) on both sides (Fig. 2). Even when the Onodi cell or SS extended forward and was displayed in the posterior superior of the nasal septum on the coronal plane, the anterior of the cell was also adjacent to the PEA (Figs. 5–7).

DISCUSSION

At present, the cell is described and named SPEC because it is a medially and superiorly extended PE that is located the posterior superior of the nasal septum between the SS/PE and the PPE. This air cell is also called the supraseptal ethmoid sinus cell, sphenoseptal cell or ethmoidal origin of nasal roof pneumatization [4, 14, 16]. Nevertheless, the meaning of "supraseptal ethmoid sinus cell" and "sphenoseptal cell" does not accurately describe the fact that this cell originates from the PE [4, 16]. Therefore, the present study adopts the name supraseptal posterior ethmoid cell — SPEC.

Initially, the SPEC was a focus owing to the pneumatization seen in the posterior superior of the nasal septum on the coronal plane [5, 13]. In fact, identification of the SPEC must be made using combined imaging from the sagittal and axial planes; indeed, there would be many erroneous judgments if the SPEC was confirmed based only on coronal plane observations [14]. Anterior-superior expansion of the SS and sphenoethmoidal cell can also appear in the posterior superior of the nasal septum on the coronal plane (Figs. 5–7). The present results show that anterior expansion of the Onodi cell (21.57%) and the SS (22.88%) is significantly more common than the SPEC (5.88%) ($p < 0.05$). Therefore, we should pay attention to distinguishing the SPEC from the Onodi cell and SS (Table 1).

Based on the present observation, the nature of the SPEC is that the PE extends medially and superiorly along the sphenoid planum to the posterior superior of the nasal septum. The SPEC is still in the sphenoid bone, but it does not further pneumatize to the SS and is not close to the optic canal, which is different from the Onodi cell [9, 11]. The SPEC, as a type of outward expansion of the PE, reflects the extreme variation characteristics of the PE [3, 9, 10]. Similar to previous reports, the PE extends from the superior, superolateral, lateral, inferolateral areas of the SS into the sphenoid bone to form the Onodi cell, Jinfeng cell and central Onodi cell [1, 7, 9]. In addition, as the PE extends to the orbital roof and maxillary sinus [6, 18], it is not surprising that PE extends to the posterior superior of the nasal septum. Sex differences in the morphology of the craniofacial bone and paranasal sinus have also been reported [2, 17]. However, according to the present results, the SPEC incidence in females (7.84%) was slightly higher than that in males (4.90%), even though the difference was not significant [16].

The SPEC is located outside of the conventional area of ethmoidal cells, which is easy to ignore during ESS. Therefore, we should recognize the possibility of isolated PE appearance in the central area under the sphenoid planum (5.88%) when reviewing CT before ESS. Furthermore, the presence of the SPEC may increase ESS difficulty and surgical risk [4, 14]. The SPEC shows a small space and narrow drainage channels, and the anterior and superior regions of the SPEC are adjacent to the skull base, cribriform plate and PPE. In the event that an SPEC appears and there are lesions or opacities in it (Fig. 4), the SPEC should be opened inferiorly and posteriorly to avoid injury to the skull base and to allow adequate opening, which can also avoid residual lesions or poor drainage during ESS [4, 14].

Moreover, the SPEC and Onodi cell can appear simultaneously (2/9 cases), which should be carefully identified to avoid a missed SPEC and insufficient surgery [16]. The SPEC is the highest ethmoidal cell and is close to the skull base. The roof of the SPEC is the sphenoid planum and can be used as a marker of the skull base. Overall, precise identification and localization of the SPEC during surgery is very important. Moreover, our observations show that the SPEC is located behind the PEA; thus, when opening the SPEC during ESS, we should pay attention to avoid damage to the PEA. Even when the Onodi cell or the

SS extends forward and is displayed in the posterior superior of the nasal septum on the coronal plane, the anterior area of the cell is adjacent to the PEA (Figs. 4, 5).

CONCLUSIONS

The SPEC is a rare variation; it is the PE cells extending medially and superiorly to the posterior superior nasal septum and into the sphenoid body but not close to the optic canal. The anterior SPEC is adjacent to the cribriform plate, PPE and PEA. Care should be taken to protect the skull base, cribriform plate and PEA when opening the SPEC during ESS.

Funding

Conflict of interest: None declared

REFERENCES

1. Cherla DV, Tomovic S, Liu JK, et al. The central Onodi cell: A previously unreported anatomic variation. Allergy Rhinol (Providence). 2013; 4(1): e49–e51, doi: 10.2500/ar.2013.4.0047, indexed in Pubmed: 23772328.
2. Demiralp KO, Kursun Cakmak S, Aksoy S, et al. Assessment of paranasal sinus parameters according to ancient skulls' gender and age by using cone-beam computed tomography. Folia Morphol. 2019; 78(2): 344–350, doi: 10.5603/FM.a2018.0089, indexed in Pubmed: 30280374.
3. Gibelli D, Cellina M, Gibelli S, et al. Anatomical variants of ethmoid bone on multidetector CT. Surg Radiol Anat. 2018; 40(11): 1301–1311, doi: 10.1007/s00276-018-2057-6, indexed in Pubmed: 29934677.
4. Gore MR. The supraseptal ethmoid sinus cell: A previously unreported ethmoid sinus variant. Clin Case Rep. 2019; 7(7): 1306–1308, doi: 10.1002/ccr3.2215, indexed in Pubmed: 31360472.
5. Huang D, Li W, Gao L, et al. Study on computed tomography features of nasal septum cellule and its clinical significance. Lin Chung Er Bi Yan Hou Tou Jing Wai Ke Za Zhi. 2008 ; 22(5): 217–219, indexed in Pubmed: 18476611.
6. Liu J, Dai J, Wen X, et al. Imaging and anatomical features of ethmomaxillary sinus and its differentiation from surrounding air cells. Surg Radiol Anat. 2018; 40(2): 207–215, doi: 10.1007/s00276-018-1974-8, indexed in Pubmed: 29368251.
7. Liu J, Liu Q, Wang N. Posterior ethmoid cell expansion towards the inferolateral region of the sphenoid sinus: a computed tomography study. Surg Radiol Anat. 2019; 41(9): 1011–1018, doi: 10.1007/s00276-019-02277-w, indexed in Pubmed: 31250138.
8. Liu J, Qian Z, Yan Z, et al. Asymmetry of inferior turbinate in patients with nasal septum deviation and its significance for nasal ventilation surgery. Eur Arch Otorhinolaryngol. 2022; 279(5): 2423–2431, doi: 10.1007/s00405-021-07012-z, indexed in Pubmed: 34302496.
9. Liu J, Yuan J, Dai J, et al. The Whole Lateral Type of the Sphenoethmoidal Cell and Its Relevance to Endoscopic Sinus Surgery. Ear Nose Throat J. 2021; 100(9): NP416––NP423, doi: 10.1177/0145561320922119, indexed in Pubmed: 32396389.
10. Márquez S, Tessema B, Clement PAr, et al. Development of the ethmoid sinus and extramural migration: the anatomical basis of this paranasal sinus. Anat Rec (Hoboken). 2008; 291(11): 1535–1553, doi: 10.1002/ar.20775, indexed in Pubmed: 18951481.
11. Meloni F, Mini R, Rovasio S, et al. Anatomic variations of surgical importance in ethmoid labyrinth and sphenoid sinus. A study of radiological anatomy. Surg Radiol Anat. 1992; 14(1): 65–70, doi: 10.1007/BF01628046, indexed in Pubmed: 1589850.
12. Mladina R, Antunović R, Cingi C, et al. Sinus septi nasi: anatomical study. Clin Anat. 2017; 30(3): 312–317, doi: 10.1002/ca.22850, indexed in Pubmed: 28192871.
13. Mureşan AN, Mogoantă CA, Stănescu R, et al. The sinus septi nasi and other minor pneumatizations of the nasal septum. Rom J Morphol Embryol. 2021; 62(1): 227–231, doi: 10.47162/RJME.62.1.22, indexed in Pubmed: 34609425.
14. Mureşan AN, Rusu MC, Rădoi PM, et al. Patterns of pneumatization of the posterior nasal roof. Tomography. 2022; 8(1): 316–328, doi: 10.3390/tomography8010026, indexed in Pubmed: 35202191.
15. Rimmer J, Hellings P, Lund VJ, et al. European position paper on diagnostic tools in rhinology. Rhinology. 2019; 57(Suppl S28): 1–41, doi: 10.4193/Rhin19.410, indexed in Pubmed: 31376816.
16. Saka C, Öcal B, Çadallı Tatar E, et al. How important is the sphenoseptal cell in identifying the skull base? Recent incidence and demonstration of endoscopic surgical steps. Turk J Med Sci. 2021; 51(4): 1889–1893, doi: 10.3906/sag-2012-187, indexed in Pubmed: 33862672.
17. Tomaszewska IM, Frączek P, Gomulska M, et al. Sex determination based on the analysis of a contemporary Polish population's palatine bones: a computed tomography study of 1,200 patients. Folia Morphol. 2014; 73(4): 462–468, doi: 10.5603/FM.2014.0069, indexed in Pubmed: 25448904.
18. Zhou J, Xie Y, Huang Xi, et al. The supraethmoidal roof cell: an unreported sinus anatomic variation. OTO Open. 2021; 5(2): 2473974X211022318, doi: 10.1177/2473974X211022318, indexed in Pubmed: 34164594.

V M
VIA MEDICA

O R I G I N A L   A R T I C L E

Sex prediction with morphometric measurements of first and fifth metatarsal and phalanx obtained from X-ray images by using machine learning algorithms

D. Senol[1], F. Bodur[1], Y. Secgın[2], R.S. Bakıcı[2], N.E. Sahin[2], S. Toy[2], S. Oner[3], Z. Oner[4]

[1]Department of Anatomy, Faculty of Medicine, Düzce University, Düzce, Turkey
[2]Department of Anatomy, Faculty of Medicine, Karabük University, Karabük, Turkey
[3]Department of Radiology, Faculty of Medicine, İzmir Bakırçay University, İzmir, Turkey
[4]Department of Anatomy, Faculty of Medicine, İzmir Bakırçay University, İzmir, Turkey

Background: The aim of this study is to predict sex with machine learning (ML) algorithms by making morphometric measurements on radiological images of the first and fifth metatarsal and phalanx bones.

Materials and methods: In this study, radiologic images of 263 individuals (135 female, 128 male) between the ages of 27 and 60 were analysed retrospectively. The images in digital imaging and communications in medicine (DICOM) format were transferred to personal workstation Radiant DICOM Viewer programme. Length and width measurements of the first and fifth metatarsal and foot phalanx bones were performed on the transferred images. In addition, the ratios of the total length of the first proximal and distal phalanx and length of the first metatarsal and total length of fifth proximal, middle, and distal phalanx and maximum length of fifth metatarsal were calculated.

Results: As a result of machine learning algorithms, highest accuracy, specificity, sensitivity, and Matthews correlation coefficient values were found as 0.85, 0.86, 0.85, and 0.71, respectively with decision tree algorithm. It was found that accuracy rates of other algorithms varied between 0.74 and 0.83.

Conclusions: As a result of our study, it was found that sex estimation was made with high accuracy rate by using machine learning algorithms on X-ray images of the first and fifth metatarsal and foot phalanx. We think that in cases when pelvis, cranium and long bones are harmed and examination is difficult, bones of the first and fifth metatarsal and foot phalanx can be used for sex estimation. (Folia Morphol 2023; 82, 3: 704–711)

Key words: decision tree, machine learning algorithms, metatarsus, phalanx, radiography, sex prediction, X-ray

Address for correspondence: Dr. D. Senol, Düzce University, Faculty of Medicine, Department of Anatomy, Düzce, Turkey,
e-mail: denizanatomi@gmail.com

INTRODUCTION

For years, sex has been one of the most important parameters used for identity determination. In medical and forensic cases, especially anthropometric measurements taken from the parts of an unidentified decomposed or decayed body are important in terms of predicting the height, sex and age of the individual [29]. These anthropometric measurements are frequently used in sex determination and data obtained as a result of studies are very useful especially in terms of identity determination of victims of large-scale disasters and deadly attacks [17].

In identity determination, sex determination draws attention as the first and most important point [11]. For sex determination, there are bones that have been studied many times and the reliability of which has been proven. Of these bones, cranium, pelvis, and long bones are the most examined ones. Both metrically and morphologically, pelvis is the best area in sex determination and it is reported to give correct results with a rate of 95–98% [4, 15, 31, 33]. It is followed by cranium and long bones [24, 35]. In cases when pelvis, cranium and long bones are harmed and examination is difficult, sex prediction is tried with less dimorphic parts of the human skeleton.

Today, although DNA technologies are considered as the method with highest reliability in sex determination, they also have disadvantages such as accessibility, taking time, need for qualified personnel and cost. Because of this, methods such as osteometry, which are easier to access, less costly, highly accurate, easily accessible, fast, and not requiring expertise have begun to be preferred in sex prediction [14, 27].

Machine learning (ML) is specialised data analysis method that automates model building with machines that learn to use certain algorithms [5]. ML algorithms are grouped in three as supervised learning, unsupervised learning and reinforcement learning. Supervised learning is the algorithm that models the relationship between input and output data [18]. Unsupervised learning is the ML algorithm which is based on observations and which allows to reveal the features of previously unknown data. Reinforcement learning is the algorithm matching the input data with desired output data [21]. Building a sex prediction model is based on solving a classification task and this classification is one of the most frequently performed exploratory tasks in ML algorithms. ML helps forensic teams, anatomists,

and anthropologists in many aspects in areas such as crime prevention, individual identity analysis, forensic cyber security, forensic informatics and forensic criminology [2, 3]. Foot bones are among the bones frequently used in sex determination studies due to their presence in both forensic and archaeological contexts, their small and robust structures, being less exposed to taphonomic elements, their resistance to post-mortem changes and being protected by shoes [22, 25, 26]. Literature review shows that sex estimation studies on foot bones generally focus on the shape of the first metatarsal bone and transverse arch of foot in both gender [10].

The aim of this study was sex prediction with ML algorithms by making osteometric measurements on radiological images of the first and fifth metatarsal and phalanx bones.

MATERIALS AND METHODS

Population sample

The study was initiated with 2021/760 numbered decision of Karabuk University Non-Interventional Clinical Studies Ethics Committee. X-ray images of a total of 263 individuals (135 females, 128 males) between the ages of 27 and 60 were included in the study. The X-ray images were selected as randomised among the people admitted to the hospital with various problems in 2021. The exclusion criteria were determined as pathology, fracture, tumour and degeneration of the metatarsal bones.

Image protocol and processing

Images in the study were obtained by the digital single tube X-ray device at Karabuk University Training and Research Hospital. The images in digital imaging and communications in medicine (DICOM) format were transferred to personal workstation Radiant DICOM Viewer (Version: 2020.2) programme. Length and width measurements were made on the transferred images (Table 1, Figs. 1, 2). In addition, the ratios of the total length of the first proximal and distal phalanx and length of the first metatarsal and total length of fifth proximal, middle, and distal phalanx and maximum length of fifth metatarsal were calculated. Parameters were measured once by a specialist radiologist with at least 10 years of experience.

Statistical analysis

In descriptive statistics, Minitab 17 package programme was used for median, minimum and max-

Table 1. Length and width measurements

Measurement parameters	
Length	**Width**
Maximum length of metatarsal I	Medio-lateral width of the first metatarsal head
Maximum length of metatarsal V	Shaft width of metatarsal I
Length of proximal phalanx I	Width of metatarsal base I
Length of distal phalanx I	Medio-lateral width of the fifth metatarsal head
Length of middle phalanx V	Shaft width of metatarsal V
Length of proximal phalanx V	Width of metatarsal base V
Length of distal phalanx V	Width of proximal phalanx I
Total length of first proximal and distal phalanx	Width of distal phalanx I
Total length of fifth proximalis, middle and distalis phalanx	Width of proximal phalanx V
	Width of middle phalanx V
	Width of distal phalanx V

Figure 1. Length measurements of the first and fifth metatarsals and foot phalanx bones; 1 — length of the first distal phalanx; 2 — length of the first proximal phalanx; 3 — maximum length of the first metatarsal; 4 — length of the fifth distal phalanx; 5 — length of the fifth middle phalanx; 6 — length of the fifth distal phalanx; 7 — maximum length of the fifth metatarsal.

Figure 2. Width measurements of the first and fifth metatarsals and foot phalanx bones; 1 — width of the first distal phalanx; 2 — width of the first proximal phalanx; 3 — medio-lateral width of the first metatarsal head; 4 — width of the middle shaft first metatarsal; 5 — width of the first metatarsal base; 6 — width of the fifth distal phalanx; 7 — width of the fifth middle phalanx; 8 — width of the fifth proximal phalanx; 9 — medio-lateral width of the fifth metatarsal head; 10 — middle shaft width of the fifth metatarsal; 11 — width of the fifth metatarsal base.

Table 2. Median, minimum, and maximum values of the length measurements taken from radiological measurements of male and female

Parameters [cm]	Sex	Median [cm]	Minimum [cm]	Maximum [cm]
Maximum length of metatarsal I	Male	6.185	4.600	7.780
	Female	5.650	4.690	6.950
Maximum length of metatarsal V	Male	7.400	6.020	8.910
	Female	6.790	5.580	8.040
Length of proximal phalanx I	Male	3.230	2.490	3.980
	Female	2.930	1.760	3.530
Length of distal phalanx I	Male	2.715	2.040	3.430
	Female	2.470	1.920	2.950
Length of proximal phalanx V	Male	2.420	1.910	2.940
	Female	2.230	1.640	2.690
Length of middle phalanx V	Male	0.700	0.340	1.410
	Female	0.630	0.320	0.910
Length of distalis phalanx V	Male	0.915	0.310	1.320
	Female	0.830	0.480	1.130
Total length of first proximal and distal phalanx	Male	5.915	4.670	7.230
	Female	5.380	4.020	6.210
Total length of fifth proximal, middle and distal phalanx	Male	4.050	2.810	5.130
	Female	3.680	2.890	4.580
Total length of first proximal and distal phalanx/ /maximum length of metatarsal I	Male	1.050	1.900	1.290
	Female	1.050	1.890	1.480
Total length of fifth proximal, middle and distal phalanx/ /maximum length of metatarsal V	Male	1.820	1.470	2.230
	Female	1.820	1.550	2.210

imum values. Mann-Whitney U test was performed for age parameter.

Machine learning algorithms

For ML algorithms, Python programming language (Version 3.7.1) and scikit-learn framework (Version 0.20.0) was used as 80% training set and 20% test set [30]. Quadratic discriminant analysis, linear discriminant analysis, decision tree, random forest, extra tree classifier, logistic regression algorithms were used in our study.

Performance criteria

Accuracy (Acc), Matthews correlation coefficient (Mcc), specificity (Spe), sensitivity (Sen) values were included in the study.

RESULTS

Median, minimum (min) and maximum (max) values were included in descriptive statistics. Median, min, max values of the length measurements taken from radiological measurements of men and women

are shown in Table 2, while median, min, max values of the width measurements are shown in Table 3. Median age of the women in the study was 44 years, while the median age of the men in the study was 49 years. No statistically significant difference was found according to Mann-Whitney-U test in terms of age according to sex groups (p = 0.098).

As a result of ML algorithm analysis, highest Acc, Spe, Sen, Mcc values were found as 0.85, 0.86, 0.85, and 0.71, respectively with decision tree algorithm. It was found that accuracy rates of other algorithms varied between 0.74 and 0.83 (Table 4).

As a result of our study, confusion matrix of decision tree algorithm with the highest Acc rate was included (Fig. 3).

DISCUSSION

The aim of this study was to predict sex with ML algorithms by making morphometric measurements on radiological images of the first and fifth metatarsal and phalanx bones of a total of 263 individuals (135 females, 128 males) between the ages of 27 and 60.

Table 3. Median, minimum, and maximum values of the width measurements taken from radiological measurements of male and female

Parameters [cm]	Sex	Median [cm]	Minimum [cm]	Maximum [cm]
Medio-lateral width of first metatarsal head	Male	2.380	1.790	3.040
	Female	2.140	1.680	2.690
Width of metatarsal corpus I	Male	1.650	1.150	2.010
	Female	1.430	1.120	1.860
Width of metatarsal base I	Male	2.450	1.820	3.160
	Female	2.150	1.680	2.840
Medio-lateral width of metatarsal head V	Male	1.480	0.970	2.110
	Female	1.430	0.940	1.810
Width of metatarsal corpus V	Male	0.940	0.730	1.250
	Female	0.910	0.610	1.210
Width of metatarsal base V	Male	2.560	1.940	3.280
	Female	2.320	1.820	2.870
Width of proximal phalanx I	Male	1.570	1.140	1.950
	Female	1.360	0.940	1.780
Width of distal phalanx I	Male	1.200	0.850	1.640
	Female	1.060	0.790	1.330
Width of proximal phalanx V	Male	0.580	0.370	0.780
	Female	0.510	0.380	0.700
Width of middle phalanx V	Male	0.855	0.470	1.180
	Female	0.790	0.480	1.040
Width of distal phalanx V	Male	0.520	0.350	0.830
	Female	0.470	0.330	0.700

Table 4. Machine learning algorithms performance values

Algorithms	Accuracy	Specificity	Sensitivity	Mcc
QDA	0.83	0.83	0.83	0.69
LDA	0.81	0.81	0.81	0.62
DT	**0.85**	**0.86**	**0.85**	**0.71**
RF	0.83	0.85	0.83	0.68
ETC	0.74	0.75	0.74	0.48
LR	0.81	0.82	0.81	0.62

QDA — quadratic discriminant analysis; LDA — linear discriminant analysis; DT — decision tree; RF — random forest; ETC — extra tree classifier; LR — logistic regression; Mcc — Matthews correlation coefficient

Figure 3. Confusion matrix of decision tree algorithm.

As a result of ML algorithm analysis, highest Acc, Spe, Sen, Mcc values were found as 0.85, 0.86, 0.85 and 0.71, respectively with decision tree algorithm. It was found that accuracy rates of other algorithms varied between 0.74 and 0.83.

When the literature is reviewed, it can be seen that hip bone and cranial bones are the first preferred bones in sex determination. This is because some parts of the pelvis and cranial bones show sex specific morphological differences [13, 34, 37]. In cases when these bones are not present, it can be seen that femur [8], tibia and fibula [12], patella [27], sternum [28], humerus [19], ulna and radius [16], foot and hand bones [36] have also been tried in sex prediction.

Akhlaghi et al. [1] measured the length, width, length-width ratio (L/W) and length-width (L×W)

of right foot metatarsal bones of 184 individuals by using radiographic images. In the study, as a result of logistic regression analysis, it was found that L×W value of the first metatarsal bone and L×W values of all metatarsal bones had the highest accuracy (86% and 85%) in sex prediction. It was found that first metatarsal width and mean width of all metatarsal bones had an accuracy ratio of 82% and 84%, respectively. In our study, they were found to have an accuracy ratio of 74% and 85% as a result of ML analysis. In line with these results, the study conducted by Akhlaghi et al. [1] and our study are similar.

In literature review, as a result of the discriminant analysis performed on the patella and metatarsal bones of 160 individuals, the accuracy of the measurements from metatarsal bones was found to be between 85% and 100%. Therefore, metatarsal bones were found to be more reliable and valid than patella [25].

In another study conducted on metatarsal and phalanx, sex prediction was aimed by measuring the length of phalanx first and fifth toes and first and fifth metatarsal bones by using artificial neural network technique. The model was found to have Acc of 0.95, Spe of 0.97, Sen of 0.95 and Mcc of 0.92 [38]. In our study, the highest Acc, Spe, Sen, Mcc values were found as 0.85, 0.86, 0.85, and 0.71, respectively, with decision tree algorithm. It was found that accuracy rates of other algorithms varied between 0.74 and 0.83. The differences in the results may be resulting from differences in method.

As a result of the study that aimed to predict sex with osteometric methods, Mountrakis et al. [26] reported that metatarsal bones showed significant sexual dimorphism and the Acc of discriminant function equations for sex prediction was between 80% and 90%. In another study, the lengths of the metatarsal bones of 100 individuals were measured by using Vernier calliper. The measurements were evaluated by using discriminant function and logistic regression analysis and as a result of the evaluation, various combinations of metatarsal bones have been shown to give high mean Acc (between 79% and 84%) for sex prediction [6]. In a study conducted with dry metacarpal and metatarsal bones by using digital calliper for sex prediction, as a result of discriminant functions it was found that the accuracy of metacarpal bones varied between 79% and 85%, while the Acc of metatarsal bones varied between 77% and 83% [36]. In our study, as a result of ML algorithms,

Acc was found to be between 74% and 85% with quadratic discriminant analysis, linear discriminant analysis, decision tree, random forest, extra tree classifier, logistic regression algorithms. In line with these results, in addition to other sex prediction techniques, it was shown that metatarsal bones could be used for sex prediction and the results of our study were found to be in parallel with the literature.

Although the methods used for sex prediction in length measurements performed on dry metatarsal bones and foot phalanx bones are different, it has been found that length measurements show significant difference between genders. As a result of the analysis of these studies, a mean accuracy range varying between 70% and 84% has been shown and it has been found that the results are in parallel with the results of our study [6, 7, 9, 32]. All metatarsal bones show sex based biomechanical differences. In a study which examined the length and width measurements of metatarsal bones by using three-dimensional foot scanning data, women were found to have smaller rates [23]. In studies conducted on different populations, foot length and width have been shown to differ in women and men [20].

Limitations of the study

The limitations of our study are the difficulty in taking the images of metatarsal and foot phalanx bones due to their small structure, small sample size, the fact that foot morphology may be affected by ethnic origin, the study was conducted only on a specific population and superposition disadvantage since X-ray is a two-dimensional imaging technique.

CONCLUSIONS

In this study, mean first metatarsal and fifth metatarsal values of men were found to be higher than mean values of women and this result was found to be in parallel with other studies conducted. As a result of our study, X-ray images of the first and fifth metatarsal and phalanx can be used for sex determination by using ML algorithms.

Conflict of interest: None declared

REFERENCES

1. Akhlaghi M, Bakhtavar K, Bakhshandeh H, et al. Sex determination based on radiographic examination of metatarsal bones in Iranian population. Int J Med Toxicol Forensic Med. 2017; 7(4): 203–208, doi: 10.22037/ijmtfm.v7i4(Autumn).17059.

2. Ariu D, Giacinto G, Roli F. Machine learning in computer forensics (and the lessons learned from machine learning in computer security). Proceedings of the 4th ACM workshop on Security and artificial intelligence. 2011, doi: 10.1145/2046684.2046700.

3. Awais M, Naeem F, Rasool N, et al. Identification of sex from footprint dimensions using machine learning: a study on population of Punjab in Pakistan. Egypt J Forensic Sci. 2018; 8(1): 72, doi: 10.1186/s41935-018-0106-2.

4. Best KC, Garvin HM, Cabo LL. An investigation into the relationship between human cranial and pelvic sexual dimorphism. J Forensic Sci. 2018; 63(4): 990–1000, doi: 10.1111/1556-4029.13669, indexed in Pubmed: 29044526.

5. Bhardwaj R, Nambiar A, Dutta D. A study of machine learning in healthcare. 2017 IEEE 41st Annual Computer Software and Applications Conference (COMPSAC). 2017; 2: 236–241, doi: 10.1109/compsac.2017.164.

6. Bidmos MA, Adebesin AA, Mazengenya P, et al. Estimation of sex from metatarsals using discriminant function and logistic regression analyses. Australian J Forensic Sci. 2020; 53(5): 543–556, doi: 10.1080/00450618.2019.1711180.

7. Case DT, Ross AH. Sex determination from hand and foot bone lengths. J Forensic Sci. 2007; 52(2): 264–270, doi: 10.1111/j.1556-4029.2006.00365.x, indexed in Pubmed: 17316220.

8. Colman KL, Janssen MCL, Stull KE, et al. Dutch population specific sex estimation formulae using the proximal femur. Forensic Sci Int. 2018; 286: 268.e1–268.e8, doi: 10.1016/j.forsciint.2017.12.029, indexed in Pubmed: 29548547.

9. Cordeiro C, Muñoz-Barús JI, Wasterlain S, et al. Predicting adult stature from metatarsal length in a Portuguese population. Forensic Sci Int. 2009; 193(1-3): 131.e1–131.e4, doi: 10.1016/j.forsciint.2009.09.017, indexed in Pubmed: 19854594.

10. Domínguez-Maldonado G, Munuera-Martinez PV, Castillo-López JM, et al. Normal values of metatarsal parabola arch in male and female feet. Sci World J. 2014; 2014: 505736, doi: 10.1155/2014/505736, indexed in Pubmed: 24688397.

11. Eshak GA, Ahmed HM, Abdel Gawad EAM. Gender determination from hand bones length and volume using multidetector computed tomography: a study in Egyptian people. J Forensic Leg Med. 2011; 18(6): 246–252, doi: 10.1016/j.jflm.2011.04.005, indexed in Pubmed: 21771554.

12. Fasemore MD, Bidmos MA, Mokoena P, et al. Dimensions around the nutrient foramina of the tibia and fibula in the estimation of sex. Forensic Sci Int. 2018; 287: 222.e1–222.e7, doi: 10.1016/j.forsciint.2018.03.015, indexed in Pubmed: 29678345.

13. Funayama M, Aoki Y, Kudo T, et al. Sex determination of the human skull based upon line drawing from roentgen cephalograms. Tohoku J Exp Med. 1986; 149(4): 407–416, doi: 10.1620/tjem.149.407, indexed in Pubmed: 3775765.

14. Giurazza F, Schena E, Del Vescovo R, et al. Sex determination from scapular length measurements by CT scans images in a Caucasian population. Annu Int Conf IEEE Eng Med Biol Soc. 2013; 2013: 1632–1635, doi: 10.1109/EMBC.2013.6609829, indexed in Pubmed: 24110016.

15. Iscan MY, Steyn M. The human skeleton in forensic medicine. Charles C Thomas Publisher, Springfield, IL 2013.

16. Issa S, Khanfour A, Kharoshah M. A model for stature estimation and sex prediction using percutaneous ulnar and radial lengths in autopsied adult Egyptians. Egypt J Forensic Sci. 2016; 6(2): 84–89, doi: 10.1016/j.ejfs.2016.05.013.

17. Kanchan T, Krishan K, Sharma A, et al. A study of correlation of hand and foot dimensions for personal identification in mass disasters. Forensic Sci Int. 2010; 199(1-3): 112.e1–112.e6, doi: 10.1016/j.forsciint.2010.03.002, indexed in Pubmed: 20382487.

18. Karslı ÖB. Makine Öğrenme Algoritmaları ile Karaciğer Hastalığının Teşhisi. Turkish Studies-Information Technologies and Applied Sciences. 2020; 15(1): 75–83, doi: 10.29228/turkishstudies.39612.

19. Khan MA, Gul H, Mansor Nizami S. Determination of gender from various measurements of the humerus. Cureus. 2020; 12(1): e6598, doi: 10.7759/cureus.6598, indexed in Pubmed: 32064180.

20. Kim W, Kim YM, Yun MH. Estimation of stature from hand and foot dimensions in a Korean population. J Forensic Leg Med. 2018; 55: 87–92, doi: 10.1016/j.jflm.2018.02.011, indexed in Pubmed: 29474990.

21. Krems RV. Bayesian machine learning for quantum molecular dynamics. Phys Chem Chem Phys. 2019; 21(25): 13392–13410, doi: 10.1039/c9cp01883b, indexed in Pubmed: 31165115.

22. Krishan K. Determination of stature from foot and its segments in a north Indian population. Am J Forensic Med Pathol. 2008; 29(4): 297–303, doi: 10.1097/PAF.0b013e3181847dd3, indexed in Pubmed: 19259013.

23. Lee YC, Wang MJ. Taiwanese adult foot shape classification using 3D scanning data. Ergonomics. 2015; 58(3): 513–523, doi: 10.1080/00140139.2014.974683, indexed in Pubmed: 25361465.

24. MacLaughlin SM, Oldale KN. Vertebral body diameters and sex prediction. Ann Hum Biol. 1992; 19(3): 285–292, doi: 10.1080/03014469200002152, indexed in Pubmed: 1616286.

25. Moneim WMA, Hady RHA, Maaboud RMA, et al. Identification of sex depending on radiological examination of foot and patella. Am J Forensic Med Pathol. 2008; 29(2): 136–140, doi: 10.1097/PAF.0b013e318173f048, indexed in Pubmed: 18520480.

26. Mountrakis C, Eliopoulos C, Koilias CG, et al. Sex determination using metatarsal osteometrics from the Athens collection. Forensic Sci Int. 2010; 200(1-3): 178.e1–178.e7, doi: 10.1016/j.forsciint.2010.03.041, indexed in Pubmed: 20430546.

27. Oner S, Turan M, Oner Z. Estimation of gender by using decision tree, a machine learning algorithm, with patellar measurements obtained from MDCT images. Med Rec. 2021; 3(1): 1–9, doi: 10.37990/medr.843451.

28. Oner Z, Turan MK, Oner S, et al. Sex estimation using sternum part lenghts by means of artificial neural networks. Forensic Sci Int. 2019; 301: 6–11, doi: 10.1016/j.forsciint.2019.05.011, indexed in Pubmed: 31128410.

29. Ozden H, Balci Y, Demirüstü C, et al. Stature and sex estimate using foot and shoe dimensions. Forensic Sci Int. 2005; 147(2-3): 181–184, doi: 10.1016/j.forsciint.2004.09.072, indexed in Pubmed: 15567624.

30. Pedregosa F, Varoquaux G, Gramfort A, et al. Scikit-learn: machine learning in python. J Mach Learn Res. 2011; 12: 2825–2830, doi: 10.48550/arXiv.1201.0490.

31. Pellico LG, Camacho FF. Biometry of the anterior border of the human hip bone: normal values and their use in sex determination. J Anat. 1992; 181(Pt 3): 417, indexed in Pubmed: 1304579.

32. Robling AG, Ubelaker DH. Sex estimation from the metatarsals. J Forensic Sci. 1997; 42(6): 1062–1069, indexed in Pubmed: 9397547.

33. Rogers TL. Determining the sex of human remains through cranial morphology. J Forensic Sci. 2005; 50(3): 1–8, doi: 10.1520/jfs2003385, indexed in Pubmed: 15932077.

34. Secgin Y, Oner Z, Turan M, et al. Gender prediction with parameters obtained from pelvis computed tomography images and decision tree algorithm. Med Sci | Int Med J. 2021; 10(2): 356–361, doi: 10.5455/medscience.2020.11.235.

35. Spradley MK, Jantz RL. Sex estimation in forensic anthropology: skull versus postcranial elements. J Forensic Sci. 2011; 56(2): 289–296, doi: 10.1111/j.1556-4029.2010.01635.x, indexed in Pubmed: 21210801.

36. Torres G, Garmendia AM, Sánchez-Mejorada G, et al. Estimation of gender from metacarpals and metatarsals in a Mexican population. Span J Leg Med. 2020; 46(1): 12–19, doi: 10.1016/j.remle.2018.09.004.

37. Toy S, Secgin Y, Oner Z, et al. A study on sex estimation by using machine learning algorithms with parameters obtained from computerized tomography images of the cranium. Sci Rep. 2022; 12(1): 4278, doi: 10.1038/s41598-022-07415-w, indexed in Pubmed: 35277536.

38. Turan MK, Oner Z, Secgin Y, et al. A trial on artificial neural networks in predicting sex through bone length measurements on the first and fifth phalanges and metatarsals. Comput Biol Med. 2019; 115: 103490, doi: 10.1016/j.compbiomed.2019.103490, indexed in Pubmed: 31606585.

Correlation between glenoid bone structure and recurrent anterior dislocation of the shoulder joint

Q. Zhao, D. Jin, H. Yuan

Department of Radiology, Peking University Third Hospital, China

Background: The aim of the study was to investigate the anatomical characteristics and symmetry of the bilateral glenoid structures of Chinese people and to explore the relationship between the glenoid bone structure and recurrent anterior dislocation.

Materials and methods: The control group included 131 individuals with no history of shoulder dislocation. The dislocation group consisted of 131 patients with a history of unilateral shoulder dislocation. All subjects underwent computed tomography scans. Glenoid shape (pear-shaped, inverted comma-shaped, oval-shaped), width, height, depth, version angle, area, maximum fitting circle area and volume were measured.

Results: There was no significant difference in normal bilateral glenoid of Chinese people (p > 0.05). There were statistically significant differences in depth, height to width ratio, maximum fitting circle area and shape between the dislocation and control groups (p < 0.05). Regression analyses showed that the glenoid depth (odds ratio [OR] 0.48; p < 0.01), the glenoid height to width ratio (OR 28.61; p < 0.01), the glenoid maximum fitting circle area (OR 1.01; p < 0.01) and the glenoid shape (p <0.05; pear-shaped OR 0.432; inverted comma-shaped OR 0.954) were associated with anterior shoulder instability. Pear-shaped and inverted comma-shaped glenoid had lower risk of recurrent anterior shoulder dislocation compared to oval glenoid. Receiver operating characteristic curve analysis showed that individuals with anterior shoulder instability had smaller glenoid depth and larger height to width ratio and the glenoid maximum fitting circle area compared with the control group.

Conclusions: The normal bilateral glenoids of Chinese people are basically symmetrical. The glenoid shape, depth, height to width ratio and maximum fitting circle area are risk factors for recurrent anterior shoulder dislocation. Evaluation of the glenoid bone structure enables more accurate prediction of the risk of recurrent shoulder dislocation. (Folia Morphol 2023; 82, 3: 712–720)

Key words: shoulder glenoid, recurrent anterior shoulder dislocation, bony structures, glenoid shape

---

Address for correspondence: Dr. H. Yuan, Peking University Third Hospital, Huayuan North Road No. 49, Haidian District, Beijing, China, 100191, tel: 86-010-82264567, e-mail: huishuy@bjmu.edu.cn

INTRODUCTION

The glenohumeral joint is the most unstable joint and has the largest range of motion in the human body [9, 26]. Glenohumeral joint dislocation accounts for more than 40% of joint dislocations in the whole body [8], resulting in shoulder pain or dysfunction. It often occurs in young patients, with an average age of 20 years old, and more often in male patients than in female patients, the vast majority of which experience anterior dislocations (85–95%) [3, 6, 20, 25]. Unfortunately, this injury is associated with a very high rate of recurrence (85%) in younger athletes after the initial injury [8]. The first dislocation causes structural damage to the shoulder joint, and the external force required for the second dislocation is smaller than that required for the first dislocation. When dislocation occurs repeatedly, the structural damage is further aggravated, thereby making the next dislocation more likely to occur, forming a vicious cycle.

Previous studies have shown that the risk factors of anterior shoulder instability include soft tissues such as rotator cuff, ligaments, labrum, joint capsule, and bone anatomic features such as the glenoid morphology [19]. The bony structure of the glenoid plays an important role in maintaining the stability of the glenohumeral joint. The glenoid bone structure includes the glenoid width, height, depth, version angle, glenoid area and shape [5, 14]. However, the effect of the glenoid shape on anterior shoulder instability has been rarely studied.

Approximate glenoid symmetry is a feature of the human body [12], and this is the basis for using the contralateral normal side as the reference for analysing the correlation between the bony structure of the glenoid and recurrent shoulder dislocation. To date, the recognition of side-to-side glenoid symmetry has been based on basic measurements of maximum glenoid width, length, circumference, and area [22]. This presumed side-to-side symmetry nevertheless requires a more robust and detailed analysis before management decisions based on this assumption can reliably be undertaken.

The purpose of this study were to evaluate the anatomical characteristics and symmetry of the glenoid bone structures (width, height, depth, version angle, area, maximum fitting circle area, volume, shape) in the bilateral glenoids of Chinese patients and to explore the relationship between the glenoid bone structure and recurrent anterior dislocation.

MATERIALS AND METHODS

Internal review board approval was obtained for this retrospective study. The study was designed as a matched retrospective case-control study.

Compliance with ethical standards

The requirement for informed patient consent was waived for the retrospective study. The study protocol was approved by the institutional review board (number: IRB00006761-M2020544).

Subjects

Patients who were referred to the institution during the period between June 2018 and February 2021 were retrospectively reviewed. The dislocation group consisted of 131 patients with a history of unilateral shoulder dislocation with at least 2 or more anterior dislocations, including 108 males and 23 females, aged 28.16 ± 10.75 years. Patients were excluded if there was evidence of injuries to the previous shoulder dislocation with other direction, glenoid damage, tumour or previous surgery of the glenoid. The control group consisted of 131 individuals with no history of shoulder dislocation, shoulder joint developmental deformity or other disease that may lead to abnormal morphology of the shoulder glenoid. Individuals in the control group were matched by age, sex and height to the dislocation group, in order to increase confidence in the validity of the statistical results.

Imaging protocol

Images were acquired on a Germany Siemens 64-slice spiral computed tomography (CT) system with a 1-mm slice thickness and a 1-mm increment, a pitch of 1. All scans were performed according to a pre-established protocol. All images were acquired with the patient supine, the body centred on the scanning bed, the upper limbs in a neutral position during the examination. All subjects underwent CT examination, including complete imaging of the bilateral glenoids. Multiplanar reconstruction were accomplished and measurement were made on oblique coronal, sagittal and axial images, respectively. Three-dimensional volume rendered reconstructions with humerus-subtracted were accomplished on the CT images of the bilateral glenoid, and the glenoid cavities were rotated to create standardized en face views.

Measurements of the following variables were performed on corrected images:

713
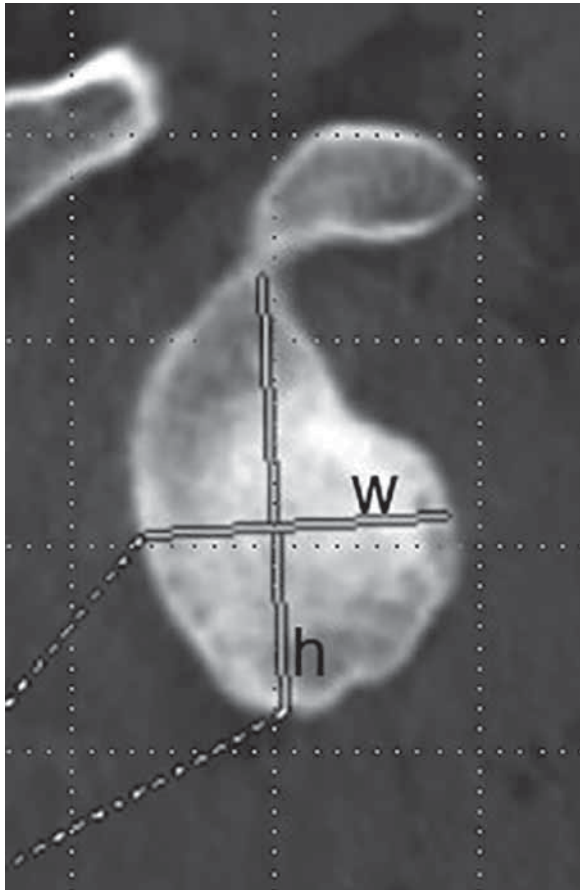
Figure 1. Measurement of glenoid height (shown as h) and glenoid width (shown as w).
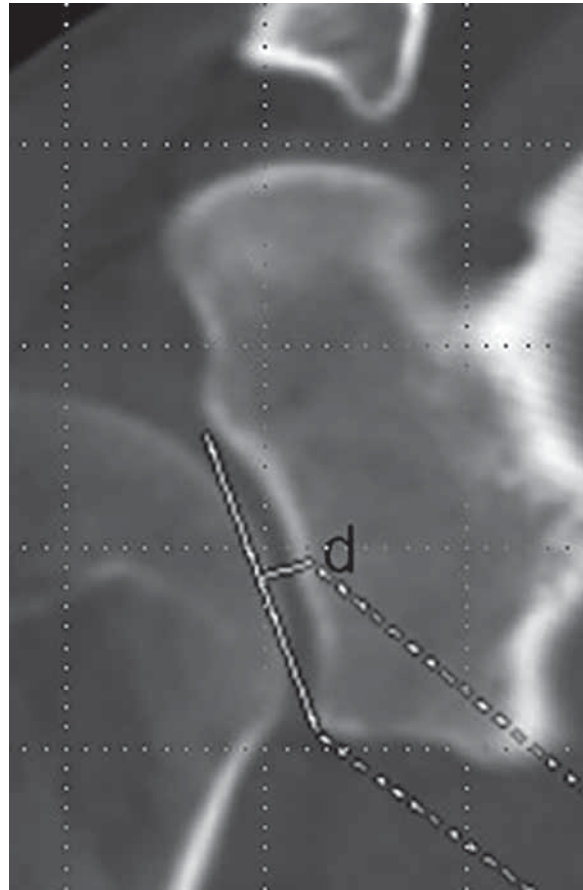
Figure 2. Measurement of glenoid depth (shown as d).

— glenoid width: length of the line connecting the anterior and posterior edges of the glenoid on oblique sagittal images (Fig. 1);
— glenoid height: length of the line connecting the supraglenoid tubercle to the infraglenoid tubercle on oblique sagittal images. Two lines (glenoid width and height) perpendicular to each other (Fig. 1);
— glenoid depth: on oblique coronal images a parallel line connecting the superior and inferior glenoid edges of the scapula through the deepest point of the articular surface was made. The distance between the two lines is the depth of the glenoid depression (Fig. 2);
— Glenoid area: draw a free hand region of interest delineated along the glenoid rim on oblique sagittal images, and measure area automatically (Fig. 3);
— maximum fitting circle area: first, a vertical line along the long axis of the glenoid through the supraglenoid tubercle was drawn. Then a best-fit

circle with its centre on this line was placed along the inferior edge of the glenoid, and measure circle area automatically (Fig. 4);
— glenoid volume: automatically identify glenoid contours in oblique sagittal images, adjust contours as needed, and measure volumes (Fig. 5);
— version angle: defined as 90 minus the angle between the scapular plane and the glenoid circle on corrected oblique axial images, with a negative value representing retroversion (Fig. 6);
— glenoid shape: there are three types of glenoid shape, inverted comma shape — the glenoid cavity has a distinct notch; pear shape — the glenoid cavity has an indistinct notch; oval shape — the glenoid cavity has no notch. The shape assessed directly on the volume rendered images (Fig. 7).

Each glenoid was measured 3 times. To establish inter- and intraobserver reliability, 10 random CTs were selected. Two investigators used the methods described and correlation coefficients were calculated. The correlation coefficients for intraobserver
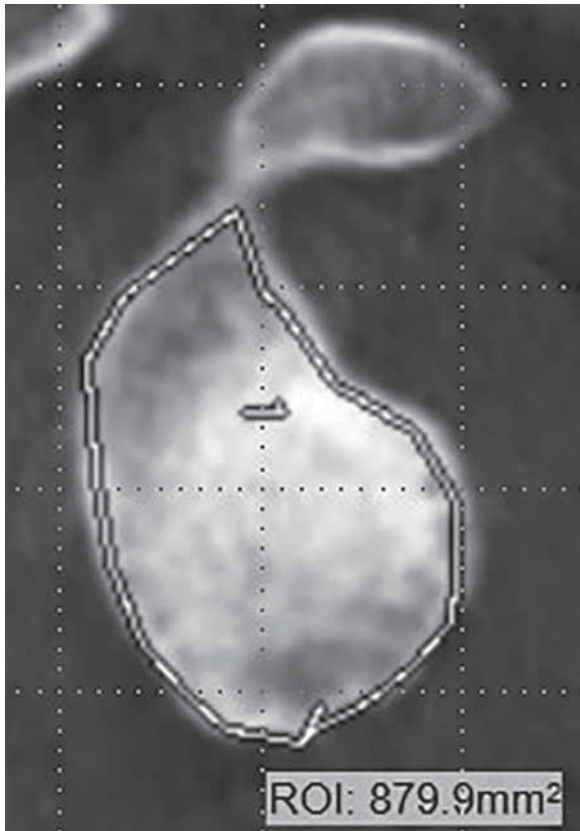
Figure 3. Measurement of glenoid area; ROI — region of interest.
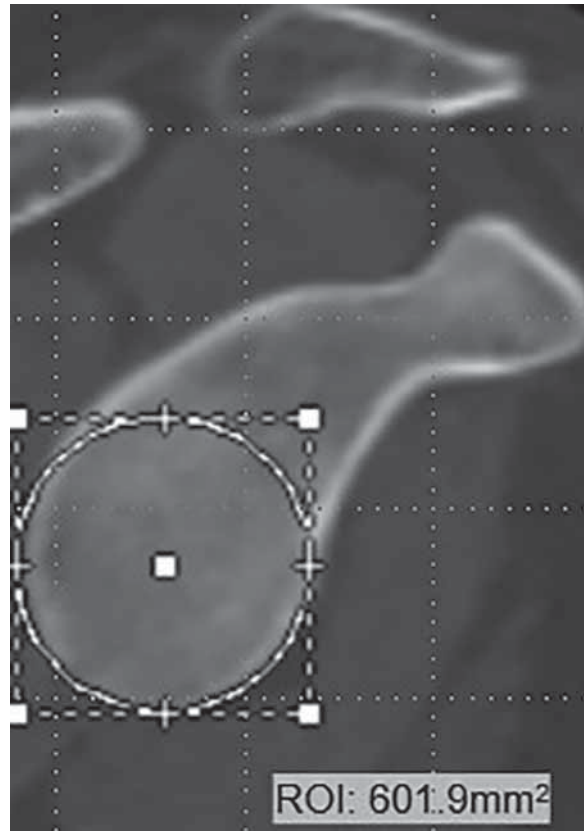
Figure 4. Measurement of glenoid maximum fitting circle area; ROI — region of interest.
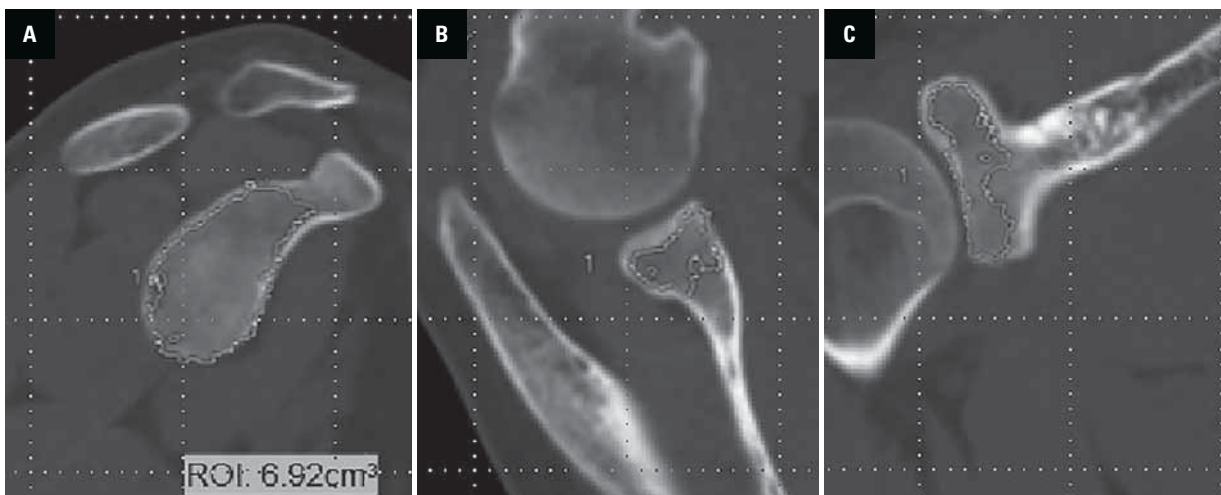
Figure 5. A–C. Measurement of glenoid volume; ROI — region of interest.

had higher scores than interobserver. Given the comparative nature of the project and the higher scores for intraobserver reliability, selection of CTs and all measurements were subsequently performed by the independent research associate only.

Statistical analysis

For continuous variables, we used paired t tests to examine the differences between participants who experienced anterior instability events and those who did not. For categorical variables, we examined the

association between the variables and shoulder anterior instability using the χ^2 test. The parameters were further examined using binary logistic regression analysis. Due to the considerable number of patients, cutoff points were determined after using receiver operating characteristic (ROC) curve analysis as a complementary method. All measurements were presented as mean ± standard deviation unless otherwise stated.

RESULTS

There were no significant differences in the height, width, height to width ratio, depth, area, maximum fitting circle area, volume, or version angle of the normal bilateral glenoids of Chinese patients (p > 0.05) (Table 1). There were no significant differences in demographic characteristics between the dislocation group and the control group. No significant differences were found between the control and dislocation group with respect to the glenoid width, height, version angle, area and volume. In contrast, there were statistically significant differences in depth, height to width ratio, maximum fitting circle area and shape between the dislocation and control groups (p < 0.05) (Table 2).

Because the values of depth, height to width ratio, maximum fitting circle area and shape had

Figure 6. Measurement of glenoid version.

Table 1. Skeletal anatomical parameters of bilateral glenoid in normal population

Parameters	Left	Right	P
Glenoid width [mm]	26.1 ± 2.14	26.53 ± 2.32	0.08
Glenoid height [mm]	41.43 ± 2.89	42.24 ± 3.2	0.06
Height to width ratio	1.59 ± 0.13	1.60 ± 0.12	0.81
Glenoid depth [mm]	4.26 ± 0.74	4.47 ± 0.88	0.11
Area [mm²]	761.85 ± 85.27	774.55 ± 86.41	0.13
Maximum fitting circle area [mm²]	526.39 ± 79.75	540.78 ± 81.31	0.06
Volume [cm³]	5.94 ± 1.43	6.18 ± 1.6	0.16
Version angle [o]	–3.52 ± 3.59	–3.58 ± 3.81	0.61
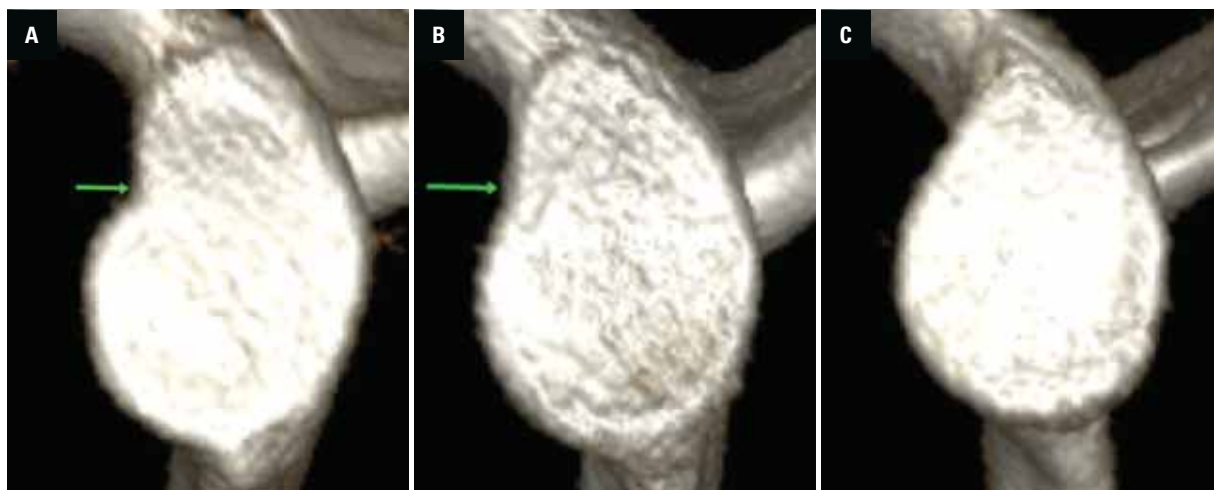
Figure 7. Inverted comma shape (A), pear shape or tear drop shape (B) and ovoid, oval or round shape (C).

Table 2. Comparison of glenoid bone anatomy between the dislocation group and the control group

	The dislocation group (n = 131)	The control group (n = 131)	χ^2/t	P
Gender, male [%]	108	108	–	1
Age	28.16 ± 10.75	28.4 ± 10.55	0.16	> 0.05
Height [cm]	171.62 ± 4.3	171.21 ± 3.6	–0.92	> 0.05
Glenoid width [mm]	25.48 ± 2.56	25.86 ± 2.41	0.99	> 0.05
Glenoid height [mm]	41.44 ± 3.2	41.06 ± 3.32	–0.81	> 0.05
Height to width ratio	1.63 ± 0.16	1.59 ± 0.13	–2.07	0.04
Glenoid depth [mm]	3.99 ± 0.77	4.32 ± 0.72	3.09	< 0.01
Version angle [º]	–2.6 ± 3.27	–3.54 ± 3.75	1.83	> 0.05
Area [mm²]	748.91 ± 103.89	748.38 ± 104.69	–0.03	> 0.05
Maximum fitting circle area [mm²]	552.76 ± 93.65	497.26 ± 90.49	–4.27	< 0.01
Volume [cm³]	6.31 ± 1.32	6.16 ± 1.74	–0.73	> 0.05
Shape:				
Inverted common shape	9	11	17.29	< 0.01
Pear shape	66	95		
Oval shape	56	25		

Table 3. Logistic regression analysis of risk factors for recurrent shoulder dislocation

Parameters	Odds ratio	95% confidence interval		P
		Minimum	Maximum	
Depth	0.48	0.305	0.757	< 0.01
Height to width ratio	28.61	3.018	271.266	< 0.01
Maximum fitting circle area	1.011	1.007	1.016	< 0.01
Shape:				
Oval shape	1			0.01
Pear shape	0.432	0.228	0.816	
Inverted common shape	0.954	0.231	3.937	

a $p < 0.05$, they were further examined using conditional logistic regression analysis, as reported in Table 3. Regression analyses showed that the glenoid depth (odds ratio [OR] 0.48; $p < 0.01$), the glenoid height to width ratio (OR 28.61; $p < 0.01$), the glenoid maximum fitting circle area (OR 1.01; $p < 0.01$) and the glenoid shape ($p < 0.05$; pear-shaped OR 0.432; inverted comma-shaped OR 0.954) were associated with anterior shoulder instability. Pear-shaped and inverted comma-shaped glenoids had lower risk of recurrent anterior shoulder dislocation compared to oval glenoids (Table 3).

Subsequently, ROC curve analysis was performed on parameters such as the glenoid depth, the glenoid height to width ratio and the glenoid maximum fitting circle area (Fig. 8). A comparison of cutoff points showed that individuals with anterior shoulder instability had smaller glenoid depth and larger height to width ratio and the glenoid maximum fitting circle area than those in the control group, identified by ROC curve analyses. The cutoff point for the glenoid depth was 4.25 mm, for the height to width ratio was 1.62, for the glenoid maximum fitting circle area was 515.55 mm² using ROC curves in these analyses.

DISCUSSION

In this study, data on the shoulder structure of patients with anterior shoulder dislocation were assessed by CT. CT has the advantages of extremely high spatial resolution and density resolution, and multiplanar reconstruction and quantitative analysis of the bone structure of the glenoid. We used
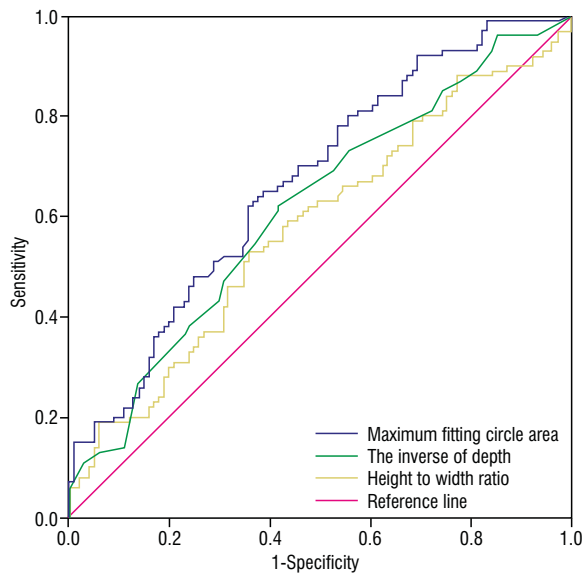
Figure 8. Receiver operating characteristic curves showed that individuals with anterior shoulder instability had smaller glenoid depth and larger height to width ratio and the glenoid maximum fitting circle area compared with the control group.

post-processing technologies such as three-dimensional volume-rendered reconstructions, which made it more intuitive and convenient for us to evaluate the shape of the glenoid [13, 23]. It is readily and rapidly available in most hospitals compared with magnetic resonance imaging [7]. The study shows that the normal bilateral glenoids of Chinese Han population is symmetrical in terms of height, width, height to width ratio, depth, area, maximum fitting circle area, volume and version angle, which implies that we can use the contralateral normal side as the reference for analysing the bony anatomy of the glenoid in patients with recurrent anterior shoulder dislocation.

For the first time, we have performed an analysis of the shape of the glenoid in Chinese patients. The glenoid fossa of the scapula is a shallow oval depression on the lateral corner of the scapula. There may be a notch at the anterior and superior edges of the glenoid. This notch is consequently a common finding, rather than a rare anatomical variant, but is often overlooked in studies [17, 18]. The notch is situated somewhat above the middle of the anterior margin of the cavity and can be very prominent, very shallow or absent. Preschers [17, 18] classified the shape of glenoid according to the presence or absence of glenoid notch. One hundred twenty-nine (55%) scapulae showed a more or less recognisable glenoid notch at the anterior margin of the glenoid cavity and were pear-shaped; 107 (45%) scapulae showed no notch

and were of oval form [17, 18]. Sangeeta Gupta et al. [10] classified 60 scapula glenoid anatomical specimens into inverted comma-shaped, pear-shaped or teardrop-shaped, and oval-shaped, and the left and right sides were not always identical. The inverted comma-shaped was 38%, the pear-shaped was 42% and the oval-shaped was 20%, and the relationship with shoulder instability needs further study [10]. In this study, inverted comma-shaped, pear-shaped, and oval-shaped glenoid of the bilateral glenoids accounted for 8%, 72%, and 20% in the control group, including 118 (90%) symmetrically shaped scapular pairs and 13 (10%) asymmetrically shaped scapular pairs. The difference between the sides was not significant. In the dislocation group inverted comma-shaped, pear-shaped, and oval-shaped glenoid of the unaffected glenoids accounted for 7%, 50%, and 43%, respectively. The study showed that the control group had fewer oval-shaped glenoids compared with Preschers [17, 18], but the proportion of oval-shaped in the dislocation group was significantly increased.

This study showed that the shape of the glenoid was an important factor in cases of anterior instability of the shoulder. Pear-shaped and inverted comma-shaped glenoid had lower risk of recurrent anterior shoulder dislocation compared to oval glenoid. The results suggested that the pear-shaped and inverted comma-shaped glenoids were protective factors for recurrent anterior shoulder dislocation, the oval-shaped glenoid was a risk factor and may be prone to recurrent anterior shoulder dislocation. This may be inconsistent with the hypothesis of Preschers [18] that the labrum does not attach to the bone at the notch and liable to be sheared of (Bankart lesions). There is no doubt that evaluating the risk factors of recurrent shoulder dislocation by simple shape analysis is still a preliminary study, we also need to analyse the relationship between glenoid shape and soft tissues such as the glenoid labrum, ligaments, and whether there are racial differences. There was no priority of side for the glenoid notch, so that an influence of handedness on the shaping of the glenoid cavity is unlikely. This study used CT to analyse the shape of the glenoid in Chinese people. Unfortunately, visualising soft tissues in a CT scan is not possible without the use of contrast agents, so the relationship between the glenoid notch and the glenoid labrum could not be determined. If the notch was present, the glenoid labrum was not attached in this area to the anterior margin of the glenoid cavity.

A small recess of the articular cavity was regularly found at the glenoid notch. It was mentioned in the paper by Preschers [17, 18]. The middle glenohumeral ligament, a broad, thick structure with a variety of presentations, also originates at the superior part of the articular lip; whether it is related to the notch requires further study. In addition, the notch is mentioned by Frazer (1958) [4], who stated that the position of the notch indicates the line of the junction between the 'coracoid' and the 'scapular' parts of the glenoid cavity. However, the glenoid notch is located a few millimetres below the junction between these two developmental parts of the glenoid cavity.

The distance between the supraglenoid tubercle and the infraglenoid tubercle of the glenoid determines the height of the glenoid. The distance between the anterior and posterior edges of the glenoid determines the width of the glenoid. Saygi et al. [21] found that the height of the dislocation group was significantly different from that of the control group. This study showed that the differences of height and width between the dislocation and control group were not significant. Owens et al. [15] analysed the glenoid height of 714 young athletes and found that a tall and narrow glenoid was more unstable and associated with a higher risk of dislocation than a short and wide glenoid. Hong et al. [11] found that an increased ratio of glenoid height to width was a risk factor for anterior glenohumeral joint instability. The same conclusion was reached in this study. While neither height nor width was a significant risk factor in its own right, the glenoid height to width ratio was a significant finding. There were significant differences in the ratio of glenoid height to width between the dislocation group and the control group, suggesting that height to width ratio was a risk factor for recurrent anterior shoulder dislocation.

Previous studies did not consider glenoid depth to be risk factor of anterior shoulder instability [16]. In contrast, the glenoid depth played an important role in anterior shoulder instability. In our study, the depth of the dislocation group was significantly lower than that of the control group. We revealed that the glenoid depth was a risk factor for anterior shoulder instability. The cutoff point for glenoid depth was 4.25 mm.

The glenoid osseous Bankart injury is an avulsion fracture of the anterior inferior glenoid when the shoulder dislocation occurs, resulting in the reduction of the glenoid area. It is an important cause of shoulder instability and recurrent anterior dislo-cation. Previous studies showed that glenoid bone defects were generally measured by the maximum fitting circle method [8, 24]. This study we measured the maximum fitting circle area on one side of the control group and the unaffected side of the dislocation group. This study also found that there was a significant difference in the maximum fitting circle area between the dislocation group and the control group, and the dislocation group had a larger glenoid area. We revealed that the maximum fitting circle area was a risk factor for anterior shoulder instability. The cutoff point for maximum fitting circle area was 515.55 mm^2.

The version angle is the angle between the scapular plane and the glenoid plane in the cross-sectional view, with a positive value representing anterior tilt of the glenoid and a negative value representing posterior tilt, reflecting the anteversion or retroversion of the glenoid in the axial position. Churchill et al. [2] measured version angles using anatomical specimens and concluded that there were differences among different ethnic groups. Aygun et al. [1] concluded that the angles of glenoid version on the dislocated side were significantly more anteverted in the study group than in the dominant and nondominant shoulders of the control group. However, in our study, we did not identify a significant relationship between glenoid version and anterior shoulder instability in the Chinese Han population. The results of the glenoid version angle in this study were similar to previous study [11].

Limitations of the study

This study has several limitations. One possible limitation is the select and homogeneous nature of our study. The included population is ideal for a clinical study, but the sample may not be representative of the normal healthy population and could lead to the selective bias in this study. For version measurement, the results of intraclass correlation coefficient for intra- and interobserver reliability showed that intraobserver intraclass correlation coefficient was significantly more reliable; therefore, only one independent examiner did this work, but this may lead to bias.

CONCLUSIONS

The normal bilateral glenoids of Chinese people are basically symmetrical. The glenoid shape, depth, height to width ratio and maximum fitting circle area

are risk factors for recurrent shoulder dislocation. Evaluation of the glenoid bone structure enables more accurate prediction of the risk of recurrent shoulder dislocation.

Conflict of interest: None declared

REFERENCES

1. Aygün Ü, Çalik Y, Işik C, et al. The importance of glenoid version in patients with anterior dislocation of the shoulder. J Shoulder Elbow Surg. 2016; 25(12): 1930–1936, doi: 10.1016/j.jse.2016.09.018, indexed in Pubmed: 27855874.

2. Churchill RS, Brems JJ, Kotschi H. Glenoid size, inclination, and version: an anatomic study. J Shoulder Elbow Surg. 2001; 10(4): 327–332, doi: 10.1067/mse.2001.115269, indexed in Pubmed: 11517362.

3. Cofield RH, Kavanagh BF, Frassica FJ. Anterior shoulder instability. Instr Course Lect. 1985; 34: 210–227, indexed in Pubmed: 3833942.

4. Frazer JE, Viii LP. The Anatomy of the Human Skeleton. 5th ed. Churchill, London 1958.

5. Gervasi E, Sebastiani E, Spicuzza A. Multidirectional shoulder instability: arthroscopic labral augmentation. Arthrosc Tech. 2017; 6(1): e219–e225, doi: 10.1016/j.eats.2016.09.025, indexed in Pubmed: 28409104.

6. Grana WA, Buckley PD, Yates CK. Arthroscopic Bankart suture repair. Am J Sports Med. 1993; 21(3): 348–353, doi: 10.1177/036354659302100304, indexed in Pubmed: 8346746.

7. Green GL, Arnander M, Pearse E, et al. CT estimation of glenoid bone loss in anterior glenohumeral instability: a systematic review of existing techniques. Bone Jt Open. 2022; 3(2): 114–122, doi: 10.1302/2633-1462.32.BJO-2021-0163.R1, indexed in Pubmed: 35109662.

8. Griffith JF. Measuring glenoid and humeral bone loss in shoulder dislocation. Quant Imaging Med Surg. 2019; 9(2): 134–143, doi: 10.21037/qims.2019.01.06, indexed in Pubmed: 30976536.

9. Guan H, Zhang B, Ye Z, et al. Glenoid bony morphology along long diameter is associated with the occurrence of recurrent anterior shoulder dislocation: a case-control study based on three-dimensional CT measurements. Int Orthop. 2022; 46(8): 1811–1819, doi: 10.1007/s00264-022-05463-5, indexed in Pubmed: 35668240.

10. Gupta S, Magotra R, Kour M. Morphometric analysis of glenoid fossa of scapula. J Evol Med Dental Sci. 2015; 4(45): 7761–7766, doi: 10.14260/jemds/2015/1129.

11. Hong J, Huang Y, Ma C, et al. Risk factors for anterior shoulder instability: a matched case-control study. J Shoulder Elbow Surg. 2019; 28(5): 869–874, doi: 10.1016/j.jse.2018.09.014, indexed in Pubmed: 30509611.

12. Huijsmans PE, Haen PS, Kidd M, et al. Quantification of a glenoid defect with three-dimensional computed tomography and magnetic resonance imaging: a cadaveric study. J Shoulder Elbow Surg. 2007; 16(6): 803–809, doi: 10.1016/j.jse.2007.02.115, indexed in Pubmed: 18061117.

13. Hurley ET, Matache BA, Wong I, et al. Anterior Shoulder Instability International Consensus Group. Anterior Shoulder Instability Part I-Diagnosis, Nonoperative Management, and Bankart Repair-An International Consensus Statement. Arthroscopy. 2022; 38(2): 214–223.e7, doi: 10.1016/j.arthro.2021.07.022, indexed in Pubmed: 34332055.

14. Moroder P, Hitzl W, Tauber M, et al. Effect of anatomic bone grafting in post-traumatic recurrent anterior shoulder instability on glenoid morphology. J Shoulder Elbow Surg. 2013; 22(11): 1522–1529, doi: 10.1016/j.jse.2013.03.006, indexed in Pubmed: 23664749.

15. Owens BD, Campbell SE, Cameron KL. Risk factors for anterior glenohumeral instability. Am J Sports Med. 2014; 42(11): 2591–2596, doi: 10.1177/0363546514551149, indexed in Pubmed: 25248922.

16. Peltz CD, Zauel R, Ramo N, et al. Differences in glenohumeral joint morphology between patients with anterior shoulder instability and healthy, uninjured volunteers. J Shoulder Elbow Surg. 2015; 24(7): 1014–1020, doi: 10.1016/j.jse.2015.03.024, indexed in Pubmed: 25958216.

17. Prescher A. Anatomical basics, variations, and degenerative changes of the shoulder joint and shoulder girdle. Eur J Radiol. 2000; 35(2): 88–102, doi: 10.1016/s0720-048x(00)00225-4, indexed in Pubmed: 10963915.

18. Prescher A, Klümpen T. The glenoid notch and its relation to the shape of the glenoid cavity of the scapula. J Anat. 1997; 190(Pt 3): 457–460, doi: 10.1046/j.1469-7580.1997.19030457.x, indexed in Pubmed: 9147231.

19. Provencher MT, Midtgaard KS, Owens BD, et al. Diagnosis and management of traumatic anterior shoulder instability. J Am Acad Orthop Surg. 2021; 29(2): e51–e61, doi: 10.5435/JAAOS-D-20-00202, indexed in Pubmed: 33275397.

20. Rutgers C, Verweij LPE, Priester-Vink S, et al. Recurrence in traumatic anterior shoulder dislocations increases the prevalence of Hill-Sachs and Bankart lesions: a systematic review and meta-analysis. Knee Surg Sports Traumatol Arthrosc. 2022; 30(6): 2130–2140, doi: 10.1007/s00167-021-06847-7, indexed in Pubmed: 34988633.

21. Saygi B, Karahan N, Karakus O, et al. Analysis of glenohumeral morphological factors for anterior shoulder instability and rotator cuff tear by magnetic resonance imaging. J Orthop Surg (Hong Kong). 2018; 26(2): 2309499018768100, doi: 10.1177/2309499018768100, indexed in Pubmed: 29635957.

22. Shi L, Griffith JF, Huang J, et al. Excellent side-to-side symmetry in glenoid size and shape. Skeletal Radiol. 2013; 42(12): 1711–1715, doi: 10.1007/s00256-013-1728-y, indexed in Pubmed: 24077754.

23. Stefaniak J, Lubiatowski P, Kubicka AM, et al. Clinical and radiological examination of bony-mediated shoulder instability. EFORT Open Rev. 2020; 5(11): 815–827, doi: 10.1302/2058-5241.5.200049, indexed in Pubmed: 33312708.

24. Stillwater L, Koenig J, Maycher B, et al. 3D-MR vs. 3D-CT of the shoulder in patients with glenohumeral instability. Skeletal Radiol. 2017; 46(3): 325–331, doi: 10.1007/s00256-016-2559-4, indexed in Pubmed: 28028575.

25. Walton J, Paxinos A, Tzannes A, et al. The unstable shoulder in the adolescent athlete. Am J Sports Med. 2002; 30(5): 758–767, doi: 10.1177/03635465020300052401, indexed in Pubmed: 12239016.

26. Wermers J, Raschke MJ, Wilken M, et al. The anatomy of glenoid concavity-bony and osteochondral assessment of a stability-related parameter. J Clin Med. 2021; 10(19), doi: 10.3390/jcm10194316, indexed in Pubmed: 34640334.

C A S E   R E P O R T

Bilateral vertebral arteries entering the C4 foramen transversarium with the left vertebral artery originating from the aortic arch

C.J. Dean[1], K. Labagnara[1], A.K. Lee[1], D.J. Yun[1], Z. Dong[1], P.L. Mishall[1, 2], A. Pinkas[1]

[1]Department of Pathology, Albert Einstein College of Medicine, Bronx, NY, United States
[2]Department of Ophthalmology and Visual Science, Albert Einstein College of Medicine, Bronx, NY, United States

Vertebral arteries (VAs) serve as major blood vessels to the central nervous system. VAs typically arise from the subclavian arteries and ascend separately within the transverse foramina of the cervical vertebrae (C6-C1) before entering the skull at the foramen magnum and joining at the base of the pons to form the basilar artery of the vertebrobasilar circulation. Therefore, variations in the origin and anatomic course of the VAs have implications for invasive medical procedures involving the superior thoracic/cervical regions or the cervical vertebrae. The current case report describes variation in the entry point of both VAs and the site of origin of the left vertebral artery. The variation was revealed during routine dissection of a 72-year-old female cadaver. It was found that the left vertebral artery originated directly from the aortic arch to abnormally enter the transverse foramen of C4 instead of the transverse foramen of C6. The right vertebral artery arose as usual from the right subclavian artery. However, the right vertebral artery also directly entered the transverse foramen of C4 instead of the transverse foramen of C6.
(Folia Morphol 2023; 82, 3: 721–725)

Key words: vertebral artery, aortic arch, cervical vertebrae, transverse foramen

INTRODUCTION

The vertebral arteries (VAs) and their branches provide the blood supply to a majority of important structures of the central nervous system, including the brainstem, spinal cord, cerebellum, and cranial meninges. The VAs typically originate in the root of the neck, branching from the first part of the right and left subclavian arteries. The VAs have an extracranial and intracranial course. For the extracranial course, the VAs pass superiorly to enter the transverse foramina of the C6 vertebra and continue to run through the transverse foramina of each superior cervical vertebra before passing through the foramen magnum to enter the skull. For the intracranial course, the right and left VAs run on the posterior surface of the medulla oblongata and join at the base of the pons to form the basilar artery. The basilar artery then branches into posterior cerebral arteries. This forms the posterior part of the circle of Willis — the arterial circle that provides blood supply to the brain.

Variations in vertebral artery (VA) origin, branching pattern, and course have been seen in both cadaveric [3, 5, 11] and patient populations [1, 4, 6–12]. A study examining existing variations of VA

Address for correspondence: A. Pinkas, PhD, Ass. Prof., Department of Pathology, Albert Einstein College of Medicine, 1300 Morris Park Ave, Forchheimer Building Room 620SD, Bronx, NY 10461, USA, tel: +1 (718) 430-4260, fax: +1 (718) 430-8996, e-mail: adi.pinkas@einsteinmed.edu

origin in both cadavers and living patients found that unilateral abnormalities are most common and was seen in greater than 95% of cases. Of the cases with a unilateral aberrant origin, the left vertebral artery (LVA) was found to be the affected vessel 85.6% of the time. The site of aberrant origin of the LVA was most commonly at the aortic arch, occurring in 97.4% of cases [11]. Another study reported on variations in the entry point of VAs into the transverse foramina of the cervical vertebrae. The study findings showed that the incidence of abnormal entry of VAs into the transverse foramina is as high as 7%. The same study reported on the laterality of the abnormally entering VAs. Investigators found that the majority of VAs that entered the transverse process of the cervical vertebrae at an abnormal level were unilateral (31/33 individuals with an abnormality; 31/250 individuals studied) with only minimal incidence of a bilateral abnormality (2/33 individuals with an abnormality; 2/250 individuals studied) [1].

Knowledge of abnormal origins and unique courses of the VA is crucial for ensuring patient safety during invasive procedures near the thoracic outlet or involving an anterior or lateral approach to the cervical spine. This case report documents cadaveric findings of a LVA originating from the aortic arch and bilateral VAs with abnormal entry points into the transverse foramina of the cervical vertebrae at the level of C4.

CASE REPORT

The superior mediastinum of a 72-year-old female cadaver was dissected by faculty members during the preparation of prosected cadavers for a first-year anatomy course. While utilising Grant's Dissector [2], the sternum and anterior rib cage were reflected inferiorly to gain access to the thoracic cavity. The heart and lungs were carefully dissected and removed to fully expose the ascending aorta, aortic arch, and all relevant vascular branches. The bodies of the left and right clavicles were removed for adequate visualisation of the subclavian arteries. It was noted that the LVA arose directly from the aortic arch and the right vertebral artery arose appropriately from the right subclavian artery. The anterior and lateral neck were then dissected to visualise the courses of the VAs. It was found that both VAs did not enter the transverse foramina of C6. As a result, the anterior and lateral neck were further dissected. The deep muscles of the neck close to the transverse and spinous processes of the cervical vertebrae were reflected to better visualise the abnormal entry and courses of the

VAs. It was found that the VAs entered the transverse foramina of the C4 vertebra instead of the C6 vertebra. The VAs continued to travel through the cervical transverse foramina before entering the skull via the foramen magnum. It was found that the VAs then followed a normal intracranial course.

During dissection of the superior mediastinum, an abnormal origin of the LVA was noted. Rather than originating from the first part of the left subclavian artery, it originated directly from the aortic arch. Specifically, its origin was located distal to the origin of the left common carotid artery and proximal to the origin of the left subclavian artery (Fig. 1).

Anterior and lateral neck dissections revealed that the LVA travelled superiorly but did not enter the transverse foramen of C6 as would be expected. Instead, it continued superiorly outside of the transverse foramina of C6 and C5 before entering the transverse foramen of the C4 vertebra (Fig. 2).

Of note, the right vertebral artery was found to have an anatomically normal origin at the first part of the right subclavian artery (Fig. 3). However, it also appears to follow an atypical anatomic course, ascending outside of the transverse foramina of C6 and C5 before entering the transverse foramen of the C4 vertebra (Fig. 2).

After entering the transverse foramina of C4, both VAs were found to ascend normally through the cervical transverse foramina before entering the skull via the foramen magnum. It was noted that the VAs then followed a normal intracranial course.

DISCUSSION AND CONCLUSIONS

This case report involves two different variations of the LVA and one variation of the right vertebral artery found within a single cadaveric donor. In this unique case, the LVA originated as the third direct branch of the aortic arch distal to the origin of the left common carotid artery and proximal to the origin of the left subclavian artery. Furthermore, both VAs followed an abnormal ascending course outside of the transverse foramina of C6 and C5 until entering the transverse foramina at the level of C4 and continuing to ascend normally. Within the existing literature, a LVA originating directly from the aortic arch has been a commonly observed anatomic variant [3, 6, 11]. One study involving analysis of 955 cases of the LVA originating from the aortic arch found that the location of origin seen in this case report — between the left common carotid and left subclavian arter-
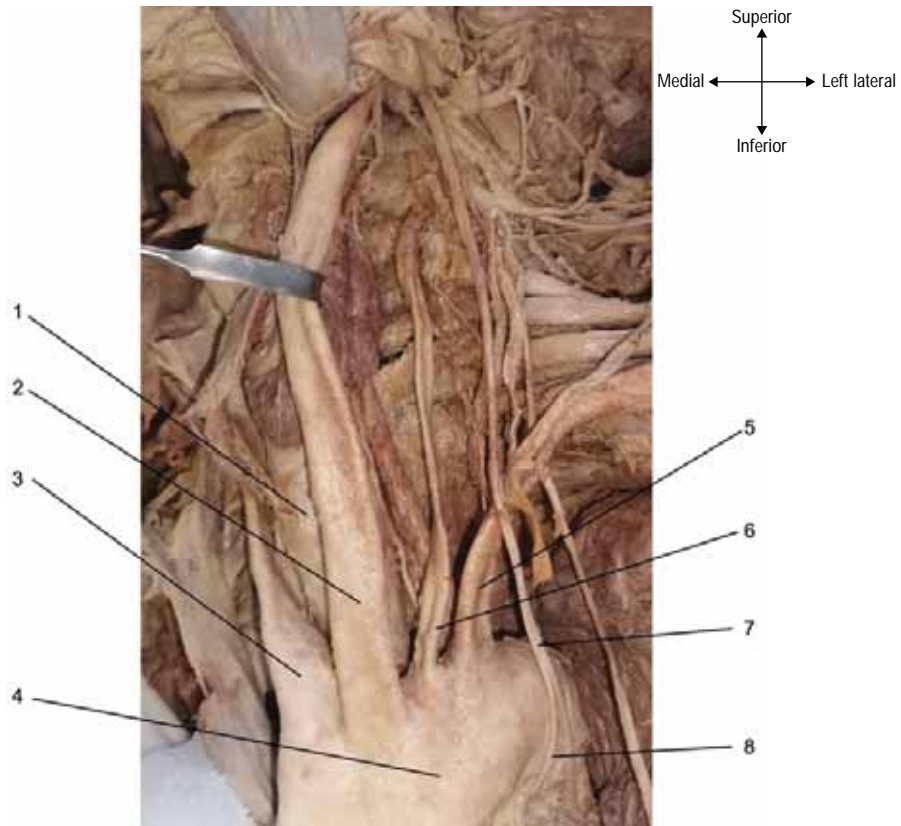
Figure 1. Aortic arch and direct arterial branches. Left vertebral artery originates between left common carotid and left subclavian arteries; 1 — trachea; 2 — left common carotid artery; 3 — brachiocephalic artery; 4 — aortic arch; 5 — left subclavian artery; 6 — left vertebral artery; 7 — left vagus nerve; 8 — left recurrent laryngeal nerve.
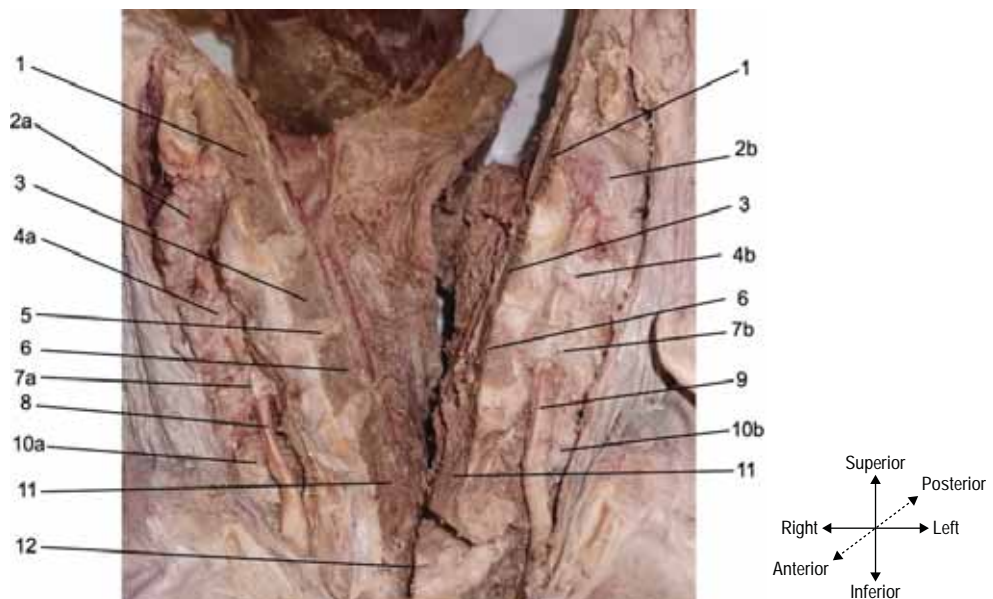
Figure 2. Anterior view of bisected cervical vertebral column. Right and left vertebral arteries directly enter C4 transverse foramen and continue to pass through C3-C1 transverse foramina; 1 — C2 vertebral body; 2a — C2 transverse process (right); 2b — C2 transverse process (left); 3 — C3 vertebral body; 4a — C3 transverse process (right); 4b — C3 transverse process (left); 5 — intervertebral disc; 6 — C4 vertebral body; 7a — C4 transverse process (right); 7b — C4 transverse process (left); 8 — right vertebral artery; 9 — left vertebral artery; 10a — C5 transverse process (right); 10b — C5 transverse process (left); 11 — C5 vertebral body; 12 — C6 vertebral body.

723
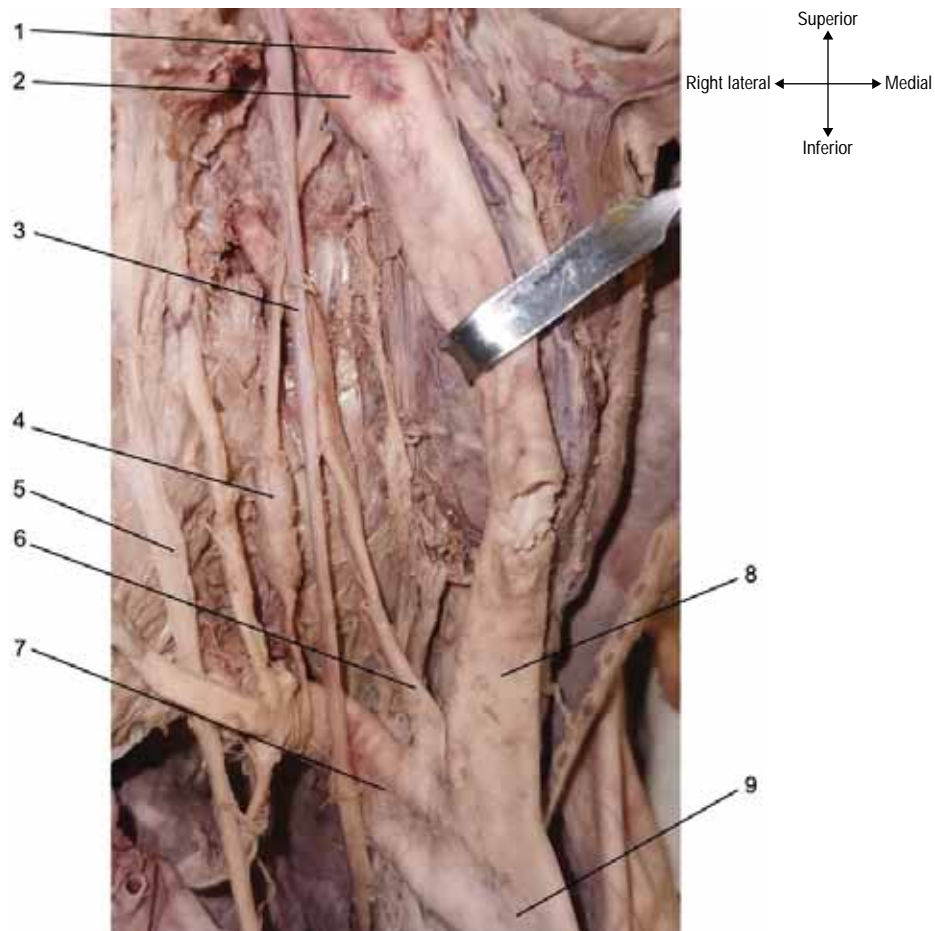
Figure 3. Right vertebral artery originates from right subclavian artery; 1 — right internal carotid artery; 2 — right external carotid artery; 3 — right vagus nerve; 4 — inferior cervical sympathetic ganglion; 5 — right phrenic nerve; 6 — right vertebral artery; 7 — right subclavian artery; 8 — right common carotid artery; 9 — brachiocephalic artery.

ies — was the most common variant, occurring in 782 (81.9%) cases [11]. The same study noted other abnormal sites of origin for the LVA, including 71 (7.4%) cases originating between the right common carotid and left common carotid arteries, 37 (3.9%) cases originating distal to the left subclavian artery, and 46 (4.8%) cases originating at the root of the left subclavian artery [11]. Additional case reports have also noted the LVA originating both completely and partially (i.e. having multiple origins) as the third direct branch of the aortic arch [3, 8]. Right and LVAs that enter the cervical transverse foramina above the level of C6 are a significantly less common variation. A study utilising magnetic resonance imaging of 500 VAs in living individuals cited the incidence of VAs entering the transverse cervical foramina at the level of C6 as being greater than 90% [1]. Entrance at more superior levels was cited as being significantly less common, with the incidence of entrance at the

level of C4 being as little as 1% [1]. Furthermore, the same study found most cases of abnormal VA courses to be unilateral, occurring in 31/33 individuals with noted abnormalities, while bilaterally abnormal courses were significantly less common, occurring in only 2/33 individuals noted to have abnormal anatomy [1]. These findings are corroborated in other studies that have examined the anatomy of VAs in living patients via a variety of imaging modalities, including multi-detector computed tomography [9], magnetic resonance imaging [4], and computed tomography angiography [7, 12]. Similar findings have also been noted via direct observation in cadaveric specimens [5]. While each of the individual VA abnormalities exhibited in this report has been documented, the unique combination found here with the LVA originating from the aortic arch and both left and right VAs entering the transverse foramina of the C4 vertebra appears to be exceedingly rare. No known cases that

match the precise anatomy of this cadaveric donor were found within the available literature.

There are many clinical implications that warrant a more widespread awareness of such VA variants among physicians. For example, a case report of a 16-year-old male with a LVA that ascended outside of the transverse foramina of C6-C3 with entrance into the transverse foramen of C2 documented that this individual experienced dizziness and syncope as a result of arterial folding with neck flexion [10]. This case highlights the possibility of abnormal VA anatomy predisposing patients to cerebral ischaemia likely involving the posterior circulation. Such ischaemic changes may have dangerous and potentially life-threatening implications for patients with such anatomy, which warrants clinical consideration. Perhaps a more important application of the knowledge of VA variations is surgical. Iatrogenic injury of the VA is a potentially disastrous complication of surgeries involving the anterolateral neck and cervical vertebrae or injections of the cervical epidural space in patients with cervical radiculopathies. Potential complications include arterial dissection, vasospasm, fistula formation, pseudoaneurysm formation, cerebral ischaemia, or even patient death. This case report highlights the possibility of a VA that ascends outside of the transverse foramina of the cervical vertebrae and therefore without the protection offered by the bony transverse processes. Thus, an awareness of the anatomy of the VAs prior to initiation of surgical procedures that risk injury to these vessels is of paramount importance for patient safety. Preoperative mapping of the VAs may be accomplished via commonly utilised imaging studies such as colour doppler ultrasonography, computed tomographic angiography, or magnetic resonance angiography and may therefore be both widely available and clinically useful in avoiding injury to these vessels. The possible clinical utility of such imaging practices warrants further studies to better characterise the prevalence of anatomic variants of the VAs in specific patient populations as well as the impact on patient outcomes in those who undergo preoperative mapping of the vertebral vasculature.

The findings of this report may therefore be of particular interest to clinicians, as similar unidentified variations of the VAs may increase the potential for complications during invasive procedures in the superior thoracic or cervical regions. The use of preoperative imaging in order to determine the course of the VAs may thus be warranted to avoid such complications and enhance patient safety.

REFERENCES

1. Bruneau M, Cornelius JF, Marneffe V, et al. Anatomical variations of the V2 segment of the vertebral artery. Neurosurgery. 2006; 59(1 Suppl 1): ONS20–4; discussion ONS20, doi: 10.1227/01.NEU.0000219931.64378.B5, indexed in Pubmed: 16888547.
2. Detton AJ. Grant's Dissector. 17th ed. Wolters Kluwer Health/Lippincott Williams & Wilkins, Philadelphia, PA 2020.
3. Einstein EH, Song LH, Villela NLA, et al. Anomalous origin of the left vertebral artery from the aortic arch. Aorta (Stamford). 2016; 4(2): 64–67, doi: 10.12945/j.aorta.2015.15.022, indexed in Pubmed: 27757404.
4. Eskander MS, Drew JM, Aubin ME, et al. Vertebral artery anatomy: a review of two hundred fifty magnetic resonance imaging scans. Spine (Phila Pa 1976). 2010; 35(23): 2035–2040, doi: 10.1097/BRS.0b013e3181c9f3d4, indexed in Pubmed: 20938397.
5. Gitkind AI, Olson TR, Downie SA. Vertebral artery anatomical variations as they relate to cervical transforaminal epidural steroid injections. Pain Med. 2014; 15(7): 1109–1114, doi: 10.1111/pme.12266, indexed in Pubmed: 25202774.
6. Goray VB, Joshi AR, Garg A, et al. Aortic arch variation: a unique case with anomalous origin of both vertebral arteries as additional branches of the aortic arch distal to left subclavian artery. AJNR Am J Neuroradiol. 2005; 26(1): 93–95, indexed in Pubmed: 15661708.
7. Hong JT, Park DK, Lee MJ, et al. Anatomical variations of the vertebral artery segment in the lower cervical spine: analysis by three-dimensional computed tomography angiography. Spine (Phila Pa 1976). 2008; 33(22): 2422–2426, doi: 10.1097/BRS.0b013e31818938d1, indexed in Pubmed: 18923317.
8. Satti SR, Cerniglia CA, Koenigsberg RA. Cervical vertebral artery variations: an anatomic study. AJNR Am J Neuroradiol. 2007; 28(5): 976–980, indexed in Pubmed: 17494682.
9. Shin HY, Park JiK, Park SK, et al. Variations in entrance of vertebral artery in Korean cervical spine: MDCT-based analysis. Korean J Pain. 2014; 27(3): 266–270, doi: 10.3344/kjp.2014.27.3.266, indexed in Pubmed: 25031813.
10. Siedlecki Z, Szostak M, Nowak K, et al. Atypical course of vertebral artery outside the cervical spine: case report and review of the literature. World Neurosurg. 2021; 145: 405–408, doi: 10.1016/j.wneu.2020.10.028, indexed in Pubmed: 33059082.
11. Yuan SM. Aberrant origin of vertebral artery and its clinical implications. Braz J Cardiovasc Surg. 2016; 31(1): 52–59, doi: 10.5935/1678-9741.20150071, indexed in Pubmed: 27074275.
12. Zhang M, Dayani F, Purger DA, et al. Extraforaminal vertebral artery anomalies and their associated surgical implications: an epidemiologic and anatomic report on 1000 patients. World Neurosurg. 2020; 141: e971–e975, doi: 10.1016/j.wneu.2020.06.110, indexed in Pubmed: 32585381.

CASE REPORT

VIA MEDICA

An aberrant right subclavian artery in a 63-year-old male cadaver

P. Ostrowski, M. Bonczar, W. Przybycień, I. Zamojska, B. Kołodziejczyk, J. Walocha, M. Koziej

Department of Anatomy, Jagiellonian University Medical College, Krakow, Poland

An aberrant right subclavian artery (ARSA), also called "arteria lusoria", is described as a right subclavian artery (RSA) with a retro-oesophageal course that most frequently originates as the most distal branch of the aortic arch. The aim of the following study was to present and thoroughly describe a case of an ARSA, its course, branches, and relation to the surrounding anatomical structures and discuss the clinical significance and embryology of this variant. During routine dissection, a 63-year-old male cadaver with an abnormal variant of the RSA was found. The RSA branched off from the aortic arch as the most distal branch. Subsequently, it coursed posteriorly to the trachea and oesophagus at the level of T2 and T3. Abnormalities in the branching pattern of the RSA were also discovered, such as the right vertebral artery originating from the right common carotid artery as its first branch. This study presents a case of an ARSA, which is a rare anatomical variant of the branches of the aortic arch. The course and branching pattern of an aberrant subclavian artery is quite variable, and each variant can be associated with different possible complications. Furthermore, the ARSA is associated with other cardiovascular anomalies, such as the Kommerell's diverticulum. Therefore, knowledge about the possible variations of this anomaly may be of great importance for physicians who encounter this variant in their practice. (Folia Morphol 2023; 82, 3: 726–731)

Key words: subclavian artery, aberrant right subclavian artery, arteria lusoria

INTRODUCTION

An aberrant right subclavian artery (ARSA), also called "arteria lusoria" is the most common variation of the aortic arch [16, 29]. It is described as a right subclavian artery (RSA) with a retro-oesophageal course that most frequently originates as the most distal branch of the aortic arch [17]. Embryologically, a left aortic arch with an ARSA results from interruption of the right arch between the right common carotid and right subclavian arteries [23]. When the pharyngeal arches develop during the 4th and 5th weeks of embryological development, each pharyngeal arch obtains its own artery, or aortic arch, which arises from the aortic sac, and cranial nerve. The common carotids and the first part of the internal carotid arteries are formed by the third aortic arch. Furthermore, the fourth aortic arch persists on both sides and forms different structures on the right and left sides. The left 4th aortic arch forms part of the arch of the aorta, between the left common carotid and the left subclavian arteries. On the right side, it forms the proximal segment of the RSA. The distal part of the said artery is formed by a portion of the right dorsal aorta and the 7th intersegmental artery [27].

Address for correspondence: Dr. M. Koziej, Department of Anatomy, Jagiellonian University Medical College, ul. Mikołaja Kopernika 12, 33–332 Kraków, Poland, tel: +48 888 202 628, e-mail: mateusz.koziej@gmail.com
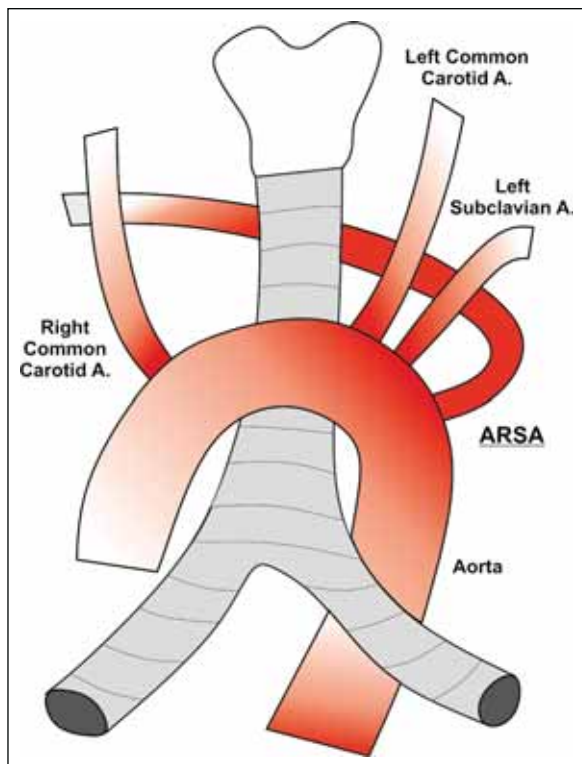
Figure 1. Scheme presenting aberrant right subclavian artery (ARSA).

The prevalence of this vascular anomaly is said to be ranging from 0.16% to 4.4% in the general population, with a female predominance [16, 20]. The ARSA was first described by Hunauld in 1735 [9]. However, the term "dysphagia lusoria" was first mentioned by Bayford in 1787 [3] in a study about a patient with a long history of dysphagia caused by an ARSA. A scheme presenting ARSA can found in Figure 1.

Being aware of the possible anomalies of the aortic arch is important because they might be associated with vascular rings, heart diseases, and chromosomal abnormalities [7, 24]. Congenital variants such as the left circumflex aorta or the right-sided aortic arch are examples of anomalies that have been associated with the formation of vascular [7, 22]. Furthermore, the prevalence of the ARSA is said to be higher in patients with trisomy 21 (35%) [5].

Variations of the arterial system are frequently observed by medical professionals of many distinct specialties worldwide and oftentimes influence daily clinical practice in the form of treatment options [11, 15, 31]. Patients with an ARSA are usually asymptomatic. However, when symptoms are present, they usually consist of dysphagia, chest pain, haemoptysis, and hoarseness, among others [30]. Puri et al. [26] described the symptoms, when present, as manifest-

ing at two extremes of life. In children, dysphagia and symptoms associated with tracheal compression might occur. However, respiratory symptoms associated with the ARSA rarely occur because the adult trachea is more rigid compared to the infant trachea which is more compressible.

The aim of the following study was to present and thoroughly describe a case of an ARSA, its course, branches, and relation to the surrounding anatomical structures. Furthermore, the clinical significance and embryology of this variant will be discussed.

CASE REPORT

During routine dissection, a 63-year-old male cadaver with an abnormal variant of the RSA was found. The RSA originated from the aortic arch as the most distal branch. Subsequently, it coursed posteriorly to the trachea and oesophagus at the level of T2 and T3. At the level of the 1st intercostal space, a costocervical trunk branched off posteriorly. Afterward, a thyrocervical trunk originated superiorly to the first rib. Subsequently, the RSA exited the thorax via the superior thoracic aperture between the anterior and middle scalene muscles. The further course shows no exceptions from the currently adopted normal anatomy of the human body.

In the present case, the brachiocephalic trunk was absent, and the right common carotid artery originated directly from the aortic arch. Furthermore, the right vertebral artery did not originate from the RSA. Instead, at the level of the sternum manubrium, anteriorly to the trachea, the right vertebral artery branched off the right common carotid artery as its first branch. Subsequently, the right vertebral artery entered the transverse foramen at the level of C2. The left subclavian and common carotid arteries branched off normally from the aortic arch, and presented with no abnormalities in their anatomy (Figs. 2, 3).

The diameters of the aortic arch and its branches were measured using a calliper. All measurements were taken two times by two independent researchers (W.P. and P.O.) and a mean value was established taking both measurements into account. The diameter of the ascending aorta at its origin was set at 30.4 mm. The diameter of the RSA at its origin was found to be 12.9 mm. The diameter of the RSA when it courses posteriorly to the trachea and oesophagus was set at 9.9 mm. The diameter of the RSA where it gave off the costocervical trunk was found to be 8.4 mm. The aforementioned measurements, and

additional diameters of the branches of the RSA are presented in Table 1.
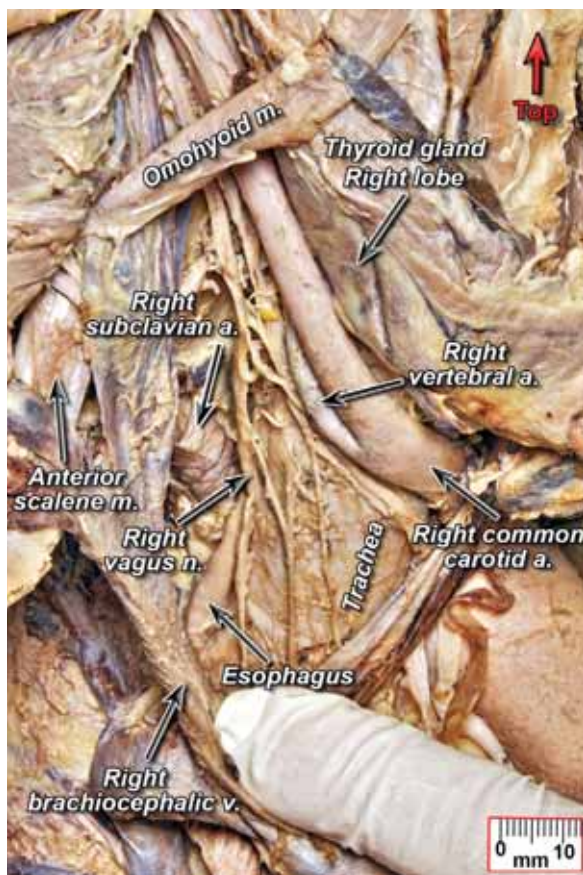
Figure 2. Subclavian artery and its close anatomical area — the aberrant right subclavian artery from the superior view.

Ethical concern

All procedures performed in studies involving human participants were in accordance with the ethical standards of the institutional and/or national research committee and with the 1964 Helsinki Declaration and its later amendments or comparable ethical standards. The material used for this research was obtained from a body donation programme.

Table 1. Mean results of the measurements

Diameters	Mean value [mm]
Ascending aorta at its origin	30.4
Right subclavian artery at its origin	12.9
Right subclavian artery when it courses posteriorly to the trachea and oesophagus	9.9
Right subclavian artery where it gave off the costocervical trunk	8.4
Right costocervical trunk	2.1
Right thyrocervical trunk	4.4
Right common carotid artery at its origin	10.3
Right vertebral artery at its origin	3.8
Left common carotid artery at its origin	8.2
Left subclavian artery at its origin	8.3
Left vertebral artery at its origin	3.9
Left costocervical trunk	3.3
Left thyrocervical trunk	4.5
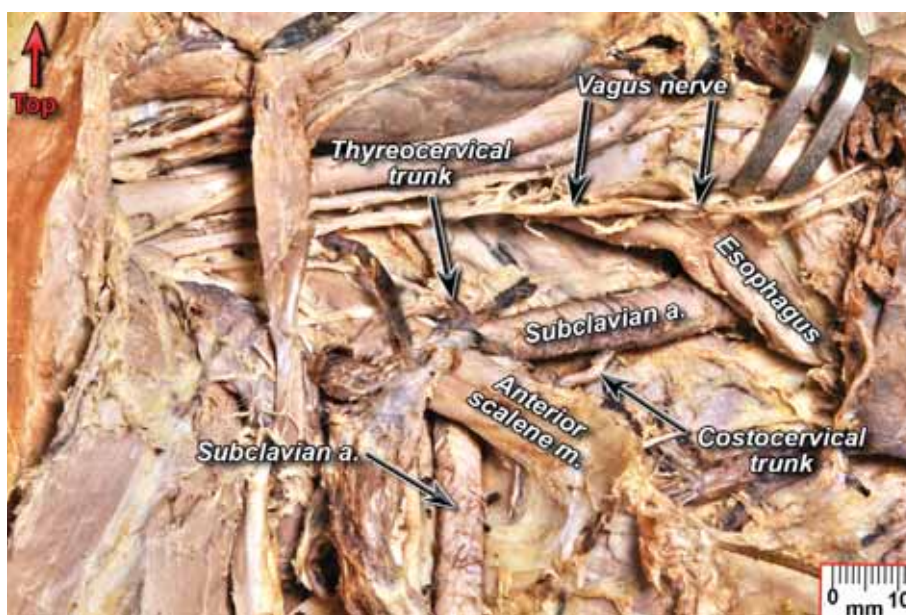
Figure 3. A photograph of the aberrant right subclavian artery — an inferior view.

DISCUSSION

The RSA usually develops from the right 4th aortic arch and 7th cervical intersegmental artery. However, the ARSA results from the regression of the right arch, between the right subclavian and right common carotid arteries, including the right ductus arteriosus. Subsequently, the proximal RSA arises from the distal right dorsal aorta, rather than from the right 4th aortic arch. This forms the retroesophageal portion of the ARSA [1, 8].

The course of the ARSA is quite variable. In most cases, it courses behind the oesophagus and the trachea. However, the artery can also pass between the trachea and oesophagus, and rarely, also anteriorly to the trachea [20]. The current case presents an ARSA with the most frequently seen retroesophageal course. Natsis et al. [20] conducted a retrospective cadaveric study about the ARSA. In the study, they reported that the bicarotid trunk with an ARSA is present in 0.16–19.2% of the cases. However, in the present case, the carotid arteries originated independently from the aortic arch.

The ARSA is associated with other vascular and neural anatomic variations. A prime example is the Kommerells diverticulum, which is a remnant of the dorsal aortic arch [7]. Kommerell [13] was the first to describe this anomaly in 1936, as a retroesophageal outpouching at the origin of an ARSA. However, the aforementioned retroesophageal outpouching at the origin of an aberrant subclavian artery, is actually more prevalent in an aberrant left subclavian artery with a right aortic arch [2, 25]. Nevertheless, this vascular anomaly was not found in the present case study. The presence of an ARSA is also quite common in disorders such as Down's, and Edwards' syndromes, amongst others [28]. Furthermore, aberrant subclavian arteries are also associated with other cardiac anomalies, such as the tetralogy of Fallot [19]. Nakajima et al. [19] reported that the incidence of an aberrant subclavian artery in patients with tetralogy of Fallot was 6%.

Variations of the branching pattern in aberrant subclavian arteries have been discussed in the literature. Keiffer et al. [12] presented a study about the surgical treatment in patients with aberrant subclavian arteries. In the study, they highlighted the coexistence of an ARSA with a vertebral artery originating from the right common carotid artery. Interestingly, this phenomenon was also observed in the present cadaver. Other abnormalities in the branching pattern

of the subclavian artery were noted. The costocervical trunk had a more inferior origin in the thoracic cavity, more specifically, originating at the level of the 1st intercostal space, rather than posteroinferiorly to the clavicle. The branching pattern of this arterial trunk has been proven to be quite variable [4]. However, no abnormalities considering the branches of the costocervical trunk were observed in the present case. Furthermore, other studies have presented cases where the thyroid ima artery originated from the ARSA [12, 20].

An ARSA can compress the respiratory pathways, resulting in an increased risk of pulmonary infections and cyanosis [23]. However, respiratory symptoms in adults with an aberrant subclavian artery are rare. Polguj et al. [23] stated that the reason for the different clinical manifestations of this anomaly is the difference in the anatomy of the trachea. In an infant, the trachea is more compressible, and therefore, more prone to damage that can be caused by an ARSA. However, the adult trachea is more rigid and with that more resistant to compression by an aberrant subclavian artery. The sudden occurrence of symptoms in adults has been associated with age-related morphological alterations of the vessel due to atherosclerosis, and fibromuscular dysplasia among others [20]. Furthermore, in cases where stenosis or tortuosity of the aberrant subclavian artery is present, unequal upper extremity blood pressure, splinter haemorrhages, or vertebrobasilar ischaemia might be present [21]. Patients with an ARSA that arises from the Kommerell diverticulum are also more susceptible to the development of an aneurysm [30]. The rupture of the said aneurysm is a life-threatening complication, and therefore, early detection is very important.

Gross performed the first successful surgical repair of an ARSA in 1946 on a 4-month-old infant [6]. Previously, ARSA, and other aortic arch anomalies were diagnosed by endoscopy or upper gastrointestinal barium imaging. Nowadays, computed tomography-angiography or magnetic resonance-angiography the most common method for diagnosing vascular anomalies, such as the ARSA [14]. Initial management, for mild symptoms, includes lifestyle changes, such as taking smaller sips and chewing well. Use of proton pump inhibitors for acid reduction has also been described [18]. If the conservative treatment does not work, surgical management is advised. The surgical treatment of a symptomatic aberrant subcla-

vian artery consists of both endovascular and surgical treatments. A surgical approach to a symptomatic ARSA consists of dissection of the vessel and end-to-end anastomosis to the unilateral carotid artery [30]. However, Morris et al. [18] presented a hybrid technique using both an endovascular approach with the use of an Amplatzer plug, and a surgical carotid subclavian bypass procedure to treat patients with an ARSA and dysphagia lusoria. In the case study, the patient that underwent the said procedure recovered fully without any neurological deficits.

CONCLUSIONS

The present study presents a case of an ARSA, which is a rare anatomical variant of the branches of the aortic arch. The course and branching pattern of an aberrant subclavian artery is quite variable, and each variant can be associated with different possible complications. Furthermore, the ARSA is associated with other cardiovascular anomalies, such as the Kommerells diverticulum. Therefore, knowledge about the possible variations of this anomaly may be of great importance for physicians who encounter this variant in their practice.

Acknowledgements

Conflict of interest: None declared

REFERENCES

1. Alghamdi MA, Al-Eitan LN, Elsy B, et al. Aberrant right subclavian artery in a cadaver: a case report of an aortic arch anomaly. Folia Morphol. 2021; 80(3): 726–729, doi: 10.5603/FM.a2020.0081, indexed in Pubmed: 32748949.
2. Backer CL, Ilbawi MN, Idriss FS, et al. Vascular anomalies causing tracheoesophageal compression. Review of experience in children. J Thorac Cardiovasc Surg. 1989; 97(5): 725–731, indexed in Pubmed: 2651808.
3. Bayford D. An Account of a Singular Case of Obstructed Deglutition. Memoirs of the Medical Society of London, London 1787.
4. Bonczar M, Ostrowski P, Dziedzic M, et al. The costocervical trunk: a detailed review. Clin Anat. 2022; 35(8): 1130–1137, doi: 10.1002/ca.23929, indexed in Pubmed: 35796160.
5. Fehmi Yazıcıoğlu H, Sevket O, Akın H, et al. Aberrant right subclavian artery in Down syndrome fetuses. Prenat Diagn. 2013; 33(3): 209–213, doi: 10.1002/pd.4042, indexed in Pubmed: 23319208.
6. Gross RE. Surgical treatment for dysphagia lusoria. Ann Surg. 1946; 124(3): 532–534, indexed in Pubmed: 17858859.
7. Hanneman K, Newman B, Chan F. Congenital variants and anomalies of the aortic arch. Radiographics. 2017; 37(1): 32–51, doi: 10.1148/rg.2017160033, indexed in Pubmed: 27860551.
8. Hanneman K, Newman B, Chan F. Congenital variants and anomalies of the aortic arch. Radiographics. 2017; 37(1): 32–51, doi: 10.1148/rg.2017160033, indexed in Pubmed: 27860551.
9. Hunauld PM. Examen de quelques parties d'un singe. Histoire de l'Academie Royale des Sciences. 1735; 2: 516–523.
10. Iwanaga J, Singh V, Ohtsuka A, et al. Acknowledging the use of human cadaveric tissues in research papers: Recommendations from anatomical journal editors. Clin Anat. 2021; 34(1): 2–4, doi: 10.1002/ca.23671, indexed in Pubmed: 32808702.
11. Kahn C, MacNeil M, Fanola C, et al. Complex arterial patterning in an anatomical donor. Transl Res Anat. 2018; 12: 11–19, doi: 10.1016/j.tria.2018.06.001.
12. Kieffer E, Bahnini A, Koskas F. Aberrant subclavian artery: surgical treatment in thirty-three adult patients. J Vasc Surg. 1994; 19(1): 100–110, doi: 10.1016/s0741-5214(94)70125-3, indexed in Pubmed: 8301723.
13. Kommerell B. Verlagerung des ösophagus durch eine abnorm verlaufende arteria subclavia dextra (arteria lusoria). Fortschr Geb Roentgenstr. 1936; 54: 590–595.
14. Leon M, Garibaldi M, Virgen F, et al. Hybrid treatment of aberrant right subclavian artery causing dysphagia lusoria by subclavian to carotid transposition and endovascular plug. Vasc Specialist Int. 2020; 36(4): 258–262, doi: 10.5758/vsi.200042, indexed in Pubmed: 33293486.
15. Mishra A, Sah B, Yadav R, et al. Five vascular variations in a male cadaver: An anatomical case report. Transl Res Anat. 2022; 28: 100208, doi: 10.1016/j.tria.2022.100208.
16. Molz G, Burri B. Aberrant subclavian artery (arteria lusoria): sex differences in the prevalence of various forms of the malformation. Evaluation of 1378 observations. Virchows Arch A Pathol Anat Histol. 1978; 380(4): 303–315, doi: 10.1007/BF00431315, indexed in Pubmed: 153045.
17. Moore KL, Dalley AF, Agur A. Clinically oriented anatomy. 8th ed. Lippincott Williams and Wilkins 2017.
18. Morris ME, Benjamin M, Gardner GP, et al. The use of the Amplatzer plug to treat dysphagia lusoria caused by an aberrant right subclavian artery. Ann Vasc Surg. 2010; 24(3): 416.e5–416.e8, doi: 10.1016/j.avsg.2009.06.027, indexed in Pubmed: 20004549.
19. Nakajima Y, Nishibatake M, Ikeda K, et al. Abnormal development of fourth aortic arch derivatives in the pathogenesis of tetralogy of Fallot. Pediatr Cardiol. 1990; 11(2): 69–71, doi: 10.1007/BF02239564, indexed in Pubmed: 2349144.
20. Natsis K, Didagelos M, Gkiouliava A, et al. The aberrant right subclavian artery: cadaveric study and literature review. Surg Radiol Anat. 2017; 39(5): 559–565, doi:

10.1007/s00276-016-1796-5, indexed in Pubmed: 27999944.

21. Natsis K, Didagelos M, Manoli SM, et al. A bicarotid trunk in association with an aberrant right subclavian artery. Report of two cases, clinical impact, and review of the literature. Folia Morphol. 2011; 70(2): 68–73, indexed in Pubmed: 21630225.

22. Ostrowski P, Popovchenko S, Bonczar M, et al. A left circumflex aorta with a displaced thoracic duct in a 94-year-old male cadaver: a case report with discussion on embryology. Folia Morphol. 2022 [Epub ahead of print], doi: 10.5603/FM.a2022.0043, indexed in Pubmed: 35481702.

23. Polguj M, Chrzanowski Ł, Kasprzak JD, et al. The aberrant right subclavian artery (arteria lusoria): the morphological and clinical aspects of one of the most important variations: a systematic study of 141 reports. Sci World J. 2014; 2014: 292734, doi: 10.1155/2014/292734, indexed in Pubmed: 25105156.

24. Popieluszko P, Henry BM, Sanna B, et al. A systematic review and meta-analysis of variations in branching patterns of the adult aortic arch. J Vasc Surg. 2018; 68(1): 298–306.e10, doi: 10.1016/j.jvs.2017.06.097, indexed in Pubmed: 28865978.

25. Poterucha J, Anavekar N, Niaz T, et al. Incidence and clinical presentation of Kommerell diverticulum and aneurysm.

J Am Coll Cardiol. 2015; 65(10): A524, doi: 10.1016/s0735-1097(15)60524-1.

26. Puri SK, Ghuman S, Narang P, et al. CT and MR angiography in dysphagia lusoria in adults. Indian J Radiol Imaging. 2005; 15(4): 497, doi: 10.4103/0971-3026.28782.

27. Sadler TW, Langman J. Langman's medical embryology. Lippincott Williams & Wilkins, Philadelphia 2004.

28. Singh S, Grewal PD, Symons J, et al. Adult-onset dysphagia lusoria secondary to a dissecting aberrant right subclavian artery associated with type B acute aortic dissection. Can J Cardiol. 2008; 24(1): 63–65, doi: 10.1016/s0828-282x(08)70552-x, indexed in Pubmed: 18209773.

29. Tapia-Nañez M, Landeros-Garcia GA, Sada-Treviño MA, et al. Morphometry of the aortic arch and its branches. A computed tomography angiography-based study. Folia Morphol. 2021; 80(3): 575–582, doi: 10.5603/FM.a2020.0098, indexed in Pubmed: 32844389.

30. Ye Y, Nikolla Z, Hebbar R, et al. A tight spot. Am J Med. 2011; 124(10): 921–923, doi: 10.1016/j.amjmed.2011.02.006.

31. Żytkowski A, Tubbs R, Iwanaga J, et al. Anatomical normality and variability: Historical perspective and methodological considerations. Transl Res Anat. 2021; 23: 100105, doi: 10.1016/j.tria.2020.100105.

Abnormal vein patterns on the feet: two case reports

B. Karip[1] , A. Ertaş[2]

[1]Department of Anatomy, Hamidiye Faculty of Medicine, University of Health Sciences, Istanbul, Turkey
[2]Department of Anatomy, Faculty of Medicine, İstanbul University-Cerrahpaşa, Istanbul, Turkey

There are many variable variants of the posterior tibial veins and these are extremely important for the venous circulation of the feet. Due to the complex and variable nature of the lower extremity veins, their drainage is particularly important in some surgical operations including flap operations and the treatment of important pathological conditions such as deep vein thrombosis. The plantar surface of the foot and the tarsal tunnel have significant neurovascular structures. Therefore it is extremely difficult to determine a safe zone when working in this region, especially for surgeons.

In these two cases, abnormal vein patterns with rare anastomoses with their different drainage patterns and the fenestration were observed in the right and left feet and medial region of the ankle of male cadavers during the routine dissection. The clinical importance of this condition was particularly discussed.

There are very limited cadaver studies to find out the relationship between the posterior tibial veins and great saphenous vein due to the difficulty of working on surgically deep vein thrombosis and some flap techniques. Therefore the region should be well known anatomically. Thanks to the variations and the anastomoses in our study, we aim to contribute to the studies to understand the complex structure of the region. (Folia Morphol 2023; 82, 3: 732–734)

Key words: posterior tibial veins, great saphenous vein, deep vein thrombosis, anastomosis

INTRODUCTION

Considering the venous drainage of the foot, after the dorsal digital veins of the foot drain into dorsal venous arch on the dorsal surface, it continues as lateral marginal vein and drains into small saphenous vein (SSV). In the medial side, medial marginal vein drains into great saphenous vein (GSV). When the plantar region is examined, it continues with plantar digital veins, medial plantar vein and lateral plantar vein and drains into posterior tibial veins. Then the GSV drains into the femoral vein and posterior tibial veins drain into popliteal vein [1]. At the same time, important perforating veins such as Cockett's perforators drain into the GSV and posterior tibial veins. Although it varies in the foot and ankle region, it is known that there may be about 3–4 medial perforator veins [5]. This area has so many complex structures but there are not enough cadaver studies on this region. We hope that our study will guide clinicians in terms of surgical approaches to this area, especially the veins that we showed in Figures 1 and 2.

Address for correspondence: B. Karip, DDS, PhD, Department of Anatomy, Hamidiye Faculty of Medicine, University of Health Sciences, Üsküdar, 38000 İstanbul, Turkey, tel: +90 538 860 94 10, e-mail: krpbrk@gmail.com

Figure 1. The medial aspect of the ankle; 1 — the vein which arises from the posterior compartment; 2 — the large vein; 3 — an anastomosis between them; 4 — the drainage junction, arrows — cutaneous branches.

Figure 2. The anteromedial aspect of the ankle; 1 — the anastomosis between great saphenous vein (GSV) and posterior tibial vein (PTV); 2 — the vein that arises from the skin of the medial surface of the ankle; 3 — the vein that arises from the medial plantar region of the foot; black asterisk — GSV, white asterisk — PTV.

CASE REPORT

During the educational dissection for medical students in two male cadavers, we observed unusual vein patterns when lifting the skin and the superficial fascia of the plantar region of the feet and the medial ankle regions.

In the case 1, although it is known that there are many perforating veins in this region that first drain the superficial fascia, then pierce the deep fascia, and then drain into SSV and GSV on the dorsal surface, the posterior tibial veins (PTV) in the plantar surface and posterior compartment, it has not been reported before that a vein from the posterior compartment and a large vein from the dorsal surface of the foot anastomose and drain into PTV (Fig. 1).

On the other hand, it was observed that a cutaneous branch given to the posterior compartment by the posterior tibial artery passed through a fenestration thought to occur congenitally in PTV.

In the case 2, we observed a very large anastomosis between the GSV and PTV in which one of each branches drains from the medial plantar region of the foot and from the skin of the medial surface of the ankle (Fig. 2). Other than those conditions, no variations were observed for the other structures.

DISCUSSION AND CONCLUSIONS

These two conditions contain rare abnormal drainage patterns. Although there are many articles in the literature on supplying and drainage of the foot and ankle, the rate of cadaver dissection studies especially on venous drainage are very few. Beyond all veins of the leg and foot, the most important disorder for the veins is deep vein thrombosis (DVT) which can cause motor function deficiency in the lower limb, especially in the elderly patients [4].

Deep vein thrombosis seen in patients with acute strokes is usually peripheral type. 12.7% of acute stroke seen in PTV occur with haemorrhagic stroke and 7.6% with ischaemic stroke [7]. In addition, according to Bergan et al. [3], the incidence of DVT

after cardiovascular surgery for venous disorders as a complication is average 1.8%.

According to the studies performed, the catheter-directed thrombolysis method has an important place in the treatment of DVT. For this method, some studies indicate that PTV is an ideal entry point [10]. Although it is known that the prognosis of the catheter-directed thrombolysis method performed over PTV is better than the popliteal vein according to long-term studies, it is recommended to be careful because of the high variation and small diameter rate of PTV [2].

Due to the fact that it receives more pressure, the vascular structure on the palmar surface of the hand, as well as the plantar surface of the foot, is very thin and the connections between them are very weak. This condition may cause difficulties in some flap operations in terms of reconstructive surgery. On the other hand, the structural architecture of perforating and superficial veins can be seen as an alternative and facilitating factor in flap operations allowing drainage to be performed directly to the deep veins or with anastomoses between deep veins and superficial veins [11].

The perforating veins of the feet act as a connection between the deep veins and the superficial veins as they follow a path from the deep to the surface. This is very important in ascending venous pump activation [9]. When the pathology is examined, it is obvious how important it is in vein structures as well as the organization of arterial and nerve structures for surgical operations to be performed on the dorsal surface and plantar surface of the foot and for the ankle region. In addition, the thrombosis in PTV can be seen in some different conditions such as the antiphospholipid syndrome, some metabolic syndromes, or in some developmental venous malformations [6, 8].

We know that the dissection of the areas that we mentioned is hard, that is why almost all studies are done with radiological images of the areas. It is foreseen that our study will provide a new perspective on the initiatives to be made in this region.

Conflict of interest: None declared

REFERENCES

1. Baccellieri D, Ardita V, Carta N, et al. Anterior accessory saphenous vein confluence anatomy at the sapheno-femoral junction as risk factor for varicose veins recurrence after great saphenous vein radiofrequency thermal ablation. Int Angiol. 2020; 39(2): 105–111, doi: 10.23736/S0392-9590.20.04271-6, indexed in Pubmed: 32043339.
2. Bendix SD, Nolan R, Banipal S, et al. Posterior tibial vein approach to catheter-directed thrombolysis for iliofemoral deep venous thrombosis. J Vasc Surg Venous Lymphat Disord. 2019; 7(5): 629–634, doi: 10.1016/j.jvsv.2019.01.064, indexed in Pubmed: 31231054.
3. Bergan J, Pascarella L, Mekenas L. Venous disorders: treatment with sclerosant foam. J Cardiovasc Surg (Torino). 2006; 47(1): 9–18, indexed in Pubmed: 16434941.
4. Debela D, Ababulgu E, Desu G, et al. Distal deep vein thrombosis in a patient cured of severe COVID-19 pneumonia at Jimma, Oromia, Ethiopia 2021: a rare case report. Int Med Case Rep J. 2021; 14: 519–522, doi: 10.2147/IMCRJ.S322301, indexed in Pubmed: 34393520.
5. Hill BG, van Rij AM. The lower limb perforator veins in normal subjects. J Vasc Surg Venous Lymphat Disord. 2022; 10(3): 669–675.e1, doi: 10.1016/j.jvsv.2022.01.010, indexed in Pubmed: 35134574.
6. Khan AA, Asari MA, Hassan A, et al. An interconnected duplicated femoral vein and its clinical significance. Folia Morphol. 2013; 72(1): 82–85, doi: 10.5603/fm.2013.0014, indexed in Pubmed: 23749717.
7. Liu XC, Chen XW, Li ZL, et al. Anatomical distribution of lower-extremity deep venous thrombosis in patients with acute stroke. J Stroke Cerebrovasc Dis. 2020; 29(7): 104866, doi: 10.1016/j.jstrokecerebrovasdis.2020.104866, indexed in Pubmed: 32404283.
8. Przepiera-Będzak H, Brzosko M. Antiphospholipid syndrome with antiβ2glicoprotein-1 antibodies as the cause of recurrent tibial vein thrombosis in SAPHO syndrome. Acta Dermatovenerol Croat. 2016; 24(4): 305–306, indexed in Pubmed: 28128085.
9. Uhl JF, Lo Vuolo M, Gillot C. Anatomy of foot and ankle perforator veins. Phlebolymphology. 2021; 50: 59–75, doi: 10.1055/a-1246-6030.
10. Yi KH, Kim HJ. Is variation in posterior tibial veins a risk factor for deep-vein thrombosis? Clin Anat. 2021; 34(6): 829–834, doi: 10.1002/ca.23691, indexed in Pubmed: 32996214.
11. Zhong SZ, Wang GY, Yuan L, et al. Anatomic basis of venous drainage in donor flaps. Surg Radiol Anat. 1994; 16(4): 349–354, doi: 10.1007/BF01627652, indexed in Pubmed: 7725188.

VIA MEDICA

CASE REPORT

A unique variation of a four-bellied digastric muscle named "real quadrigastric muscle": a case report and literature review

B. Landzhov[1] , L. Gaydarski[1], R.S. Tubbs[2], V. Kirkov[3], G.P. Georgiev[4]

[1]Department of Anatomy, Histology and Embryology, Medical University of Sofia, Bulgaria
[2]Department of Neurology, Tulane University School of Medicine, New Orleans, Louisiana, United States
[3]Department of Health Policy and Management, Medical University of Sofia, Bulgaria
[4]Department of Orthopaedics and Traumatology, University Hospital Queen Giovanna – ISUL,
Medical University of Sofia, Bulgaria

From a topographical standpoint, the digastric muscle is key to the formation of several triangles of the neck, which are of the utmost clinical significance. Herein, we present a previously unrecognised variation of the digastric muscle: a quadrigastric muscle with two accessory bellies originating from the body and angle of the mandible and inserting to the intermediate tendon. Three new triangles are demarcated between the four bellies of the aberrant muscle. Detailed knowledge of variations of the digastric muscle, changing the borders and relationships of the topographic triangles, is paramount for radiologists and surgeons operating on the anterior region of the neck. (Folia Morphol 2023; 82, 3: 735–739)

Key words: neck topography, novel triangles, clinical significance

INTRODUCTION

The digastric muscle (DM) belongs to the suprahyoid muscle group. It normally comprises an anterior belly (AB), an intermediate tendon (IMT), and a posterior belly (PB). The posterior belly of the digastric muscle (PBDM) is usually marginally longer and originates from the mastoid notch of the temporal bone. It passes ventrally and inferiorly as it continues into the intermediate tendon. The anterior belly of the digastric muscle (ABDM) originates from the digastric fossa of the mandible and passes caudally and inferiorly as it inserts into the IMT, thus connecting with the PB and constituting the whole muscle. The IMT perforates the tendon of the stylohyoid muscle and attaches to the body and greater horns of the hyoid bone [19].

The AB is innervated by the mylohyoid branch of the inferior alveolar nerve, a branch of the third branch of the trigeminal nerve, the mandibular nerve. The blood supply for the AB is carried by the submental artery, a branch of the facial artery. The PB is innervated by the digastric branch of the facial nerve. Its blood supply is carried by muscle branches of the posterior auricle and occipital arteries [19]. This duality in innervation and blood supply is explained by embryological development. The ABDM, the mandibular branch of the trigeminal nerve and the facial artery are derived from the first pharyngeal arch; the PBDM, the facial nerve and the stapedial artery are derived from the second. The stapedial artery is only present during early development. Later, it obliterates and is substituted by muscle branches of the posterior

auricular and occipital arteries [5, 18, 19]. With that in mind, it is only logical to assume that the development of the two accessory bellies is a result of division in the mesenchyme tissue of the first pharyngeal arch during the 4th week of gestation [18].

The DM is important for topographic landmarks in the neck. It is involved in the formation of several triangles, which a plethora of medical specialties such as radiologists, general surgeons, neck surgeons, endocrinologists, and maxillofacial surgeons use as landmarks in the anterior region of the neck [10, 20].

CASE REPORT

A 78-year-old male cadaver had undergone standard anatomical dissection in the dissection hall of the Department of Anatomy, Histology, and Embryology in the Medical University of Sofia for the education of medical students, as approved by the Medico-Legal Office and Local Ethics Committee. During the dissection of the cadaver's neck, a unique unilateral variation of the left DM was observed. After the deviant muscle was thoroughly cleaned of the surrounding connective tissue and its fascia had been gently peeled off, the aberrant muscle proved to have two accessory bellies. The posterior accessory belly (PAB) originated from the angle of the mandible, passed anteriorly and inferiorly and inserted on to the IMT. The anterior accessory belly (AAB) originated from the inferior margin of the body of the mandible, approximately in the middle. It passed inferiorly and nearly vertically and inserted on to the IMT. The left and right digastric muscles were measured with a standard ruler. The AB of the left DM was 35 mm long from the digastric fossa to its continuation into the IMT, and 11 mm wide. The AB of the right DM was 37 mm long from the digastric fossa to its continuation into the IMT, and 17 mm wide. The AAB was 22 mm long from the inferior margin of the mandible to the point of its insertion on to the IMT, and 9 mm wide. The PAB was 23 mm long from the angle of the mandible to its insertion on to the IMT, and 7 mm wide (Fig. 1). No variations of the PB of the left DM were noted, as it originated from the mastoid notch and continued into the IMT. Both accessory bellies were supplied with blood from the submental branch of the facial artery, and both were innervated by branches of the facial nerve.

The two accessory bellies subdivided the submandibular triangle into three smaller triangles: anterior triangle, bounded by the AB and the AAB; middle
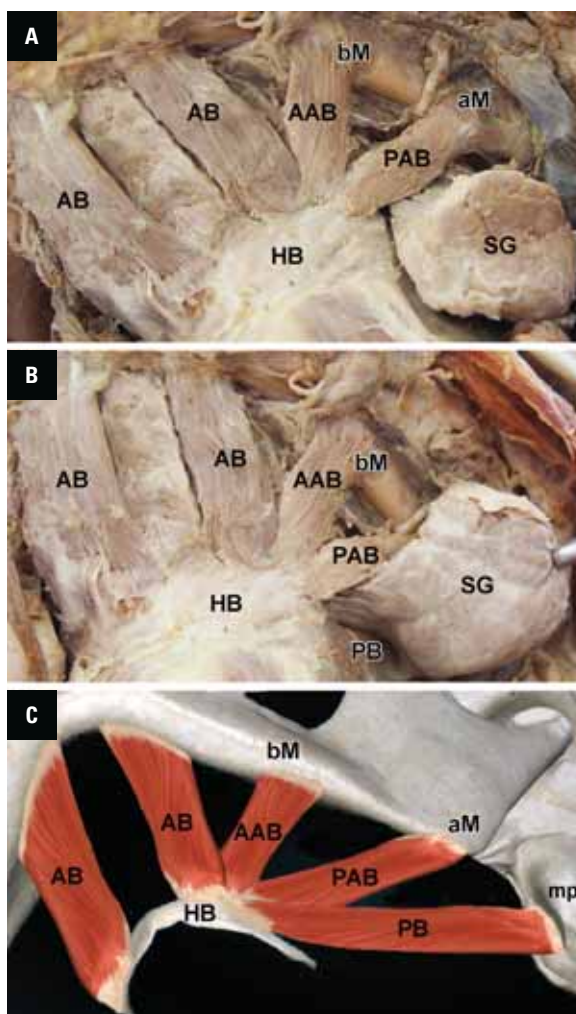
Figure 1. Anterolateral view of the neck. An unusual variation of the digastric muscle: a "real quadrigastric muscle"; **A.** Anterior triangle, bounded by the AB and the AAB; middle triangle, situated between the AAB and the PAB; **B.** Posterior triangle, demarcated by the PAB and the PB; **C.** A schematic presentation of unilateral "real quadrigastric muscle"; AB — anterior belly; PB — posterior belly; AAB — anterior accessory belly; PAB — posterior accessory belly; HB — hyoid bone; SG — submandibular gland; bM — base of mandible; aM — angle of mandible; mp — mastoid process.

triangle, situated between the AAB and the PAB; and posterior triangle, demarcated by the PAB and the PB of the digastric muscle. In addition, owing to the presence of the two accessory bellies, the topography of the three small triangles (of Béclard [1], Lesser [see 7], and Pirogoff [17]) normally situated inside the submandibular triangle, was altered. Those three small triangles could not be observed on the left side since their boundaries were overlapped by the accessory bellies. After the right side of the neck of the same cadaver had been dissected, it was established that the right DM had two normal bellies. It was concluded that the unique abnormality of the

quadribellied DM (two accessory bellies) was unilateral, present only on the left side of the neck. Medical records of the cadaver showed no history of surgical interventions of any kind in the region of the neck, nor were any scars observed prior to the dissection.

DISCUSSION

The ABDM is a highly variable structure with an extensive range of variations in its number, form, and points of origin and insertion. According to Lee and Yang [11] incidence rate of doubling of the ABDM is 66.7%. Kim and Loukas [9] have summarized all the more common cases of AAB, including cases of crossing the midline and inserting contralaterally, both uni- and bi-laterally, arising from the IMT, the hyoid bone, or the main AB. However, there are only a handful cases describing unique variations of the DM with two AABs. Macalister described an independent muscle originating from the body of the hyoid bone, passing alongside the medial border of the ABDM and inserting on to the symphysis of the mandible: the mentohyoid muscle. Furthermore, Macalister [12] described a hyoangularis muscle, which originated from the hyoid bone and inserted into the angle of the mandible. Natsis et al. [14] described a three-headed right ABDM. The main ABDM originated from the digastric fossa and the accessory bellies originated from the inferior margin of the mandible. Natsis et al. [14] also reported two accessory muscle bundles in the submental region, forming a triangle. Harvey et al. [4] reported a unique waving pattern of bilateral variation of the ABDM; the aberrant AB had two heads, deep and superficial. Furthermore, Harvey et al. [4] described two more accessory heads bilaterally, again superficial and deep, as the right superficial accessory head and both deep accessory heads crossed in the midline. Celik et al. [2] presented a rare case of quadrification of the ABDM. The aberrant muscle belly had four insertion points in the digastric fossa, but posteriorly the four muscle bellies united and continued into the IMT [2]. Ozgur et al. [16] described a bilateral quadrification of the DM. All four ABs originated for the digastric fossa and inserted to the hyoid bone. Moreover, Ozgur et al. [16] described two more accessory muscles situated medially to the medial ABDM. Those two aberrant muscles fused at the midline and covered the underlying mylohyoid muscle. Uzun et al. [22] reported a rare case of bilateral variation of the ABDM. Medially to the main anterior belly was an accessory belly,

originating from the digastric fossa on both sides. The accessory bellies inserted to the hyoid bone via a common fibrous band [22]. With that in mind, it is apparent that the variation found in our case has never been described throughout the literature. It therefore appears to be unique.

During our extensive literature review we found several different types of classification, summarizing the variations of the ABDM in several ways. Žlábek [24] first classified the variations of the AB of the digastric muscle in terms of ontogenetic and phylogenetic development. Afterwards, Yamada [23] developed a six-types classification based on the relationships between the AABs and their points of origin and insertion. Mori [13] classified the variations of the ABDM into seven types on the basis of their points of origin and insertion, along with the presence or absence of aberrant muscle fibres. De-Ary--Pires et al. [3] classified the variations in the DM into three large categories containing different numbers of subtypes. The first category comprised five types of variations of the AB based on the number of ABs inserting to the mandible or mylohyoid, both ipsi- or contra-laterally [3]. Type 5 was the unique mentohyoid muscle described by Macalister [12]. The second category comprised variations of the IMT based on the relationship between the IMT of the DM and the tendon of the stylohyoid muscle. The third category comprised variations of the PBDM based on its point of origin [3]. Hsiao and Chang [6] studied 15 cadavers and found three with variations of the ABDM, which they classified as "unilateral type", "crossed type" and "mixed type" depending on whether the aberrant muscle fibres crossed the midline. Ozgur et al. [15] proposed a simplified classification with three types based on the origin and insertion of the ABDM: Classical type — normal digastric; digastric fossa type — ipsilateral origin and insertion; crossed type — one or more accessory bellies crosses the midline. The aberrant muscle we report as a unique muscle cannot be included in any of the abovementioned classifications.

The DM is not only anatomically important owing to its participation in vital processes such as mastication, swallowing, and phonation [19], but also of the utmost clinical significance as a paramount landmark for several clinically significant triangles on the anterior region of the neck: submental, submandibular, Béclard's, Lesser's, and Pirogoff's triangles [8, 19].

According to Tubbs et al. [21], Béclard's triangle was present in 82.4% of cases, while Lesser's

and Pirogoff's triangles were found in 88.2%. The reason for the absence of Béclard's triangle was a consequence of variations of the PBDM, while the absence of Lesser's and Pirogoff's triangles was due to the inferior passage of the hypoglossal nerve.

The fact that the bellies of the DM are used as margins of these various triangles is enough to demonstrate the clinical significance of variations in the DM; a deviation in the course or number of bellies results in complete reorganisation of the triangular spaces of the anterior neck. In our case, the topography of the submandibular triangle was completely changed because of the two accessory bellies. Instead of the three small triangles (Béclard's, Lesser's and Pirogoff's) there were three different triangles that we described as anterior, middle, and posterior accessory. As shown, the muscle is paramount for the topography of the suprahyoid region of the neck; hence, variations in the DM are of definite clinical significance, as aberrant bellies can be misinterpreted as tumour masses or metastatic lymph nodes [10]. In addition, the DM has a key role in plastic surgery for facial reconstruction [20].

CONCLUSIONS

Comprehensive knowledge of the variations of the ABDM is paramount for every medical specialism regarding the suprahyoid region of the neck because of the great topographical and clinical significance of the DM for a plethora of surgical and radiological procedures. The aim of this article was therefore to elucidate the variability of the ABDM.

Acknowledgements

Conflict of interest: None declared

REFERENCES

1. Béclard PA, Knox R. Third section. Of the external muscles. In: Knox R (ed). Elements of general anatomy. MacLachlan and Stewart, Edinburgh 1830: 311–321.
2. Celik HH, Aldur MM, Ozdemir B, et al. Abnormal digastric muscle with unilateral quadrification of the anterior belly. Clin Anat. 2002; 15(1): 32–34, doi: 10.1002/ca.1088, indexed in Pubmed: 11835541.
3. De-Ary-Pires B, Ary-Pires R, Pires-Neto MA. The human digastric muscle: patterns and variations with clinical and surgical correlations. Ann Anat. 2003; 185(5): 471–479, doi: 10.1016/S0940-9602(03)80110-3, indexed in Pubmed: 14575275.
4. Harvey JA, Call Z, Peterson K, et al. Weave pattern of accessory heads to the anterior digastric muscle. Surg Radiol Anat. 2015; 37(8): 1001–1004, doi: 10.1007/s00276-014-1401-8, indexed in Pubmed: 25501489.
5. Hitier M, Zhang M, Labrousse M, et al. Persistent stapedial arteries in human: from phylogeny to surgical consequences. Surg Radiol Anat. 2013; 35(10): 883–891, doi: 10.1007/s00276-013-1127-z, indexed in Pubmed: 23640742.
6. Hsiao TH, Chang HP. Anatomical variations in the digastric muscle. Kaohsiung J Med Sci. 2019; 35(2): 83–86, doi: 10.1002/kjm2.12012, indexed in Pubmed: 30848024.
7. Jamieson GG. Head and neck operations. In: Jamieson GG (ed). Anatomy of general surgical operations, 2nd ed. Churchill Livingstone/Elsevier, Edinburgh 2006: 1–240.
8. Kikuta S, Iwanaga J, Kusukawa J, et al. Triangles of the neck: a review with clinical/surgical applications. Anat Cell Biol. 2019; 52(2): 120–127, doi: 10.5115/acb.2019.52.2.120, indexed in Pubmed: 31338227.
9. Kim SD, Loukas M. Anatomy and variations of digastric muscle. Anat Cell Biol. 2019; 52(1): 1–11, doi: 10.5115/acb.2019.52.1.1, indexed in Pubmed: 30984445.
10. Larsson SG, Lufkin RB. Anomalies of digastric muscles: CT and MR demonstration. J Comput Assist Tomogr. 1987; 11(3): 422–425, doi: 10.1097/00004728-198705000-00010, indexed in Pubmed: 3571582.
11. Lee HY, Yang HE. Anterior neck muscles. In: Tubbs RS, Shoja MM, Loukas M (eds.) Bergman's comprehensive encyclopedia of human anatomic variation, 1st ed. Wiley & Sons, Hobokken, New Jersey 2016: 228.
12. Macalister A. Additional observations on muscular anomalies in human anatomy (third series), with a catalogue of the principal muscular variations hitherto published. Trans Roy Irish Acad Sci. 1875; 25(1): 1–134.
13. Mori M. Statistics on the musculature of the Japanese. Okajimas Folia Anat Jpn. 1964; 40: 195–300, doi: 10.2535/ofaj1936.40.3_195, indexed in Pubmed: 14213705.
14. Natsis K, Piagkou M, Vrochidis P, et al. Unilateral asymmetrical anterior bellies of the digastric muscle in coexistence with accessory muscle bundles in the submental triangle: A rare case report. Morphologie. 2018; 102(337): 83–86, doi: 10.1016/j.morpho.2017.10.001, indexed in Pubmed: 29496384.
15. Ozgur Z, Govsa F, Ozgur T. The cause of the difference in the submental region: aberrant muscle bundles of the anterior belly of the digastric muscle. J Craniofac Surg. 2007; 18(4): 875–881, doi: 10.1097/scs.0b013e31806844da, indexed in Pubmed: 17667681.
16. Ozgur Z, Govsa F, Ozgur T. Bilateral quadrification of the anterior digastric muscles with variations of the median accessory digastric muscles. J Craniofac Surg. 2007; 18(4): 773–775, doi: 10.1097/scs.0b013e318068ff09, indexed in Pubmed: 17667663.
17. Pirogoff NI. Sectiones capitis, colli et columne vertebrarum triplici directioneductae. In: Pirogoff NI (ed.) Anatome topographica sectionibus per corpus humanum congelatum.

Triplice directione ductis illustrate. First Ed. Typis Jacobi Trey, St. Petersburg 1852: 1–248.

18. Sadler TW. Head and neck. In: Sadler TW (ed.) Langman's medical embryology, 10th ed. Lippincott Williams & Wilkins, Philadelphia 2006: 259–261.

19. Standring S. Head and neck. In: Standring S (ed.) Gray's Anatomy. The Anatomical Basis of Clinical Practice, 40th ed. Churchill Livingstone/Elsevier, Edinburgh 2008: 437.

20. Tan ST. Anterior belly of digastric muscle transfer: a useful technique in head and neck surgery. Head Neck. 2002; 24(10): 947–954, doi: 10.1002/hed.10150, indexed in Pubmed: 12369074.

21. Tubbs RS, Rasmussen M, Loukas M, et al. Three nearly forgotten anatomical triangles of the neck: triangles of Beclard, Lesser and Pirogoff and their potential applications in surgical dissection of the neck. Surg Radiol Anat. 2011; 33(1): 53–57, doi: 10.1007/s00276-010-0697-2, indexed in Pubmed: 20623121.

22. Uzun A, Aluclu A, Kavakli A. Bilateral accessory anterior bellies of the digastric muscle and review of the literature. Auris Nasus Larynx. 2001; 28(2): 181–183, doi: 10.1016/s0385-8146(00)00100-0, indexed in Pubmed: 11240328.

23. Yamada S. Beobachtungen über den Venter anterior des Musculus digastricus mandibulae bei japanischen Erwachsenen und Foeten. Acta Anat Nippon. 1935; 8(1): 303–347.

24. Žlábek K. Contribution à la connaissance des anomalies du ventreantérieur du digastrique de l'Homme. Arch Anat Histol Embryol. 1933; 16: 357–406.

CASE REPORT

Extensor digitorum muscle tendon to the index finger from the extensor carpi radialis brevis: a cadaveric case report

W. Chaba[1], S. Popovchenko[1], K. Shafarenko[1], M. Piagkou[2], J.A. Walocha[1], P. Depukat[1], M.P. Zarzecki[1]

[1]Department of Anatomy, Jagiellonian University Medical College, Krakow, Poland
[2]Department of Anatomy, School of Medicine, National and Kapodistrian University of Athens, Greece

The forearm extensor compartment is known for its wide variability in terms of muscle origin, number of tendons and their distal insertion. The index finger on its dorsal aspect is the typical place of insertion of the two tendons of the extensor digitorum (ED-index) and of the extensor indicis. Being acquainted with their anatomy is of immense importance to orthopaedic surgeons in the treatment of e.g., de Quervain's syndrome.

The current report presents a rare finding of the ED-index tendon arising from the extensor carpi radialis brevis (ECRB). A routine dissection revealed their fused course from the lateral epicondyle of humerus, though separate from the extensor carpi radialis longus. The ED-index muscle belly separated from the ECRB, 119 mm distal to the lateral epicondyle. The distal insertion point of the ED-index was located radially to that of the extensor indicis. The deep branch of the radial nerve and the recurrent interosseous artery supplied the ED-index. No other musculotendinous variations were encountered neither on the ipsilateral nor the contralateral upper limb of the cadaver.

This study presents in detail a tendon of the ED-index arising from the ECRB, a knowledge that can be applied namely in the lateral epicondylitis treatment or approach to the ulnar nerve at the level of the elbow. Extensive depiction of both the proximal and distal attachment points of the muscles, their course and dimensions is indispensable to attain the best patient outcomes and avoid iatrogenic injuries. (Folia Morphol 2023; 82, 3: 740–744)

Key words: extensor digitorum, extensor carpi radialis brevis, anatomy, variation

INTRODUCTION

The extensor compartment of the forearm presents a rich variability. Most of these variants are asymptomatic [10, 14]. The index finger has two independent tendons: the tendon of the extensor digitorum (ED-index) with a single slip, usually, and the tendon of the extensor indicis (EI), variable in size, origin, and insertion locations, as well as in number of distal slips present. The most common variant is a single-slip of the EI tendon inserting on the ulnar side of the ED-index tendon [25].
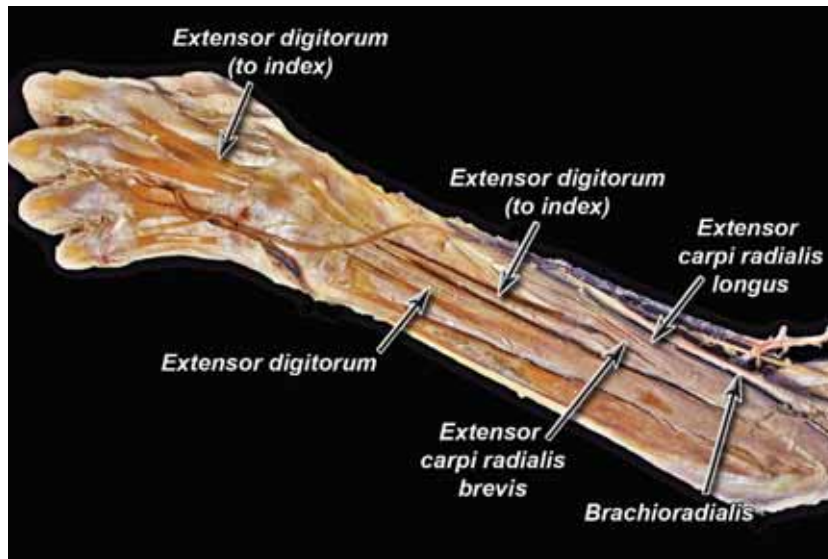
Figure 1. The posterior view of the left forearm and dorsum of hand.

The ED arises from the lateral epicondyle of humerus and divides into four tendons, inserting into the lateral and dorsal surface of the middle and distal phalanges of the 2nd–5th finger [13]. Most studies describe the ED to give off one tendon directly to the extensor expansion of hand of each one of the above-mentioned four digits [3]. The extensor carpi radialis brevis (ECRB) also arises from the lateral epicondyle of humerus and inserts as a flat tendon into the styloid process of metacarpal III [13, 24]. The ED and the ECRB muscles are both innervated by the radial nerve. The ECRB's function is mainly to extend the wrist, whereas the ED extends the proximal interphalangeal joints, the wrist, and the elbow.

Becoming thoroughly acquainted with the extensor tendons' variants may be helpful for hand surgeons in planning tendon graft surgery [3, 25] and allowing them to successfully perform tenosynovectomy for the treatment of de Quervain's syndrome [3, 19]. The detailed anatomical knowledge of the extensor tendons is a determining factor in preserving healthy tendons during orthopaedic procedures, hence accounts for good patient outcomes and improves their quality of life [3, 5].

The current case study refers to a rare origin of the ED-index tendon from the ECRB. The report offers a detailed depiction of the topography of this aberrant muscle in its clinical context and discusses its embryological significance.

CASE REPORT

During a routine dissection of a 66-year-old male formalin fixed cadaver (performed by J.A.W. and S.P.), a variant origin of the ED-index tendon from the ECRB was noted on the left upper extremity. Having removed both the superficial fat and connective tissues, digital documentation was performed prior to taking measurements with a digital calliper (Lux tools, China) and further exploration of the subsequent vascular and neural supply. The obtained values were averaged from three subsequent measurements.

The described variation involved a common origin of the musculotendinous ED-index from the ECRB. The proximal attachment site was at the lateral epicondyle of humerus. The ED-index muscle belly and tendon separated from the ECRB, 119 mm distal to the outermost palpable point of the lateral epicondyle. The separated muscle belly measured 70 mm in length and 12 mm in width (at its widest part located mid-length). The musculotendinous portion had a length of 179 mm (from the point of separation to the extensor retinaculum of wrist). The ED-index tendon coursed near the other tendons of the ED and inserted into the radial side of the tendon of the EI. The ED-index passed beneath the extensor retinaculum of wrist in the typical manner. The tendon width at the proximal entry point underneath the extensor retinaculum was approximately 2 mm and its further course was not altered (Fig. 1).

No aberrations were found in terms of the neurovascular structures supplying the variation. The

ED-index was supplied by the deep branch of the radial nerve and the recurrent interosseous artery. No variations were found regarding the ED muscle and tendons to the middle, ring, and little fingers at the ipsilateral extremity. Their origin and insertion points were typical. The EI muscle also had a typical course and inserted into the ulnar side of the ED-index. No musculotendinous variants were found at the contralateral upper limb of the cadaver.

DISCUSSION

A variation in the extensor compartment of the forearm is not an uncommon finding. The ED-index occurs in 99.8% of cases, and in the vast majority arises from a single proximal attachment of the ED [24]. Notwithstanding, to the best knowledge of the authors the prevalence of ED-index and ECRB variants is casuistic and has not been analysed in larger study samples. Henceforth, it is crucial for the researchers worldwide to continuously identify and record them to facilitate surgical procedures on the forearm.

Embryology

The muscles of the upper limb are identifiable by the seventh week of gestation. Among them, superficial and proximal muscles differentiate before the deeper and distal ones, respectively [2]. Diogo et al. [8] reported that the ED can be distinguished in the fetus of 12.0 mm. The ED and the extensor carpi ulnaris are the first muscles of the forearm to develop during ontogeny in the human. According to Straus [21], the mammalian innovation, when it comes to evolution, includes a widespread migration of the superficial marginal muscles and the complete transformation of the extensor carpi intermedius into the ED. Henceforth, it is thought to be related to more potential aberrances encountered in that region. The ED is divided into more muscle bellies in humans and that tendency is a differentiating factor between them and the three great apes (chimpanzee, gorilla, and orangutan) [21].

A more severe form of disruption in migration of the mesoderm cells in the distal upper limb than simple misalignment of muscles may be, for example, symbrachydactyly. Mesoderm germ layer gives rise not only to the musculature, but also vasculature, cartilage and bones. Nonetheless, in case of symbrachydactyly the ectoderm derivatives tend to appear normal [20]. Bavinck and Weaver [4] hypothesized that interruption to the vascular supply can play a part in certain conditions, namely Poland syndrome. A study by Simet and Cassidy [20] has found a variant distal insertion point of the EI muscle onto the 1st metacarpal in a patient with symbrachydactyly, working as an accessory extensor pollicis longus. However, similarly to the current study, the authors have not found any visible aberrances in the vasculature of the upper limb, hence possibly pointing to the disruption in the mesoderm migration and division as the embryologic mechanism responsible for the encountered variants.

ED-index and ECRB variants in the literature

An aberrant ED-index was described by Kim and Lee [13]. Similarly to the present study, it originated from the ECRB muscle and inserted into the index finger. The ED arose from the lateral epicondyle of humerus and was divided into three musculotendinous bellies. There was no index finger tendon of the ED muscle [13].

The ED has many variants. Nayak et al. [15] reported it to have five distinct tendon slips, instead of the typical four. It resulted from a tendon split that inserted into both the ring and little fingers. Arora et al. [3] found both the ED and ECRB to be aberrant. The ECRB had an accessory belly inserting into the dorsal digital expansion of the index finger and the ED was divided into three (lateral, intermediate, and medial) musculotendinous bellies [3].

Musculotendinous variant connections to the index finger are frequently described in the literature. Vaida et al. [23] reported an EI, originating from the ECRB and replacing the tendon of the ED-index. The other muscle was the EI and medii communis split to three tendons, two of which attached to the index finger and one to the middle digit. Casanova-Martinez et al. [6] described an accessory tendon located between the tendons of the ED-index and the extensor pollicis longus muscle, which arose from an independent muscle, being a part of the EI.

The ECRB can also give rise to anomalous muscles. West et al. [24], in their sample of 82 cadaveric forearms, found 7 (8.53%) cases with additional wrist extensors (4 extensor carpi radialis intermedius and 3 accessory extensor carpi radialis). The extensor carpi radialis intermedius originated from the ECRB lateral and medial part in four and one forearms, respectively. Anomalies of the radial wrist extensors were described by Albright and Linburg [1], as well. The interconnections between the ECRB and the extensor

carpi radialis longus were found in 61 out of 173 forearms (35.3%). The tendons arose from the ECRB in 21% of the cases. Such muscular linkage between the ECRB and longus was reported by Gümüşalan et al. [11]. Furthermore, they described an accessory muscle emerging from the ECRB medial side and inserting to the base of the second metacarpal bone.

Clinical significance

Meticulous knowledge of the distribution pattern of the ED and ECRB tendons is crucial in a wide range of surgical procedures. The ED may play an important role in the lateral epicondylitis (known also as "the tennis elbow"), as indicated by Fairbank and Corlett [9]. The authors suggest that the ED is a main factor in the Maudsley's test, which is positive in painful patients while resisting the extension of the middle finger, in a fully extended elbow. In such tendinopathy, a proximal disinsertion of the common extensor tendon is carried out [7]. During the procedure, the origins of both the tendons of ECRB and ED need to be located, so any possible variants in that area could have an impact on the treatment result.

Location of the ECRB tendon is also important in the dorsoradial approach to the wrist, used for corrective osteotomies [17]. Another landmark is the tendon of the extensor carpi radialis longus. The dissection is performed distally to these two tendons, and proximally between the ECRB and ED. Incision between those muscles is also made to treat elbow stiffness [18].

Tendon of the ECRB can be harvested for an autograft [22]. Multiple variations in the extensor forearm region may also influence the results of tenosynovectomy performed for the treatment of de Quervain's syndrome. The procedure, in case of coexisting variants, may not be successful in terms of reducing the inflammation and relieving pain [3, 19]. However, it is worth remembering that the ED brevis muscle can be found in the proximity of the index finger extensor tendons and might e.g., be mistaken for dorsal ganglion tenosynovitis [16]. Henceforth, it is worth bearing in mind that variation in the differential diagnosis.

Limitations and future directions of research

The main limitation of the current case description is the lack of medical history of the patient. Thus, no possibility existed to associate the cadaveric finding with clinical significance. The authors can only conclude that due to the location of the musculotendinous variant, away from the neurovascular structures, its presence was asymptomatic, although no medical record was available to reinforce this point of view. However, case reports describing rare findings such as the present one, are the first step for future studies based on larger samples. Lastly, it is worth remembering that the widely acclaimed "anatomical norm" is rather an approximation, as many reported variants are not pathological in nature, but rather pose a higher risk of iatrogenic complications during surgical interventions if one is not aware of their presence [26].

CONCLUSIONS

This report presents a rare musculotendinous variant formed by the common origin of the ED-index tendon from the ECRB in a formalin-fixed cadaver. Being thoroughly acquainted with the possible variants in the forearm extensor compartment is of dire importance to the orthopaedic surgeons performing procedures in the elbow region, namely for the tennis elbow or whilst approaching the ulnar nerve in its humeral grove. Undoubtedly, there is still a need to correlate the detected finding with its potential clinical presentation in vivo, utilizing larger study samples.

Conflict of interest: None declared

REFERENCES

1. Albright JA, Linburg RM. Common variations of the radial writs extensors. J Hand Surg Am. 1978; 3(2): 134–138, doi: 10.1016/s0363-5023(78)80060-4, indexed in Pubmed: 632542.
2. Al-Qattan MM, Yang Y, Kozin SH. Embryology of the upper limb. J Hand Surg Am. 2009; 34(7): 1340–1350, doi: 10.1016/j.jhsa.2009.06.013, indexed in Pubmed: 19700076.
3. Arora J, Dave V, Kumar A, et al. Unusual architecture of extensor digitorum muscle of hand in conjunction with accessory belly of extensor carpi radialis brevis: a clinico-anatomical insight. Clin Ter. 2013; 164(1): 31–33, doi: 10.7417/T.2013.1508, indexed in Pubmed: 23455740.

4. Bavinck JN, Weaver DD. Subclavian artery supply disruption sequence: hypothesis of a vascular etiology for Poland, Klippel-Feil, and Möbius anomalies. Am J Med Genet. 1986; 23(4): 903–918, doi: 10.1002/ajmg.1320230405, indexed in Pubmed: 3008556.

5. Carlos JS, Goubran E, Ayad S. The presence of extensor digiti medii muscle-anatomical variant. J Chiropr Med. 2011; 10(2): 100–104, doi: 10.1016/j.jcm.2010.12.004, indexed in Pubmed: 22014864.

6. Casanova Martínez D, Valdivia Gandur I, Golanó P. Extensor pollicis et indicis communis or extensor indicis radialis muscle. Anat Sci Int. 2013; 88(3): 153–155, doi: 10.1007/s12565-012-0164-8.

7. Cusco X, Alsina M, Seijas R, et al. Proximal disinsertion of the common extensor tendon for lateral elbow tendinopathy. J Orthop Surg (Hong Kong). 2013; 21(1): 100–102, doi: 10.1177/230949901302100125, indexed in Pubmed: 23629999.

8. Diogo R, Siomava N, Gitton Y. Development of human limb muscles based on whole-mount immunostaining and the links between ontogeny and evolution. Development. 2019; 146(20), doi: 10.1242/dev.180349, indexed in Pubmed: 31575609.

9. Fairbank SM, Corlett RJ. The role of the extensor digitorum communis muscle in lateral epicondylitis. J Hand Surg Br. 2002; 27(5): 405–409, doi: 10.1054/jhsb.2002.0761, indexed in Pubmed: 12367535.

10. Fontaine C, Wavreille G, Chantelot C, et al. [Surgical anatomy of the dorsal face of the hand and the wrist]. Chir Main. 2005; 24(2): 64–78, doi: 10.1016/j.main.2005.01.007, indexed in Pubmed: 15861975.

11. Gümüşalan Y, Kalaycioğlu A, Yazar F, et al. Accessory extensor carpi radialis muscle and interconnecting muscular bundle. Acta Anat (Basel). 1997; 159(1): 57–60, indexed in Pubmed: 9522898.

12. Iwanaga J, Singh V, Takeda S, et al. Acknowledging the use of human cadaveric tissues in research papers: Recommendations from anatomical journal editors. Clin Anat. 2021; 34(1): 2–4, doi: 10.1002/ca.23671, indexed in Pubmed: 32808702.

13. Kim J, Lee JH. An extensor digitorum muscle for index finger originated from the extensor carpi radialis brevis. Anat Biol Anthropol. 2020; 33(1): 31, doi: 10.11637/aba.2020.33.1.31.

14. Melo C, Coelho P, Bernardes A. [The anatomical variations of the extensor muscles of the hand fingers]. Acta Med Port. 2013; 26(3): 276–278, indexed in Pubmed: 23815845.

15. Nayak SR, Krishnamurthy A, Pai MM, et al. Multiple variations of the extensor tendons of the forearm. Rom J Morphol Embryol. 2008; 49(1): 97–100, indexed in Pubmed: 18273511.

16. Orellana-Donoso M, Valenzuela-Fuenzalida J, Gold-Semmler M, et al. Neural entrapments associated with musculoskeletal anatomical variations of the upper limb: Literature review. Transl Res Anat. 2021; 22: 100094, doi: 10.1016/j.tria.2020.100094.

17. Pichler W, Tesch NP, Clement H, et al. [The dorsal approach to the radiocarpal joint: an anatomic variant and its clinical implications]. Z Orthop Unfall. 2009; 147(3): 372–373, doi: 10.1055/s-0029-1185413, indexed in Pubmed: 19551592.

18. Ring D, Jupiter JB. Operative treatment of elbow stiffness. JBJS Essent Surg Tech. 2011; 1(3): e18, doi: 10.2106/JBJS.ST.K.00010, indexed in Pubmed: 31321123.

19. Shiraishi N, Matsumura G. Identification of two accessory muscle bundles with anomalous insertions in the flexor side of the right forearm. Okajimas Folia Anat Jpn. 2007; 84(1): 35–42, doi: 10.2535/ofaj.84.35, indexed in Pubmed: 17654842.

20. Simet S, Cassidy K. Dissection and analysis of a complex cadaveric hand dysmorphology. Transl Res Anat. 2021; 25: 100141, doi: 10.1016/j.tria.2021.100141.

21. Straus WL. The phylogeny of the human forearm extensors (Concluded). Human Biology. 1941; 13(2): 203–238.

22. Türker T, Gosey GM, Kempton DM. Surgical technique for harvesting ECRL and ECRB concurrently as upper extremity tendon autograft. Tech Hand Up Extrem Surg. 2020; 25(1): 41–44, doi: 10.1097/BTH.0000000000000294, indexed in Pubmed: 32384382.

23. Vaida MA, Gug C, Jianu AM, et al. Bilateral anatomical variations in the extensor compartment of forearm and hand. Surg Radiol Anat. 2021; 43(5): 697–702, doi: 10.1007/s00276-020-02584-7, indexed in Pubmed: 33001251.

24. West CT, Ricketts D, Brassett C. An anatomical study of additional radial wrist extensors including a unique extensor carpi radialis accessorius. Folia Morphol. 2017; 76(4): 742–747, doi: 10.5603/FM.a2017.0047, indexed in Pubmed: 28553852.

25. Yammine K. The prevalence of the extensor indicis tendon and its variants: a systematic review and meta-analysis. Surg Radiol Anat. 2015; 37(3): 247–254, doi: 10.1007/s00276-014-1352-0, indexed in Pubmed: 25096501.

26. Żytkowski A, Tubbs R, Iwanaga J, et al. Anatomical normality and variability: Historical perspective and methodological considerations. Transl Res Anat. 2021; 23: 100105, doi: 10.1016/j.tria.2020.100105.

REVIEW ARTICLES

ORIGINAL ARTICLES

←

*Cover picture: Anteroposterior diameter (depth) of the sacral hiatus at the level of its apex. For details see: E. Nastoulis et al., Folia Morphol 2023;
82, 3: 603–614.*